Dissertation zur Erlangung des Doktorgrades

der Fakultät für Chemie und Pharmazie

der Ludwig-Maximilians-Universität München

Integrated Hemithioindigo Based Molecular Motors – Transmission of Directional Motion and Potential Energy

Edgar Uhl

aus

Weilheim i.Ob.

2020

Erklärung

Diese Dissertation wurde im Sinne von § 7 der Promotionsordnung vom 28. November 2011 von Herrn Prof. Dr. Dube betreut.

Eidesstattliche Versicherung

Diese Dissertation wurde eigenständig und ohne unerlaubte Hilfe erarbeitet.

München, 2.12.2020

Edgar Uhl

Dissertation eingereicht am 2.12.2020

1. Gutachter: Prof. Dr. Henry Dube

2. Gutachter: Prof. Dr. Konstantin Karaghiosoff

Mündliche Prüfung am 21.1.2021

Danksagung

Saying Thank You and finding the right words to express gratitude and appreciation can be quite difficult. For this reason the following acknowledgements will be in german.

Ich möchte mich vorab ganz besonders bei Prof. Henry Dube bedanken. Danke für die freundliche Aufnahme und das entgegengebrachte Vertrauen, danke auch für die Freiheit eigene Ideen verwirklichen zu dürfen oder dabei zu scheitern. Vielen Dank auch dafür, dass ich in fachlichen Diskussionen stets offen meine Meinung beitragen durfte. Ich freue mich Teil der „Familie“ gewesen sein zu dürfen. Von der Freude über neuen Nachwuchs bis hin zum aktuellen Höhepunkt der Karriere, der Professur in Erlangen. Ich wünsche weiterhin Alles Gute und viel Erfolg.

Ich bedanke mich bei Prof. Karaghiosoff für lehrreiche Vorlesungen und die Übernahme der Zweitkorrektur.

Lieber *Manu,* danke, dass ich bei deinem Thema einsteigen durfte, es hat mir einen super Start verschafft. Ich hoffe wir bleiben auch weiterhin in Kontakt.

Danke *Manu*, *Moni*, *Sandra*, *Ludwig*, *Nicolai*, Esteban, *Aaron*, *Benni*, *Kerstin*, *Laura* und *Thomas* für die familiäre Atmosphäre die ihr geschaffen habt, welche diese Zeit so lebenswert gemacht hat. Danke auch für viele spannende Ausflüge und Aktivitäten die noch lange in Erinnerung bleiben werden. Danke auch an alle die Teil der *Bouldercrew* waren.

Ganz besonders bedanken möchte ich mich bei meinem Laborpartner *Chris* der sich unermüdlich um jedes noch so unscheinbare Gerät gekümmert und dieses am Laufen gehalten hat. Danke auch, dass du von Labor einrichten in der Freizeit bis hin zum Aufbau von IKEA-Möbeln über Autoprobleme und Boombox basteln Hilfsbereitschaft immer als selbstverständlich verstanden hast, ich weiß es sehr zu schätzen.

Danke *Aaron* für spannende Wanderungen („Oh Gott!“) und die Unterstützung bei zahlreichen fachlichen Fragen. Danke *Nitin*, *Thomas* und *Chris* für die wöchentliche Ablenkung vom grauen Alltag. Danke *Jasmin* für die mentale Unterstützung bei der Anfertigung dieser Arbeit.

Noch einmal bedanken möchte ich mich bei allen Korrektoren *Benni*, *Chris*, *Thomas*, *Moni* und *Manu*.

Abschließend noch ein außerordentliches Dankeschön an meine Familie. Das Wissen mich immer auf Eure Unterstützung verlassen zu können war eine gewaltige Stütze.

List of abbreviations

a	annum
Å	angstrom (10^{-10} m)
a.u.	arbitrary unit
Boc	tert-butoxycarbonyl
conc.	concentrated
°C	degree Celsius
cal	calorie
calc.	calculated
cis	double bond configuration
cw	clockwise
ccw	counterclockwise
d	doublet (NMR)
d	day(s)
δ	chemical shifts, delta scale (in ppm)
DIBAL-H	diisobutylaluminium hydride
DIPEA	N,N-diisopropylethylamine
DMAP	4-dimethylaminopyridine
DMF	*N*,*N*-dimethylformamide
DMSO	dimethyl sulfoxide
E	double bond configuration
ε	molar absorption coefficient
ECD	electronic circular dichroism
EI	electronic ionization
eq	equivalent(s)
ESI	electron spray ionization
EtOAc	ethyl acetate
EtOH	ethanol
h	hour(s)
HMBC	heteronuclear multiple bond correlation
HPLC	high performance liquid chromatography
HR	high resolution
HTI	hemithioindigo
Hz	hertz
i-Hex	isohexane
IR	infrared (spectroscopy)
J	coupling constant (NMR)
J	joule
K	kelvin
L	liter
M	helix configuration
m	meter
m	medium (IR)

m	multiplet (NMR)
M	molar
Me	methyl
MeOH	methanol
min	minute(s)
m.p.	melting point
MS	mass spectrometry
m/z	mass/charge ratio section)
$\tilde{\nu}$	wave number
NMR	nuclear magnetic resonance
NOESY	nuclear Overhauser effect spectroscopy
P	helix configuration
pss	photostationary state
q	quartet (NMR)
R	stereodescriptor
R_a	stereodescriptor (axial chirality)
S	stereodescriptor
S_a	stereodescriptor (axial chirality)
s	strong (IR)
s	second(s)
sep	septet (NMR)
s	singulet (NMR)
t	triplet (NMR)
TCNQ	tetracyanoquinodimethane
TEA	triethylamine
TFA	trifluoroacetic acid
THF	tetrahydrofuran
TICT	twisted intramolecular charge transfer
TLC	thin layer chromatography
trans	double bond configuration
UV	ultraviolet part of electromagnetic spectrum
Vis	visible part of the electromagnetic spectrum
vs	very strong (IR)
w	weak (IR)
Z	double bond configuration

Table of Contents

1 Summary

A macrocyclic system with integrated HTI based molecular motor, connecting rotor and stator, was realized with compound **81** (Figure A). Through action of the motor fragment thermal atropisomerization of the biaryl reporter is forced to proceed unidirectionally. A combination of X-ray crystallographic analysis, 2D NMR experiments, ECD spectroscopy and a comprehensive theoretical assessment revealed the stepwise directional motion of both, motor and biaryl unit, which are covalently connected by an ethylene glycol linker.

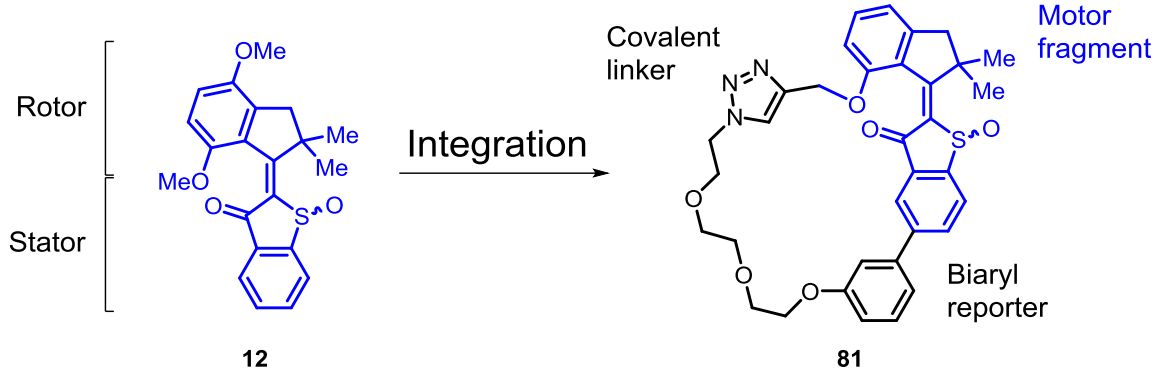

Figure A The original HTI based molecular motor **12** and the first integrated system **81**.

When rotation around the biaryl axis is impeded by increased steric demand as in **95** the motor fragment has to work actively to drive the biaryl rotation (Figure B). The amount of transmitted potential energy could be determined from the extent that energy degeneracy of the respective atropisomers is lifted. In addition, activation energies for the biaryl rotation are greatly decreased resulting in a rate acceleration of several orders of magnitude when compared to an untethered model system. Again, an in depth analysis of experimental and theoretical data gave unprecedented insight into the working mechanism of the motor fragment within the macrocycle. Additional experiments at variable temperatures were used to compare data at a unified temperature, which in turn was used to establish a quantitative energy scheme of the machines function.

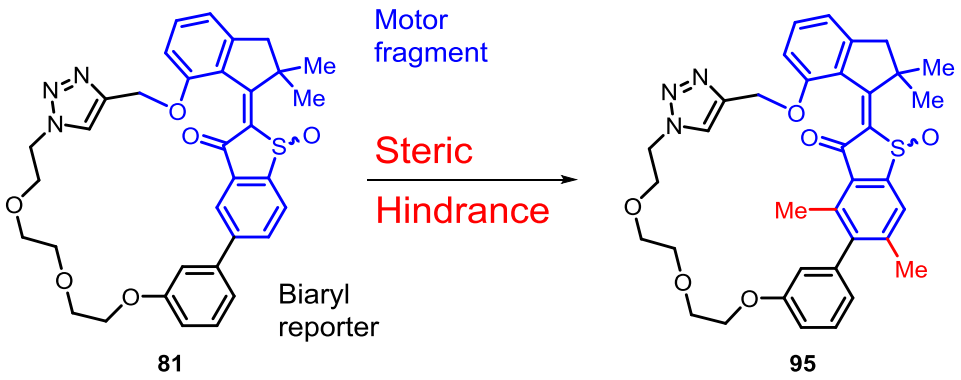

Figure B Increasing the steric demand around the biaryl axis in **81** resulted in system **95** that is now able to actively accelerate the biaryl rotation.

When the steric demand around the central double bond was reduced as in **110** a change of the rotation direction of the motor fragment was observed (Figure C, left). In this system the unidirectional motion is no longer dictated by the sulfoxide stereocenter in vicinity to the photoisomerizable double bond but instead by the absolute configuration of the fluorinated biaryl axis. Additionally, secondary effects such as hydrogen bonding become an important factor.

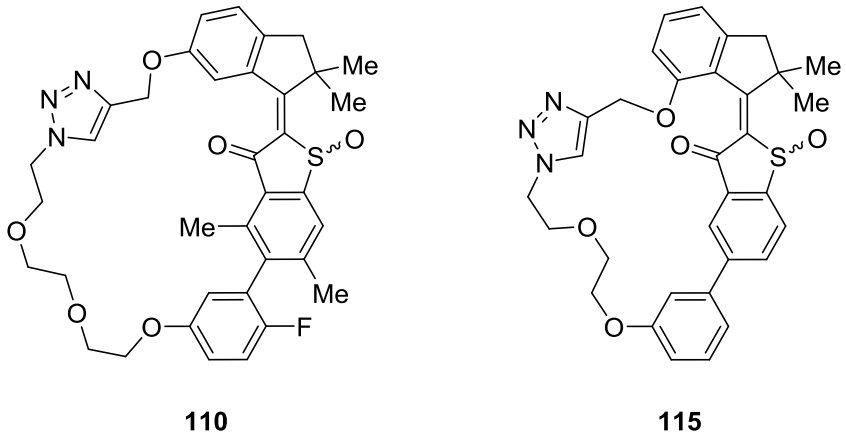

Figure C System **110** with an integrated "unsubstituted" HTI fragment (left) and integration of the motor fragment into a smaller macrocycle (**115**, right).

Integration of the motor fragment into the smaller macrocycle **115** drastically reduced the thermal stability of the *Z* configured isomer (Figure C, right). As a result isomerization processes at ambient temperatures were too fast to be observed with common spectroscopic methods. Attempts at low temperature irradiation experiments did not result in observable constructive photochemistry. This could be the result of missing population of vibronic states

that are necessary for excitation to the transition state. This issue will be clarified by ultrafast transient measurements in the near future.

Integration of the motor fragment into larger macrocycles potentially allows for the complexation of a variety of organic and inorganic cations (Figure D). A number of experiments indicate the potential complexation of guest molecules but no distinct binding site or complexation in a crown-ether type fashion could be deduced. Additional attempts to construct rotaxane- and catenane-type structures were unsuccessful so far but promising approaches are presented that offer direct routes to these complexes in a concise fashion. Still, suitable macrocyclic systems for the successful construction of sophisticated, mechanically locked systems need to be established and are currently worked on.

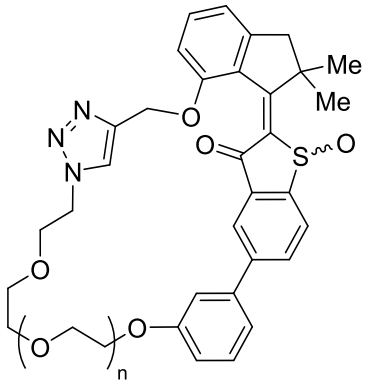

n = 4 **121**
n = 6 **149**

Figure D Larger macrocyclic systems **121** and **149** with integrated motor fragment were used to for complexation studies and the attempted construction of mechanically interlocked systems.

In a separate topic, that was worked on with *Manuel Güntner*, a recently established receptor is presented, that is based on an asymmetric bis-HTI core (Figure E). Upon irradiation the thermodynamically most stable and planar *Z*,*Z* isomer is selectively transformed into its helical *E*,*Z* isomeric form in 94% yield that can bind aromatic and electron deficient guest molecules through polar aromatic interactions. Upon heating the planar and non-binding *Z*,*Z* isomer is quantitatively restored. A series of potential guests was screened for their binding affinities which revealed **160** as a potential guest. A precise titration protocol was established to determine the binding constants and stoichiometries for *E*,*Z*-**158** ⊂ **160**. The reversibility of the photoinduced guest capture-and-release was demonstrated and repeated for a total of three cycles. Overall the presented system operates with high precision and provides a new basic type

of receptor that will be explored in future studies especially in the fields of enantioselective recognition.

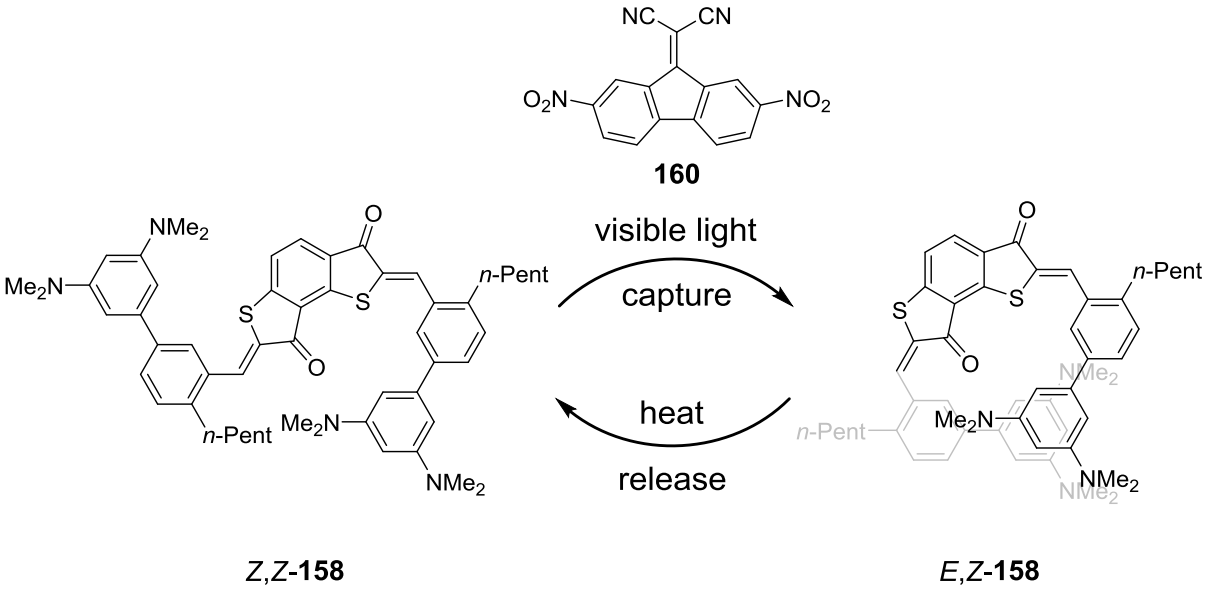

Figure E The bis-HTI based receptor **158** for the photocontrol of polar aromatic interactions. The planar *Z*,*Z*-**158** isomer is selectively transformed to its helical *E*,*Z*-**158** conformer upon irradiation with light. Heating is used to restore the initial conformation. The *E*,*Z*-**158** is able to selectively and reversibly bind electron-deficient aromatic guest molecules such as **160**.

Lastly, a photolabile protecting group from the 2-nitrobenzyl family was used to construct photocaged analogs of the proteasome inhibitor MG132 (Figure F). As the proteasome is responsible for the degradation of the majority of proteins in all eukaryotic cells investigated to date, it represents a highly attractive target for i.e. cancer treatment, induction of metaphase arrest and even apoptosis upon prolonged exposure of cells to the inhibitor. In a first approach, part of the MG132 core structure was substituted by a photolabile NVOC moiety (**163**, Figure F). The compound showed similar inhibitory potency compared to MG132, most likely because of the still active "war head" aldehyde functional group. Removal of the photocage was used to alter the structure and therefore binding properties of the compound but with neglectable modulation of its activity.

Having established the experimental setup and biological assessment in collaboration with the laboratory of *Esther Zanin* a second approach was attempted. A photocaging methodology that used the nitroveratryl moiety to protected small model molecules was successfully employed to mask the aldehyde function of MG132 as mixed acetal rendering it completely inactive *in vivo*. Upon exposure to 405 nm light effective release of MG132 from the caged compound was

demonstrated with overall highly comparable potency. A series of control experiments was conducted to link the observed inhibitory function directly to the release of MG132 and additional washout experiments showed the reversibility of the inhibition. With this a versatile photopharmacological tool was established for spatio-temporal control of proteasome inhibition that could attract great interest for future research in related fields.

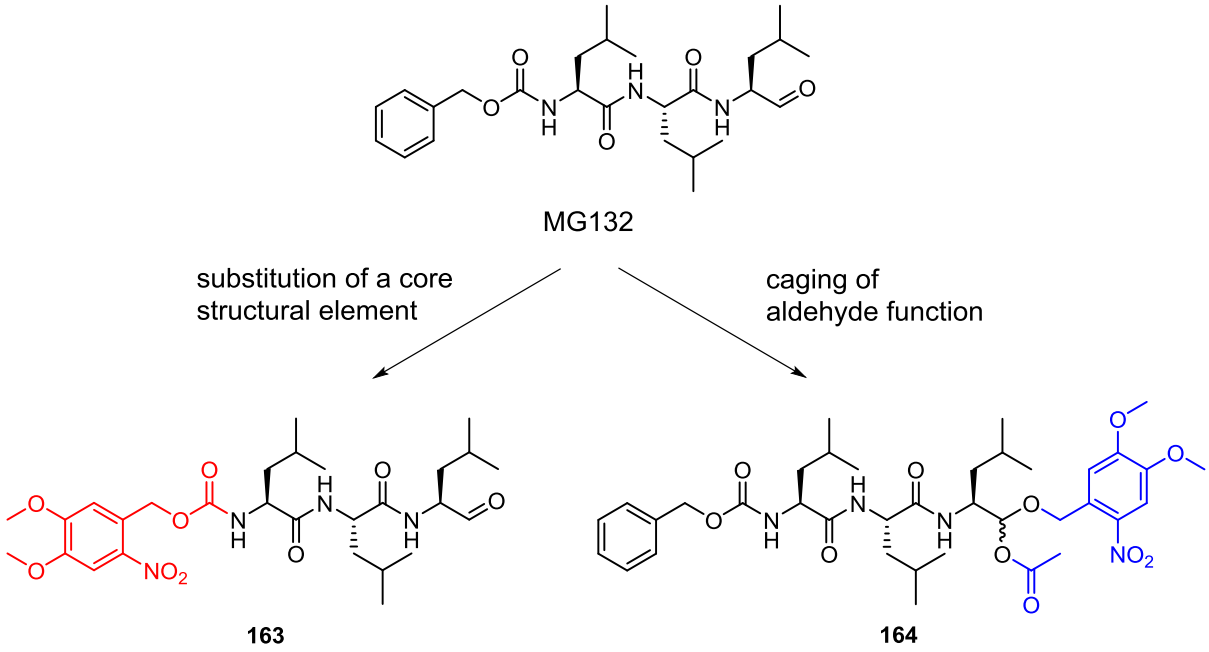

Figure F The established proteasome inhibitor MG132 and investigated analogs **163** and **164**. The photolabile 2-nitrobenzyl moieties (hightlighted in red or blue) are readily removed upon irradiation with 405 nm light to modulate the activity of the compounds.

2 Introduction

2.1 HTI as a photoswitch

Despite its early discovery in 1906 by Friedländer[1], it took over a century to fully unravel the immense potential of hemithioindigo (HTI) as a photoswitch. HTIs belong to the class of indigoid photoswitches that are derived from the parent indigo dye[2] (Figure 1a) and were first synthesized from benzothiophenone and benzaldehydes as mostly yellow colored compounds. HTIs are composed of a thioindigo and a stilbene fragment that are connected through a central double bond (Figure 1b). They are commonly obtained as a mixture of *cis* (*Z*) and *trans* (*E*) isomers that were not distinguished until *Mostoslavskii* et al. first reported on less stable HTI conformers that are generated by irradiation with UV light.

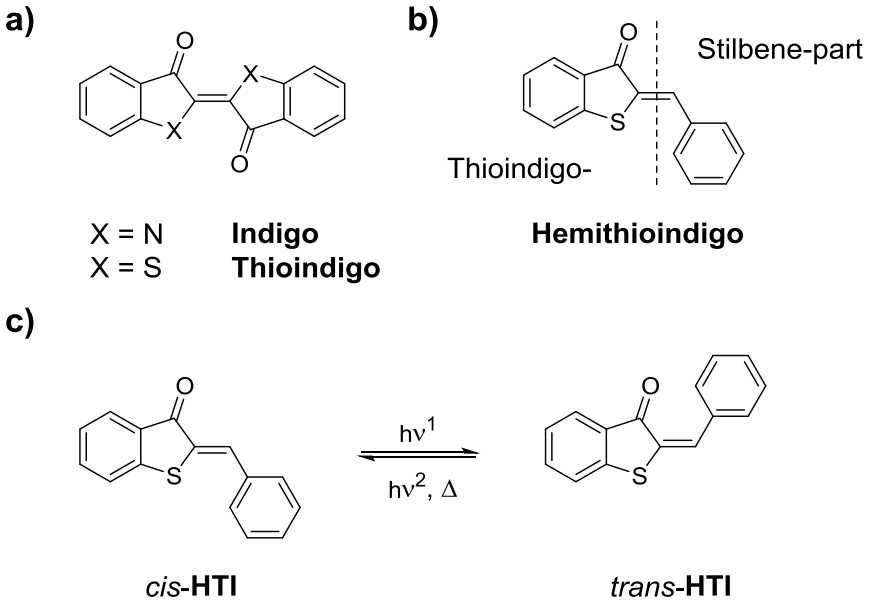

Figure 1 The (Thio)Indigo dye and the derived hemithioindigo (HTI) photoswitch. a) The parent compound indigo and the sulfur analog thioindigo. b) The hemithioindigo chromophore is composed of a thioindigo and stilbene fragment that are connected by a central double bond. c) Isomerization of the central double bond from *cis* to *trans* is commonly achieved by irradiation with ~400 nm light. Isomerisation of the thermally less stable *trans* isomer is achieved by heating or irradiation with wavelengths of ~500 nm.

The metastable products were identified as the *trans* isomers that show increased steric interactions due to carbonyl and aryl interactions and the photoisomerization reaction was reversed by heating, treatment with base or irradiation with light of different wavelengths. Studies by *Réamonn* and *O'Sullivan* unveiled that despite their different stabilities the isomer ratios obtained from condensation reactions of e.g. benzothiophenone and benzaldehyde are not

controlled by sterics of the products. Instead the outcome of the reaction is a result of *overlap control*[3] in the elimination step that favors transition states with unhindered electron delocalizing groups.[4] In depth studies on the photochromism showed that the *E* isomer can be generated in > 80% yield using a wavelength of around 400 nm. This makes HTIs highly interesting for applications in biochemistry related fields due to the non-damaging visible light that is required for their operation. The metastable *Z*-isomer shows a batochromic shift that lies in the range of $\Delta\lambda_{max}$ = 30 nm with λ_{max} = 450±15 nm and ε > 10 000 $L \cdot mol^{-1}cm^{-1}$ for the *E* and *Z* configured isomers. *E*/*Z*-photoisomerization can be achieved with wavelengths up to 500 nm giving the *Z*-isomer quantitatively in most reported cases.[5,6] HTIs also show high fatigue resistance and can be switched repeatedly from *E* to Z and *vice versa* for > 10^4 cycles with minor loss of material.[7] The photoisomerization process takes place in the ultrafast picosecond timescale with quantum yields of 20±5% for the *Z*/*E* isomerization (in CH_2Cl_2) and lower quantum yields for the *E*/*Z* isomerization for most HTIs due to an additional deexcitation pathway that leads back to the *E* isomer via internal conversion.[8] This fast and nonradiative loss channel is also responsible for the descreased fluorescence that is observed for the *E* isomer and can even turn HTIs into a one-way switch at very low temperatures in the gas phase.[9]

The thermal- and photoisomerization rate of HTIs can be tuned by substituents at different parts of the molecule with a strong relation to their *Hammett* constants.[10,11] An approximately linear increase in thermal isomerization barriers with increasing donor strength at the *para* stilbene position is observed. Electron withdrawing groups (EWG) at the thioindigo part increase photoisomerization rates as do electron donating groups (EDG) at the stilbene part and *vice versa*. While stilbene substitution affects the rate by both, inductive- and resonance-interactions, thioindigo substitution is limited to mostly inductive effects. A detailed investigation of the underlying reaction mechanism reveals a limit to the *Hammett* correlation.[8] Substitution with an electron donating group on the *para* position of the stilbene part enhances the donor-acceptor character around the central double bond and with increasingly stronger donating groups an enhanced photoisomerization rate is observed. This is explained by the presence of two excited states, S_1 and S_2 that are separated by a barrier (Figure 2). The S_1 state with a negative charge at the carbonyl and a positive charge at the sulfur atom are unaffected by substituents at the stilbene part. The strongly polarized S_2 with a positive charge at the stilbene fragment is stabilized by electron donating groups lowering its energy and thus the $S_1 \rightarrow S_2$ barrier for photoisomerization. The acceleration however is limited and an unexpected reverse trend is observed when the very strong donating groups NMe_2 and julolidine are used.

This is due to a change of the electronic character of the S_1 state where the positive charge at the sulfur is stabilized. As a result both S_1 and S_2 energies are lowered and the photoisomerization barrier is increased.

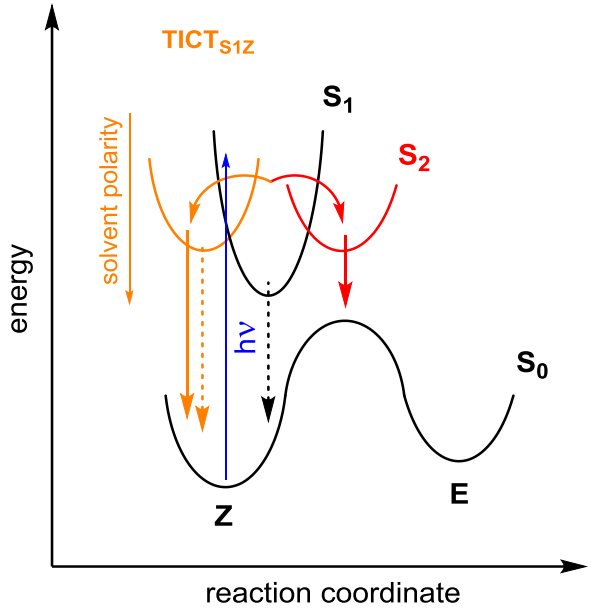

Figure 2 Pathways for the *Z*/*E* photoisomerization of HTI. S_2 energies are lowered by weak donating *para* substituents at the stilbene part, lowering $S_1 \rightarrow S_2$ photoisomerization barriers. Strong donors lower both S_1 and S_2 energies, again increasing the barrier. The TICT$_{S1Z}$ state is observed in pre-twisted, electron donor substituted HTIs and becomes a predominant reaction pathway in increasingly polar solvents.

A second light induced rotation pathway becomes available when a strong electron donor at the *para* position of the stilbene part is combined with pretwisting around the single bond by i.e. methyl groups at the *ortho* positions.[12] In polar solvents a twisted intramolecular charge transfer (TICT) state with a 90° torsion around the single bond is now populated. Deexcitation takes place without rotation of the adjacent double bond which allows to selectively address one of the two rotational axes depending on the choice of solvent. Time-resolved absorption spectra are invaluable tools to identify these excited states that are supported by additional characteristics such as occurrence of dual fluorescence and low isomerization quantum yields in highly polar solvents.[13] A related study by *Rueck-Braun* on *para*-N,N'-diarylamine HTIs found that increasing the push-pull strength of the donor-acceptor system of HTIs in general can result in favorable formation of intramolecular charge transfer (ICT) states.[14]

Groundbreaking new insights into light induced single-bond rotation (SBR) and coupled single-bond/double-bond isomerization (DBI) in the form of the Hula-Twist[15] (HT, Figure 3a) were

obtained from studies on HTIs.[16] A sterically strongly encumbered molecule was used to uncouple photoreactions from fast thermal conversion processes. Introduction of a chiral sulfoxide stereocenter established four different ground states that were characterized at ambient conditions by NMR spectroscopy and crystal structural X-ray analysis. By controlling the temperature and nature of the surrounding medium (polarity and viscosity) the elusive HT and SBR photoreactions were unambiguously proven to occur and yields of 82% and 99%, respectively were obtained depending on the applied conditions. Also, evidence is presented that SBR and HT are the more space-demanding motions compared to DBI, which is opposite to previous suggestions for retinal.[17,18]

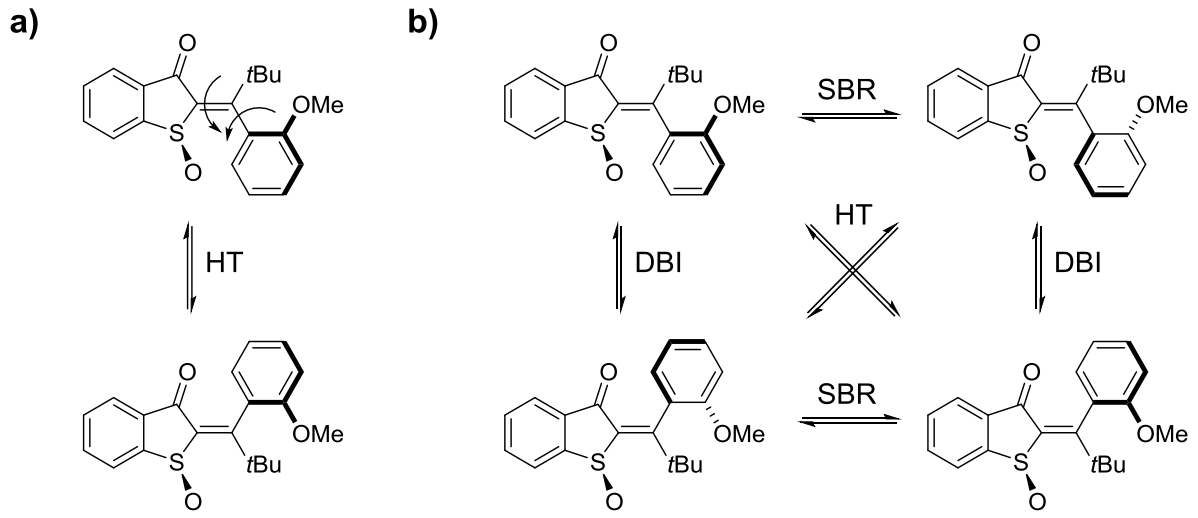

Figure 3 Photoisomerization mechanisms observed in a single HTI molecule. a) The Hula-Twist (HT) mechanism of the coupled motion of adjacent double and single bond rotation results in out of plane C-*t*Bu inversion. Other parts of the molecule are reoriented within the plane. b) Photoconversion products that prove the underlying single-bond rotation (SBR), double-bond isomerization (DBI) and HT processes (benzene-d_6, 405 nm light).

2.2 From switch to molecular rotary motor

In a non-chiral photoswitch light induced bond rotation in one direction is statistically counterbalanced by the opposite rotation as it occurs with identical probability. As a result the total work performed by such a molecule will be zero. Introduction of additional steps that break microscopic reversibility enable the transformation of energy into active, directional motion like their macroscopic counterparts. Such nanomachines that seem to (or do) defy the laws of thermodynamics like the Brownian Ratchet made famous by *Feynman* in the 1960s were

envisioned decades ago but it took until 1999 for the first experimental realization by *Kelly* that introduced a chemically powered ratcheting step within a molecular machine that resulted in a single unidirectional 120° rotation (Figure 4).[19] The setup **1** consists of a triptycene that is connected to a helicene via a single bond. In the first step isocyanate **2** is formed by addition of phosgene. From the ground state only clockwise rotation of the triptycene results in sufficient vicinity of the reactive groups and urethane formation, covalently trapping the molecule in a pretwisted, high-energy ground state **3**. Ambient thermal energy then drives the unidirectional rotation of the triptycene over the helicene, a step that was reported to be irreversible. The tether in **4** can then be cleaved to complete the 120° rotation. The system however could not undergo full and repetitive 360° rotation.

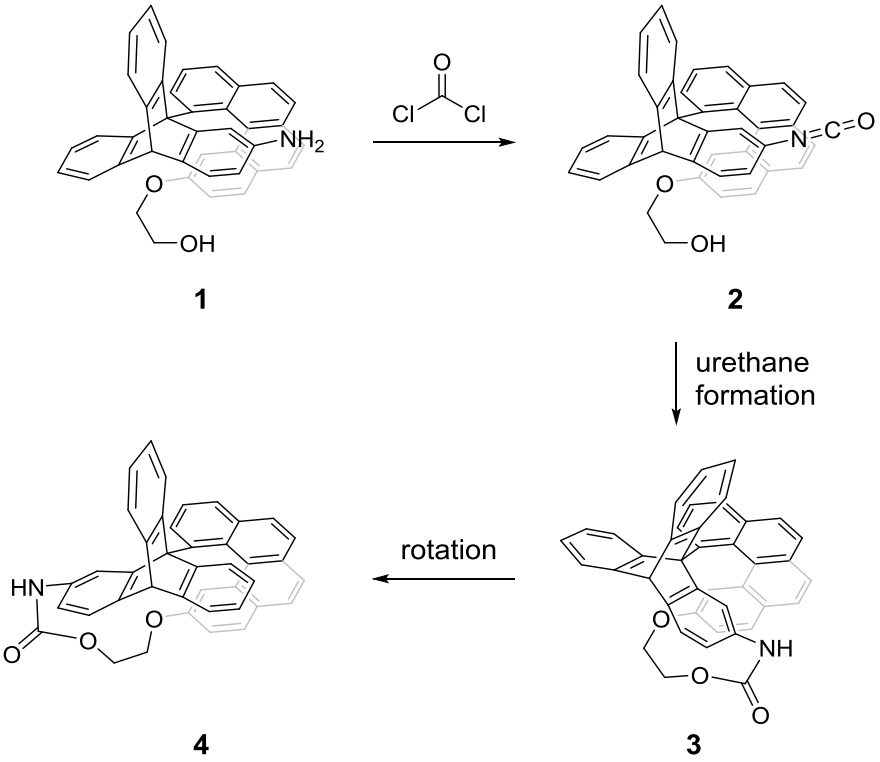

Figure 4 Chemically induced unidirectional 120° rotation by *Kelly*. The setup **1** consists of a triptycene that is covalently attached to a helicene. Isocyanate **2** is prepared by addition of phosgene. Urethane formation is enabled by spontaneous clockwise rotation of triptycene that traps the molecule in a high-energy conformation **3**. Ambient thermal energy then drives the unidirectional and irreversible 120° rotation to reach **4**.

Around the same time a light-driven molecular motor that achieved such a rotation was published by *Feringa* and coworkers.[20] The setup utilizes a central carbon-carbon double-bond that is sterically strongly encumbered (thus termed *overcrowded alkene*) forcing the two

connected molecular halves, arbitrarily termed *rotor* and *stator*, out of the plane (Figure 5). As a result the molecule adopts a helical shape (*P* or *M*) that is inverted upon photoisomerization of the central double bond. In this metastable form two terminal methyl groups are forced into an energetically unfavorable equatorial conformation. The strain is released in a thermal step where one half of the molecule flips over the other again inverting helicities. This thermal helix inversion (THI) constitutes the ratcheting step that breaks the reversibility of the motion and finishes the first 180° of the rotational cycle. A second photoisomerization step follows and the corresponding product then undergoes another THI at elevated temperatures finishing the full 360° cycle.

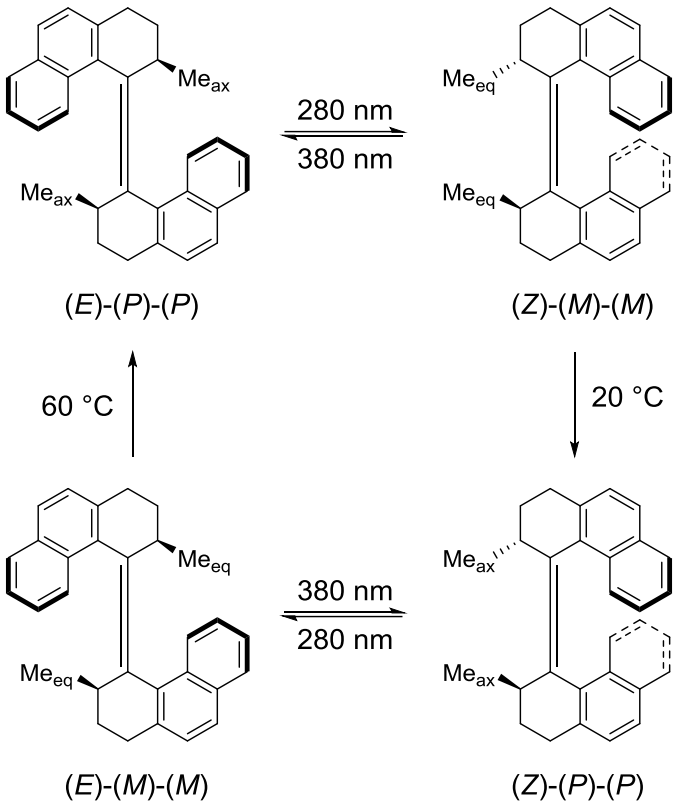

Figure 5 First generation light-driven molecular motor by *Feringa*. A central double bond connects two sterically demanding *rotor* and *stator* halves resulting in a helical (*E*)-(*P*)-(*P*) conformation. UV-light induced photoisomerization to (*Z*)-(*M*)-(*M*) inverses helicities, forcing two terminal methyl groups into an energetically unfavorable equatorial position. The strain is released in a thermal ratcheting step that flips one half of the molecule over the other. The resulting (*Z*)-(*P*)-(*P*) isomer again undergoes photoisomerization to (*E*)-(*M*)-(*M*). The unidirectional cycle is completed by a second ratcheting step at elevated temperatures giving the initial (*E*)-(*P*)-(*P*) conformer.

Drawbacks of the system are the different THI barriers that are encountered during rotation and temperatures above 60 °C required to operate the system. In the second generation of the motor

5 the "lower half" is replaced with a symmetric moiety (commonly termed the *stator* part) resulting in identical energies for the THI steps while maintaining the general working mechanism (Figure 6a).[21] The setup uses a single stereogenic center at the rotor part to induce a more uniform directional movement. This also facilitated the extensive search for motors with increased rotational speeds[22,23] which culminated in system **6** possessing half-lives of metastable ground state intermediates as low as $6x10^{-3}$ s at 20 °C.[24]

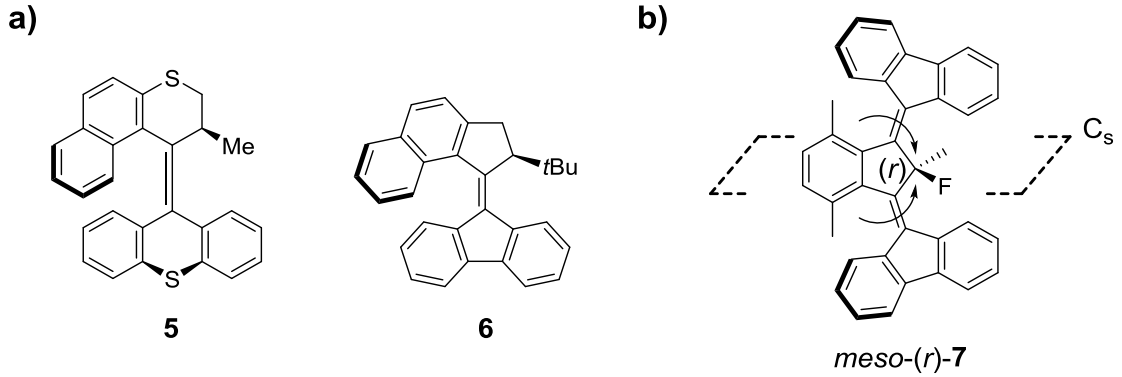

Figure 6 Second and third generation *overcrowded alkene* molecular motors. a) The original second generation molecular motor **5** (left) and a redesigned second generation motor **6** with very fast rotational speeds (right). b) Achiral third generation molecular motor **7** constructed by fusing two second generation motors with mirror plane C_s. A pseudo-asymmetric carbon atom establishes opposite helicities of the connected rotor fragments and unidirectional rotation around the double bonds. Both units move in the same direction with respect to their surroundings resulting in overall directional rotation.

An achiral third generation motor was constructed by fusing two second generation motors (Figure 6b).[25] The *meso* structure **7** features a central pseudo-asymmetric carbon atom that establishes opposite helicities (*P*,*M* or *M*,*P*) of the two rotor parts. The different size of substituents at the pseudo-asymmetric center stabilizes one of the two possible *meso* forms. Upon irradiation one double bond undergoes isomerization which is directly followed by THI. When observed from the mirror plane one fluorene unit rotates clockwise and the other anticlockwise. For the external observer these rotations are in the same forward direction, like wheels on an axle resulting in an intrinsic directional movement.

A fourth generation molecular motor that does not rely on intrinsic asymmetry achieves unidirectional rotation by non-covalent interaction with a chiral guest molecule.[26] The stiff-stilbene[27] receptor **8** features two (thio)urea binding sites that can strongly interact with phosphate ions through hydrogen bonding (Figure 7). The receptor exists in two configurations,

the planar *E*-**8** and helical (*P*,*M*)-*Z*-**8** that can be interconverted by light. The thermal *P*/*M* isomerization of *Z*-**8** encounters a very low thermal barrier and the two isomers interconvert rapidly at ambient temperatures. Irradiation of *E*-**8** generates both *Z* isomers with equal probabilities. Addition of a chiral phosphate salt (*S*)-**9** stabilizes one of the two helical forms and as a result *Z*/*E*-photoisomerization occurs predominantly from the stabilized isomer resulting in a net directionality of the double bond rotation.

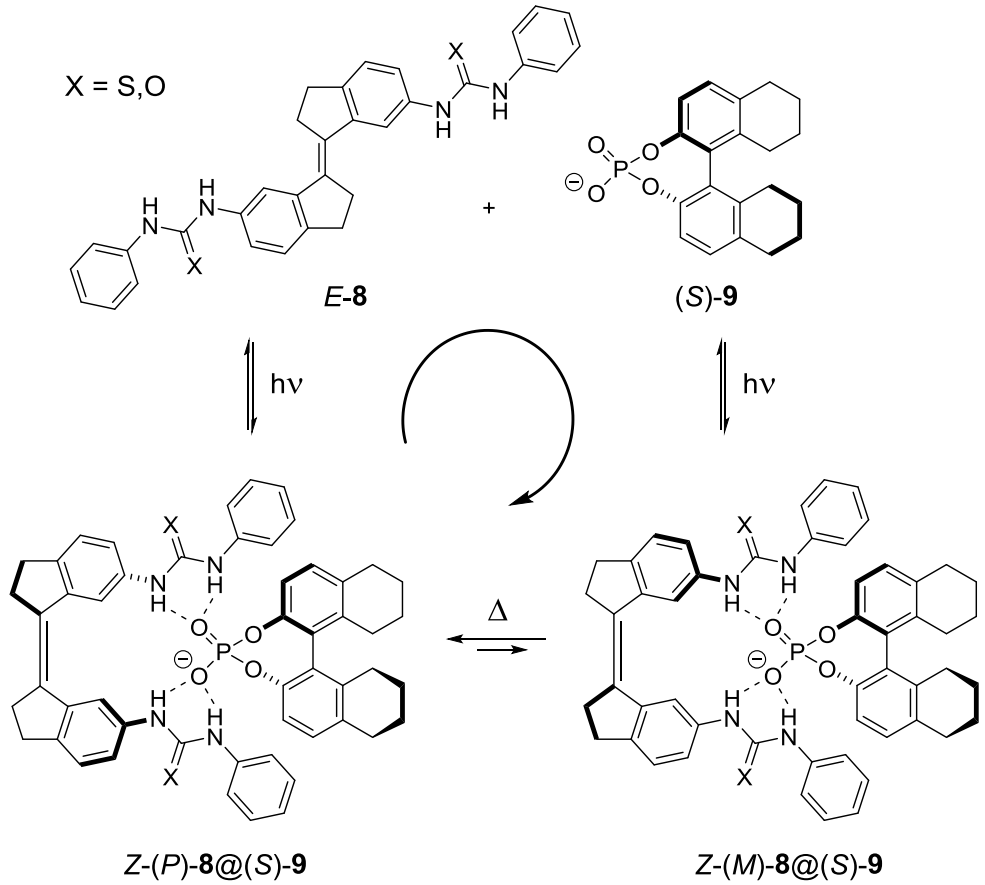

Figure 7 Fourth generation *overcrowded alkene* molecular motor. Bis-(thio)urea receptor **8** can be switched between planar, non-binding *E*-**8** and helical, binding (*P*,*M*)-*Z*-**8**. Interconversion between the two helical *Z* isomeric forms is rapid and one isomer becomes stabilized upon addition of a chiral phosphate salt **9**. *Z*/*E*-photoisomerization to *E*-**8** occurs preferentially via the stabilized isomer resulting in a net unidirectional rotation.

A different light-powered motor system based on imines was proposed by *Lehn* in 2006.[28] It was hypothesized that two different isomerization mechanisms, that is photochemical, out-of-plane double bond isomerization in combination with thermal, in-plane nitrogen inversion (NI) can be used to established unidirectional rotation (Figure 8). If the symmetry in such a thermally- and light-driven molecular switch is broken, one trajectory will be preferred over

the other and substituents at the imine carbon and nitrogen will undergo directional motions. To constitute a real motor however, the additional condition that at least one of the two steps – photoisomerization or thermal isomerization – is directional must be met. Therefore, a source of asymmetry needs to be introduced that prevents statistic 50/50 rotations in either step – clock and counterclockwise.

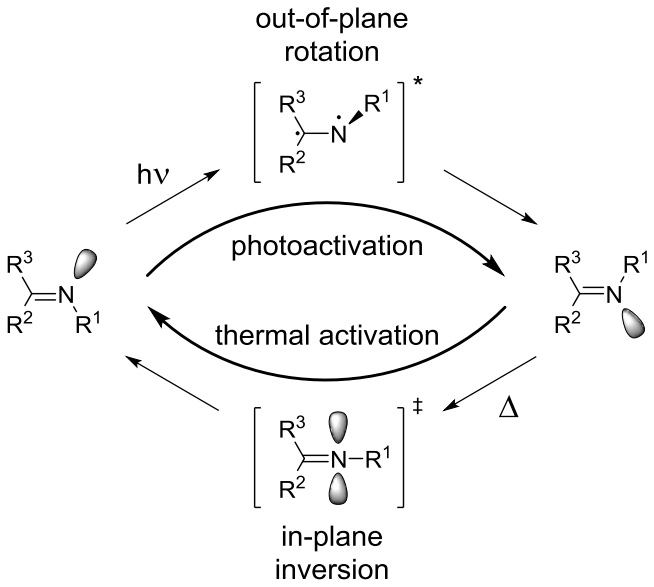

Figure 8 Proposed working mechanism of an imine based molecular motor by *Lehn*. Photoactivated double bond isomerization follows an out-of-plane trajectory. The second isomerization step proceeds by nitrogen in-plane inversion via a different geometry change therefore establishing overall unidirectional rotation.

An experimental realization of such two-step motor is depicted in Figure 9a.[29] An asymmetric cycloheptatriene stator is connected to a chiral amine via a central C-N double bond. Irradiation of (*M*)-(*Z*)-**10** gives (*P*)-(*E*)-**10** in an out-of-plane rotation. Thermal inversion at the nitrogen leads back to (*M*)-(*Z*)-**10** in a different symmetry rendering the system a molecular motor. The stator gains conformational flexibility when one of the benzene rings, fused to the tricyclic core is removed thus lowering the energy of cycloheptatriene ring inversion (RI) with only minor effects on the NI barrier. In (*M*)-(*E*/*Z*)-**11** (Figure 9b) RI is of significantly lower energy compared to NI and thus constitutes the preferred thermal relaxation pathway. As a result unidirectional four-step rotation with alternating photoactivated DBI and thermal RI is achieved that is very similar to the working mechanism of *overcrowded alkene* motors.

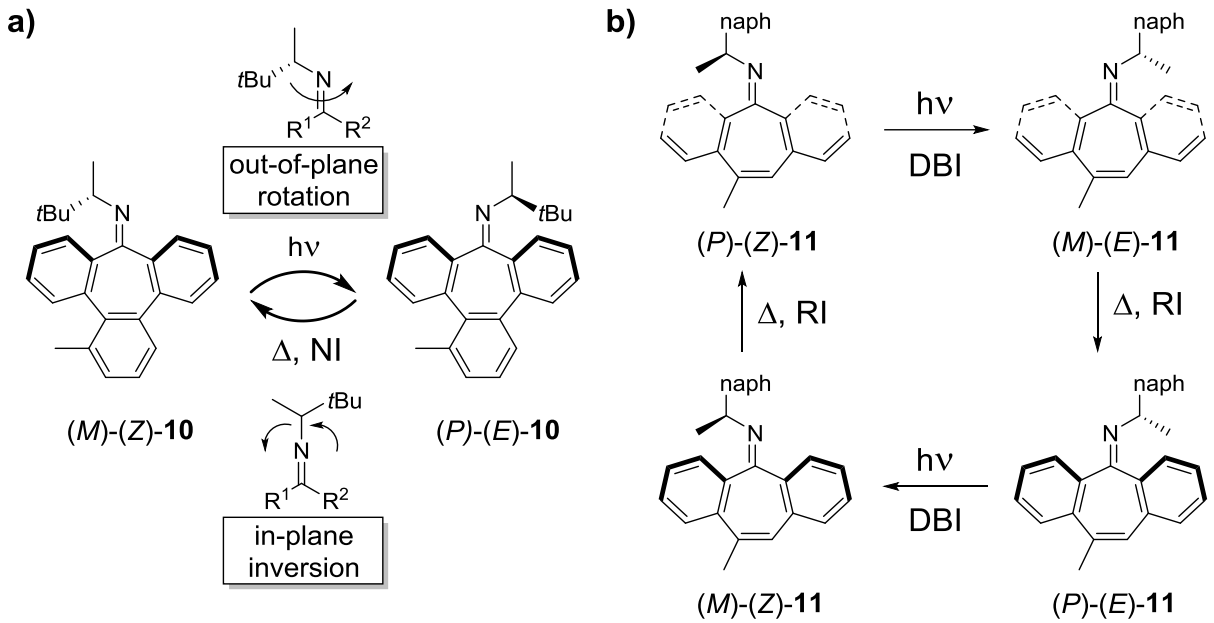

Figure 9 Two- and four-stroke imine-based molecular motors. a) Two-step molecular motor. Unidirectional rotation is established by photoactivation of (*M*)-(*Z*)-**10** and concomitant double bond isomerization to (*P*)-(*E*)-**10**. Thermal nitrogen inversion (NI) restores the initial conformer. b) Four-step molecular motor **11**. Ring inversion (RI) of the tricyclic core is the major thermal relaxation pathway due to the higher flexibility of the cycloheptatrien stator. The unidirectional rotation consists of alternating double bond isomerization (DBI) and ring inversion (RI) steps.

In 2015 a HTI-based molecular motor **12** was reported that presented the first example of visible light-driven motion with very fast rotation at ambient temperatures (Figure 10).[30] To achieve this the sulfur atom in HTI was oxidized to the sulfoxide, generating a chiral center in close proximity to the central double bond. Rotation around the single-bond is prevented by ring-fusion and a pronounced helical twisting is introduced by additional steric demand of the stilbene-fragment. A single enantiomer (*R* or *S* configured sulfoxide) can assume four diastereomeric forms that are interconverted by light induced DBI or (irreversible) THI in a working mechanism that is closely related to *overcrowded alkene* motors or four-stroke imine motors. The very fast THI of the system comes at the cost of metastable intermediates that can elude characterization by common spectroscopic methods (e.g. *Z*-(*S*)-(*M*)-**12** in Figure 10 with a very low THI barrier).

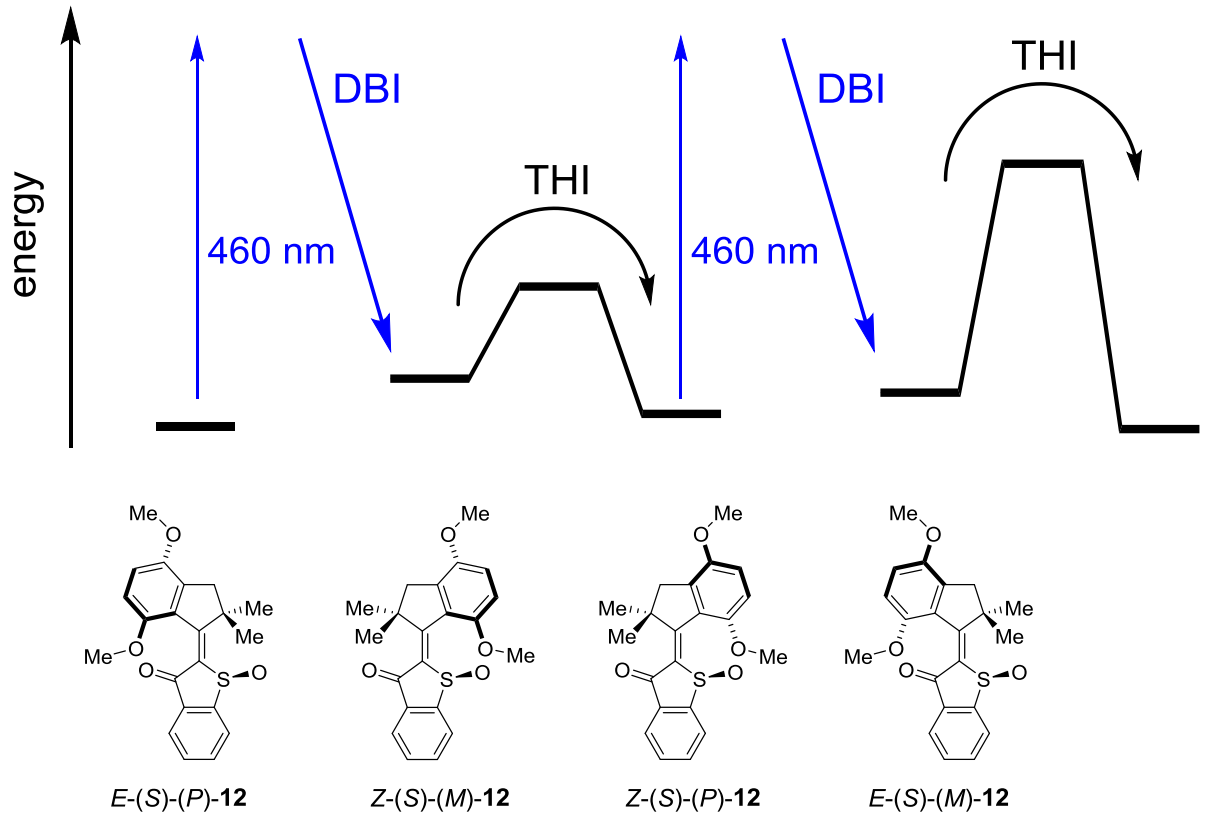

Figure 10 Qualitative energy profile for the four-step unidirectional rotation of HTI-based molecular motor **12**. Only isomers with *S* configured sulfoxide are shown. Irradiation of *E*-(*S*)-(*P*)-**12** generates the highly unstable *Z*-(*S*)-(*M*)-**12** via double-bond isomerization (DBI) that is followed by very fast thermal helix inversion (THI) to *Z*-(*S*)-(*P*)-**12**. DBI to metastable *E*-(*S*)-(*M*)-**12** and THI gives the initial isomer *E*-(*S*)-(*P*)-**12**.

A molecular setup that made all four steps accessible was realized by further increasing the steric demand of the stilbene-fragment. The isopropyl HTI derivative **13** encounters a THI barrier for the *Z*-(*S*)-(*M*)-**13** to *Z*-(*S*)-(*P*)-**13** conversion above 11 kcal·mol^{-1} (Figure 11a). The corresponding rotational speed is slowed to the point that observation by NMR spectroscopy at –105 °C becomes possible, thus revealing the full sequence of the stepwise rotation.[31]

On the other hand, reducing ground state barriers can be used to increase rotational speeds. A prospective ultrafast HTI motor was reported with maximum rotational speeds in the THz regime based on experimental evidence and theoretical calculations (Figure 11b).[32] In this system the aromatic ring of the stilbene-fragment is replaced by a heterocyclic pyridine. This reduces THI energy barriers to the point that an isomer corresponding to *Z*-(*S*)-(*M*)-**13** is not found as a stable minimum structure, reducing the working mechanism to only three steps.

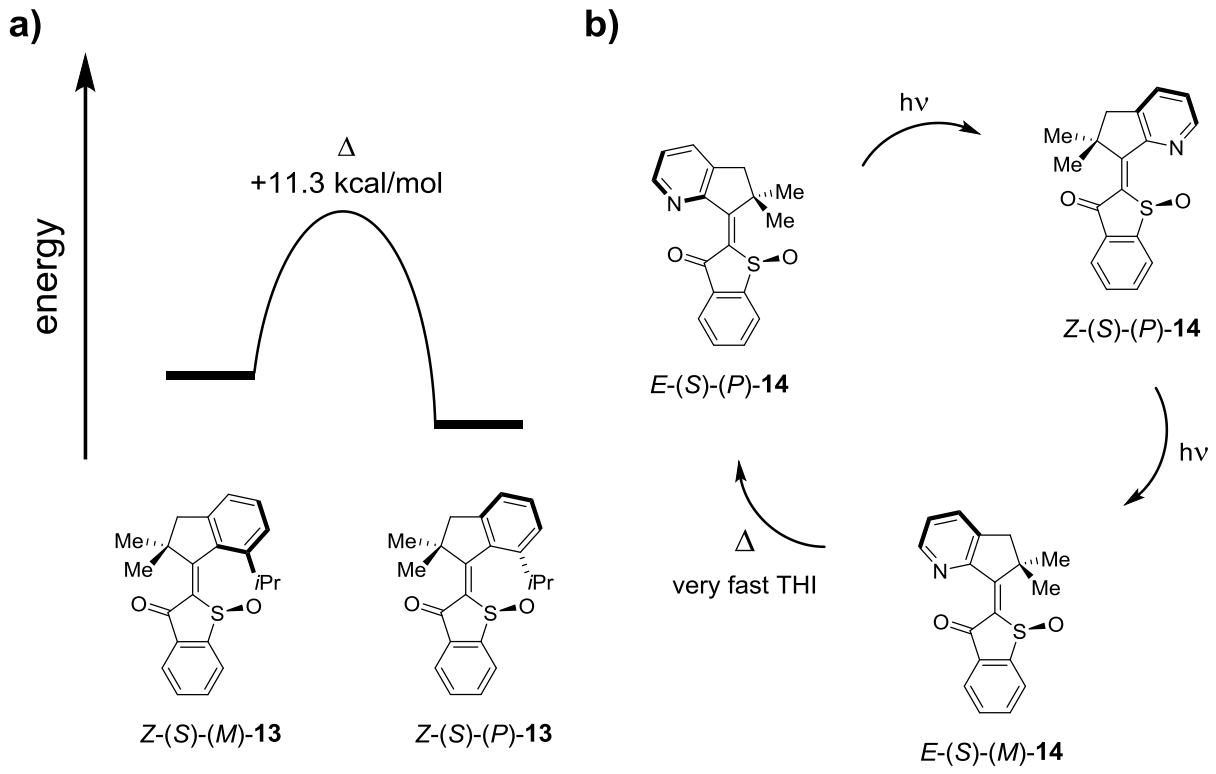

Figure 11 HTI analogs used to modulate rotational speeds. a) Increased steric hindrance at the stilbene-fragment in **13** allowed direct observation of the sequential, four-step motor sequence. b) Replacing the stilbene fragment with a pyridine moiety reduces ground state barriers. HTI **14** is a prospective three-step motor with ultrafast rotational speeds.

A photon-only driven motor system was established on basis of the different HTI photoreactions (see also Figure 3). HTI **15** can assume four diastereomeric forms that are stable at ambient temperatures and can be analyzed individually (Figure 12). Quantum yield measurements were used to determine the probability of SBR, DBI and HT photoreactions for each of the four isomers and the resulting photoisomerization sequences. To create a directional process at least three different reactions have to occur in sequence. Cycles that include more steps were omitted due to their negligible probability. At 20 °C HTI **15** follows two major unidirectional pathways **ABC** and **ABD** with a monodirectionality, that is the preference of one cycle, of 81%. At lower temperatures B→C transition is greatly enhanced compared to B→D resulting in 98% probability of the **ABC** sequence at increased motor speeds which is an unprecedented behavior to this point.

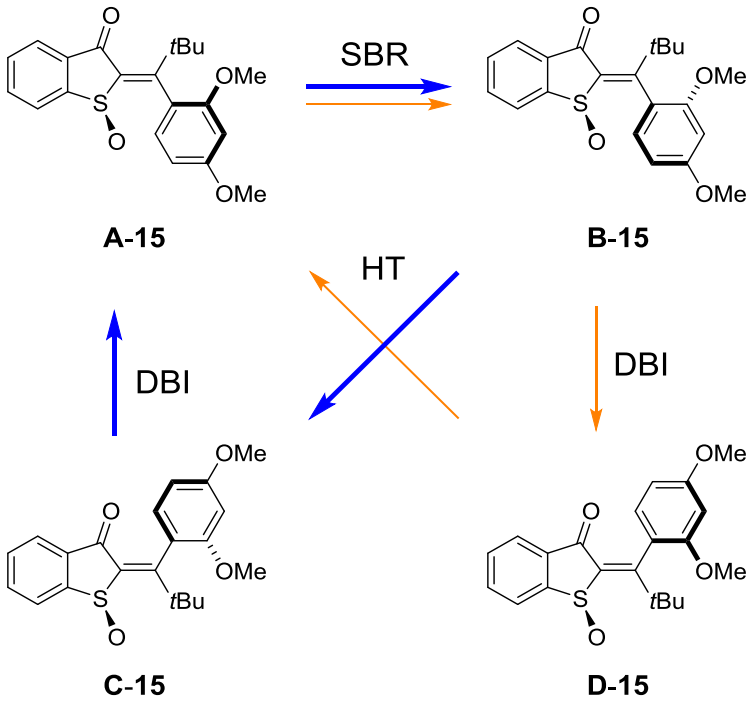

Figure 12 The two major monodirectional three-step sequences in photon-only molecular motor **15**. At 20 °C (442 nm light, CD_2Cl_2) the unidirectional **ABC** sequence occurs with 81% probability (indicated by blue arrows) followed by **ABD** with 16% probability (indicated by orange arrows). At –50% the quantum yield of **B→C** increases and the quantum yield of **B→D** decreases resulting in 98% monodirectionality for the **ABC** cycle.

As molecular motors only present the powering unit of potential future nanomachinery, the transmission of such light-generated directional motion to secondary units becomes increasingly relevant. An important step in this direction was achieved on the basis of a second generation *overcrowded alkene* motor **16** (Figure 13).[33] A naphthalene substituent at the rotor part is introduced that closely follows the unidirectional movement of the motor. Biaryl rotation (BR) around the connecting single bond is prevented by a high thermal barrier which is critical to distinguish between atropisomers and to follow the naphthalene movement in detail. During the 360° rotation of the motor one side of the naphthalene continuously faces the stator half of the motor. This locked synchronous motion consists of two parts, a sliding movement during DBI where the torsion around the single bond is adjusted from a synclinal to an anticlinal orientation, followed by THI where the naphthalene group rotates around the fluorene moiety. A methoxy "brake" is implemented to further increase the barrier for BR compared to THI which guarantees the locked movement. While the system represents a first example of repetitive motion coupled to a light-driven molecular motor it is still far from achieving active transmission of unidirectional motion to a remote and passive component.

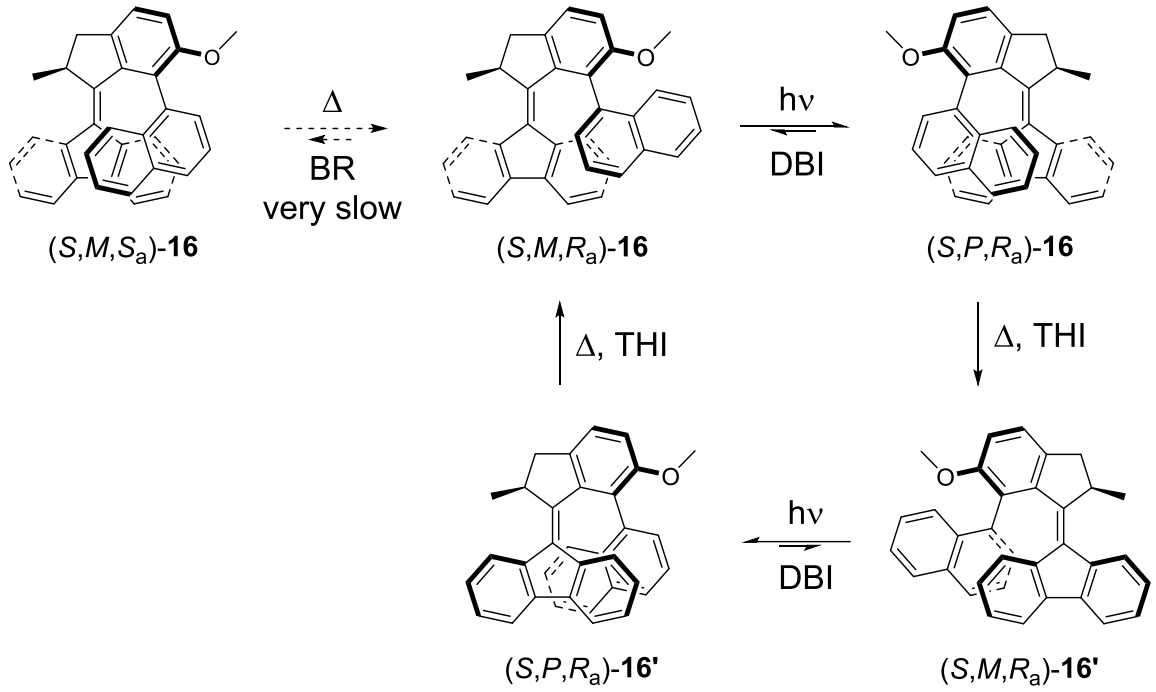

Figure 13 Coupled motion in a second generation *overcrowded alkene* motor **16**. Upon DBI the naphthalene moiety slides along the lower half of the motor. THI results in rotation around the fluorene. A methoxy "brake" at the indanyl part further increases the thermal barrier for biaryl rotation (BR) which becomes negligible. During 360° rotation the motor always faces the same side of the naphthyl resulting in a locked synchronous motion.

2.3 Chemistry of polyethylene glycol macrocycles

Crown-ethers

Since the presented work is in a great deal concerned with HTIs integrated into macrocycles, a brief overview of the basic chemistry with focus on polyethers and ion complexation will be given. Crown ethers are cyclic polyethers that are constructed from multiple ethylene oxide units and were discovered 1967 by *Pederson* (Figure 14).[34] Their trivial names are constructed from 1) the number of atoms forming the ring 2) the class name *crown* 3) the number of oxygen atoms in the ring. It must be noted that this methodology was introduced in order to avoid the complicated IUPAC nomenclature but names can be ambiguous in some cases (see i.e. Figure 14e) and clear assignment to the respective structures is recommended. Crown-ether rings are of variable size and common functionalizations include incorporation of aromatic moieties, nitrogen or sulfur substitution or longer alkyl chains (Figure 14).

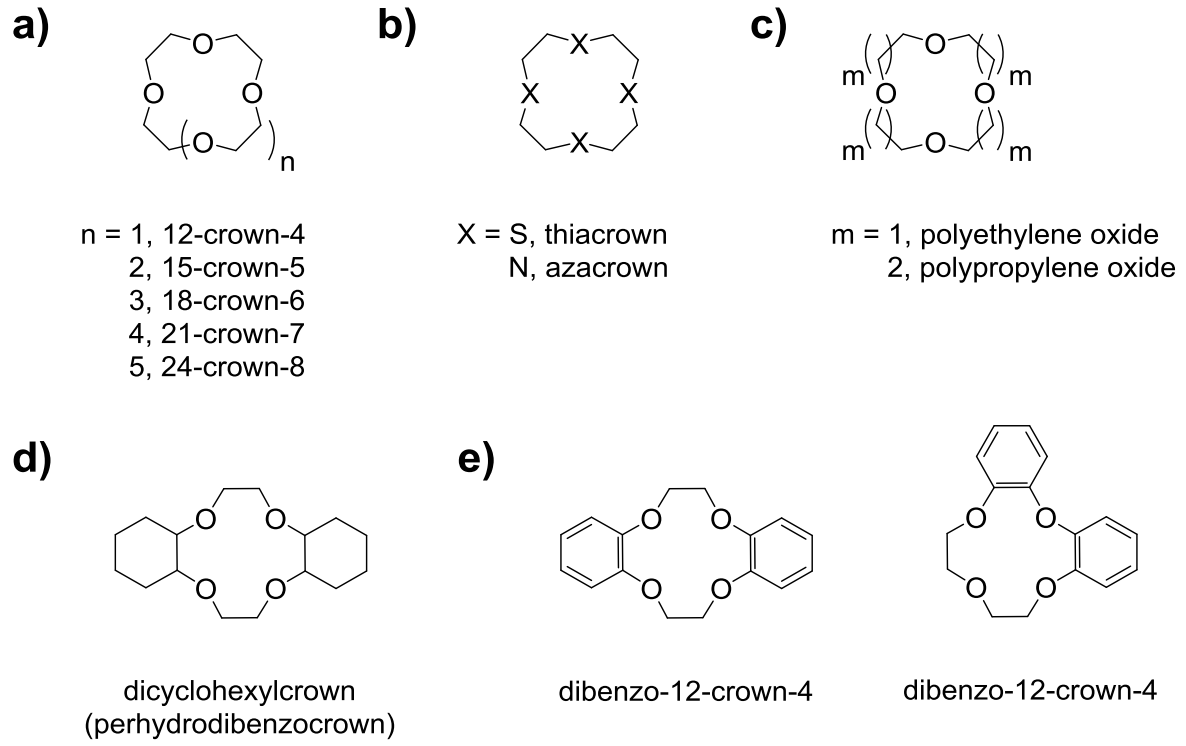

Figure 14 Selection of crown-ethers and crown-ether analogs with their nomenclature. a) Different ring sizes. b) Substitution of oxygen by sulfur or nitrogen. c) Different alkyl chain lengths. d) Substitution of alkyl units. e) Ambiguity of the non-IUPAC nomenclature.

Crown ethers are naturally colorless and occur as viscous liquids or solids with low melting points. They are neutral molecules and form stable complexes with alkali- and alkaline earth metals as well as a variety of heavy metals.[34] In many cases addition of polyethers results in solubilization of otherwise hardly solubable inorganic salts. Small amounts of methanol or analog compounds can increase solubility significantly through completion of the solvent sphere or solvation of the anion. Complexes with 1:4 up to 2:1 polyether:cation stoichiometries are formed by ion-dipole interactions between the cation and the negatively charged oxygen atoms of the ring.[35] The stability of the complexes is primarily determined by how well the cations fit into the polyether resulting in pronounced ion selectivity.[36] Values given in Table 1 for example suggest that 18-crown-6 has higher selectivity for K^+ compared to Na^+. Complex stability increases with the number of oxygen atoms, given a coplanar geometry and even distribution of oxygen atoms in the ring. The oxygen atoms are considered coplanar if they lie in the same plane and the apex of the C-O-C angles is directed towards the center. A coplanar configuration is not possible when the number of oxygens exceeds 6. Polyethers then arrange themselves around the surface of a cylinder with C-O-C angles pointing towards the center.

Table 1 Selected polyether ring sizes and ionic diamaters.

Polyether	Hole Diameter (Å)	Ion	Ionic dameter crystal (Å)
14-crown-4	1.2[a] – 1.5[b]	Li^+	1.36
15-crown-5	1.7 – 2.2	Na^+	1.94
18-crown-6	2.6 – 3.2	K^+	2.66
21-crown-7	3.4 – 4.3	NH_4^+	2.86
		Cs^+	3.34

[a] According to *Corey-Pauling-Coltun*. [b] According to *Fisher-Hirschfelder-Taylor*.

The best fit of cations is illustrated by the binding constants of the complexes that are formed. They are defined as the equilibrium constants K (in $L \cdot mol^{-1}$) for the complexation reactions ((equation **1** and (equation 2)

$$P + M^+ \overset{K_1}{\rightleftharpoons} PM^+ \qquad \text{(equation 1)}$$

$$PM^+ + P \overset{K_2}{\rightleftharpoons} P_2M^+ \qquad \text{(equation 2)}$$

where P is the polyether and M^+ the cation. The stability constant K_1 describes the formation of complex PM^+ with a 1:1 stoichiometry and K_2 formation of the complex with 2:1 stoichiometry where the cation is sandwiched between two rings. K_1 values of cyclohexyl-18-crown-6 in water for example pass through a maximum for K^+ with increasing cation size (Table 2).[37]

Table 2 Stability constants in water and methanol (25 °C).

		$\log_{10}(K_1)$				
Polyether	**solvent**	Li^+	Na^+	K^+	NH_4^+	Cs^+
Cyclohexyl-18-crown-6	water	< 0.7	0.8	1.9	1.1	0.8
	methanol	–	4.1	5.9	–	4.3

This can be explained by the competition of hydration versus complexation where the polyether has to compete with coordinated water to fit the cation into the ring. The polyether cannot

compete well with small and highly charged cations and strip them off their hydration sphere. Larger cations with comparably low charge density on the other hand have a low affinity for both polyether and water. Cs^+ is too large to fit into the whole of the polyether ring prohibiting complexation with coplanar geometry. When compared with stability constants in methanol (Table 2) the respective K_1 values are three to four orders of magnitude larger. This is due to the weaker solvation of methanol that competes less with the polyether for cations.

Crown ethers can also be interpreted as "two dimensional" ligands that leave part of the cations coordination sphere exposed to other interactions.[38] As a result crown ether complexes occur in many variation of the classical ring-fit approach. In the anhydrous complex [K(18-crown-6)]NO_3 for example the potassium cations resides above the plane of the polyether ligand exposing more of the surface to the nitrate anion that is coordinated in a bidentate fashion (Figure 15a). As a result the cation is pulled out of the cavity adopting a "domed" position with ca. 0.2 Å longer K-O distances compared to the intra-cavity structure.[38]

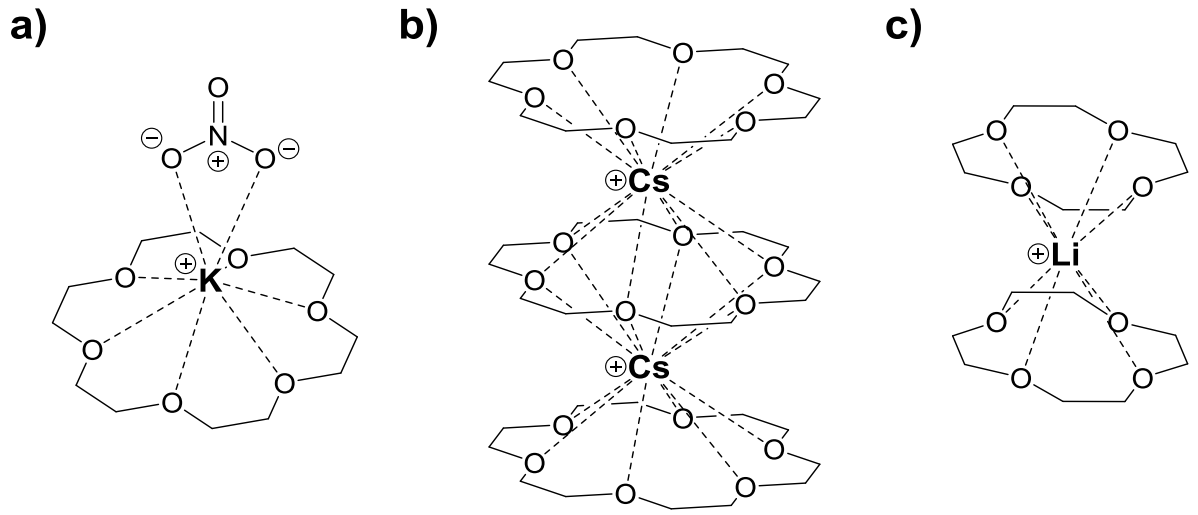

Figure 15 Schematic illustration of complexes that deviate from classical ring-fit geometries. a) [K(18-crown-6)]NO_3. b) $[Li(12\text{-crown-}4)_2]^+$ c) $[Cs_2(18\text{-crown-}6)_3]^{2+}$

As mentioned earlier polyether cation ratios can deviate from classical 1:1 stoichiometries. When cations such as Cs^+ are too large to fit into the polyether rings sandwich complexes with 2:1 or 3:2 stoichiometries can be formed as in the α-cyanobenzothiazole-α-carbaldehyde oximate complex of $[Cs_2(18\text{-crown-}6)_3]^{2+}$ (Figure 15b).[39] Similar complexes with higher polyether to cation ratio can be found when ions such as Li^+ are too small to fit even into the smallest rings. An example is the sandwich-type $[Li(12\text{-crown-}4)_2][PPh_2]$ complex with 2:1 stoichemetry (Figure 15c).[40] Complexes with higher cation to polyether ratios are found for 18-

crown-6 and Li^+ for example. In the lithium phenoxide complex two cations are encapsulated by the ring in a coplanar fashion resulting in a 1:2 stoichiometry (Figure 16a).[41] A different geometry is adopted with the BH_4^- anion.[42] Here two lithium ions are complexed by one distorted 18-crown-6 ring which is stabilized by additional BH–Li hydrogen bonds. These given examples represent only a small fraction of crown-ether complexes that have been found to date and serve to highlight the vast number of structures that can be obtained.

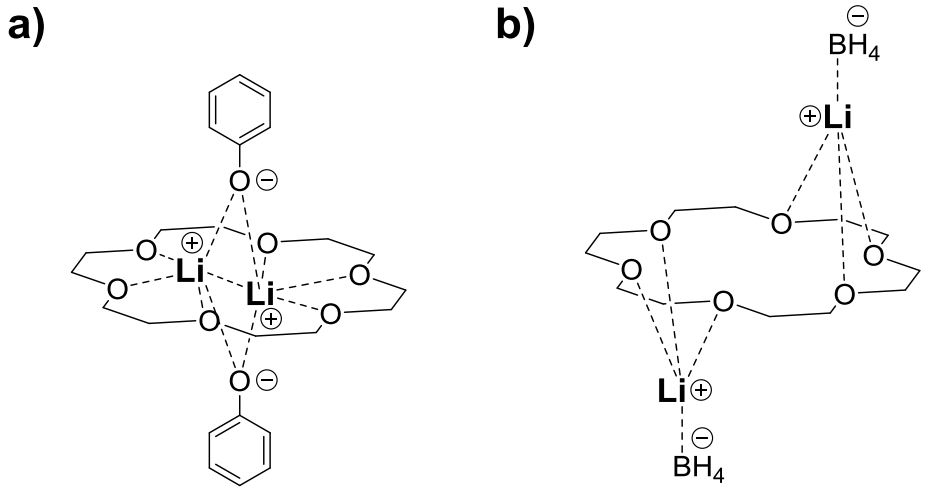

Figure 16 Schematic illustration of complexes with lower polyether to cation ratios. a) Phenoxide complex of Li_2(18-crown-6) b) [Li_2(18-crown-6)][BH_4]$_2$.

Cryptands and podands

Even more structural variation arises from cryptands and podands as complexing ligands. Cryptands are a class of macrobicyclic ligands that were mentioned as early as 1969 by *Lehn*.[43] They are constructed by capping the crown-ether cavity with an additional polyether chain that is attached to nitrogen atoms at the polyether ring. Cryptands form highly selective inclusion complexes that follow the *size selectivity* argument where the cation is contained in the eponymous *crypt*.[44] The cryptand complexes (*cryptates*) are often orders of magnitude more stable than their natural or synthetic macrocyclic counterparts. The [K⊂[2.2.2]cryptand]$^+$ complex for example is 10^5 times more stable than its monocyclic analog (Figure 17a). This cryptate effect can even exceed the macrocyclic effect where ring fusion of an open chain polyether leads to the discussed, stable crown-ether complexes (Figure 17b). The well-defined size of the intramolecular cavity comes with an extraordinary cation selectivity. Smaller size [2.1.1], [2.2.1] and [2.2.2] cryptands preferentially form complexes with the alkali cations Li^+,

Na^+ and K^+ with peak selectivities for a certain cation.[45] The larger [3.2.2], [3.3.2] and [3.3.3] cryptands show increasing selectivity towards the larger cations with plateauing stability for the K^+, Rb^+ or Cs^+ complexes due to their larger and more flexible cavities.

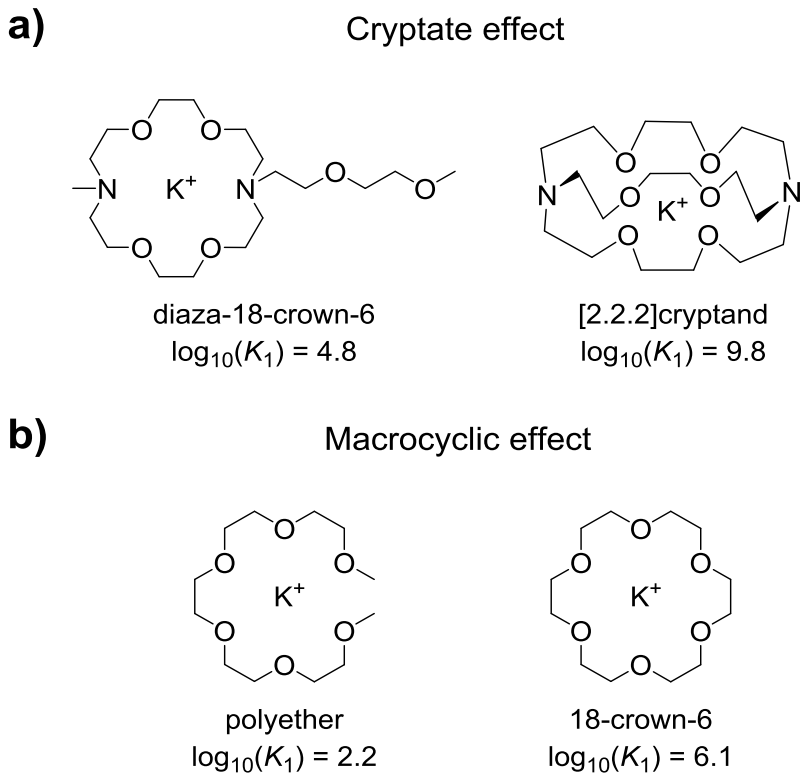

Figure 17 Effect of ring numbers of the polyether ligand on stability constants. a) The cryptate effect leads to a 10^5 more stable complex (methanol:water = 95:5). b) Ring-fusion of a polyether to the respective 18-crown-6 results in a 10^4 more stable complex due to the macrocyclic effect (methanol).

Another manifestation of the cryptate effect is the reversed selectivity for earth-alkali cations over alkali cations compared to some macrocyclic ligands.[46] [2.2.2]Cryptand complexes with cations of similar size, e.g. Ba^{2+}/K^+ reveal a ratio of their binding constants of 10^3-10^4 in favor of barium (Figure 18). The C_8-bridged, tricyclic [2.2.C_8]cryptand on the other hand reveals a Ba^{2+}/K^+ affinity ratio in the range of 10^{-2}. The cation ratios of monocyclic diaza-18-crown-6 are again in the same range as [2.2.2]cryptand. Since the macrocycle leaves part of the coordination sphere open solvation of the cation can be completed by solvent molecules. On the other hand [2.2.C_8]cryptand lacks two oxygen binding sites and access of solvent to the cation is effectively shielded resulting in a drastically lower stability of the Ba^{2+} complex.

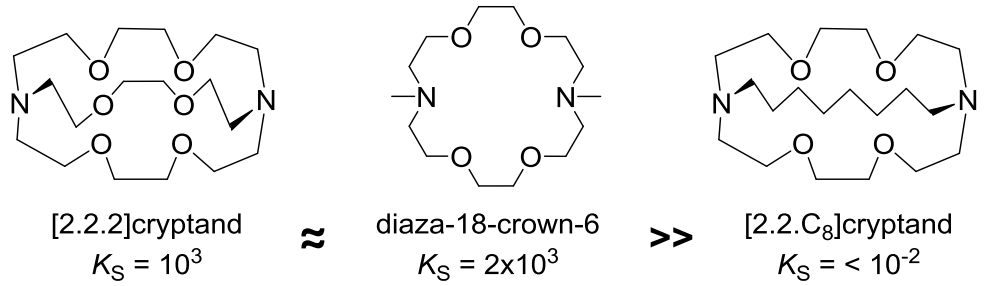

Figure 18 Selectivity of cryptands for earth-alkali metal cations over alkali metal cations on the basis of the cryptate effect.

Another aspect of complexation that has been omitted to this point is preorganization of the ligands. In its uncomplexed state 18-crown-6 reveals randomly arranged binding sites.[47] The free energy cost of arranging the macrocycle into its binding conformation has to be paid during complexation. This energy is drastically raised for open-ring ethers or *podands* as **18** (Figure 19). They come in a large variety of conformations focused on maximizing their entropy. The energy for spherand **17** for example that is necessary to assume its binding conformation and desolvate its oxygens has already been paid during synthesis, which delivers a structure with a single, ideal conformation for binding Li^+ and Na^+. As a result free energies differ by up to 17 kcal·mol^{-1} and a corresponding difference in K_1 of > 10^{12} for the complexation of these cations. The same principle applies to cryptands compared to crown-ethers as they are more rigid and well preorganized due to their additionally bridged nitrogen atoms, which is manifested in the remarkable property of cryptands to decomplex crown-ethers.

One way of increasing stability of crown-ether complexes is through the introduction of additional side-chains that can interact with the bound cation or add additional functionality. These *lariat ethers* (Figure 19) are yet another group of polyethers, which demonstrates that compounds containing multiple polyethylene oxide units cannot always be allocated to a distinct class of structures in straightforward manner.[48,49]

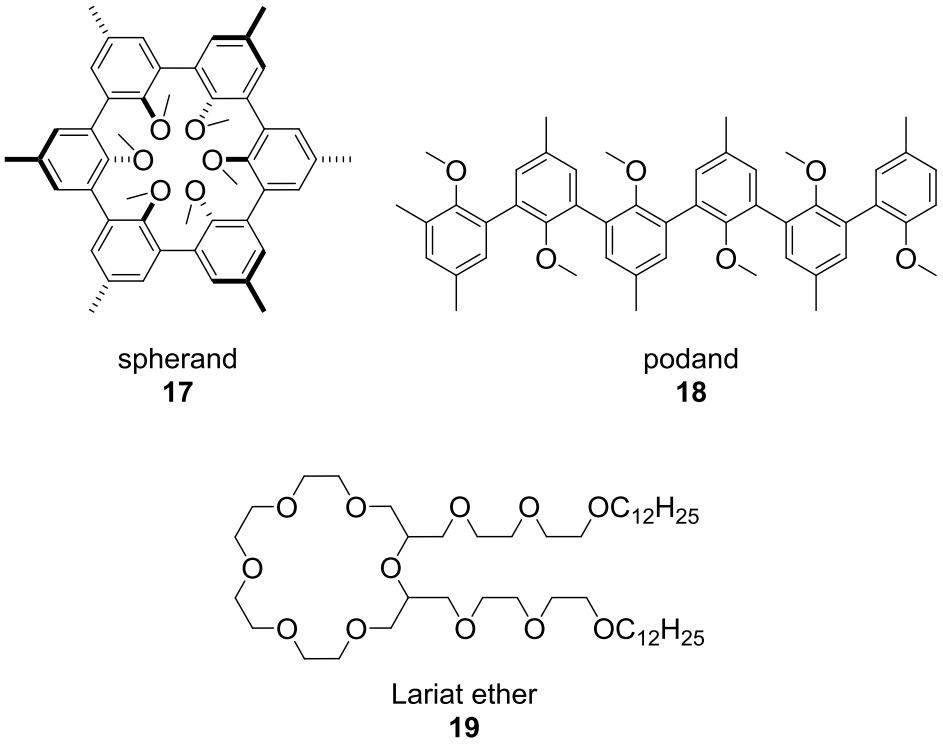

Figure 19 Preorganization in spherand **17** results in drastically more stable Li^+ and Na^+ complexes compared to podand **18**. Lariat ethers are crown ethers with additional functional sidearms such as **19** which is used for the formation of bilayer membranes.

2.4 Rotaxanes and catenanes

The idea of mechanically interlocking cyclic molecules is commonly attributed to *Willstätter* who discussed the new type of structures in the early 20th century[50,51] and the first successful synthesis was achieved half a decade later by *Wasserman* in 1960.[52] The architecture of two macrocycles connected through a "mechanical bond" that cannot be separated without breaking a covalent bond was termed *catenane* (**20**, Figure 20, left). In the first synthesis a cyclic C_{34} hydrocarbon was prepared and the reaction was then repeated in the presence of the macrocyclic product. From this small fractions of the mechanically interlocked complex could be isolated terming the new architecture a *topological isomer*, which also applies to the isomerism between i.e. knotted and unknotted loops or Möbius strips. In 1961 *Frisch* et al. suggested that a complex like **21** might be of similar stability as **20** when dethreading of the macrocycle is prevented by large enough end groups (Figure 20, right).[50] A first synthesis that was also based on statistical probability like the preparation of the first catenane was achieved in 1967 by *Harrison*.[53] The idea was that when an alkyl chain is reacted with bulky stopper groups in the presence of a

macrocycle small amounts of complex such as **21** would be formed. After 70 treatments of a resin bound macrocycle small amounts (6%) of the stable complex were obtained that was readily purified by column chromatography. This type of structure where a macrocycle is threaded on dumbbell shaped chain was later termed *rotaxanes*.

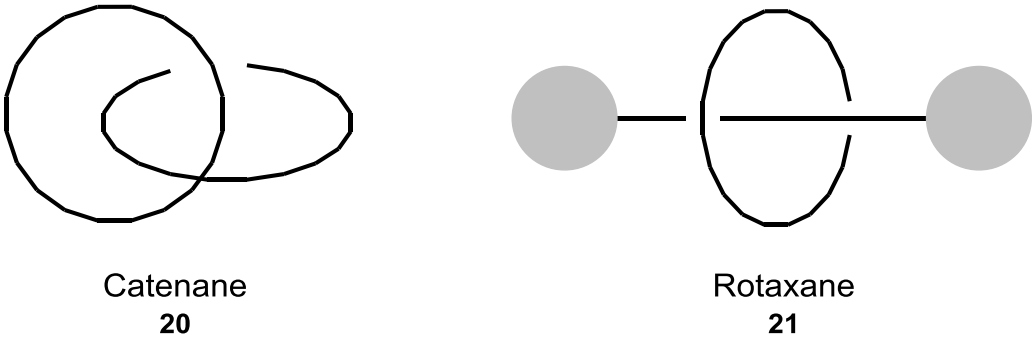

Figure 20 Schematic representation of a [2]catenane (**20**, left) featuring two interlocked cyclic compounds and a rotaxane (**21**, right) with a cyclic compound threaded onto a dumbbell shaped axle that prevents dethreading through bulky end groups.

Since then the synthesis of mechanically interlocked molecules has been greatly improved from the first directed synthesis of a catenane by *Schill* and *Lüttringhaus* in 1964[54] towards templated synthesis introduced by *Sauvage* in 1983.[55] The latter is a robust and versatile method that exploits the highly ordered arrangement of ligands around transition metal cations to preorganize the crossings of the target compounds. In the first reported templated synthesis the tetrahedral coordination of copper was used to thread a phenanthroline moiety **22** into a related macrocycle **23** (Scheme 1). Catenane **24** was obtained in 42% yield by fusing of the second ring via *Williamson* ether synthesis. The templating metal can then be removed by treating **24** with potassium cyanide, which allows the interlocked macrocycles to rearrange within the topological limits.[56] The synthesis of [2]catenanes was improved drastically when olefin metathesis was employed in the templated synthesis approach providing yields of > 90%.[57]

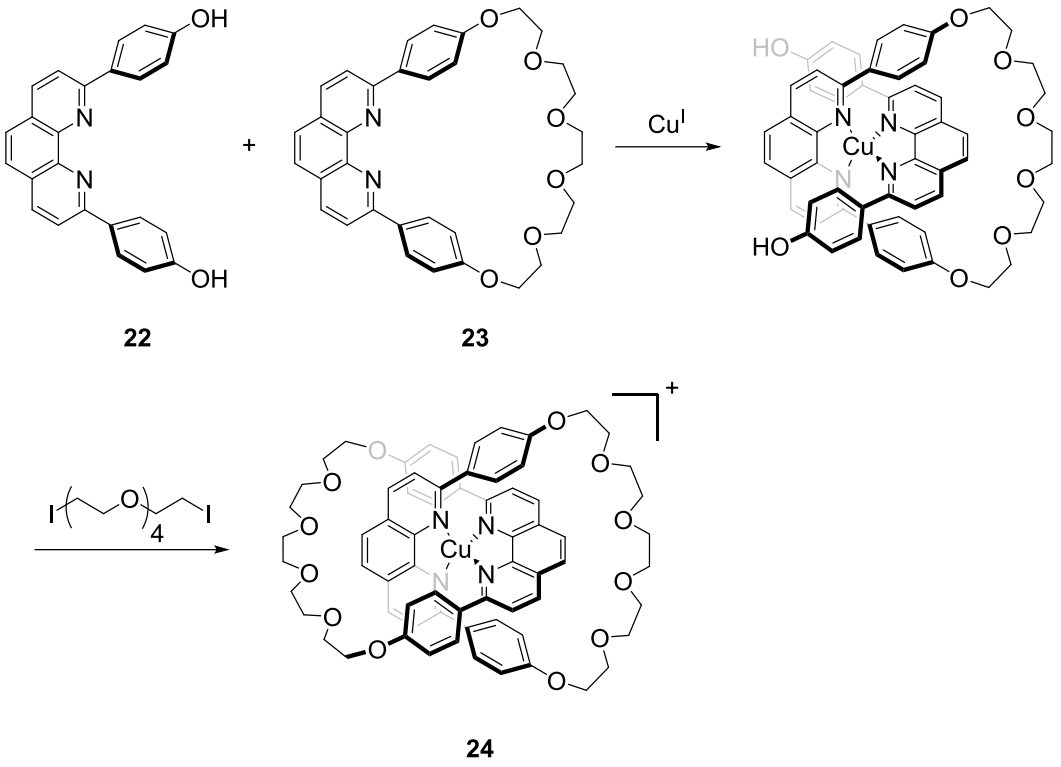

Scheme 1 First reported metal-templated catenane synthesis. The tetrahedral coordination of copper was used to preorganize ligand **22** and macrocycle **23** in an orthogonal fashion. [2]Catenane **24** was obtained in 42% yield through ring fusion via *Williamson* ether synthesis using a short ethylene glycol linker.

Another groundbreaking catenane synthesis was developed by *Stoddart*. Prior a series of bisphenylene macrocycles and analogs were found to form stable complexes with paraquat and diquat that are stabilized by electrostatic and charge transfer interactions (Figure 21a).[58–60] This observation was soon followed by the first [2]catenane synthesis that exploited that fact, that the role of host and guest could be reversed.[61] Bisparaquat **25** and macrocycle **26** form stacks of alternating electron-poor and electron-rich aromatic π-systems that have a templating effect on the synthesis. The product **27** was obtained in 70% yield which encouraged the development of countless interlocked systems.[62]

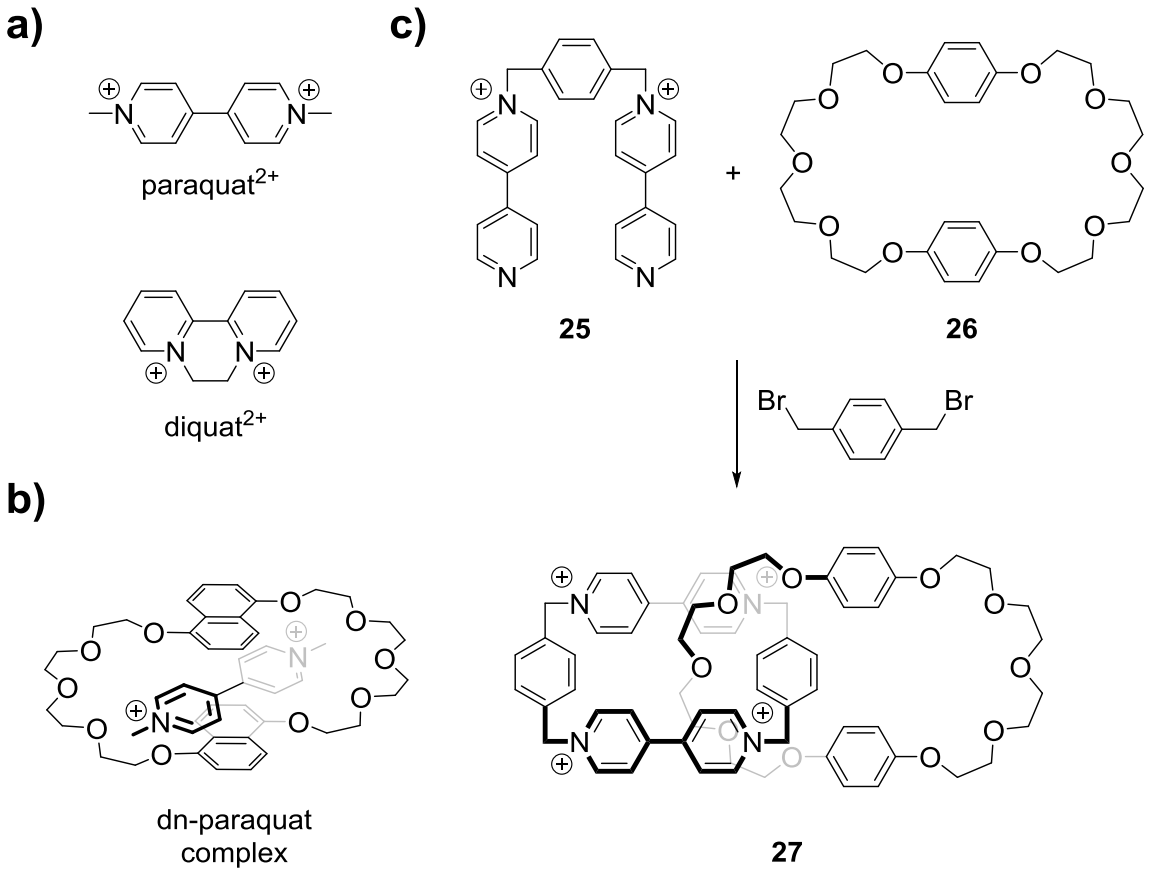

Figure 21 Templated catenane synthesis on the basis of polar aromatic interactions. a) Electron-poor paraquat and diquat form stable complexes with a series of crown ether macrocycles where the donor and acceptor stack in an alternating fashion. b) Exemplary dihydroxynaphto (dn) crown ether paraquat complex. c) First reported templated synthesis using the bisparaquat receptor **25** and macrocycle **26**. Catenane **27** was obtained in 70% yield.

The establishing of mechanically locked systems in general has fueled the development of a plethora of artificial molecular machines[63] and motors.[64] An example of a chemically fueled motor reported by *Leigh* is given in Figure 22. The system works on the basis of a linear molecular pump[65] that uses acid/base oscillations to transport a substrate away from its equilibrium positions. In the initial isomeric structure of **28**-H^+ obtained from synthesis the macrocycle resides on the dibenzylammonium site. Movement of the ring to either side is prevented by a bulky disulfide (green) and hydrazone (blue). Addition of base (Et_3N) deprotonates the dibenzylammonium rendering the triazolium the thermodynamically favored binding site. At the same time the disulfide is temporarily removed through exchange with **29** allowing movement of the ring. Acidification (CF_3CO_2H) reprotonates the dibenzylamine moiety while the hydrazone undergoes exchange with **30** thus enabling full directional 360° rotation of the macrocycle.

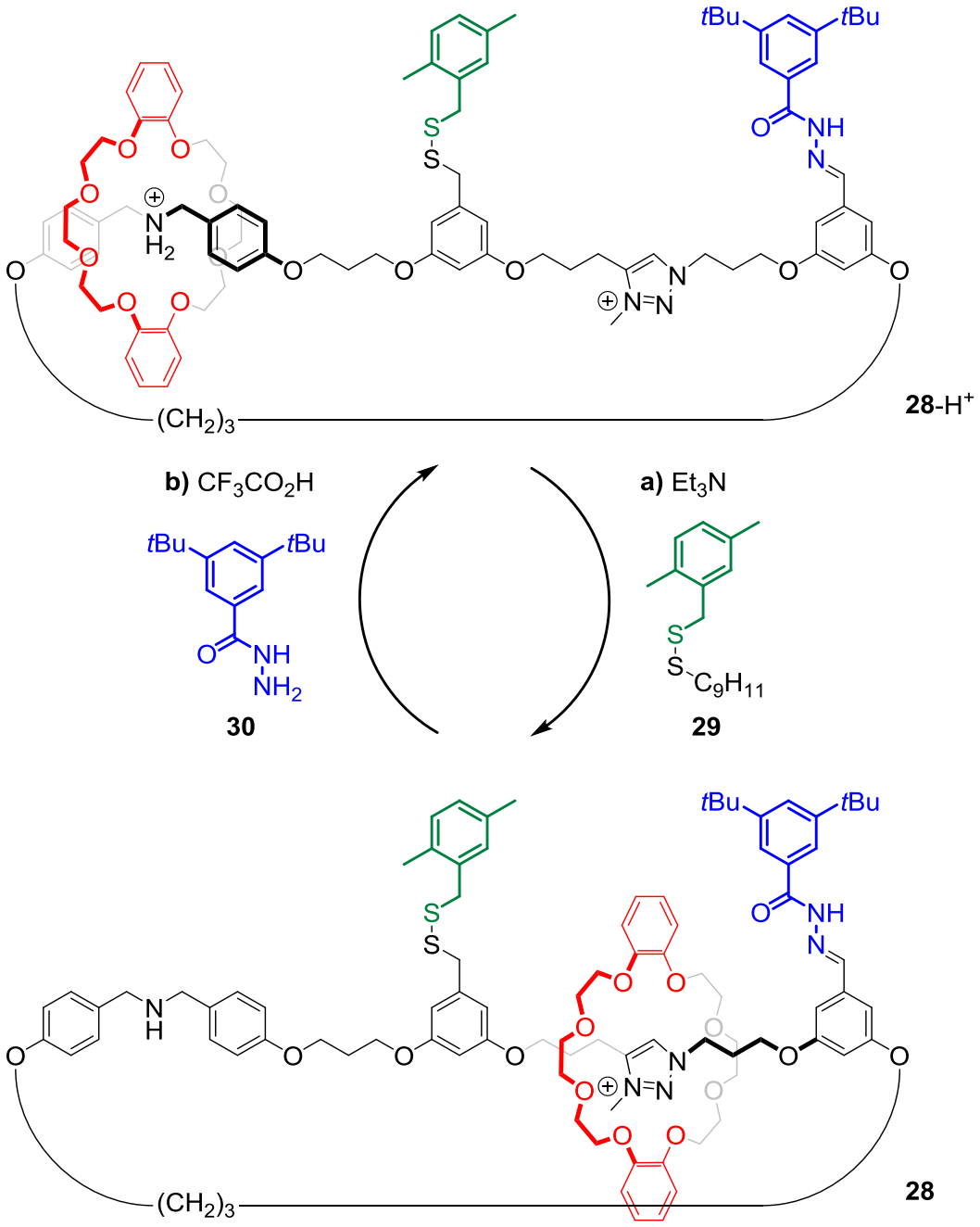

Figure 22 Example of a chemically-fueled molecular motor **28** on the basis of a linear rotaxane pump by *Leigh*.

2.5 Photoswitches integrated into macrocyclic systems

Interesting property changes can be observed when photoswitches are integrated into macrocycles. Reducing the size of the macrocycles in general can be expected to build up strain that can be used to tune the photochemical properties of the chromophores as well as thermal izomerisation rates. When *Huang* et. al integrated stiff-stilbene **31** into 17-membered

macrocycle **32** the *E* isomer is now metastable and not the *Z* isomer (as in the parent stilbene itself). The thermal half-life $\tau_{1/2}$ of the metastable isomer dropped from 10^9 years (*Z* isomer in the parent stilbene) to 17 days (*E* isomer in the macrocycle) as shown in Figure 23a.[66] When the size of the ring is reduced by an additional atom (**33**) the half-life experiences a sharp drop to 100 ms. Similar effects are observed when a methylene group in diazocine is substituted with heteroatoms of different sizes (Figure 23b).[67] Also in this case the metastable isomer of the diazocine is now *E* configured – directly opposite to the parent azobenzene with metastable *Z* isomer. When the azobenzene-bridge in diazocine includes a sulfur atom a half-life of the metastable *E* isomer of 3.5 d is observed (**34**, 27 °C). Replacing the sulfur with oxygen on the other hand significantly reduces the thermal stability to a half-life of 89 seconds (**35**, 20 °C). This shows that minor changes in the size and constitution of the macrocycle can have a great impact on the properties of the integrated switch.

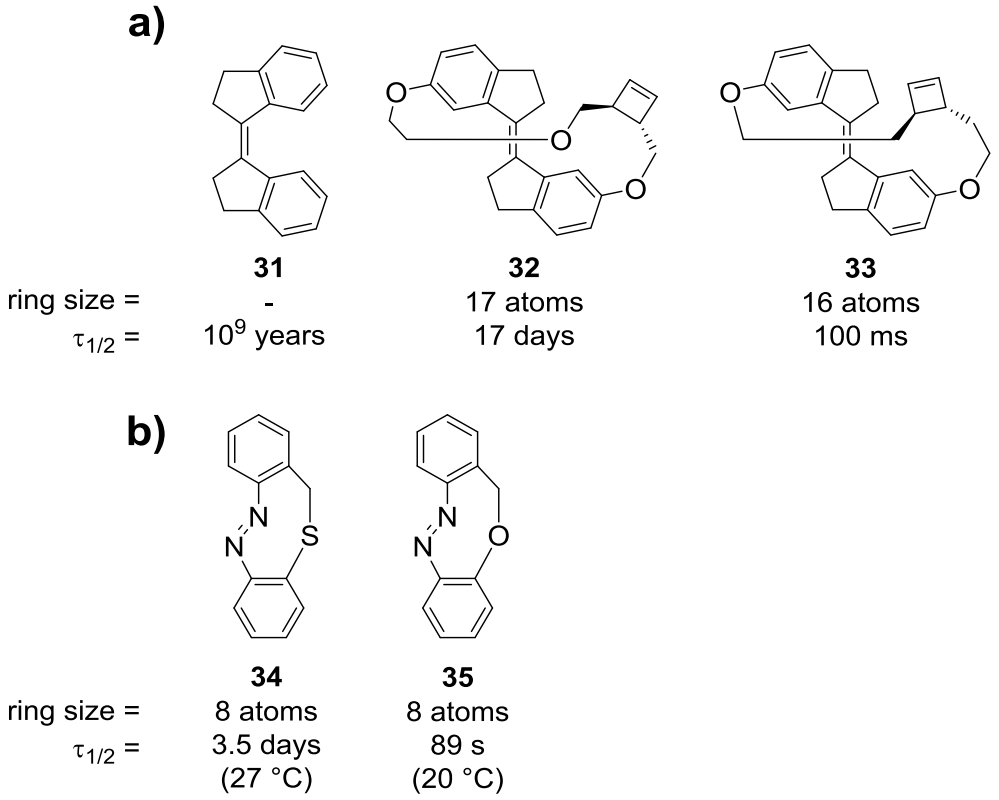

Figure 23 Effects of ring-size and heteroatoms on thermal half-lives of metastable photoswitching states. a) The half-life of parent stiff stilbene *Z*-**31** of 10^9 years is reduced to 17 days when it is integrated into the *trans* configured 17-membered ring *Z*-**32**. The isomerization rate is increased sharply when the ring size is reduced to 16 atoms in *Z*-**33** ($\tau_{1/2}$ at 300 K). b) Changes in thermal half-lives of bridged *E*-azobenzenes **34** and **35** based on the integrated heteroatom.

A series of bridged hydrazone photoswitches was used to study the effect of ring size on the thermal isomerization rates of the metastable states in greater detail.[68,69] Kinetic and crystallographic data supported by DFT calculations reveal that isomerization rates are controlled by combined enthalpic and entropic contributions that experience great variation. Compounds with shorter aliphatic linker lengths **C3** to **C5** exhibited the expected behavior of faster isomerization rates towards smaller linkers (Figure 24). This is readily explained by angle (Baeyer) strain, which is commonly found in small cycloalkanes and the negative change in entropy, which results from less conformational freedom in the ground state. Surprisingly the half-life experiences a significant drop at **C6**, which continues up to **C8** which was attributed to a combination of Baeyer, Prelog (transannular), and Pitzer (torsional) strain[70] that is not counterbalanced by entropic penalties. Overall the half-lives of the metastable switching states range from 15 (**C3**) over 10^3 (**C5**) to 0.05 years (**C8**) which shows that effects of ring-size does not only stem from the intuitively understood angle strain but substantial strain can also be introduced through larger macrocycles.

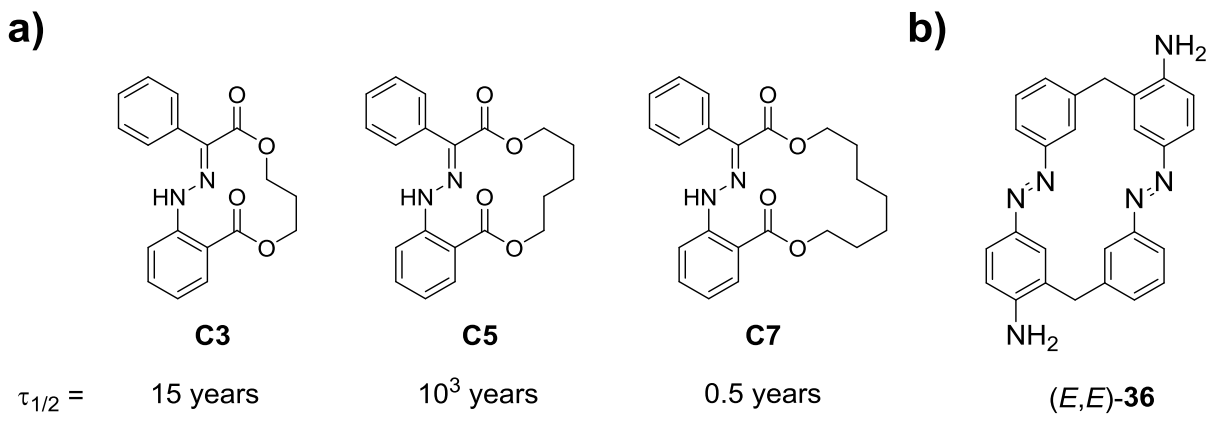

Figure 24 a) Exemplary hydrazone macrocycles with aliphatic linkers of varying lengths (**C3**, **C5**, **C7**) and respective half-lives for the thermal isomerization of metastable *E* to stable *Z* forms via nitrogen inversion. b) Azobenzenophane **36** with two integrated azo units.

The incorporation of multiple photoswitches i.e. azobenzenes into a single macrocycle has attracted much attention over the years.[71] Such macrocycles termed azobenzenophanes are of high interest due to their multiple accessible states in a single molecule. A system that is constructed from two *para*-aminoazobenzenes bridged by two methylene groups (**36**, Figure 24b) shows significantly reduced photoconversion rates for the *E* to *Z* isomerization compared to free aminoazobenzene and the thermal *Z* to *E* isomerization also occurs twice as fast.[72] Both are the result of the pronounced strain of the mixed E/Z-**36** isomer. Despite stabilizing hydrogen

bonds that were calculated to counterbalance the strain in the Z/Z-**36** isomer this photoproduct could not be obtained suggesting that the strain induced by the macrocycle can greatly affect the reactivity of the excited states of the azobenzene units.

A symmetrical macrocycle with four integrated azo units was used to demonstrate that the photoswitching of a single azo units is not statistically controlled (**37**, Figure 25).[73] With four integrated switches photoisomerization of (*E*,*E*,*E*,*Z*)-**37** can result in two different products (*E*,*Z*,*E*,*Z*)-**37** or (*E*,*E*,*Z*,*Z*)-**37**. The group of *Wegner* found, that (*E*,*E*,*Z*,*Z*)-**37** is formed preferably in the photostationary state (pss). This is most likely the result of minor changes in quantum yield and absorption maxima of the products. It can also be excluded that the observations are based on differences in thermal stabilities as (*E*,*Z*,*E*,*Z*)-**37** showed the highest and (*E*,*E*,*Z*,*Z*)-**37** the lowest thermal stability of all possible isomers. The systems demonstrates that ring strain does not only influence thermal isomerization rates but can also be used to change the photoswitching properties of the incorporated chromophore.

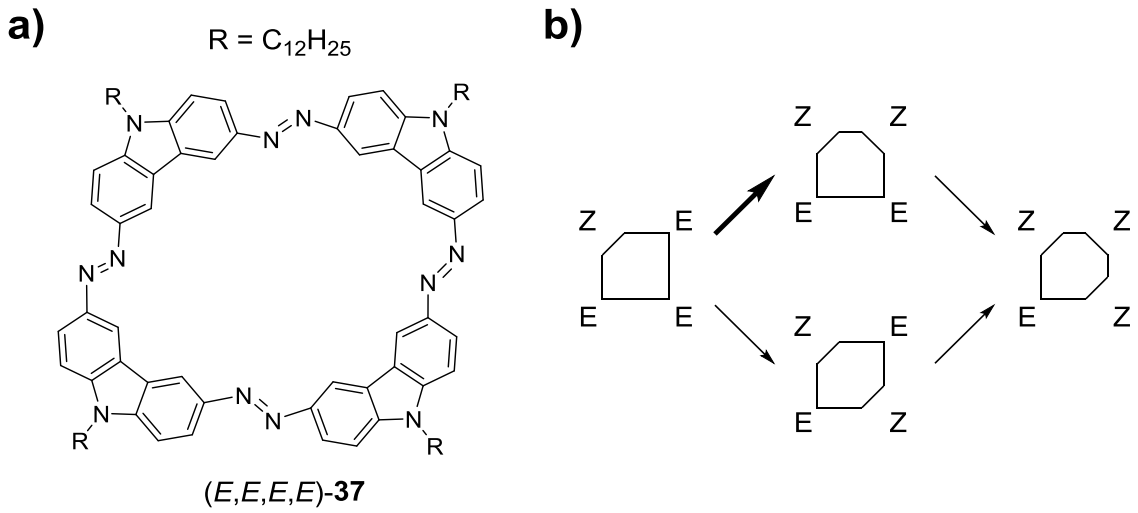

Figure 25 Example of a highly symmetric oligobenzenophane **37** with a total of four azobenzene units. a) The azocarbazole macrocycle (*E*,*E*,*E*,*E*)-**37** used in the study. b) Preferred formation of (*E*,*Z*,*E*,*Z*)-**37** is observed in the pss indicated by the bold arrow.

An intriguing way to tune the rotational speeds of a molecular motor was achieved through the combination of a second generation *overcrowded alkene* motor and a macrocycle. In the setup **38** the stator part of the motor is integrated into a monothia 18-crown-6 ether that forms complexes with selected alkali and earth alkali metal cations (Figure 26).[74] Upon addition of the metal salts a notable decrease of the activation energy of the THI was observed. As this also represents the rate limiting step observed rotational speeds were up to twice as fast, reducing

the corresponding half-lives from 14 min down to 7 min at 20 °C (in MeCN). Also concentrations of the metastable photoisomer in the pss were significantly improved increasing the yield from 65% up to > 95%. Complexation of cations can result in contractions of the molecular structure, which has been reported earlier.[75,76] The studies suggest that distortion of the stator fragment results in reduced steric hindrance around the central double bond which explains the increased rotational speeds. These effects can be fully reversed in the presented system when the competing ligand [2.2.2]cryptand is used for decomplexation, thus establishing full control over the rotational properties of the motor within its intrinsic limits.

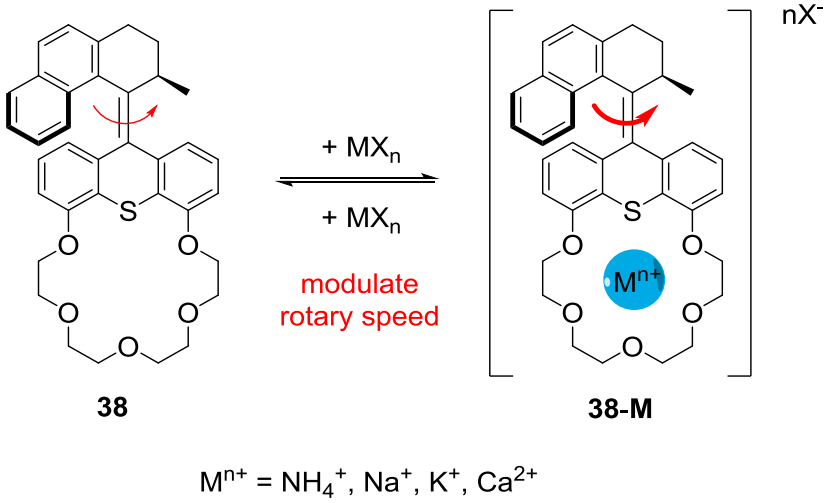

Figure 26 Tuning of rotational speeds in crown ether functionalized molecular motor **38**.

Yet another way to control the rotational speeds within a motor-macrocycle system is the use of a chemical "lock". In this setup the xanthene stator of a second generation motor is integrated into a dibenzo 24-crown-8 ether and the rotor is functionalized with a short alkyl chain featuring a secondary amine (**39**, Figure 27). Acid is added to give the protonated $R_2NH_2^+$ species, which undergoes intramolecular self-complexing forming the locked pseudorotaxane *Z*-**39**-H^+. In this state irradiation does not result in observable isomerization processes. When base is added the pseudorotaxe is dethreaded and becomes unlocked reestablishing full functionality of the motor. The results demonstrate that hydrogen-bonding interactions in an intramolecular crown ether complex are strong enough to prevent the conformational changes that are required for the rotational motion of the motor.

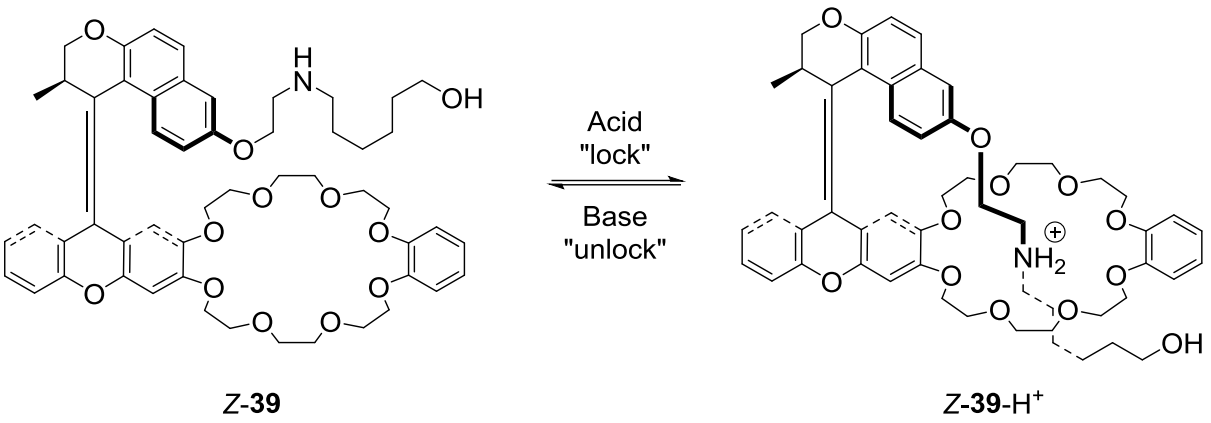

Z-**39** *Z*-**39**-H$^+$

Figure 27 Second generation *overcrowded alkene* motor with a self-complexing lock. Upon addition of acid the short alkyl chain is threaded through the crown ether moiety forming pseudorotaxane *Z*-**39**-H$^+$. In this state unidirectional rotation of the motor is effectively blocked. Addition of base results in dethreading restoring the motor function.

Taken together integration of photoswitches into macrocycles can result in drastic changes of their photophysical properties that cannot be predicted in a straightforward manner. On the other hand extended control is obtained that cannot be achieved through simple substitution. It is also clear that the combination of photoswitches and macrocycles opens up great possibilities for the construction of highly sophisticated machinery with unmet complexity. In the main part of the here presented work the integration of a HTI based molecular motor into different macrocyclic systems was used to gain unprecedented insight into the working mechanism of the motor fragment and the amount of work that can be performed by such a nanoscale powering unit. Most importantly new concepts for the transmission of directional rotation at the molecular scale and active driving of passive, secondary units were successfully developed, which opens up exciting possibilities for building integrated nanomachinery in the future.

3 Transmission of unidirectional motor rotation

3.1 General design principles

Establishing an atomic scaffold for the conversion of light into unidirectional motion at the molecular scale is only the first step towards complex nanomachinery. While conceiving a functional molecular setup that allows generation of unidirectional molecular motion requires genius in the first place, the visualization and experimental prove of these motions is another obstacle that needs to be overcome either by sophisticated analytical methods or additional synthetic efforts. A further logical step in building machinery at the smallest scale is to use the motor rotation to drive a remote unit. Coming up with structures, which allow for such a transmission of motion is not straightforward but it is evident to assume that simple introduction of any rigidly linked moiety to a molecular motor should result in unidirectional rotation of this additional part. However, more complex or non-rigidly linked functions require some sort of readout that allows for the observation of the individual parts moving in relation to each other. As mentioned earlier for unidirectional rotation a minimum of three observable conformations must be experimentally accessible in order to prove the underlying motion.

Integration of a HTI based molecular motor unit into such a machine was the first logical step as the chromophore allows photoswitching in the visible range of the spectrum with a high bistability. Attachment of a *receiver* unit was envisioned by a covalent linker to the indanone part of the motor, the latter being arbitrarily assigned the *rotor* part. A sketch of the required functional parts of the nanomachine is presented in Figure 28. Communication of the benzothiophenone *stator* and the remote receiver over long intramolecular distances via a dedicated reporter unit in order to prove the unidirectional rotation of the individual parts in relation to each other was not feasible. Consequently, connection of the receiver unit directly to the stator fragment of the molecule was a logical step in the design of the molecular machine. Next, a connection must be established that can be used as a reporter for the different geometries that are adopted during the 360° rotation cycle. By this means an aryl moiety was integrated as the receiving unit, establishing a biaryl reporter by connecting it to the benzothiophenone stator.

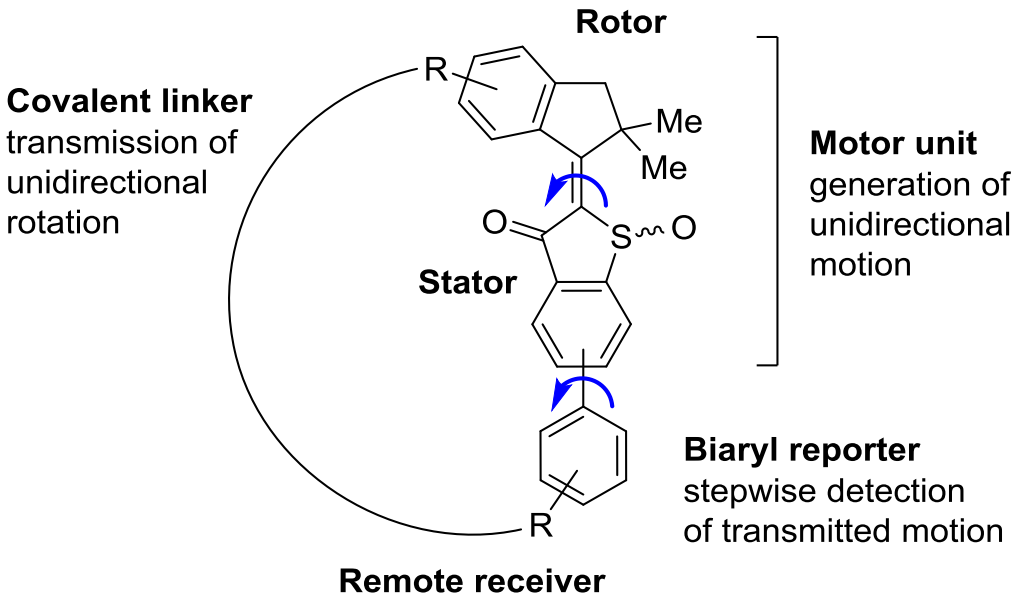

Figure 28 Schematic representation of the design of the molecular machine. Stator and Rotor fragments were arbitrarily assigned to facilitate understanding of the system. Generation of unidirectional motion is achieved by integration of a HTI-based molecular motor. Transmission of the rotation to a receiving aryl unit is realized by a covalent linker. Together with the benzothiophenone-based stator a biaryl reporter unit is established that enables a straightforward readout of the molecules geometry.

The electronic circular dichroism (ECD) response of asymmetric biaryls does not only differentiate between the two atropisomers, which would be the result of the rotation but also distinguishes tilts of atropisomers to either side[77] and therefore matches the four step rotation of the motor unit perfectly. As a result, ECD experiments in combination with a comprehensive 2D NMR analysis should enable the elucidation of the motion in detail.

3.2 Retrosynthetic analysis

From the discussed design principles a retrosynthetic roadmap can be derived. This breaks down the molecule into major building blocks, which are shown in Scheme 2. The target compound synthesis was planned to provide a general access to macrocyclic HTIs in a highly modular fashion employing reliable reactions with high tolerance for functional groups to pave the way for more advanced systems in the future.

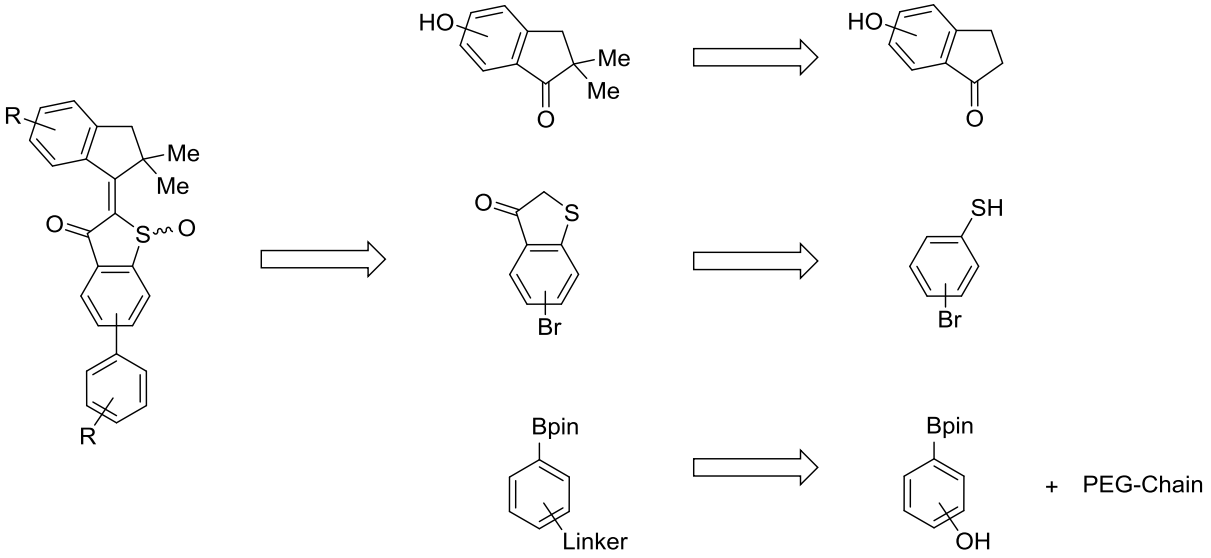

Scheme 2 Retrosynthetic analysis of the required building blocks for the synthesis of a functional macrocyclic HTI.

A common approach to HTIs is realized by the condensation of benzothiophenone with a substituted benzaldehyde, or in this case indanone. Two modifications were deemed as indispensable for the motor function. First, dimethylation in *alpha* position of the carbonyl. This increases the steric hindrance around the central double bond and facilitates experimental access to the elusive metastable states of the molecular motor. Second, an aromatic ether functionality at the 7-position of the indanone to induce steric repulsion by lone-pair interactions between the oxygen and the carbonyl or sulfoxide of the benzothiophenone stator. Since methylation in *alpha* position to the carbonyl of hydroxylated indanone precursors will give the methoxy byproduct a “protecting group” had to be introduced to the hydroxyl group before the reaction could be carried out. As introduction of a functional group for the attachment of the covalent linker was also required this opened up the possibility to introduce an attachment site that simultaneously serves this purpose.

The benzothiophenone stator had to be modified in a way that allows establishment of the biaryl unit in a later stage of the synthesis. An obvious approach is the *Suzuki-Miyaura* cross-coupling of the two arenes from an organohalide and a boronic acid. As preparation of benzothiophenones and later condensation had proven to require very delicate reaction conditions with low tolerance of functional groups, introduction of a bromine was a straightforward approach. From the three possible substitution patterns the benzothiophenone with bromine in *ortho* postion results in an unfavorable geometry of the macrocyclic HTI

because of the close proximity to the sulfoxide and the huge difference in potential ring strain in between the *E* and *Z* isomers (Figure 29).

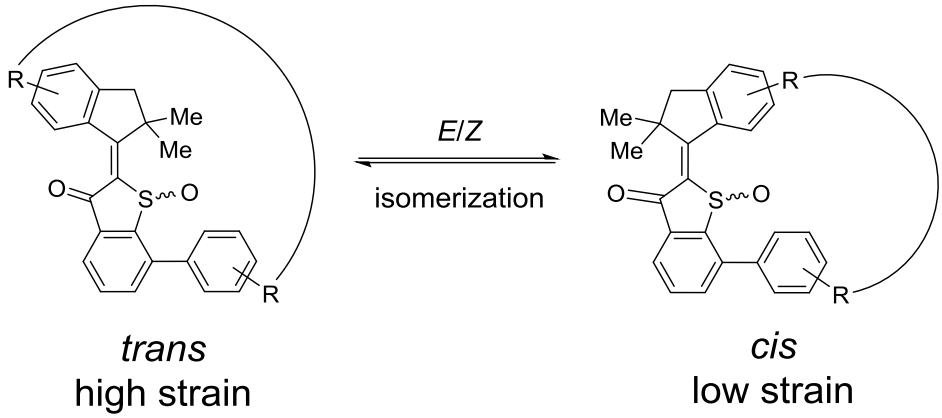

Figure 29 Illustration of the macrocycle geometry obtained from integration of a benzothiophenone with a bromo substituent in *ortho* position to the sulfur. The aryl receiver unit of the target compound is in close proximity to the sulfoxide allowing for unwanted interactions. The ring strain in the *E* isomer is potentially much higher than in the *Z* isomer and could result in unfavorable leverage effects.

The *meta* substituted benzenethiol was discarded as starting material, as synthesis of the benzothiophenone affords two regioisomers that required tedious purification efforts to separate (Scheme 3). As a result, the *para* substitution pattern of 5-bromobenzothiophenone was chosen.

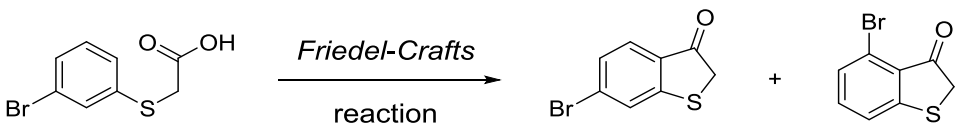

Scheme 3 Intramolecular *Friedel-Crafts* acylation of 3-bromophenylthioacetic acid afforded a mixture of two benzothiophenone regioisomers.

Hydroxyl and amine functional groups were considered for the boronic acid building block to allow the attachment of the covalent linker. Since aniline as a starting material would be converted to a secondary amine which could interfere in later stages of the synthesis in an unpredictable manner a hydroxyl substitution was preferred. Attachment of the covalent linker in *para* position could result in it having no leverage effect on the biaryl axis (Figure 30). Instead unidirectional motion, transmitted by the chain, could be dissipated by rotation around the (Ar)C-O single bond. Attachment in *ortho* position would interfere with atropisomerization barriers in an unpredictable manner, which left 3-hydroxyphenylboronic acid as a building block.

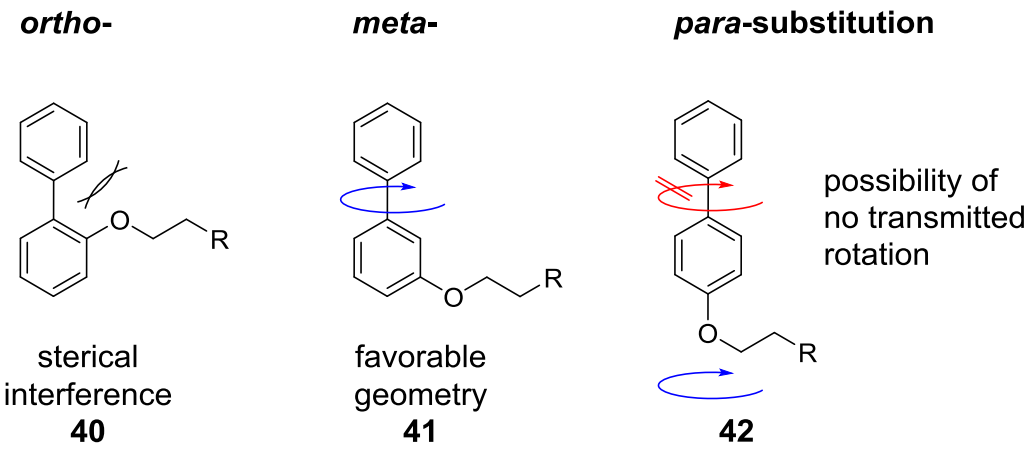

Figure 30 Consideration of possible attachment sites for the covalent linker. Substitution in *ortho* position leads to unpredictable interactions with the biaryl rotational barrier (**40**, left). *Meta* substitution results in the most favorable geometry (**41**, middle). Unidirectional motion of the covalent linker, which is connected in *para* position might not be transmitted to the biaryl axis (**42**, right).

Long-chain aliphatic diols or dicarboxylic acids can be employed as covalent linkers as well as polyethers such as polyethylene oxides (Figure 31). A polyethylene glycol type chain offers several advantages. Chain lengths up to PEG-12 (37 atoms chain length before integration as building block) are commercially available at reasonable prices. Substitution of an ethylene glycol unit, for example by catechol is synthetically realized in a highly modular fashion and can be used to tailor the properties of the linker. In addition a potentially higher crystallinity and interactions of the PEG chain with cations in more sophisticated systems were taken into consideration.

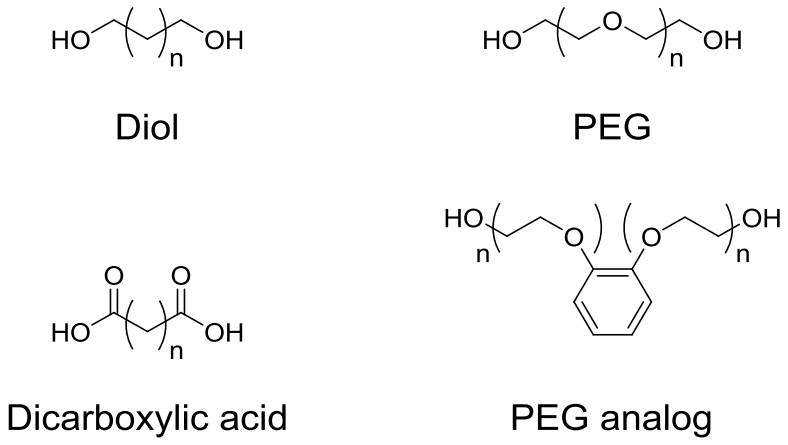

Figure 31 Possible building blocks for the use as covalent linker in the synthesis of macrocyclic HTIs.

Finally, possibilities to close the macrocycle had to be considered for their feasibility. In the literature this is commonly realized by olefin metathesis or 1,3 dipolar cycloadditions, the latter is also known as *Huisgen* cycloaddition or *click* reaction (Scheme 4). Introduction of allyl or propargyl functional groups seemed straightforward by reaction of the respective hydroxyl groups with an allyl- or propargyl halide. The introduction of an azide can be realized in two steps by conversion of the hydroxyl functional group to a leaving group, for example via the *Appel* reaction or tosylation and subsequent substitution utilizing an azide source.

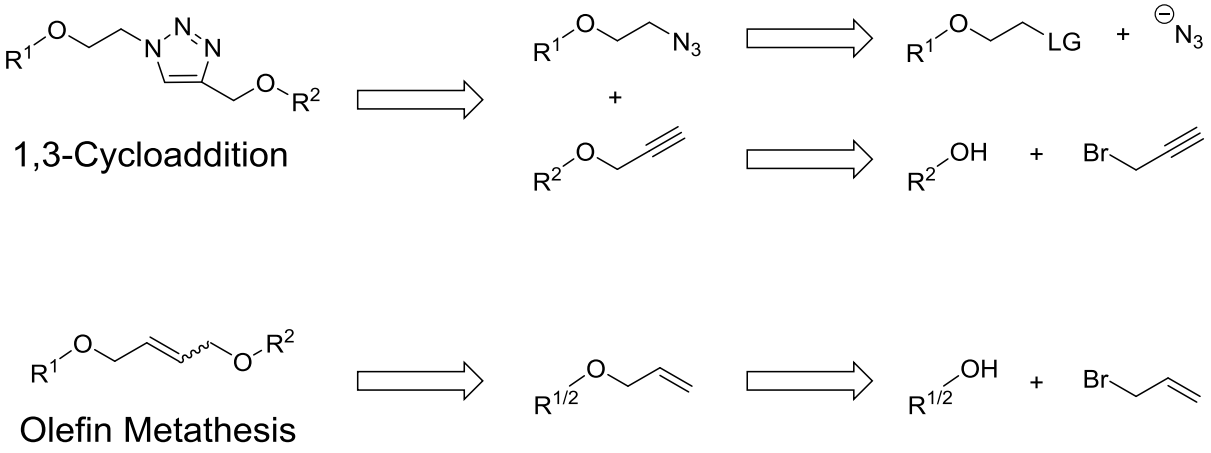

Scheme 4 Retrosynethetic analysis of prospective compounds obtained from macrocyclic ring-closing reactions.

3.3 Synthesis of macrocyclic HTI 81

3.3.1 Possible synthesis of functional HTI motor analogues

There are two general approaches that are commonly applied for the synthesis of HTI-based molecular motors and their applicability will be discussed briefly. The pioneering HTI motor **12** was synthesized in five steps. Two one-pot reactions shorten this to only three steps in total that required workup. A short outline is given in Scheme 5.

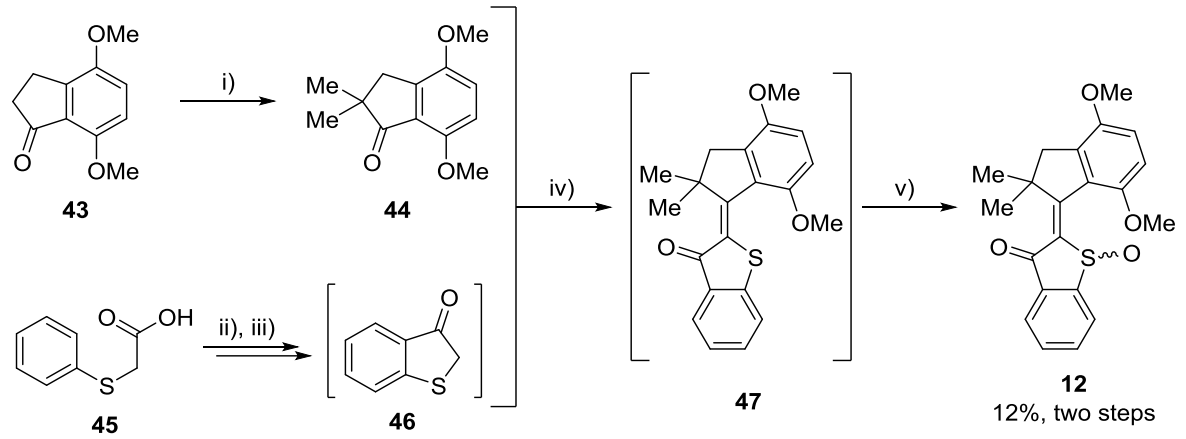

Scheme 5 Synthesis of the first HTI based molecular motor **12**. i) NaH, MeI, $(CH_2OMe)_2$, 75%. ii) $SOCl_2$, cat. DMF. iii) $AlCl_3$, $(CH_2Cl)_2$. iv) $BF_3 \cdot OEt_2$, CH_2Cl_2. v) H_2O_2, AcOH, 12%, two steps. Only the *Z* configured isomers are shown.

Since functionalized analogs of HTI **12** should be utilized in the synthesis of macrocyclic HTIs, applicability of this route had to be evaluated in detail. Methylation of indanone **43** afforded the product **44** in good yields. However, phenolic functional groups have to be protected/functionalized prior to the reaction as discussed above. Benzothiophenone **46** and several analog precursors are accessible by *in situ* generation of the acid chloride of **45** and subsequent intramolecular *Friedel-Crafts* acylation. The target compound **12** was obtained in poor yields which can be attributed to the condensation reaction to **47** as key step. The yield was sufficient to allow elucidation of the motor function in detail but is unsatisfactory to be applied in the synthesis of the motor building block for the construction of macrocyclic HTIs. These results had already prompted the development of a multi-step workaround which increases steric hindrance stepwise by construction of a functional motif required for a *Meyer-Schuster* rearrangement which is then followed by an intramolecular cyclization reaction (Scheme 6).[31]

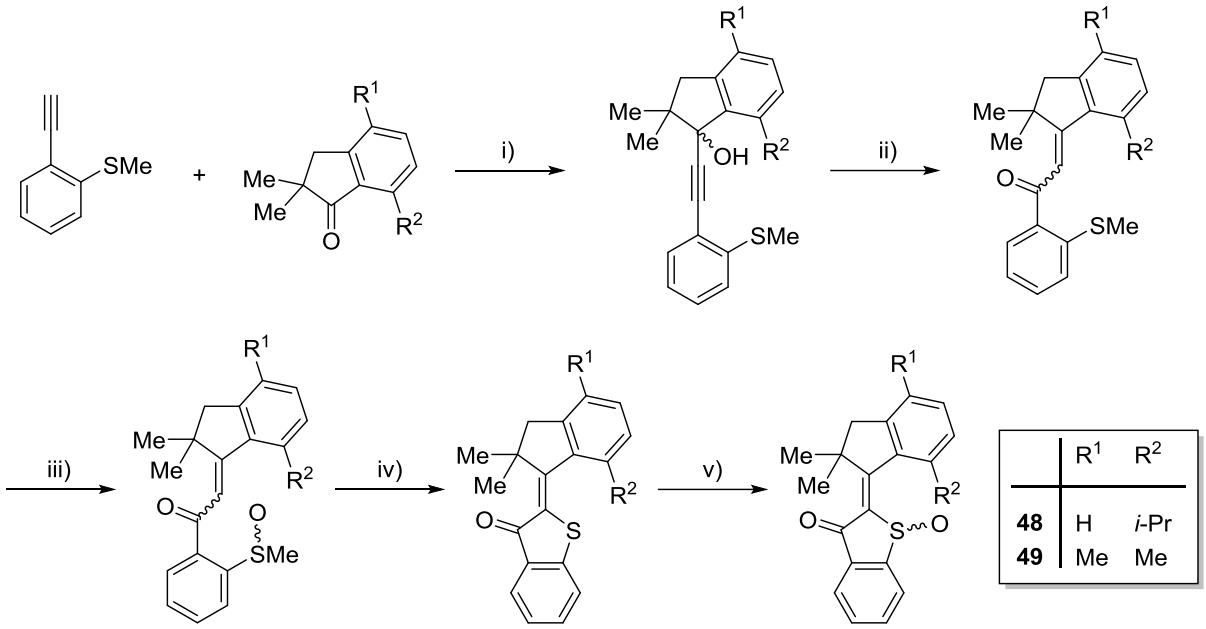

Scheme 6 Synthesis of sterically hindered HTI motors utilizing a *Meyer-Schuster* rearrangement as key step. i) *n*-BuLi, THF. ii) H_2SO_4, THF. iii) $NaBO_3 \cdot 4H_2O$, AcOH. iv) Oxalyl chloride, CH_2Cl_2. v) $NaBO_3 \cdot 4H_2O$, AcOH. The yield over five steps is 52% for motor **48** and 67% for motor **49**. Only the *Z* configured isomers are shown.

The synthesis provides an ingenious way to overcome steric hindrance around the central double bond but is limited by the number of accessible acetylide species as well as low functional group tolerance which is required in the first reaction step. Consequently, optimization of the originally employed condensation reaction was attempted to realize the macrocycle synthesis in the desired modular fashion.

3.3.2 Synthesis of HTI 81

The literature known benzothiophenone **52** was synthesized in two steps starting from commercially available 4-bromothiophenol **50** and bromoacetic acid. Reaction of the starting compounds in acetone proceeded under mildly basic conditions through addition of potassium carbonate (Scheme 7). Excess bromoacetic acid was removed upon aqueous workup giving the phenylthioacetic acid **51** in good yields. Conversion to the acid chloride was done *in situ* by heating of **51** in $SOCl_2$. Addition of $AlCl_3$ afforded 5-bromobenzothiophenone **52** in an intramolecular *Friedel-Crafts* acylation in excellent yields.

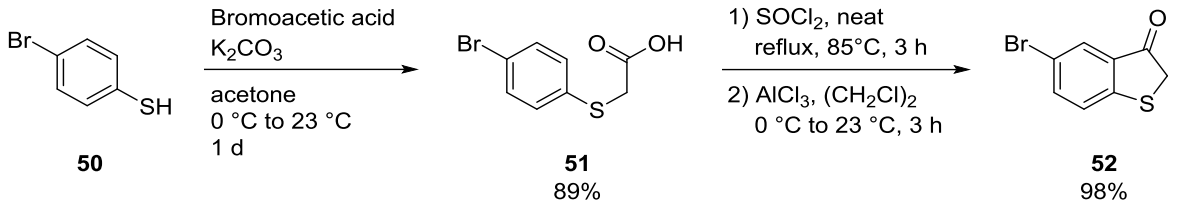

Scheme 7 Synthesis of 5-bromobenzothiophenone **52**. Thiophenol **50** was reacted with bromoacetic acid to phenylthioacetic acid **51**. Intramolecular *Friedel-Crafts* acylation gave **52**.

Protection and simultaneous functionalization of 7-hydroxyindanone was achieved by reaction with propargyl bromide providing **53** in very good yields (Scheme 8). It was also attempted to separate the alkyne functional group from the phenolic oxygen through a longer alkyl chain to avoid unwanted interactions. However, reaction of the indanone with 4-bromo-1-butyne under identical conditions showed only traces of product **54** as judged by TLC and GC-MS analysis and the route was not further pursued. In addition to the alkyne for a later cycloaddition, a suitable metathesis substrate **55** was generated by reaction with allyl bromide in moderate yields. Subsequent methylation using sodium hydride and iodomethane gave the desired indanones **56** and **57** in good yields.

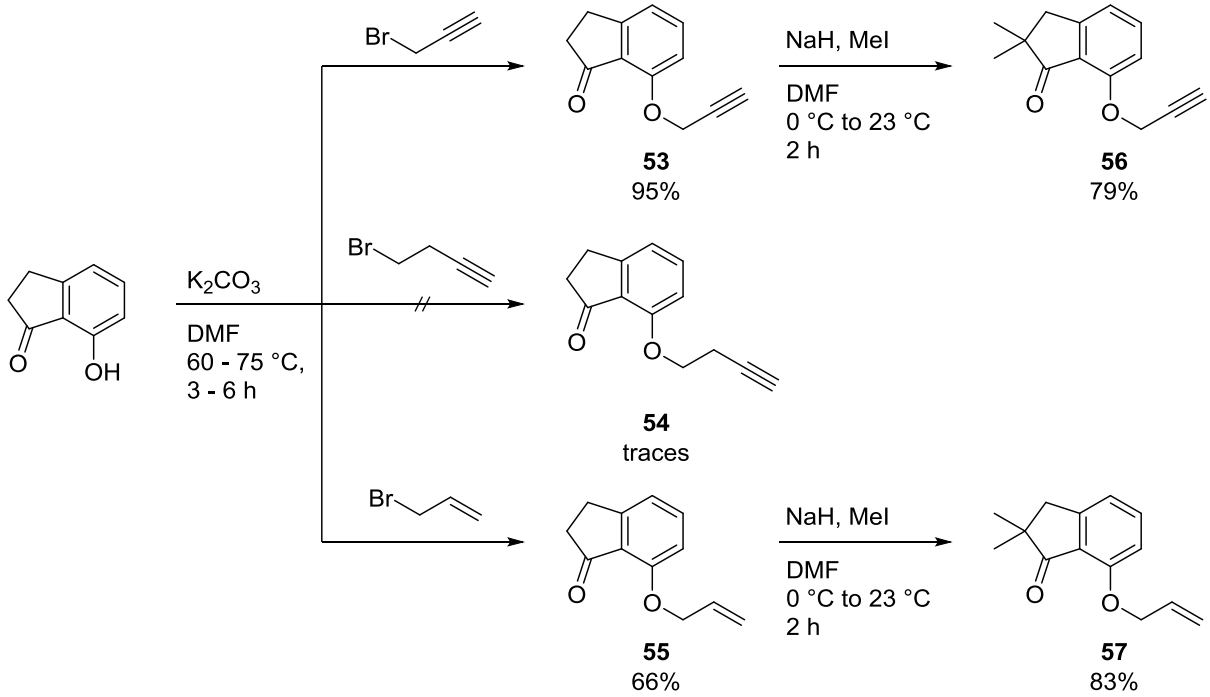

Scheme 8 Synthesis of propargyl and allyl protected/functionalized 7-hydroxy indanones **53** and **55**. The butinyl product **54** was obtained only in traces as judged by GC-MS and TLC. Subsequent methylation afforded compounds **56** and **57** in good yields.

Next, synthesis of functionalized PEG-based covalent linkers and their attachment to the 3-hydroxy phenylboronic acid building block was attempted. Reaction of diethylene glycol with potassium *tert*-butoxide and propargyl bromide afforded **58** in good yields (Scheme 9).

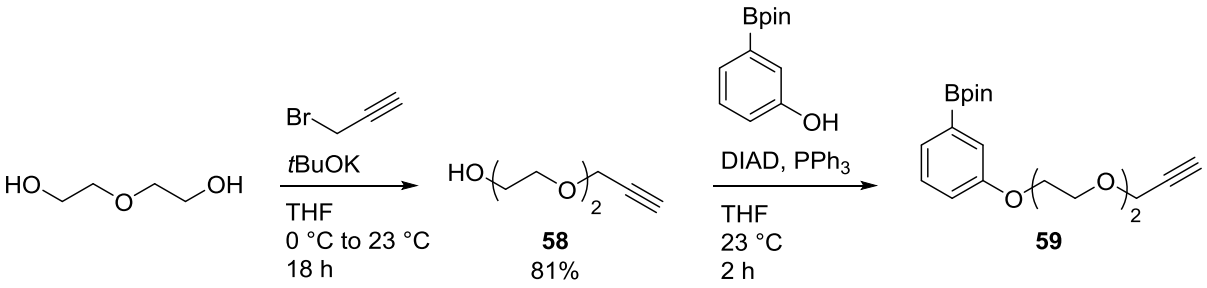

Scheme 9 Reaction of diethylene glycol with propargyl bromide and potassium *tert*-butoxide gave **58** in good yields. Conversion with 3-hydroxy phenylboronic acid pinacol ester in a *Mitsunobu* reaction afforded **59** as judged by GC-MS analysis. Workup was impeded by partial hydrolysis and reaction byproducts.

There are countless examples in the literature for the direct attachment of PEG-type alcohols to phenols under *Mitsunobu* reaction conditions. Indeed, reaction of **58** with 3-hydroxyphenylboronic acid using diisopropyl azodicarboxylate (DEAD) and PPh_3 in THF showed very good conversion upon GC-MS analysis. Unfortunately, partial hydrolysis of the product **59** on silica prohibited separation from triphenylphosphine oxide and diisopropyl hydrazodicarboxylate, which are byproducts of the reaction. To circumvent this problem, an additional reaction step was implemented (Scheme 10).

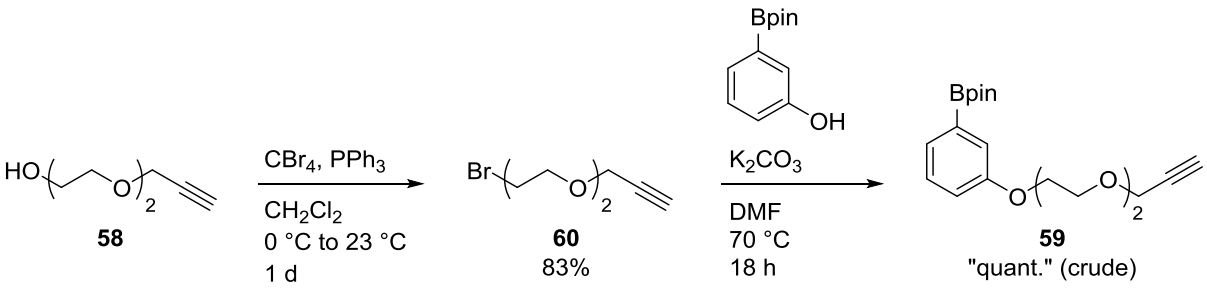

Scheme 10 Conversion of **58** under *Appel* conditions afforded **60** in good yields. Reaction with 3-hydroxy phenylboronic acid pinacol ester under mild conditions gave **59** that was used as crude product in the following synthetic steps. (A "quantitative" yield of crude product was obtained indicating good conversion rates for this reaction but the actual yield could not be determined.)

Conversion of **58** under *Appel* conditions afforded the brominated product **60** in good yields. Tethering to 3-hydroxy phenylboronic acid pinacol ester proceeded under mild conditions.

Generated potassium bromide is readily removed upon aqueous workup. The crude product **59** was obtained quantitatively in sufficient purity for the use in subsequent reactions. Small amounts of byproduct were attributed to onset of boronic ester hydrolysis upon aqueous workup as judged by ^{1}H NMR analysis and therefore definite yields of the reaction could not be determined.

Having established the route to **59**, synthesis of differently functionalized analogs was attempted. To this end PEG-based linkers with complementary functional groups for the macrocyclic ring closing reaction were prepared, the precurosors of which bearing a bromine substituent at the other end for the attachment to the phenylboronic acid. Synthesis of the allyl functionalized linker **62** proceeded analog to the synthesis of **60** with triethylene glycol as starting material (Scheme 11).

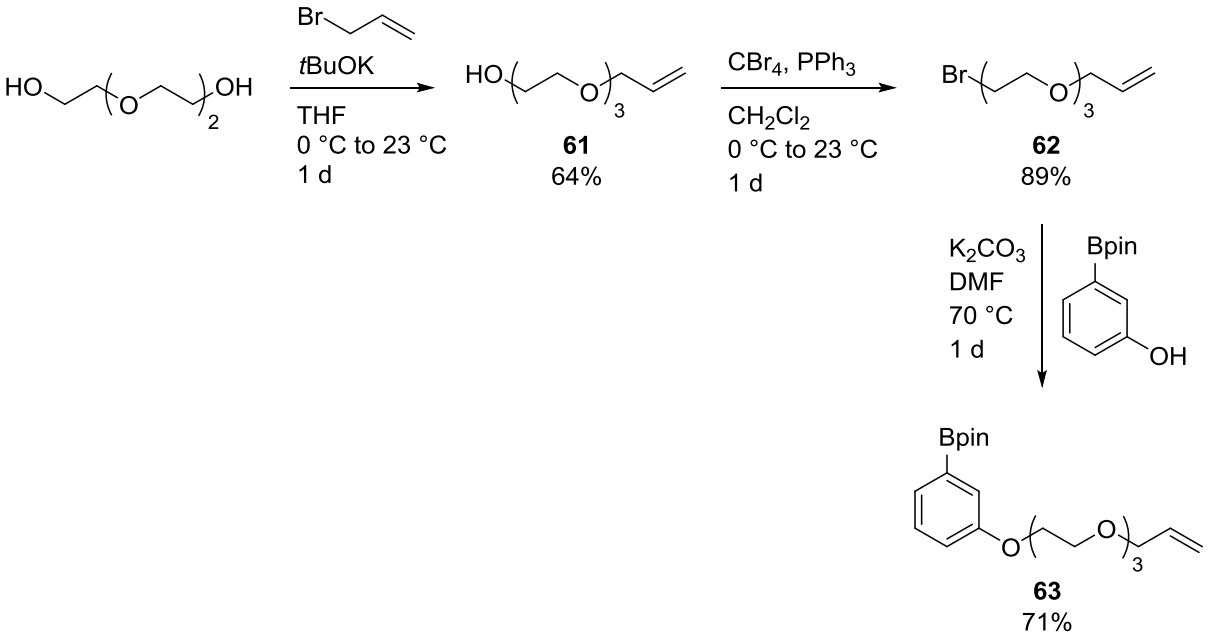

Scheme 11 Synthesis of building block **63**. Reaction of triethylene glycol with allyl bromide gives **61**. Bromination under *Appel* conditions afforded **62**, which was followed by substitution with 3-hydroxyphenylboronic acid pinacol ester to **63**.

A modified approach was used for the synthesis of the azide analog. Synthesis of the PEG chain is commonly done by (mono)tosylation, followed by substitution with sodium azide and conversion of the remaining alcohol to the alkyl bromide (Scheme 12).[78,79] Using an excess of the cheap triethylene glycol, the intermediate **64** is obtained in good yields based on tosyl chloride. The synthesis of **66** is completed in a straightforward manner over a total of three steps with good yields.

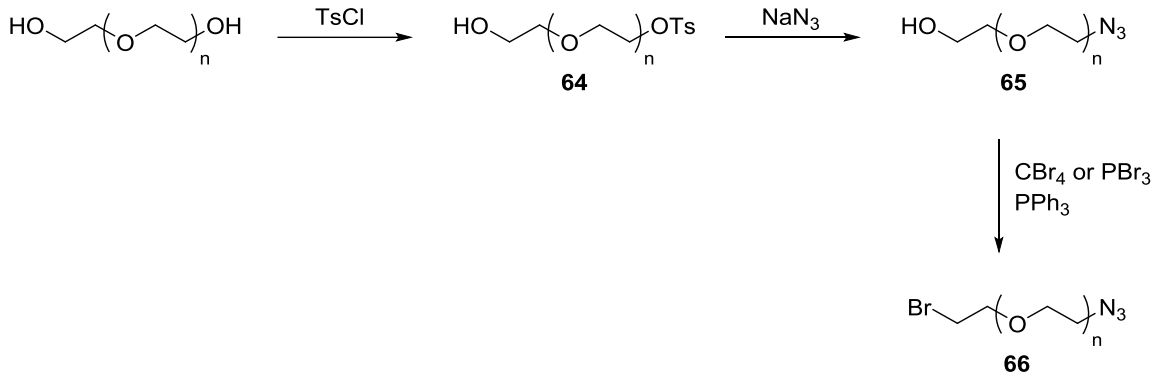

Scheme 12 A common approach to bromo/azide functionalized PEG fragments that is frequently found in the literature. Tosyl chloride is reacted with an excess of PEG starting material to give the monotosylated product **64**. Subsequent substitution with sodium azide gives **65**, which is brominated to **66** in an *Appel* reaction.

A shorter approach that could not be found in the literature would proceed via double bromination of the respective polyethylene glycol followed by monosubstitution with azide. The second reaction step is similar to the monotosylation of PEG (Scheme 12, first synthetic step) with a statistical distribution of products. If an excess of the dibrominated compound (**67** in Scheme 13) would be used, high yields for the monoazide can be expected. However, based on **67** the theoretical maximum obtainable yield of **69** is 50% if one equivalent of each reagent is used and the reaction proceeds with a statistical distribution of products (Scheme 13).

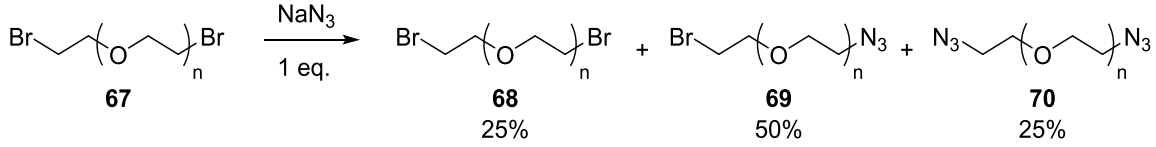

Scheme 13 Theoretical distribution of products from the reaction of polyethylene glycol with one equivalent of azide. After full conversion of the starting material a statistical distribution of 1:2:1 is expected, reducing the maximum obtainable yield of **69** to 50%.

The synthesis was attempted using triethylene glycol as starting material (Scheme 14). Bromination under *Appel* conditions afforded **71** in 79% yield. Reaction with sodium azide gave the product **72** in the expected poor yields (30%). Separation of monosubstituted **72** from the discussed byproducts was straightforward but can pose a serious problem when the PEG chains become longer, which will be discussed later. However, as this route constitutes a faster approach to the intermediate **73** it was implemented in the total synthesis. With the three

differently functionalized arylboronic acid building blocks at hand the macrocycle synthesis could be advanced further.

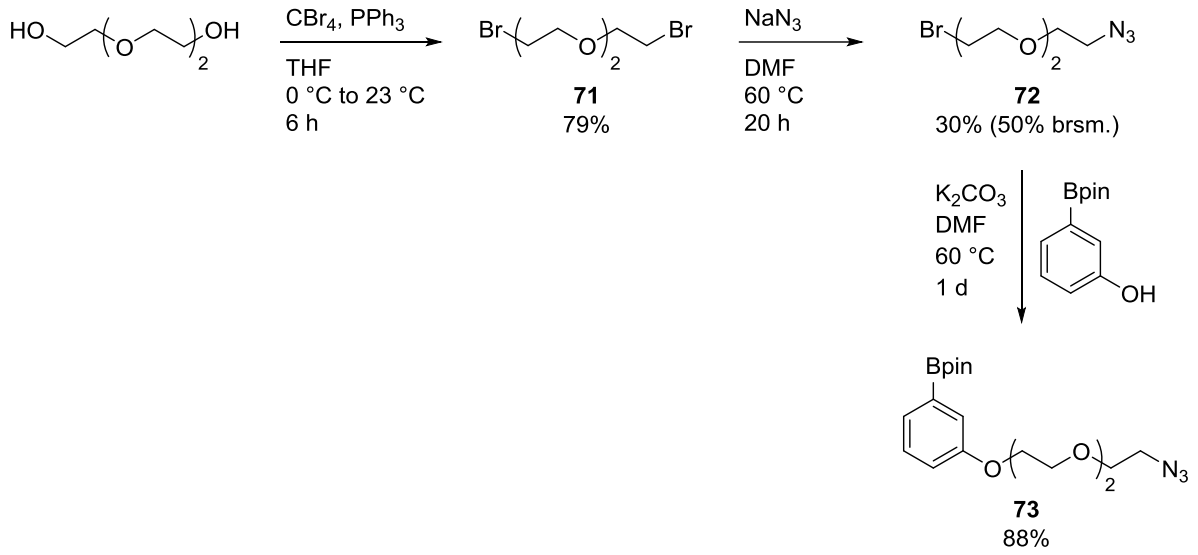

Scheme 14 Synthesis of building block **73**. Double bromination of triethylene glycol under *Appel* conditions afforded **71**. Substitution with sodium azide gave **72** in 30% yield (50% yield based on recovered **71**) that was reacted with 3-hydroxyphenylboronic acid pinacol ester to give **73**.

After the successful synthesis of **59**, cross-coupling with functionalized benzothiophenone **52** to **74** was attempted (Scheme 15).

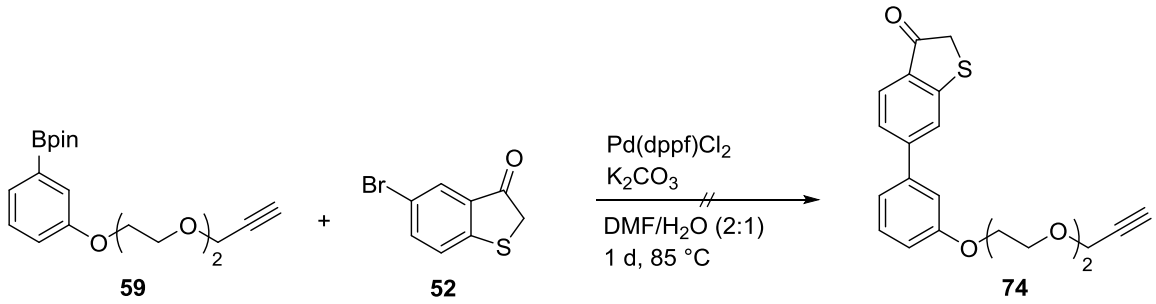

Scheme 15 Attempted *Suzuki-Miyaura* cross-coupling of building block **59** with benzothiophenone **52**. Decomposition of the starting materials was observed and no product was formed.

Reaction of the compounds in DMF/H_2O with Pd(dppf)Cl_2 as catalyst in the presence of K_2CO_3 resulted in quantitative decomposition of organic material as judged by TLC. Simultaneous precipitation of solid compounds was observed. It is commonly known that benzothiophenone and its analogs readily react to the respective thioindigo derivatives or decompose under unsuitable reaction conditions. As a result this route was not pursued further.

As the reactivity of benzothiophenone **52** that causes the unwanted side reactions stems most likely from the acidic alkyl position *alpha* to the carbonyl the respective HTI (**75**) was considered a more robust substrate for the attempted cross-coupling reaction. To this end the *Lewis* acid promoted condensation reaction had to be optimized as discussed earlier. With the required compounds already at hand, condensation was attempted applying the reaction conditions used in the synthesis of the original HTI motor (Scheme 16). However, treating a solution of benzothiophenone **52** and indanone **56** in CH_2Cl_2 with $BF_3 \cdot OEt_2$ did not show any conversion on GC-MS or TLC and the majority of the indanone **56** could be recovered.

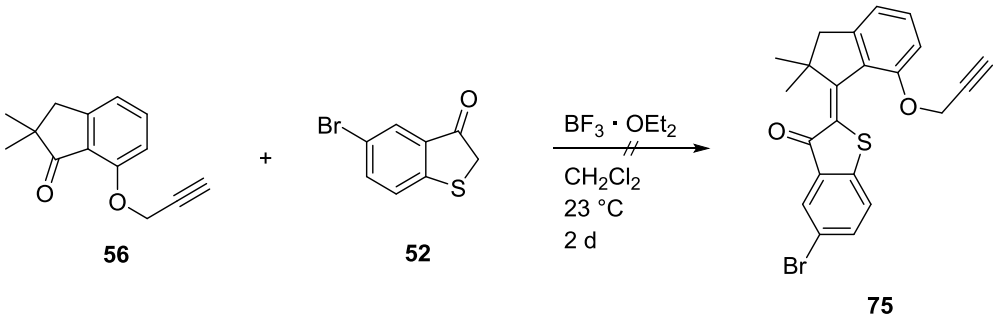

Scheme 16 Attempted condensation of benzothiophenone **52** with indanone **56** using $BF_3 \cdot OEt_2$. No formation of HTI **75** could be observed. Only the *Z* configured isomer is shown.

Based on these results the reaction was reattempted with the stronger *Lewis* acid BCl_3 (1 M solution in heptane). This time the solution quickly turned orange within minutes indicating the successful construction of the HTI chromophore. GC-MS analysis revealed small amounts of product and an orange colored reaction product on the TLC plate could easily be spotted with the naked eye. The reaction was monitored further for a total of 24 h. GC-MS and TLC analyses suggested that reaction times exceeding one hour do not result in higher yields, instead decomposition of starting materials and potentially also product was observed. Because of this, isolation of the target compound was not possible under these reaction conditions.

For the next attempt the reaction time was cut to six hours and the equivalents of BCl_3 were reduced from five to one. HTI **75** was obtained in 5% yield and the structure was confirmed by NMR and HRMS analysis. Changing the solvent of the BCl_3 solution had no observable effect on the product yield (Table 3). Increasing the equivalents of the *Lewis* acid resulted in a byproduct, which was attributed to the deprotected/defunctionalized indanone, explaining the observed decomposition when multiple equivalents of BCl_3 were used. This is not surprising as cleavage of phenolic ethers with *Lewis* acids is well known in the literature and cleaving of

propargyl ethers can occur much faster compared to methyl ethers.[80] To further suppress this undesired side reaction the temperature was lowered to –78 °C for the addition of BCl_3. TLC monitoring of the reaction showed fast reaction and no observable progress for reaction times exceeding five minutes. Interestingly, indanone ether **56** can be selectively cleaved in the presence of benzothiophenone **52** at –78 °C when the BCl_3 solution is cooled below 0 °C before addition. This can be realized by slow addition of the *Lewis* acid over the inside of the flask (which is already cooled to –78 °C), allowing it to cool down before coming in contact with the solution containing the starting materials. When the reaction was attempted in toluene only traces of product were observed. Taken together the results indicate that the condensation reaction proceeds very fast and is accompanied by a slower side reaction that cleaves the aryl ether, which is the major cause of product loss. To prevent local oversaturation with *Lewis* acid upon addition and to minimize the side reaction of indanone **56** with BCl_3, a solution of benzothiophenone **52** was premixed with one equivalent of the *Lewis* acid at –78 °C and the mixture was immediately transferred to a solution of the indanone, which was prepared in a separate flask and held at –78 °C. The reaction mixture immediately turned to a very dark red and the reaction was stopped after five minutes. Workup afforded HTI **75** in 53% yield enabling this route to be employed in the total synthesis of macrocyclic HTIs.

Table 3 Reaction conditions for the condensation of benzothiophenone **52** with indanone **56** to HTI **75**. The *Lewis* acid BCl_3 was used as a 1.0 M solution with the respective solvent given in brackets.

***Lewis* acid**	**eq**	**solvent**	**temp.**	**time**	**yield**
$BF_3 \cdot OEt_2$	5.0	CH_2Cl_2	23 °C	18 h	–
BCl_3 (heptane)	5.0	CH_2Cl_2	0 °C	1 d	traces
BCl_3 (heptane)	1.0	CH_2Cl_2	–78 °C	6 h	5%
BCl_3 (CH_2Cl_2)	1.0	CH_2Cl_2	–78 °C	7.5 h	8%
BCl_3 (Toluene)	1.0	CH_2Cl_2	–78 °C	3 h	(25%)*
BCl_3 (Toluene)	2.0	toluene	–78 °C	1 h	traces
BCl_3 (Toluene)	1.0	CH_2Cl_2	–78 °C	5 min	53%

*crude product with significant amounts of impurities as judged by ^{1}H NMR

During the optimization process it was also attempted to premix the BCl_3 solution at 0 °C with benzothiophenone **52** before addition to the indanone solution. These conditions were tested

using indanone **57** and afforded HTI **76** in 28% yield (Scheme 17). Because the product was not required in greater amounts, synthesis of **76** was not repeated under the optimized reaction conditions (premixing at –78 °C).

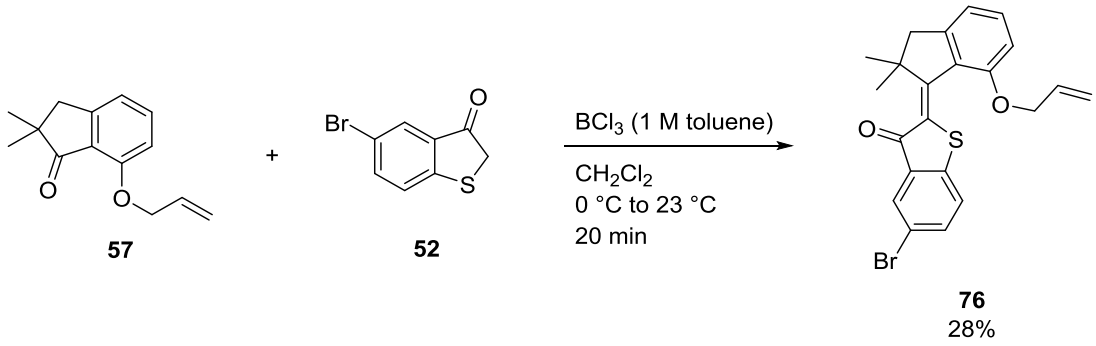

Scheme 17 Condensation of indanone **57** with benzothiophenone **52** at 0 °C using BCl_3 (1.0 M in toluene). The yield for this reaction was 28% and has not been repeated under the optimized reaction conditions. Only the *Z* configured isomer is shown.

Next, cross-coupling of HTI **75** with building block **73** was attempted (Scheme 18). The azide and propargyl substituents provide the necessary functional groups to subsequently close the macrocycle in a 1,3-dipolar cycloaddition.

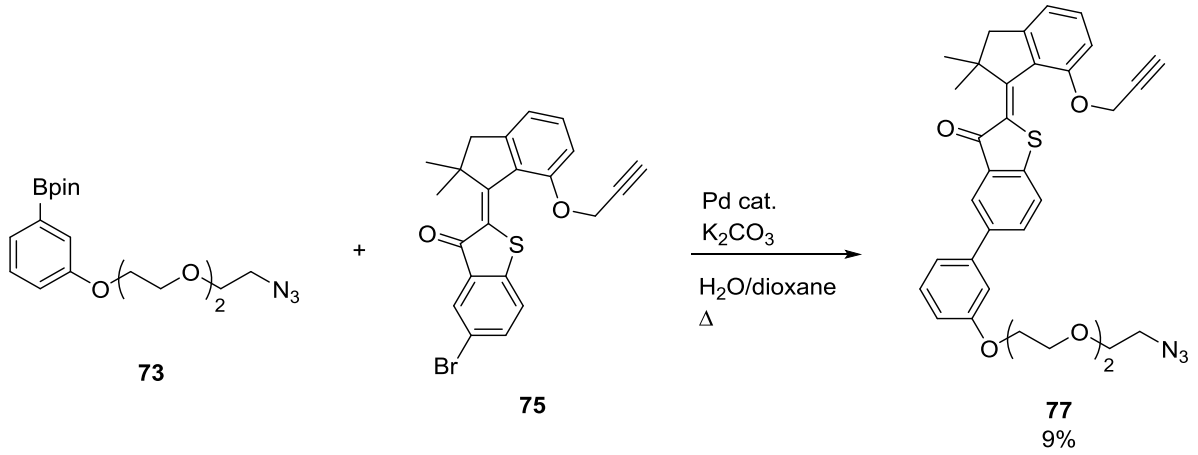

Scheme 18 Attempted *Suzuki-Miyaura* cross-coupling of building block **73** with HTI **75**. Biphenyl **77** was obtained in 9% yield under optimized reaction conditions. Only the *Z* configured isomers are shown.

First attempts were carried out in H_2O:Dioxan (2:1) with K_2CO_3 as base at elevated temperatures. $Pd(PPh_3)_4$ and $Pd(dppf)Cl_2$ were used as catalyst. TLC monitoring showed onset of decomposition after one hour with complete decomposition after 8 h at 90 °C. These results prompted the screening of more sophisticated palladium catalysts and traces of the product

could be observed on TLC for several reaction mixtures. See Table 4 for an overview of applied conditions.

Table 4 Reaction conditions applied to the palladium catalyzed cross-coupling of HTI **75** with one equivalent of boronic acid pinacol ester **73** and three equivalents of K_2CO_3.

catalyst	**ligand**	**eq**	**solvent H_2O:dioxan**	**temp.**	**time**	**product formation**
$Pd(PPh_3)_4$	–	5 mol%	2:1	90 °C	18 h	–
$Pd(dppf)Cl_2$	–	5 mol%	1:5	90 °C	1 d	–
sSPhos Pd G2	–	2 mol%	1:5	60 °C	16 h	✓
$Pd(amphos)Cl_2$	–	2 mol%	1:5	60 °C	16 h	–
PEPPSI™-IPr	–	2 mol%	1:5	60 °C	16 h	✓
PEPPSI™-IPent	–	2 mol%	1:5	60 °C	16 h	✓
$Pd_2(dba)_3$	SPhos	5/15 mol%	1:5	60 °C	16 h	–
PEPPSI™-IPr	–	1 mol%	1 drop water	40 °C	1 d	✓
PEPPSI™-IPr	–	6 mol%	1 drop water	40 °C	1 d	✓

The most promising results were obtained from reactions using Pd-PEPPSI™-IPr and Pd-PEPPSI™-IPent catalysts as they showed full conversion of the starting material and the most evident traces of product as judged by TLC. Still, decomposition was the predominantly observed reaction. Because of the small scale all reactions were worked up together. This way sufficient amounts of product were obtained to confirm the structure of **77**. Additional attempts using Pd-PEPPSI™-IPr at lower temperatures (40 °C) did not prevent decomposition and identical results were obtained. Because of the small total amount of isolated product (2.7 mg) the subsequent intramolecular cycloaddition was not carried out.

Cross-coupling of the allyl functionalized building block **63** and HTI **76** was attempted using palladium based catalysts and K_2CO_3 as base in DMF at room temperature and elevated temperatures (Scheme 19).

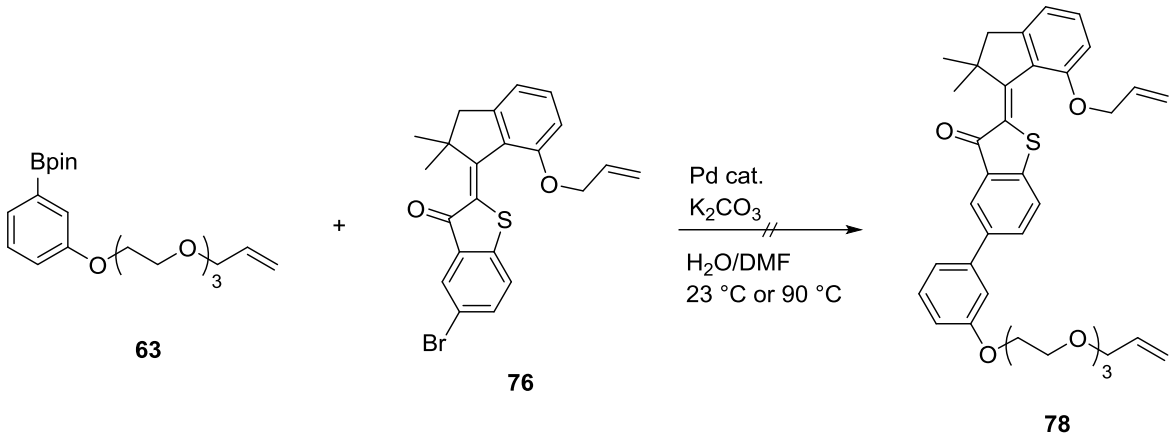

Scheme 19 Attempted *Suzuki-Miyaura* cross-coupling of building block **63** with HTI **76**. The product **78** could not be isolated. Only the *Z* configured isomers are shown.

In the first attempt the starting materials were reacted at 90 °C with $Pd(PPh_3)_4$ in DMF with an additional drop of water. After nine hours complete decomposition had occurred, with no visible traces of the potential product. The reaction was repeated at 23 °C but workup did not afford any detectable product after one day. The reaction was repeated with a variety of catalysts and monitored for a total of three days but apart from decomposition no product formation could be observed (Table 5).

Table 5 Reaction conditions applied to the palladium catalyzed cross-coupling of HTI **76** with one equivalent of boronic acid pinacol ester **63**. Three equivalents of K_2CO_3 were used. DMF was used as solvent and water was added to promote boronic ester hydrolysis.

catalyst	**ligand**	**eq**	**solvent H_2O:DMF**	**temp.**	**time**	**product formation**
$Pd(PPh_3)_4$	–	10 mol%	1 drop water	90 °C	9 h	–
$Pd(PPh_3)_4$	–	10 mol%	DMF	23 °C	3 d	–
PEPPSI™-IPr	–	10 mol%	1 drop water	23 °C	3 d	–
sSPhos Pd G2	–	10 mol%	1 drop water	23 °C	3 d	–
$Pd(dppf)Cl_2$	–	10 mol%	1 drop water	23 °C	3 d	–
PEPPSI™-IPent	–	10 mol%	1 drop water	23 °C	3 d	–
$Pd_2(dba)_3$	SPhos	5/15 mol%	1 drop water	23 °C	3 d	–

In conclusion cross coupling reactions between HTI **75** and boronic acid **73** as well as between HTI **76** and boronic acid **63** predominantly lead to decomposition of the starting materials. This might be due to many possible interactions of the palladium catalyst with functional groups of the reagents, especially complexation of allylic and propargylic ethers as well as the central double bond and adjacent carbonyl and/or sulfide might lead to unpredictable interactions. Therefore, cross-coupling reactions between these two building blocks were not pursued further.

With several approaches to assemble the macrocycle already ruled out, copper catalyzed 1,3-dipolar cycloaddition of azide functionalized building block **73** and propargyl functionalized HTI **75** was attempted. This reaction allowed to test the general feasibility of the reaction with the prepared compounds and to potentially facilitate subsequent cross-coupling by preorganizing the reagents in an intramolecular fashion. In addition, side reactions of the unsaturated alkyl ether functional groups might be prevented in the palladium catalyzed cross-coupling reaction that has emerged as the key step.

A common approach to 1,3-dipolar cycloadditions uses copper(II) sulfate as source for the active Cu(I) catalyst, which is generated *in situ* through reduction by sodium ascorbate. A successful reaction would allow implementation of this step in the total synthesis in a very versatile and affordable fashion compared to use of sophisticated Cu(I) catalysts.

The starting materials were suspended in H_2O/*t*BuOH and catalytical amounts of $CuSO_4 \cdot 5\ H_2O$ (2 mol%) and sodium ascorbate (10 mol%) were added. Upon workup mostly starting materials were recovered which was attributed to the low solubility of the reactants. As a consequence DMF was used as solvent and the reaction was repeated under identical conditions. This time complete conversion of the starting materials was observed after one day as judged by TLC monitoring (Scheme 20).

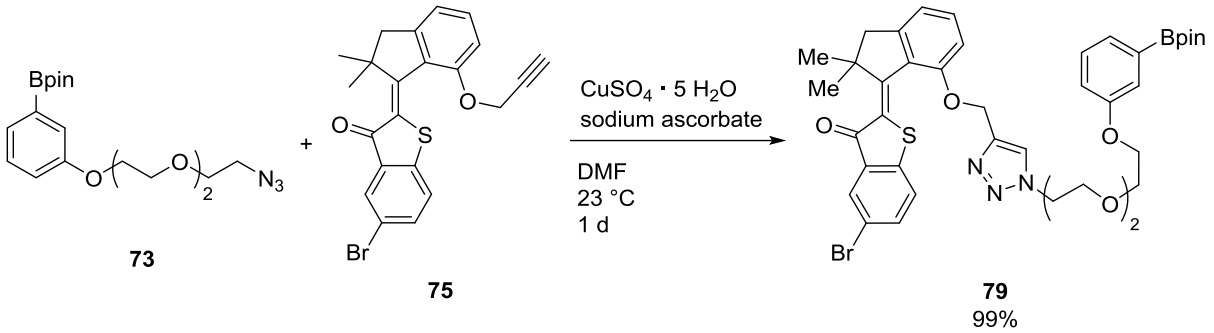

Scheme 20 Copper catalyzed 1,3-dipolar cycloaddition of boronic acid pinacol ester **73** and HTI **75**. $CuSO_4 \cdot 5H_2O$ (2 mol%) and sodium ascorbate (10 mol%) were used to generate the catalytically active Cu(I) species *in situ*. A mixture of *Z* and *E* configured boronic esters and their corresponding hydrolyzed boronic acids was obtained that translates to an excellent overall yield for the boronated species. Only the *Z* configured isomers are shown.

A pair of orange colored product spots were observed on TLC which were assigned to *E* and *Z* configured **79**, accompanied by an additional pair of orange compounds which were attributed to the hydrolyzed *E* and *Z* configured products. This is in agreement with the observations from synthesis of **73** (and analogous building blocks) where partial hydrolysis of the boronic ester had occurred. The polarity of the potential products drastically increased, which is characteristic for this reaction and stems from the newly established 1,4-triazol moiety. The presence of two isomers (*E* and *Z*) along with the hydrolyzed products did not allow separation and in depth analysis of the compounds. However, due to the highly increased polarity flash column chromatography was used to separate the product mixture from apolar impurities. This way a boronated product mixture was obtained that would translate to excellent yields (99%). HRMS confirmed the identity of the target compounds.

Due to these excellent results ring-closing metathesis of the previously prepared alkenes **63** and **76** was not attempted. Instead, intramolecular cross-coupling reactions were conducted to obtain macrocycle **80** (Scheme 21). $Pd(PPh_3)_4$ was used as catalyst together with K_2CO_3 at elevated temperatures, which is a common approach to assess the feasibility of the reaction before screening of more sophisticated catalysts and a general optimization of reaction conditions.

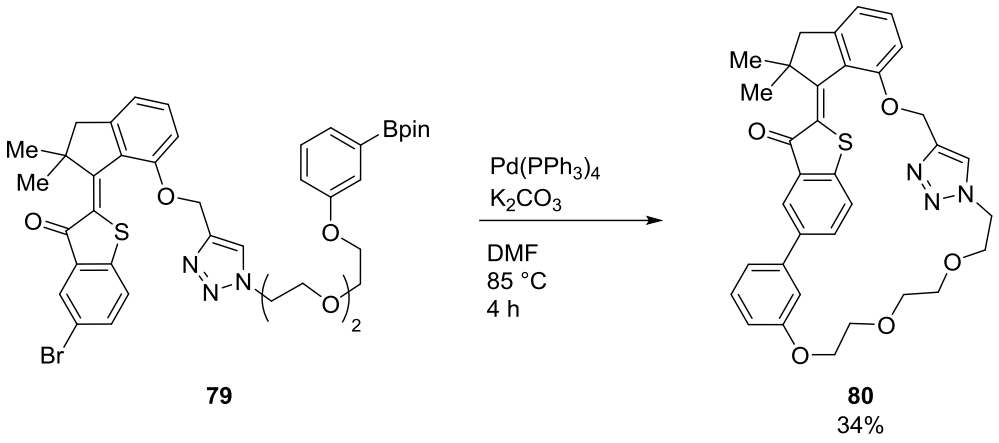

Scheme 21 Intramolecular *Suzuki-Miyaura* cross-coupling of **79** afforded macrocycle **80**. Only the *Z* configured isomers are shown.

The product **80** was obtained in 34% yield, which was very encouraging given the many failed attempts when *Suzuki-Miyaura* couplings were applied in earlier stages of the synthesis. Also, palladium catalyzed coupling reactions are somewhat unusual for macrocyclic ring closure and this approach was therefore not considered as an option initially.

Not surprisingly an indefinite number of byproducts was observed that is readily explained by intermolecular side reactions, which result in polymerization or macrocycles containing multiple units of the starting compound when the polymerization is terminated by ring closing. To prevent polymerization the reaction was conducted in tenfold dilution but no significant change in terms of yield was observed. Isolation of compound **80** from the polymerization byproducts posed a challenge but could be realized by two consecutive separations by flash column chromatography using two different solvent mixtures. To further facilitate separation from byproducts the reaction time was extended to one day. This was supposed to guarantee a complete conversion of reactive intermediates (e.g. dimers) to polymers or macrocycles that are more readily removed upon workup. However, the efficiency of this approach was not further evaluated.

In the concluding step the sulfide **80** was oxidized to the corresponding sulfoxide **81** using sodium perborate tetrahydrate, which is a versatile alternative to hydrogen peroxide that is commonly applied in this type of reaction (Scheme 22).[81] In combination with acetic acid the oxidation strength is increased further and the reaction proceeds via a peracetic intermediate.[82] Monitoring of the reaction is crucial when multiple equivalents of perborate are used as oxidation will continue to the respective sulfone.

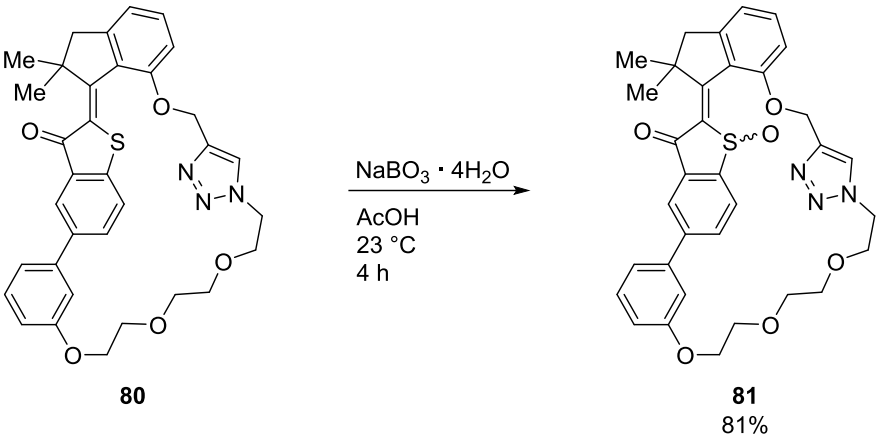

Scheme 22 Oxidation of **80** to sulfoxide **81** using sodium perborate tetrahydrate in acetic acid. The target compound was obtained in good yields. Only the *Z* configured isomers are shown.

The oxidation afforded the target macrocycle **81** in good yields. With this the first integration of a molecular motor fragment into a macrocyclic compound, connecting rotor and stator part, was realized. Next, extensive studies should reveal the working mechanism of the molecular machine in detail.

3.4 Structure of HTI 81

The target molecule **81** can be divided into the four fragments, stator, rotor, linker and follower/receiver (Figure 32). It is constructed in a way that conformational changes around the central double bond are transmitted to an aryl via a PEG-type linker, which is covalently attached to the rotor. This aryl is furthermore connected to the stator fragment to establish a biaryl reporter unit. The construction of the biaryl unit was carried out, avoiding substitutents in *ortho* positions adjacent to the connecting single bond to guarantee free rotation. This way a passive follower unit is realized, which experiences conformational changes depending on the geometry around the central double bond. Consequently, this stereoinformation is also reflected in a tilt around the biaryl axis, which can be used for the stepwise detection of the transmitted unidirectional motion.

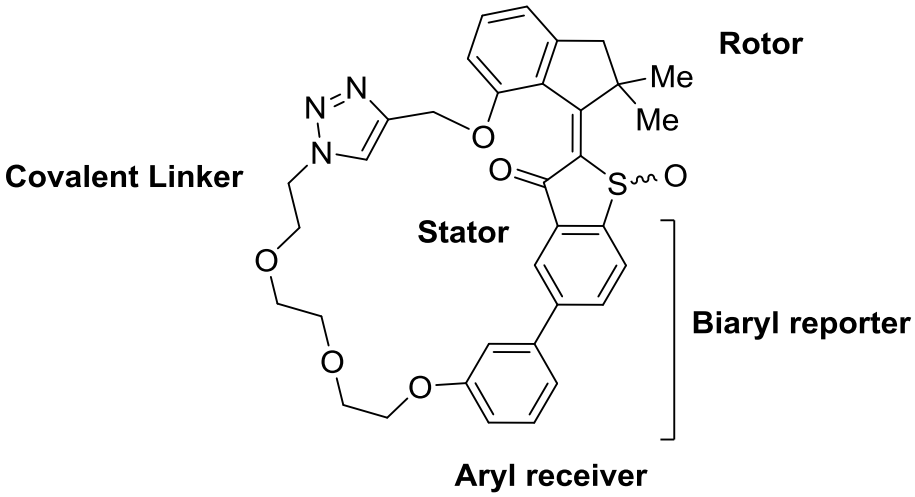

Figure 32 Synthetically realized molecular machine **81** derived from the proposed design (described in section 3.1).

The structure of **81**, including all observable conformers, was elucidated by a combination of methods including crystallographic data obtained from single crystal X-ray diffraction, 2D NMR experiments, UV-Vis spectroscopy as well as ECD spectroscopy. It was further supported by a comprehensive quantum chemical analysis. The theoretical assessment of **81** was conducted by *Stefan Thumser*. For an in depth analysis and additional information also see the literature.[83] Experiments were conducted in CH_2Cl_2 if not stated otherwise as it offers excellent solubility, a favorable range of temperatures for experiments (40 °C to –96 °C) as well as residual NMR signals of deuterated CD_2Cl_2 that are likely not to interfere with indicative signals of **81** including all its conformers.

3.4.1 Structure of *E*-81 in the crystalline state

The macrocycle **81** possesses several stereogenic elements that can be analyzed in solution by complementary use of 2D NMR experiments and ECD spectroscopy and in the crystalline state by single crystal X-ray diffraction. These elements are the *R* or *S* configured sulfoxide, *P* or *M* helicity around the central double bond – which is either *E* or *Z* configured – and the biaryl unit with axial R_a or S_a chirality.

The described synthesis afforded compound **81** purely in its *E* isomeric form. Crystals suitable for single crystal X-ray diffraction were obtained from a racemic mixture. In Figure 33 the *E*-(*R*)-(*M*)-(S_a) configured isomer is shown. The crystal data confirmed the configuration of the central double bond. The helicity of the motor unit in combination with the configuration of the

adjacent sulfoxide is in agreement with the original HTI based molecular motor where an *R* configured sulfoxide resulted in *M* helicity of the stable *E* configured isomer and *vice versa*. The indanone fragment and the aryl follower are tilted out of the benzothiophenone plane counterclockwise (the viewing direction is defined as the *follower* to *stator* to *rotor* direction) with a torsion angle of –14° around the central double bond and a corresponding tilt of 44° around the biaryl single bond. This indicates a biaryl geometry that is determined by the rotor fragment. However, the biaryl tilt can also be a result of crystal packing effects and additional experiments are required to elucidate the structure in solution.

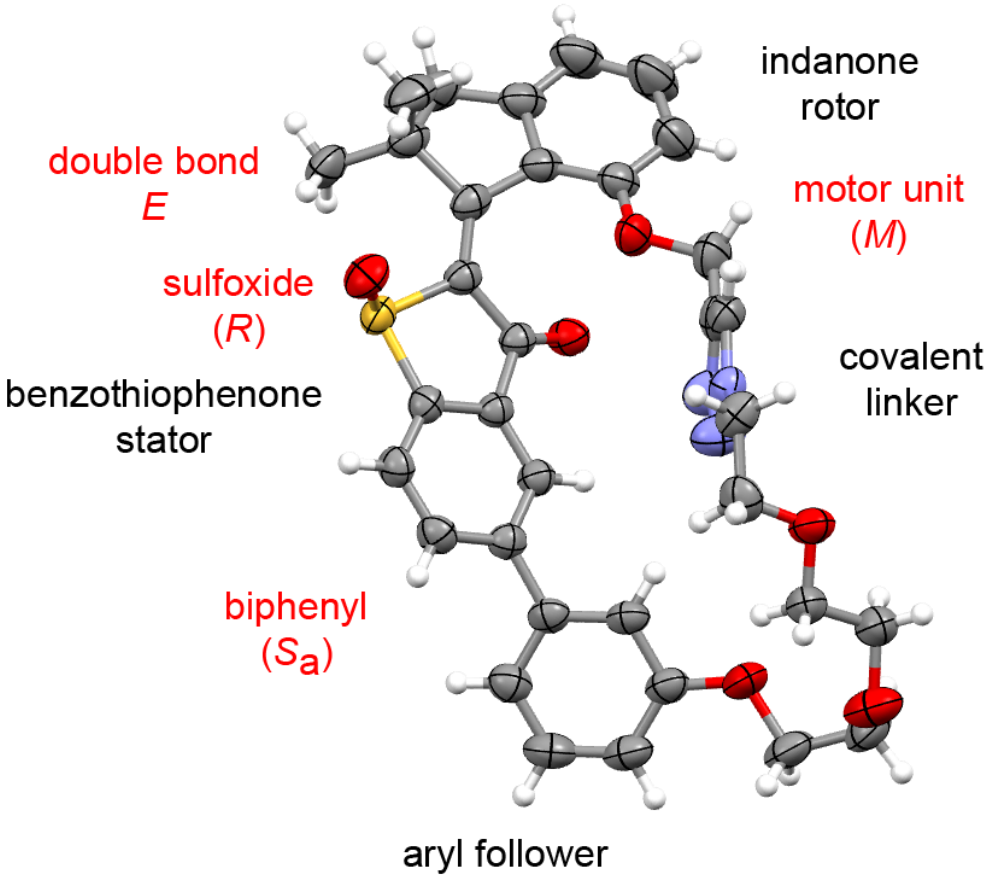

Figure 33 Structure of racemic *E*-**81** in the crystalline state (50% probability ellipsoids). Assignments of stereodescriptors are given in red. Only the *E*-(*R*)-(*M*)-(S_a) isomer is shown. The indanone rotor and aryl follower are tilted counterclockwise out of the plane indicating a biaryl tilt whicht reflects the geometry of the motor unit.

3.4.2 Structure of *E*-81 in solution

For assignments of ^{1}H and ^{13}C signals and a detailed analysis of 2D NMR experiments see the corresponding publication.[83] The NOESY NMR experiment is an important tool to elucidate the three dimensional structure of molecules in solution. For *E*-**81** this includes the configuration of the central double bond, the tilt of the biaryl axis and the chain geometry/position in relation to the other fragments. The 2D NOESY NMR experiment is based on dipole-dipole interactions and stands out methodically due to its ability to reveal protons that are in spatial proximity. Different to most NMR methods it does not require through-bond scalar coupling. This can be used to support assignment of *E* or *Z* configuration of the central double bond if indicative interactions of the linker chain with one side of the benzothiophenone stator (carbonyl side for the *E* isomer or sulfoxide side for the *Z* conformer) are visible. In addition, a preferential tilt (dihedral angle $\neq \pm 90°$) of the biaryl axis towards one side can be visible. However, the NOESY experiment cannot differentiate between R_a or S_a axial chirality or *R* and *S* configured sulfoxides.

For *E*-**81** in CD_2Cl_2 solution a preferred tilt of the biaryl axis towards the carbonyl side of the benzothiophenone stator is observed (Figure 34). Because of the similarity in chemical shifts of the indicative protons 14 and 16 the cross-signals overlap. However, the maximum intensity of the signals is centered at the junctions with protons 24 and 20, respectively as indicated by black lines in Figure 34. A very weak interaction between the triazole proton 31 and the stator proton 14 confirms an *E* configured central double bond.

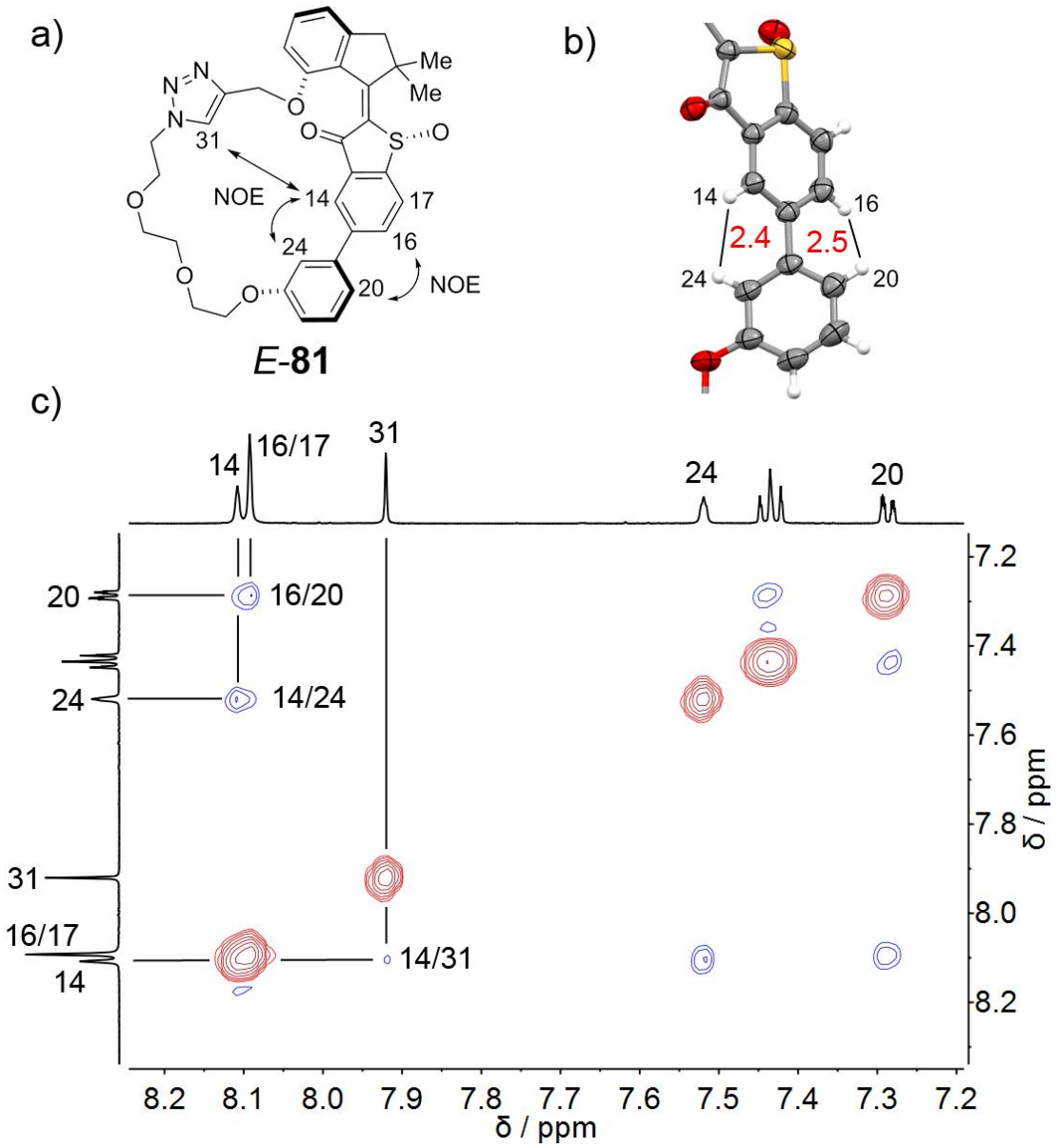

Figure 34 Geometry of *E*-**81** in solution and in the crystalline state. a) Schematic structure of *E*-(*R*)-(*M*)-(*S*$_a$)-**81**. Interacting protons that result in NOESY NMR cross signals are highlighted. b) Detail of the structure of *E*-(*R*)-(*M*)-(*S*$_a$)-**81** in the crystalline state. A preferred tilt of the biaryl axis towards the carbonyl side of the benzothiophenone stator is observed. Distances are given in Å (red numbers). c) NOESY NMR spectrum (CD_2Cl_2, 599 MHz, 27 °C) of the aromatic region of racemic *E*-**81**. Indicative cross signals are highlighted by black lines. Cross signals between protons 14 and 24 as well as 16 and 20 show a preferred tilt of the biaryl axis towards the carbonyl side of the benzothiophenone stator. A very weak interaction between protons 14 and proton 31 supports the assignment of an *E* configured central double bond.

Cross-signals between the covalent linker to both *ortho* protons of the phenol ether attachment site indicate a flexible chain geometry shown in Figure 35. The lack of additional cross-signals between the linker and the stator also suggests an overall flexible chain geometry.

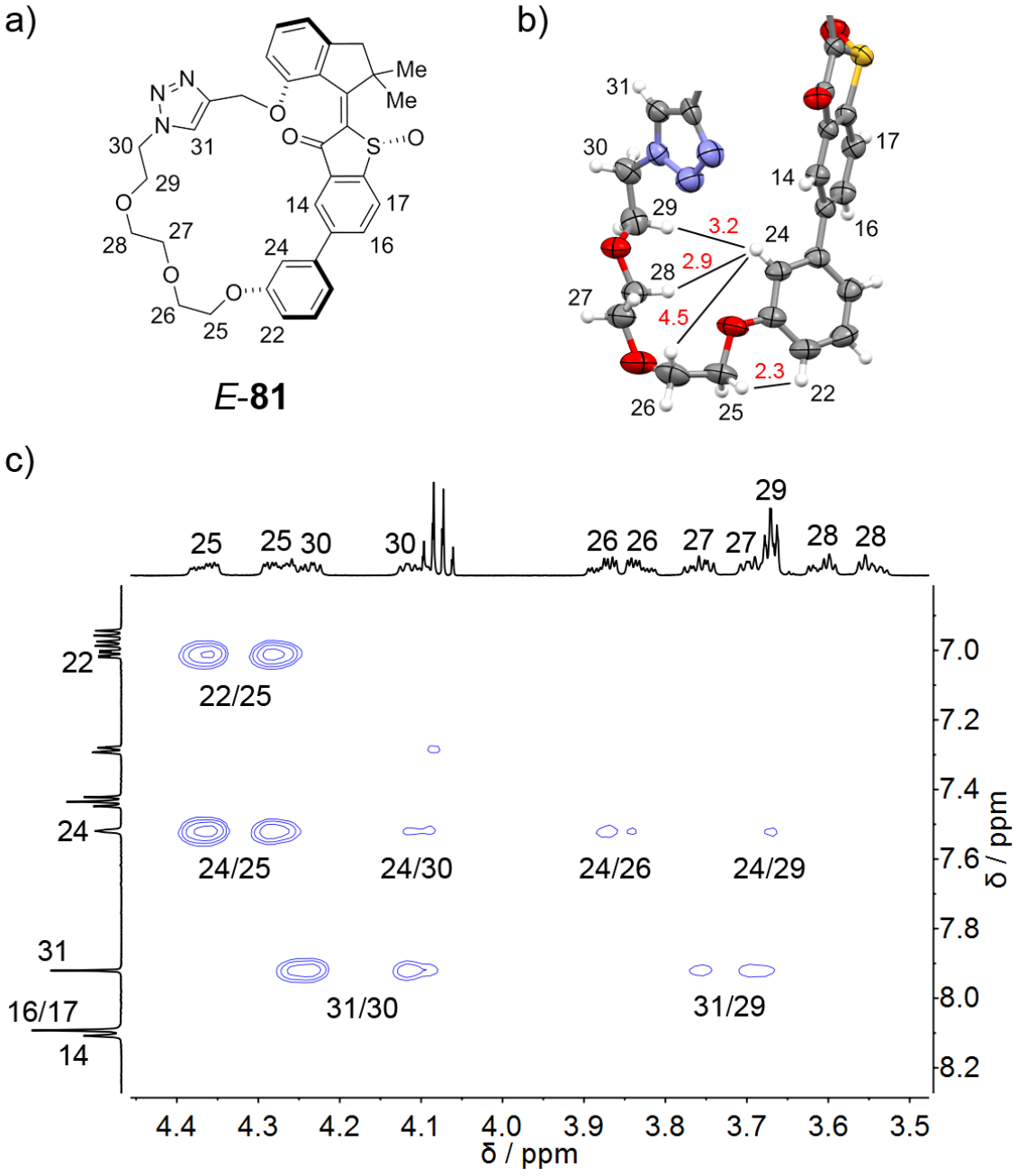

Figure 35 Geometry of *E*-**81** in solution and in the crystalline state. a) Schematic structure of *E*-(*R*)-(*M*)-(S_a)-**81**. b) Detail of the structure of *E*-(*R*)-(*M*)-(S_a)-**81** in the crystalline state. Close proximity of the flexible linker chain and the phenol ether is observed. Distances are given in Å (red numbers). The distance between proton 24 and proton 30 amounts to 5.0 Å (not depicted) c) NOESY NMR spectrum (CD_2Cl_2, 599 MHz, 27 °C) of racemic *E*-**81**. Cross-signals between protons 22 and 25 as well as 24 and 25 are equally visible indicating a flexible chain geometry. Additional weak cross-signals between proton 24 and protons of the covalent linker support assignment of an *E* configured central double bond, since proton 24 is also found to be in proximity to proton 14 and not 16 (see Figure 34 above). No additional cross-signals between protons of the benzothiophenone stator and the covalent linker are observed.

3.4.3 Structure of *Z*-81 in the crystalline state

The *Z* isomer of **81** is obtained when a solution of *E*-**81** is irradiated with light of a certain wavelengths (see chapter 3.4.5). Crystals suitable for single crystal X-ray diffraction were obtained from a racemic *Z*-**81** mixture. In Figure 36 the *Z*-(*R*)-(*M*)-(R_a) configured isomer is shown. The crystal data confirm *Z* configuration of the central double bond. Analogously to the *E* conformer the helicity of the motor unit in combination with the configuration of the adjacent sulfoxide is in agreement with the original HTI motor where an *R* configured sulfoxide results in stable *M* helicity and *vice versa*. The indanone fragment and the aryl follower are tilted out of the benzothiophenone plane counterclockwise with a torsion of –22° around the central double bond, which is reflected in the biaryl tilt with a corresponding angle of 35°.

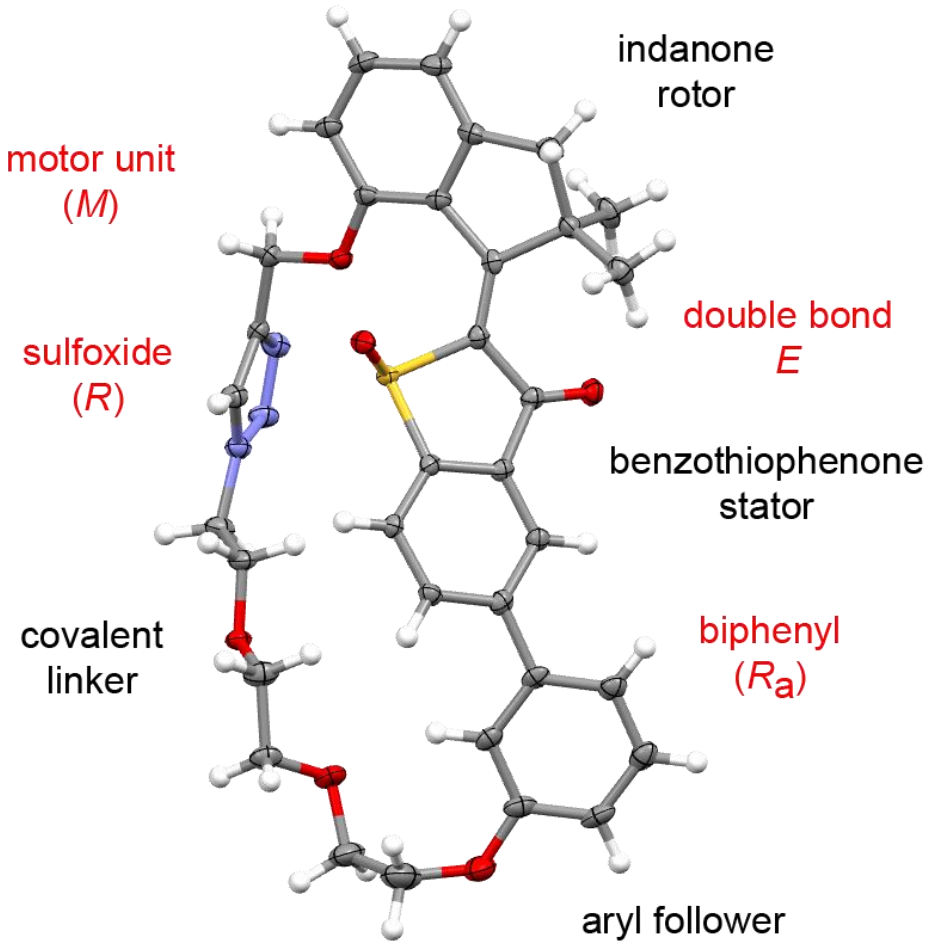

Figure 36 Structure of racemic *Z*-**81** in the crystalline state (50% probability ellipsoids). Assignments of stereodescriptors are given in red. Only the *Z*-(*R*)-(*M*)-(R_a) isomer is shown. The indanone rotor and aryl follower are tilted counterclockwise out of the plane indicating a biaryl tilt which reflects the geometry of the motor unit.

3.4.4 Structure of *Z*-81 in solution

Again, NMR NOESY experiments were conducted to obtain information regarding the tilt of the biaryl axis and the chain geometry in *Z*-**81** (Figure 37).

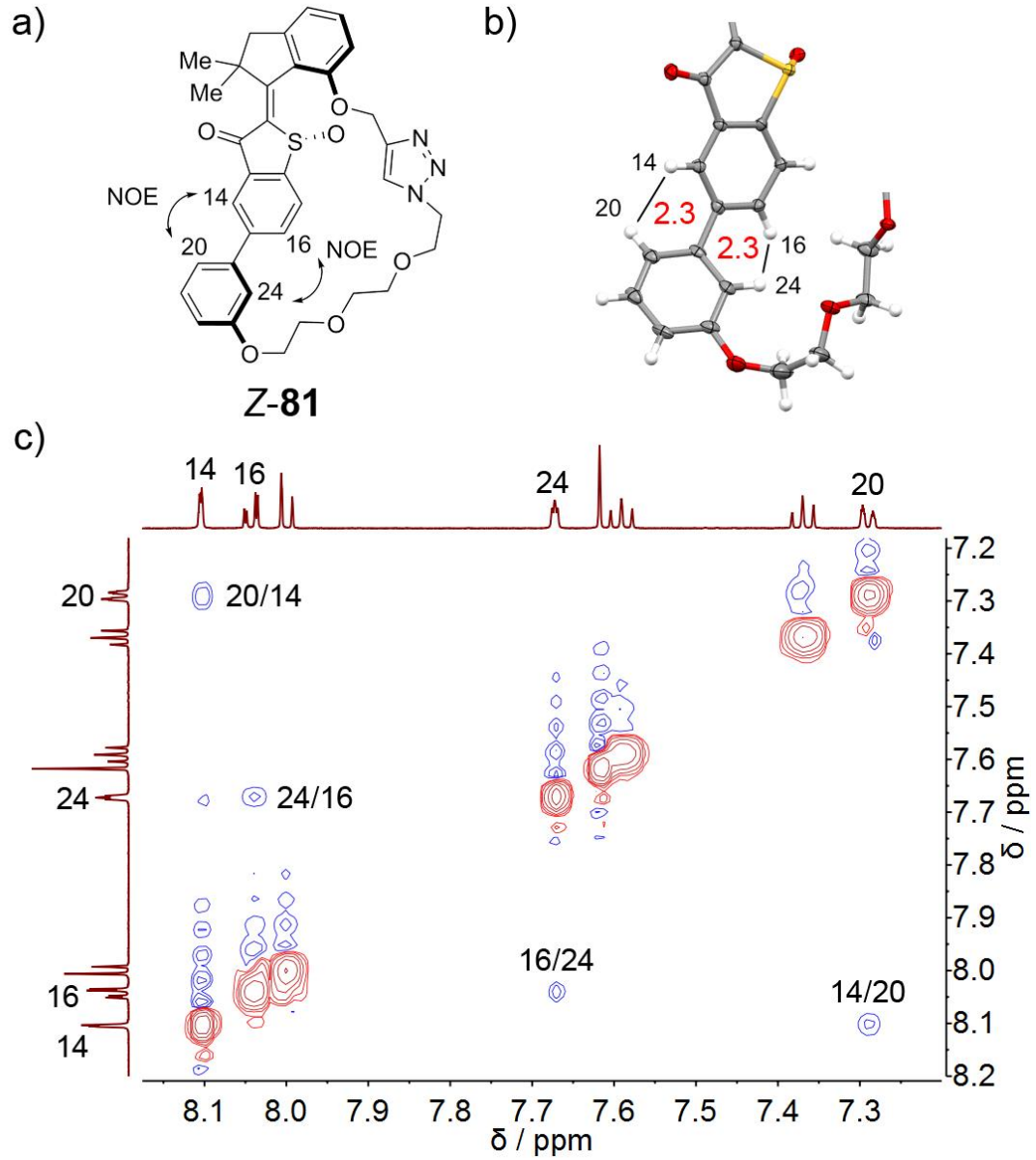

Figure 37 Geometry of *Z*-**81** in solution and in the crystalline state. a) Schematic structure of *Z*-(*R*)-(*M*)-(R_a)-**81**. Interacting protons that result in NOESY NMR cross signals are highlighted. b) Detail of the structure of *Z*-(*R*)-(*M*)-(R_a)-**81** in the crystalline state. A preferred tilt of the biaryl axis towards the sulfoxide side of the benzothiophenone stator is observed. Distances are given in Å (red numbers). c) NOESY NMR spectrum (CD_2Cl_2, 599 MHz, 27 °C) of the aromatic region of racemic *Z*-**81**. Cross signals between protons 14 and 20 as well as 16 and 24 show a preferred tilt of the biaryl axis towards the sulfoxide side of the benzothiophenone stator.

A clear preferential tilt of the aryl follower toward the sulfoxide side of the benzothiophenone stator was observed. This is also reflected in the crystalline state and stands in contrast to the *E*-**81** conformer where the aryl fragment is tilted to the opposite, carbonyl side. Taken together this is a first indication of transmitted motion from the indanone rotor fragment to the aryl follower. Analysis of cross-signals between aryl follower and the attached covalent linker chain show a limited flexibility of the chain. In contrast to *E*-**81** no interactions can be seen for indicative protons 22 and 25 (indicated by red arrows in Figure 38). Also, shorter distances are found between the covalent linker chain and the benzothiophenone stator in the crystalline state. This is reflected in solution by weak cross-signals between protons 16 and 28 as well as protons 17 and 29 (Figure 38). The latter interactions confirm the *Z* configuration of the double bond.

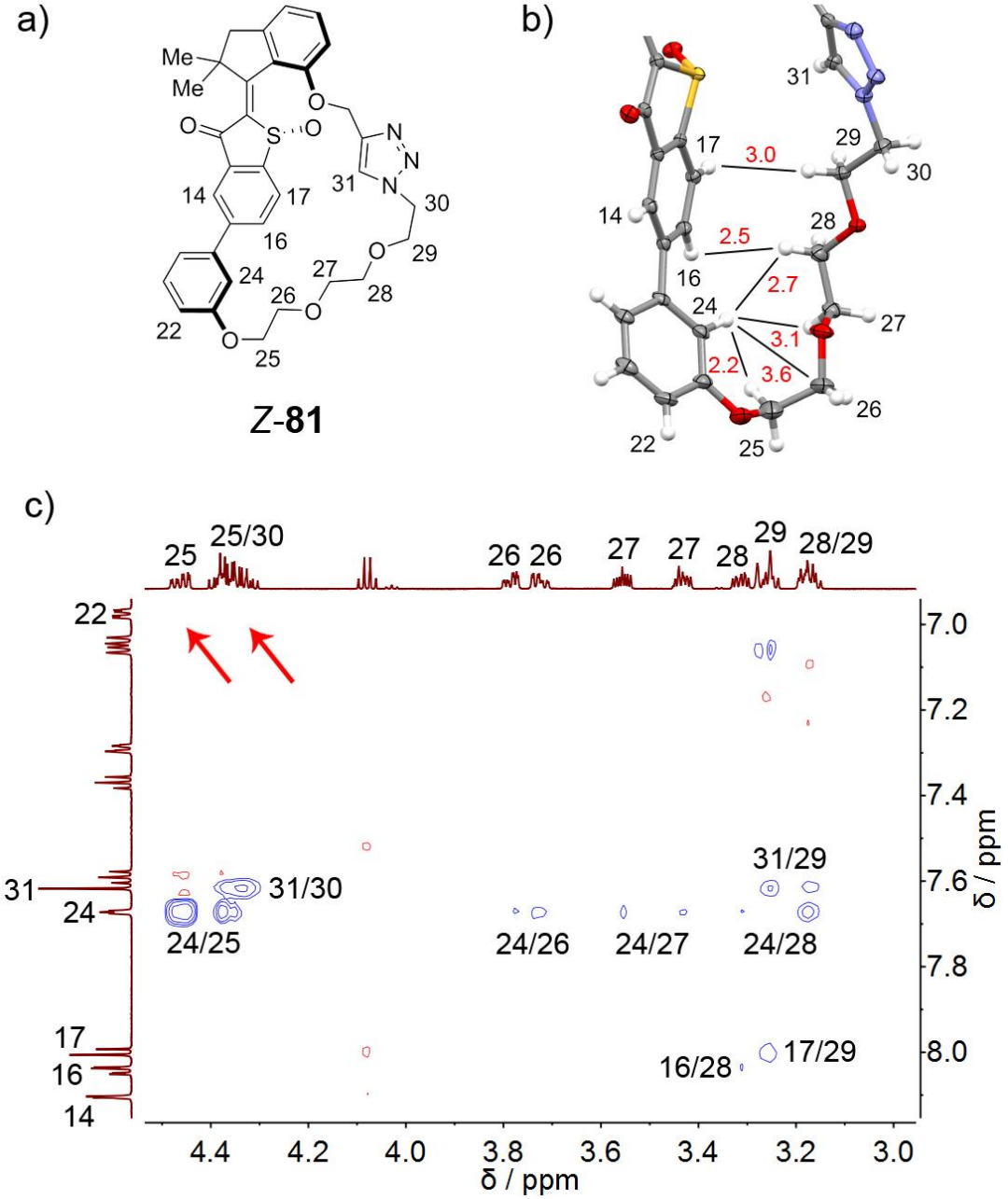

Figure 38 Geometry of *Z*-**81** in solution and in the crystalline state. a) Schematic structure of *Z*-(*R*)-(*M*)-(R_a)-**81**. b) Detail of the structure of *Z*-(*R*)-(*M*)-(R_a)-**81** in the crystalline state. A preferred tilt of the biaryl axis towards the sulfoxide side of the benzothiophenone stator is observed. Distances are given in Å (red numbers). c) NOESY NMR spectrum (CD_2Cl_2, 599 MHz, 27 °C) of racemic *Z*-**81** showing cross-signals between the biphenyl unit and the covalent linker. Cross signals between protons 24 and chain protons 25 to 29 together with missing cross-signals between protons 22 and 25 (red arrows) show a restrained geometry of the covalent linker. This is supported by additional cross-signals between protons 16 and 28 as well as protons 17 and 29.

3.4.5 UV-Vis spectra and molar absorption coefficients of *E*-81 and *Z*-81

The *Z*-**81** isomer is obtained by irradiation of a solution of *E*-**81** in CH_2Cl_2 at room temperature (Figure 39). The highest yield is observed when light with a wavelength of 450 nm is used and the solution is irradiated to the photostationary state (pss).

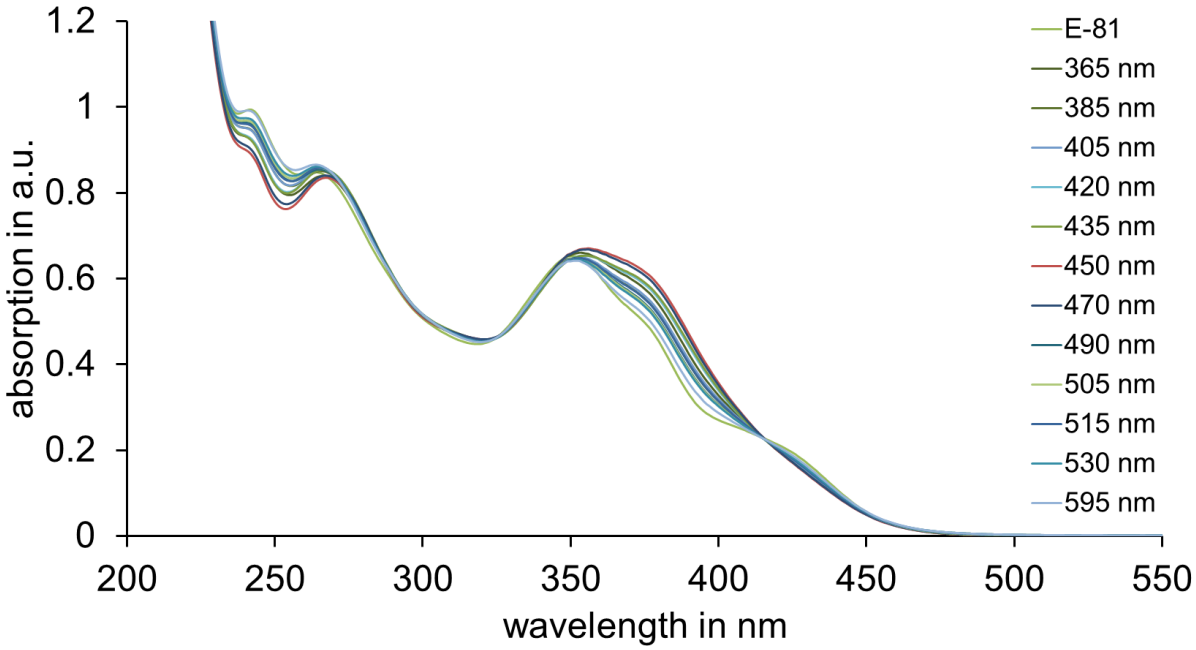

Figure 39 UV-Vis spectra of a solution of *E*-**81** (40 µM, CH_2Cl_2, 23 °C) obtained after irradiation with wavelengths between 365 nm and 595 nm to the pss.

Separation on a preparative HPLC column afforded pure *Z*-**81**, which was analyzed further. UV-Vis absorption spectra of pure *E*-**81** and *Z*-**81** with known concentrations were used to calculate the molar absorption coefficients ε (Figure 40).

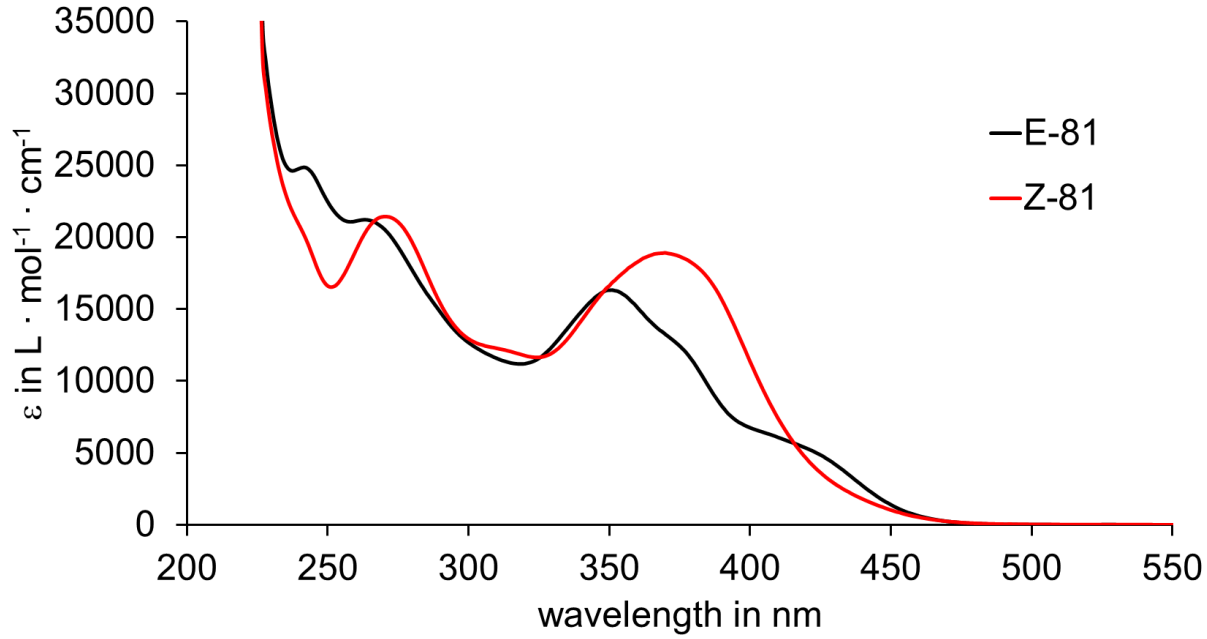

Figure 40 Molar absorption coefficients ε of *E*-**81** and *Z*-**81** (CH_2Cl_2, 23 °C).

3.4.6 Elevated temperature behavior

Due to its boiling point at around 40 °C CD_2Cl_2 was replaced by $(CDCl_2)_2$ (tetrachloroethane) for high temperature NMR experiments. *E*-**81** is the thermodynamically most stable conformer. At elevated temperatures the *Z*-**81** isomer is almost completely (96%) converted to the *E*-**81** isomeric form (Figure 41, top and bottom spectrum).

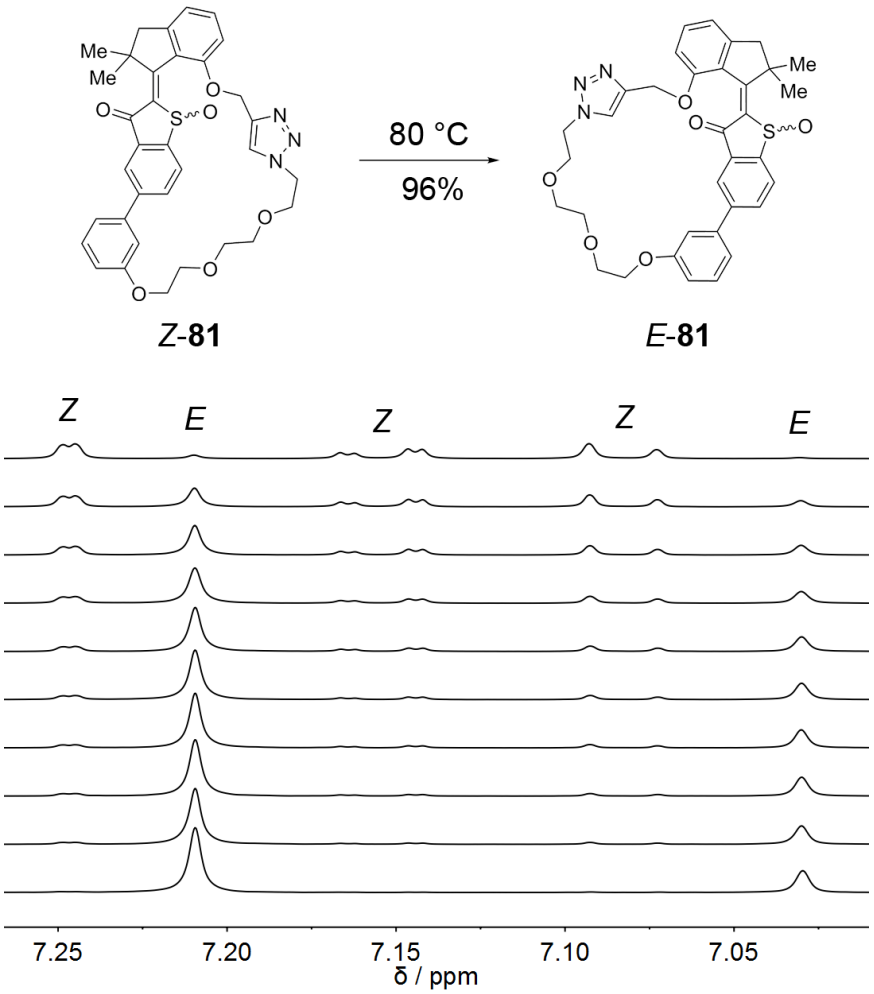

Figure 41 ^{1}H NMR spectra ($(CDCl_2)_2$, 400 MHz, 25 °C) acquired during the thermal conversion of *Z*-**81** to *E*-**81** at 80 °C. Indicative signals of the aromatic region of the *Z* and *E* isomers are shown. The spectra were taken in 30 min intervals and an additional spectrum (bottom) was measured after 16 h to obtain the isomer distribution at equilibrium.

A kinetic analysis was conducted (Figure 42 and Figure 43) to assess the energy barriers associated with thermal *Z* to *E* isomerization of **81**. To this end a *Z*-**81** enriched solution in $(CDCl_2)_2$ was heated to 80 °C and ^{1}H NMR spectra were measured in 30 minute intervals for 6 h in total. After that the solution was heated for 16 more hours at 80 °C to obtain the equilibrium distribution that is 96% *Z*-**81** and 4% *E*-**81**.

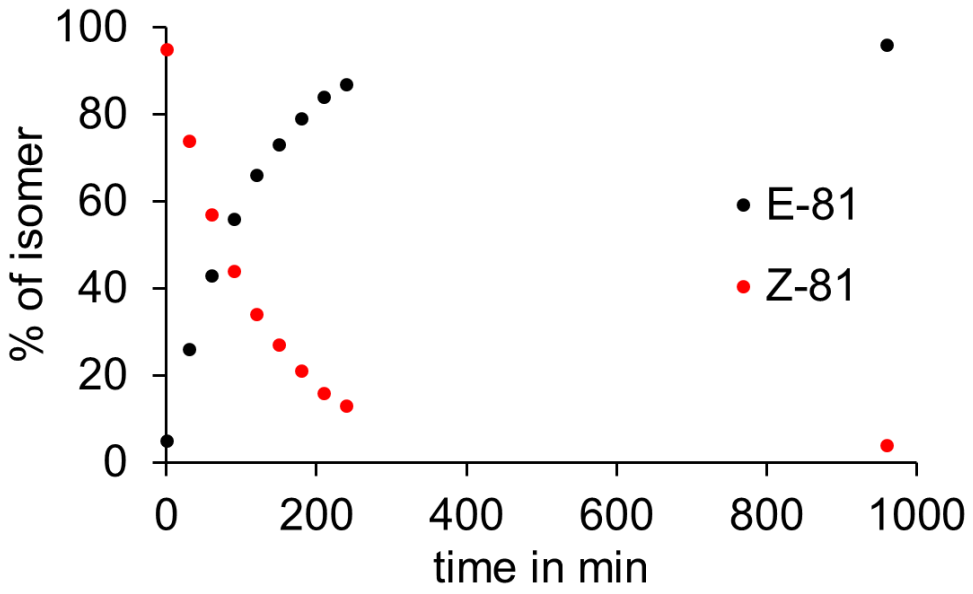

Figure 42 Isomer distribution during the thermal *Z*-**81** to *E*-**81** conversion starting from a $(CDCl_2)_2$ solution containing 95% *Z*-**81** and 5% *E*-**81** and heating in 30 min intervals. After heating for a total of 16 h a stable ratio of 4% *Z*-**81** to 96% *E*-**81** is established.

A first-order rate constant was determined from the thermal decay of the *Z*-**81** isomer. As the thermal conversion does not proceed to 100% the result is a dynamic equilibrium of the two isomerization processes *Z*-**81** to *E*-**81** and *vice versa*, which is described by (equation *3*:

$$\ln\left(\frac{c(Z_0)-c(Z_{eq})}{c(Z_t)-c(Z_{eq})}\right) = \big(k(Z \rightarrow E) + k(E \rightarrow Z)\big) \cdot t \qquad \text{(equation 3)}$$

where $c(Z_0)$ is the initial concentration of the *Z*-**81** isomer, $c(Z_{eq})$ is the concentration of *Z*-**81** at equilibrium, $c(Z_t)$ is the concentration of *Z*-**81** after the elapsed time *t*, $k(Z \rightarrow E)$ is the rate constant of the *Z*-**81** to *E*-**81** isomerization and $k(E \rightarrow Z)$ is the rate constant of the *E*-**81** to *Z*-**81** isomerization.

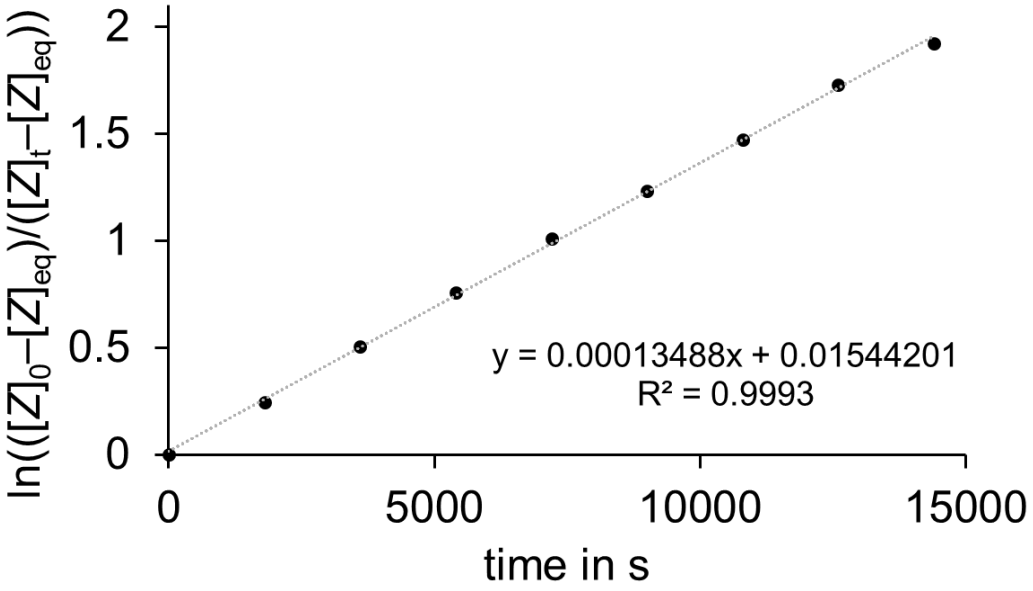

Figure 43 First-order kinetic analysis taking into account the dynamic equilibrium gives a linear relationship. The formula of the linear fit is given in the diagram. The slope m = 0.00013488 is used to calculate the rate constant $k(Z \rightarrow E)$ according to (equation **4)**.

The slope m of the logarithmic function can be used to calculate the rate constant $k(Z \rightarrow E)$ of the thermal *Z*-**81** to *E*-**81** conversion according to (equation 4:

$$k(Z \rightarrow E) = \frac{m}{1 + \frac{c(Z_{eq})}{c(E_{eq})}} \qquad \text{(equation 4)}$$

when taking into account the law of mass action:

$$\frac{c(Z_{eq})}{c(E_{eq})} = \frac{k(E \rightarrow Z)}{k(Z \rightarrow E)} \qquad \text{(equation 5)}$$

The Gibbs free energy of activation $\Delta G^{\ddagger}$ for the thermal *Z*-**81** to *E*-**81** isomerization can be calculated using the *Eyring* equation:

$$k(Z \rightarrow E) = \frac{k_B T}{h} e^{\frac{-\Delta G^{\ddagger}}{RT}} \qquad \text{(equation 6)}$$

where k_B is the Boltzmann constant ($1.381 \cdot 10^{-23}$ J·K^{-1}), T is the temperature in K, h is the Planck constant ($6.626 \cdot 10^{-34}$ J·s) and R is the gas constant (8.314 J·K^{-1}·mol^{-1}).

After rearranging (equation 6 and insertion of the numerical values $\Delta G^{\ddagger}$ is given by:

$$\Delta G^{\ddagger} = 8.314 \cdot T \cdot \left[23.760 + \ln\left(\frac{T}{k(Z \rightarrow E)}\right)\right] \qquad \text{(equation 7)}$$

With the experimentally obtained value for $k(Z \rightarrow E)$ the Gibbs free energy of activation is 27.04 kcal·mol^{-1} for the thermal *Z*-**81** to *E*-**81** isomerization. This translates into a half-live of 1.5 hours at 80 °C or 121 days at 23 °C.

The relative energy difference between *Z*-**81** and *E*-**81** can be calculated from the equilibrium composition (4% *Z*-**81** to 96% *E*-**81**) at 80 °C according to (equation 8:

$$-\Delta G = \ln(K) \cdot R \cdot T \qquad \text{(equation 8)}$$

where K is the equilibrium constant *Z*-**81**/*E*-**81**, R is the gas constant (8.314 J·K^{-1}·mol^{-1}) and T the temperature in K.

With K = 4/96 and T = 353.15 K a $-\Delta G$ of 9.33 kJ·mol^{-1} = 2.23 kcal·mol^{-1} is obtained.

3.5 Elucidation of motor function

The motor fragment of macrocycle **81** reveals the characteristic features of the original HTI motor that were deemed necessary for the unidirectional rotation around the central double bond (Figure 44).

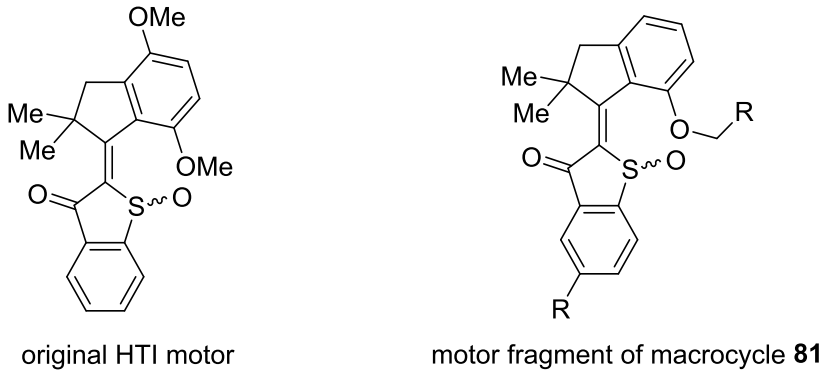

Figure 44 Comparison of the structural features of the original HTI motor and the analogous fragment that is integrated into macrocycle **81**.

In the original setup irradiation of *Z*-(*S*)-(*P*)/*Z*-(*R*)-(*M*) generates the metastable *E*-(*S*)-(*M*)/*E*-(*R*)-(*P*) isomer that is frozen out at low temperatures. The *E*-(*S*)-(*P*)/*E*-(*R*)-(*M*) isomer is obtained after a thermal ratcheting step. It is assumed that photoisomerization from *E*-(*S*)-(*M*)/*E*-(*R*)-(*P*) to *Z*-(*S*)-(*P*)/*Z*-(*R*)-(*M*) proceeds analogously via a *Z*-(*S*)-(*M*)/*Z*-(*R*)-(*P*) intermediate but the energy barrier for this thermal conversion is too low to obtain direct experimental evidence with the available analytical methods. To facilitate understanding, the different conformers of the original motor and its analogs will be termed **A**, **B**, **C**, and **D** as shown in Figure 45.

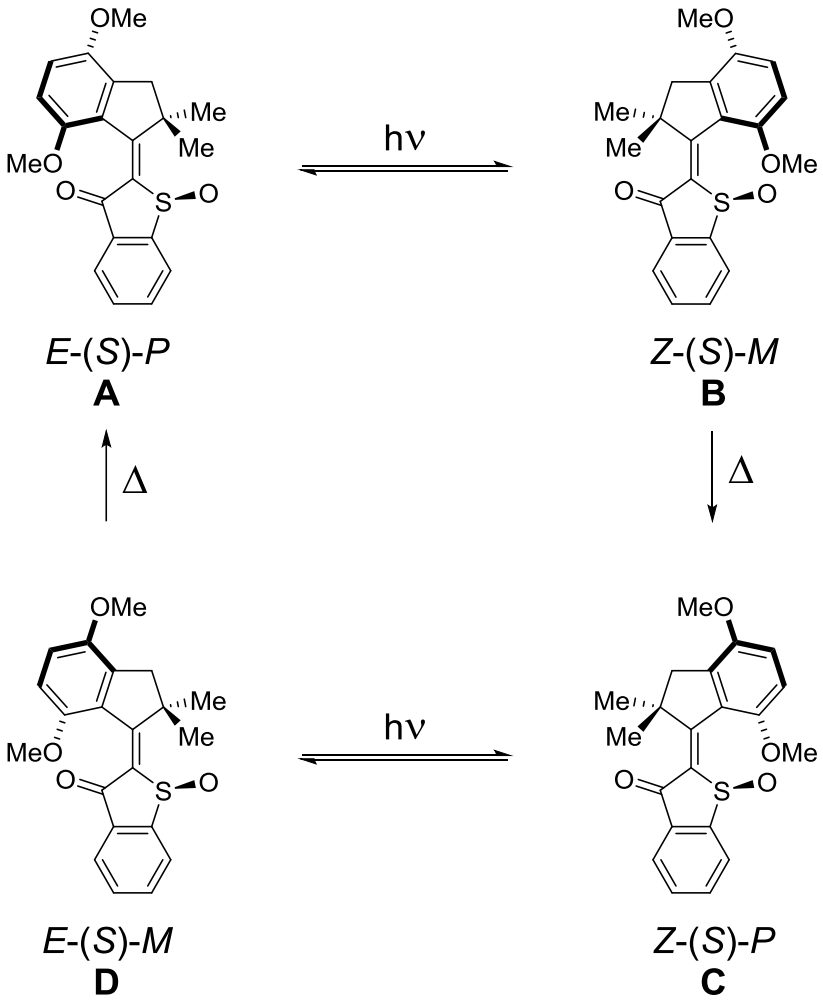

Figure 45 Simplified depiction of the working mechanism of the original HTI motor. Only the conformers with *S* configured sulfoxide are shown. To facilitate understanding the different conformers including their enantiomeric counterparts in racemic mixtures will be termed **A**, **B**, **C**, and **D**.

To confirm the successful implementation of the functional motor analog into the macrocycle, low temperature ^{1}H NMR experiments with simultaneous irradiation were carried out. To this end a solution of **C-81** in CD_2Cl_2 was cooled to –80 °C and irradiated with 470 nm light using an LED. A new set of signals emerged that was attributed to the **D-81** isomer (Figure 46a).

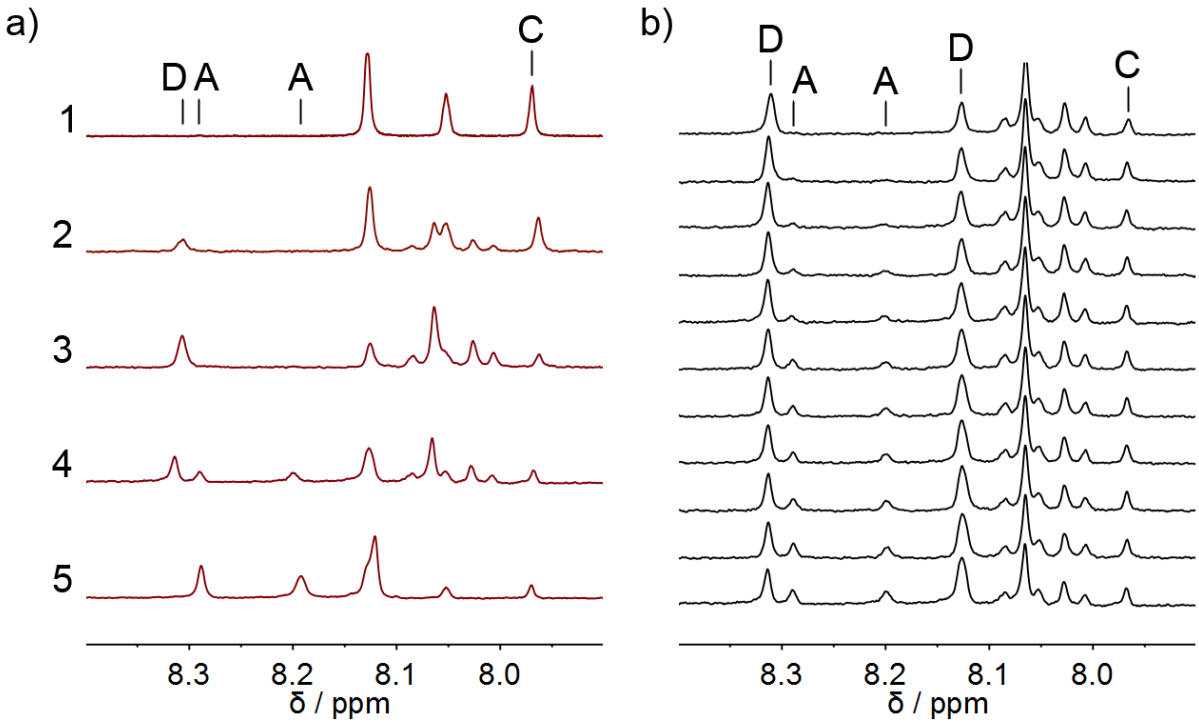

Figure 46 ^{1}H NMR spectra of **81** (400 MHz, CD_2Cl_2) acquired at –80 °C. a) 1. A solution of **C-81** at –80 °C before irradiation. 2. After 1 min of irradiation with 470 nm light. 3. After 5 min of irradiation with 470 nm light the pss is reached. 4. After 33 min in the dark at –80 °C (see b) for details). 5. After warming the sample to 23 °C and cooling back to –80 °C. b) At –80 °C thermal conversion of **D-81** exclusively to **A-81** is observed.

When the light was turned off **D-81** was slowly and exclusively converted to the **A-81** isomer. After warming to room temperature and recooling to –80 °C a full conversion of **D-81** to **A-81** was observed. A kinetic analysis was conducted to obtain the energy barrier of this process (Figure 47 and Figure 48). This time, thermal conversion did not result in a dynamic equilibrium and (equation *3* is simplified to:

$$\ln\left(\frac{c(Z_0)}{c(Z_t)}\right) = \big(k(Z \rightarrow E)\big) \cdot t \qquad \text{(equation 9)}$$

As a result the slope of the logarithmic plot *m* directly translates to the rate constant $k(Z \rightarrow E)$. A Gibbs free energy of activation $\Delta G^{\ddagger}$ of 14.5 kcal·mol^{-1} was obtained. This is significantly higher than the energy barrier of 13.1 kcal·mol^{-1} of the original HTI motor system and cannot be readily explained. This 10fold deceleration (1.4 kcal·mol^{-1} difference in free enthalpy of activation corresponds to roughly a factor of 10 in terms of rate) of the thermal helix inversion from isomer **D** to isomer **A** is most probably an effect of macrocyclization and/or the missing

second methoxy substituent at the rotor fragment. Which effect is most important can only be determined in future studies involving control compounds lacking e.g. macrocycles.

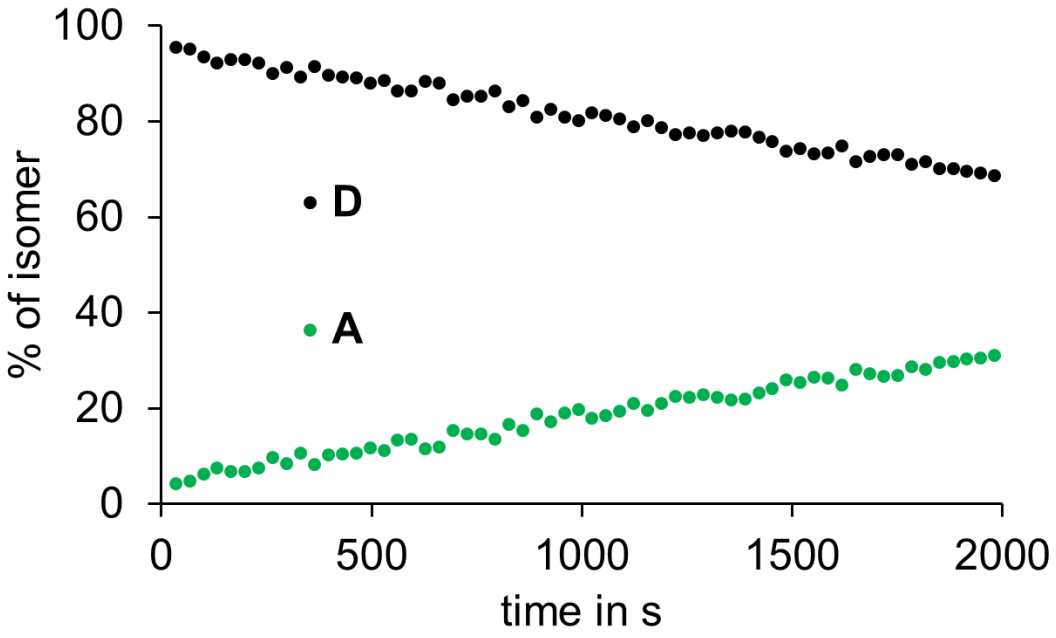

Figure 47 Isomer distribution during the thermal conversion of **D-81** to **A-81** at –80 °C (CD_2Cl_2).

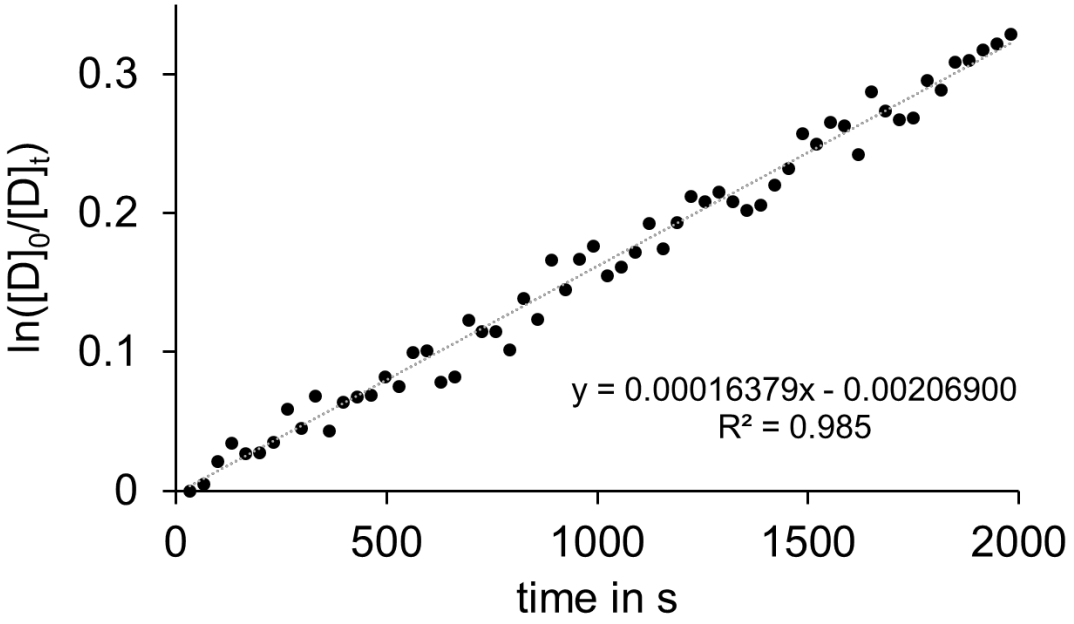

Figure 48 Kinetic analysis of the thermal conversion of **D-81** to **A-81** at –80 °C (CD_2Cl_2). The slope m = 0.00016379 (formula given in the diagram) directly translates to the rate constant $k(Z \rightarrow E)$. The corresponding Gibbs free energy of activation is 14.5 kcal·mol^{-1}.

To gain further insight into the working mechanism of the motor fragment the **A-81** isomer was irradiated at low temperatures. At –80 °C signals of **C-81** and **D-81** emerge almost simultaneously (Figure 49).

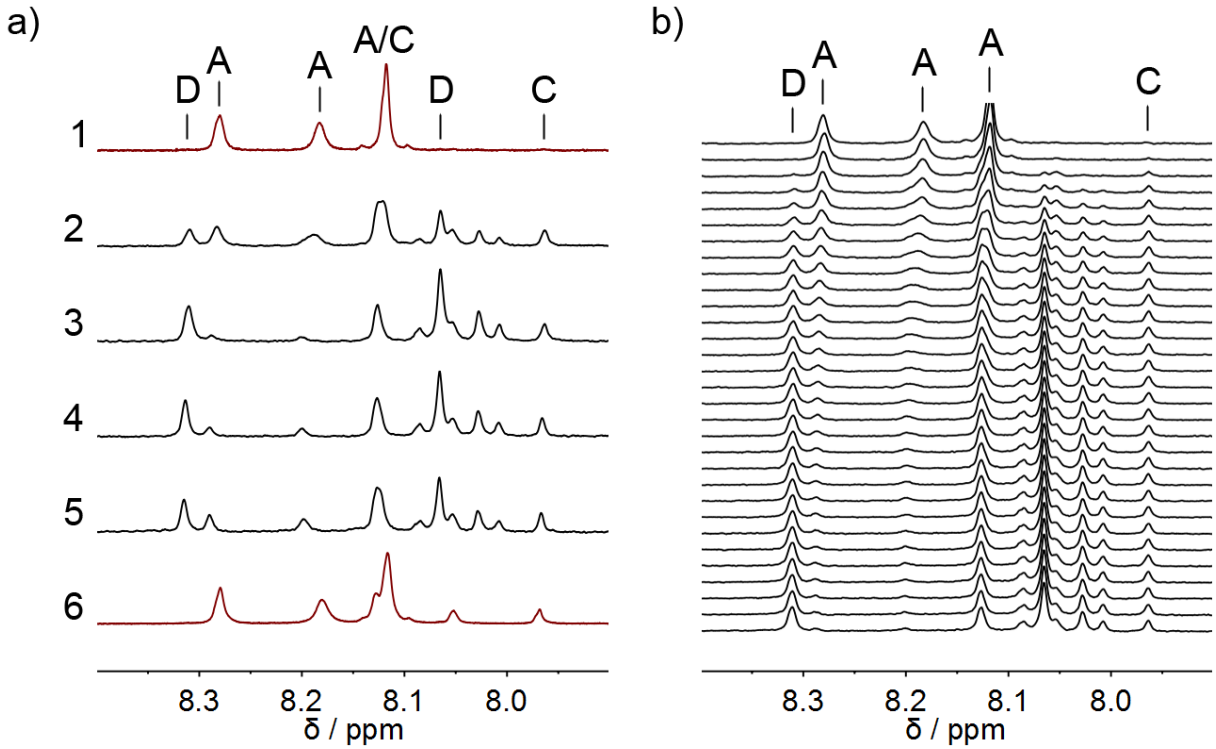

Figure 49 ^{1}H NMR spectra of **81** (400 MHz, CD_2Cl_2) acquired at –80 °C. a) 1. A solution of **A-81** at –80 °C before irradiation. 2. After 1 min of irradiation with 470 nm light (see b) for details). 3. After 5 min of irradiation with 470 nm light the pss is reached. 4. After 16 min in the dark at –80 °C. 5. After 33 min in the dark at –80 °C. 6. After warming the sample to 23 °C and cooling back to –80 °C. b) Irradiation of **A-81** at –80 °C results in formation of **C-81** first, which is closely followed by formation of **D-81**.

A detailed analysis of the isomer distribution during the irradiation process revealed a steeper initial increase of the **C-81** concentration that plateaud after several minutes (Figure 49b and Figure 50). An initially slower but constant increase of the **D-81** concentration confirmed that **D-81** is the follow-up product of the photoisomerization of already present **C-81**. After 20 minutes the solution was almost completely depleted of **A-81**. Analogously to the original system no traces of a fourth species were visible that could have been attributed to the elusive **B-81** conformer.

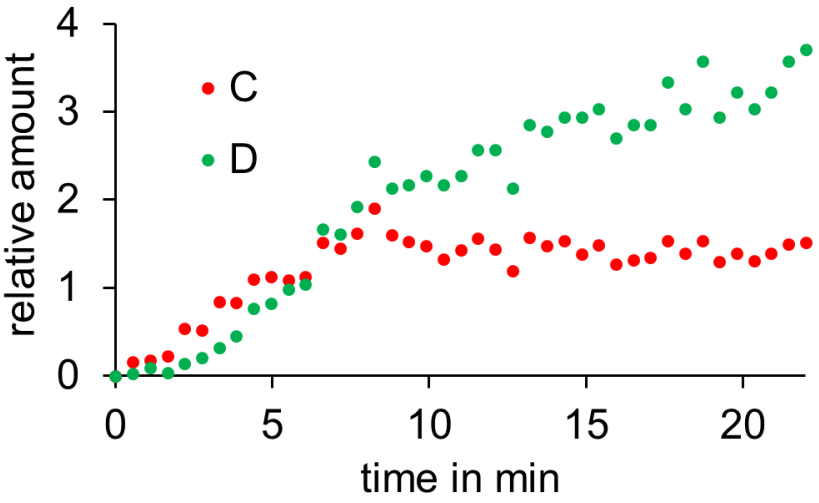

Figure 50 Increase of **C-81** and **D-81** during continuous irradiation of a solution of pure **A-81** in CD_2Cl_2 at –80 °C with 470 nm light.

3.6 ECD spectra at different temperatures

3.6.1 ECD spectra of A-81 and C-81 at room temperature

So far three conformers, i.e. **A-81**, **C-81** and **D-81** were identified and unidirectionality of the rotation around the central double bond was proven by low temperature NMR experiments. For an in depth analysis of the different geometries that are adopted during the stepwise rotation ECD spectra of the conformers were measured. Enantiopure samples of **A-81** and **C-81** were obtained by HPLC separation on a semi preparative CHIRALPAK® IC column. Room temperature spectra were taken in CH_2Cl_2 (Figure 51 and Figure 52).

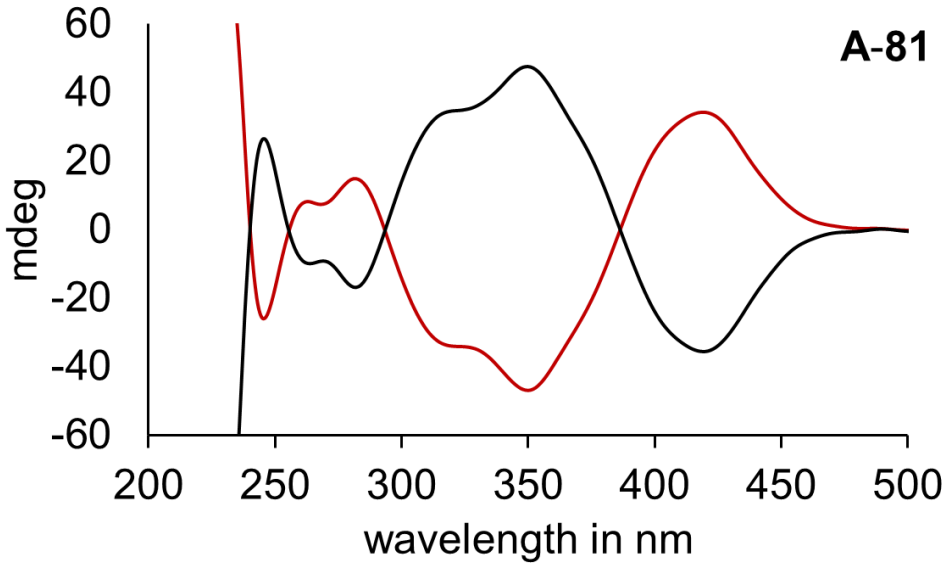

Figure 51 ECD spectra of **A-81** with *R* (black) and *S* (red) configured sulfoxide (CH_2Cl_2, 23 °C)

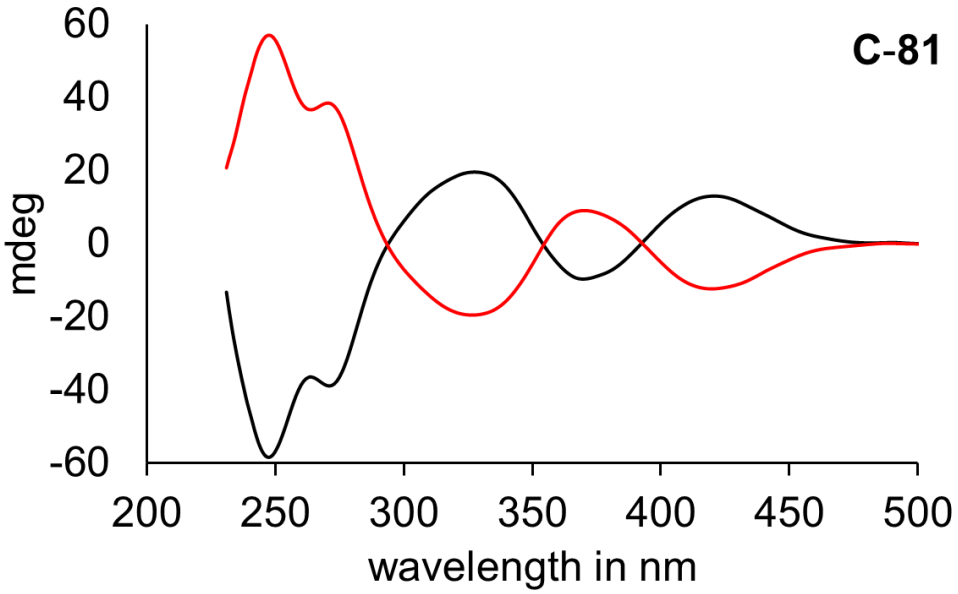

Figure 52 ECD spectra of **C-81** with *R* (black) and *S* (red) configured sulfoxide (CH_2Cl_2, 23 °C)

3.6.2 ECD spectra of D-81 at low temperatures

NMR experiments have shown that irradiation of **C-81** at low temperatures leads exclusively to generation of the **D-81** isomer. The result is a mixture that contains remaining **C-81** (25% in the pss at 470 nm irradiation) and newly formed **D-81** (75% in the pss at 470 nm irradiation). When the mixture is annealed at room temperature and cooled back, the metastable **D-81** is quantitatively converted to the **A-81** isomer. The result is a mixture of initial **C-81** and **A-81** and the isomer distribution is identical to the ratio of **C-81** and **D-81** before annealing. These correlations can be applied to an analogous ECD experiment. The isomer distribution of the resulting solution containing **C-81** and **A-81** can be determined by fitting of the known ECD spectra of enantiopure **C-81** and **A-81**. The concentration of **A-81** equals the concentration of **D-81** before the annealing step. The concentrations of **C-81** before and after annealing are identical. Subtraction of the respective **C-81** contribution from the mixed **C-81** and **D-81** ECD spectrum therefore results in a pure **D-81** ECD spectrum. For low temperature ECD experiments a cryo cuvette was used (see experimental section for details). A solution of enantiopure **C-81** in CH_2Cl_2 was irradiated at –80 °C for 40 minutes using an LED with a wavelength of 450 nm (Figure 53). The sample was then warmed to 23 °C for five minutes in the dark and cooled back to –80 °C. Additionally spectra of enantiopure **A-81** were taken at –80 °C to allow fitting of the mixed spectrum. The annealed spectrum (green spectrum, Figure 53) is clearly composed of pure **C-81** and **A-81**.

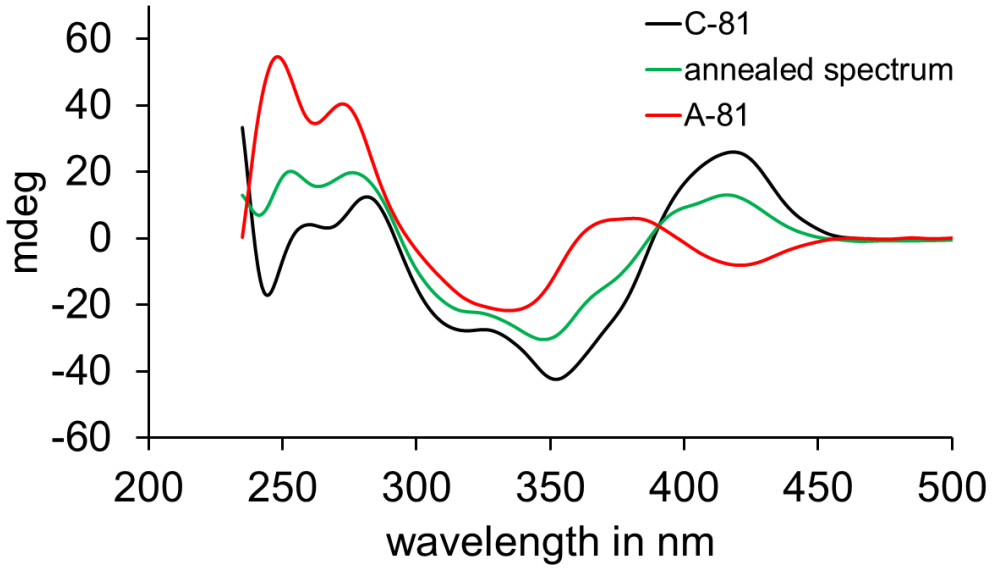

Figure 53 ECD spectra of **81** with *S* configured sulfoxide acquired at –80 °C in CH_2Cl_2. Spectrum of **C-81** (red) before irradiation with 450 nm light. Spectrum measured at –80 °C after annealing the solution at 23 °C (green) to obtain a mixture of **C-81** and **A-81** in an unknown ratio. Spectrum of pure **A-81** measured at –80 °C (black) to allow fitting of the annealed (green) spectrum.

The best fit for the annealed spectrum was found for a ratio of 60% **A-81** and 40% **C-81** (Figure 54). Consequently, the isomer distribution of the solution before annealing was composed of 60% **D-81** and 40% **C-81**. This is different to the pss ratio of 75% **D-81** and 25% **C-81** observed in the analogous NMR experiment (using 470 nm light), which could be the result of less efficient irradiation of the sample within the cryo cuvette setup or the different wavelength that was used.

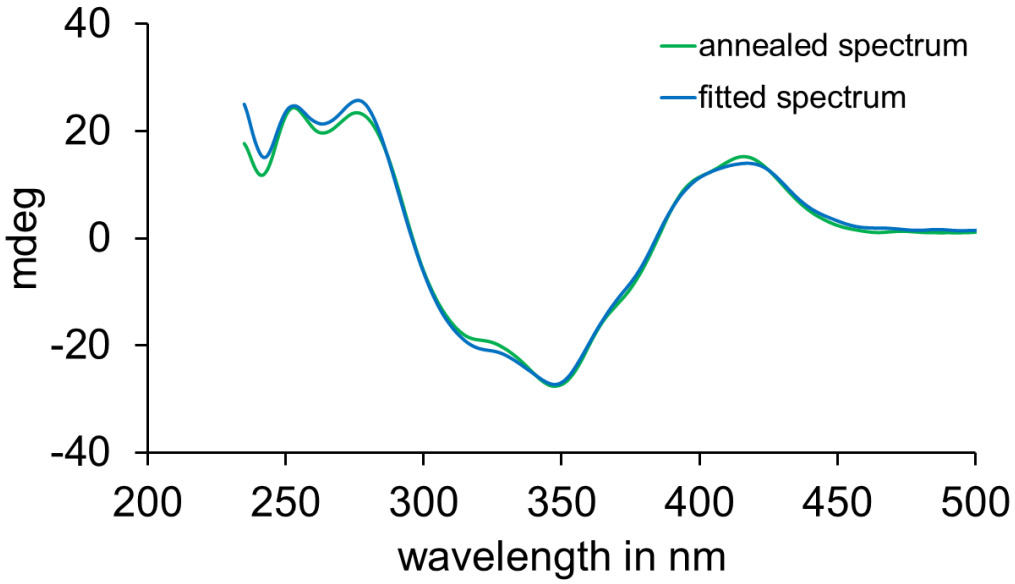

Figure 54 Experimental ECD spectrum (green) composed of **A-81** and **C-81** with *S* configured sulfoxide in an unknown ratio. The spectrum was obtained after irradiation of a solution of **C-81** in CH_2Cl_2 at –80 °C with 450 nm light for 40 min, warming to 23 °C for 5 min and recooling to –80 °C. Fitted ECD spectrum (blue) obtained from a combination of pure **A-81** and **C-81** spectra, taken at –80 °C, with a ratio of 60% **A-81** and 40% **C-81**.

Subtraction of the 40% **C-81** contribution gives a pure **D-81** spectrum (Figure 57). Because the total concentration of **81** does not change throughout the experiment this was done by subtracting the initial pure **C-81** spectrum with 40% intensity. For a better comparability the concentration of the extracted **D-81** spectrum was corrected to match the initial **C-81** concentration by multiplication with a correction factor (that is 1/0.6).

The experiment was repeated for the second set of enantiomers (Figure 55). The best fit for the annealed spectrum was found for a ratio of 55% **A-81** and 45% **C-81** in this case (Figure 56).

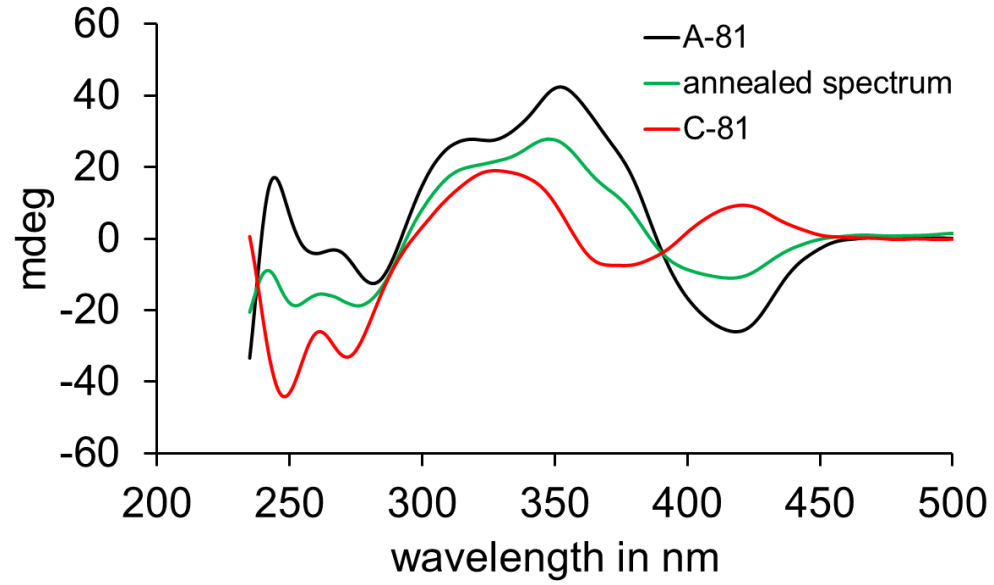

Figure 55 ECD spectra of enantiopure **81** with *R* configured sulfoxide acquired at –80 °C in CH_2Cl_2. Spectrum of **C-81** (red) before irradiation with 450 nm light. Spectrum measured at –80 °C after annealing at 23 °C (green) resulting in a mixture of **C-81** and **A-81** in an unknown ratio. Spectrum of **A-81** measured at –80 °C (black) to allow fitting of the annealed (green) spectrum.

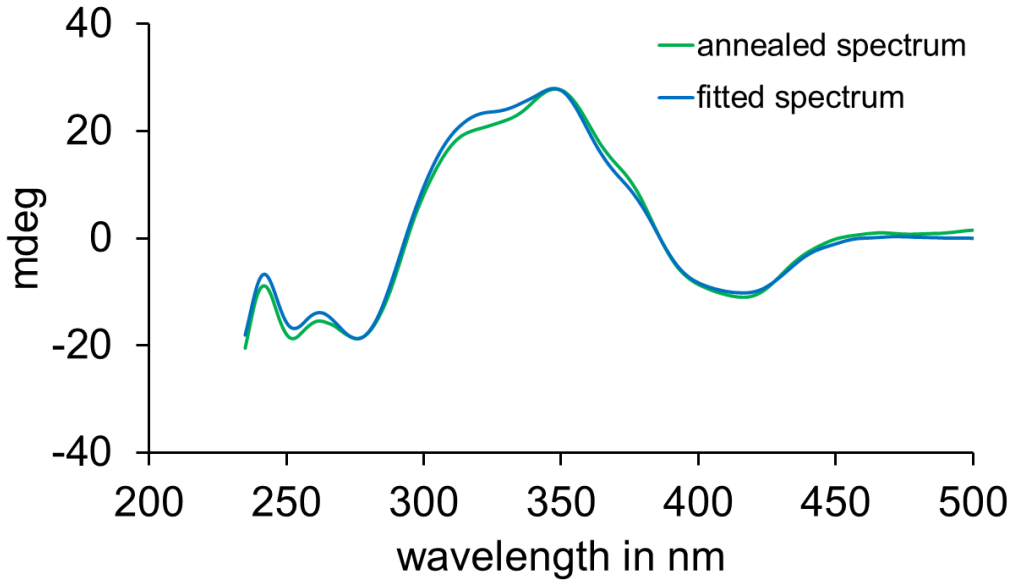

Figure 56 Experimental ECD spectrum (green) of a mixture of **A-81** and **C-81** with *R* configured sulfoxide in an unknown ratio. The spectrum was obtained after irradiation of a solution of **C-81** in CH_2Cl_2 at –80 °C with 450 nm light for 40 min, warming to 23 °C for 5 min and recooling to –80 °C. Fitted ECD spectrum (blue) obtained from a combination of pure **A-81** and **C-81** ECD spectra, taken at –80°C, using a ratio of 55% **A-81** and 45% **C-81**.

The extracted **D-81** spectrum is the mirror image of the extracted **D-81** spectrum that was obtained from the first set of enantiomers (Figure 57). This independently proved the quality of the conducted experiments.

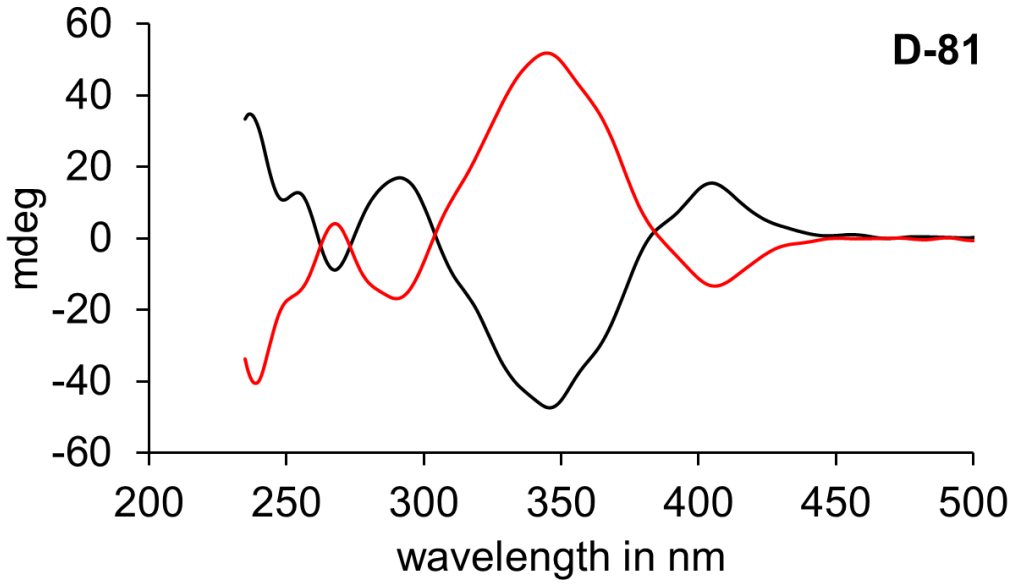

Figure 57 Extracted ECD spectra of **D-81** (CH_2Cl_2, –80 °C) with *R* (black) and *S* (red) configured sulfoxide.

In addition, the data have been extensively tested for robustness. Calculations with up to 5% errors of the fitting ratios results in almost identical extracted spectra (Figure 58).

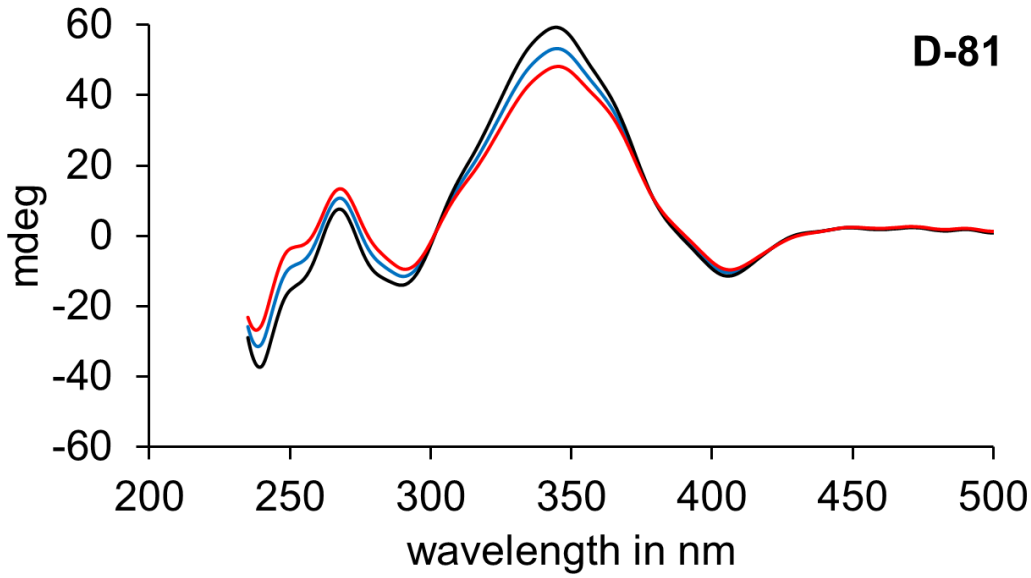

Figure 58 Extracted ECD spectra of **D-81** (CH_2Cl_2, –80 °C) with *S* configured sulfoxide. Spectrum obtained from the best fit of 60% **A-81** and 40% **C-81** (blue). Spectrum obtained from a 55% **A-81** and 45% **C-81** fit (black). Spectrum obtained from a 65% **A-81** and 35% **C-81** fit (red).

3.7 Comparison of experimental and calculated ECD spectra

A comprehensive theoretical analysis of the ground state geometries was conducted to compare the experimentally obtained ECD spectra with calculated ones and to assign the absolute configurations from measured ECD spectra. Optimizations were carried out exclusively for structures with an *R* configured sulfoxide. Calculations of **81** including all its conformers were conducted by *Stefan Thumser*. Molecular dynamics simulations were carried out to obtain a set of 50 to 70 starting structures for each conformer (**A-81**, **B-81, C-81** and **D-81**) within a 30 kJ·mol^{-1} threshold. Ground state optimizations were calculated on the B3LYP-GD3BJ/6-311G(d,p) IEFPCM (CH_2Cl_2) level of theory. Electronic excitation spectra were obtained from B3LYP-GD3BJ/6-311+G(d,p) IEFPCM (CH_2Cl_2) calculations, which were then compared to the experimental spectra. Only conformers with free energies between 0.0 and 2.0 kcal·mol^{-1} were taken into consideration. For further details see the corresponding publication.[83]

The ECD spectrum of **A-81** is in very good agreement with the Boltzmann-averaged calculated ECD spectrum. The contributing ground state conformers reflect the structure found in the crystalline state with an exception for the configuration of the biaryl axis. Structures with R_a and S_a configuration were both found to significantly contribute to the experimental spectrum (Figure 59a) whereas the crystal only contained the S_a configured conformer. It is therefore assumed that the chain has some flexibility in solution but still restricts the tilt of the aryl follower to the carbonyl side of the benzothiophenone stator as demonstrated earlier by NOESY NMR experiments (for the S_a configured conformer the tilt of the biaryl unit is thus opposite to the R_a conformer as shown in Figure 59a).

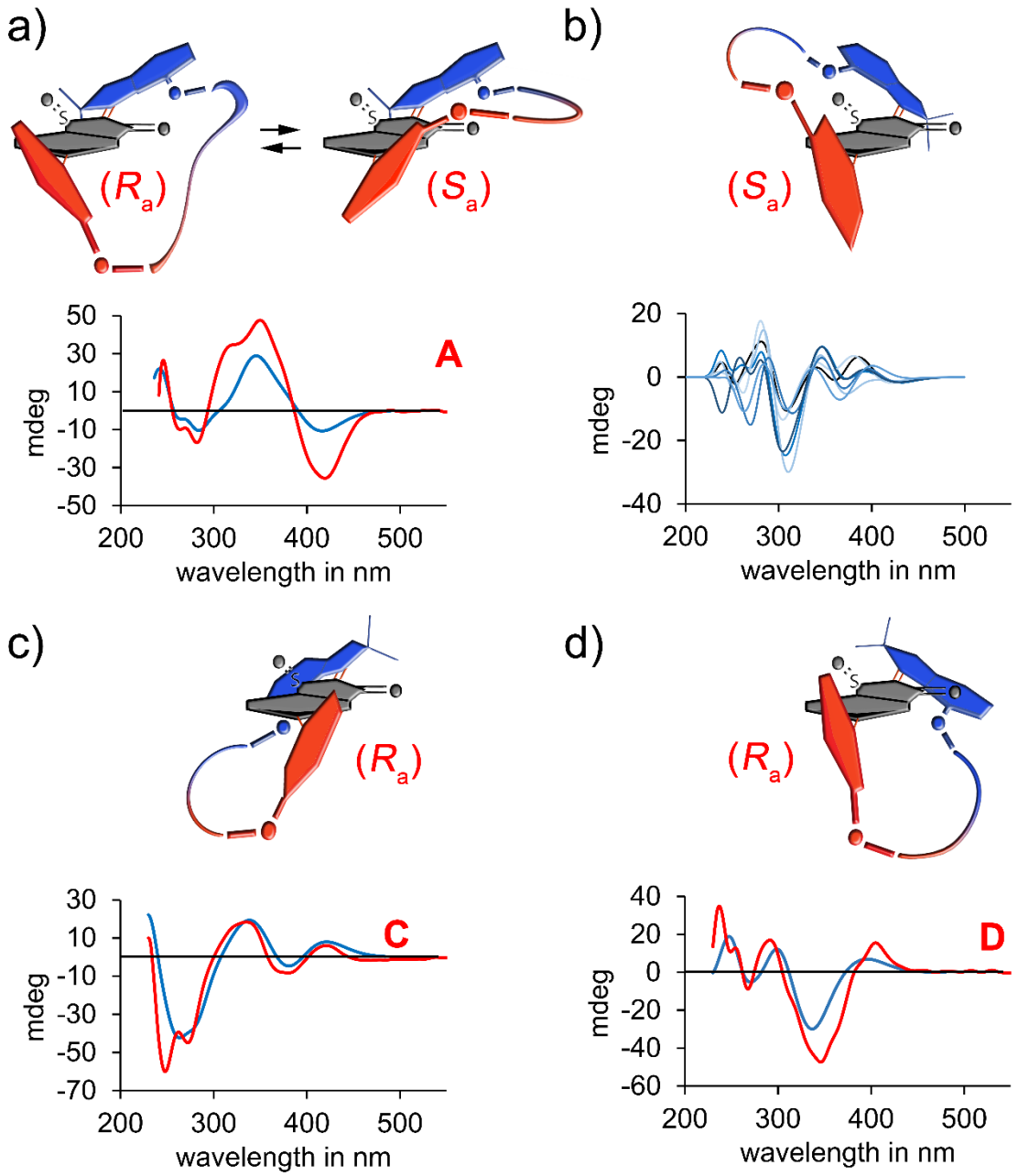

Figure 59 Assessment of the ground state geometries of **81** in solution. Structures were assigned by comparison of experimental (red) and calculated (blue) spectra. The calculated spectra were blue-shifted 10-15 nm for better comparability. a) The experimental spectrum of **A-81** is best reproduced by the Boltzmann weighed contributions of the calculated spectra containing R_a and S_a configured biaryl units. b) Calculated ECD spectra for all low energy conformers, which were found to have exclusively S_a configured biaryl units. c) The best fit to the experimental spectrum was found for a conformer with R_a configured biaryl unit. d) Calculated structures were found with R_a configured biaryl units. The experimental spectrum is best represented by structures with a tilt of the biaryl towards the carbonyl side of the benzothiophenone stator. From these the ECD spectrum of the conformer with the best fit is shown. Reprinted with permission from *Angew. Chemie - Int. Ed.* **57**, 11064–11068 (2018). Copyright 2018 Wiley and Sons.

The **B**-**81** conformer was not experimentally accessible due to its low kinetic stability. However, all minimum structures within the 2.0 kcal·mol^{-1} energy window possess an S_a configuration of the biaryl which reflects the geometry of the motor fragment (Figure 59b). This indicates a restricted movement of the aryl follower that is dictated by the indanone stator for **B**-**81**.

Optimized structures of **C**-**81** were found exclusively with R_a configuration of the biaryl axis. Included are structures with a tilt of the aryl follower toward the sulfoxide as well as the carbonyl side of the benzothiophenone stator. The best agreement with the experimental data was found for a structure with a tilt toward the sulfoxide (Figure 59c) which also reflects the conformation of **C**-**81** found in the crystalline state. A clear preferential tilt toward this side was also observed earlier in NOESY NMR experiments.

The experimental **D**-**81** spectrum was extracted from low temperature ECD experiments. Calculated structures were found exclusively with R_a configuration of the biaryl axis (Figure 59d). Similar to **C**-**81** tilts of the aryl follower towards both sides of the benzothiophenone stator were found as energetic minima. However, structures with a tilt toward the carbonyl side were in much better agreement with the experimental data. Attempts at low temperature NOESY NMR experiments were unsuccessful and no additional information regarding the tilt could be obtained in this case.

3.8 Conclusion

Taken together a comprehensive picture of the motor motion sequence is drawn. Irradiation of **81** in CH_2Cl_2 with 450 nm light results in a four step unidirectional rotation around the central double bond. The motion of the indanone rotor in relation to the benzothiophenone stator is transmitted to the aryl receiver and as a result, the geometry of the motor fragment is reflected by the tilt of the biaryl axis. The linker allows for a limited conformational freedom regarding this tilt where each step confines the movement of the aryl follower to either one side (sulfoxide or carbonyl) of the benzothiophenone stator or to the same or opposite half-space as the sulfoxide oxygen atom (Figure 60). With this integrated molecular machine the first direct observation of a transmitted unidirectional motion to a passive and remote receiving unit was realized. Next steps in this field imply the construction of more advanced nanomachinery that

can use the transmitted motion for productive tasks such as enantioselective catalysis, repeated construction of chiral molecules or active driving of secondary, independent parts.

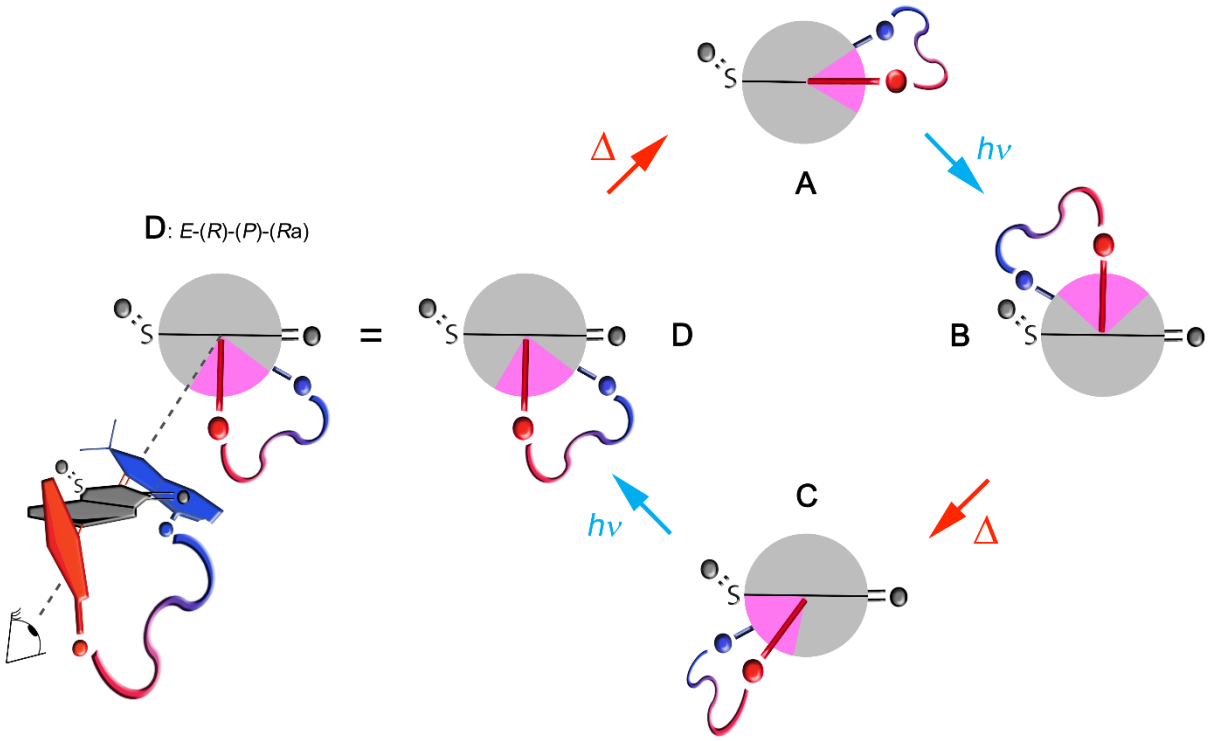

Figure 60 Schematic representation of the transmitted unidirectional rotation of the rotor fragment to the aryl receiver in four consecutive steps. a) View along the imaginary axis created running through the biaryl axis and the central double bond. b) Unidirectional rotation of the rotor fragment (blue) is closely followed by the aryl receiver (red). The tilt around the biaryl axis is confined to a certain range for each conformer indicated by the pink colored area. Reprinted with permission from *Angew. Chemie - Int. Ed.* **59**, 5730–5737 (2020). Copyright 2020 Wiley and Sons.

4 Active and unidirectional acceleration of biaryl rotation by a molecular motor

4.1 General design principles

The transmission of directional rotation to a passive and remote receiving unit was realized with macrocycle **81**. In addition, a biaryl reporter unit was introduced as a tool to grant direct experimental access to each step of the underlying processes. A molecular system that utilizes this setup to gain unprecedented insight into the mechanism of the motor fragment was conceived. To this point, the passive rotation of the aryl follower is dictated by the light induced isomerization of the central double bond or the subsequent thermal ratcheting step. With increased steric hindrance at the biaryl unit the energy barrier for the atropisomerization can be increased above the barrier of the thermal helix inversion that was determined to be 14.5 kcal·mol^{-1} for the conversion from **D-81** to **A-81** in the above described system. This allows the biaryl unit to work as a "brake" in conjunction with the motor fragment if the thermal ratcheting takes place while the rotation around the biaryl is hindered (Figure 61).

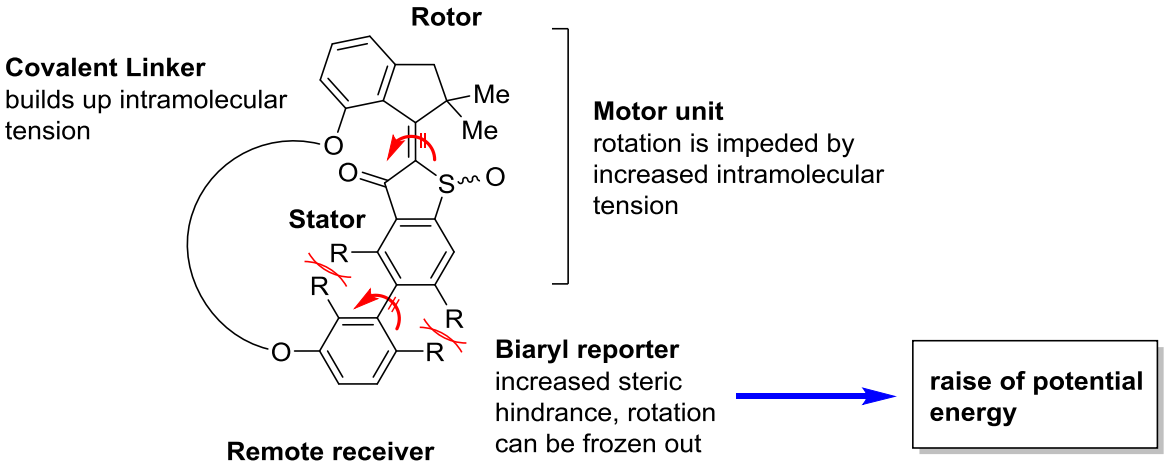

Figure 61 Schematic representation of the design of the second generation molecular machine. Rotation around the biaryl axis can be frozen out due to increased steric hindrance. Rotation of the motor fragment increases intramolecular tension through the strain caused by the covalent linker and results in an overall raise of potential energy.

The impeded biaryl rotation is transmitted to the motor fragment through the covalent linker by an increase in intramolecular tension. In return, the built up tension also effects the rotation of the biaryl, which is forced to proceed unidirectionally. The establishment of such a system requires an energy barrier of around 20 kcal·mol^{-1} for the biaryl axis rotation. This allows for a clear distinction from the thermal ratcheting/helix inversion step from **D** to **A** and guarantees

free rotation of the system at elevated temperatures. This rotational barrier also does not interfere with the thermal *Z* to *E* isomerization that was determined to encounter an energy barrier of 27.0 kcal·mol^{-1} for the previous system. The modified building blocks that are required to furnish the incorporated sterically hindered biaryl axis had to be synthetically accessible in a straightforward fashion within the limits of the free Gibbs energy values discussed above. Even though an exact value cannot be predetermined, the literature suggests a free Gibbs energy of ca. 20 kcal·mol^{-1} for the atropisomerization of 2,6-dimethylbiphenyl.[84] Dimethyl substitution of the aryl follower would require phenylboronic acid **82** which is not described in the literature and was ruled out as potential building block (Scheme 23a). Synthesis of benzothiophenone **83** that bears two methyl groups should proceed via the thiophenol **84** that can be synthesized in three steps starting from the commercially available phenol (Scheme 23b).[85] As these are the only modifications to the established route, synthesis of the new benzothiophenone building block was attempted next.

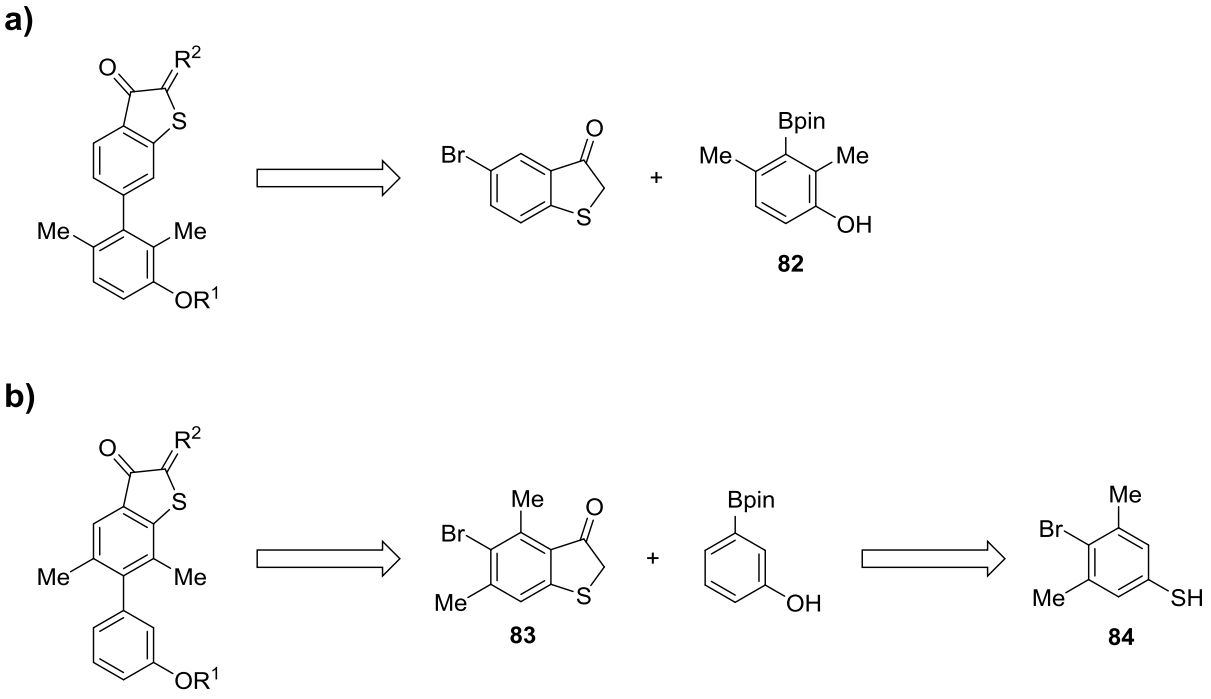

Scheme 23 Retrosynthetic pathways to a modified biaryl fragment. a) Synthesis starts with 2,6-dimethylphenylboronic acid pinacol ester **82** that is not reported in the literature. b) Benzothiophenone **83** could be synthesized from literature known thiophenol **84**.

4.2 Synthesis of HTI 95

The synthesis of the target compound **95** (shown in Scheme 31) proceeded in a highly modular fashion, which was established for the preceding system **81**. All building blocks except for the benzothiophenone are identical to the ones used in the synthesis of the previous system. Thiophenol **88** was obtained from the respective phenol in three steps via a *Newman-Kwart* rearrangement.

The synthesis commenced with esterification of 4-bromo-3,5-dimethylphenol **85** and dimethylthiocarbamoylchloride, which afforded **86** in very good yields (Scheme 24).

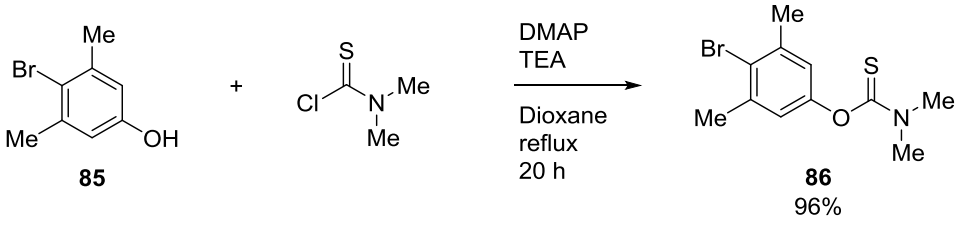

Scheme 24 Reaction of the phenol precursor **85** with dimethylthiocarbamoylchloride gave *O*-aryl thiocarbamate **86**.

Above 250 °C the *S*-aryl thiocarbamate **87** was formed in 86% yield (Scheme 25). The reaction proceeds via a four-membered cyclic intermediate and is driven by the energetically favorable conversion of the thione to the carbonyl.

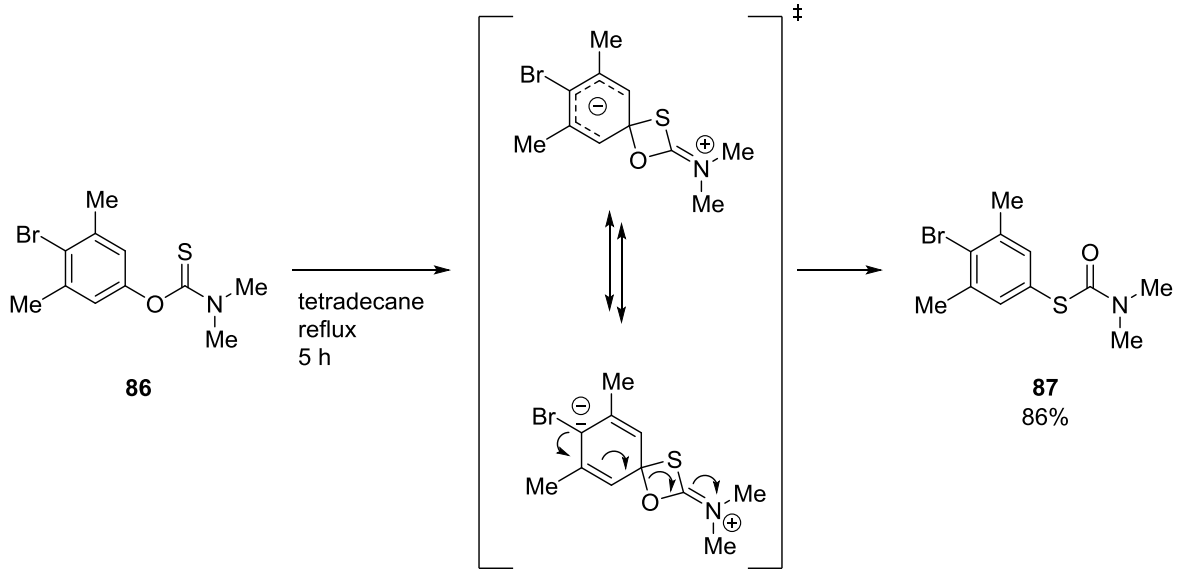

Scheme 25 *Newman-Kwart* rearrangement of the thiocarbamic acid *O*-aryl ester **86** to the *S*-aryl ester **87** via a cyclic intermediate. The reaction is driven by the formation of an energetically favorable carbon-oxygen double bond.

Cleaving of the ester using potassium methoxide gave thiophenol **84** in 88% yield (Scheme 26). The disulfide dimer **88** was observed as a minor byproduct whose formation could not be prevented even when the reaction was carried out under an inert nitrogen gas atmosphere.

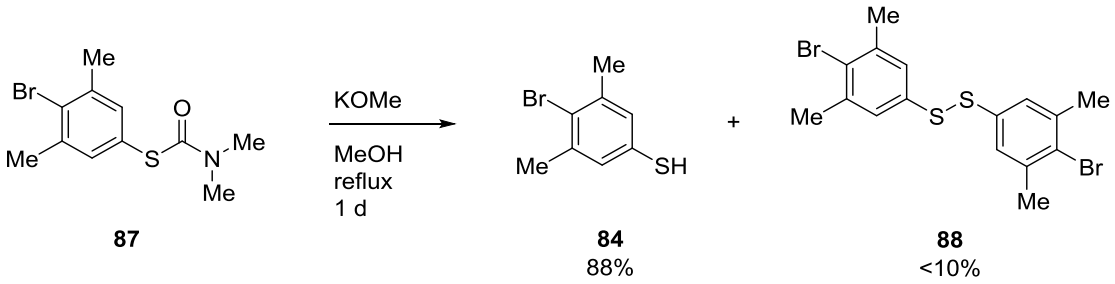

Scheme 26 Cleaving of the thioester **87** with potassium methoxide gave thiophenol **84** in 88% yield. The disulfide **88** was found as a minor byproduct.

Upon drying under high vacuum, the disulfide **88** crystallized (Figure 62) and could be partially separated from the liquid phenol **84**. Separation by flash column chromatography was not feasible as both products were extremely apolar. Minor amounts of **88** did however not visibly hamper the subsequent reactions.

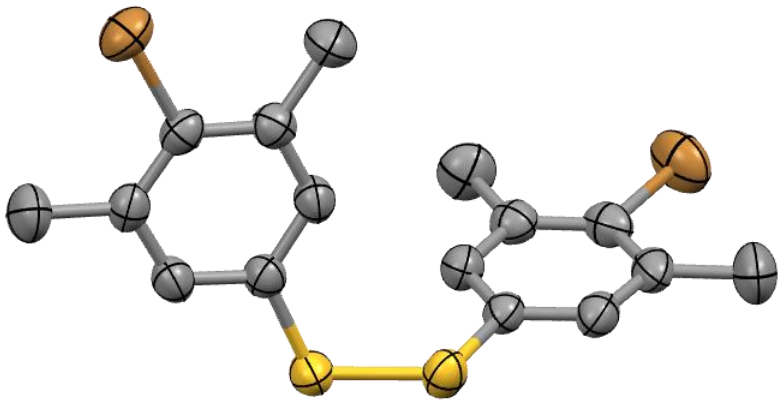

Figure 62 Structure of **88** in the crystalline state (50% probability ellipsoids). The torsion angle around the central disulfide bond is 92.8°. The unit cell also contains the respective enantiomer.

Reaction of **84** with bromoacetic acid in acetone afforded thioacetic acid **89** in good yields (Scheme 27). Conversion with thionyl chloride gave the reactive acetyl chloride that was treated *in situ* with aluminum chloride. When three equivalents of *Lewis* acid were added and standard conditions were applied an almost quantitative halogen migration was observed (**90**). The macrocycle obtained from this byproduct is discussed briefly in section 4.14. Addition of

aluminum chloride in portions over five minutes and reduction of equivalents from three to one prevented halogen migration and afforded the desired benzothiophenone **91** in excellent yields.

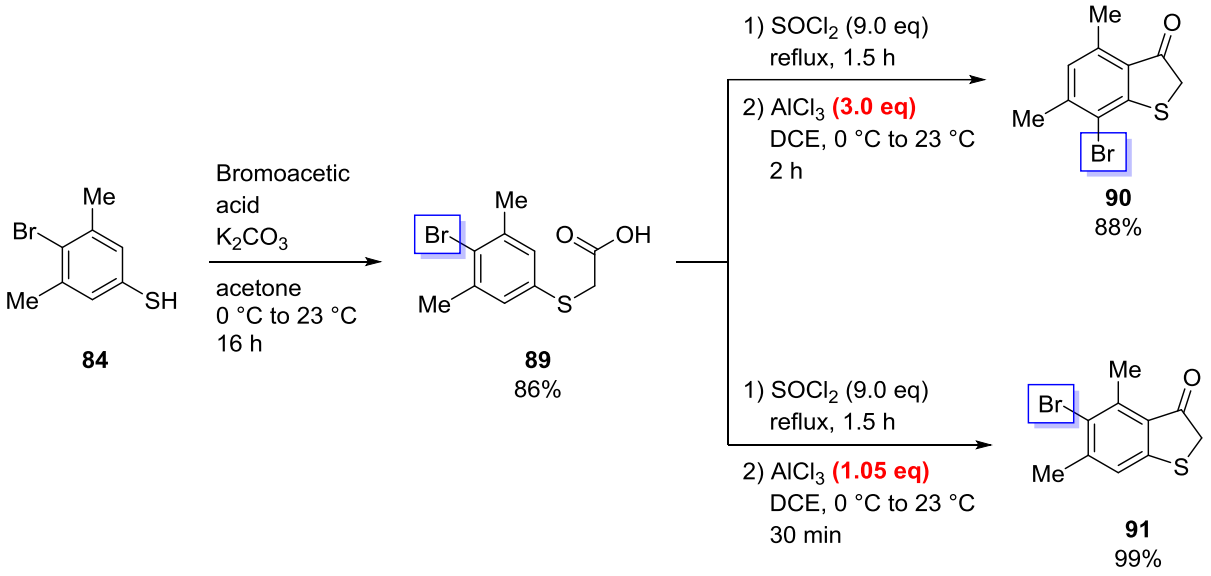

Scheme 27 Synthesis of dimethylbenzothiophenones. Reaction of thiophenol **87** with bromoacetic acid gave thioacetic acid **89**. Heating in thionyl chloride was used to generate the acid chloride that was reacted *in situ* with $AlCl_3$. Excess *Lewis* acid resulted in halogen migration (highlighted by blue boxes) and gave benzothiophenone **90**. The desired product **91** was obtained in excellent yields under optimized reaction conditions using less $AlCl_3$.

The following reaction steps proceeded analogously to the synthesis of macrocyclic HTI **81**. Condensation of benzothiophenone **91** and indanone **56** using BCl_3 gave HTI **92** in 61% yield as a mixture of *E* and *Z* isomers (Scheme 28).

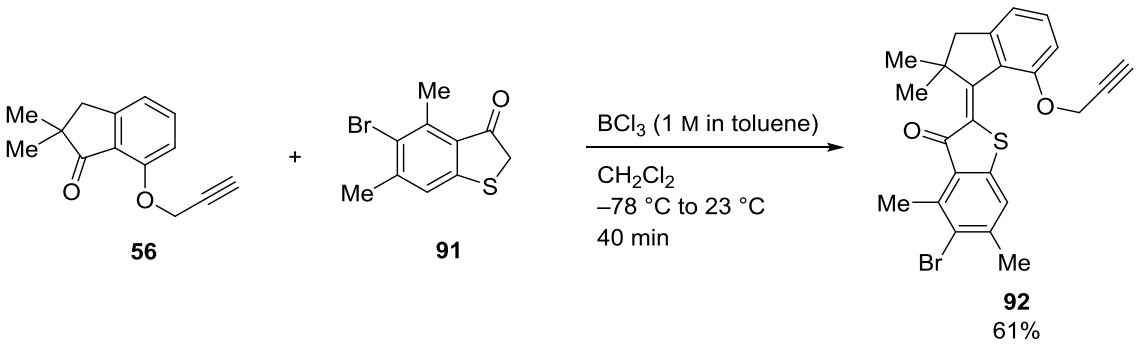

Scheme 28 Condensation of indanone **56** and benzothiophenone **91** at –78 °C in CH_2Cl_2 using BCl_3. HTI **92** was obtained as a mixture of *E* and *Z* isomers. Only the *Z* configured isomer is shown.

Reaction of the motor fragment **92** with the already established building block **73** by a 1,3-dipolar cycloaddition afforded **93** in good yields (Scheme 29).

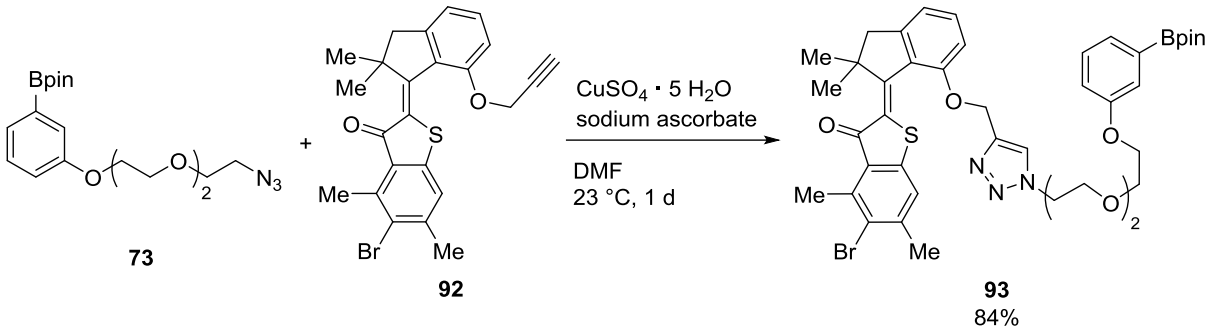

73 **92** **93** 84%

Scheme 29 Copper catalyzed 1,3-dipolar cycloaddition of boronic acid pinacol ester **73** and HTI **92**. $CuSO_4 \cdot 5H_2O$ (2 mol%) and sodium ascorbate (10 mol%) were used to generate the catalytically active Cu(I) species *in situ*. The product **93** was obtained as a mixture of *E* and *Z* isomers. Only the *Z* configured isomers are shown.

Intramolecular *Suzuki-Miyaura* cross-coupling furnished macrocycle **94** in poor yields (Scheme 30). The decreased yield compared to the preceding system (34% yield) can be attributed to the increased steric demand at the aryl halide reactive site.

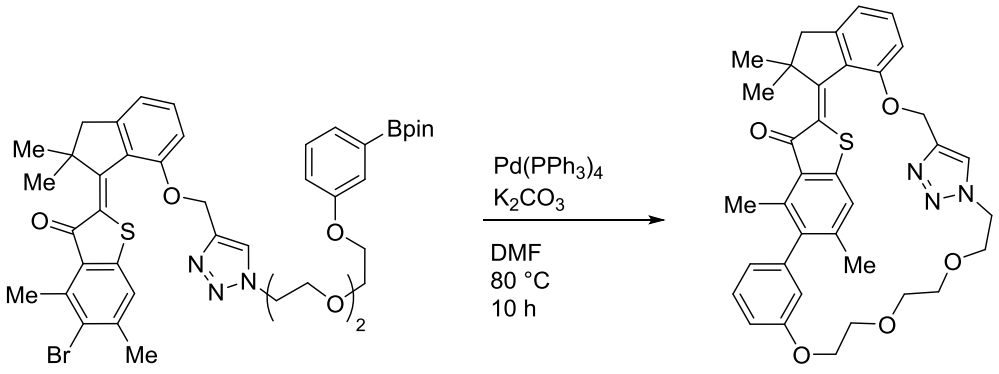

93 **94** 23%

Scheme 30 Intramolecular *Suzuki-Miyaura* cross-coupling of **93**. The product **94** was obtained in 23% yield. Only the *Z* configured isomers are shown.

The synthesis was completed with the oxidation of **94** to the corresponding sulfoxide using sodium perborate tetrahydrate in acetic acid. After four hours target compound **95** was obtained in 80% yield as a mixture of *E* and *Z* isomers (Scheme 31). The sulfone was obtained as a minor byproduct, indicating that the reaction can be further optimized using shorter reaction times or reduced equivalents of oxidant.

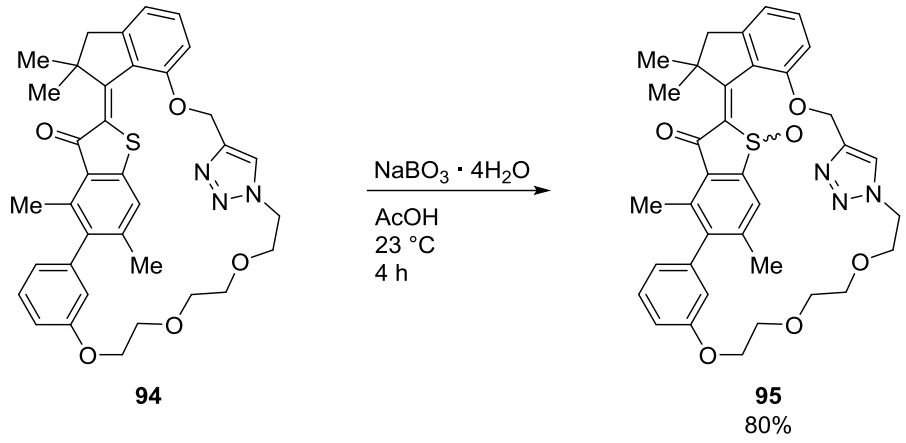

Scheme 31 Oxidation of **94** to the sulfoxide **95** using sodium perborate tetrahydrate in acetic acid. Only the *Z* configured isomers are shown.

4.3 Structure of HTI 95

4.3.1 Structure of *E*-95 in the crystalline state

Crystals suitable for single crystal X-ray analysis were obtained from a racemic mixture of *E*-**95**. For convenience, only the *E*-(*R*)-(*M*)-(S_a) configured isomer is discussed (Figure 63). *R* configuration of the sulfoxide in combination with *M* helicity of the motor unit is in agreement with analogous structures of HTI motors. The aryl follower is tilted slightly towards the carbonyl side of the benzothiophenone stator with a torsion angle of 81°, which reflects the geometry around the central double bond. The oxygen-atoms of the indanone rotor and the aryl follower that connect to the PEG linker chain point to the same half-space as the sulfoxide oxygen atom. The pronounced loop between the triazole moiety and the attachment point to the biphenyl fragment indicates a relaxed geometry of the covalent linker.

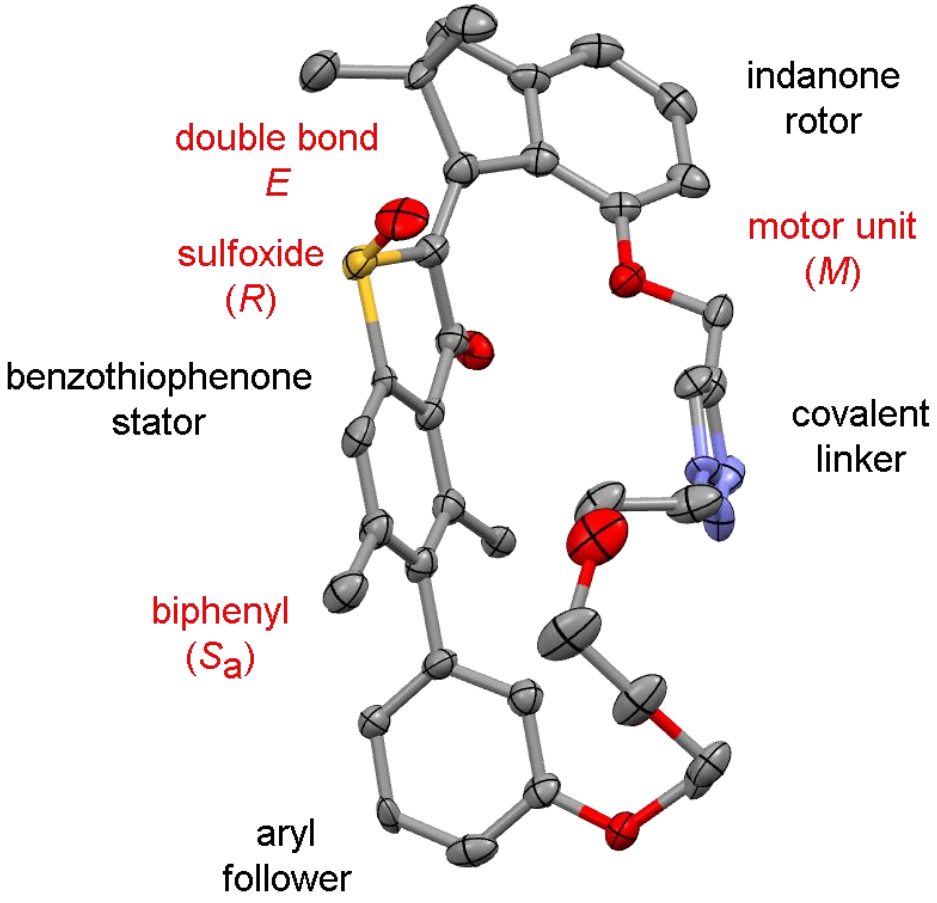

Figure 63 Structure of racemic *E*-**95** in the crystalline state (50% probability ellipsoids). Assignments of stereodescriptors are given in red. Only the *E*-(*R*)-(*M*)-(S_a) isomer is shown. The oxygen atoms of the indanone rotor and aryl follower that are connected to the covalent linker chain point to the same half-space as the sulfoxide oxygen atom. Hydrogen atoms are omitted for clarity.

4.3.2 Structure of *E*-95 in solution

For assignments of ^{1}H and ^{13}C signals and a detailed analysis of 2D NMR experiments see the corresponding publication.[86] Proton numbers were arbitrarily assigned to the structure. A cross signal between protons 17 and 35 in the NOESY NMR spectrum was used to distinguish the methyl groups adjacent to the biaryl axis (Figure 64). Cross signals between methyl group protons 34 and 35 to protons 20 and 24 have almost similar intensities, indicating a minor tilt to the carbonyl side of the benzothiophenone stator. This is also observed in the crystalline state with a torsion angle of 81° around the biaryl axis. An indicative cross signal between protons 31 and 34 suggests a preferred orientation of the covalent linker in proximity to the carbonyl side of the stator, proving the assignment of an *E* configured central double bond.

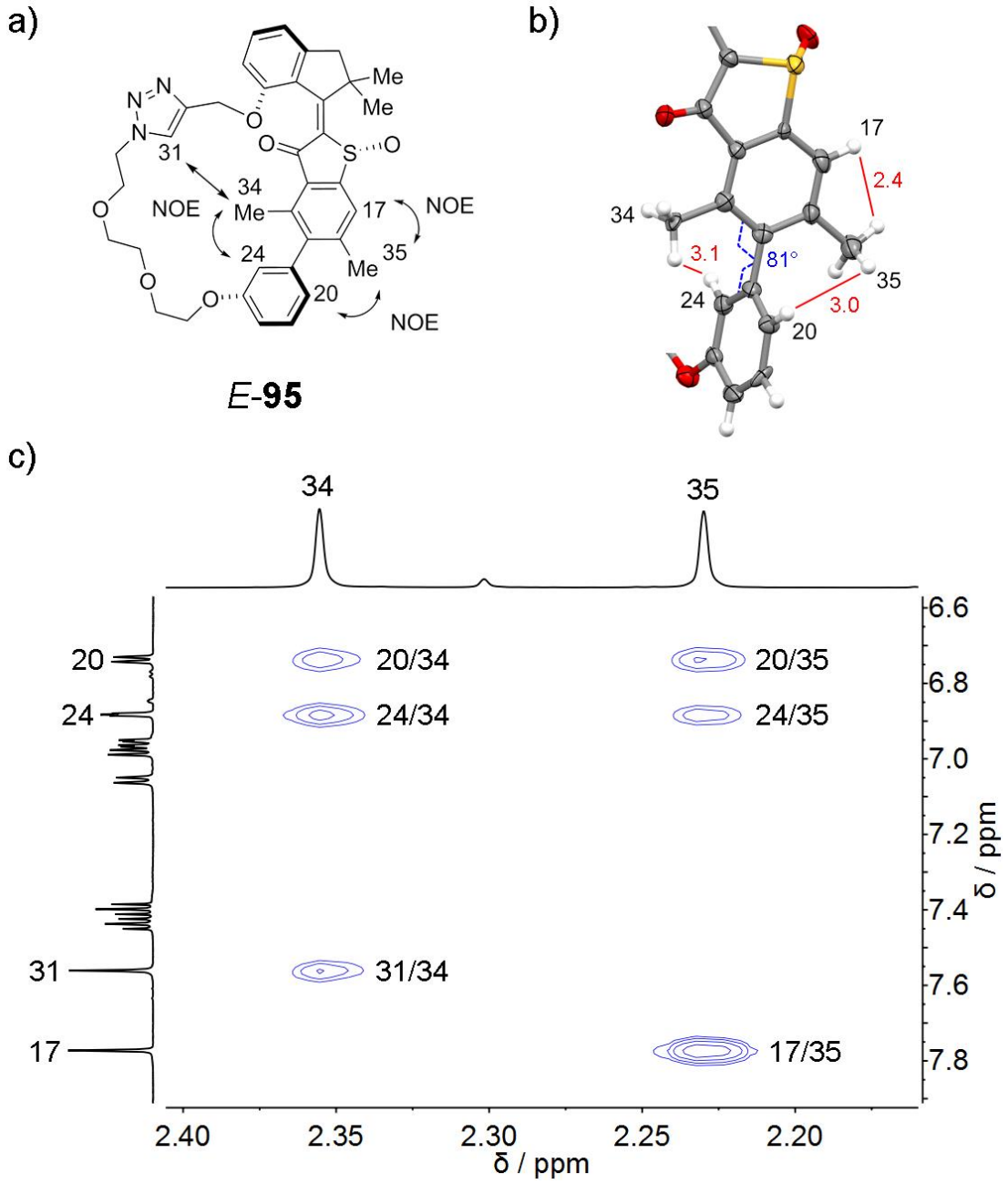

Figure 64 Geometry of *E*-**95** in solution and in the crystalline state. a) Schematic structure of *E*-(*R*)-(*M*)-(*S*$_a$)-**95**. Interacting protons that result in NOESY NMR cross signals are highlighted. b) Detail of the structure of *E*-(*R*)-(*M*)-(*S*$_a$)-**95** in the crystalline state. A minor tilt of the biaryl axis towards the carbonyl side of the benzothiophenone stator is observed with a torsion angle of 81°. Distances are given in Å (red numbers). The distance between protons 24 and 35 as well as between protons 20 and 34 is 3.3 Å (not shown). c) Detail of the NOESY NMR spectrum (CD_2Cl_2, 599 MHz, 27 °C) of racemic *E*-**95**. Cross signals between protons 34 and 35 to protons 20 and 24 have almost similar intensities, revealing a minor tilt of the biaryl axis to the carbonyl side of the stator, which reflects the structure found in the crystalline state. A cross signal between protons 31 and 34 confirms *E* configuration of the central double bond.

The *E* configuration is further supported by distinct cross signals between the PEG units of the covalent linker to methyl group protons 34 and only weak interactions between the linker and methyl group protons 35 (Figure 65).

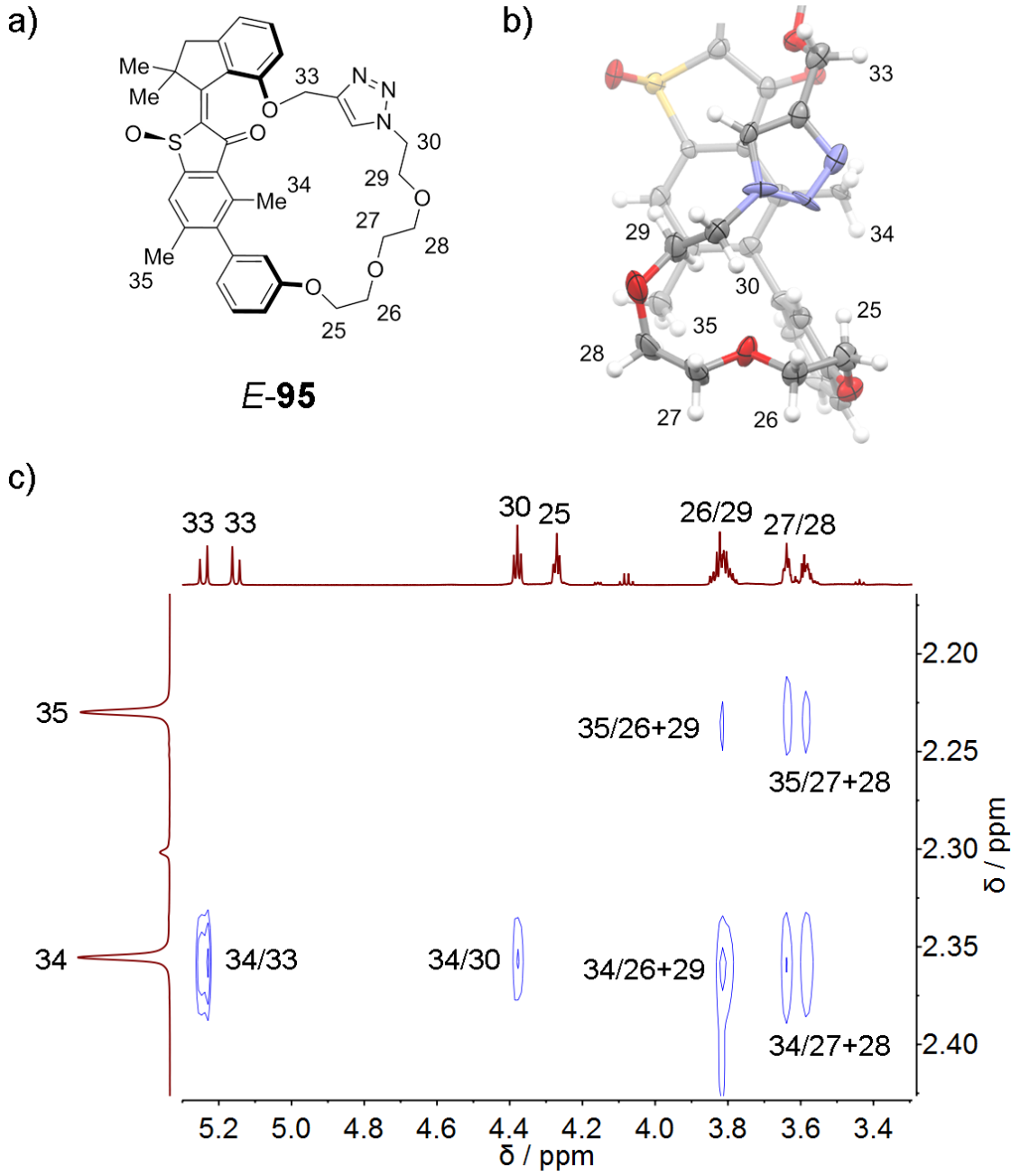

Figure 65 Geometry of *E*-**95** in solution and in the crystalline state. a) Schematic structure of *E*-(*R*)-(*M*)-(S_a)-**95**. Interacting protons that result in NOESY NMR cross signals are highlighted. b) Detail of the structure of *E*-(*R*)-(*M*)-(S_a)-**95** in the crystalline state. The PEG tether reveals a pronounced loop towards the sulfoxide side of the stator. c) NOESY NMR spectrum (CD_2Cl_2, 599 MHz, 27 °C) of racemic *E*-**95**. Cross-signals between the covalent linker and methyl group protons 34 are more pronounced, indicating a preferred orientation of the chain to the carbonyl side of the stator in solution.

This is in contrast to the structure in the crystalline state where the PEG tether resides in the same half-space of the benzothiophenone stator as the sulfoxide oxygen atom with a pronounced loop resulting in close proximity to methyl group protons 35. This demonstrates an overall high flexibility of the covalent linker in the *E*-**95** conformer.

4.3.3 Structure of E_A-95 in solution

The atropisomer of *E*-**95** was found to be stable in CH_2Cl_2 solution at temperatures below –60 °C and can be accumulated by irradiating a mixture of *E*/*Z*-**95** at this temperature (see section 4.7 for a detailed description). Interactions between protons 34 and proton 24 as well as protons 35 and and 20 in the NOESY NMR spectrum of E_A-**95** reveal a pronounced tilt of the biaryl axis towards the carbonyl side of the benzothiophenone stator (Figure 66). An additional cross signal between methyl group protons 34 and triazol proton 31 confirms *E* configuration of the central double bond.

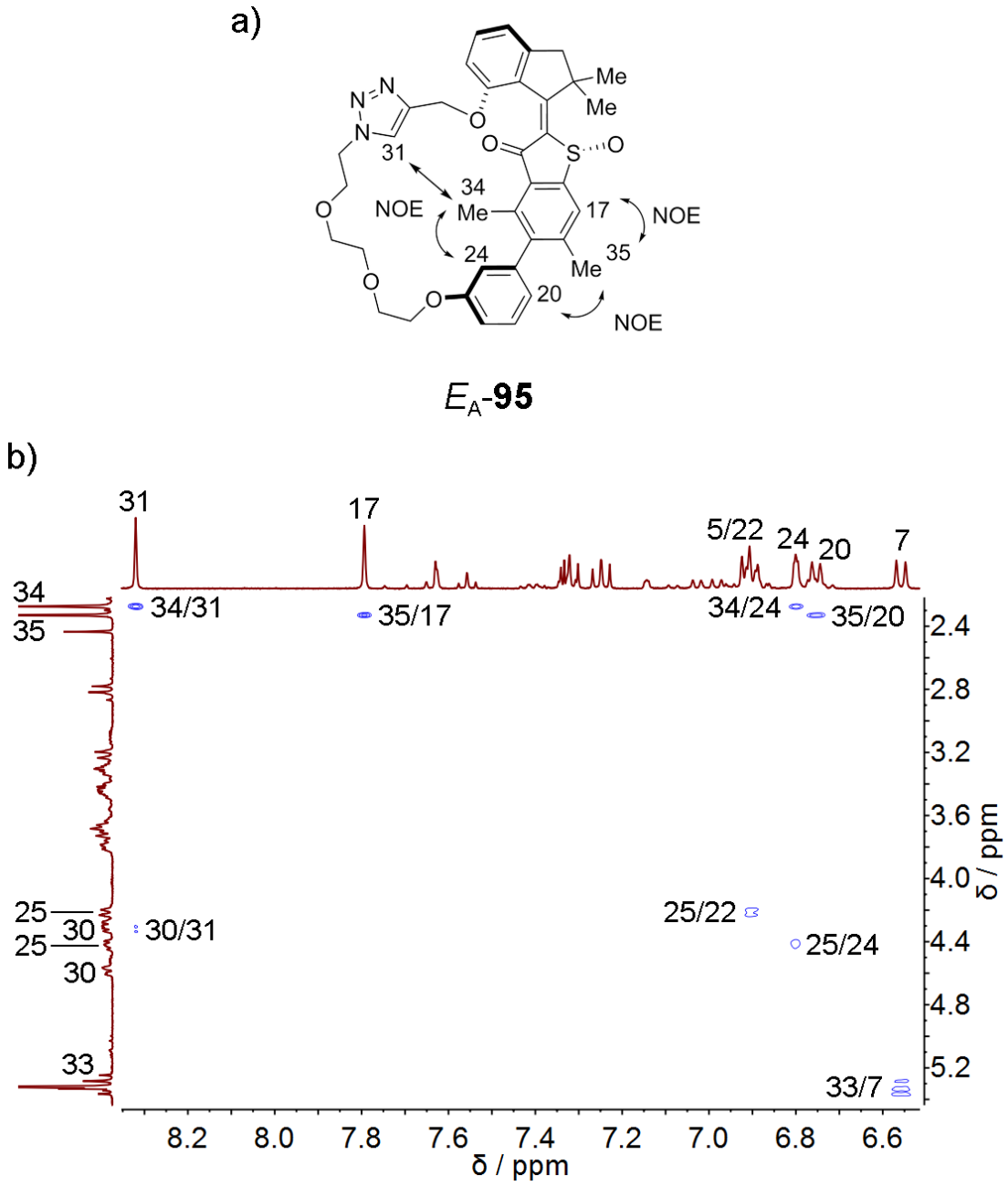

Figure 66 Geometry of E_A-**95** in solution. a) Schematic structure of *E*-(*R*)-(*M*)-(R_a)-**95**. Interacting protons that result in NOESY NMR cross signals are highlighted. b) NOESY NMR spectrum (CD_2Cl_2, 400 MHz, –60 °C) of racemic E_A-**95**. Cross-signals between protons 34 and proton 24 as well as protons 35 and 20 reveal a pronounced tilt of the biaryl axis towards the carbonyl side of the stator. A cross-signal between protons 34 and proton 31 confirms *E* configuration of the central double bond.

4.3.4 Structure of *Z*-95 in the crystalline state

Crystals suitable for X-ray analysis of *Z*-**95** were obtained from a racemic mixture (Figure 67). The oxygen atoms of the indanone rotor and the aryl follower point to the same half space of the benzothiophenone stator with the sulfoxide oxygen atom pointing towards the opposite side. The aryl follower is tilted to the sulfoxide side of the stator with a torsion angle of 68°, which reflects the *M* helicity of the motor unit. The tilt is significantly more pronounced compared to the *E*-**95** isomer and can be attributed to a more confined geometry. Also, the covalent linker connects the aryl follower and the rotor fragment in a straight, linear fashion, which also indicates less flexibility.

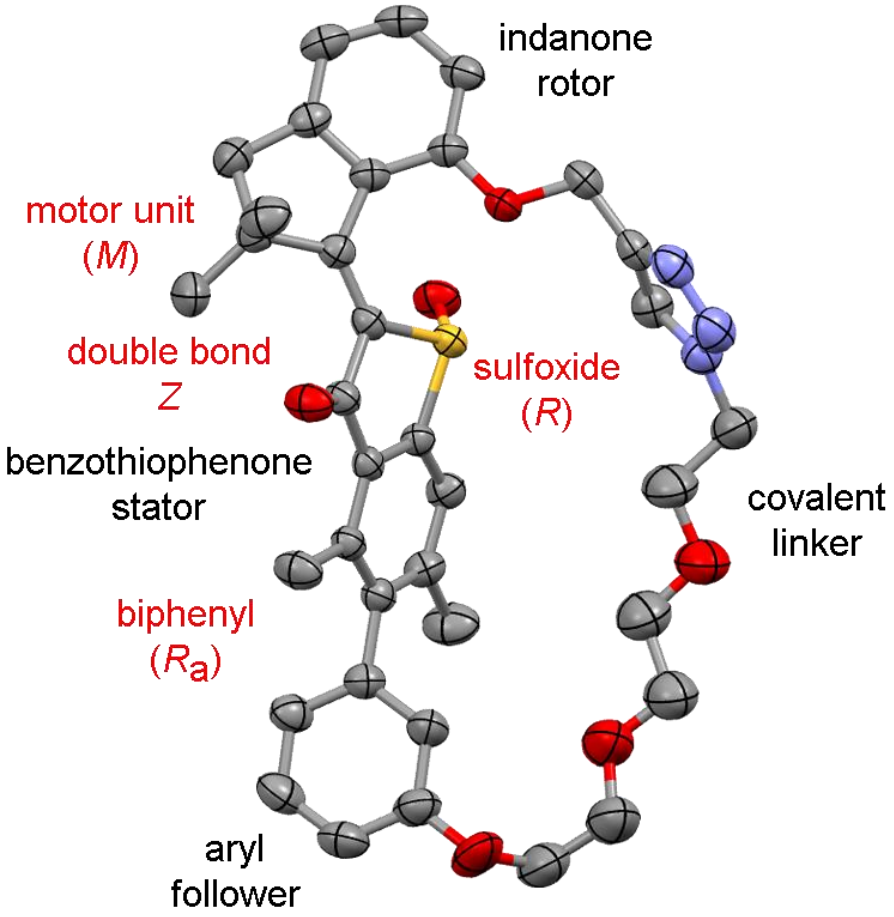

Figure 67 Structure of racemic *Z*-**95** in the crystalline state (50% probability ellipsoids). Assignments of stereodescriptors are given in red. Only the *Z*-(*R*)-(*M*)-(R_a) isomer is shown. The oxygen atoms of the indanone rotor and the covalently linked aryl follower point to the opposite half-space as the sulfoxide oxygen atom. Hydrogen atoms are omitted for clarity.

4.3.5 Structure of *Z*-95 in solution

In solution, NOESY NMR cross signals between methyl group protons 34 and 35 to protons 20 and 24 reveal no difference in intensity, indicating a dihedral biaryl torsion angle that is close to 90° (Figure 68).

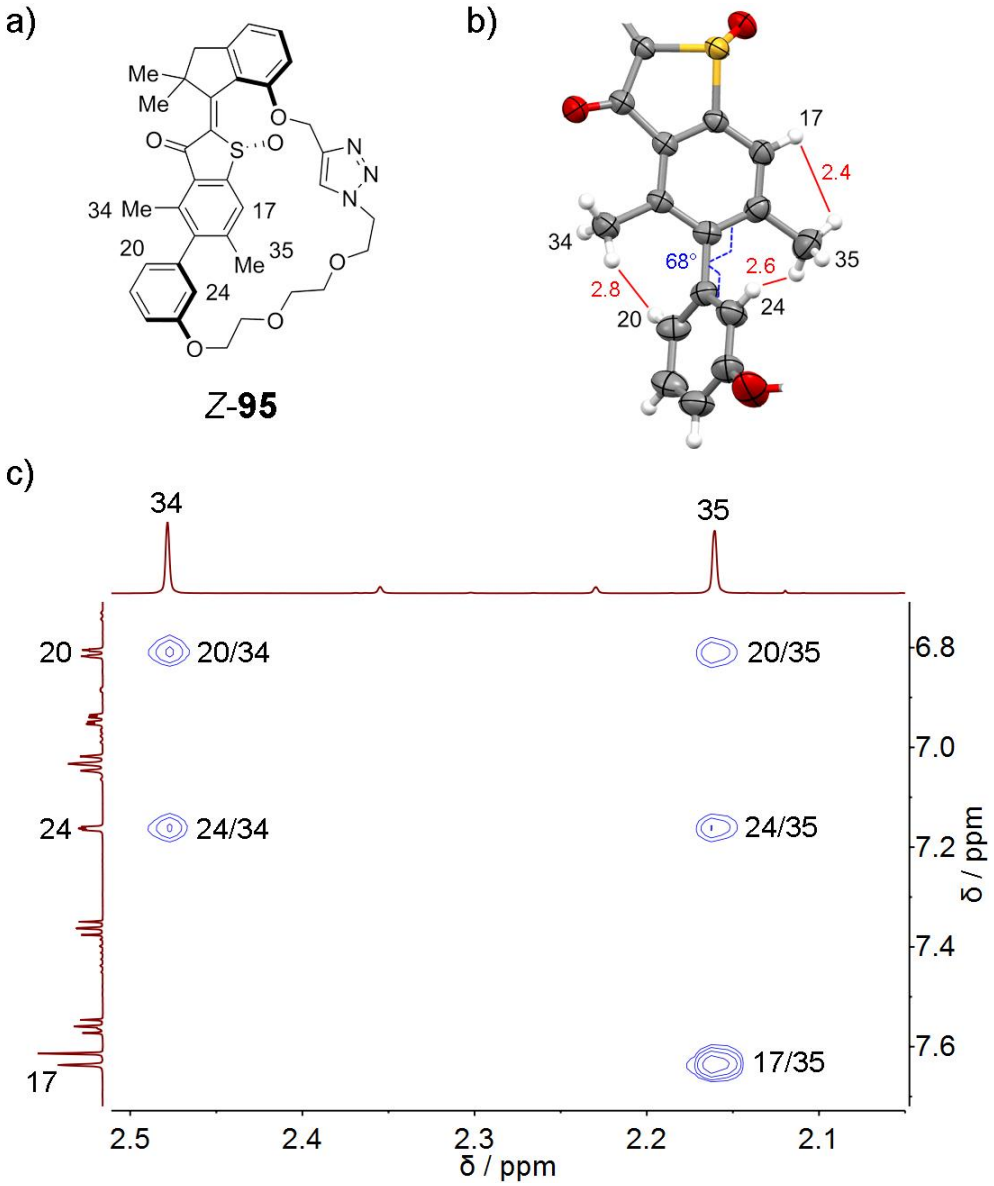

Figure 68 Geometry of *Z*-**95** in solution and in the crystalline state. a) Schematic structure of *Z*-(*R*)-(*M*)-(*R*$_a$)-**95**. Interacting protons that result in NOESY NMR cross signals are highlighted. b) Detail of the structure of *E*-(*R*)-(*M*)-(*S*$_a$)-**95** in the crystalline state. A tilt of the biaryl axis towards the sulfoxide side of the benzothiophenone stator is observed with a torsion angle of 68°. Distances are given in Å (red numbers). The distance between protons 20 and 35 as well as between protons 24 and 34 is 3.6 Å (not shown). c) Detail of the NOESY NMR spectrum (CD_2Cl_2, 599 MHz, 27 °C) of racemic *Z*-**95**. Cross signals between protons 34 and 35 to protons 20 and 24 are equally visible revealing no preferential tilt of the biaryl axis. A cross signal between protons 31 and 34 confirms *E* configuration of the central double bond.

This is in contrast to the structure in the crystalline state with a torsion angle of 68°, which, as a result, can be attributed to crystal packing effects. The difference in cross-signal intensities between the methyl groups of the biaryl unit and the PEG tether reveal a closer proximity of the linker to the sulfoxide side of the benzothiophenone stator (Figure 69). The shortest distance between methyl group protons 34 and the PEG tether in the crystalline state amounts to 5.2 Å.

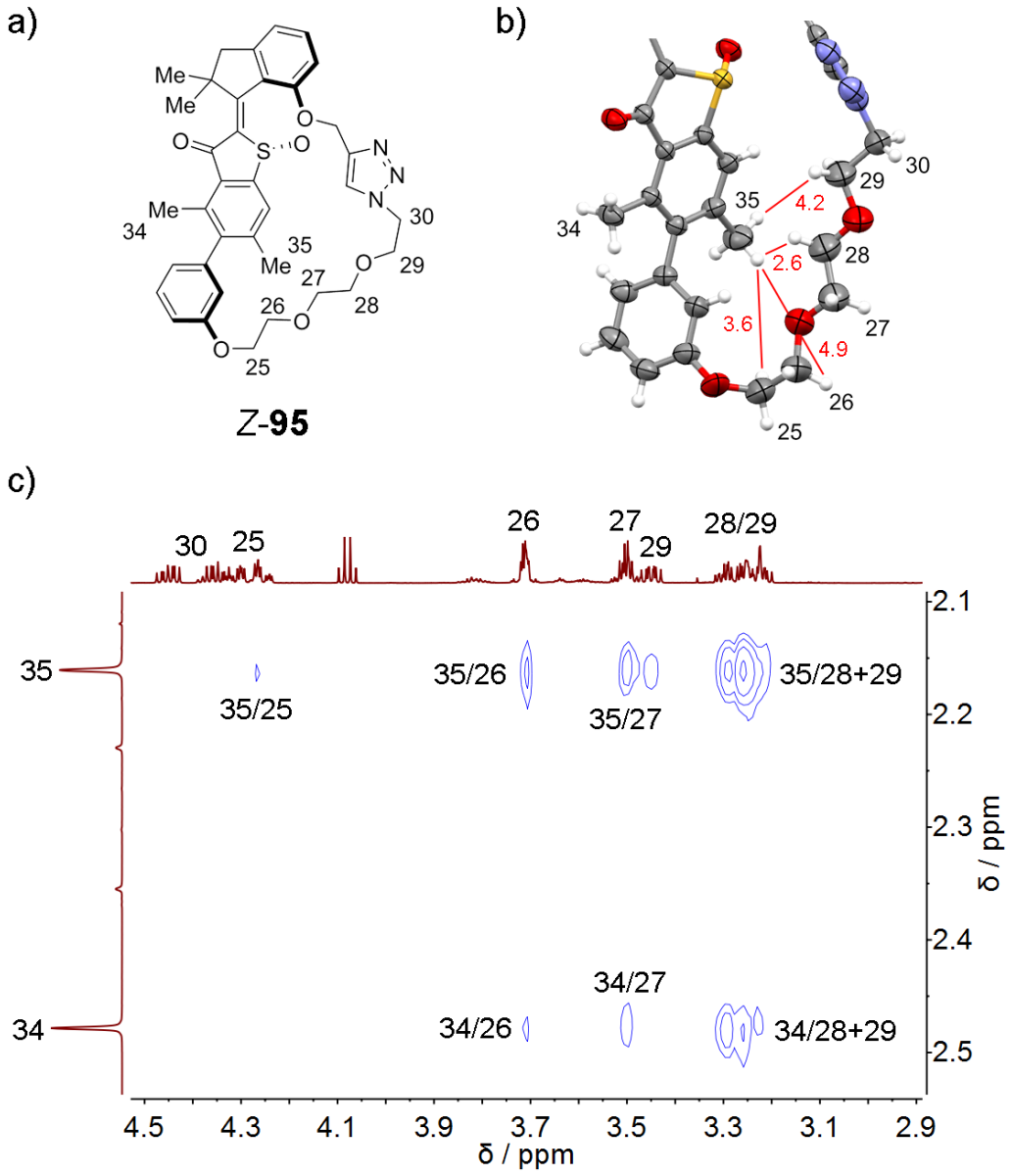

Figure 69 Geometry of *Z*-**95** in solution and in the crystalline state. a) Schematic structure of *Z*-(*R*)-(*M*)-(R_a)-**95**. Interacting protons that result in NOESY NMR cross signals are highlighted. b) Detail of the structure of *Z*-(*R*)-(*M*)-(R_a)-**95** in the crystalline state. The PEG tether is tilted towards the sulfoxide side of the stator. Distances are given in Å (red numbers). c) NOESY NMR spectrum (CD_2Cl_2, 599 MHz, 27 °C) of racemic *E*-**95**. Cross-signals between the covalent linker and methyl group protons 34 are more pronounced, indicating a preferred orientation of the chain to the sulfoxide side of the stator.

Indicative cross signals between proton 17 and the covalent linker confirm *E* configuration of the central double bond (Figure 70). Taken together, the structure of *Z*-**95** in solution is in very good agreement with the crystal structure data.

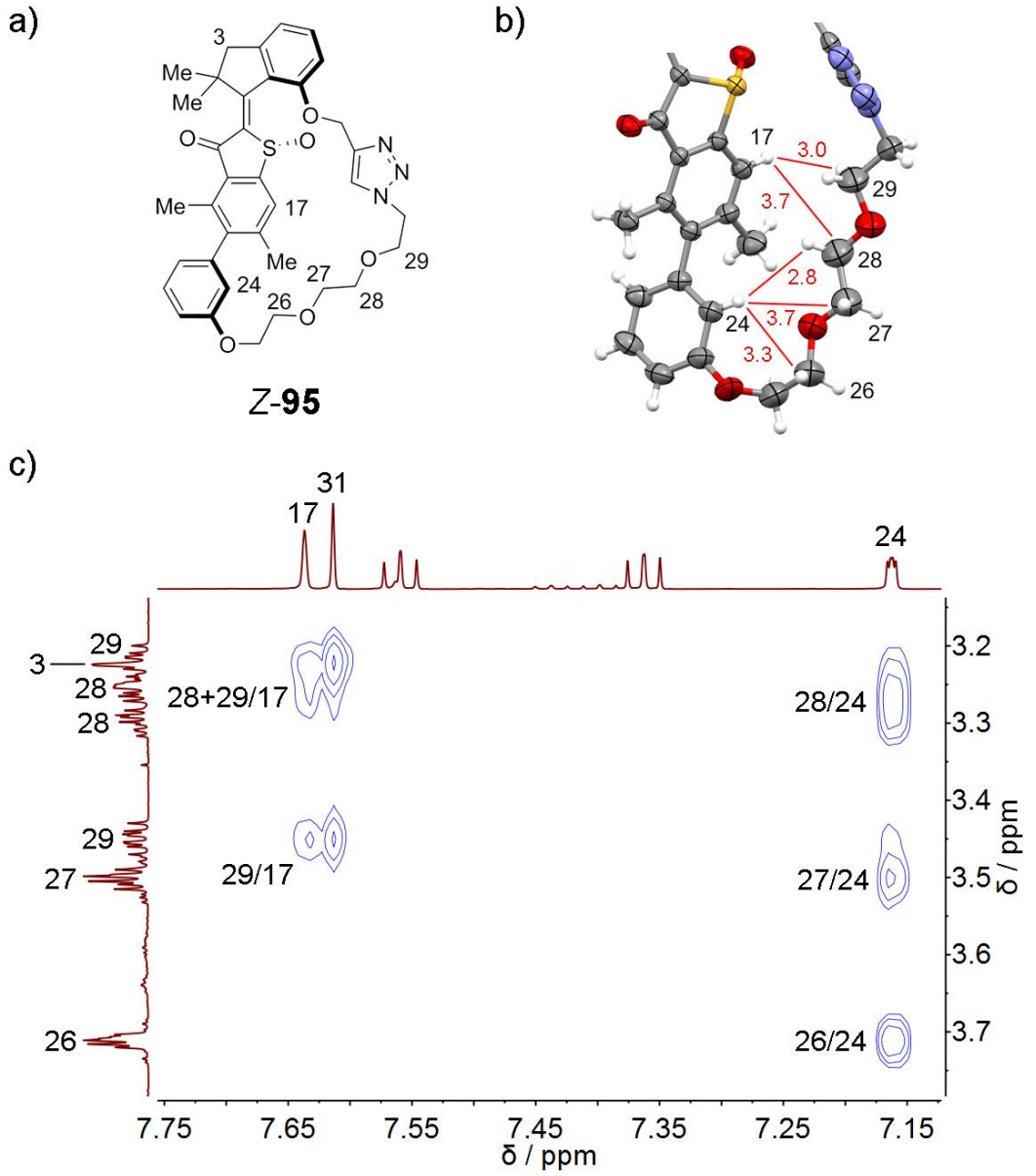

Figure 70 Geometry of *Z*-**95** in solution and in the crystalline state. a) Schematic structure of *Z*-(*R*)-(*M*)-(R_a)-**95**. Interacting protons that result in NOESY NMR cross signals are highlighted. b) Detail of the structure of *Z*-(*R*)-(*M*)-(R_a)-**95** in the crystalline state. The PEG tether is tilted towards the sulfoxide side of the stator. Distances are given in Å (red numbers). c) NOESY NMR spectrum (CD_2Cl_2, 599 MHz, 27 °C) of racemic *E*-**95**. Cross-signals between proton 17 and the covalent linker confirm *E* configuration of the central double bond.

4.4 Molar absorption coefficients and isomer distribution in the pss

The UV-Vis spectra of pure *E*-**95** and *Z*-**95** in CH_2Cl_2 solution with known concentrations were used to calculate the molar absorption coefficients (Figure 71).

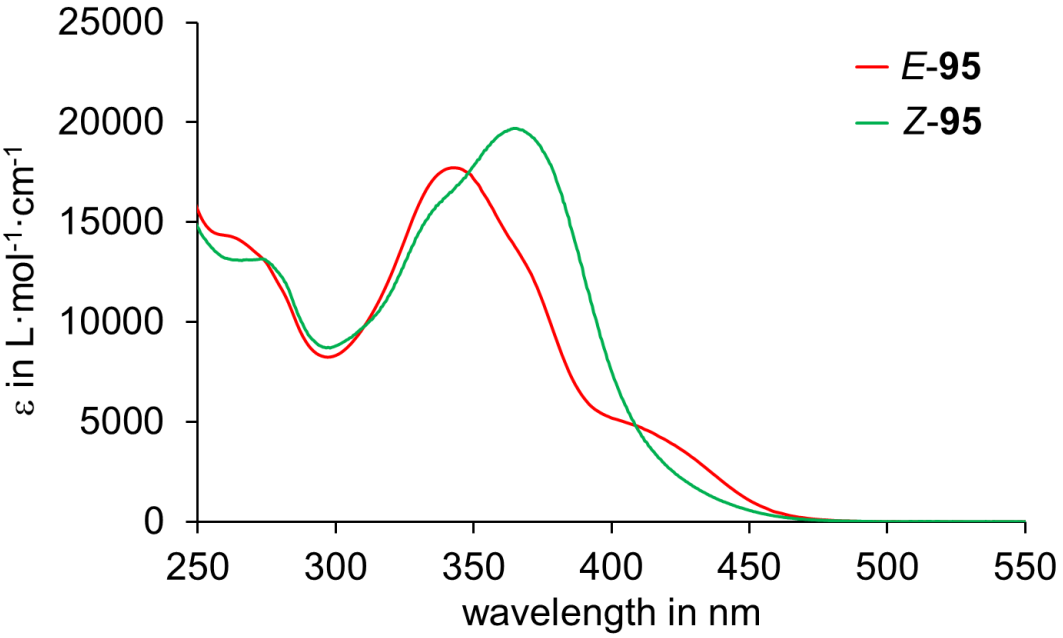

Figure 71 Molar absorption coefficients ε of *E*-**95** and *Z*-**95** (68 µM, CH_2Cl_2, 23 °C).

In addition, a solution of *E*-**95** was irradiated to the pss using different wavelengths (Figure 72). The highest concentration of *Z*-**95** is observed when 450 nm light is used.

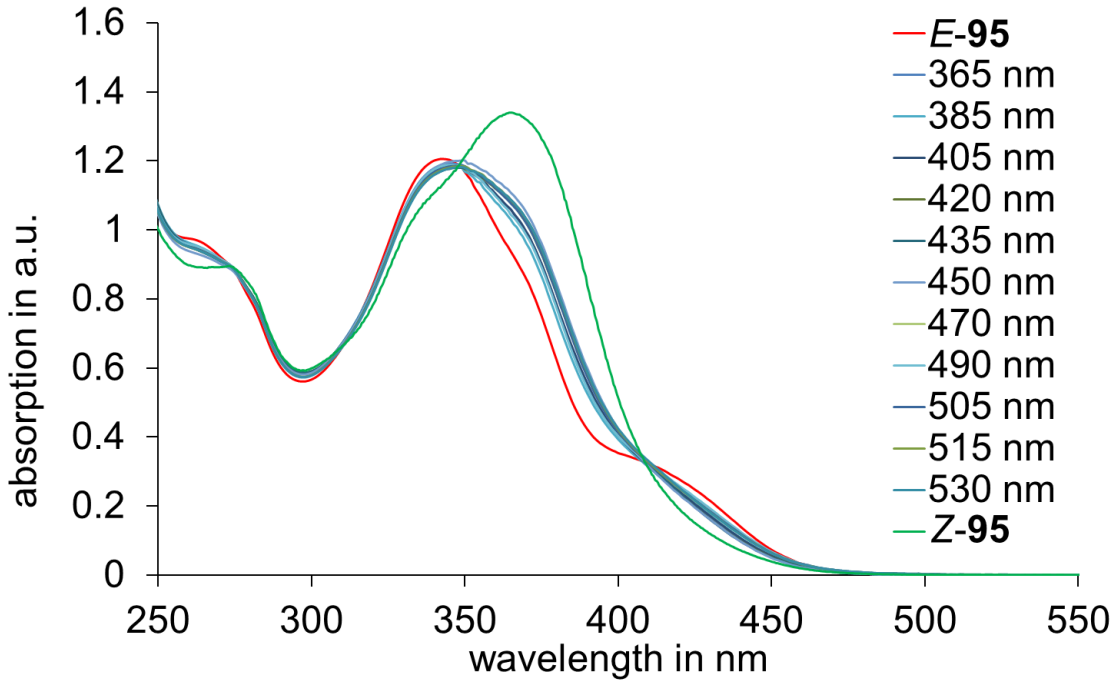

Figure 72 UV-Vis spectra of a solution of **95** (68 µM, CH_2Cl_2, 23 °C) obtained after irradiation to the pss using wavelengths between 365 nm and 530 nm. The initial pure *E*-**95** spectrum (red line) and a pure *Z*-**95** spectrum (green line) are shown for comparison.

Irradiations with different wavelengths were repeated for a solution of *E*-**95** in CD_2Cl_2 and the isomer distributions in the pss were obtained by integration from the corresponding ^{1}H NMR spectra (Figure 73). Analogously to the UV-Vis experiments the highest concentration of *Z*-**95** was observed when a wavelength between 435 nm and 470 nm was used (Table 6).

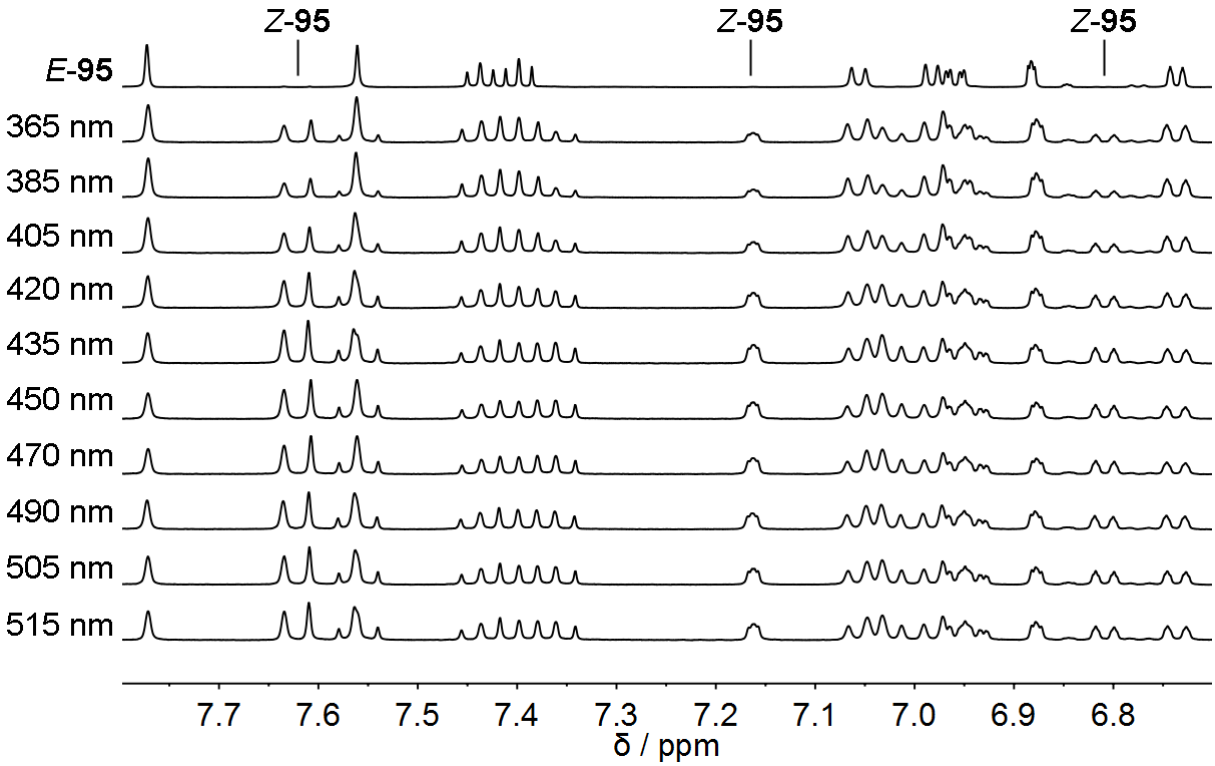

Figure 73 ^{1}H NMR spectra of a solution of *E*-**95** (CD_2Cl_2, 400 MHz, 22 °C) obtained after irradiation to the pss using different wavelengths. The highest concentration of *Z*-**95** was observed using wavelengths between 435 nm to 470 nm.

Table 6 Distribution of *E*-**95** and *Z*-**95** isomers after irradiating a solution of *E*-**95** (CD_2Cl_2, 400 MHz, 22 °C) to the pss using light of different wavelengths.

wavelength	**time**	***E*-95**	***Z*-95**
365 nm	2 h	69 %	31 %
385 nm	2 h	73 %	27 %
405 nm	1 h	65 %	35 %
420 nm	1 h	53 %	47 %
435 nm	4 h	48 %	52 %
450 nm	1 h	48 %	52 %
470 nm	1 h	47 %	53 %
490 nm	1 h	51 %	49 %
505 nm	1.5 h	50 %	50 %
515 nm	1.5 h	51 %	49 %

4.5 Quantum yield determination

The quantum yield Φ for the photoisomerization from *E*-**95** to *Z*-**95** and *vice versa* was determined at ambient temperatures. It is defined by the number of isomerized molecules per absorbed photons according to (equation *10*:

$$\Phi = \frac{n\ (isomerized\ molecules)}{n\ (absorbed\ photons)} \qquad \text{(equation 10)}$$

The measurement was conducted within a published experimental setup by the group of *Riedle*.[87] Solutions of pure *E*-**95** or *Z*-**95** in CH_2Cl_2 with known concentrations were prepared and defined portions were irradiated in a cuvette with a focused light beam of a 450 nm LED under vigorous stirring. The individual solutions were irradiated repeatedly for 10 seconds and a UV-Vis spectrum was taken after every step (Figure 74 and Figure 77). This way the change in concentration and therefore the number of *isomerized molecules* could be determined using the molar absorption coefficient (see previous section). As the isomerization process reaches a saturation only the initial linear change in concentration is used for the quantum yield determination.

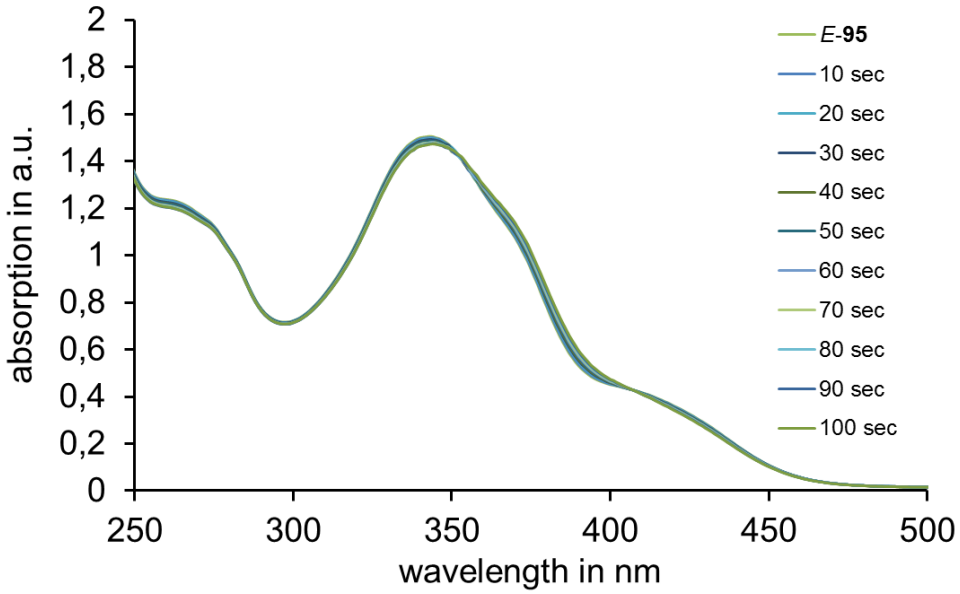

Figure 74 UV-Vis absorption spectra acquired during irradiation of a solution of *E*-**95** (85 µM, CH_2Cl_2, 23 °C) with 450 nm light. Spectra were taken in 10 sec intervals.

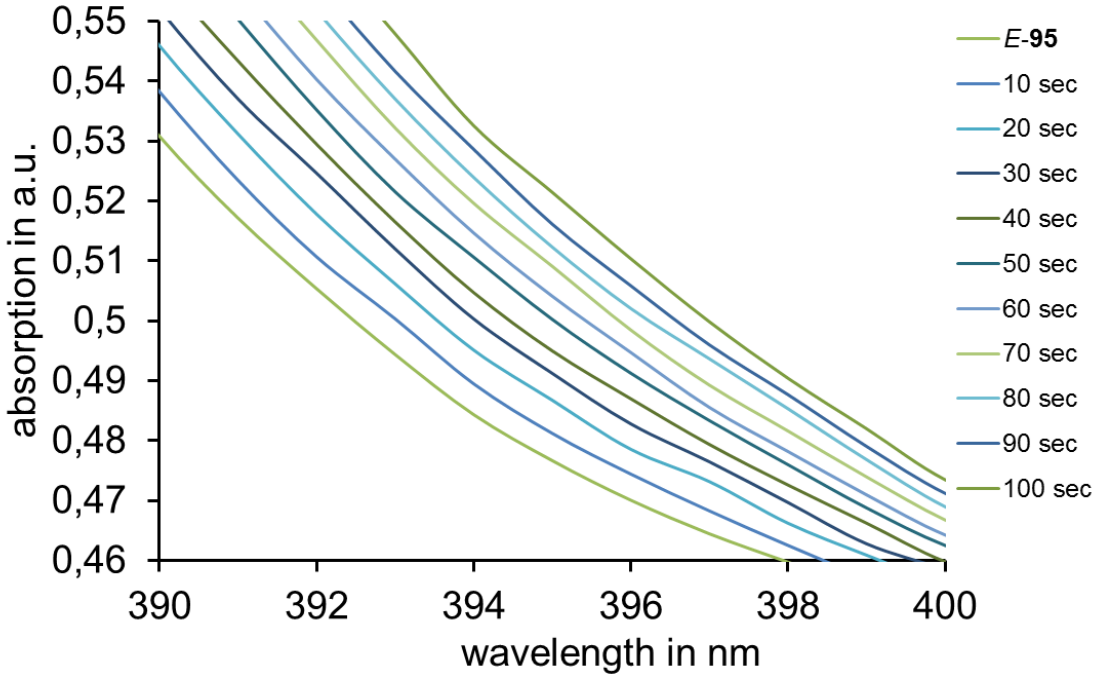

Figure 75 Detail of the UV-Vis absorption spectra acquired during irradiation of a solution of *E*-**95** (85 µM, CH_2Cl_2, 23 °C) with 450 nm light. Spectra were taken in 10 sec intervals.

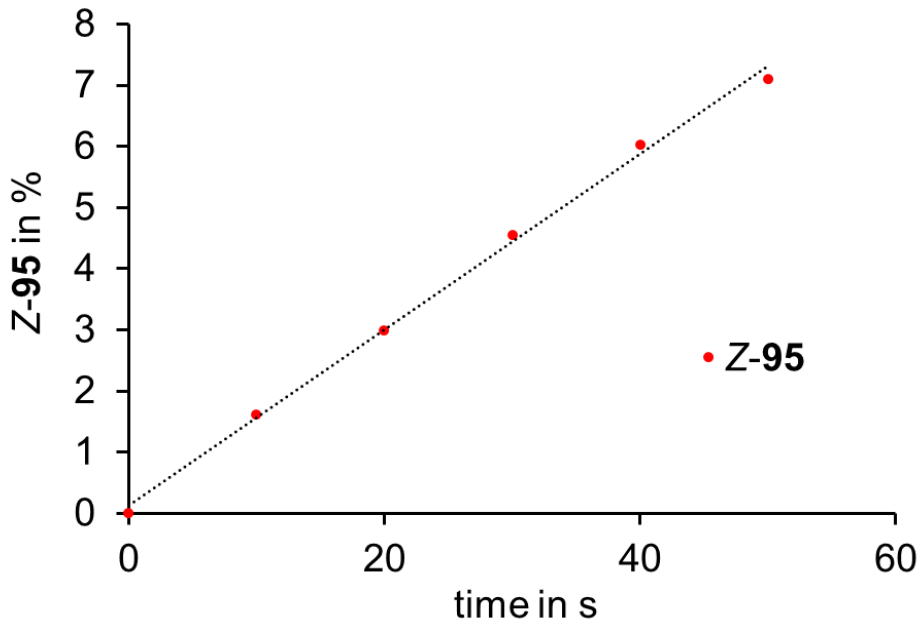

Figure 76 Plot of the concentration of *Z*-**95** during the photoconversion of *E*-**95** to *Z*-**95** by irradiation with 450 nm light. Concentrations were calculated every 10 sec from UV-Vis spectra using the molar absorption coefficient. The first five data points were used for the quantum yield determination.

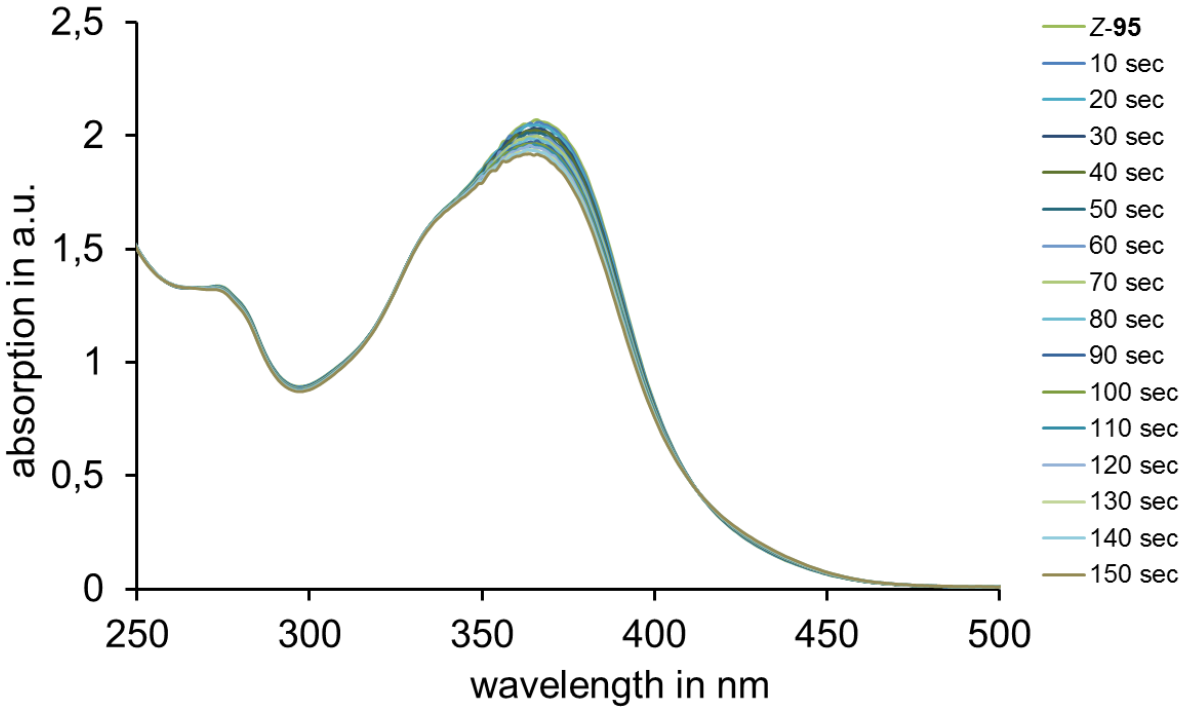

Figure 77 UV-Vis absorption spectra acquired during irradiation of a solution of *Z*-**95** (104 µM, CH_2Cl_2, 23 °C) with 450 nm light. Spectra were taken in 10 sec intervals.

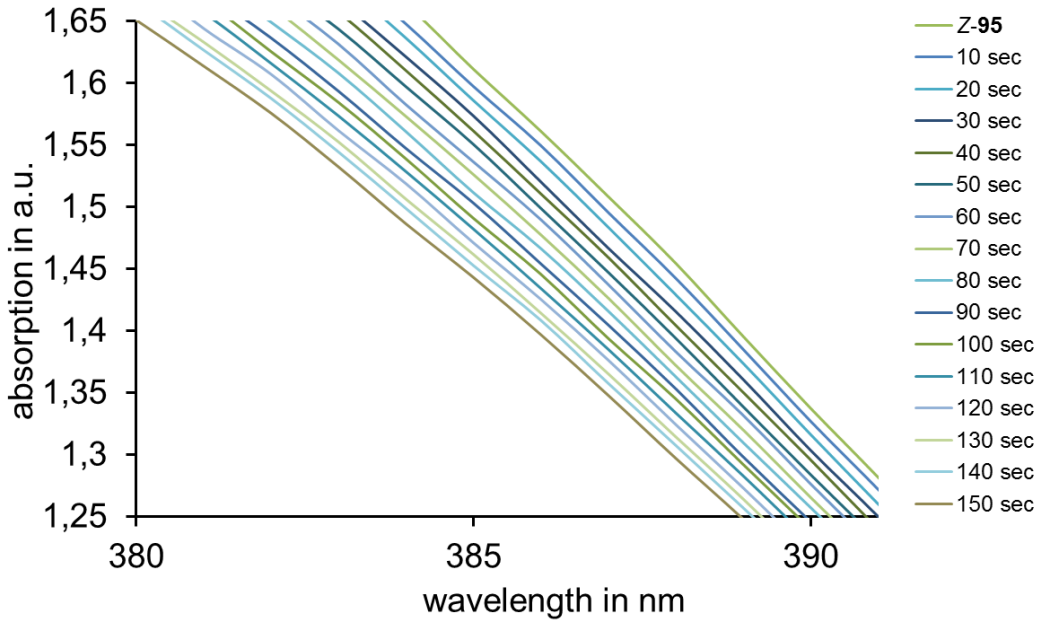

Figure 78 Detail of the UV-Vis absorption spectra acquired during irradiation of a solution of *Z*-**95** (85 µM, CH_2Cl_2, 23 °C) with 450 nm light. Spectra were taken in 10 sec intervals.

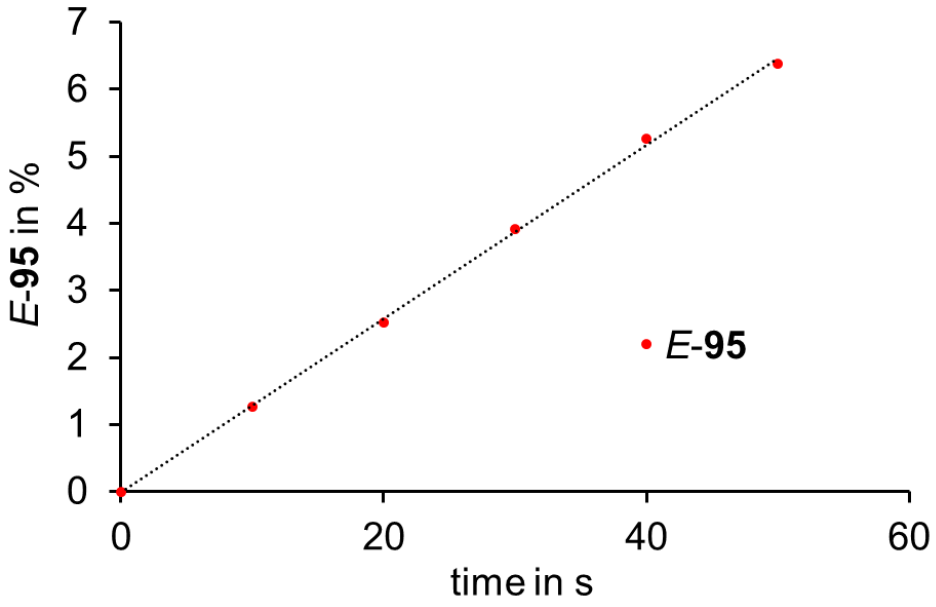

Figure 79 Plot of the concentration of *E*-**95** during the photoconversion of *Z*-**95** to *E*-**95** by irradiation with 450 nm light. Concentrations were calculated every 10 sec from UV-Vis spectra using the molar absorption coefficient. The first five data points were used for the quantum yield determination.

The number of *absorbed photons* was calculated from the power readout at the thermal photometer using (equation *11*

$$n\,(absorbed\ photons) = \frac{\Delta P \cdot \lambda_{ex} \cdot t}{c \cdot h} \qquad \text{(equation 11)}$$

where λ_{ex} is the excitation wavelength, t is the elapsed time during irradiation, c is the speed of light ($2.99792.10^8$ m·s^{-1}), h is the Planck's constant ($6.62607 \cdot 10^{-34}$ J·s), and ΔP is the difference in power readouts at the thermal photometer between a cuvette filled with solvent (P_0) and a cuvette containing the sample solution (P_t) ((equation *12*). The power read out during irradiation did not change substantially (~1%) and was averaged over the 5 steps that were used for the calculations.

$$\Delta P = P_t - P_0 \qquad \text{(equation 12)}$$

The determined quantum yields are 3.7% for the photoreaction of *E*-**95** and 6.4% for the photoreaction of *Z*-**95** (450 nm, 23 °C).

4.6 Elevated temperature behavior

The *E*-**95** isomer was determined as the thermodynamically most stable form. At 80 °C the *Z*-**95** isomer is slowly converted to the *E* isomeric form until an equilibrium state of 9% *Z*-**95** and 91% *E*-**95** is reached (Figure 80).

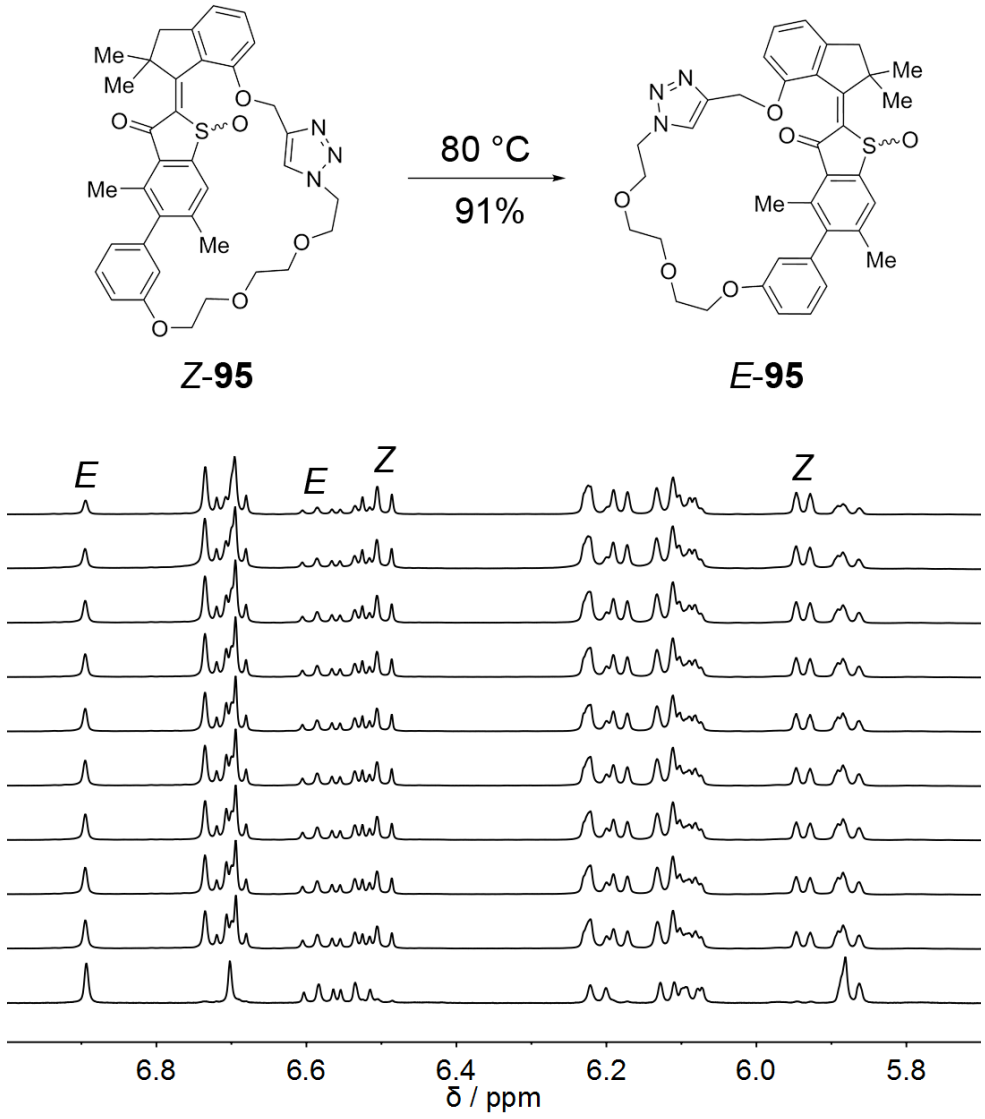

Figure 80 ^{1}H NMR spectra ($(CDCl_2)_2$, 400 MHz, 22 °C) acquired during the thermal conversion of *Z*-**95** to *E*-**95** at 80 °C. Exemplary signals of the aromatic region of the *Z* and *E* isomers are highlighted. The spectra were taken in 30 min intervals and an additional spectrum (bottom) was measured after 3 d to obtain the isomer distribution at the equilibrium composition.

The changing isomer distribution during heating to 80 °C was followed in 30 min intervals (Figure 81). A first-order rate constant was determined from the thermal decay kinetics taking into account the thermal equilibrium. The slope *m* of the logarithmic plot (Figure 82) can be used to calculate the rate constant *k* according to (equation 4.

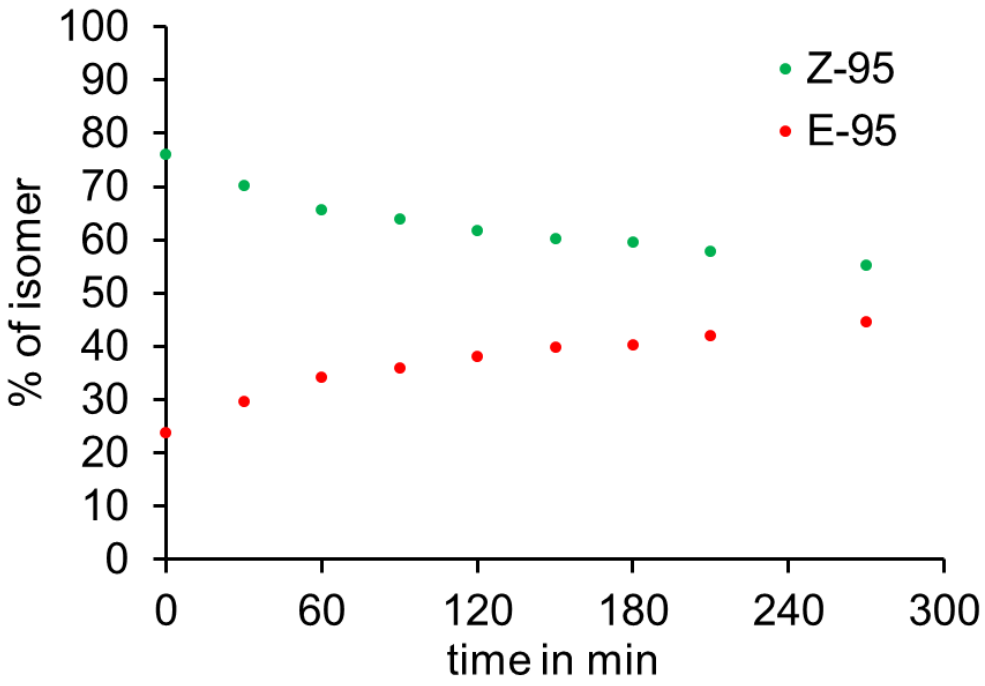

Figure 81 Isomer distribution during the thermal *Z*-**95** to *E*-**95** isomer conversion starting from a $(CDCl_2)_2$ solution containing 76% *Z*-**95** and 24% *E*-**95** isomer and heating in 30 min intervals. After 3 d of thermal annealing, a stable isomeric ratio of 9% *Z*-**95** to 91% *E*-**95** is established (data point omitted for clarity).

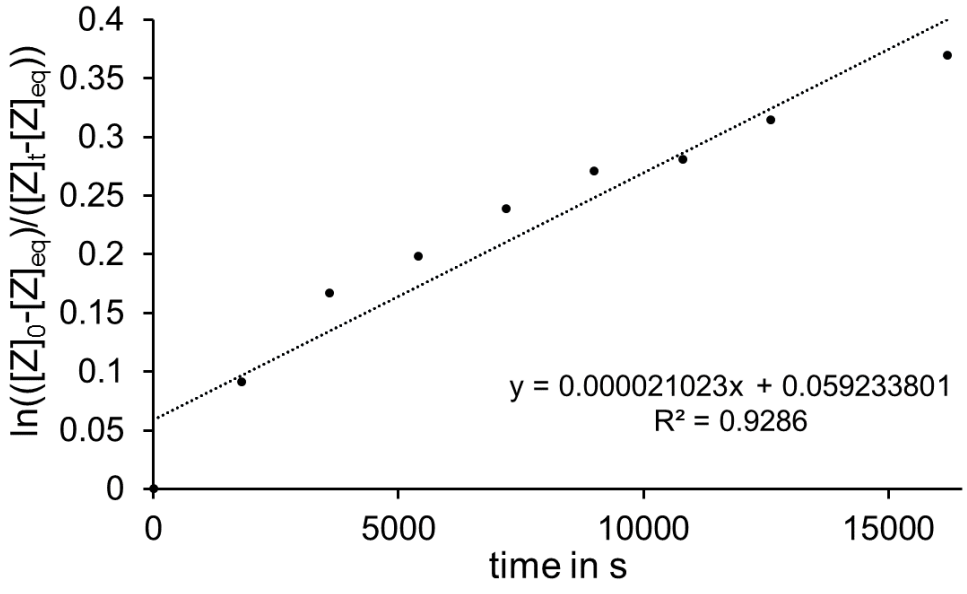

Figure 82 First-order linearization of the kinetic analysis. The formula of the linear fit is given in the diagram. The slope m = 0.000021023 is used to calculate the rate constant $k(Z \rightarrow E)$ according to (**equation 4**.

After insertion of the numerical values into the *Eyring* equation (equation 7) a Gibbs free energy $\Delta G^{\ddagger}$ = 28.4 kcal·mol^{-1} is obtained for the thermal *Z*-**95** to *E*-**95** isomerization reaction. This

translates into a half-life of 10 hours at 80 °C or 3.3 years at 23 °C. With an equilibrium constant of K = 9/91 at 80 °C, the relative energy difference between the two isomeric states can be calculated using (equation 8) and a value of ΔG = 1.62 kcal·mol^{-1} is obtained.

4.7 Elucidation of machine function

4.7.1 Conformational overview

Upon close inspection of the ^{1}H NMR spectrum of *E*-**95**, an additional set of signals is visible for protons in close proximity to the biaryl axis (Figure 83). Separation of *E*-**95** from the additional compound was not possible via preparative HPLC and the second species is found in a stable 1 to 9 ratio at room temperature compared to the *E*-**95** isomer. Based on these results, the set of signals was attributed to an atropisomer of *E*-**95**.

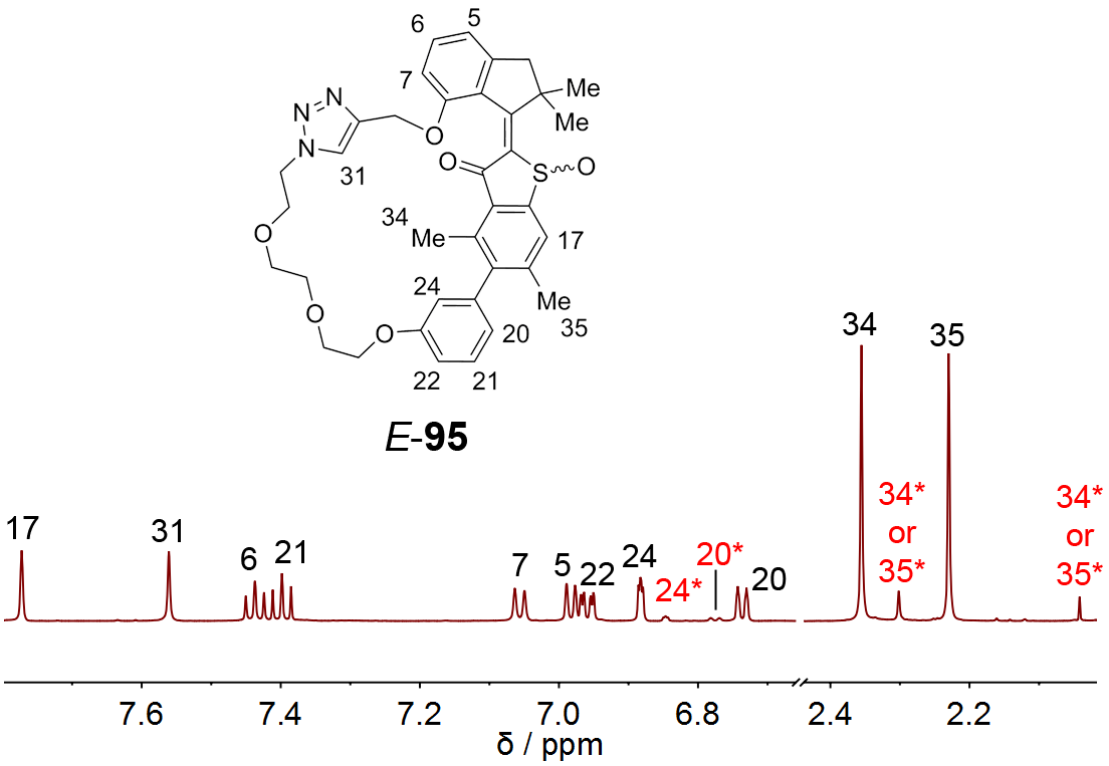

Figure 83 Selected regions of the ^{1}H NMR spectrum of *E*-**95** (CD_2Cl_2, 599 MHz, 27 °C) and respective signal assignment. An additional set of signals is observed for protons in close proximity to the biaryl axis (red numbers). Integration of the additional set of signals reveals a ratio of 1:9 compared to the signals of *E*-**95**.

Here, the covalent linker runs from one half-space of the benzothiophenone stator to the opposite half-space (**A$_T$-95**, Figure 84). This results in a more strained conformation which is

in accordance to the observed 1:9 isomer distribution and was termed **T**ensed *E*-**95** or **A$_T$-95** in accordance with the earlier introduced **A-D** nomenclature. As a consequence, all experiments conducted on *E*-**95** (= **R**elaxed *E*-**95** or **A$_R$-95)** contain some amount of **A$_T$-95** in the respective ratio. Six possible conformers were identified as energetic minima for molecular machine **95** (Figure 84). The letters **A**, **B**, **C**, and **D** were assigned to the individual conformers that result from the 360° unidirectional motor rotation analogously to the previous system **81** (see section 3.5 for a detailed description).

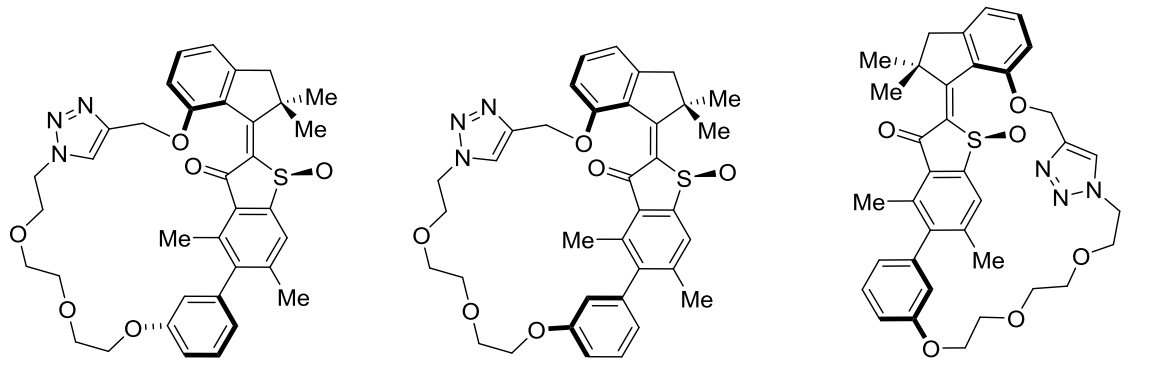

A$_T$-95
E-(*S*)-(*P*)-(*S*$_a$)

A$_R$-95
E-(*S*)-(*P*)-(*R*$_a$)

B$_R$-95
Z-(*S*)-(*M*)-(*R*$_a$)

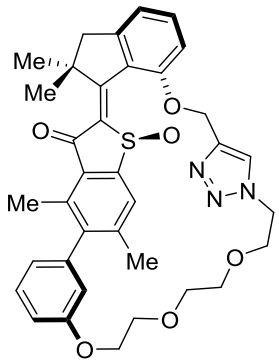

C$_T$-95
Z-(*S*)-(*P*)-(*R*$_a$)

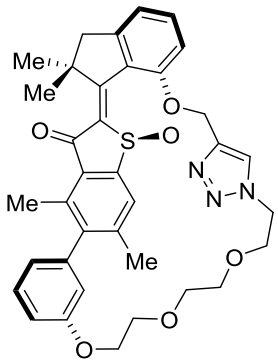

C$_R$-95
Z-(*S*)-(*P*)-(*S*$_a$)

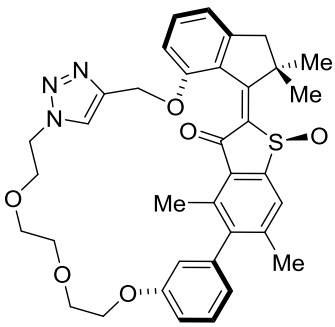

D$_R$-95
E-(*S*)-(*M*)-(*S*$_a$)

Figure 84 Overview of the conformers of **95** that represent local and global energetic minima. Only structures with an *S* configured sulfoxide are shown for clarity. The subscript **R** is used for structures with a **R**elaxed covalent linker, the subscript **T** is used for structures with a **T**ensed linker.

No additional signals of other conformers were found in the spectrum of *Z*-**95** at room temperature. This can be attributed to the overall higher strain in the *Z*-isomeric form that results in a significant increase of the relative energy of a possible **C$_T$-95** structure.

4.7.2 Irradiation and thermal conversion at low temperatures

In order to gain insight into the detailed working mechanism of the machine **95**, NMR experiments with *in situ* irradiation were conducted at low temperatures. A solution of **C_R-95** in CD_2Cl_2:CS_2 (4:1) was cooled to –105 °C and irradiated with 450 nm light to accumulate the metastable **D_R-95** isomer (Figure 85).

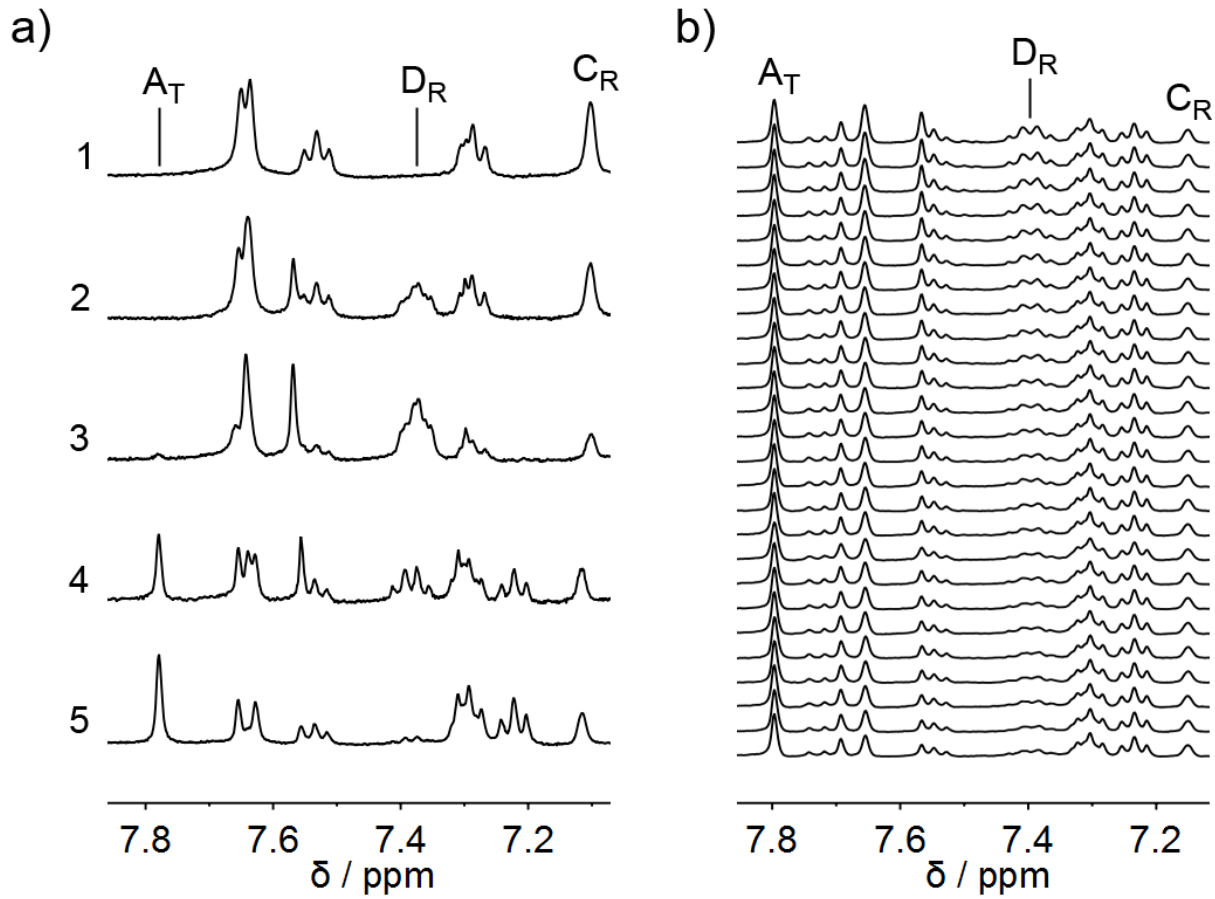

Figure 85 ^{1}H NMR spectra of **95** (400 MHz, CD_2Cl_2:CS_2 (4:1)). a) 1. **C_R-95** at –105 °C before irradiation. 2. After 29 min of irradiation with 450 nm light. 3. After 55 min of irradiation with 450 nm light 70% of the **D_R-95** isomer is accumulated. Slow onset of thermal **D_R-95** to **A_T-95** conversion is visible. 4. After turning off the light and warming to –80 °C 5. After 23 min at –80 °C almost full conversion of the **D_R-95** conformer exclusively to **A_T-95** is observed (see b) for details). b) At –80 °C thermal conversion of **D_R-95** exclusively to **A_T-95** is observed.

After 55 minutes of irradiation a maximum of 70% **D_R-95** was observed in the ^{1}H NMR spectrum. The solution was warmed to –80 °C and a kinetic analysis was conducted for the thermal decay of this metastable isomer (Figure 86 and Figure 87). A slow conversion was observed at this temperature and a new set of signals emerged that is identical to the signals that were attributed to **A_T-95**. The newly formed isomer was found to be in a dynamic equilibrium

with **D$_R$-95** with a stable isomer composition of 12:88 at –80 °C. A Gibbs free energy of activation of 13.9 kcal·mol^{-1} was determined for the isomerization process. From the equilibrium ratio, a relative energy difference of 0.76 kcal·mol^{-1} was calculated between the **A$_T$-95** and **D$_R$-95** isomers.

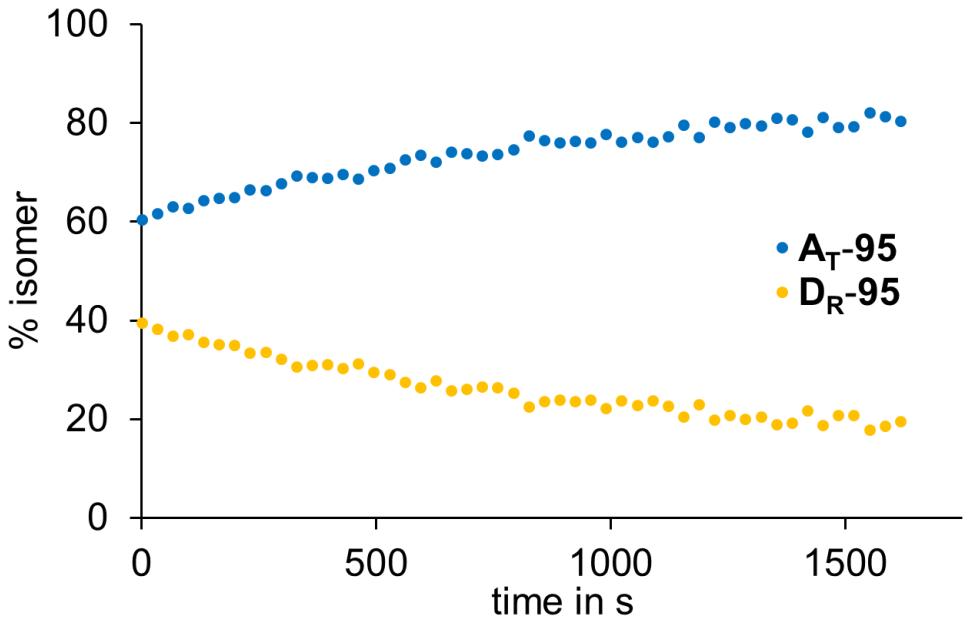

Figure 86 Isomer distribution during the thermal conversion of **D$_R$-95** to **A$_T$-95** at –80 °C in CD_2Cl_2:CS_2 (4:1) solution.

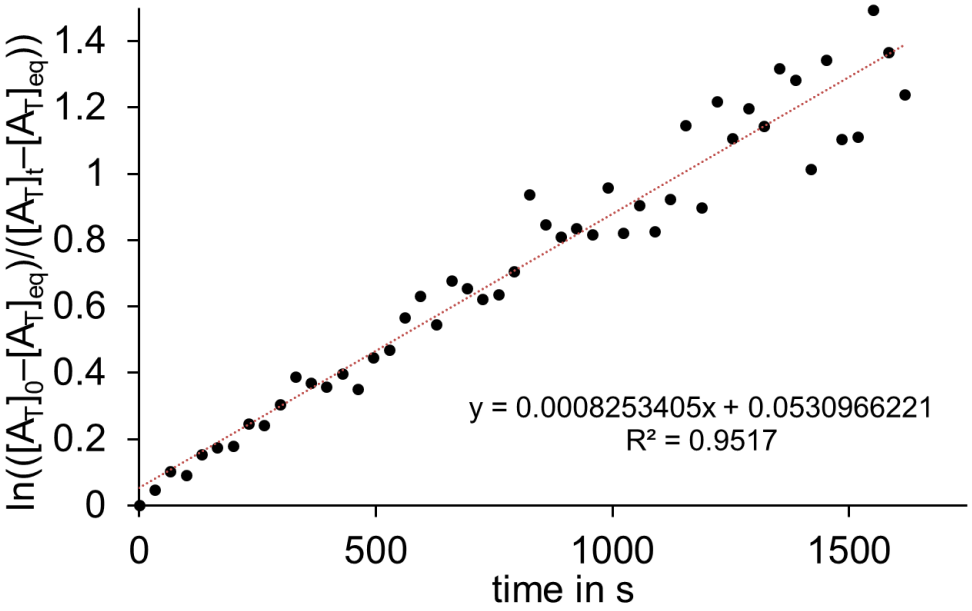

Figure 87 Kinetic analysis of the thermal conversion of **D$_R$-95** to **A$_T$-95** at –80 °C in CD_2Cl_2:CS_2 (4:1) solution. The slope m = 0.0008253405 (formula given in the diagram) is used to calculate the rate constant k(**D$_R$-95** → **A$_T$-95**) according to (equation **4**. The Gibbs free energy of activation amounts to 13.9 kcal·mol^{-1}.

Upon warming to –20 °C, the signal set of **A_T-95** decayed and conversion exclusively to **A_R-95** was observed (Figure 88). Again, the interconverting isomers were found to be in a dynamic equilibrium with a stable isomer distribution of 1:9 that was already observed in earlier experiments (see Figure 83).

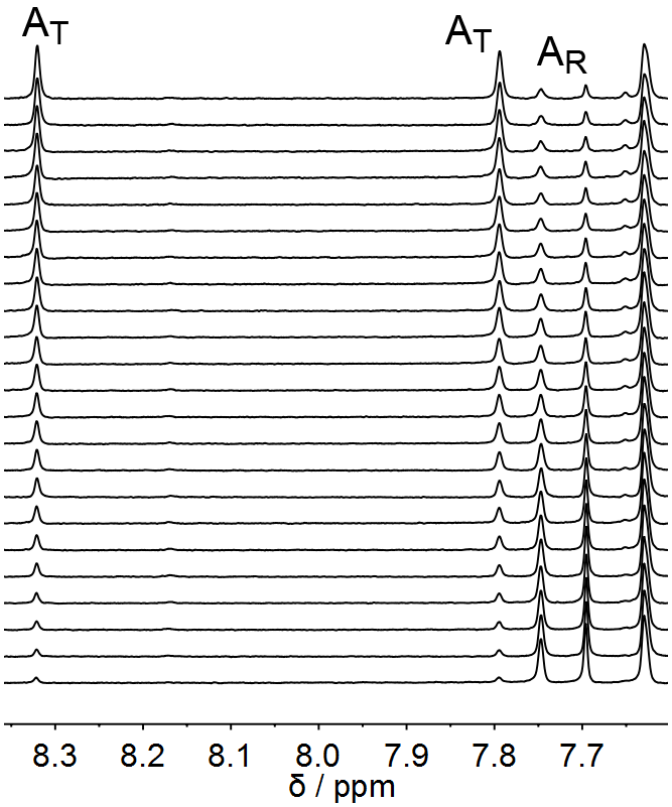

Figure 88 ^{1}H NMR spectra (400 MHz, CD_2Cl_2, –20 °C) acquired during the thermal conversion of **A_T-95** to **A_R-95** starting from an **A_T-95** enriched solution.

A kinetic analysis revealed an energy of activation of 18.8 kcal·mol^{-1} for the isomerization process from **A_T-95** to **A_R-95** and a relative energy difference of 1.29 kcal·mol^{-1} between the two isomers was derived from the resulting dynamic equilibrium (Figure 89 and Figure 90).

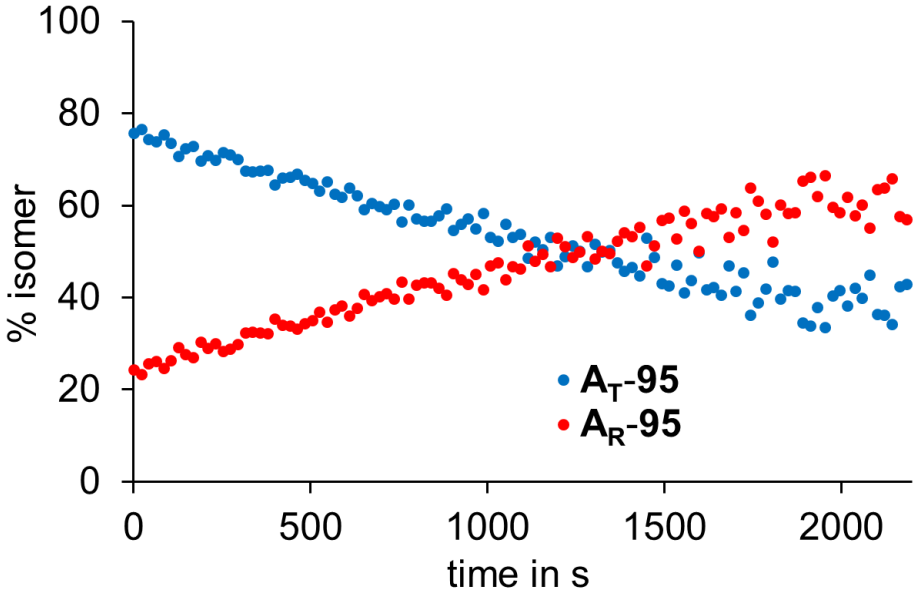

Figure 89 Isomer distribution during the thermal conversion of **A$_T$-95** to **A$_R$-95** at –20 °C in CD_2Cl_2 solution.

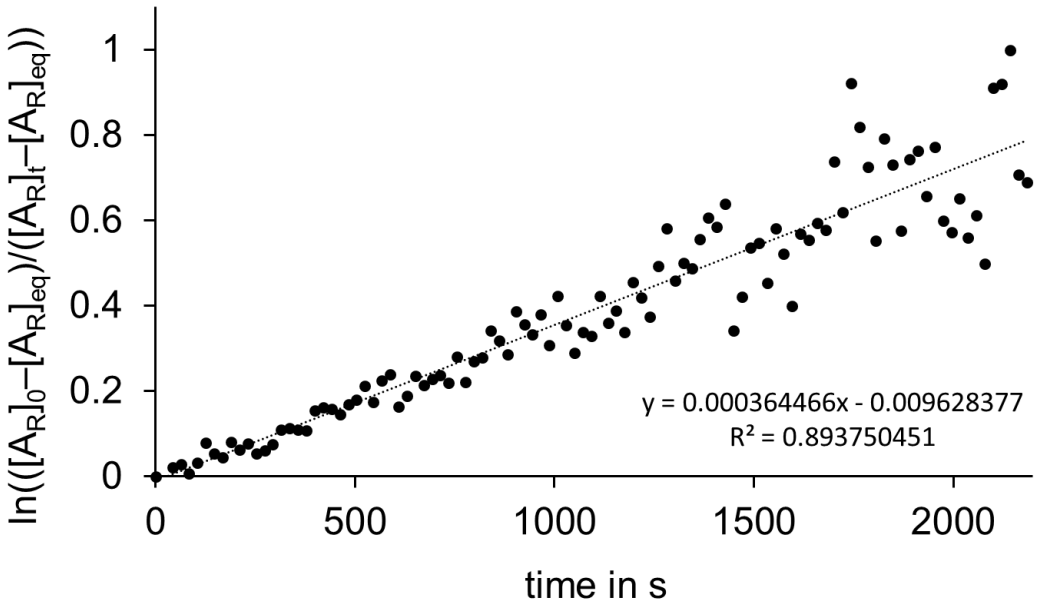

Figure 90 Kinetic analysis of the thermal conversion of **A$_T$-95** to **A$_R$-95** at –20 °C in CD_2Cl_2 solution. The slope m = 0.000364466 (formula given in the diagram) is used to calculate the rate constant k(**A$_T$-95** → **A$_R$-95**) according to (equation **4**. The Gibbs free energy of activation is 18.8 kcal·mol^{-1}.

The thermal helix inversion from **D$_R$-95** to **A$_T$-95** is in agreement with the underlying motor function. Due to the increased steric hindrance around the biaryl axis, the atropisomerization cannot occur at very low temperatures, leading to the unprecedented tensed intermediate **A$_T$-95**,

in which the motor helix has thermally already relaxed but the biaryl follower unit has not yet rotated. At elevated temperatures (–20°C), atropisomerization of **A_T-95** to **A_R-95** is observed. This releases the tension on the biaryl axis that was induced by the **D_R-95** to **A_T-95** helix inversion and completes the transmittance of the unidirectional motion to the aryl moiety for the first 180° of the unidirectional cycle.

Next, isomerization experiments starting from **A_R-95** were conducted at low temperatures in order to observe the expected metastable intermediates. To this end, a solution of **A_R-95** in CD_2Cl_2:CS_2 (4:1) was prepared and cooled to –105 °C. Irradiation with 450 nm light generated a new set of signals that could be accumulated to a maximum of 42% and corresponds to a new isomer (Figure 91).

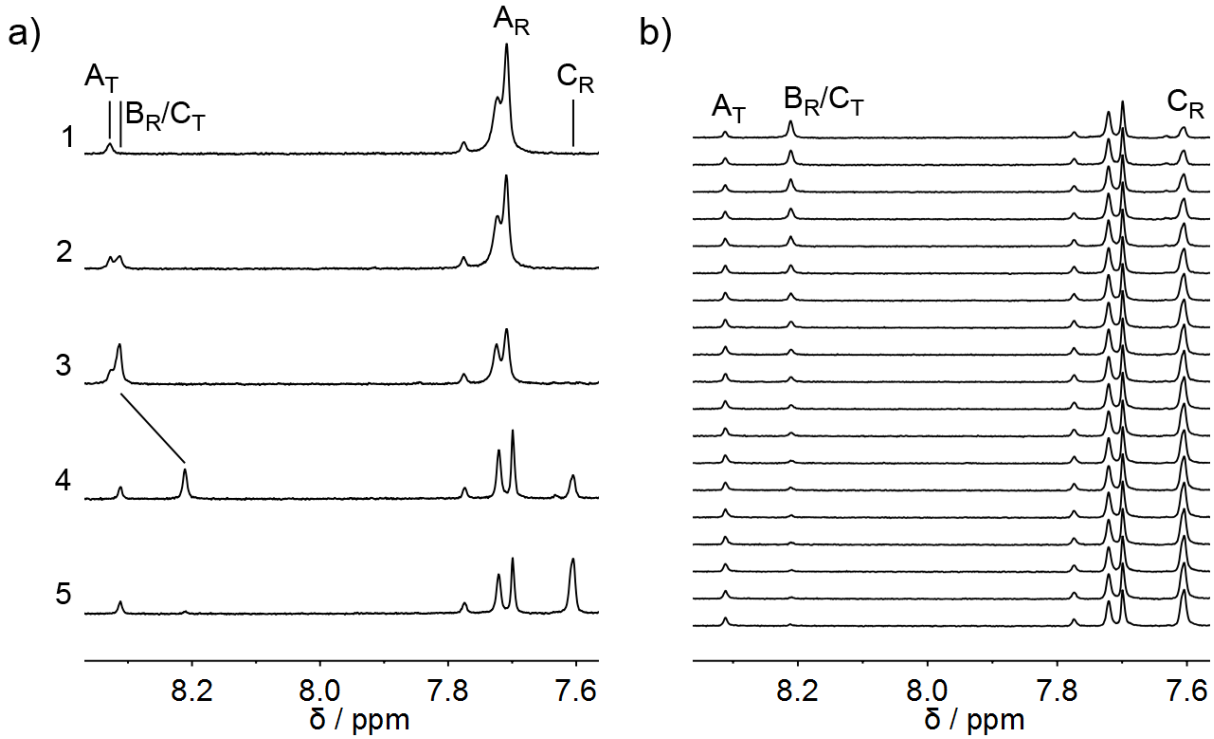

Figure 91 ^{1}H NMR spectra of **95** (400 MHz, CD_2Cl_2:CS_2 (4:1)). a) 1. A solution of **A_R-95** (**A_R**:**A_T** = 9:1) at –105 °C before irradiation. 2. After 5 min of irradiation with 450 nm light. 3. After 34 min of irradiation with 450 nm light 42% of **B_R-95**/**C_T-95** are accumulated. 4. After turning off the light and warming to –80 °C 5. After 28 min almost full conversion of the **B_R-95**/**C_T-95** conformers exclusively to **C_R-95** is observed (see b) for details). b) At –80 °C a complete thermal conversion of **B_R-95**/**C_T-95** exclusively to **C_R-95** is observed.

At –80 °C a full thermal conversion of this metastable species exclusively to **C_R-95** was observed. As a result, no relative energy difference between the intermediate and **C_R-95** can be derived from the experiment. Assuming a resolution limit of 5% for the NMR experiment, the

relative energy difference amounts to at least 1.1 kcal·mol^{-1}. This value is obtained from (equation 8 with an equilibrium constant of K = 5/95 at the temperature T = 193.15 K (–80 °C). The kinetic analysis of the decaying intermediate resulted in an energy of activation of 13.4 kcal·mol^{-1} for this process (Figure 92 and Figure 93).

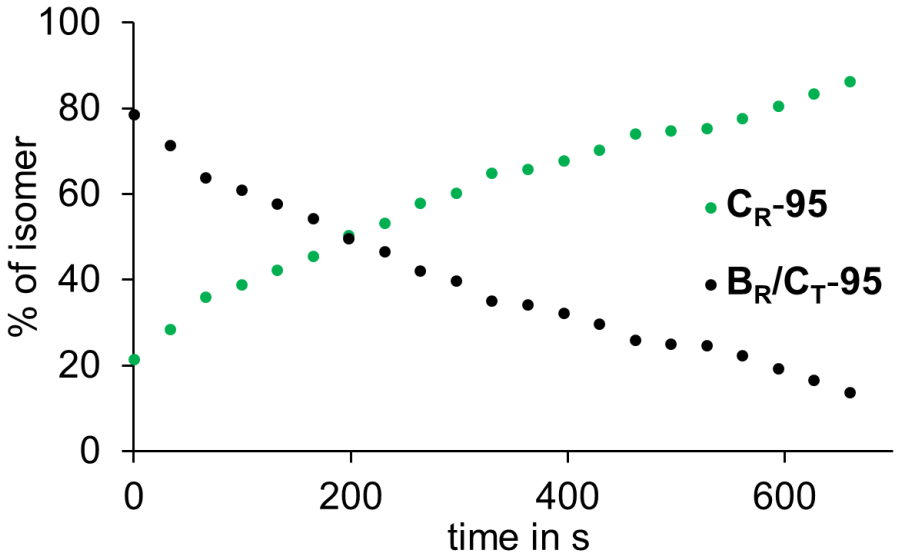

Figure 92 Isomer distribution during the thermal conversion of **B$_R$-95**/**C$_T$-95** to **C$_R$-95** at –80 °C in CD_2Cl_2:CS_2 (4:1) solution.

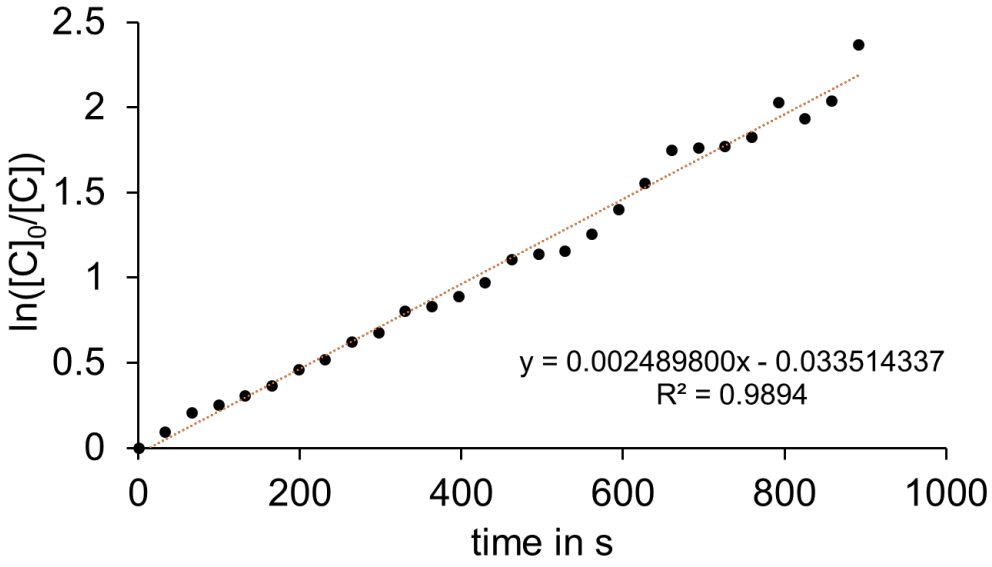

Figure 93 Kinetic analysis of the thermal conversion of **B$_R$-95**/**C$_T$-95** to **C$_R$-95** at –80 °C in CD_2Cl_2:CS_2 (4:1) solution. The slope m = 0.0024898 (formula given in the diagram) is used to calculate the rate constant k(**B$_R$-95**/**C$_T$-95** → **C$_R$-95**) according to (equation **4**. The Gibbs free energy of activation amounts to 13.4 kcal·mol^{-1}.

The conformational analysis (see Figure 84) suggests two possible intermediates **B_R-95** and **C_T-95** that could account for the ^{1}H NMR signals of the new metastable species. If the relative energy of **B_R-95** was significantly higher compared to **C_T-95** and a reduced activation barrier (significantly smaller than 13.0 kcal·mol^{-1}) for their thermal interconversion would be present, accumulation of the latter would be possible through irradiation at low temperatures (< –80 °C). The NMR irradiation experiment at –105 °C, however, has shown that the maximum relative concentration of the intermediate is 42% under continuous irradiation. This can be explained by a fast thermal equilibrium between **B_R-95** and **C_T-95** in combination with a photoequilibrium between **B_R-95** and the initial **A_R-95** isomer. A fast thermal equilibrium between the metastable species could also explain the occurrence of only one set of signals in the low temperature ^{1}H NMR spectrum.

Low temperature irradiation experiments have shown that the thermal atropisomerization from **A_T-95** to **A_R-95** with an energy barrier of 18.8 kcal·mol^{-1} is the rate limiting step of the unidirectional cycle. At –60 °C this isomerization process is frozen out and **A_T-95** can be accumulated by irradiating a mixture of **A_R-95** and **C_R-95** with light of a suitable wavelength for prolonged times. The changes of isomer distribution during the irradiation process gives a detailed insight into the working mechanism of machine **95** (Figure 94).

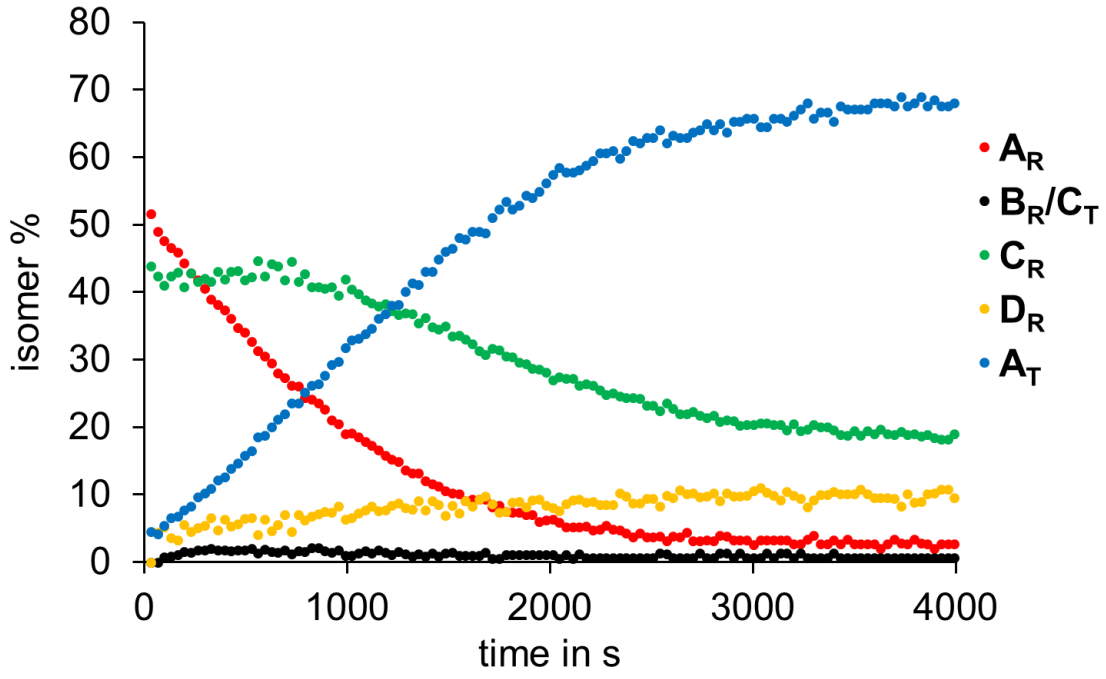

Figure 94 Isomer distribution of **95** (CD_2Cl_2) during irradiation with 450 nm light at –60 °C starting from a mixture containing **A_R-5** (**A_R**:**A_T** = 9:1) and **C_R-95**. Concentrations were determined from ^{1}H NMR spectra in intervals of 33 sec.

Photoconversion of **A_R-95** (Figure 94, red dots) leads to observable amounts of **B_R-95**/**C_T-95** at –60 °C (Figure 94, black dots) that quickly decays as the initially high concentration of **A_R-95** decreases. Thermal conversion of **B_R-95**/**C_T-95** to **C_R-95** results in a stable concentration of the latter over several minutes (Figure 94, green dots) even though **C_R-95** is simultaneously converted to **D_R-95** through irradiation. Photoconversion of **C_R-95** to **D_R-95** results in an initially fast increase of the **D_R-95** concentration (Figure 94, orange dots) that is then slowly converted to **A_T-95**. The thermal atropisomerization from **A_T-95** to **A_R-95** is frozen out at –60 °C resulting in a constant increase of the **A_T-95** concentration (Figure 94, blue dots) and a constant decrease of the **A_R-95** population over the course of the experiment. Because of the thermal equilibrium between **D_R-95** and **A_T-95** in combination with the photoequilibrium between **D_R-95** and **C_R-95**, a maximum accumulation of 70% **A_T-95** is possible.

4.8 ECD spectra of 95 at different temperatures

Enantiopure compounds **A_R-95** and **C_R-95** were obtained by HPLC separation on a semi preparative CHIRALKPAK® IC column. All spectra were measured in a CH_2Cl_2:DMF = 6:4 mixture (remains liquid down to –130 °C). Spectra of **A_R-95** and **C_R-95** were measured directly (Figure 95). A cryo cuvette was used for low temperature experiments (see experimental section for details).

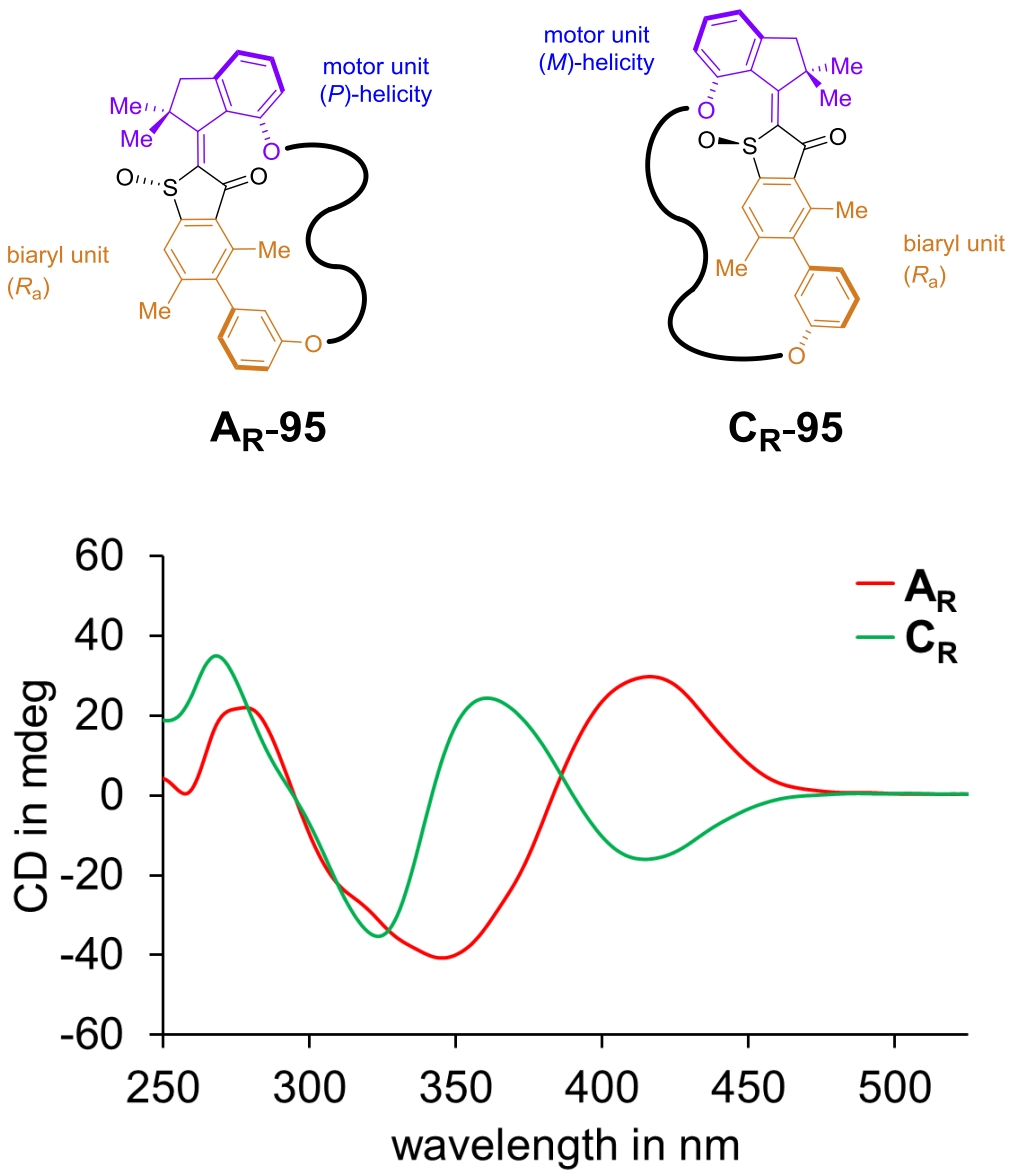

Figure 95 ECD spectra of *S* configured **A**$_{R}$**-95** (red line) and **C**$_{R}$**-95** (green line) in CH_2Cl_2:DMF = 6:4 at 23 °C.

NMR experiments have shown that irradiation of a **C**$_{R}$**-95** solution at –105 °C results in a mixture of **C**$_{R}$**-95** and **D**$_{R}$**-95** (see Figure 85 for details). The pure ECD spectrum of **D**$_{R}$**-95** was extracted from the corresponding mixed solution ECD spectrum by subtraction of the **C**$_{R}$**-95** contribution according to the isomer ratio in the pss (**C**$_{R}$:**D**$_{R}$ = 3:7, Figure 96).

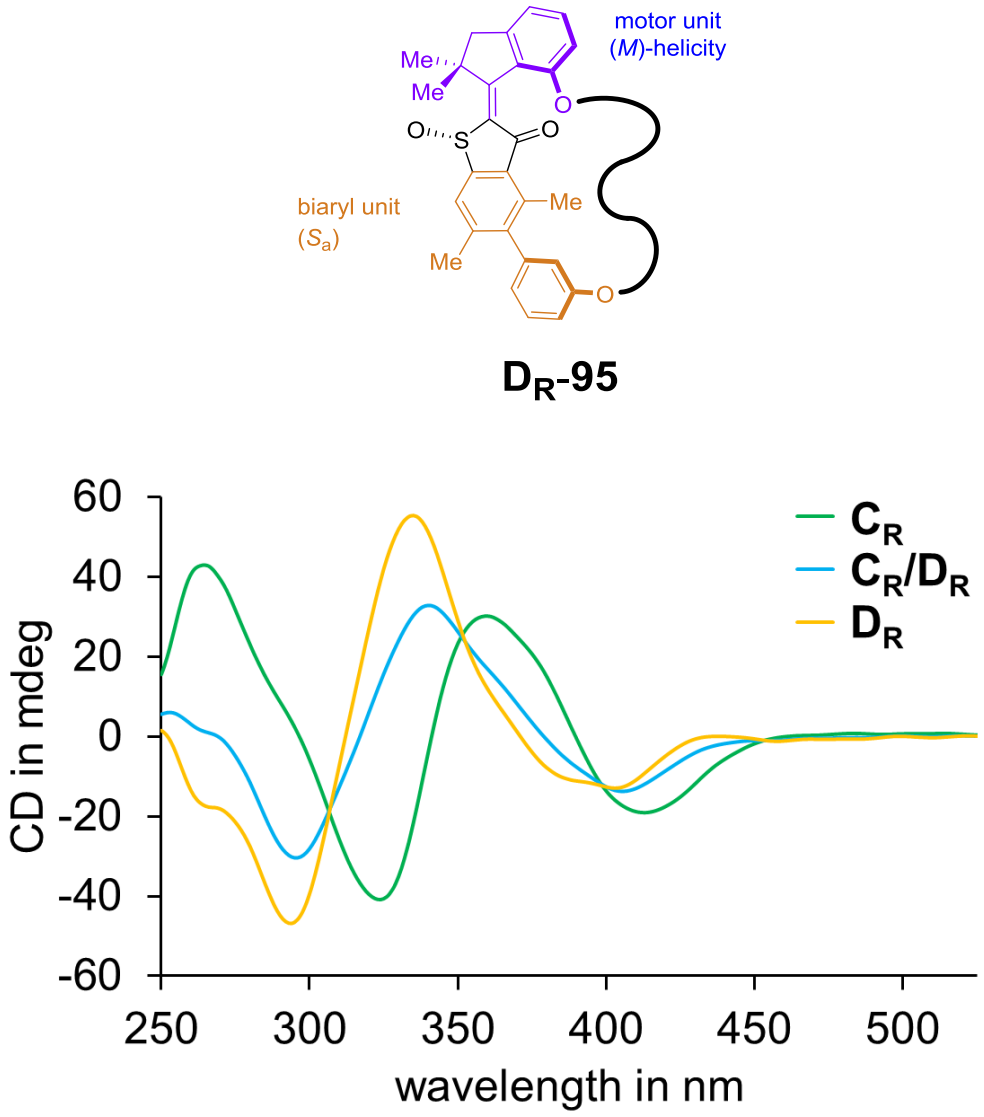

Figure 96 ECD spectra of **95** (CH_2Cl_2:DMF = 6:4). ECD spectrum of *S* configured **C_R-95** (–105 °C, green line). ECD spectrum obtained after 15 min of 450 nm irradiation of a solution of **C_R-95** at –105 °C to the pss resulting in a **D_R-95** enriched mixture (**C_R**:**D_R** = 3:7, light blue line). Extracted ECD spectrum of pure **D_R-95** (orange line).

At elevated temperatures (–50 °C) the **D_R-95** contribution of the spectrum is almost quantitatively converted to the **A_T-95** isomer. This selectivity was used to calculate the pure **A_T-95** ECD spectrum, analogously to **D_R-95** (Figure 97).

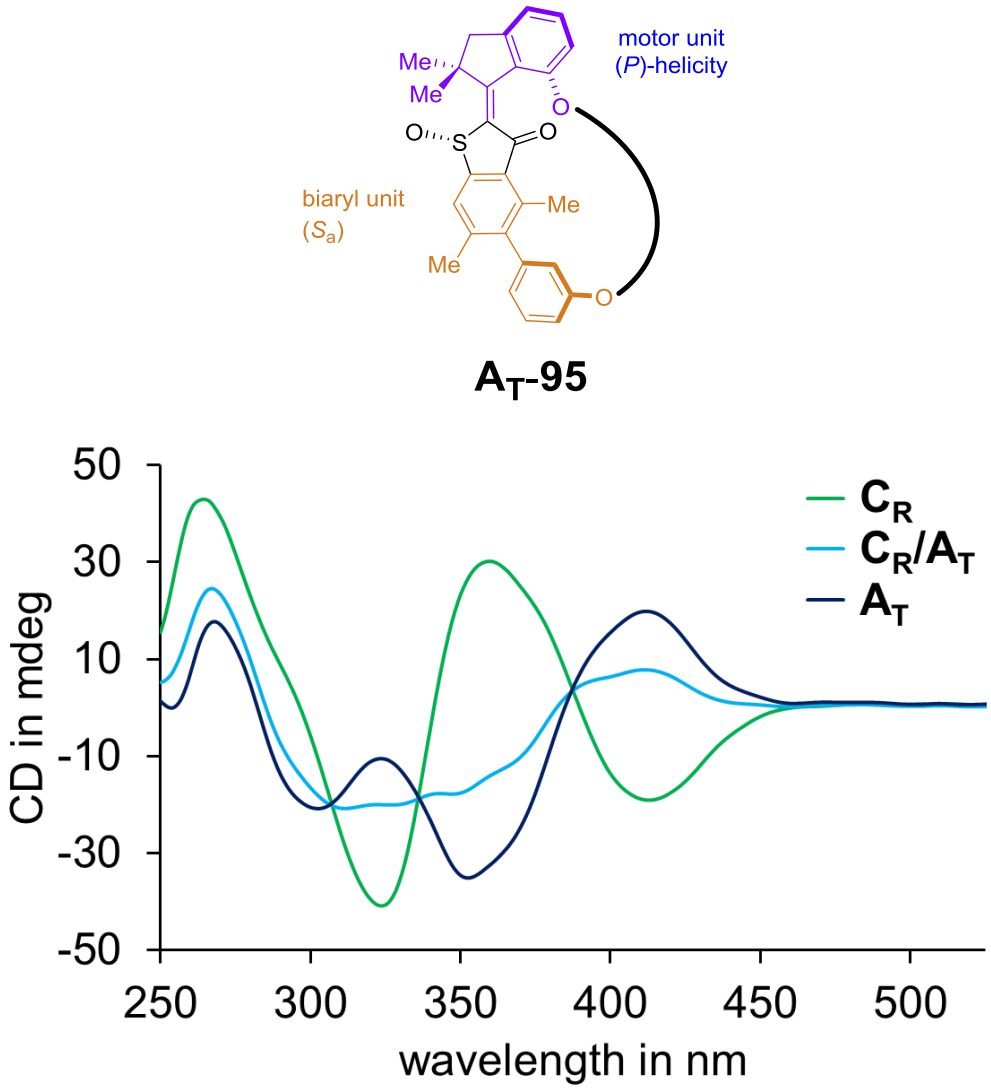

Figure 97 ECD spectra of **95** (CH_2Cl_2:DMF = 6:4). ECD spectrum of *S* configured **C_R-95** (–105 °C, green line). ECD spectrum obtained after 15 min of 450 nm irradiation of a solution of **C_R-95** at –105 °C to the pss followed by warming to –50 °C and additional waiting 10 min in the dark resulting in an **A_T-95** enriched mixture (**C_R**:**A_T** = 3:7, light blue line). Extracted ECD spectrum of pure **A_T-95** (dark blue line).

NMR experiments have shown that irradiation of **A_R-95** at low temperatures generates **B_R-95**/**C_T-95** (see Figure 91 for details). Extraction of the **B_R-95**/**C_T-95** contribution from the corresponding ECD spectrum can be done according to the isomer ratios obtained in the pss as judged from NMR experiments (composition **A_R**:**B_R**/**C_T** = 58:42). Figure 98 shows the extracted spectrum composed purely of **B_R-95**/**C_T-95** (black line). The initial spectrum of "pure" **A_R-95** (Figure 98, red line) contains **A_T-95** in the ratio **A_R**:**A_T** = 9:1 as discussed above. The 10% **A_T-95** contribution remains constant throughout the experiment and was subtracted for the calculation of the pure **B_R-95**/**C_T-95** spectrum. As a result, the extracted spectrum does

not intersect the isosbestic points that were obtained from 450 nm irradiation. Because of the underlying dynamic equilibrium, individual spectra of **B_R-95** and **C_T-95** are not accessible by this methodology.

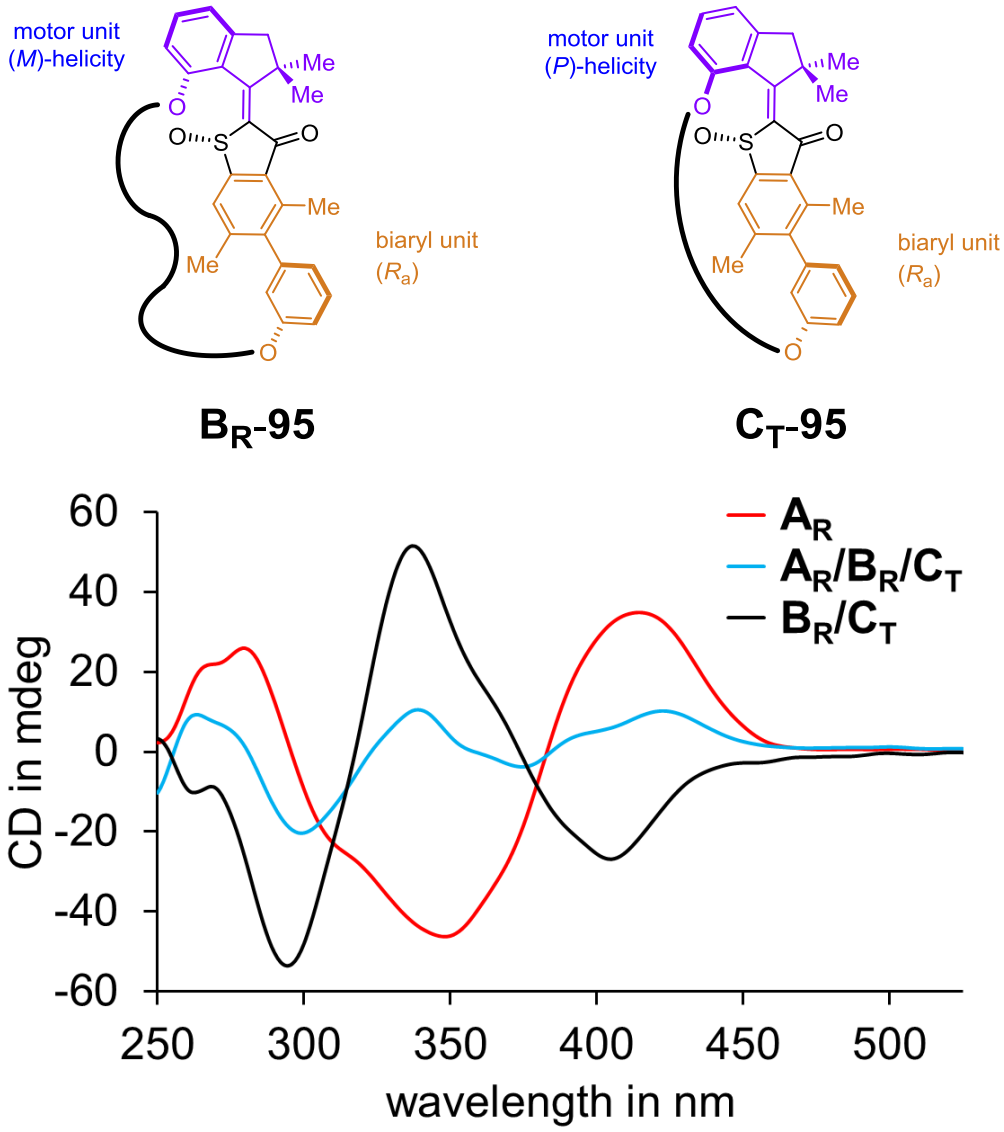

Figure 98 ECD spectra of **95** (CH_2Cl_2:DMF = 6:4). ECD spectrum of *S* configured **A_R-95** (–105 °C, **A_R**:**A_T** = 9:1, red line). ECD spectrum obtained after 15 min of 450 nm irradiation at –105 °C to the pss resulting in a **B_R-95**/**C_T-95** enriched mixture (composition **A_R**:**B_R**/**C_T** = 58:42, light blue line). Extracted ECD spectrum composed of pure **B_R-95** and **C_T-95** in an unknown ratio (black line).

4.9 Theoretical description of 95 and comparison with calculated spectra

Analogously to the first integrated molecular machine **81**, a computational study was conducted to obtain calculated ECD spectra of the different isomers (**A_R-95**, **B_R-95**, **C_T-95**, **C_R-95**, **D_R-95**, and **A_T-95**) that can be compared to experimental spectra. The individual ECD spectrum of each isomer is composed of different conformers that contribute according to their Boltzmann distribution. To account for this, a comprehensive theoretical study of the different conformers was conducted using enantiomers with exclusively *R* configured sulfoxide.

Initial structures for each isomer were obtained from molecular dynamics simulations on the force field level of theory. An **A_R-95** and **C_R-95** structure was loaded into the *MacroModel* package of the *Schrödinger* software and a mixed torsional/low-mode sampling within a sampling threshold of 80 kJ·mol^{-1} was carried out. The resulting set of structures contained conformers of each of the six isomers. A structure of each isomer was again loaded into *MacroModel* and a mixed torsional/low-mode sampling was carried out with a sampling threshold of 12 – 80 kJ·mol^{-1} to obtain 11 to 28 different conformers for each of the six isomers. The structures were then optimized on the B3LYP-GD3BJ/6-311G(d,p) IEFPCM (CH_2Cl_2) level of theory. A subsequent frequency analysis confirmed that the obtained structures were minimum structures. Redundant structures were discarded and a TD-B3LYP-GD3BJ/6-311+G(d,p) IEFPCM (CH_2Cl_2) calculation was carried out to obtain the electronic excitation spectra (ECD and UV-Vis). Only structures with a relative energy difference up to 3.0 kcal·mol^{-1} were taken into consideration for each isomer, which represents > 99% of the Boltzmann contributions. Taking into account the relative energies a Boltzmann averaged spectrum of each isomer was generated and compared to the experimental spectrum. All calculations were performed on structures with an *R* configured sulfoxide. The experimental spectra of **A_R-95** and **C_R-95** are in agreement with the mirror images of the calculated spectra (Figure 99 and Figure 100).

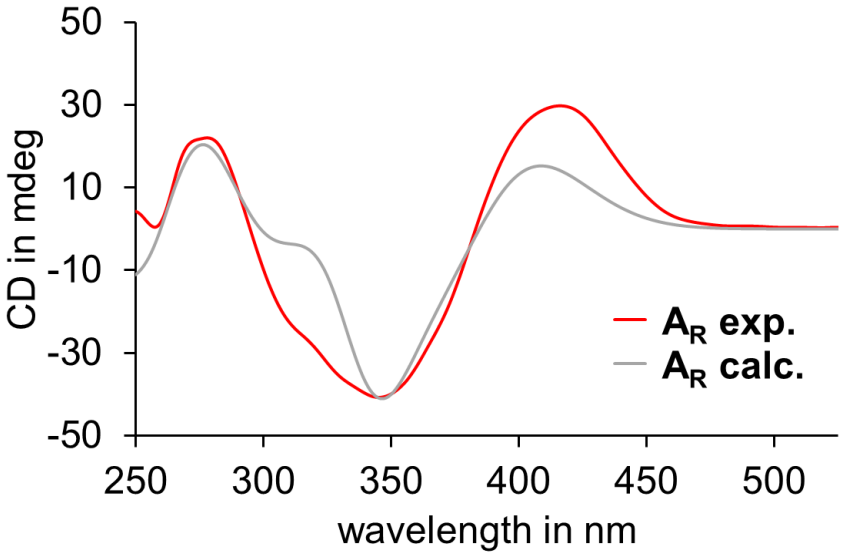

Figure 99 Comparison of the experimental spectrum of *S* configured **A$_R$-95** (**A$_R$**:**A$_T$** = 9:1, CH_2Cl_2:DMF = 6:4, 23 °C, red line) and the 10 nm blue-shifted calculated spectrum (grey line).

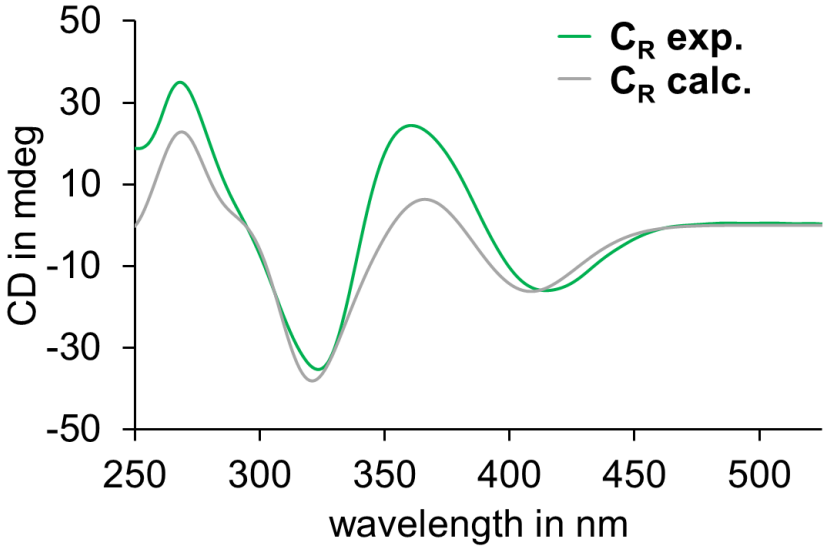

Figure 100 Comparison of the experimental spectrum of *S* configured **C$_R$-95** (CH_2Cl_2:DMF = 6:4, 23 °C, green line) and the 25 nm blue-shifted calculated spectrum (grey line).

Based on these results, the experimental ECD spectra could be unambiguously assigned to the respective enantiomers with *S* configuration of the sulfoxide. All experimental spectra were taken from the *S* configured enantiomers and consequently all depicted calculated spectra were mirrored to match the experimental results. The extracted spectra of **D$_R$-95** and **A$_T$-95** were also found to be in very good agreement with the calculations (Figure 101 and Figure 102). Overall, a blue-shift of 5 to 25 nm of the calculated spectra resulted in a better match.

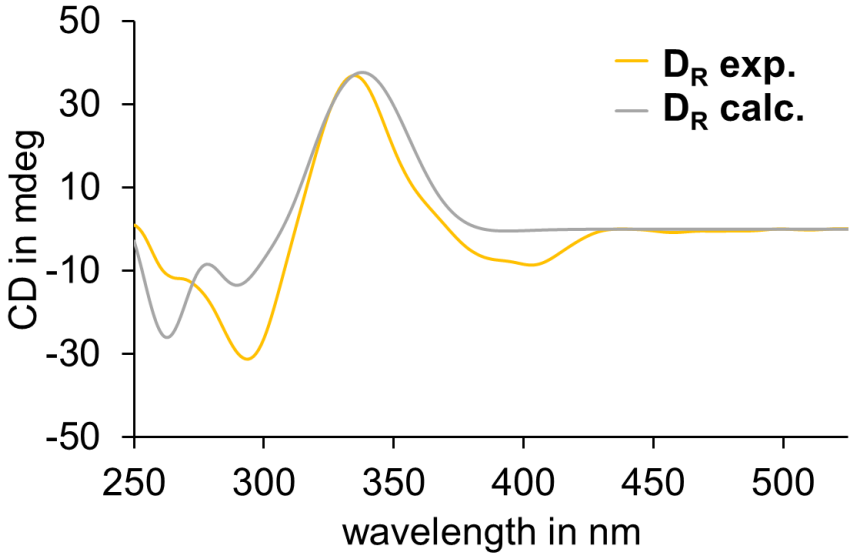

Figure 101 Comparison of the extracted experimental spectrum of *S* configured **D_R-95** (CH_2Cl_2:DMF = 6:4, –105 °C, orange line) and the 20 nm blue-shifted calculated spectrum (grey line).

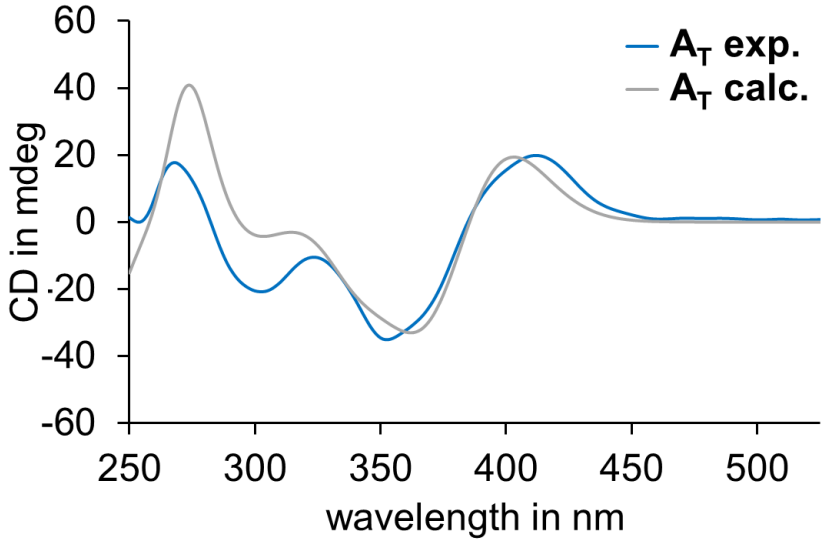

Figure 102 Comparison of the extracted experimental spectrum of *S* configured **A_T-95** (CH_2Cl_2:DMF = 6:4, –105 °C, blue line) and the 5 nm blue-shifted calculated spectrum (grey line).

The extracted experimental spectrum of **B_R-95**/**C_T-95** with unknown ratio of the contributing isomers was compared to the calculated spectra of **B_R-95** and **C_T-95** (Figure 103 and Figure 104). The spectra did not match in both cases.

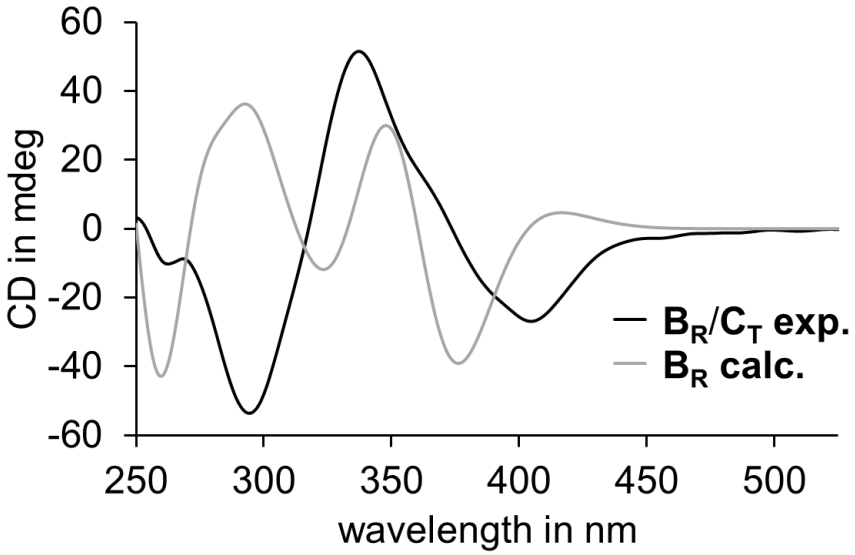

Figure 103 Comparison of the extracted experimental spectrum of *S* configured **B_R-95**/**C_T-95** (CH_2Cl_2:DMF = 6:4, –105 °C, black line) and the calculated spectrum of **B_R-95** (grey line).

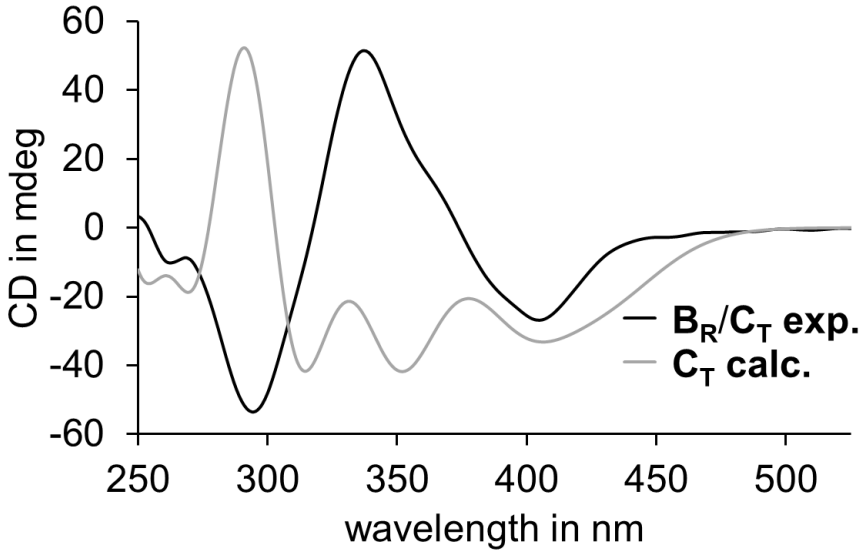

Figure 104 Comparison of the extracted experimental spectrum of *S* configured **B_R-95**/**C_T-95** (CH_2Cl_2:DMF = 6:4, –105 °C, black line) and the calculated spectrum of **C_T-95** (grey line).

Comparing the experimental spectrum with mixed spectra composed of **B_R-95** and **C_T-95** in different ratios did not improve the match. An exemplary comparison to a theoretical spectrum where each isomer contributes to 50% is shown in Figure 105.

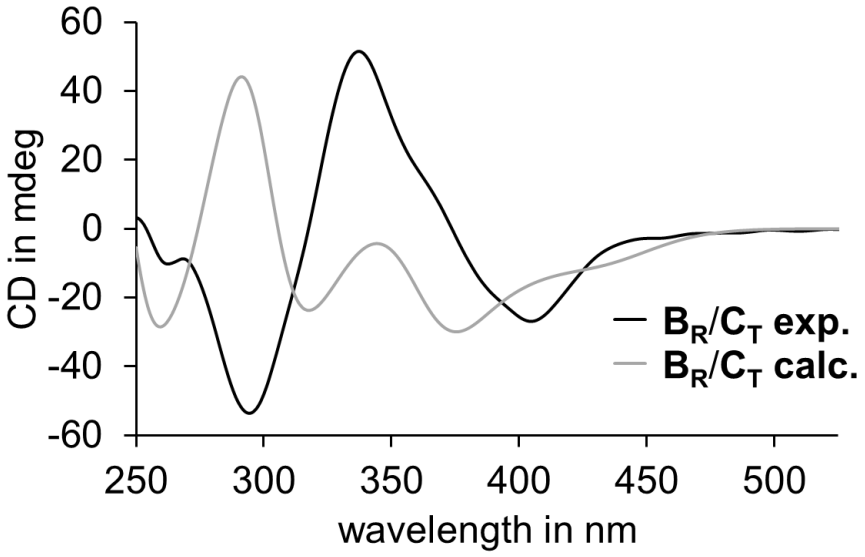

Figure 105 Comparison of the extracted experimental spectrum of *S* configured **B_R-95**/**C_T-95** (CH_2Cl_2:DMF = 6:4, –105 °C, black line) to a mixed calculated spectrum of **B_R-95** and **C_T-95** (grey line) with an isomer distribution of 1:1.

4.10 Model system 103

4.10.1 Synthesis and structure in the crystalline state

In order to explore the potential energy surface of the untethered biaryl, model system **103** was synthesized. For this molecule the covalent linker of the parent system was removed and the phenolic attachment sites were capped by methyl groups. The synthesis started with methylation of 7-methoxyindanone that gave **100** in excellent yields (Scheme 32). Condensation with building block **91**, which was established earlier, gave HTI **101** in 50% yield, which is within the expected range for this condensation method. The product readily crystallizes in orange needles by slow evaporation of an EtOAc solution.

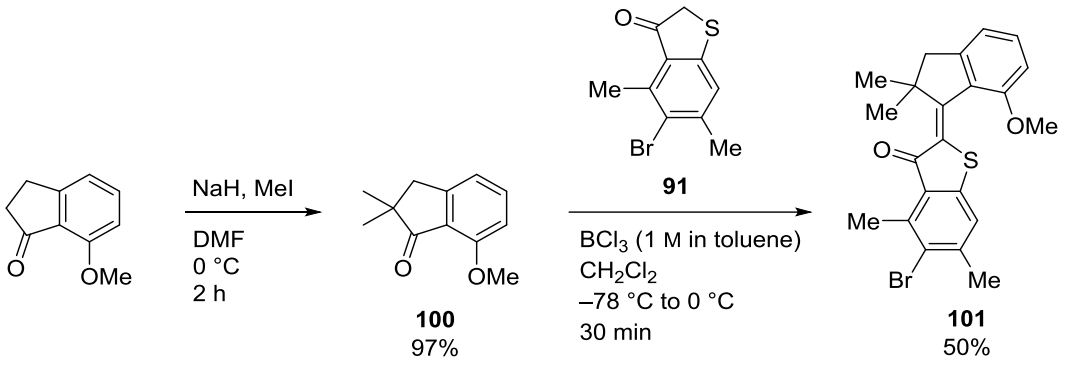

Scheme 32 Methylation of 7-methoxyindanone gave **100**. Subsequent condensation with building block **91** using BCl_3 gave HTI **101** as a mixture of *E* and *Z* isomers. Only the *Z* configured isomer is shown.

Suzuki-Miyaura-type coupling reactions of HTIs bearing a 7-alkoxy indanone moiety were unsuccessful so far (see chapter 3.3.2). However, this was attributed to the unsaturated allyl- and propargyl functional groups at the indanone part of the reactant. Indeed, the reaction of HTI **101** with 3-methoxyphenyl boronic acid pinacol ester proceeded smoothly and the product **102** was obtained in 41% yield (Scheme 33). Significant amounts of HTI **101** could be recovered, which translates to a yield of 94% based on the recovered material. Use of multiple equivalents of the boronic acid are expected to improve the yield.

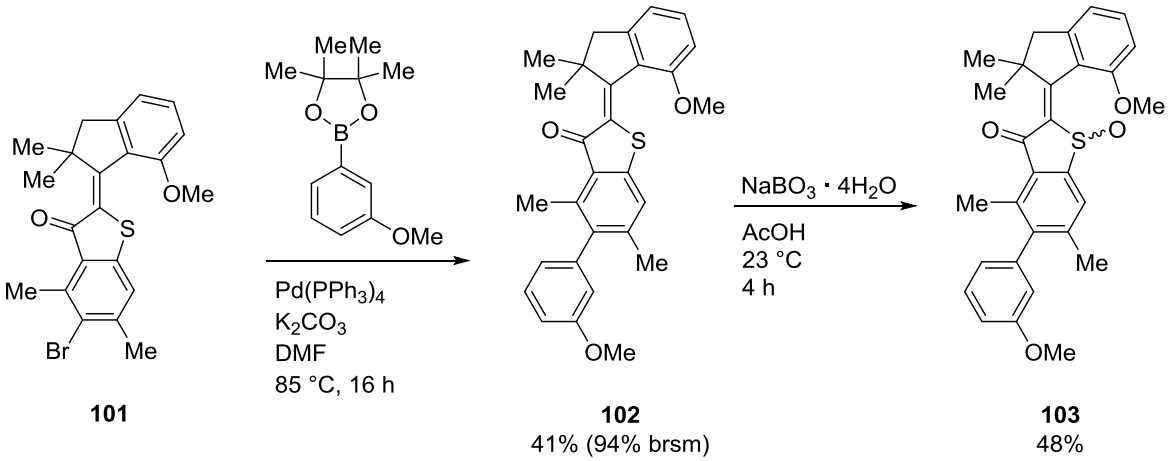

Scheme 33 *Suzuki-Miyaura* coupling of **101** with 3-methoxyphenylboronic acid pinacol ester gave **102**. Oxidation with sodium perborate afforded the target compound **103** as a mixture of *E* and *Z* isomers. Only the *Z* configured isomers are shown.

Oxidation with sodium perborate gave **103** in 48% yield. The product was obtained as a mixture of *E* and *Z* isomers (3:1) that could be separated by flash column chromatography. Crystals suitable for single crystal X-ray diffraction were obtained from a racemic mixture of the *E*-**103** isomer. Interestingly, only one conformation of the biaryl is found within the unit cell where

the methoxy group and the sulfoxide oxygen atom are pointing to opposite sides of the benzothiophenone stator (Figure 106).

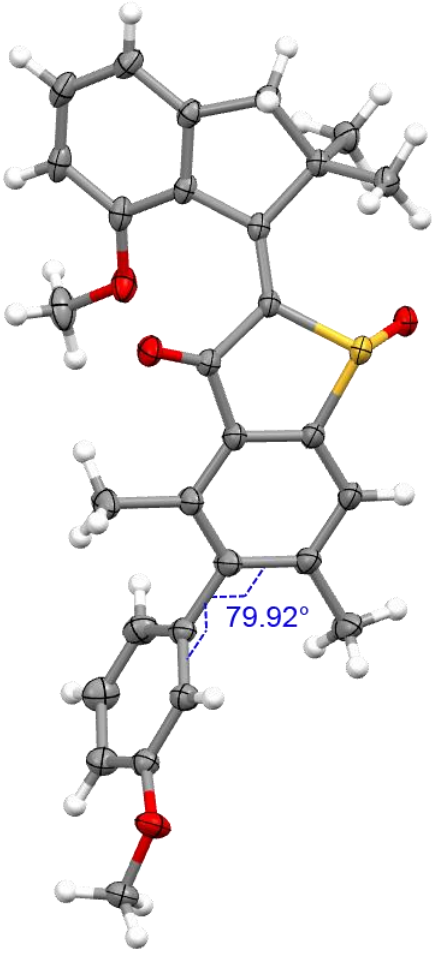

Figure 106 Structure of racemic *E*-**103** in the crystalline state. Only the *E*-(*R*)-(*M*)-(R_a) isomer is depicted for clarity. The methoxy group at the lower aryl part and the sulfoxide oxygen atom point to opposite sides of the benzothiophenone core. The respective atropisomer *E*-(*R*)-(*M*)-(S_a) is not found within the crystals unit cell.

4.10.2 Theoretical description of model system 103

Ground state as well as transition state energies of **103** were assessed on the B3LYP-GD3BJ/6-311G(d,p) IEFPCM (CH_2Cl_2) level of theory (Figure 107). All calculations were done for structures with *R* configuration of the sulfoxide. First, ground state energies for both atropisomers of *E*-**103** and *Z*-**103** were determined. The energies were found to be nearly degenerate in the range of 0.1 kcal·mol^{-1}, which translates roughly to a 1:1 mixture of atropisomers at room temperature.

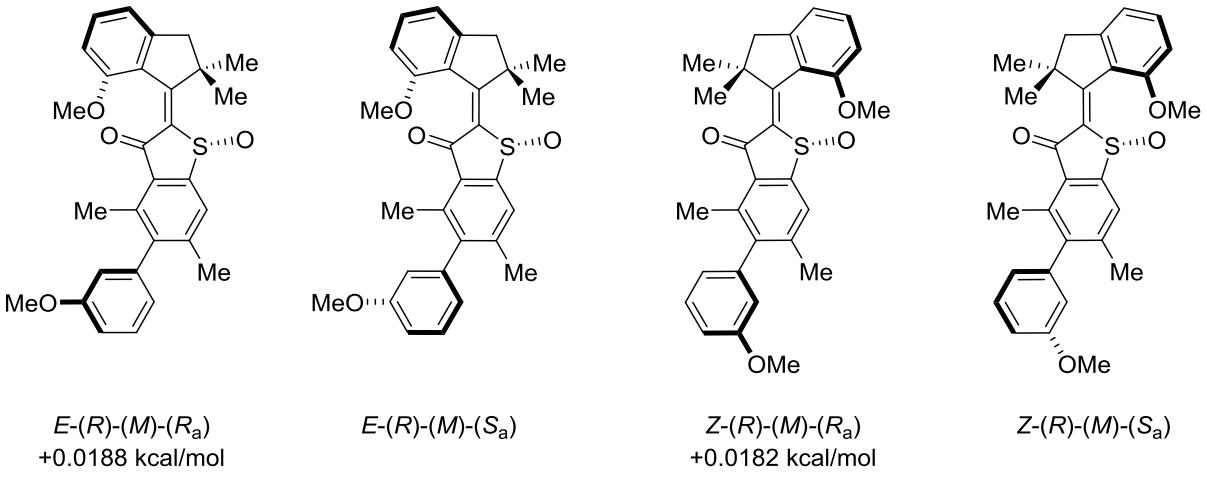

Figure 107 Ground state energies calculated on the B3LYP-GD3BJ/6-311G(d,p) IEFPCM (CH_2Cl_2) level of theory for the atropisomers of *E*-**103** and *Z*-**103**.

Next, seeding structures for the transition states were generated by 360° scans around the biaryl axis. The scans were conducted in 2° steps at the PM6 level of theory. Since no preferential rotation direction can be expected, the calculations were performed for clockwise and counterclockwise rotations of the aryl unit. The highest energy structures were then used for transition state optimizations on the B3LYP-GD3BJ/6-311G(d,p) IEFPCM (CH_2Cl_2) level of theory. The resulting energies were compared to the lowest energy states of *E*-**103** and *Z*-**103**, respectively (Figure 108). Calculations were performed for a temperature of 0 °C to allow direct comparison with experimental data.

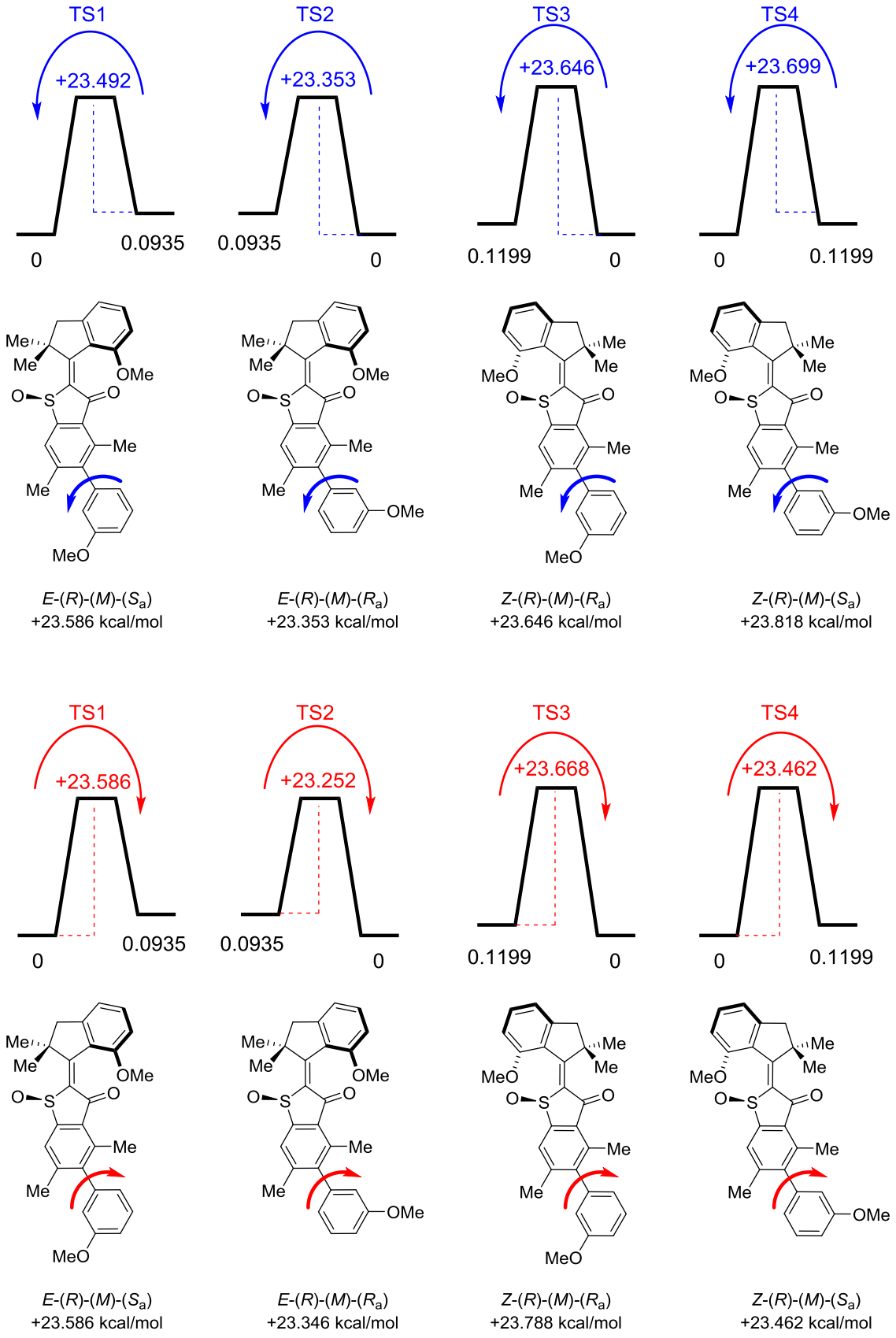

Figure 108 Activation energies for the atropisomerization reactions and the corresponding transition state energies (in kcal·mol^{-1}) at 0 °C calculated for both rotation directions on the B3LYP-GD3BJ/6-311G(d,p) IEFPCM (CH_2Cl_2) level of theory.

Differences in transition state energies, depending on the rotation direction, were found to be within the range of 0.5 kcal·mol^{-1}. The resulting differences in activation energies are in the same range due to the nearly degenerate ground states. In addition, atropisomerization barriers for *E*-**103** and *Z*-**103** show no significant differences.

4.10.3 Experimental determination of atropisomerization barriers

The computational studies suggest that activation energies for the atropisomerization reactions of **103** amount to ca. 23 kcal·mol^{-1}. However, separation attempts on a chiral HPLC column were unsuccessful so far, suggesting that the process is too fast at ambient temperatures. NMR EXSY experiments can be used to reveal such a dynamic process but require a strong difference in chemical shifts of indicative protons, which is not present for the respective pairs of atropisomers in this case. NMR coalescence experiments would require temperatures way above 100 °C for the process to be in a detectable time scale, which exceeds the maximum possible temperature of the available NMR devices.

It was therefore attempted to separate the atropisomers on HPLC by cooling of a semi preparative CHIRALPAK® IC column in an ice bath. At 0 °C, separation of mixtures of *E*-**103** and *Z*-**103** revealed up to four different species that were attributed to the *R* and *S* configured sulfoxides and the corresponding atropisomers (Figure 109). Cooling the column further down to –15 °C in a salt/ice bath or –40 °C in a dry ice/acetone filled Dewar flask results in a loss of separation efficiency. With optimized conditions, separation of a single atropisomer (note: as judged at the PDA detector, not the end of the HPLC tubing were the sample is collected) was possible for a *Z*-**103** sample at 0 °C (Figure 109, indicated by a white arrow).

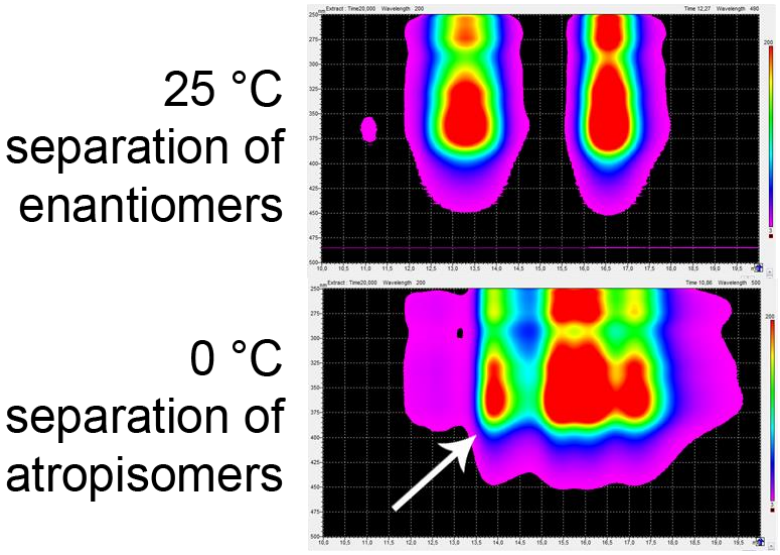

Figure 109 PDA traces of a separated racemic *Z*-**103** sample at different temperatures (CHIRALPAK® IC column, heptane:EtOAc = 7:3). At 25 °C separation of enantiomers is visible. At 0 °C the traces of the enantiomers are split into the respective pairs of atropisomers with a partial overlap of signals. The atropisomer corresponding to the signal indicated by a white arrow was isolated and used for a kinetic analysis.

The atropisomer enriched solution was collected and flash frozen in a flask, which was cooled to –78 °C using dry ice. To follow the atropisomerization kinetics this solution was again subjected to HPLC separation at 0 °C using variable retention times by varying the eluent flows (3.0, 4.0, 5.0 and 6.0 mL/min). The resulting atropisomer ratios were determined by the absorption (in mAU = milli-arbitrary units) of their individual PDA signals at 363 nm and a kinetic analysis was conducted. To obtain the equilibrium concentration of the atropisomers a portion of the sample was annealed at 23 °C and an isomer distribution of 49.6% to 50.4% was determined at 0 °C using again HPLC separation as analytical method. Kinetic analysis determined a Gibbs free energy of activation of 20.74 kcal·mol^{-1} for this process, which is in good agreement with the theoretical description (Figure 110).

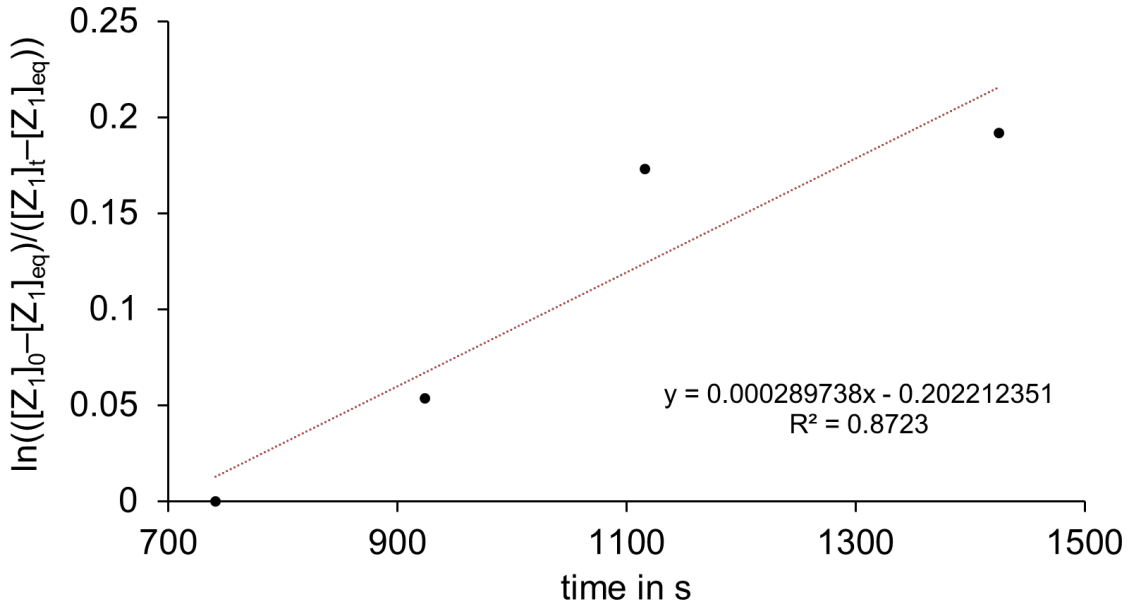

Figure 110 Kinetic analysis of the thermal atropisomerization of *Z*-**103** in heptane:EtOAc = 7:3 at 0 °C starting from an atropisomer enriched solution. First order kinetic analysis, taking into account the dynamic equilibrium of the atropisomers gives a linear relationship. The slope m = 0.000289738 (formula given in the diagram) is used to calculate the rate constant k(Atropisomer-1 → Atropisomer-2) according to (equation **4**. The Gibbs free energy of activation is 20.74 kcal·mol^{-1}.

4.11 Temperature dependence of Gibbs free energies

To this point, the energy landscape of HTI based multi-state photoswitches has been described with the approximation of temperature independent Gibbs free energies of activation $\Delta G^{\ddagger}$. This way a qualitative picture of underlying processes is obtained which holds if measurements are conducted within a small range of temperatures. For the present system, experimental values range from –80 °C (thermal conversion of **B$_R$-95**/**C$_T$-95** to **C$_R$-95)** to +80 °C (thermal conversion of **C$_R$-95** to **A$_R$-95**). Because of the resulting range of ±160 °C the experimental results were reassessed and the temperature dependence of the Gibbs free energies was studied in detail. To this end kinetic experiments were repeated for a range of experimentally accessible temperatures. *Van't Hoff* plot analysis in combination with *Eyring* plot analysis was used to extrapolate values to a unified temperature that was arbitrarily set to 0 °C.

4.11.1 Temperature dependence of ΔG($\mathbf{A_T}$-95 – $\mathbf{A_R}$-95) and $\Delta G^{\ddagger}$($\mathbf{A_T}$-95 to $\mathbf{A_R}$-95)

In order to obtain additional ΔG values for **$\mathbf{A_T}$-95**/**$\mathbf{A_R}$-95**, a solution containing **$\mathbf{A_T}$-95**/**$\mathbf{A_R}$-95** in CD_2Cl_2 was prepared and the equilibrium concentrations were determined at different temperatures. Values for 27 °C and 35 °C were measured directly. For 0 °C the solution was annealed for 1 h and measured again after 2 h to obtain a stable equilibrium concentration. From the isomer ratios at the respective temperatures, the equilibrium constants K were obtained. These constants were then used to determine the temperature dependence of ΔG. According to the *van't Hoff* equation

$$\ln(K_{\mathrm{eq}}) = -\frac{\Delta H}{RT} + \frac{\Delta S}{R} \qquad \text{(equation 13)}$$

plotting $\ln(K_{eq})$ against 1/T gives a linear relationship (Figure 111). The slope = $-\Delta H/R$ and intercept of the y-axis = $\Delta S/R$ can be used to calculate the enthalpy and the entropy of the reaction. Experimental values for ΔG, ΔH and ΔS are summarized in Table 7 at the bottom of this section.

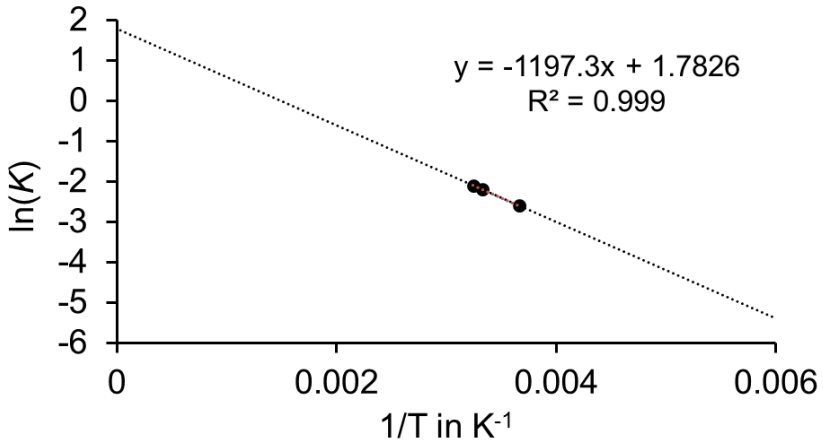

Figure 111 *Van't Hoff* plot analysis obtained from the dynamic **$\mathbf{A_T}$-95/$\mathbf{A_R}$-95** equilibrium at different temperatures (0 °C, 27 °C and 35 °C).

Next, a series of kinetic analyses was conducted. To this end, solutions of **95** in CD_2Cl_2 were irradiated at –60 °C with 450 nm light to accumulate **$\mathbf{A_T}$-95**. The solutions were then warmed to different temperatures (0 °C, –5 °C, –20 °C, –30 °C and –40 °C) and the thermal **$\mathbf{A_T}$-95** to **$\mathbf{A_R}$-95** conversion was observed by ^{1}H NMR spectroscopy. The rate constants k were determined taking into account the dynamic equilibrium that was measured directly (0 °C) or

extrapolated from the *van't Hoff* plot analysis (–5 °C, –20 °C, –30 °C and –40 °C). The results are summarized in Figure 112.

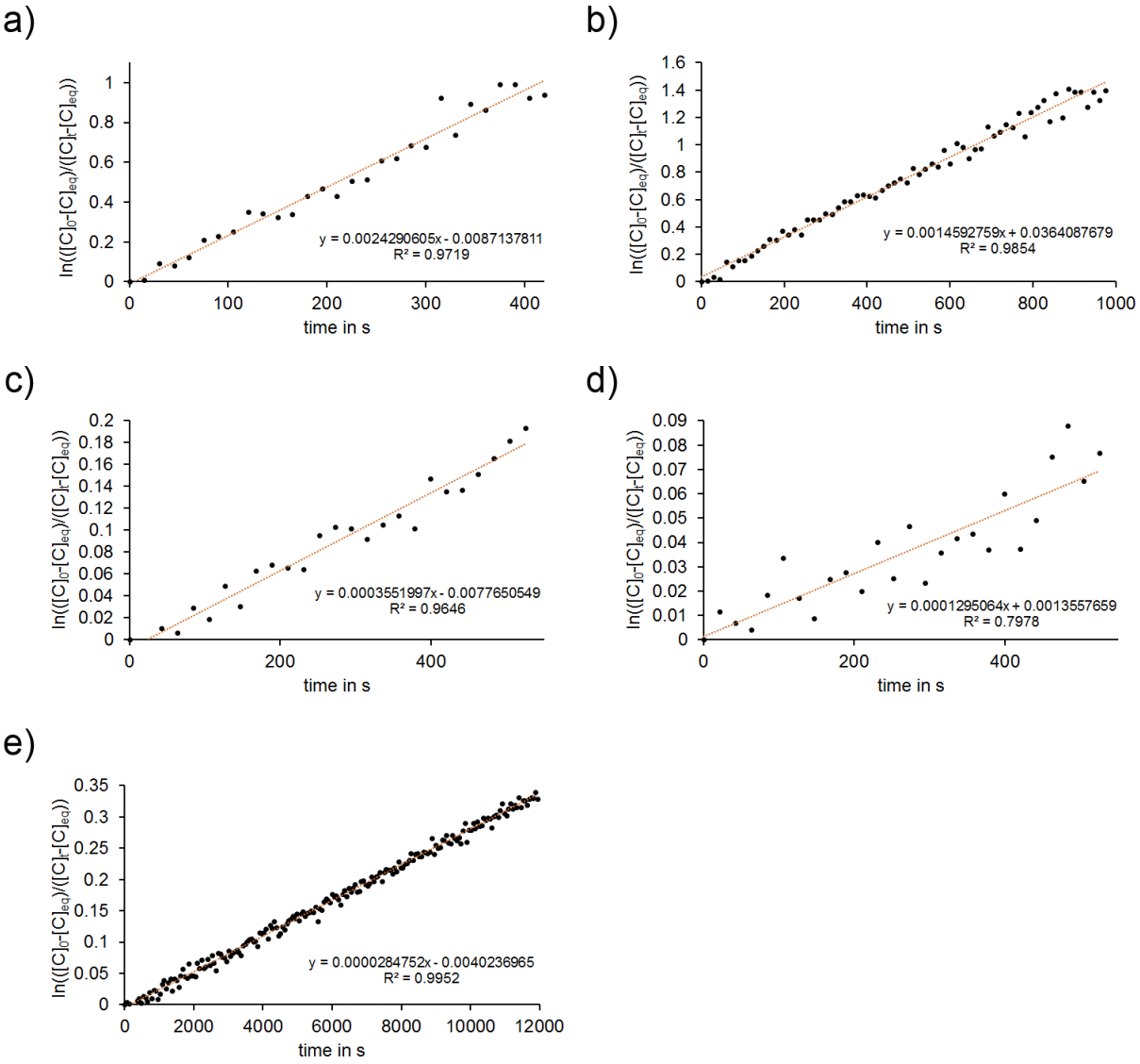

Figure 112 First order kinetic analysis of the thermal **A$_T$-95** to **A$_R$-95** conversion taking into account the dynamic equilibrium. a) –0 °C b) –5 °C c) –20 °C d) –30 °C e) –40 °C.

Due to the strong temperature dependence of the rate constant *k*, a wider temperature range is not experimentally accessible by means of ^{1}H NMR spectroscopy. The determined half-lives for the **A$_T$-95** to **A$_R$-95** conversion range from minutes at 0 °C to 1 d at –40 °C. The corresponding energy of activation $\Delta G^{\ddagger}$ was determined to be between 19.25 kcal·mol^{-1} at 0 °C and 18.40 kcal·mol^{-1} at –40 °C. According to the *Eyring* equation

$$\ln\left(\frac{k}{T}\right) = -\frac{\Delta H}{RT} + \ln\frac{k_B}{h} + \frac{\Delta S}{R} \qquad \text{(equation 14)}$$

plotting ln(k/T) against 1/T gives a linear relationship (Figure 113). The slope = $-\Delta H^{\ddagger}/R$ and intercept of the y-axis = $\ln(k_B/h) + \Delta S^{\ddagger}/R$ can be used to calculate the enthalpy of activation and entropy of activation for the reaction.

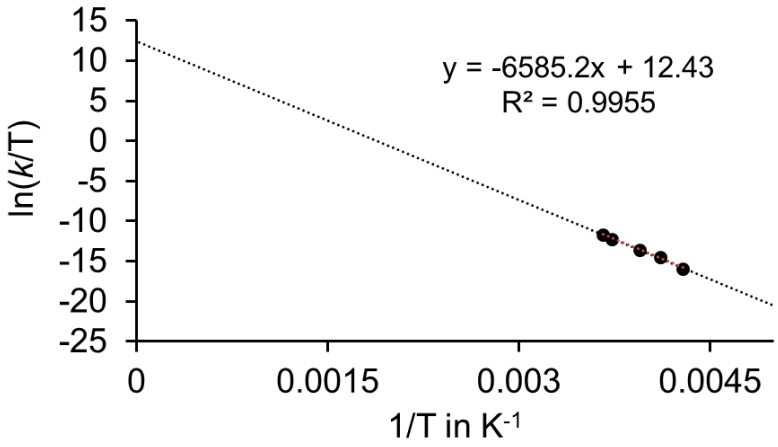

Figure 113 *Eyring* plot analysis obtained from the thermal **A$_T$-95** to **A$_R$-95** conversion at different temperatures. Rate constants k were determined at 0 °C, –5 °C, –20 °C, –30 °C and –40 °C.

From the *Eyring* plot analysis a $\Delta H^{\ddagger}$ = 13.08 kcal·mol^{-1} and $\Delta S^{\ddagger}$ = –22.50 cal·mol^{-1}·K^{-1} were obtained for the thermal **A$_T$-95** to **A$_R$-95** isomerization. Experimental values for $\Delta G^{\ddagger}$, $\Delta H^{\ddagger}$ and $\Delta S^{\ddagger}$ are summarized in Table 7 at the end of this section.

4.11.2 Temperature dependence of $\Delta G^{\ddagger}$(B$_R$-95/C$_T$-95 to C$_R$-95)

Unlike **A$_T$-95**/**A$_R$-95**, conversion of **B$_R$-95**/**C$_T$-95** to **C$_R$-95** does not result in a dynamic equilibrium detectable by ^{1}H NMR spectroscopy. The corresponding ΔG(**B$_R$-95**/**C$_T$-95** – **C$_R$-95**) could therefore not be determined.

To obtain $\Delta G^{\ddagger}$(**B$_R$-95**/**C$_T$-95** to **C$_R$-95**), a series of kinetic analyses was conducted (Figure 114). Solutions of **A$_R$-95** in CD_2Cl_2:CS_2 (4:1) were irradiated at –105 °C with 450 nm light to accumulate **B$_R$-95**/**C$_T$-95**. The solutions were then warmed to different temperatures (–75 °C, –80 °C, –85 °C, –90 °C and –100 °C) and the thermal **B$_R$-95**/**C$_T$-95** to **C$_R$-95** conversion was

observed by ^{1}H NMR spectroscopy. First order rate constants *k* were determined with the assumption of a complete conversion to **C$_R$-95**.

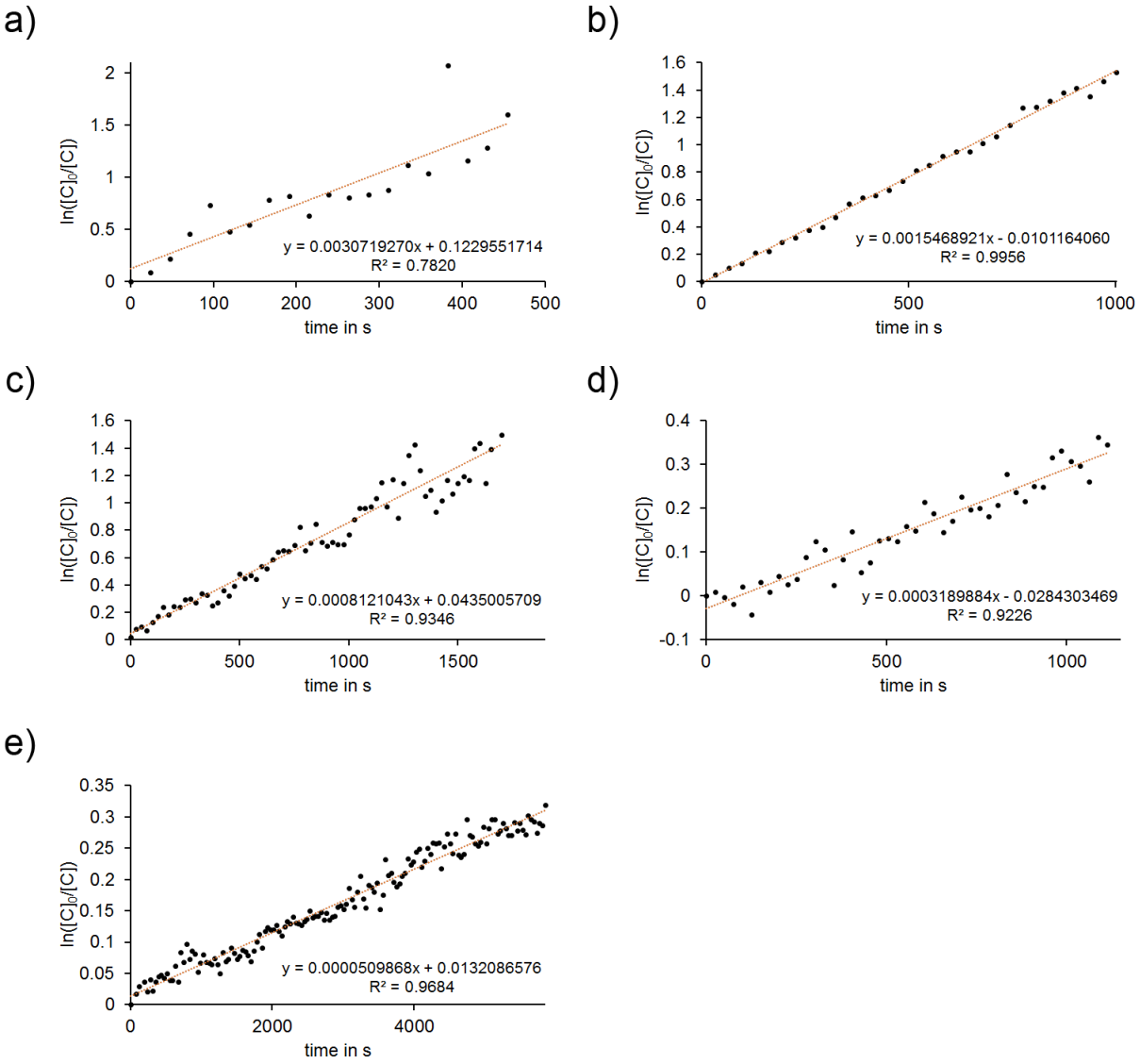

Figure 114 First order kinetic analysis of the thermal **B$_R$-95/C$_T$-95** to **C$_R$-95** conversion. a) –75 °C b) –80 °C c) –85 °C d) –90 °C e) –100 °C.

The corresponding energy of activation $\Delta G^{\ddagger}$ was determined between 13.72 kcal·mol^{-1} at –75 °C and 13.35 kcal·mol^{-1} at –100 °C. The corresponding values for $\Delta H^{\ddagger}$ = 10.86 kcal·mol^{-1} and $\Delta S^{\ddagger}$ = –14.22 cal·mol^{-1}·K^{-1} were obtained from *Eyring* plot analysis (Figure 115). Experimental values for $\Delta G^{\ddagger}$, $\Delta H^{\ddagger}$ and $\Delta S^{\ddagger}$ are summarized in Table 7 at the bottom of this section.

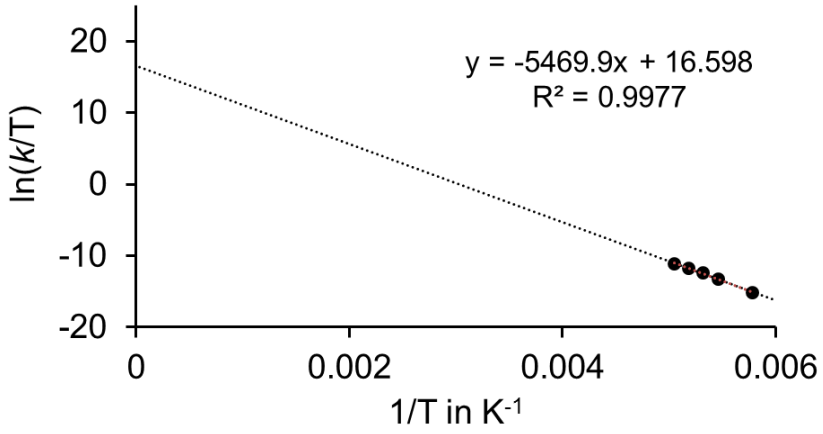

Figure 115 *Eyring* plot analysis obtained from the thermal **B$_R$-95/C$_T$-95** to **C$_R$-95** conversion at different temperatures. Rate constants *k* were determined at –75 °C, –80 °C, –85 °C, –90 °C and –100 °C.

4.11.3 Temperature dependence of Δ*G*(C$_R$-95 – A$_R$-95) and Δ*G*(D$_R$-95 – A$_T$-95)

The dynamic equilibrium concentration of **A$_R$-95**/**C$_R$-95** was measured at different temperatures. A solution of **95** (mixture of isomers) in $(CDCl_2)_2$ was heated to 80 °C, 110 °C and 140 °C for prolonged times and the resulting isomer distribution was determined by ^{1}H NMR spectroscopy. From these, Δ*G* values of 1.68 kcal·mol^{-1} (80 °C and 110 °C) and 1.69 kcal·mol^{-1} (140 °C) were calculated. *Van't Hoff* plot analysis taking into account the equilibrium constants *K* reveals a linear relationship (Figure 116).

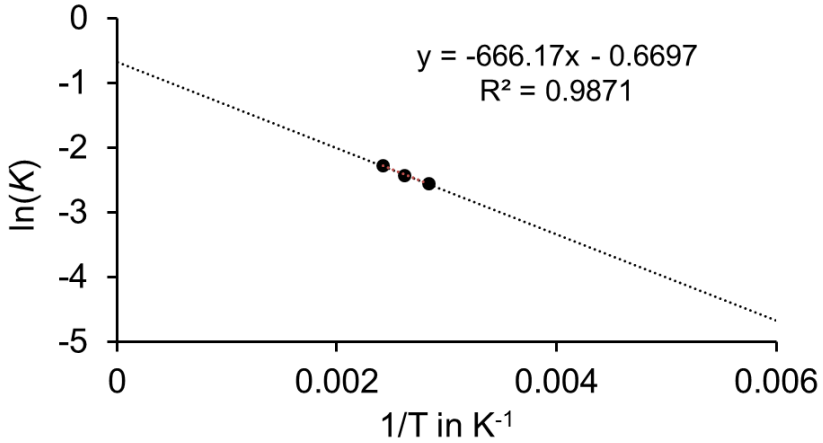

Figure 116 *Van't Hoff* plot analysis obtained from the dynamic **C$_R$-95/A$_R$-95** equilibrium at elevated temperatures (80 °C, 110 °C and 140 °C).

The equilibrium concentrations of **D_R-95**/**A_T-95** were determined at low temperatures. To this end, solutions of **C_R-95** in CD_2Cl_2 were irradiated with 450 nm light at –80 °C to accumulate **D_R-95**. The solutions were then warmed to –40 °C, –60 °C and –70 °C and kept in the dark for prolonged times. The resulting isomer concentrations were used to determine the corresponding equilibrium constants *K*. From these, ΔG values between 0.75 kcal·mol^{-1} (–40 °C) and 0.93 kcal·mol^{-1} (–70 °C) were calculated. *Van't Hoff* plot analysis reveals a linear relationship (Figure 117).

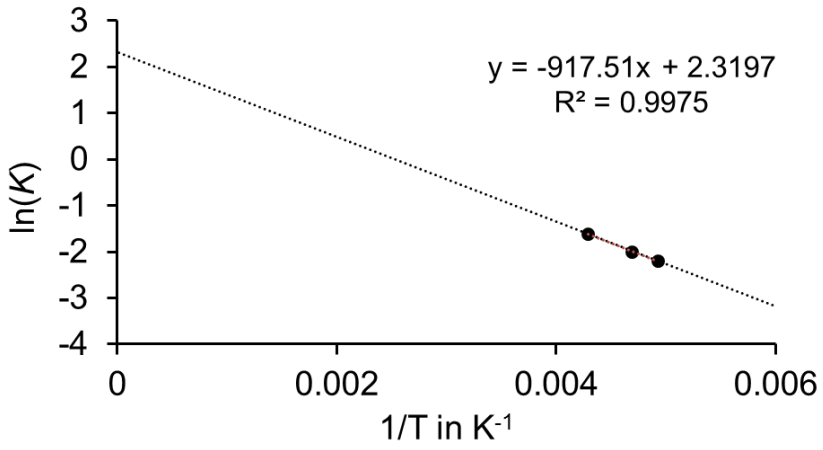

Figure 117 *Van't Hoff* plot analysis obtained from the dynamic **D_R-95/A_T-95** equilibrium at low temperatures (–40 °C, –60 °C and –70 °C).

4.12 Extrapolation and comparison of free energies at 0 °C

A qualitative energy landscape for the working mechanism of **95** had been established based on measurements with a temperature range of ±160 °C. Now, additional data points at varying temperatures for the majority of underlying reactions allowed to determine the temperature dependence of these processes. In addition, extrapolation of ΔG as well as $\Delta G^{\ddagger}$ values to a single temperature allows to directly compare energies and quantitatively evaluate the system.

All critical values were compared at 0 °C, either from direct measurements or extrapolated from *van't Hoff* plot analysis and *Eyring* plot analysis. A comprehensive overview over the quantitative experimental data is given in Table 7.

Table 7 Experimental quantitative data for the operation of motor system **95.**

Experimental values						
ΔG(**C$_R$**–**A$_R$**) [kcal/mol] (at T)	ΔG(**D$_R$**–**A$_T$**) [kcal/mol] (at T)	ΔG(**A$_T$**–**A$_R$**) [kcal/mol] (at T)	$\Delta G^{\ddagger}$(**C$_R$** to **A$_R$**) [kcal/mol] (at T)	$\Delta G^{\ddagger}$(**B$_R$**/**C$_T$** to **C$_R$**) [kcal/mol] (at T)	$\Delta G^{\ddagger}$(**D$_R$** to **A$_T$**) [kcal/mol] (at T)	$\Delta G^{\ddagger}$(**A$_T$** to **A$_R$**) [kcal/mol] (at T)
1.68 (80 °C)	0.93 (–70 °C)	1.41 (0 °C)	28.20 (80 °C)	13.35 (–100 °C)		19.25 (0 °C)
1.68 (110 °C)	0.84 (–60 °C)	1.31 (27 °C)		13.47 (–90 °C)		19.15 (–5 °C)
1.69 (140 °C)	0.75 (–40 °C)	1.30 (35 °C)		13.50 (–85 °C)	13.90 (–80 °C)	18.76 (–20 °C)
				13.62 (–80 °C)		18.48 (–30 °C)
				13.72 (–75 °C)		18.40 (–40 °C)
Values at 0 °C						
1.69[a]	0.56[a]	1.41		14.75[a]		19.25
ΔH(**C$_R$**–**A$_R$**) [kcal/mol]	ΔH(**D$_R$**–**A$_T$**) [kcal/mol]	ΔH(**A$_T$**–**A$_R$**) [kcal/mol]		$\Delta H^{\ddagger}$(**B$_R$**/**C$_T$** to **C$_R$**) [kcal/mol]		$\Delta H^{\ddagger}$(**A$_T$** to **A$_R$**) [kcal/mol]
1.32	1.82	2.38		10.86		13.08
ΔS(**C$_R$**–**A$_R$**) [cal/mol·K]	ΔS(**D$_R$**–**A$_T$**) [cal/mol·K]	ΔS(**A$_T$**–**A$_R$**) [cal/mol·K]		$\Delta S^{\ddagger}$(**B$_R$**/**C$_T$** to **C$_R$**) [cal/mol·K]		$\Delta S^{\ddagger}$(**A$_T$** to **A$_R$**) [cal/mol·K]
–1.33	4.61	3.54		–14.22		–22.50

[a] value was extrapolated from variable temperature measurements

Extrapolation of data to 0 °C does not change the qualitative statements (see chapter 4.7 for the elucidation of the machine function). A quantitative ground state energy profile of the working mechanism of motor **95** can be constructed from the ΔG and $\Delta G^{\ddagger}$ values at 0 °C (Figure 118).

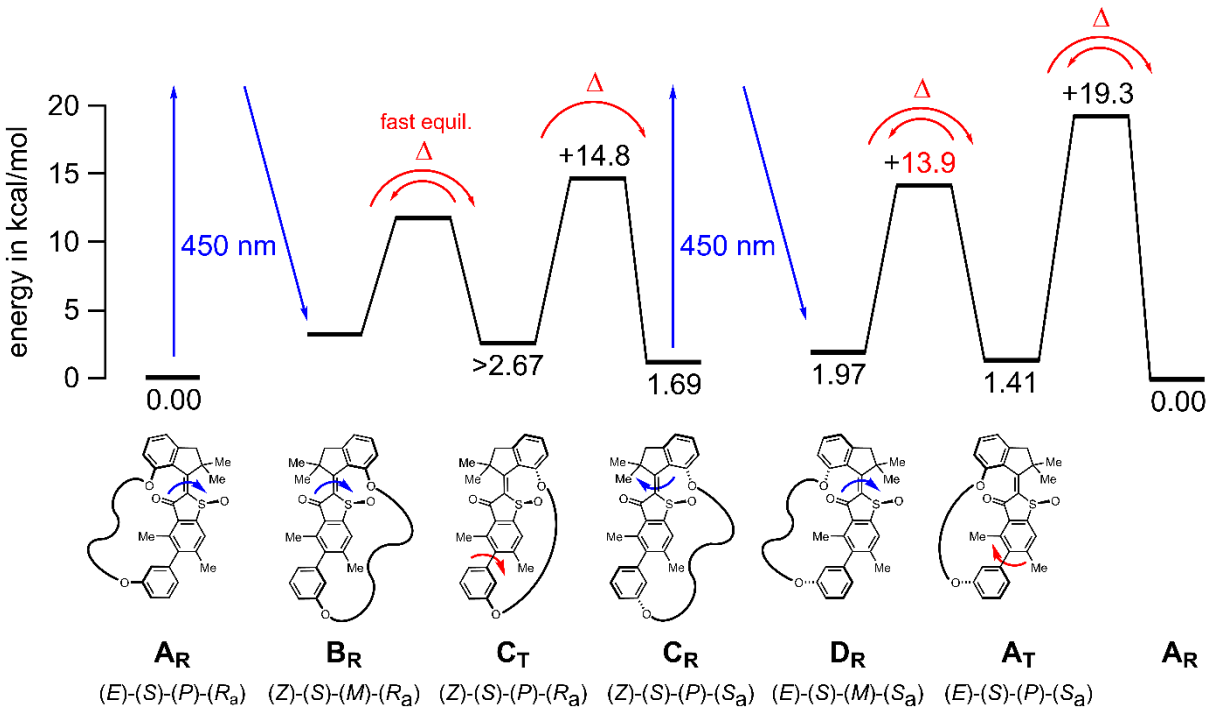

Figure 118 Quantitative ground state energy profile of motor system **95**. Six states are populated during one full unidirectional 360 °C rotation. The covalent linker is simplified for clarity reasons. Only isomers with *S* configured sulfoxide are depicted. All values with the exception of $\Delta G^{\ddagger}$(**D**$_R$**-95** to **A**$_T$**-95**) **(**value in red, measured at –80 °C) were either measured directly at 0 °C or extrapolated to this temperature.

4.13 Transmission of potential energy and active acceleration of biaryl rotation

Summarizing the experiments a comprehensive picture of the working mechanism of molecular machine **95** is drawn. Light-induced transmission of unidirectional rotation occurs over a total of six steps. Different to the preceding four-step system, thermal helix inversion of the initial photoproducts leads to the new tensed states **A**$_T$**-95** and **C**$_T$**-95**. Conversion to the respective relaxed states **A**$_R$**-95** and **C**$_R$**-95** proceeds thermally via an atropisomerization reaction. In the case of **A**$_T$**-95** and **A**$_R$**-95** both isomers are in a dynamic equilibrium with an energy difference of 1.41 kcal·mol^{-1} at 0 °C. Experimental as well as theoretical assessments of model compound **95** have demonstrated that the untethered atropisomers are energetically nearly degenerate. As a consequence, the lift in degeneracy of the **A**$_T$**-95**/**A**$_R$**-95** isomers can be seen as a direct measure of potential energy that is transmitted through action of the motor unit (Figure 119, left). This energy is raised in the initial **C**$_R$**-95** to **D**$_R$**-95** photoreaction and its maximum corresponds to the energy of **D**$_R$**-95** with 1.97 kcal·mol^{-1}. Only about 72% of this initial energy

input is then transmitted to the biaryl unit, which is reflected by the energy of **A_T-95** that is 1.41 kcal·mol^{-1}.

At low temperatures, the analogous pair of atropisomers **C_T-95**/**C_R-95** is not in a dynamic equilibrium. A lower limit of 0.98 kcal·mol^{-1}for the energy difference is established under the conservative assumption that 5% of residual **B_R-95**/**C_T-95** is not detectable by ^{1}H NMR at –105 °C (Figure 119, right). Because of the observed full conversion from **C_T-95** to **C_R-95** the actual lift in degeneracy could not be assessed experimentally. The amount of transmitted potential energy therefore amounts to at least 0.98 kcal·mol^{-1}.

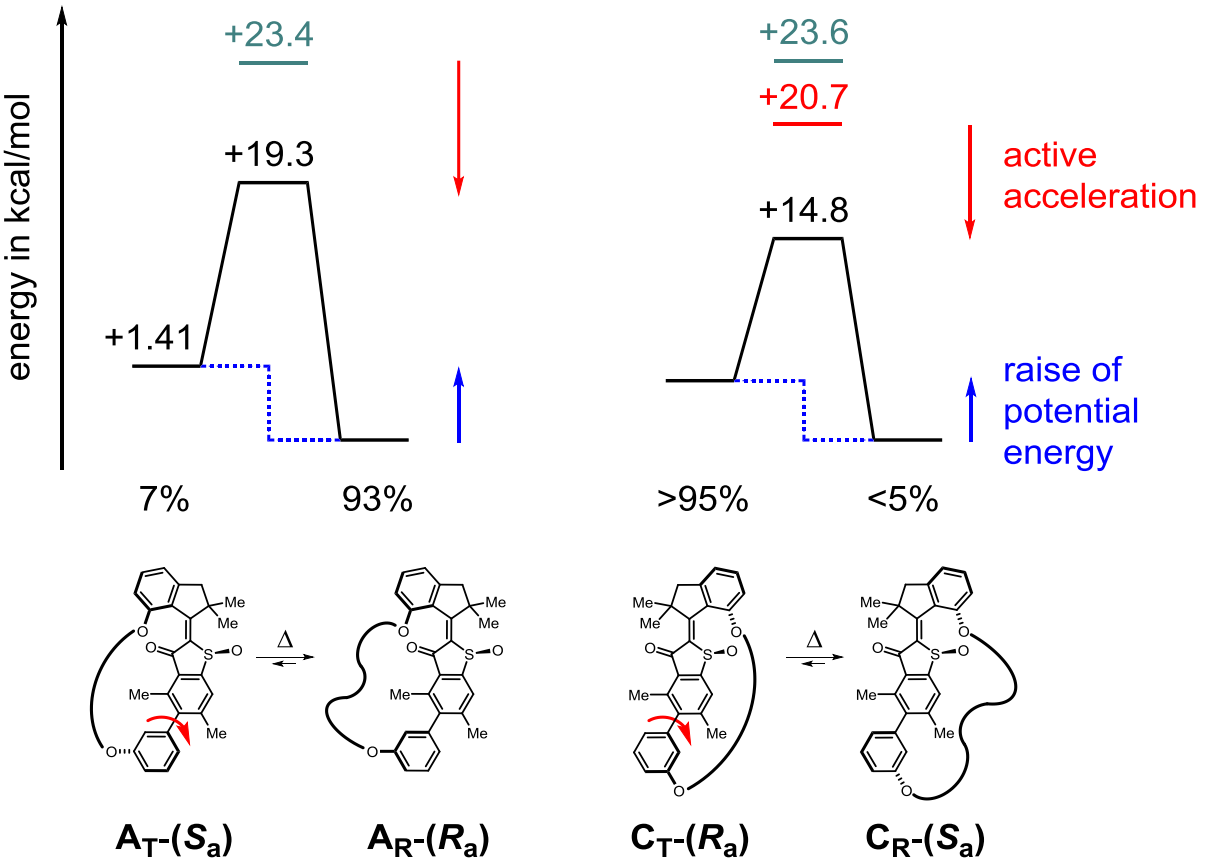

Figure 119 Raise of potential energy (blue arrows) and rate acceleration of biaryl rotation (red arrows). Calculated values for the nondirectional and untethered biaryl rotation are given in grey. All values correspond to 0 °C. Action of the integrated molecular motor results in sequential raise of potential energies. As a result, biaryl rotation proceeds unidirectionally with > 93% conversion for the individual 180° steps. The rotation cycle encounters energy barriers between 14.8 and 19.3 kcal·mol^{-1}. Activation energies are lowered by up to 5.9 kcal·mol^{-1} for the **C_T**-(R_a)/**C_R**-(S_a) atropisomerization compared to the experimental value of the untethered model system (value in red). No experimental value for the untethered biaryl rotation of the *E* configured model system could be obtained.

In theory, transmittance of more potential energy is possible in a system where the relative energy of the photogenerated isomers **B_R-95** and **D_R-95** is increased. This is independent of the energy of the tensed states as long as **A_R-95** and **C_R-95** serve as energy sinks for the subsequent thermal isomerization steps. It should be noted that the thermal equilibria between **D_R-95** and **A_T-95** as well as **A_T-95** and **A_R-95** are crucial to obtain experimental values for the corresponding ground state energies. For the conversion of **B_R-95**/**C_T-95** to **C_R-95** new experiments have to be developed to determine the lift in degeneracy and the transmitted potential energy.

Another effect of the motor unit acting on the biaryl axis is the decrease in activation energy for the atropisomerization reactions. The intrinsic barrier of the untethered biaryl rotation was determined theoretically as well as experimentally. Because of the very delicate separation process, kinetic analysis of the atropisomerization of model compound **103** could only be conducted for a single *Z* configured isomer. A corresponding Gibbs free energy of activation $\Delta G^{\ddagger}$ = 20.74 kcal·mol^{-1} was determined at 0 °C. Theoretical descriptions revealed an energy difference between *E* and *Z* configured atropisomers in the range of 0.1 kcal·mol^{-1} with no significant difference in activation energies between clockwise and counterclockwise rotations. As a result of the motor action, atropisomerization barriers for the **C_T-95** to **C_R-95** transition are lowered by up to 6.0 kcal·mol^{-1} ($\Delta G^{\ddagger}$ = 14.75 kcal·mol^{-1} at 0 °C). This constitutes a major rate enhancement that is several orders of magnitude faster compared to the untethered biaryl rotation. The experimentally determined activation energy for **A_T-95** to **A_R-95** isomerization is 19.25 kcal·mol^{-1}. Assuming an actual barrier for the free rotation that is also close to the 20.74 kcal·mol^{-1} (the calculated 23.4 kcal·mol^{-1} are probably an overestimation), atropisomerization would also occur accelerated and about 16 times faster in the tethered system.

The difference in rate acceleration between *Z* and *E* configured isomers can be in part attributed to the considerably stronger strain in the *Z* configured isomers of **95**. This is also reflected in the energy difference of 1.69 kcal·mol^{-1} between **C_R-95** and **A_R-95**. Also, strain in the tensed states is increased further in **C_T-95** compared to **A_T-95**, which can be seen in the dynamic equilibrium between **A_T-95** and **A_R-95** that is not observed for **C_T-95** and **C_R-95**. However, the difference in ground state energies cannot account for the full decrease in activation energy of 6.0 kcal·mol^{-1}, which indicates that also the transition state from **C_T-95** to **C_R-95** must be significantly stabilized by the tether strain.

Overall, the presented system **95** allowed for the first time the effective transmission of potential energy from the light powered motion of a molecular motor unto a receiving aryl unit. As a result, energy degeneracy of atropisomers is lifted and biaryl rotation is greatly accelerated and forced to proceed unidirectionally, resulting in sequential and alternating decreases in activation energies. A comprehensive study of the temperature dependence of the six-step working mechanism allowed for the quantification and direct comparison of underlying reactions in unprecedented detail. A total of 72% of maximum potential energy generated in the initial photoreaction is transmitted in one half of the 360° rotation cycle. This energy that amounts to 1.41 kcal·mol^{-1} can also be interpreted as the amount of work that can be performed by the motor unit in this particular setup. The potential energy that is transmitted by the motor in the second half of the rotational cycle could not be quantified experimentally but is expected to be equal or even higher. Due to increased intramolecular strain in the involved states, a significant rate acceleration of biaryl rotation is observed that reveals fundamental design principles for the construction of such nanomachines. In the future, efforts will be made towards more sophisticated systems that can perform highly complex motions and allow to harness the power of molecular motors for more constructive tasks.

4.14 Synthesis, structure and photophysical properties of HTI 99

4.14.1 Synthesis of HTI 99

A halogen migration side reaction during the synthesis of benzothiophenone **91** (section 4.2, Scheme 27) afforded significant amounts of the byproduct **90**. This substitution pattern allows for intriguing modifications of the core scaffold. To further explore this as a route to functional systems with an alternative attachment of the aryl follower unit, construction of the functional macrocycle was attempted. Condensation with indanone **56** furnished HTI **96** in 50% yield (Scheme 34).

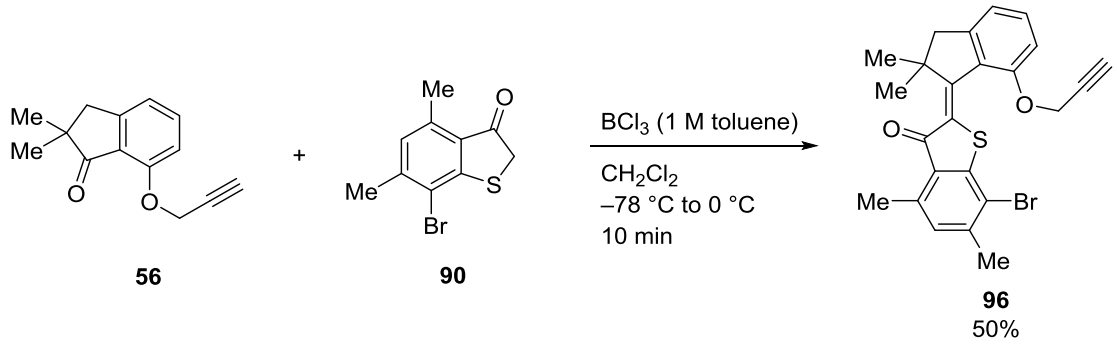

Scheme 34 Condensation of indanone **56** and benzothiophenone **90** at –78 °C in CH_2Cl_2 using BCl_3. HTI **96** is obtained as a mixture of *E* and *Z* isomers. Only the *Z* configured isomer is shown.

The following 1,3-dipolar cycloaddition with building block **73** gave triazole **97** in very good yields (Scheme 35).

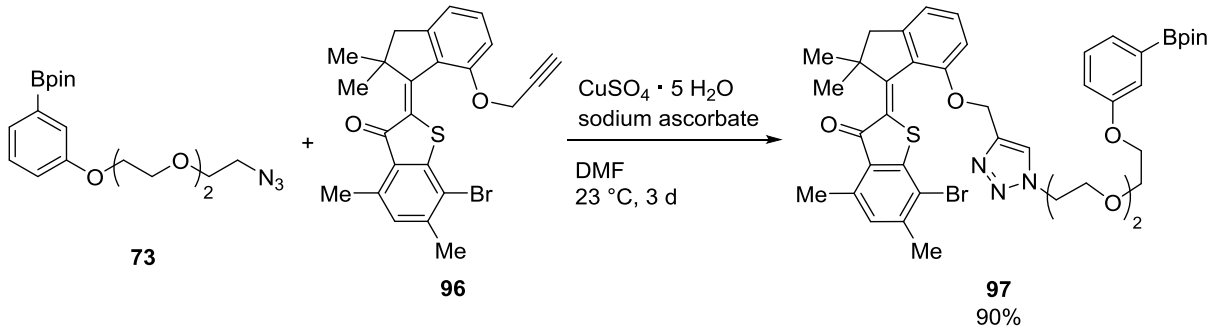

Scheme 35 Copper catalyzed 1,3-dipolar cycloaddition of boronic acid pinacol ester **73** and HTI **96** using $CuSO_4 \cdot 5H_2O$ (2 mol%) and sodium ascorbate (10 mol%). The product **97** was obtained as a mixture of *E* and *Z* isomers. Only the *Z* configured isomers are shown.

Fusion of the macrocycle in an intramolecular *Suzuki-Miyaura* coupling resulted in highly unspecific product formation. Full separation of the target compound **98** was not possible by flash column chromatography and a crude product that corresponds to 43% yield was obtained that was used directly in the next synthetic step (Scheme 36).

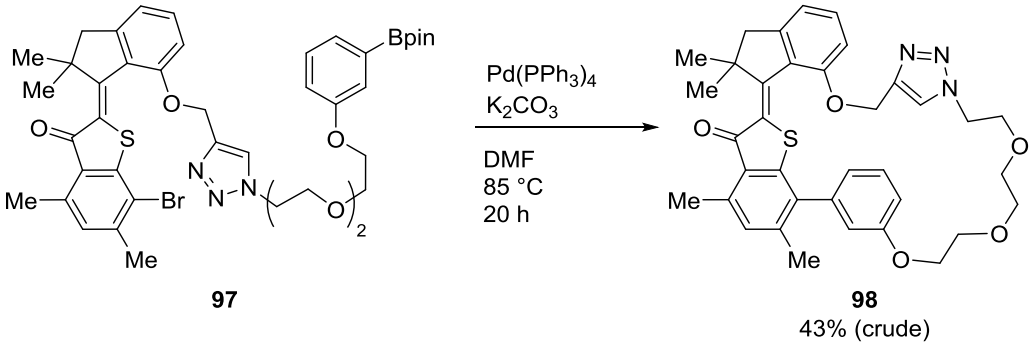

Scheme 36 Intramolecular *Suzuki-Miyaura* cross-coupling of **97**. The crude product **98** was obtained in 43% yield as a mixture of isomers. Only the *Z* configured isomers are shown.

Oxidation was accomplished using sodium perborate tetrahydrate (Scheme 37). Full separation of the target compound was achieved by preparative HPLC using a SiO_2 column and small amounts of the *E* configured macrocycle **99** were obtained. The isolated yield was 7% and sufficient to perform structural and photophysical measurements.

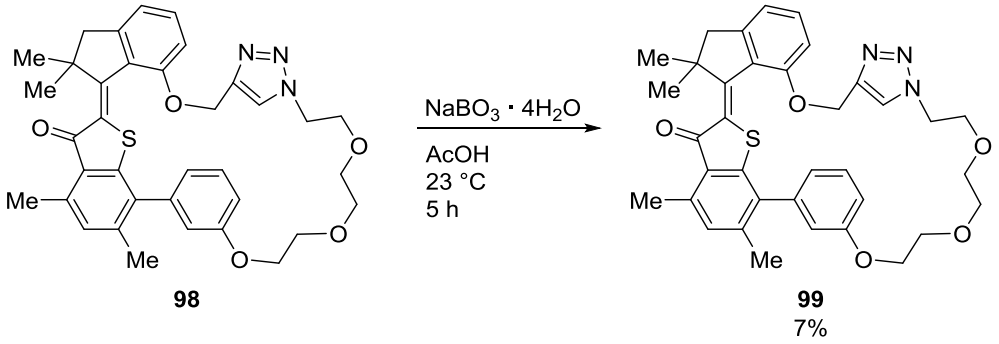

Scheme 37 Oxidation of an *E*/*Z*-isomeric mixture of **98** to the sulfoxide **99** using sodium perborate tetrahydrate in acetic acid. Only the *Z* configured isomers are shown.

4.14.2 Structure of *E*-99 in the crystalline state

Crystals suitable for single crystal X-ray analysis were obtained from a racemic mixture of *E*-**99**. The *E*-(*S*)-(*P*)-(S_a) configured isomer is shown in Figure 120. The *E*-(*S*)-(*P*)/*E*-(*R*)-(*M*)

geometry of the HTI fragment corresponds to the global energy minimum found in similarly configured macrocyclic *E* isomers of HTI motors. The phenolic oxygens of the indanone rotor and aryl follower point to the same half-space as the sulfoxide oxygen. Also, the major part of the covalent linker resides on this side of the benzothiophenone stator. The torsion of the biaryl axis is close to 90° indicating a high steric demand in proximity of the connecting single bond. In this setup, the follower plane is almost perpendicular to the benzothiophenone fragment. As a result, switching between *E*-**99** and potential *Z* isomeric forms is expected to result in a high modulation of intramolecular strain. As discussed earlier the induced strain is also likely to be greatly dependent on the length of the tether.

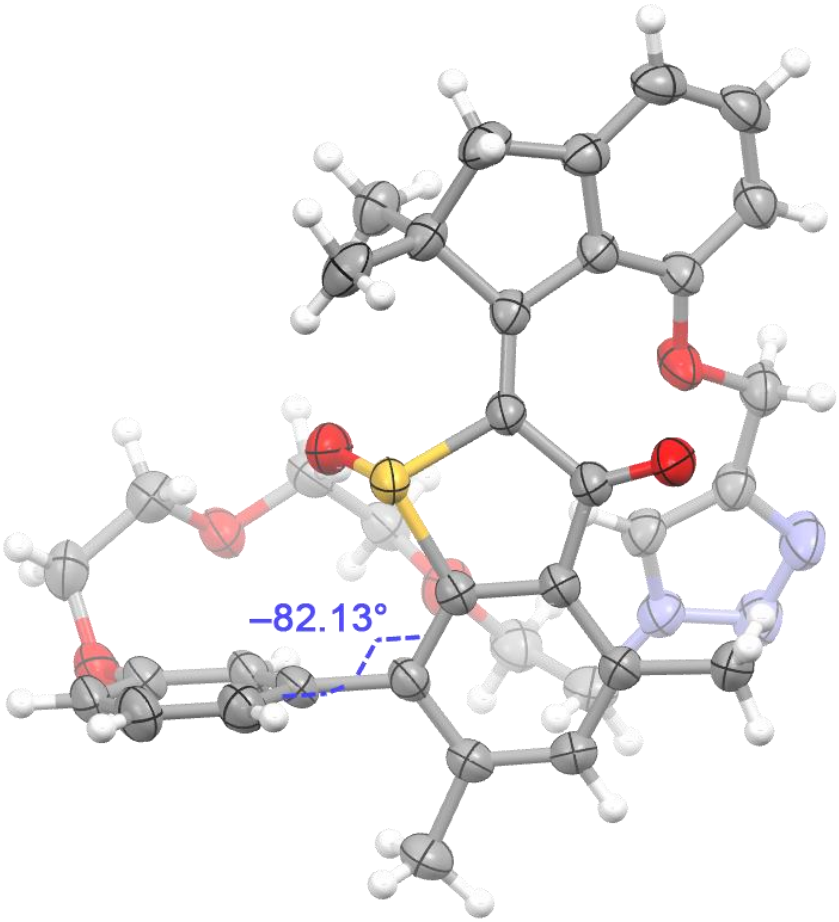

Figure 120 Structure of racemic *E*-**99** in the crystalline state (50% probability ellipsoids). Only the *E*-(*S*)-(*P*)-(S_a) isomer is shown. The oxygen atoms of the indanone rotor and aryl follower that are connected to the covalent linker point to the same half-space as the sulfoxide oxygen atom. The PEG tether also resides on this side of the benzothiophenone stator. A biaryl torsion of –82° is observed with a minor tilt of the aryl follower towards the methyl group of the stator.

4.14.3 Irradiation of 99 in solution

The isomerization behavior of **99** at ambient temperatures was elucidated in solution. A sample of *E*-**99** in CD_2Cl_2 was irradiated between 20 and 30 minutes with light of different wavelengths (Figure 121).

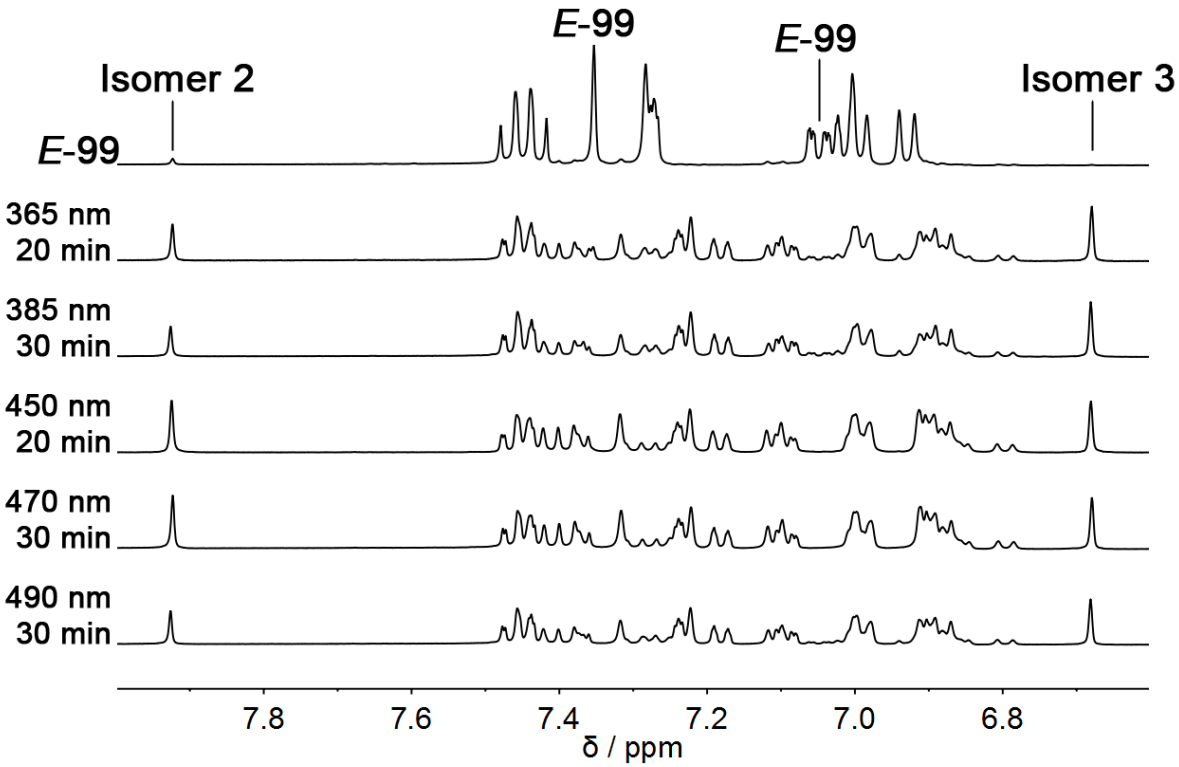

Figure 121 ^{1}H NMR spectra (CD_2Cl_2, 400 MHz, 22 °C) obtained after irradiation of *E*-**99** for 20 min or 30 min using LED light of different wavelengths.

Two new sets of signals emerged that were attributed to isomers of **99**. The product distribution is given in Table 8. The conformation of these isomers could not be further elucidated. An overall strong decrease of *E*-**99** signals is observed and the solution is almost depleted of *E*-**99** when irradiated with 450 nm or 470 nm light.

Table 8 Distribution of *E*-**99** and *Z*-**99** isomers after irradiating a solution of *E*-**99** (CD_2Cl_2, 400 MHz, 22 °C) to the pss using light of different wavelengths.

wavelength	time	*E*-99	Isomer 2	Isomer 3
365 nm	20 min	15 %	34 %	51%
385 nm	20 min	15 %	30 %	55%
450 nm	20 min	4 %	48 %	48%
470 nm	30 min	3 %	49 %	48%
490 nm	30 min	11 %	37 %	52%

The results indicate partial unidirectionality of the system as two new isomers are generated as the major photoproducts and simultaneously initial *E*-**99** concentration is greatly reduced. It is straightforward to assume that one of the two new isomers corresponds to a *Z*-(*S*)-(*P*)/*Z*-(*R*)-(*M*) structure as this constitutes the second stable product of the unidirectional photoisomerization pathway dictated by the HTI motor fragment. Also this process is expected to be accompanied by a release of intramolecular tension as stated earlier and does not necessarily require atropisomerization of the biaryl axis. Other potential isomers include the usually highly unstable *Z*-(*S*)-(*M*)/*Z*-(*R*)-(*P*) structures or require rotation around the biaryl axis. However, a photoinduced atropisomerization would result in a total of four stable conformations i.e. *E*-**99**/*Z*-**99** and their respective atropisomers but only three isomers could be identified so far. It is clear that additional experiments are required to fully unravel the underlying processes but analysis was greatly hampered by the small amounts of available compound at this point. As the main focus lied on exploration of the related macrocycle **99**, this project was not pursued any further.

5 Changing the rotation direction of the HTI motor fragment

5.1 Initial thoughts

To this point, two systems were established that allow for the transmission of unidirectional motions. Their working mechanisms were assessed by experiments that relied on an integrated biaryl reporter unit. In a next step, the biaryl setup should be employed to make photoisomerization reactions visible that are too fast to be observed by common spectroscopic methods. An example would be the potential unidirectional rotation of "unsubstituted" HTI (Figure 122).

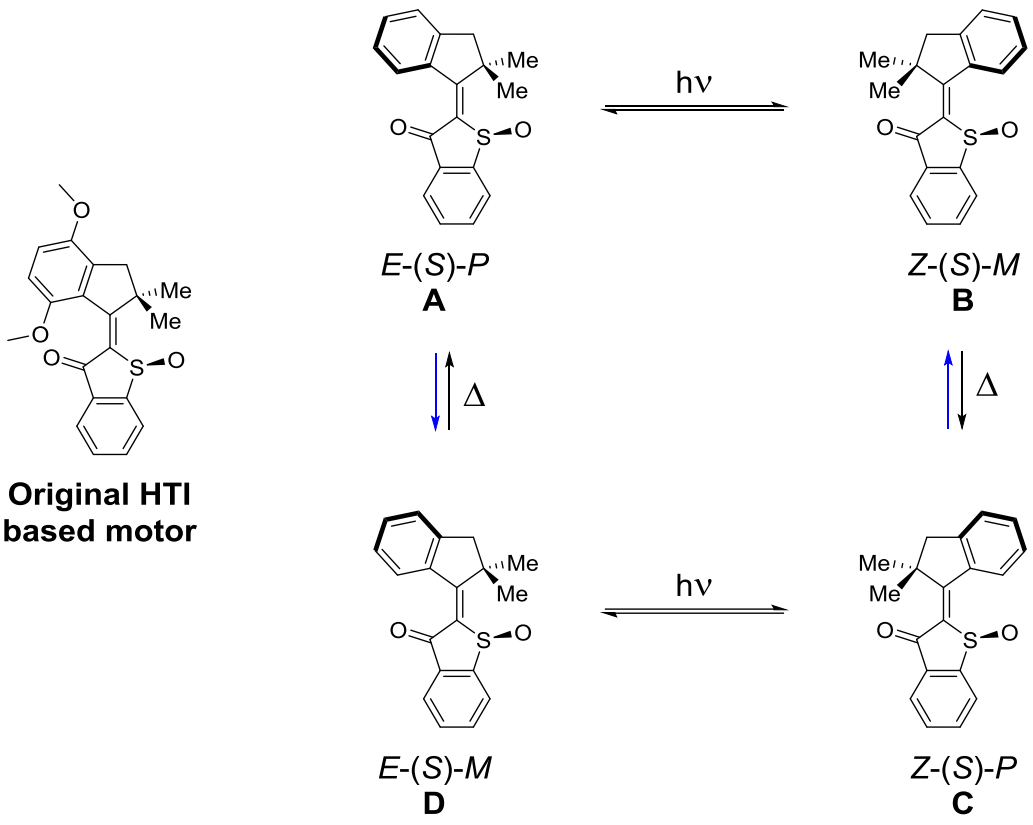

Figure 122 Schematic visualization of the potential working mechanism of "unsubstituted" HTI. Unsubstituted refers to the lack of substituents at the aromatic parts of the molecule, in particular the indanone position adjacent to the double bond, which greatly reduces steric interactions with the benzothiophenone part. This could result in a decrease of activation energy for the thermal ratcheting steps (**B** to **C** and **D** to **A**) as well as in a decrease of their respective energy differences and therefore enable rotation in either direction (indicated by blue arrows).

Compared to the parent HTI motor, repulsive interactions between an indanone substituent and the carbonyl or sulfoxide of the stator part are missing. As a result, helicity around the central double bond is expected to be less pronounced or even non-existent. Theoretical calculations at

the B3LYP-GD3BJ/6-311G(d,p) IEFPCM (CH_2Cl_2) level of theory show almost degenerate ground states with the exception of the *E*-(*S*)-(*M*) conformer with an energy difference of ΔG = 2.7 kcal·mol^{-1} (Figure 123). Also, activation energies for the helix inversion steps are expected to be much lower than in the parent system, resulting in a dynamic equilibrium of the respective isomers (indicated by blue arrows in Figure 122) and a switch-like behavior of the system. The lower helix inversion barriers imply that a potential (partial) unidirectionality of the system cannot be elucidated by common spectroscopic methods.

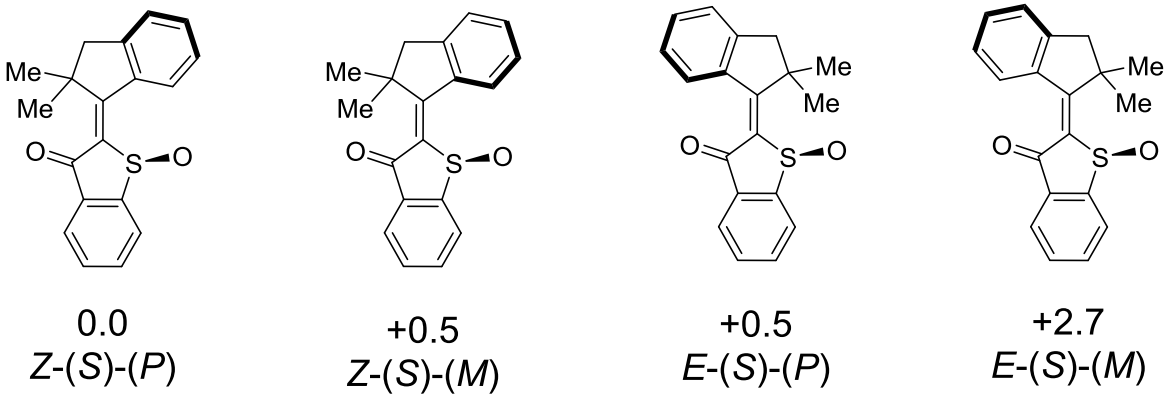

Figure 123 Ground state energies of unsubstituted HTI calculated at the B3LYP-GD3BJ/6-311G(d,p) IEFPCM (CH_2Cl_2) level of theory. Energies are nearly degenerate (ΔG = 0.5 kcal·mol^{-1}) with the exception of *E*-(*S*)-(*M*) and a corresponding ΔG = 2.7 kcal·mol^{-1} compared to the lowest energy *Z*-(*S*)-(*P*) conformer.

This problem can potentially be overcome by integration of unsubstituted HTI into a macrocyclic system. If a HTI fragment is integrated in such a system, photoirradiation of a single atropisomer results in photoproducts with a certain distribution. In the case of an integrated switch the ratio of these products is identical if the respective atropisomer is irradiated (Figure 124).

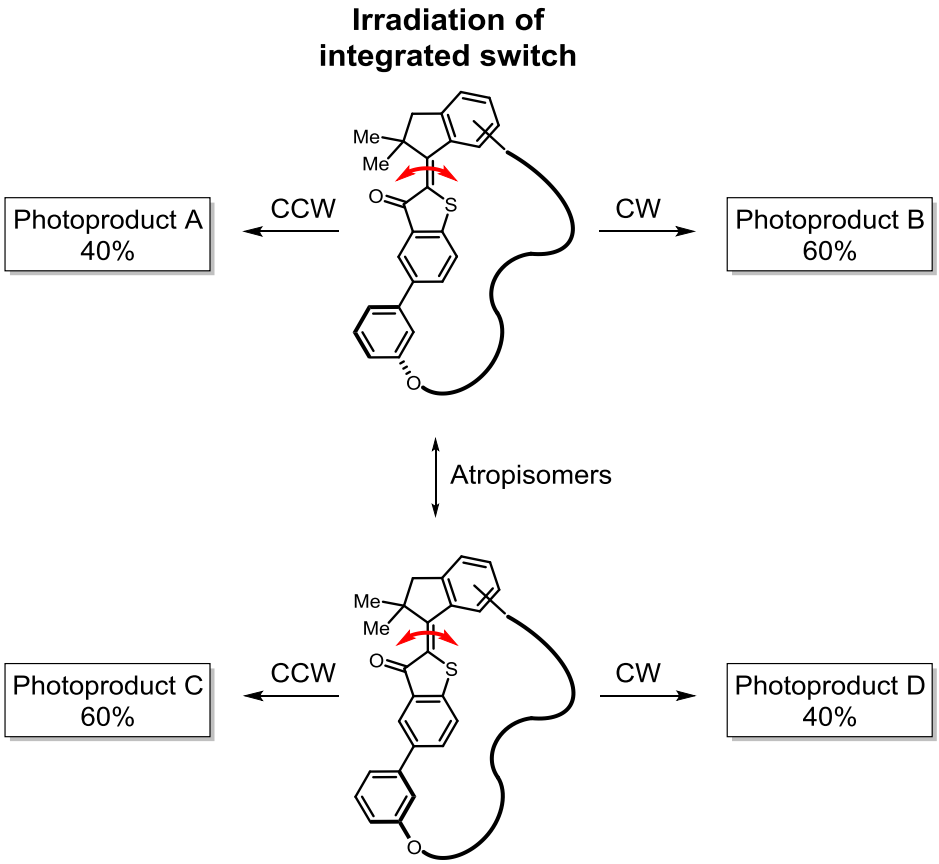

Figure 124 Schematic representation of the (arbitrarily chosen) distribution of photoproducts obtained from the irradiation of an integrated switch. Product ratios obtained from clockwise (CW) or counterclockwise (CCW) rotation are identical to the product ratios obtained from irradiation of the corresponding atropisomer from opposite rotation directions due to it being the mirror image.

If a bias is induced, for example by oxidation of the sulfide to the corresponding (chiral) sulfoxide, a shift in these photoproduct ratios can be expected for the respective atropisomers. From these ratios, a preferred rotation direction can potentially be deducted that indirectly proves the unidirectional rotation of the HTI fragment. In Figure 125 this is represented by an overall preferred clockwise (CW) rotation upon irradiation of a pair of atropisomers.

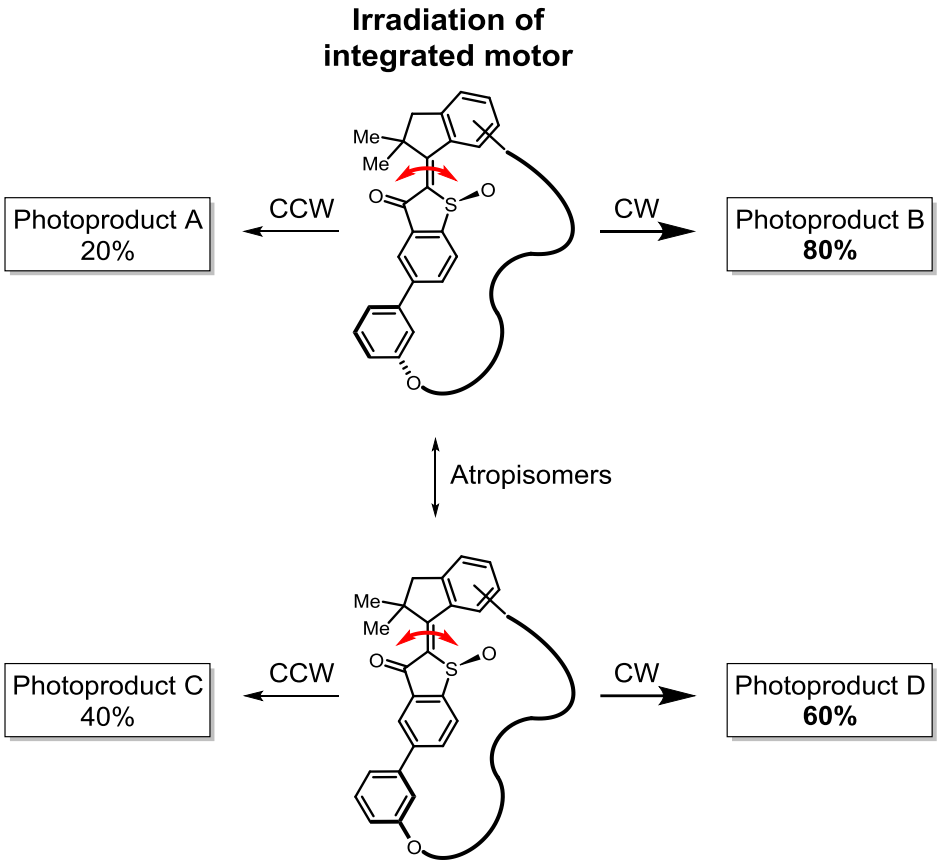

Figure 125 Schematic representation of the (arbitrary) distribution of photoproducts obtained from the irradiation of an integrated motor. Product ratios obtained from clockwise (CW) or counterclockwise (CCW) rotation reveal a bias towards one rotation direction (here CW).

In order to conduct these irradiation experiments, separation of the atropisomers must be feasible. In the previous system, two methyl groups were introduced in *ortho* position to the biaryl axis but isolating an atropisomer enriched solution was barely possible at 0 °C. Therefore, additional steric hindrance must be introduced within the new system. Ideally, the energy of activation lies in the range of 28 kcal·mol^{-1}. This translates to a half-live of > 1 years at 23 °C, making separation at ambient temperatures feasible while also allowing rotation of the system at elevated temperatures with half-lives reduced to less than an hour at 100 °C.

Theoretical calculations at the B3LYP-GD3BJ/6-311G(d,p) IEFPCM (CH_2Cl_2) level of theory were conducted to assess substitution patterns for their feasibility. In addition, the required building blocks were screened for their commercial availability to not further complicate the target compound synthesis. From these preliminary results, biaryl rotation with a 1,1-dimethyl-1'-fluoro substitution pattern showed very promising activation energies of around 28.3 kcal·mol^{-1} and was selected for the first functional system (Figure 126).

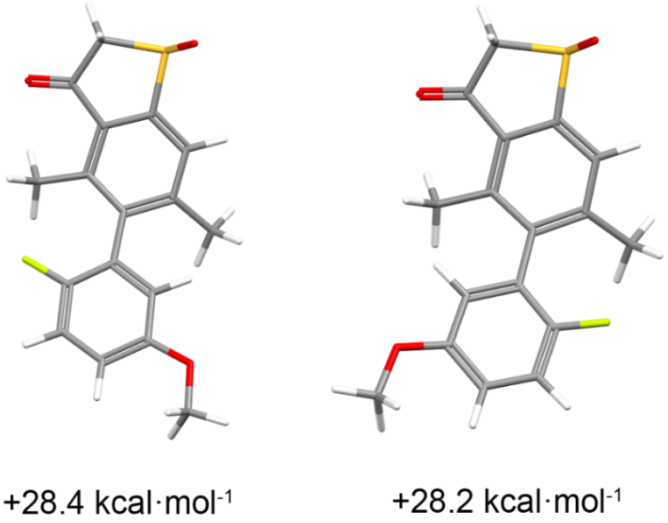

Figure 126 Transition state energies of a model 1,1-dimethyl-1'-fluoro biaryl system compared to the most stable ground state calculated on the B3LYP-GD3BJ/6-311G(d,p) IEFPCM (CH_2Cl_2) level of theory.

Lastly, attachment of the covalent linker to the rotor part had to be realized while also removing the sterically demanding substitution from the indanone rotor in *ortho*-position of the double bond. This was envisioned by shifting the attachment point of the tether to the adjacent position, which is the 6-position of the indanone. The design principles of the new system are summarized in Scheme 38.

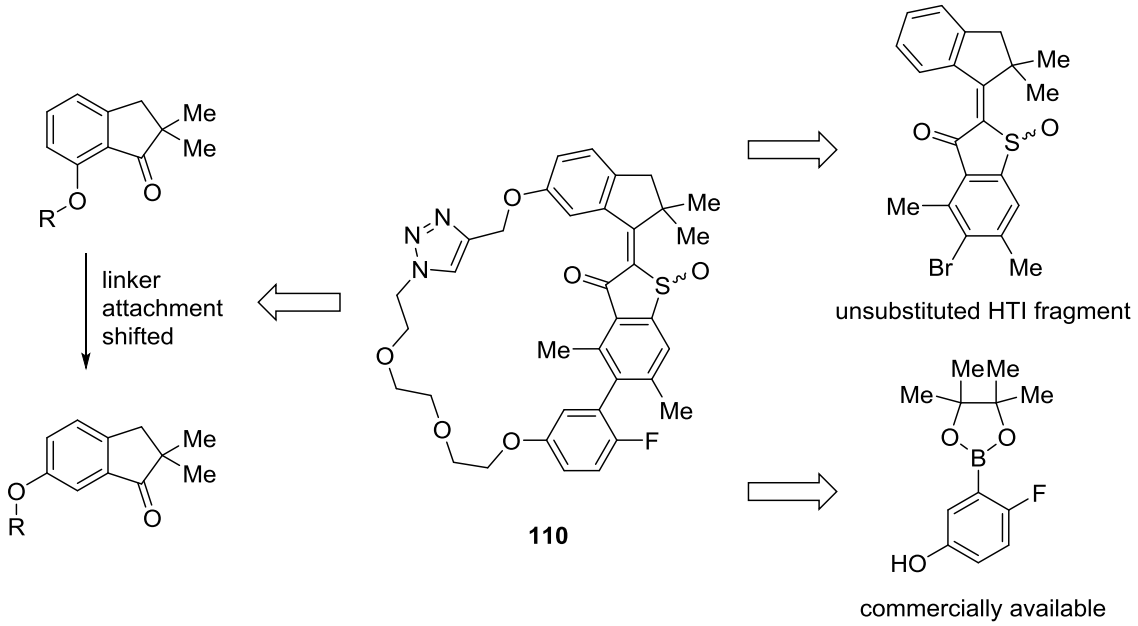

Scheme 38 Design principles for the synthesis of target compound **110**. Linker attachment at the indanone rotor part is shifted. The resulting HTI fragment is expected to be a functional analog to a HTI fragment lacking the sterically demanding substituent in *ortho*-position of the double bond on the indanone. The fluorophenyl boronic acid pinacol ester required for the modular synthesis is commercially available and does not require additional synthetic steps.

5.2 Synthesis of HTI 110

The Synthesis of HTI **110** followed the established route to macrocyclic HTIs with only minor modifications. Reaction of 6-hydroxy indanone with propargyl bromide gave indanone **104** in 84% yield (Scheme 39). Subsequent methylation proceeded in good yields and gave indanone **105** as a yellow oil.

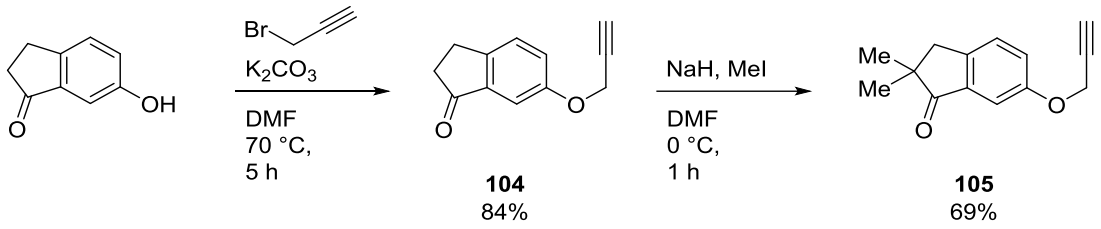

Scheme 39 Reaction of 6-hydroxy indanone with propargyl bromide and K_2CO_3 gave indanone **104**. Methylation afforded building block **105**.

Condensation of indanone **105** with the known building block **91** furnished HTI **106** in 52% yield as a mixture of *E* and *Z* isomers (Scheme 40).

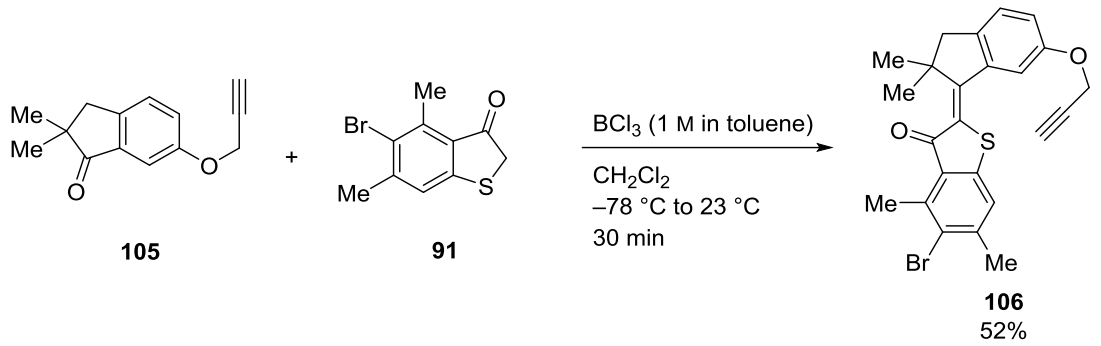

Scheme 40 Condensation of indanone **105** and benzothiophenone **91** at –78 °C in CH_2Cl_2 (followed by 30 min at 23 °C) using BCl_3. HTI **106** was obtained as a mixture of *E* and *Z* isomers (7:3). Only the *Z* configured isomer is shown.

Attachment of the bifunctionalized linker **72** to 2-fluoro-5-hydroxyphenylboronic acid pinacol ester gave compound **107** in 74% yield (Scheme 41). To avoid hydrolization of the boronic ester, the product was used crude in the following synthetic step.

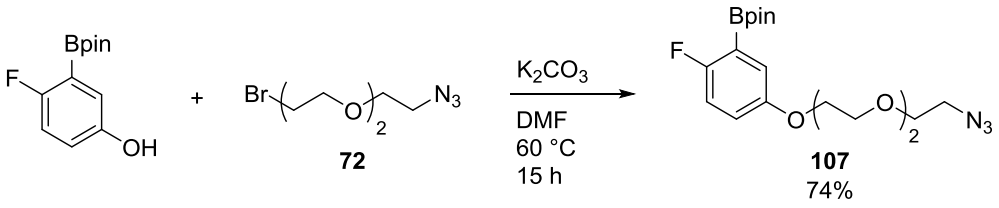

Scheme 41 Reaction of 2-fluoro-5-hydroxyphenylboronic acid pinacol ester with functionalized triethylene glycol **72** gave **107**.

With the required building blocks at hand, assembly of the macrocycle proceeded with 1,3-dipolar cycloaddition of compounds **106** and **107** (Scheme 42). Analogously to previous syntheses, minor amounts of hydrolyzed product were observed upon purification.

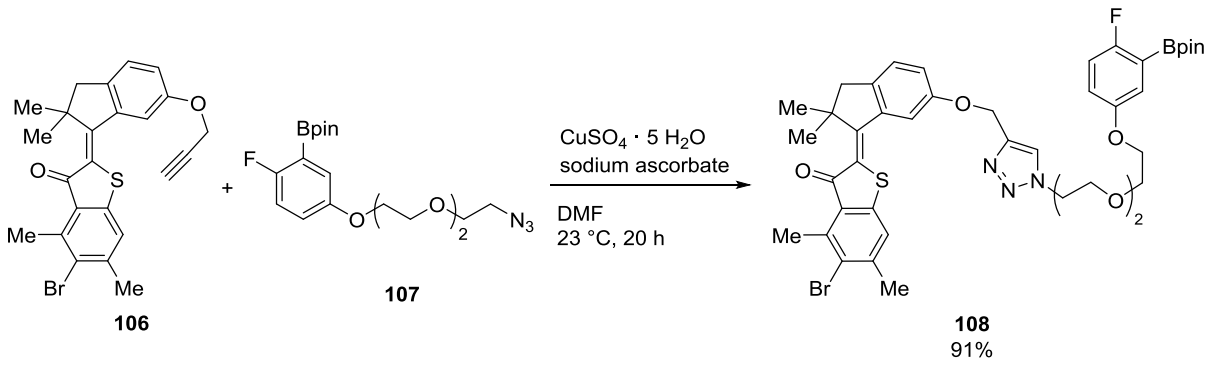

Scheme 42 Copper catalyzed 1,3-dipolar cycloaddition of HTI **106** and boronic acid pinacol ester **107**. The product **108** was obtained in 91% yield as a mixture of *E* and *Z* isomers. Only the *Z* configured isomers are shown.

The following intramolecular *Suzuki-Miyaura* cross-coupling reaction resulted in a variety of products that could not be fully separated by conventional flash column chromatography (Scheme 43). As a result, the desired product **109** was obtained as crude mixture that corresponds to 6% yield, which was directly subjected to oxidation.

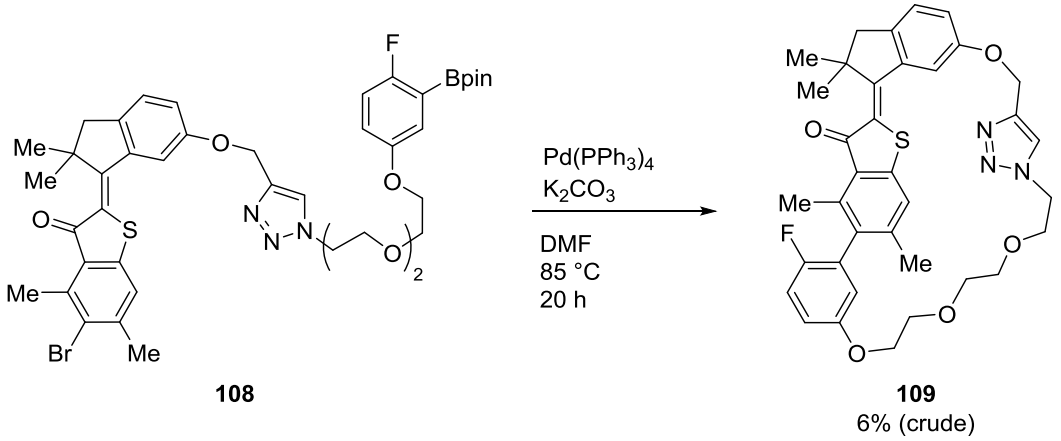

Scheme 43 Intramolecular *Suzuki-Miyaura* cross-coupling of **108**. The product **109** was obtained in 6% yield as a crude mixture. Only the *Z* configured isomers are shown.

Stirring of the solution containing crude **109** in acetic acid with four equivalents of sodium perborate resulted in the characteristic color change from orange to yellow over four hours (Scheme 44). Two conformers of compound **110** were isolated along with a variety of byproducts. The majority of these were attributed to protodeboronation since all of the corresponding ^{1}H NMR spectra revealed an additional proton signal in the aromatic region that could be assigned to the fluorinated aryl moiety. This side reaction is well known to occur in *Suzuki-Miyaura* coupling reactions and is greatly accelerated by a fluorine substituent in *ortho* or *para* position to the boronic acid.[88] Nevertheless, sufficient amounts of target compound **110** could be isolated to further elucidate the structure and working mechanism of the molecular machine.

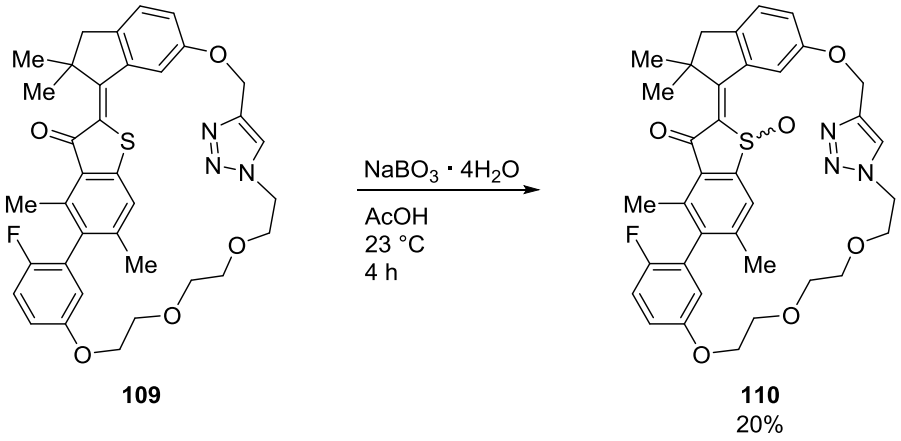

Scheme 44 Oxidation of **109** to sulfoxide **110** using sodium perborate tetrahydrate in acetic acid. Only the *Z* configured isomers are shown.

5.3 Structural analysis of 110

5.3.1 Structures in solution

Due to the extremely poor yield of the *Suzuki-Miyaura* coupling that was employed in the ring-closing step, very limited amounts of the target compound were available. Two isomers were isolated by preparative HPLC and the identity was confirmed by ^{1}H NMR and HR-MS analysis. NMR NOESY experiments were conducted to determine the configuration of the central double bond (Figure 127 and Figure 128).

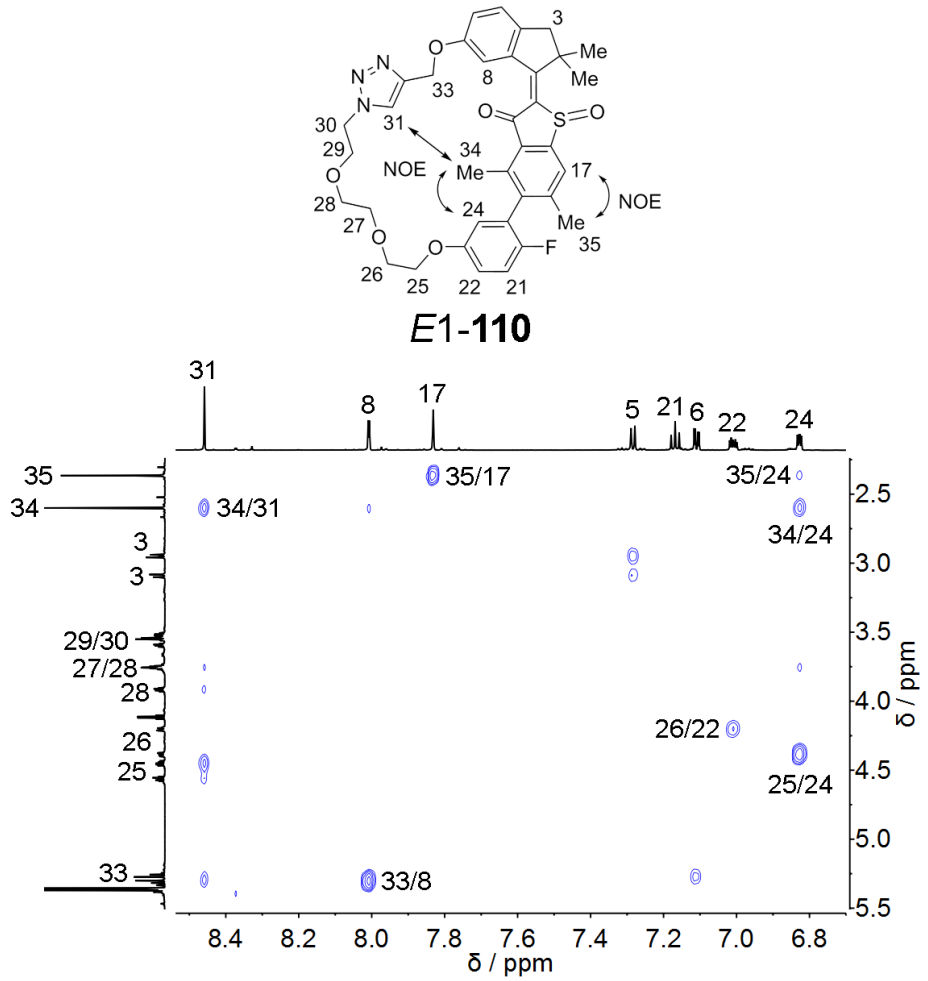

Figure 127 NOESY NMR spectrum of *E*1-**110** (CD_2Cl_2, 800 MHz, 25 °C). Indicative signals are highlighted. The cross signal between methyl group protons 34 and proton 24 is significantly stronger than the cross signal between methyl group 35 and proton 24 indicating a preferred tilt of the biaryl axis towards the carbonyl side of the benzothiophenone stator. A cross signal between proton 31 and methyl group 34 confirms *E* configuration of the central double bond.

Indicative cross signals revealed *E* configuration as a well as a preferred torsion of the dihedral angle at the biaryl single bond towards the carbonyl side of the benzothiophenone stator. This was observed for both products that were consequently assigned to a pair of atropisomers that

possess an *E* configured double bond. The biaryl torsion also indicates an overall strained geometry as a dihedral angle of approximately 90° can be expected from an untethered system.

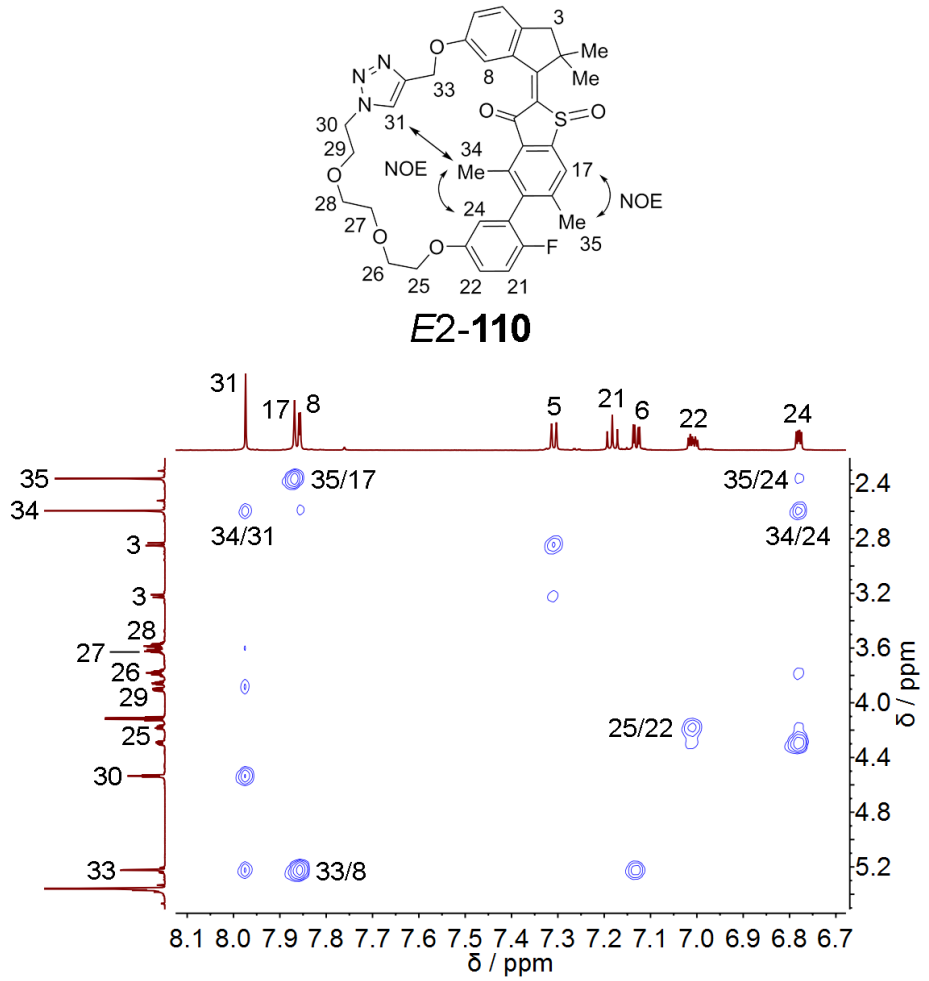

Figure 128 NOESY NMR spectrum of *E*2-**110** (CD_2Cl_2, 800 MHz, 25 °C). Indicative signals are highlighted. The cross signal between methyl group protons 34 and proton 24 is significantly stronger than the cross signal between methyl group 35 and proton 24 indicating a preferred tilt of the biaryl axis toward the carbonyl side of the benzothiophenone stator. A cross signal between proton 31 and methyl group 34 confirms *E* configuration of the central double bond.

Next, solutions of both *E*-**110** compounds in CD_2Cl_2 were irradiated with 450 nm light at 23 °C. Identical ^{1}H NMR spectra were obtained after irradiation was complete regardless of the starting *E* isomer (Figure 129). The *E*1-**110** irradiation spectrum is almost completely depleted of the initial conformer. Both irradiation spectra consist of *E*2-**110** and a new conformer that is expected to have a *Z* configured central double bond. No signals of a second atropisomer with *Z* configuration could be observed.

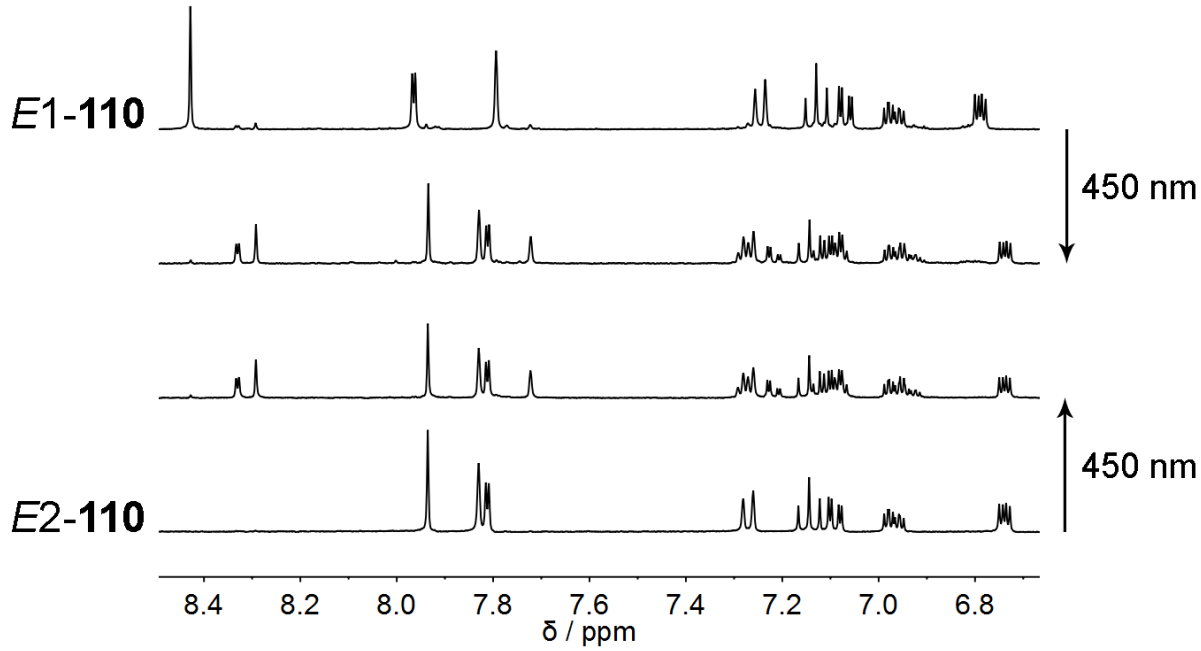

Figure 129 NMR irradiation experiments of *E*1-**110** and *E*2-**110** (CD_2Cl_2, 400 MHz, 20 °C). The solutions were irradiated with 450 nm light for 35 min resulting in identical spectra. The spectra obtained from irradiation show remaining signals of *E*2-**110** and a new conformer that is likely to possess a *Z* configured central double bond. Minor traces of *E*1-**110** remain visible.

Depending on the wavelength, different product ratios can be observed (Figure 130). Only minor amounts of the initial *E*1-**110** can be generated through irradiation. Spectra with high concentrations of *Z*-**110** show less *E*1-**110** and *vice versa*, with the exception of 490 nm irradiation experiments.

Taken together, the NMR irradiation experiments show a preferred isomerization pathway from *E*1-**110** to *Z*-**110**/*E*2-**110**. The experiments also indicate the presence of two photoisomerization processes. One being the photoisomerization between *Z*-**110** and *E*2-**110** and a second that generates *Z*-**110** from *E*1-**110**. Direct photoinduced atropisomerization from *E*1-**110** from *E*2-**110** that does not include isomerization of the central double bond is highly unlikely and cannot account for the observed isomer distribution. The depletion of *E*1-**110** upon irradiation can, however, be explained by the presence of a thermal ratcheting step, which will be discussed later in section 5.6.

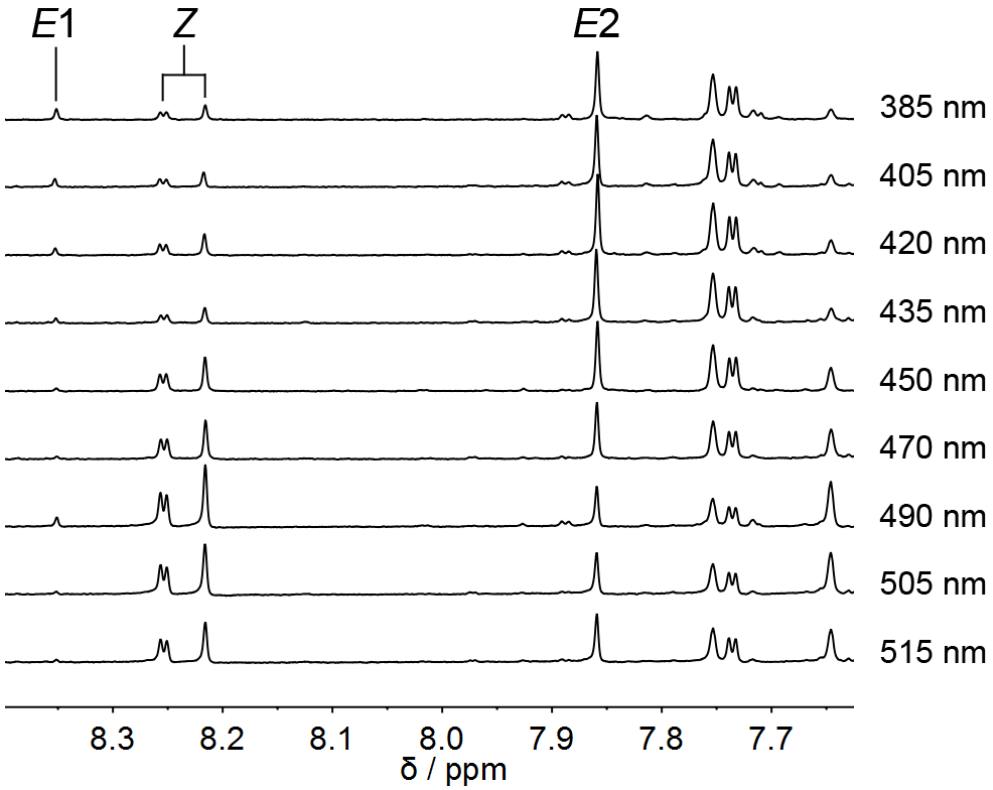

Figure 130 NMR irradiation of **110** (CD_2Cl_2, 400 MHz, 20 °C) using different wavelengths. Irradiation times were between 30 min and 35 min.

5.3.2 Structure of 110 in the crystalline state

NMR irradiation experiments revealed a total of three conformers that are stable at room temperature. This includes the new photoproduct *Z*-**110** that could be isolated by preparative HPLC. Crystals suitable for single crystal X-Ray analysis were obtained for all three conformers.

The structure of racemic *E*1-**110** in the crystalline state is shown in Figure 131. Only the *E*-(*R*)-(*M*)-(S_a) isomer is depicted for clarity. The HTI fragment reveals a helical structure with the indanone oxygen atom pointing to the same half space of the benzothiophenone stator as the sulfoxide oxygen atom. The triazole unit is almost perpendicular to the benzothiophenone fragment with a distance between the triazole proton and the carbonyl oxygen atom of 2.2 Å, suggesting intramolecular hydrogen bonding. The covalent linker is attached to the aryl follower with the phenolic oxygen pointing to the opposite half space of the benzothiophenone stator as the sulfoxide oxygen atom. This results in a geometry that was defined as *tensed* for the previous systems (see section 4.7.1).

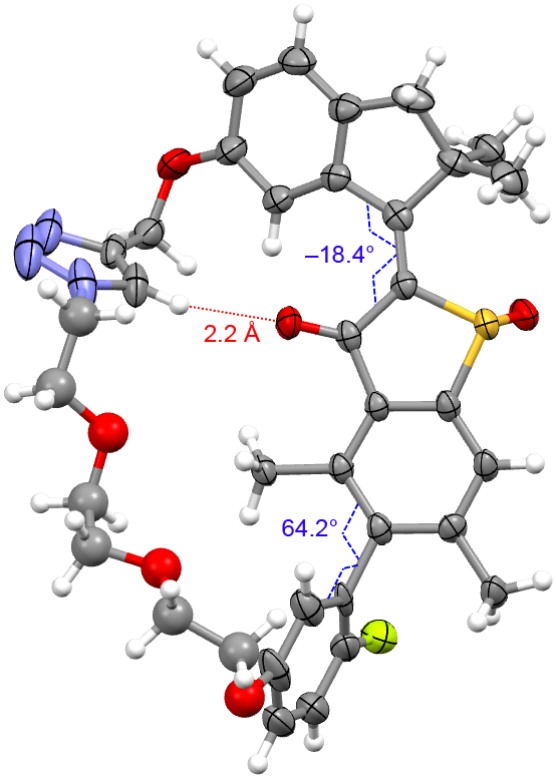

Figure 131 Structure of racemic *E*1-**110** in the crystalline state (50% probability ellipsoids). Only the *E*-(*R*)-(*M*)-(S_a) isomer is shown. The oxygen atom of the indanone rotor and the fluorine atom of the aryl unit point to the same half-space of the benzothiophenone stator as the sulfoxide oxygen atom. The covalent linker runs from one half-space of the benzothiophenone stator to the other resulting in a *tensed* structure.

The structure of racemic *Z*-**110** in the crystalline state is shown in Figure 132. Only the *Z*-(*R*)-(*P*)-(R_a) isomer is shown for clarity. The oxygen atoms of the indanone rotor and the aryl follower point to the same half-space of the benzothiophenone stator as the sulfoxide oxygen atom. The covalent linker is in a *relaxed* form, which is highlighted in Figure 132 on the right. The conformation of the HTI fragment corresponds to the elusive *Z*-(*R*)-(*P*)/*Z*-(*S*)-(*M*) isomer of the original motor system (see section 3.5). This is distinctly different to previous systems and demonstrates, that the helicity around the *Z* configured central double bond was most likely a result of the repulsive interactions between the sulfoxide oxygen atom and the alkoxy group at the 7-position of the indanone rotor. Due to the shifted attachment of the covalent linker to the 6-position in macrocycle **110**, the geometry of the HTI fragment is sterically less encumbered. As a result, helicity is controlled by other contributing factors i.e. the conformation of the biaryl unit that is transmitted via the covalent linker or crystal packing effects.

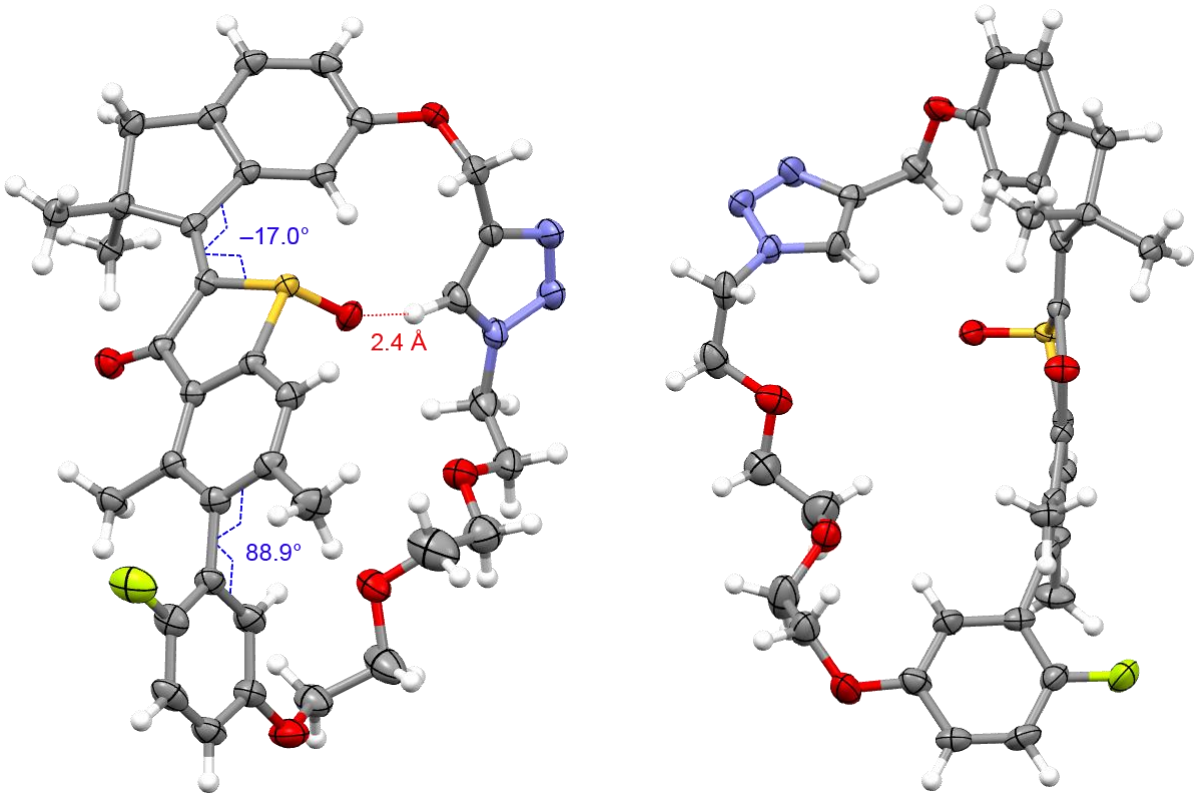

Figure 132 Structure of racemic *Z*-**110** in the crystalline state (50% probability ellipsoids). Only the *Z*-(*R*)-(*P*)-(R_a) isomer is shown. The oxygen atoms of the indanone rotor and the aryl follower point to the same half-space of the benzothiophenone stator as the sulfoxide oxygen atom.

The structure of racemic *E*2-**110** in the crystalline state is shown in Figure 133. Only the *E*-(*R*)-(*P*)-(R_a) isomer is shown for clarity. The HTI fragment reveals a helical structure with the indanone oxygen atom pointing to the opposite half space of the benzothiophenone stator as the sulfoxide oxygen atom. The covalent linker is attached to the aryl follower at the same half-space of the benzothiophenone fragment as the sulfoxide oxygen atom, resulting in a *tensed* state. Overall, the structure of *E*2-**110** strongly resembles *E*1-**110** with the exception of the differently configured sulfoxide. In other words *E*1-(*R*)-(*M*)-(S_a) is structurally analog to *E*2-(*S*)-(*M*)-(S_a) and *E*1-(*S*)-(*P*)-(R_a) analog to *E*2-(*R*)-(*P*)-(R_a). This shows that the sulfoxide stereocenter has a minor influence on the geometry of **110** in the crystalline state.

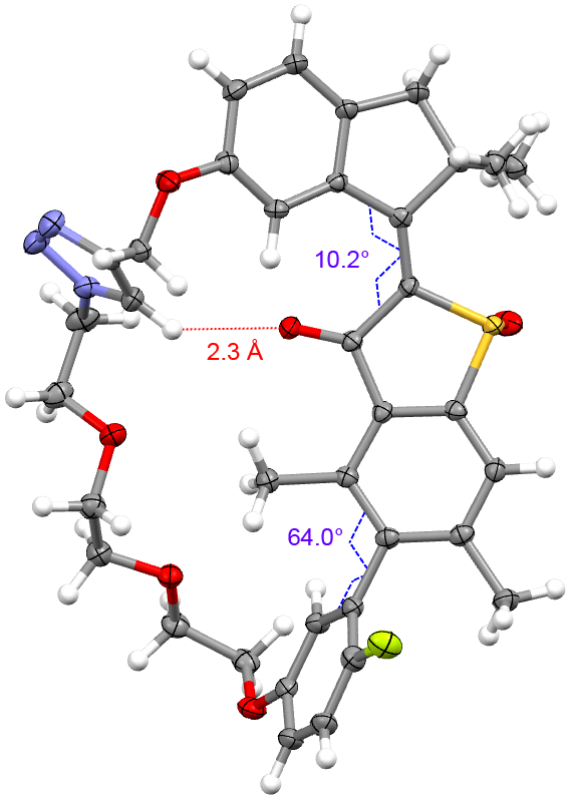

Figure 133 Structure of racemic *E*2-**110** in the crystalline state (50% probability ellipsoids). Only the *E*-(*R*)-(*P*)-(R_a) isomer is shown. The oxygen atom of the indanone rotor and the fluorine atom of the aryl unit point to the opposite half-space of the benzothiophenone stator as the sulfoxide oxygen atom.

Overall, helicity of the HTI fragment is weakly pronounced in structures of **110** in the crystalline state, indicating the successful implementation of an "unsubstituted" HTI rotor fragment that does not fit the classical behavior of the HTI based motor fragments. Very small activation energies can be expected for the thermal helix inversion steps in solution, presumably rendering them too fast to be observed by common spectroscopic methods even at low temperatures. Structures with *E* configuration of the central double bond incorporate *tensed* linkers that run from one side of the benzothiophenone stator to the other. In contrast, the *Z* configured isomer reveals a covalent linker that resides on one face of the benzothiophenone stator with a very short distance to the sulfoxide oxygen atom (Figure 132, right side), which suggests additional stabilization through intramolecular hydrogen bonding. This stands in stark contrast to the theoretical atropisomer of *Z*-**110** that cannot assume such a stabilizing conformation within a *relaxed* chain geometry and provides a first clue why only one *Z* configured isomer could be isolated to this point.

5.4 Behavior of 110 at elevated temperature

A solution containing all three isomers of **110** in $(CD_2Cl)_2$ was heated to 60 °C and ^{1}H NMR spectra were taken in 30 min intervals (Figure 134). Slow conversion of *Z*-**110** to both *E* configured isomers was observed. After 1 d at 60 °C, conversion of *Z*-**110** was complete resulting in a ratio of *E*1-**110** to *E*2-**110** of 1:4 (Figure 134, bottom spectrum). This isomer distribution did not change after two more days of heating to 60 °C.

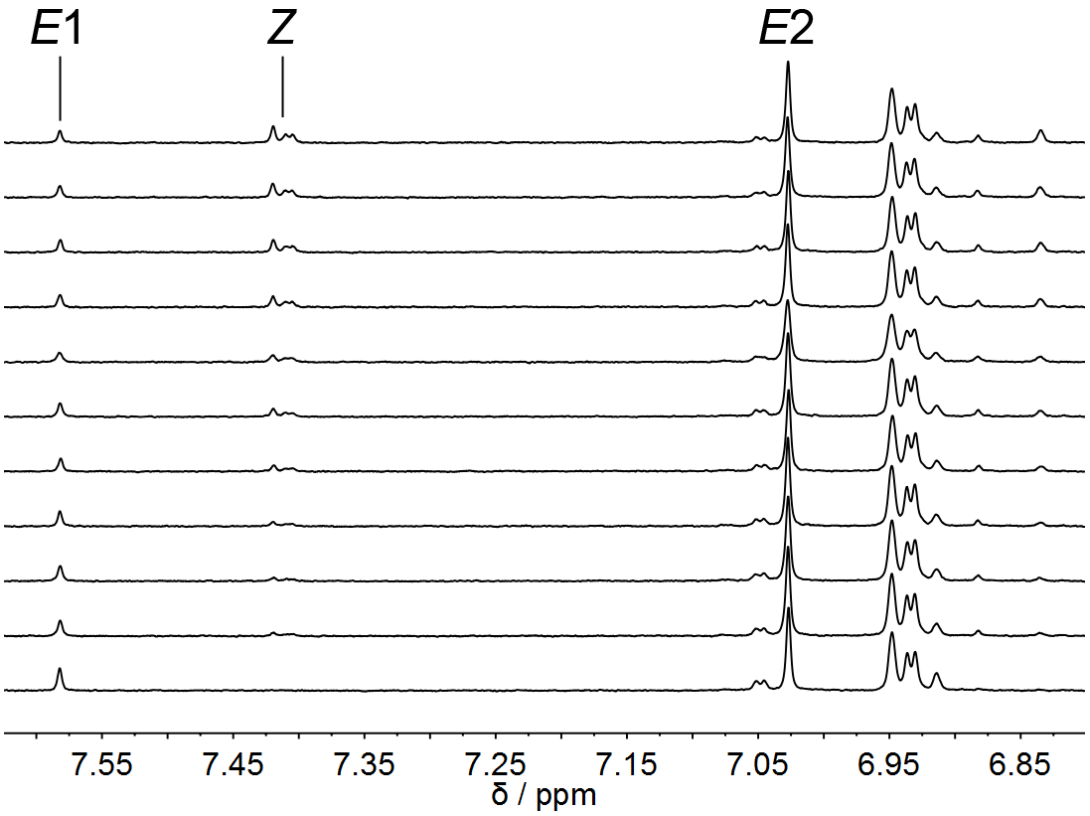

Figure 134 ^{1}H NMR spectra ($(CDCl_2)_2$, 400 MHz, 20 °C) acquired during the thermal conversion of *Z*-**110** to *E*1-**110** and *E*2-**110** at 60 °C. Indicative signals of the aromatic region of the *Z* and *E* isomers are highlighted. The spectra were taken in 30 min intervals and an additional spectrum (bottom) was measured after 1 d to obtain the isomer distribution at equilibrium.

Separate kinetic analyses were conducted for the thermal decay of *Z*-**110** assuming conversions solely to either *E*1-**110** or *E*2-**110**. A first-order kinetic rate-constant could be determined for the conversion of *Z*-**110** to *E*2-**110** (Figure 135). This process would translate to a Gibbs free energy of activation of $\Delta G^{\ddagger}$ = 25.7 kcal·mol^{-1}.

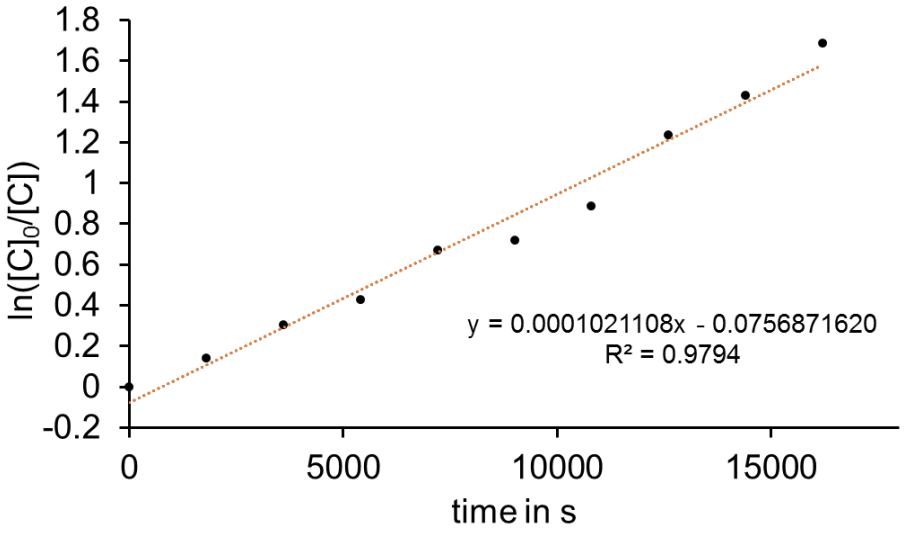

Figure 135 First-order kinetic analysis of the thermal *Z*-**110** to *E*2-**110** conversion (60 °C) gives a linear relationship. The formula of the linear fit is given in the diagram. The slope m = 0.0001021108 is used to calculate the rate constant $k(Z \rightarrow E2)$ according to (equation **4**.

First-order kinetic analysis of the *Z*-**110** to *E*1-**110** conversion does not result in a linear relationship (Figure 136). This could indicate a more complex isomerization mechanism that potentially involves the elusive atropisomer of *Z*-**110**.

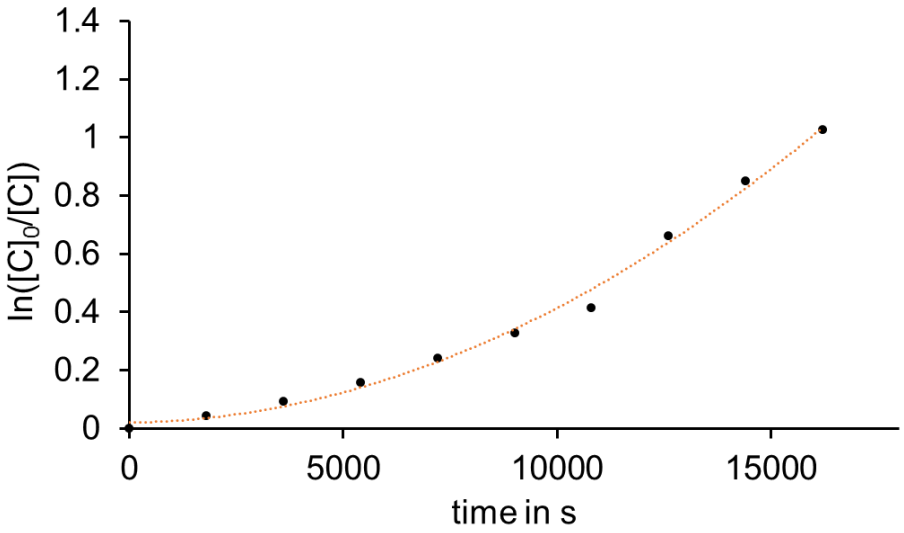

Figure 136 Kinetic analysis of the thermal *Z*-**110** to *E*1-**110** conversion (60 °C) does not give a linear relationship. A second degree polynomial fit is used to fit the data points.

When the solution containing *E*1-**110** (20%) and *E*2-**110** (80%) was heated to 100 °C a slow conversion of *E*2-**110** to *E*1-**110** was observed. Again, ^{1}H NMR spectra were taken in 30 min

intervals and another spectrum after an additional 16 h of heating to obtain the equilibrium composition that is 30% *E*1-**110** and 70% *E*2-**110** (Figure 137).

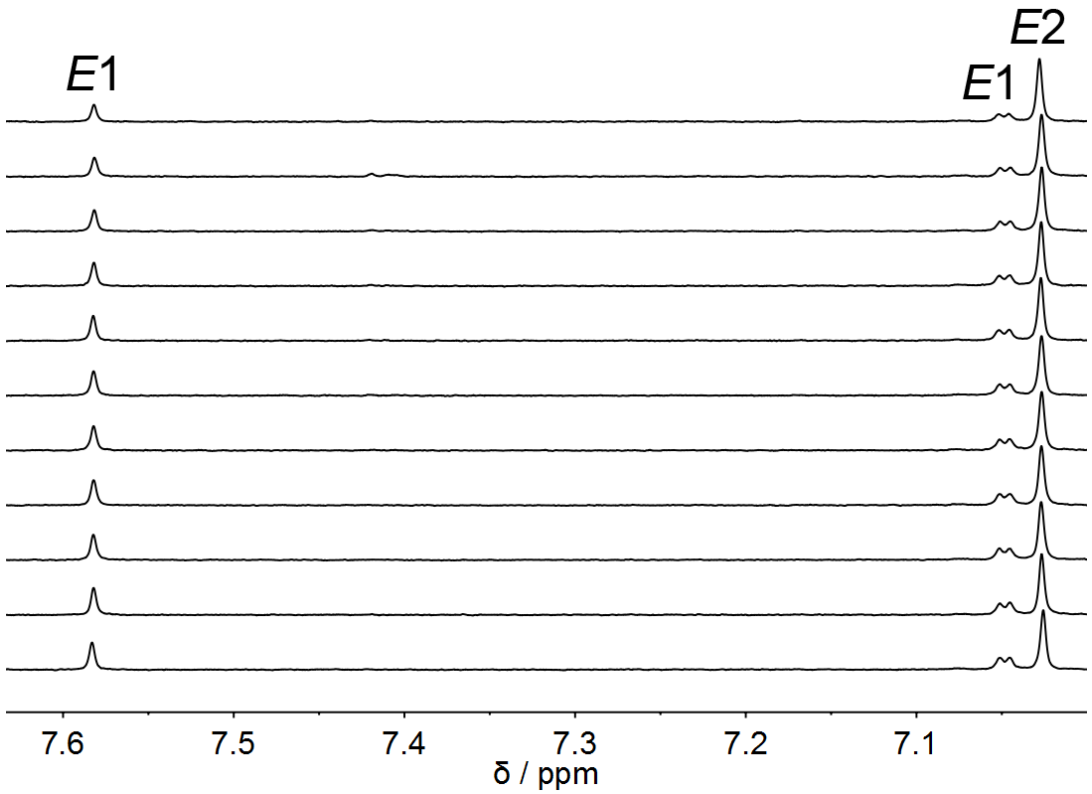

Figure 137 ^{1}H NMR spectra ($(CDCl_2)_2$, 400 MHz, 20 °C) acquired during the thermal conversion of *E*2-**110** to *E*1-**110** at 100 °C. Indicative signals of the aromatic region of the *E*1 and *E*2 isomers are highlighted. The spectra were taken in 30 min intervals and an additional spectrum (bottom) was measured after 16 h to obtain the isomer distribution at equilibrium.

A first order kinetic analysis revealed a Gibbs free energy of activation of $\Delta G^{\ddagger} = 29.5$ kcal·mol^{-1} for this process (Figure 138).

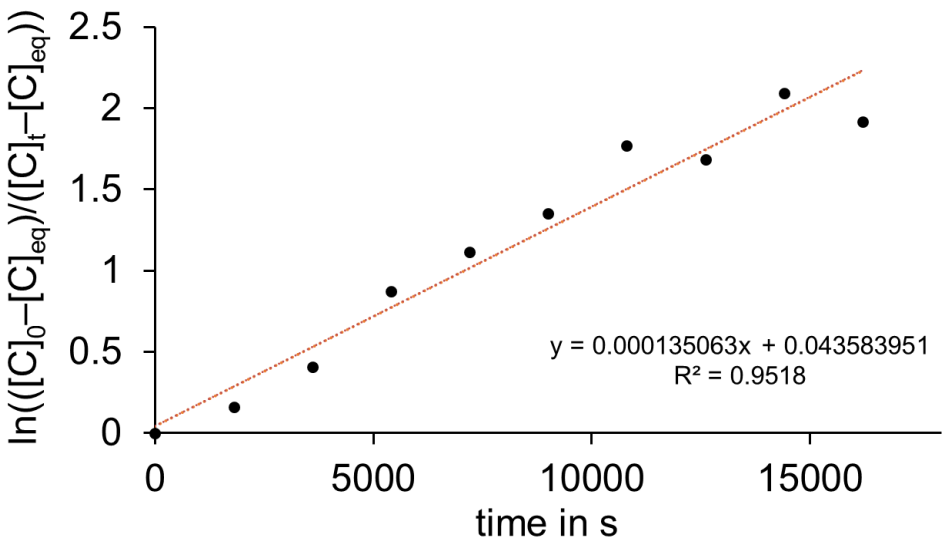

Figure 138 First-order kinetic analysis of the thermal *E*2-**110** to *E*1-**110** conversion (100 °C) gives a linear relationship. The formula of the linear fit is given in the diagram. The slope m = 0.000135063 is used to calculate the rate constant $k(E2 \rightarrow E1)$ according to (equation **4**.

From the available data it cannot be determined if this activation energy corresponds to the atropisomerization leading directly from *E*2-**110** to *E*1-**110** or if this is an equilibration process of the *E* isomers via the *Z* configured intermediates. In the latter case the 29.5 kcal·mol^{-1} would correspond to the energy of activation for the *E*2-**110** to *Z*-**110** isomerization (see also section 5.6, Figure 140).

5.5 Irradiation of 110 at low temperatures

To this point, experiments have shown that irradiation of *E*1-**110** at ambient temperatures results in an atropisomerization reaction affording the two products *Z*-**110** and *E*2-**110**. This also suggests that this isomerization process proceeds via a second *Z* configured conformer that is not stable at this temperature. It was therefore attempted to irradiate *E*1-**110** at lower temperatures in order to follow the underlying mechanism. To this end, a solution of *E*1-**110** in CD_2Cl_2 was cooled to –80 °C and an ^{1}H NMR spectrum was taken (Figure 139, top).

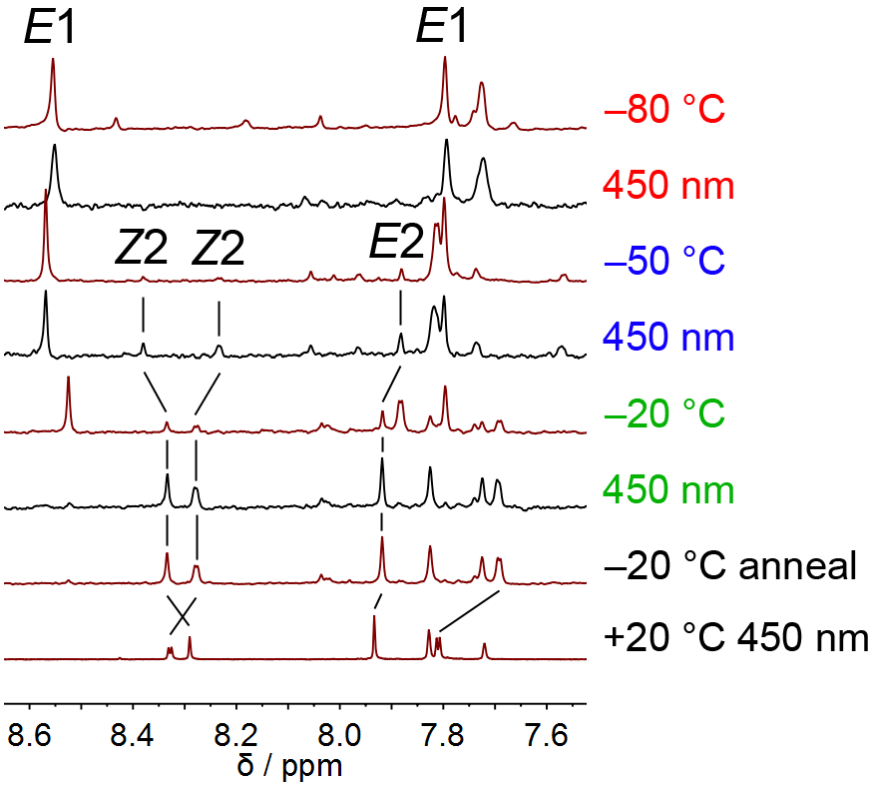

Figure 139 ^{1}H NMR spectra of **110** (CD_2Cl_2, 400 MHz) before and after irradiation with 450 nm light at different temperatures. Spectra of *E*1-**110** at –80 °C before and after irradiation (25 min) are basically identical (red). Spectra at –50 °C before and after irradiation (20 min) show traces of two new conformers (blue). At –20 °C photoconversion of *E*1-**110** to *Z*-**110** and *E*2-**110** is observed (16 min irradiation). Annealing of the sample at ambient temperatures does not result in thermal conversion of intermediates. An additional spectrum containing *Z*-**110** and *E*2-**110** (after irradiation of *E*1-**110** to the pss with 450 nm light) at 20 °C is shown for comparison.

The initial spectrum of *E*1-**110** reveals minor amounts of a second species that could not be identified. After 26 min of 450 nm irradiation at –80 °C, no new signals were observed and the solution was warmed to –50 °C. During another 20 min of 450 nm irradiation at this temperature, two new sets of signals emerged simultaneously that were attributed to the *Z*-**110** and *E*2-**110** conformers. The signals of *Z*-**110** and *E*2-**110** were shifted at –20 °C but intensities did not change, indicating that no thermal processes had occurred. At this point, photochemistry is analogous to irradiation at ambient temperatures and an almost full conversion of *E*1-**110** to *Z*-**110** and *E*2-**110** is observed. Annealing of the sample at 23 °C and cooling back to –20 °C also did not reveal any thermal conversion processes. Figure 139 shows an overview of the acquired spectra together with signal assignments and proposed chemical shifts of signals. No distinct traces of a second *Z* configured isomer were detectable throughout the experiment. Based on these results, the energy of activation for the hypothetical *Z*1-**110** to *Z*2-**110**

isomerization can be estimated to be below 13 kcal·mol^{-1}, under the assumption that the underlying kinetics are too fast to be observed on the NMR timescale at –50 °C. The required energy for the *Z*1-**110** to *Z*2-**110** isomerization could theoretically also be much higher in the case that *Z*2-**110** is not populated starting from either *E* isomer.

5.6 Discussion

Initial theoretical calculations showed an energy of activation for the atropisomerization process of a 1,1-dimethyl-1'-fluoro substituted biaryl of 28 kcal·mol^{-1}. As discussed earlier, macrocycles with a *Z* configuration of the central double bond possess a stronger intramolecular strain compared to the *E* isomeric forms. The pronounced steric hindrance around the biaryl axis, especially in comparison to the preceding dimethyl system **95** ($\Delta G^{\ddagger}(\mathbf{A_T} \rightarrow \mathbf{A_R})$ = 19.3 kcal·mol^{-1} at 0 °C), suggests that atropisomerization does not occur in the *E* configured form of machine **110** at ambient temperatures. The increased strain in the *Z* isomeric form has shown to lower atropisomerization barriers by up to 6.0 kcal·mol^{-1}. The shifted attachment of the covalent linker at the indanone rotor part in macrocycle **110** can potentially increase this even further. As a result, atropisomerization is expected to occur orders of magnitude faster between *Z* configured isomers of **110** compared to the *E* isomers. This simultaneously suggests that irradiation of *E*1-**110** to *Z*-**110**/*E*2-**110** proceeds unidirectionally via the elusive second *Z* configured isomer. Attempts at low temperature irradiation experiments could not reveal the full isomerization process. As a result, the energy of activation for the atropisomerization of the *Z*-**110** isomers lies below 13 kcal·mol^{-1}. Compared to the energy of activation for the *E*2-**110** to *E*1-**110** atropisomerization, which amounts to at least 28 kcal·mol^{-1}, this is a reduction by ≥15 kcal·mol^{-1}. This is expected to be the result of an increased ground state energy of *Z*-**110** and a stabilization of the transition state analogous to system **95**.

Close inspection of the NMR irradiation experiments at ambient temperatures revealed small amounts of *E*1-**110** in the pss that can now be explained by a second photoisomerization process between *E*1-**110** and the elusive *Z* configured isomer. This is accomplished by minor amounts of the latter being in a dynamic equilibrium with observable *Z*-**110** in solution. This is further supported by the thermal conversion of *Z*-**110** to *E*1-**110** at elevated temperatures that cannot be described by first-order kinetics. The reaction pathway of the thermal *E*2-**110** to *E*1-**110** atropisomerization cannot be elucidated for this system as thermal *Z* to *E* isomerization lies in

a similar energy range. It can, however, be expected that a lower energy of activation for the biaryl rotation would result in a unidirectional 360° rotation in an analogous system.

Overall, the proposed mechanism constitutes a reversed rotation direction compared to previous systems. This is most likely the result of the missing thermal helix inversion steps in combination with the highly stabilized conformation of the *Z*-**110** conformer compared to its (hypothetical) *Z* configured atropisomer. Together with the drastically lowered activation energy for the biaryl rotation in the *Z* configured isomers, the almost quantitative conversion of "Z1-**110**" to "Z2-**110**" constitutes the key step in the working mechanism of molecular machine **110**. An energy scheme of the proposed mechanism is given in Figure 140.

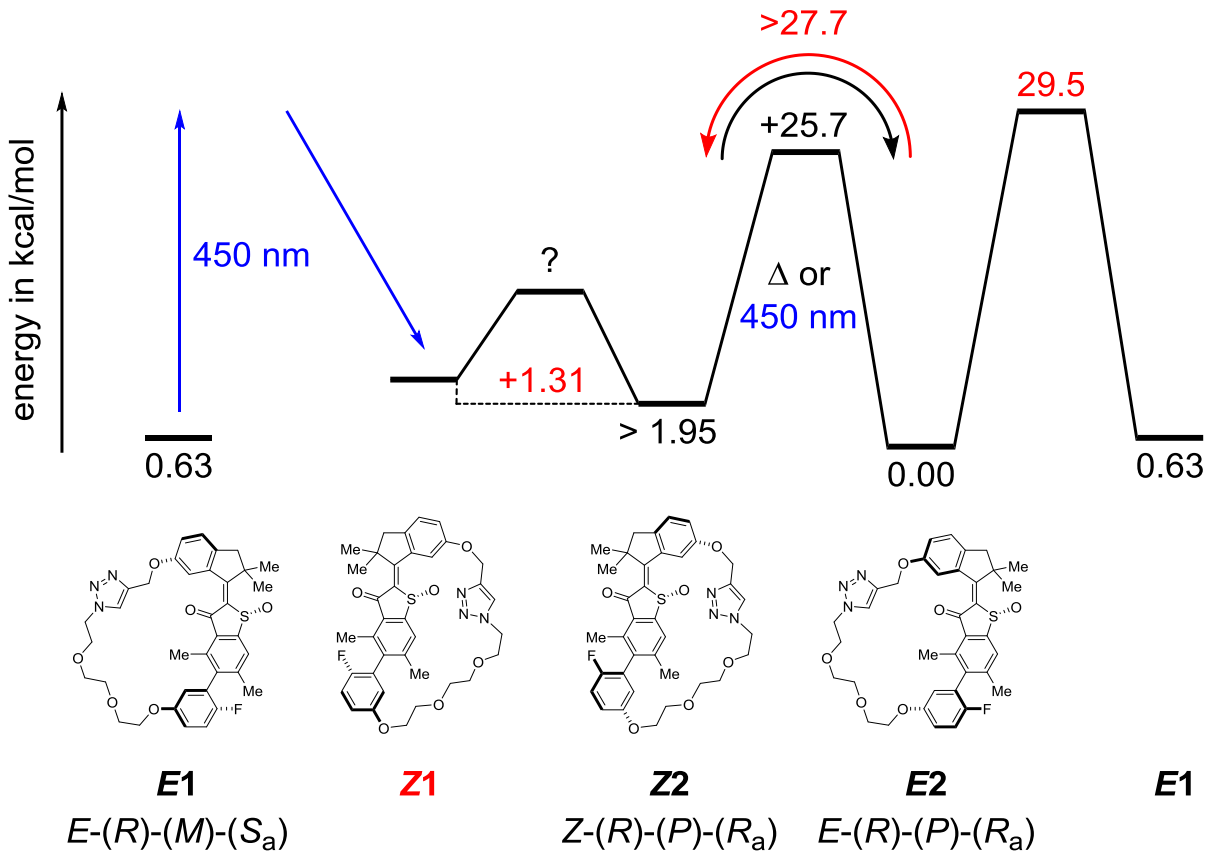

Figure 140 Qualitative ground state energy profile of machine **110**. Values are taken from experiments conducted at different temperatures. Four states are populated during one full unidirectional 360 °C rotation. Only isomers with *R* configured sulfoxide are depicted. The ground state energy of *Z*1 (ΔG(*Z*1 – *Z*2) = 1.31 kcal·mol^{-1}, value in red) is established from the conservative assumption that 5% signal intensity is not detectable by ^{1}H NMR at –50 °C. The energy of activation $\Delta G^{\ddagger}$ = 29.5 kcal·mol^{-1} could not be unambiguously assigned to either *E*2 to *E*1 atropisomerization or *E*2 to *Z*2 double bond isomerization.

To this point, *Z*1-**110** could not be accessed directly in an experimental setup and different working mechanisms have to be taken into consideration. The structure of *E*1-**110** in the crystalline state reveals an *E*-(*S*)-(*P*)/*E*-(*R*)-(*M*) conformation of the HTI fragment. In the previous systems this was the result of the thermal ratcheting step that did not allow for a "backwards" rotation around the central double bond, i.e. breaking microscopic reversibility. If this is still the case in the present system, irradiation of *E*1-**110** must lead directly to *E*2-**110** via biaryl single-bond rotation. The resulting working mechanism would also explain the missing *Z*1-**110** intermediate that now cannot be generated directly through irradiation of *E*1-**110**. However, given the reduced steric demand around the central double bond and the *tensed* geometry of *E* configured structures in the crystalline state, it is highly unlikely that states with reversed helicities are not populated at ambient temperatures. In addition, the mechanism cannot account for the almost full depletion of *E*1-**110** during irradiation.

As irradiation of *E*1-**110** results in the simultaneous formation of *Z*2-**110**/*E*2-**110**, crucial information regarding the directionality is missing. This, in combination with the elusive *Z*1-**110** isomer, prevents full elucidation of individual steps and additional experiments or the synthesis of more sophisticated systems has to be taken into consideration in order to reveal the detailed working mechanism of the system.

6 Integration of an HTI motor fragment into macrocycles of different sizes

6.1 Overview

A few macrocyclic systems with integrated HTI fragments have been established so far and minor variations of the substitution patterns at the rotor, stator and aryl follower fragments resulted in intriguing new functional molecules. However, the impact of the ring size has not been elucidated to this point. Reduction of the length of the PEG linker is naturally limited by the ring closing reaction that can introduce a finite amount of strain while expansion of the system has almost no theoretical limitations.

Reduction of the ring size can have several effects on the system. Overall an increase in macrocyclic strain results in more confined geometries and therefore reduced conformational freedom. This impacts the energy landscape of the motor fragment performing the work and significantly lowers the energy of activation of the biaryl rotation which was observed consistently throughout all preceding systems. For example it was demonstrated, that macrocycles with a *Z* configured HTI fragment experience an increased intramolecular strain compared to their *E* isomeric counterparts. However, increasing the intramolecular strain even further could eventually prevent isomerization of the HTI double bond preventing any constructive photochemistry.

An increase of the ring size will eventually reduce the intramolecular strain. A reduced strain of the covalent linker in particular will result in the rotor and follower fragment to move more independently to the point where the rotation is not transmitted anymore and a slipping motion is observed (Figure 141). The energy landscapes of the HTI fragment as well as the biaryl unit can be expected to increasingly resemble those of the isolated fragments.

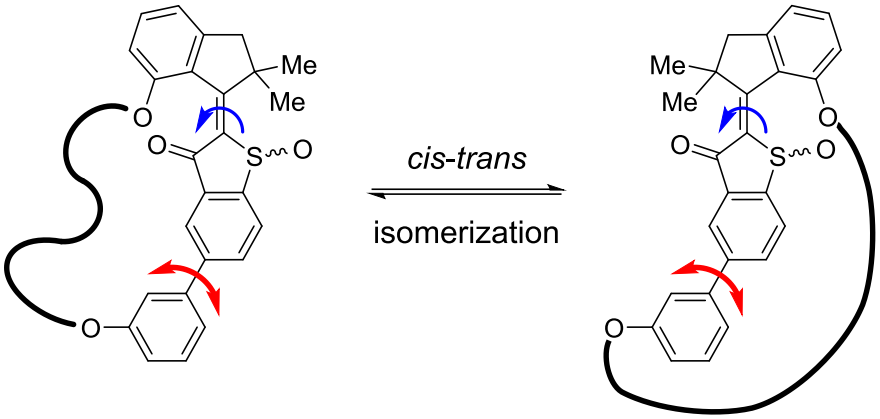

Figure 141 Schematic representation of the slipping motion at increased macrocyclic ring sizes. Rotation of the indanone rotor is not transmitted to the aryl follower by the covalent linker and can occur while the biaryl unit retains its geometry. As a result biaryl rotation can occur in both directions (red arrow). Conversely, rotation of the aryl follower can occur freely while the HTI fragment retains its geometry (not depicted).

Increasing the length of the PEG tether also opens up the possibility to bind cations in a crown ether type fashion, which will be discussed later (see section 6.3.3).

6.2 HTI 115

6.2.1 Synthesis

A straightforward approach that reduces the length of the covalent linker is accomplished by removing one ethylene glycol unit of the PEG tether (triethylene glycol to diethylene glycol). This also reduces the number of required synthetic steps as the brominated diethylene glycol is commercially available. The synthesis followed the established protocol and proceeded analogously to the synthesis of previous systems. Synthesis of the new building block **112** started with the substitution of 2-bromoethyl ether with one equivalent of azide in moderate yields (Scheme 45). The bifunctionalized PEG fragment **111** was then reacted with 3-hydroxyphenylboronic acid pinacol ester, which gave **112** in very good yields.

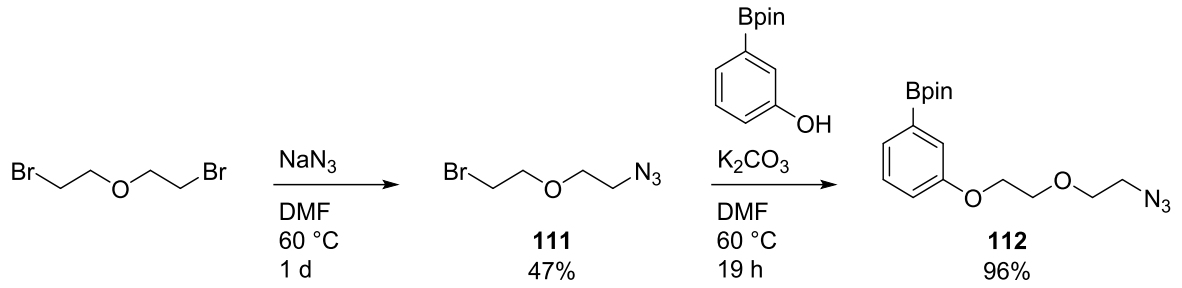

Scheme 45 Synthesis of building block **112**. Substitution of 2-bromoethyl ether with sodium azide gave **111** in 47% yield. Subsequent reaction with 3-hydroxyphenylboronic acid pinacol ester gave **112** in 96% yield.

HTI fragment **75** that was used in the next step had already been established in an earlier synthesis. Copper catalyzed 1,3-dipolar cycloaddition with compound **112** furnished triazol **113** in 87% yield (Scheme 46).

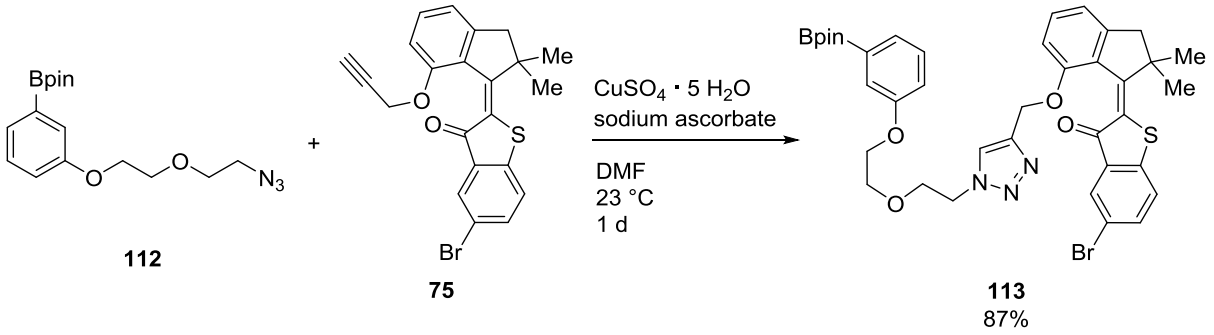

Scheme 46 Copper catalyzed 1,3-dipolar cycloaddition of boronic acid pinacol ester **112** and HTI **75**. $CuSO_4 \cdot 5H_2O$ (2 mol%) and sodium ascorbate (10 mol%) were used to generate the catalytically active Cu(I) species *in situ*. The product **113** was obtained in good yields as a mixture of *E* and *Z* configured isomers. Only the *E* configured isomers are shown.

The following intramolecular *Suzuki-Miyaura* cross-coupling reaction gave macrocycle **114** in 56% yield (Scheme 47). This is surprising as the reaction furnished a maximum yield of 34% when it was employed in the synthesis of previous systems. In addition, the ring strain that is established in this key step is expected to be significantly higher compared to macrocyclic compounds with increased ring sizes. A possible explanation is the closer proximity of the reactive sites within the present system due to the shorter tether, which consequently reduces unwanted polymerization.

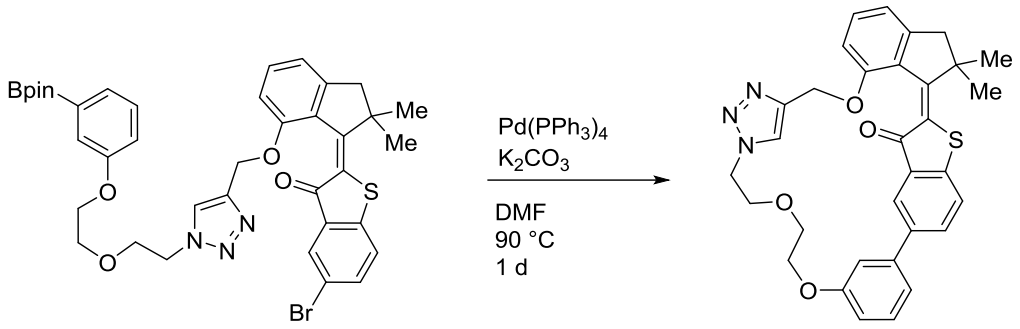

113 **114** 56%

Scheme 47 Intramolecular *Suzuki-Miyaura* cross-coupling of **113**. The product **114** was obtained in 56% yield. Only the *E* configured isomers are shown.

Oxidation with sodium perborate completed the synthesis of target compound **115** (Scheme 48). The product was obtained in moderate yields purely in its *E* isomeric form.

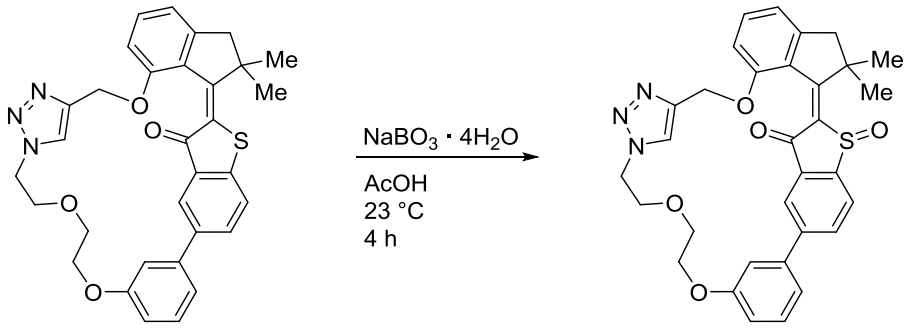

114 **115** 56%

Scheme 48 Oxidation of **114** to the sulfoxide **115** using sodium perborate tetrahydrate in acetic acid. The target molecule was obtained exclusively with *E* configuration of the central double bond. Only the *E* configured isomers are shown.

6.2.2 Structural analysis of *E*-115

Macrocycle *E*-**115** readily crystallized from a racemic EtOAc solution which was slowly evaporated at ambient conditions. In this way crystals suitable for single crystal X-ray diffraction were obtained that contained one equivalent of the solvent in the unit cell. The *E*-(*R*)-(*M*)-(S_a) isomer is shown in Figure 142. The indanone oxygen atom and the aryl follower oxygen atom point to the same half-space of the benzothiophenone stator as the sulfoxide oxygen. The biaryl unit reveals a pronounced tilt toward the carbonyl side of the

benzothiophenone stator with a torsion of 34°. This is in agreement with previous results where the tilt of the biaryl axis is determined by the helicity around the central double bond. The distance between the indanone rotor oxygen atom and the aryl follower oxygen atom is 7.97 Å and is almost identical to the distance of 8.07 Å found in the analogous system **81** with a triethylene glycol tether. This indicates that the shorter covalent linker does not impose significantly increased strain on the rigid backbone of the molecule in the case of an *E* configured central double bond.

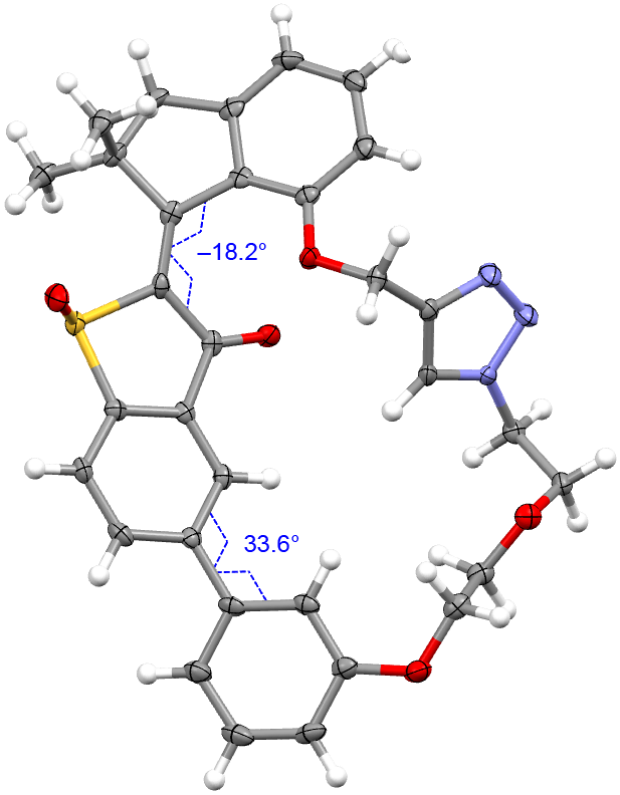

Figure 142 Structure of racemic *E*-**115** in the crystalline state (50% probability ellipsoids). Only the *E*-(*R*)-(*M*)-(S_a) isomer is shown. The co-crystallized solvent is omitted for clarity. The oxygen atom of the indanone rotor and aryl follower point to the same half-space of the benzothiophenone stator as the sulfoxide oxygen atom. The biphenyl tilt reflects the geometry around the central double bond.

At ambient temperatures *E*-**115** is the only stable conformer found in solution. NOESY NMR experiments were conducted to obtain additional structural information (Figure 143). A weak cross signal between proton 14 and proton 29 confirms *E* configuration of the central double bond that was already found in the solid state. Cross signals between proton 14 and proton 24 as well as between proton 16 and proton 20 reveal a pronounced tilt of the biaryl axis with the phenolic oxygen pointing toward the carbonyl side of the benzothiophenone stator. No additional cross signals between the PEG tether and the benzothiophenone stator were visible.

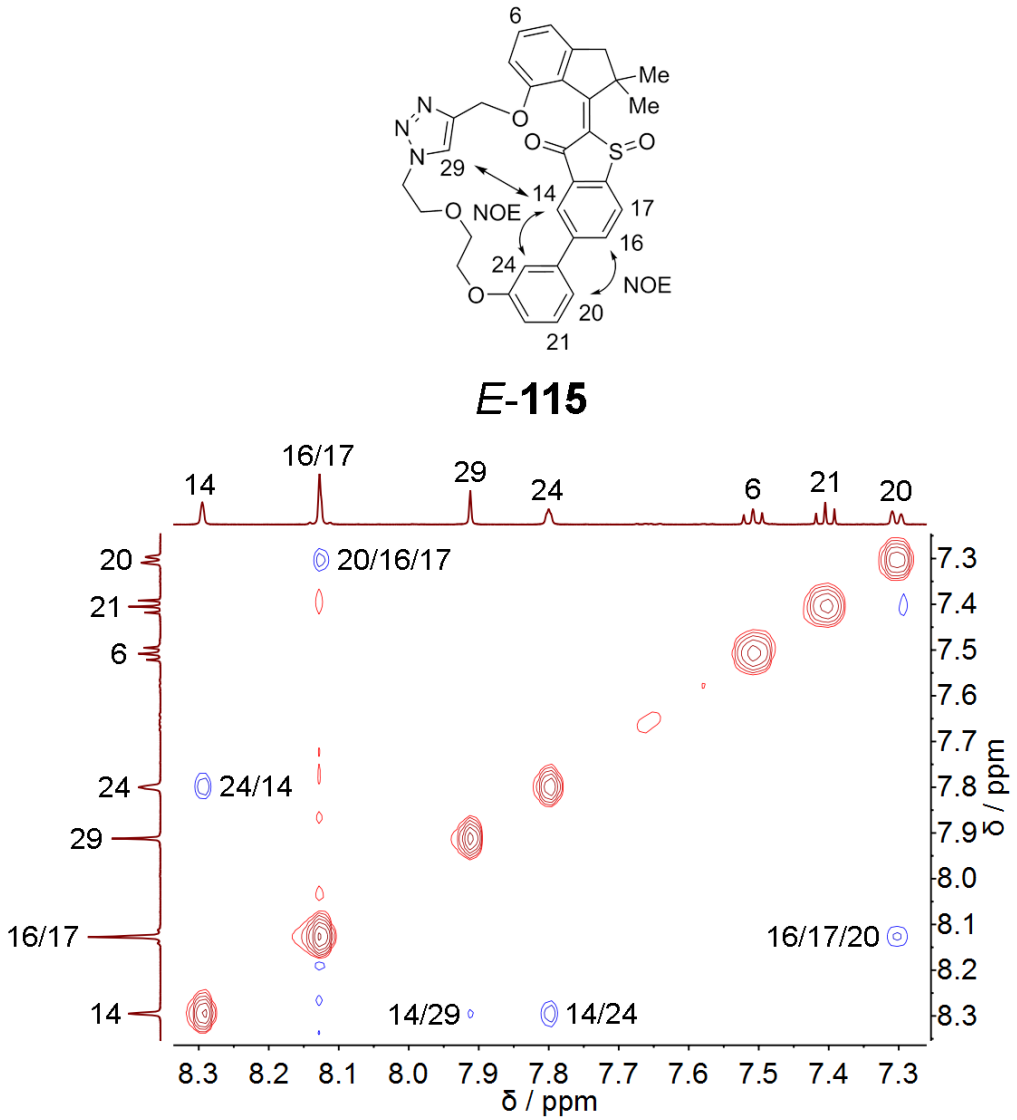

Figure 143 NOESY NMR spectrum of *E*-**115** (CD_2Cl_2, 599 MHz, 27 °C). Indicative signals are highlighted. The cross signal between proton 14 and proton 24 as well as between proton 16 and proton 20 reveals a pronounced tilt of the biaryl axis toward the carbonyl side of the benzothiophenone stator. A weak cross signal between proton 14 and proton 29 confirms *E* configuration of the central double bond.

6.2.3 UV-Vis irradiation experiments at ambient temperatures

The photochemical properties of HTI **115** were scrutinized in solution. Similar to previous compounds irradiation was first conducted in CH_2Cl_2. Macrocyclic HTI *E*-**115** was irradiated repeatedly for five minutes using light with wavelengths from 365 nm to 530 nm, the resulting spectra are shown in Figure 144. Surprisingly no constructive photochemistry was observed, which stands in stark contrast to previous systems.

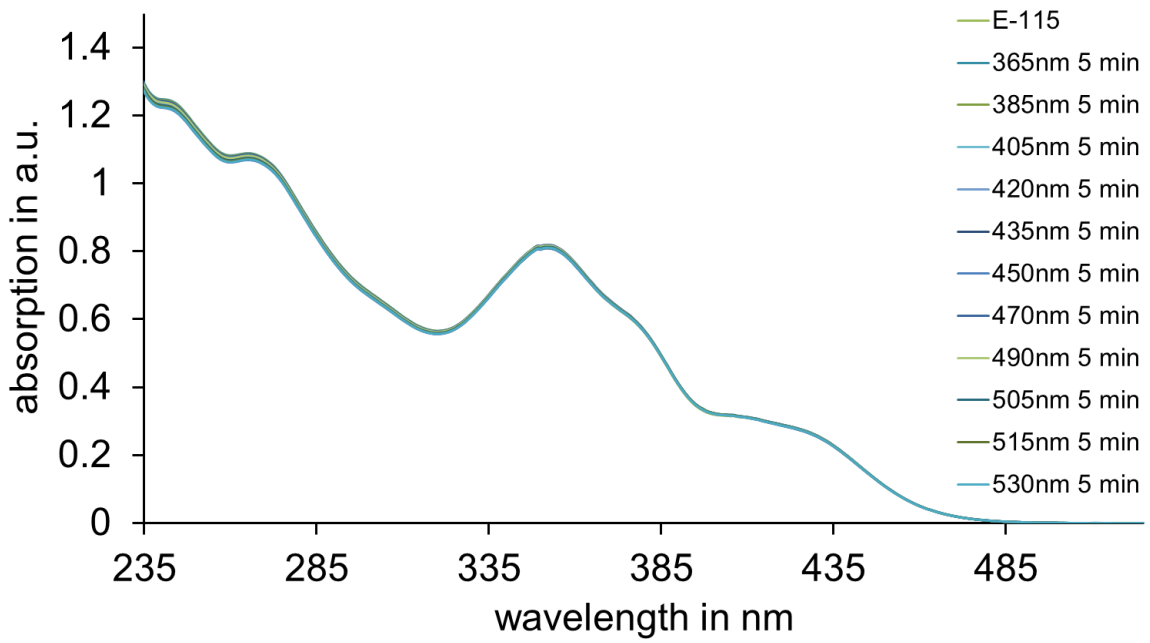

Figure 144 UV-Vis absorption spectra of **115** in CH_2Cl_2 at 23 °C. The individual spectra were taken after 5 min irradiation with the respective wavelengths.

To further elucidate on this behavior, irradiation was repeated in different solvents. When a solution of *E*-**115** in MeOH was irradiated with 450 nm light a slow loss of absorption intensity is observed (Figure 145). Similar to irradiation in CH_2Cl_2, no isomerization processes were visible through the occurrence of isosbestic points. The overall shape of the spectrum did not change either.

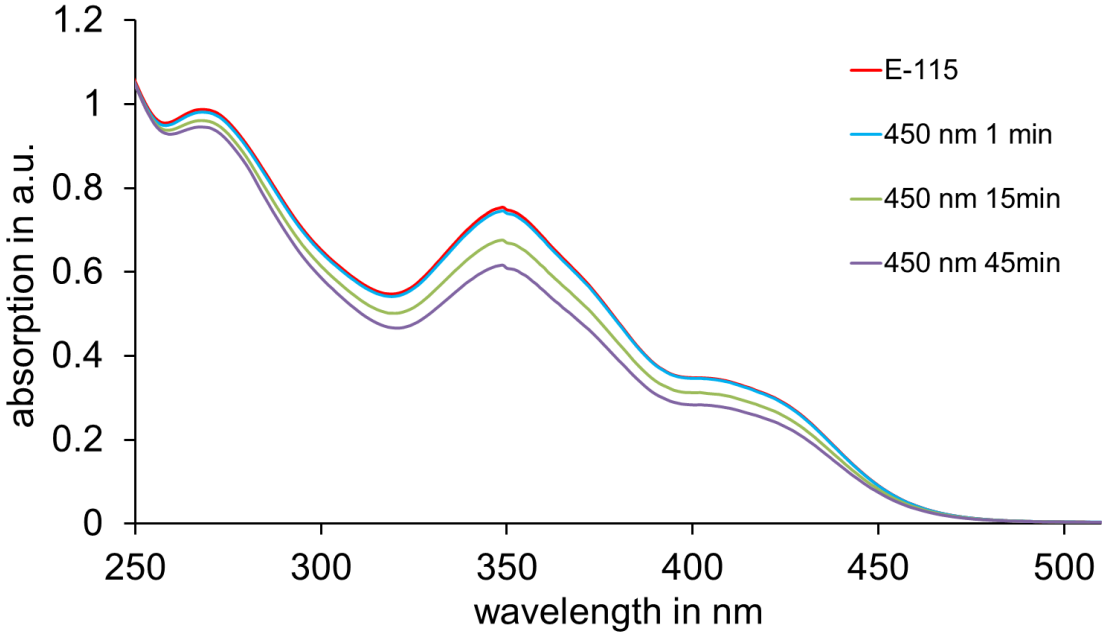

Figure 145 UV-Vis absorption spectra of **115** in MeOH at 23 °C. Irradiation with 450 nm light resulted in a slow decrease of absorption intensity.

Irradiation of *E*-**115** in toluene showed a slower decrease of absorption intensities compared to irradiation in methanol (Figure 146). The spectra revealed an isomerization process and the presence of isosbestic points was suggested (Figure 146, red arrows) but evaluation was hampered by the underlying loss of absorption intensity.

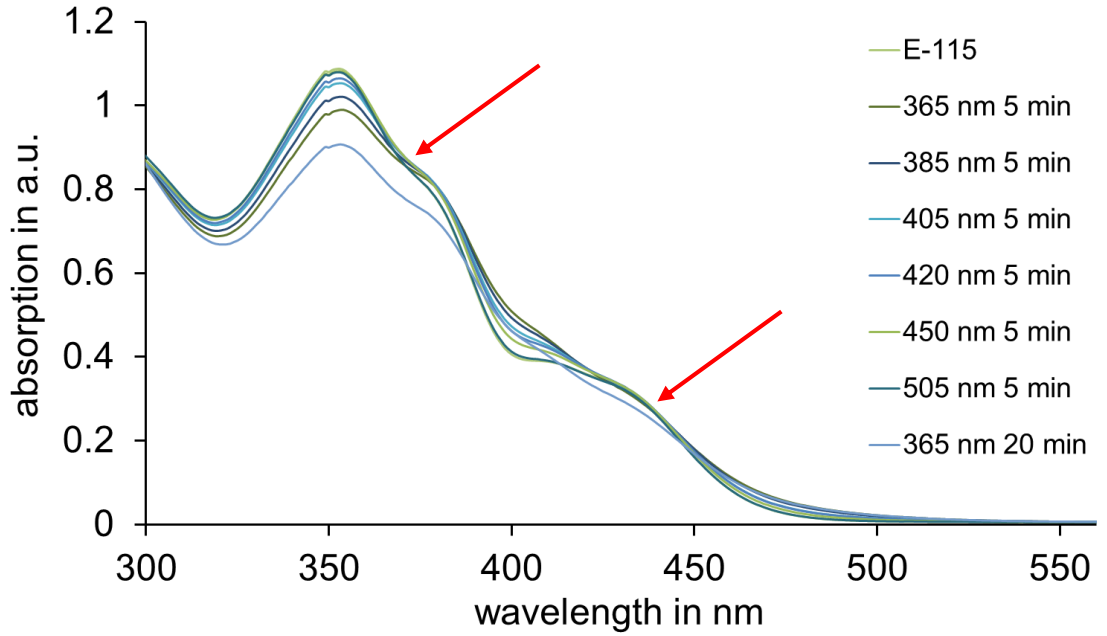

Figure 146 UV-Vis absorption spectra of **115** in toluene at 23 °C. After 5 min irradiation using different wavelengths isomerization was observed accompanied by a constant loss in absorption intensity. The decreasing absorption is highlighted by an additional spectrum taken after 20 min of 365 nm irradiation (light blue).

Taken together the experiments revealed an unprecedented irradiation behavior. No constructive photochemistry was observed in CH_2Cl_2. A decrease of absorption intensities was observed when *E*-**115** was irradiated in methanol or toluene. This can be attributed either to decomposition or precipitation of the photoproducts. The latter is supported by the retained qualitative shape of the spectra when *E*-**115** is irradiated in methanol as well as the spectra taken in CH_2Cl_2 that did not reveal any signs of photofatigue. However, no precipitation was visible to the naked eye and the underlying process cannot be concluded decisively from these experiments.

6.2.4 NMR irradiation experiments at ambient and low temperatures

Next, ^{1}H NMR irradiation experiments were conducted. Based on the results obtained from the UV-Vis experiments a solution of *E*-**115** in toluene-d_8 was irradiated with 365 nm light for prolonged times (Figure 147). Up to 20% of a new isomer were accumulated after 15 min of irradiation. The new set of signals was attributed to a *Z*-**115** conformer but the identity could not be confirmed experimentally. After 40 min the solution was again almost depleted of *Z*-**115** and precipitation of significant amounts of a pale yellow solid was observed in the NMR tube. After 120 min of 365 nm irradiation only signals of *E*-**115** were visible (Figure 147, bottom spectrum).

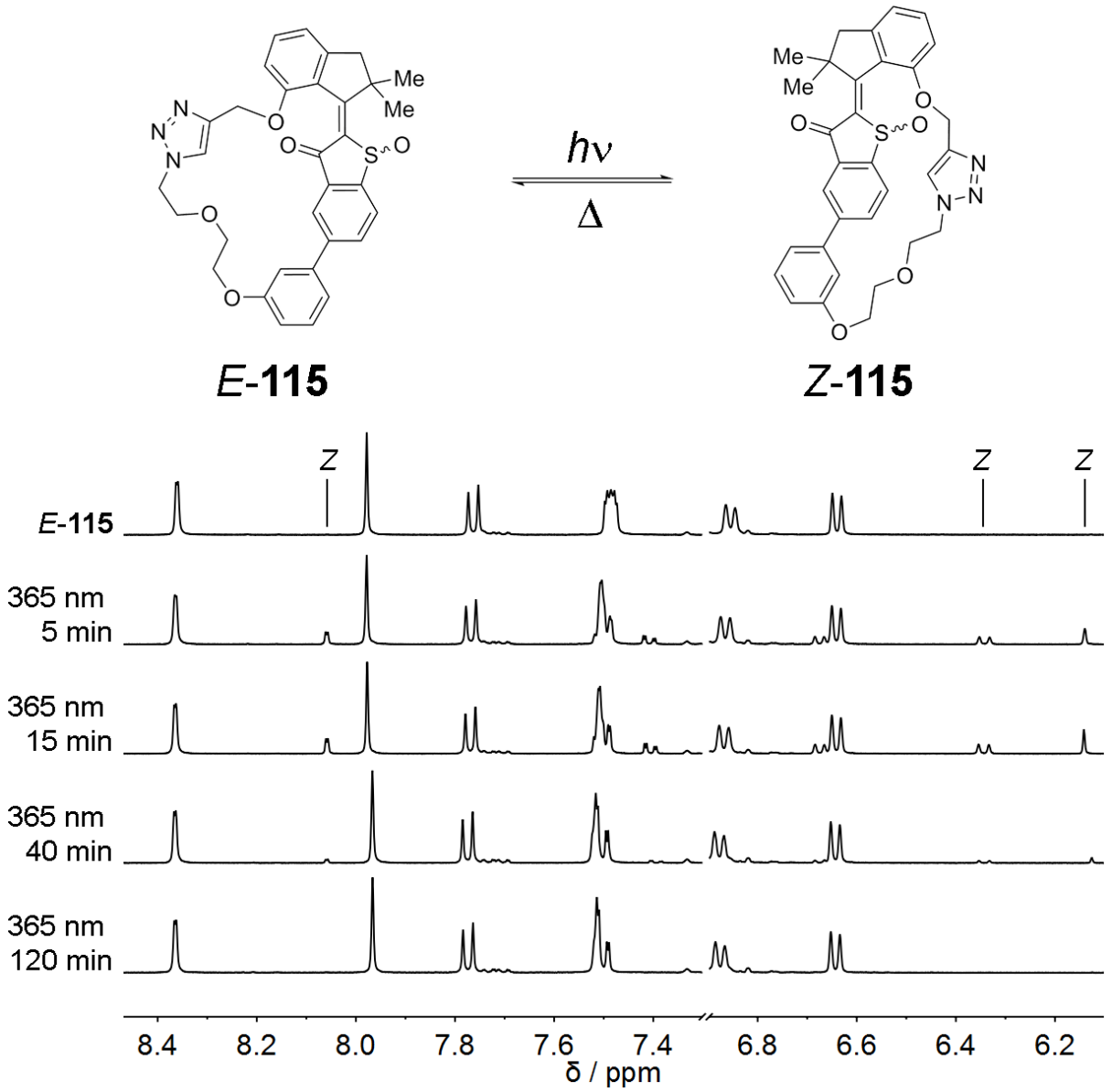

Figure 147 ^{1}H NMR spectra of *E*-**115** (400 MHz, toluene-d_8, 22 °C) acquired during irradiation with 365 nm light. The solvent signals are cut out for clarity. After 15 min a maximum of 20% *Z*-**115** were accumulated before precipitation lead to a decrease of the concentration. After 120 min of 365 nm irradiation precipitation occured very fast and the spectrum was completely depleted of *Z*-**115**.

From these observation it can be derived that precipitation occurs only after the concentration of *Z*-**115** exceeds a threshold concentration. The solids then act as crystallization seeds facilitating precipitation to the point where it is completed before an NMR spectrum is measured. This is also in agreement with the analogous UV-Vis experiment that showed initial photoisomerization followed by a decrease in absorption intensity (see Figure 146).

When an NMR tube with accumulated precipitate was kept in the dark at ambient temperatures for several minutes a homogenous solution was obtained again containing only the *E*-**115** isomer as judged by ^{1}H NMR. This indicates a low thermal stability of the *Z*-**115** isomer that isomerizes back to *E*-**115** before it is dissolved again.

In another experiment an NMR tube containing the precipitate was cooled to 0 °C and excess solution was removed. Then ice cold CD_2Cl_2 was added and a ^{1}H NMR spectrum of the solution was measured immediately revealing again only signals of the *E*-**115** isomer therefore confirming the very low thermal stability of *Z*-**115** in solution.

When a solution of *E*-**115** in CD_2Cl_2 or MeOD was irradiated with light of different wavelengths for prolonged times no isomerization or precipitation was observed (not depicted). Irradiating a solution of *E*-**115** in benzene-d_6 gave 12% *Z*-**115** after 20 min before precipitation started and the solution was again depleted of *Z*-**115** (Figure 148).

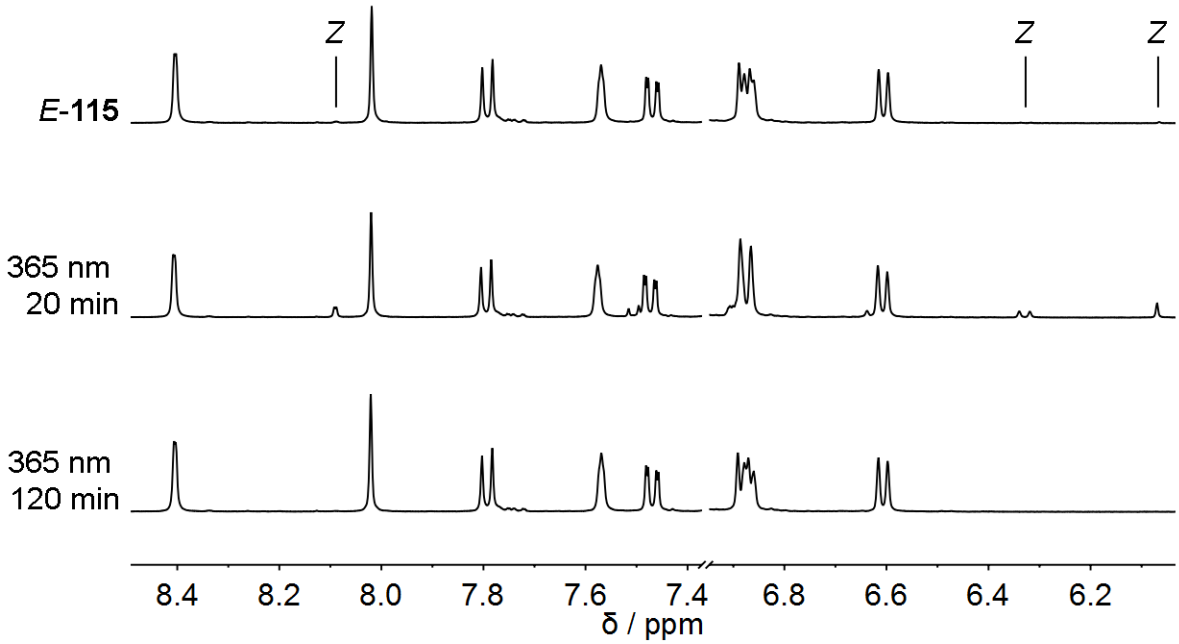

Figure 148 ^{1}H NMR spectra of *E*-**115** (400 MHz, benzene-d_6, 22 °C) acquired during irradiation with 365 nm light. The solvent signal is cut out for clarity. After 12 min 12% *Z*-**115** were accumulated before precipitation lead to a decrease of *Z*-**115** concentration. After 120 min of 365 nm irradiation precipitation occured very fast and the spectrum was completely depleted of *Z*-**115**.

Due to the low thermal stability of the *Z*-**115** isomer, irradiation at low temperatures was the next logical step. So far no isomerization has been observed when a solution of *E*-**115** in CD_2Cl_2 was irradiated. This was attributed to the very low thermal stability of *Z*-**115** in solution and

irradiations were conducted at lower temperatures ranging from –20 °C to –80 °C (Figure 149, left). Throughout the experiment no additional signals emerged that could be attributed to the *Z*-**115** isomer and individual spectra were identical to the spectra taken before irradiation. At –80 °C additional metastable intermediates were observed for analogous structures containing a HTI motor fragment but no such intermediates were detectable for **115** in CD_2Cl_2.

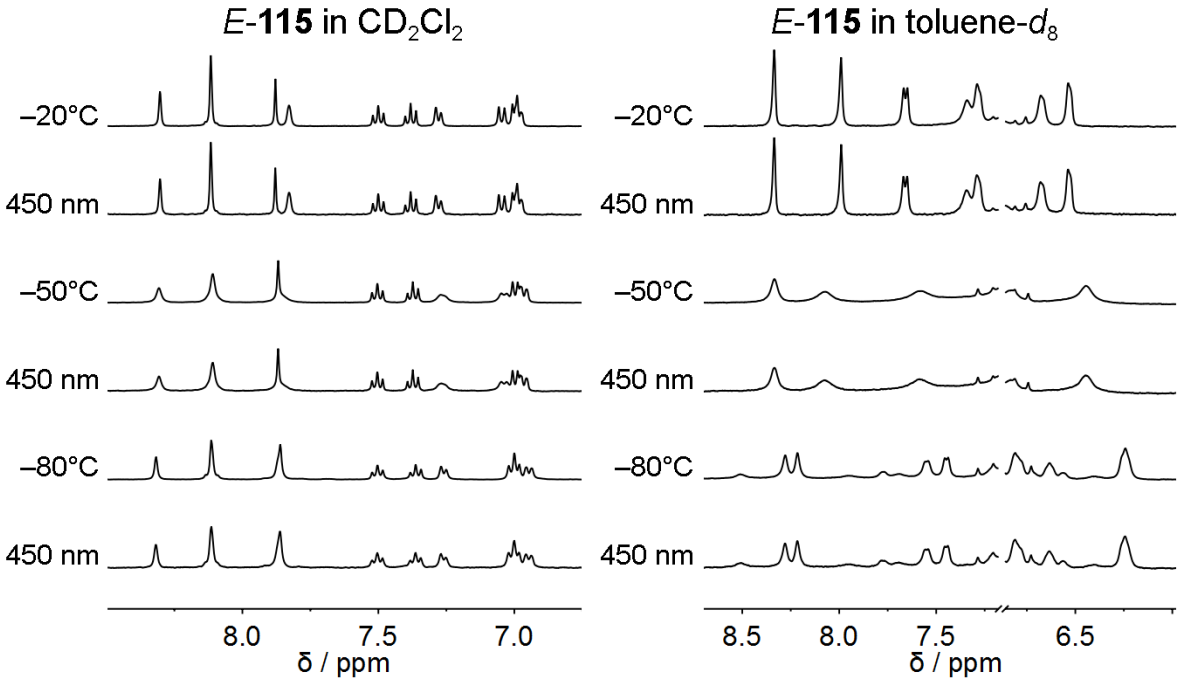

Figure 149 ^{1}H NMR spectra of *E*-**115** (400 MHz) in different deuterated solvents acquired before and after irradiation with 450 nm light at low temperatures. The toluene-d_8 solvent signal is cut out for clarity. The solutions were irradiated for 15 min each and compared to the spectra taken before irradiation. In all cases no isomerization processes were detectable. Broadening of signals in toluene-d_8 below –20 °C was observed despite sharp signals of the deuterated solvent.

The experiment was repeated using toluene-d_8 as solvent where irradiation with 450 nm light for 15 min at ambient temperatures resulted in a mixture containing 13% *Z*-**115** and 87% *E*-**115** (Figure 150, identical sample). At –20 °C, however, no such isomerization was visible (Figure 149, right). The spectra taken at –50 °C and –80 °C revealed very broad signals despite very sharp solvent signals. The quality of the spectra still sufficed to indicate the absence of constructive photoisomerization processes.

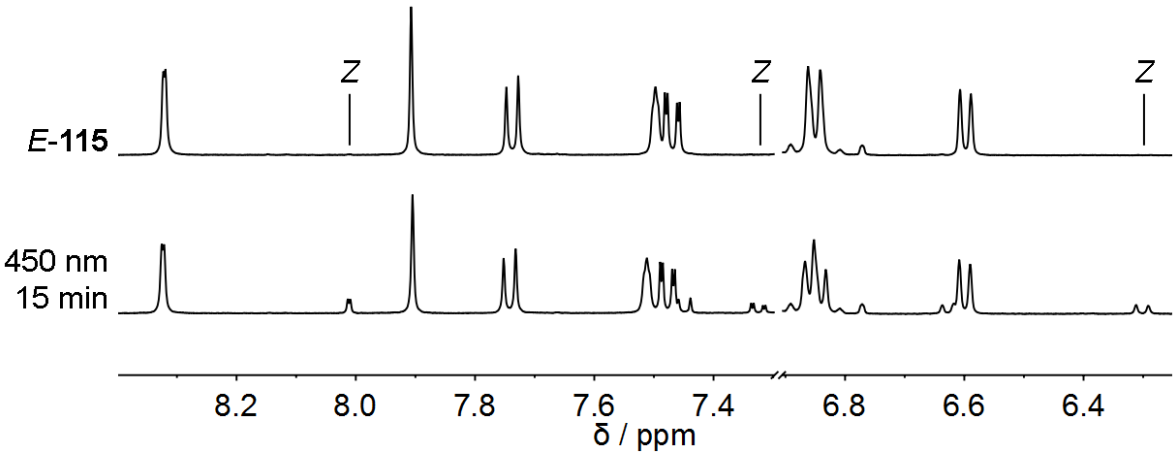

Figure 150 ^{1}H NMR spectra of *E*-**115** (400 MHz, toluene-d_8, 22 °C) acquired before and after irradiation with 450 nm light for 15 min at 23 °C. The toluene-d_8 solvent signal is cut out for clarity. The result was a mixture containing 13% *Z*-**115** and 87% *E*-**115**.

Taken together the irradiation experiments on *E*-**115** showed very limited photoisomerization. Compared to other macrocyclic HTIs the highest *Z*-**115** yields were obtained using light with significantly shorter wavelengths (365 nm compared to 450 nm or 470 nm light used previously) resulting in maximum concentrations of 20% *Z*-**115** in solution. Higher concentrations are likely achievable but impeded by the poor solubility and low thermal stability of the photoproduct. Photoisomerization was also restricted to solvents with low polarity like toluene and benzene and was greatly impeded in CH_2Cl_2 and methanol when using UV-Vis or NMR spectroscopy as detection methods. A possible explanation for these observations is the increased intramolecular strain in the *Z*-**115** conformer. The HTI fragment together with the aryl follower constitute the rigid backbone of the molecule that has very limited flexibility. As discussed for previous compounds the *Z*-**115** conformer has a significantly increased distance between the phenolic oxygens that serve as attachment points for the covalent linker. For compound **81** in the crystalline state this distance is 8.1 Å in *E*-**81** and 11.2 Å in *Z*-**81** for example. In the case of *Z*-**115** the elongated distance could be close to the threshold where structures become severely strained therefore strongly limiting the photoisomerization effectiveness and stability of the conformer in solution. An explanation for the absence of photochemistry at ambient to low temperatures could be the missing population of vibronic states that are necessary for excitation to the transition state. A deeper analysis however is impeded by the poor accessibility of the *Z*-**115** conformer.

6.3 HTI 121

6.3.1 Synthesis of HTI 121

Synthesis of the target compound **121** that features an elongated covalent linker chain followed the established route that was employed for the previous macrocyclic HTIs. The structure is composed of the known building blocks 3-hydroxyphenylboronic acid pinacol ester, HTI **75** and the longer PEG type linker **117** (Scheme 49).

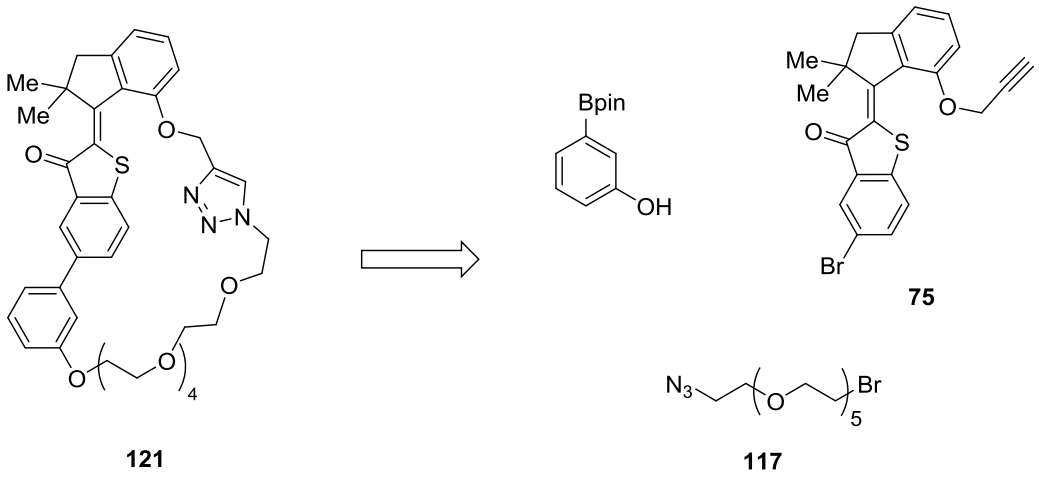

Scheme 49 Retrosynthetic aspects of the synthesis of **121**. The target compound was constructed from the known building blocks 3-hydroxyphenylboronic acid pinacol ester, HTI **75** and the new bifunctionalized hexaethylene glycol linker **117**.

First hexaethylene glycol was substituted under *Appel* conditions to give the dibromo analog **116** in poor yields (Scheme 50). The reaction did not proceed to completion giving monosubstituted hexaethylene glycol as a byproduct. Another drawback of this approach was the complicated workup as the brominated compounds as well as the starting material and the reaction byproduct triphenylphosphine oxide revealed very similar polarities hampering purification by flash column chromatography. Subsequent substitution using sodium azide gave bifunctionalized hexaethylene glycol **117** in moderate yields. Reaction with 3-hydroxyphenylboronic acid pinacol ester completed the synthesis of building block **118** with a yield of 78%.

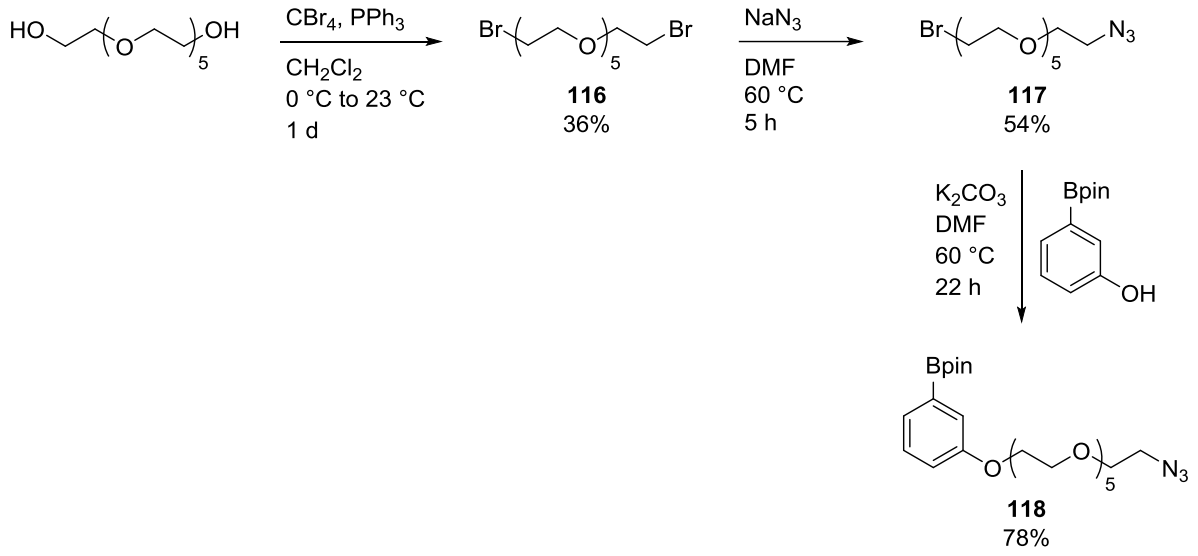

Scheme 50 Synthesis of building block **118**. Double bromination of hexaethylene glycol under *Appel* conditions afforded **116**. Substitution with sodium azide gave **117** that was reacted with 3-hydroxyphenylboronic acid pinacol ester, which afforded **118**.

Reaction of **118** with the established HTI fragment **75** in a copper catalyzed *Click* reaction gave triazole **119** in very good yields (Scheme 51).

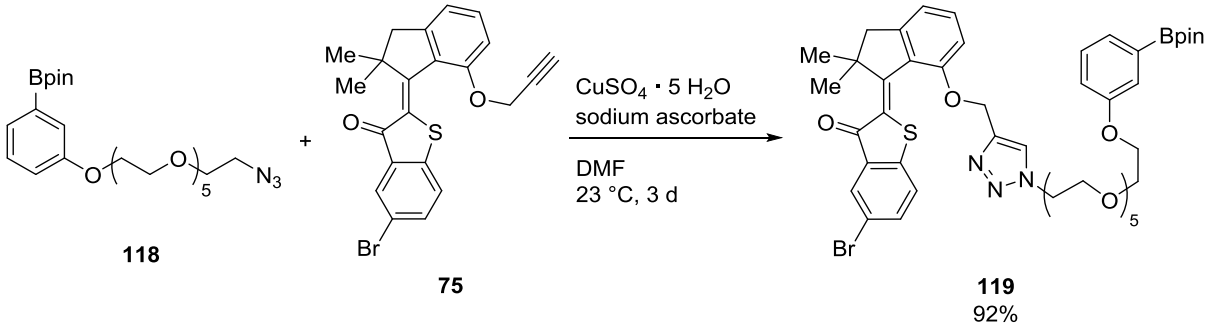

Scheme 51 Copper catalyzed 1,3-dipolar cycloaddition of boronic acid pinacol ester **118** and HTI **75**. The product **119** was obtained as a mixture of *E* and *Z* isomers. Only the *Z* configured isomer is shown.

Subsequent intramolecular *Suzuki-Miyaura* cross-coupling furnished macrocycle **120** in satisfactory 39% yield despite the increased intramolecular distance between the reactive sites (Scheme 52). Separation of polymerized byproducts was readily accomplished by two consecutive flash column chromatography separation steps using different solvent mixtures.

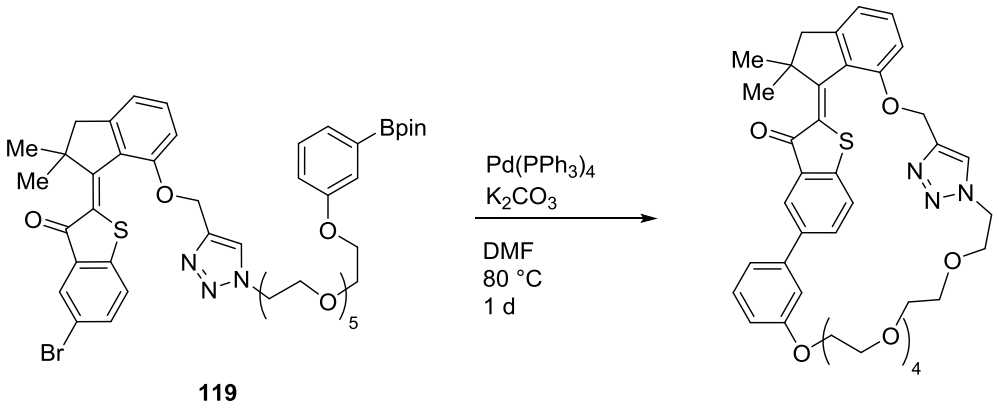

119

120
39%

Scheme 52 Intramolecular *Suzuki-Miyaura* cross-coupling of **119**. The product **120** was obtained in 39% yield. Only the *Z* configured isomers are shown.

The synthesis was completed with oxidation of **120** to the corresponding sulfoxide **121** using sodium perborate tetrahydrate in acetic acid (Scheme 53). After three hours at ambient temperatures the product **121** was obtained in 69% yield as a mixture of *E* and *Z* isomers.

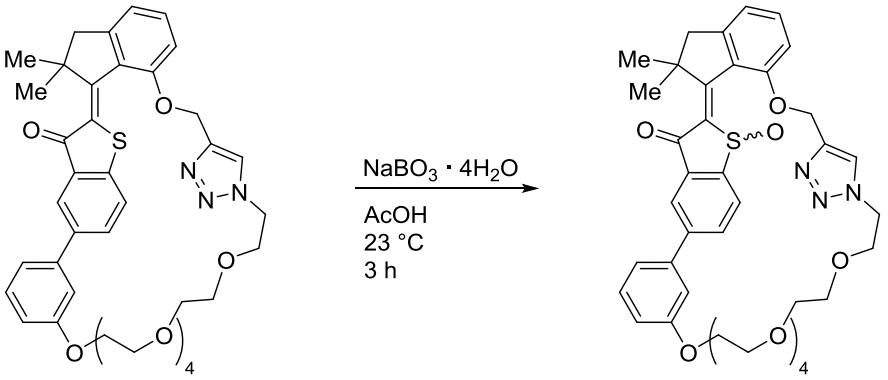

120

121
69%

Scheme 53 Oxidation of **120** to the sulfoxide **121** using sodium perborate tetrahydrate in acetic acid. Only the *Z* configured isomers are shown.

Overall the target compound **121** was synthesized in a straightforward manner. The poor accessibility of **116** under *Appel* conditions can be circumvented by an alternative route that requires an additional step and is discussed in section 6.4.1.

6.3.2 Irradiation of 121 at ambient temperatures

Racemic mixtures containing only *E* or *Z* configured isomers were readily obtained from separation on a preparative HPLC SiO_2 column. A sample of *E*-**121** in CD_2Cl_2 was irradiated at ambient temperatures to gain insight into the isomerization behavior. The solution was irradiated with wavelengths from 365 to 530 nm for 45 to 180 min. An overview is given in Figure 151.

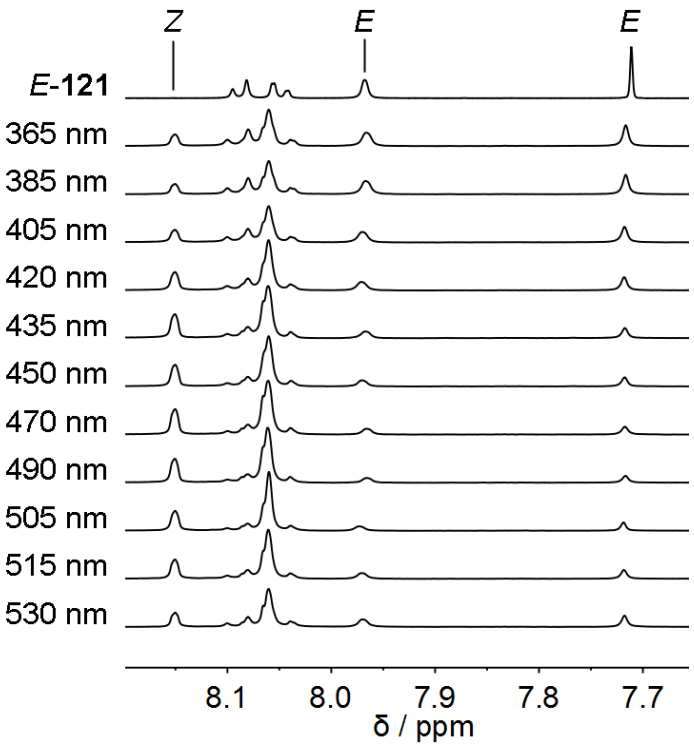

wavelength [nm]	duration [min]	%*E*	%*Z*
365	180	60	40
385	120	**63**	37
405	45	52	48
420	60	37	63
435	60	29	71
450	180	27	73
470	120	24	76
490	135	21	**79**
505	120	22	78
515	50	28	72
530	75	43	57

Figure 151 ^{1}H NMR spectra obtained after irradiation of a solution of **121** (400 MHz, CD_2Cl_2, 22 °C, left) with light of different wavelengths. The corresponding irradiation times and resulting isomer ratios are given in the table (right).

A comparatively high modulation is observed ranging from 63% *E*-**121** at 385 nm to 79% *Z*-**121** at 490 nm. The increased amount of *Z*-**121** can be a result of reduced intramolecular strain due to the increased length of the covalent linker. An in depth analysis of the motor function of the integrated HTI fragment was not conducted for this compound.

6.3.3 Complexation of inorganic salts

Upon closer inspection of the structure of macrocycle **121** the elongated PEG tether might enable complexation of suitable cations in a crown ether or podant-type fashion. An idealized

structure that emphasizes the crown-ether analogy of the linker is shown in Figure 152. To get a first idea of the binding properties the effect of ammonium and potassium cations on the chemical shifts in the ^{1}H NMR were tested. Hexafluorophosphate was chosen as counteranion as the respective salts are soluble in a variety of organic solvents. Approximately five equivalents of NH_4PF_6 and KPF_6 were added to a solution of *E*-**121** in MeOD and the resulting signal shifts in the ^{1}H NMR spectrum were analyzed (Figure 152).

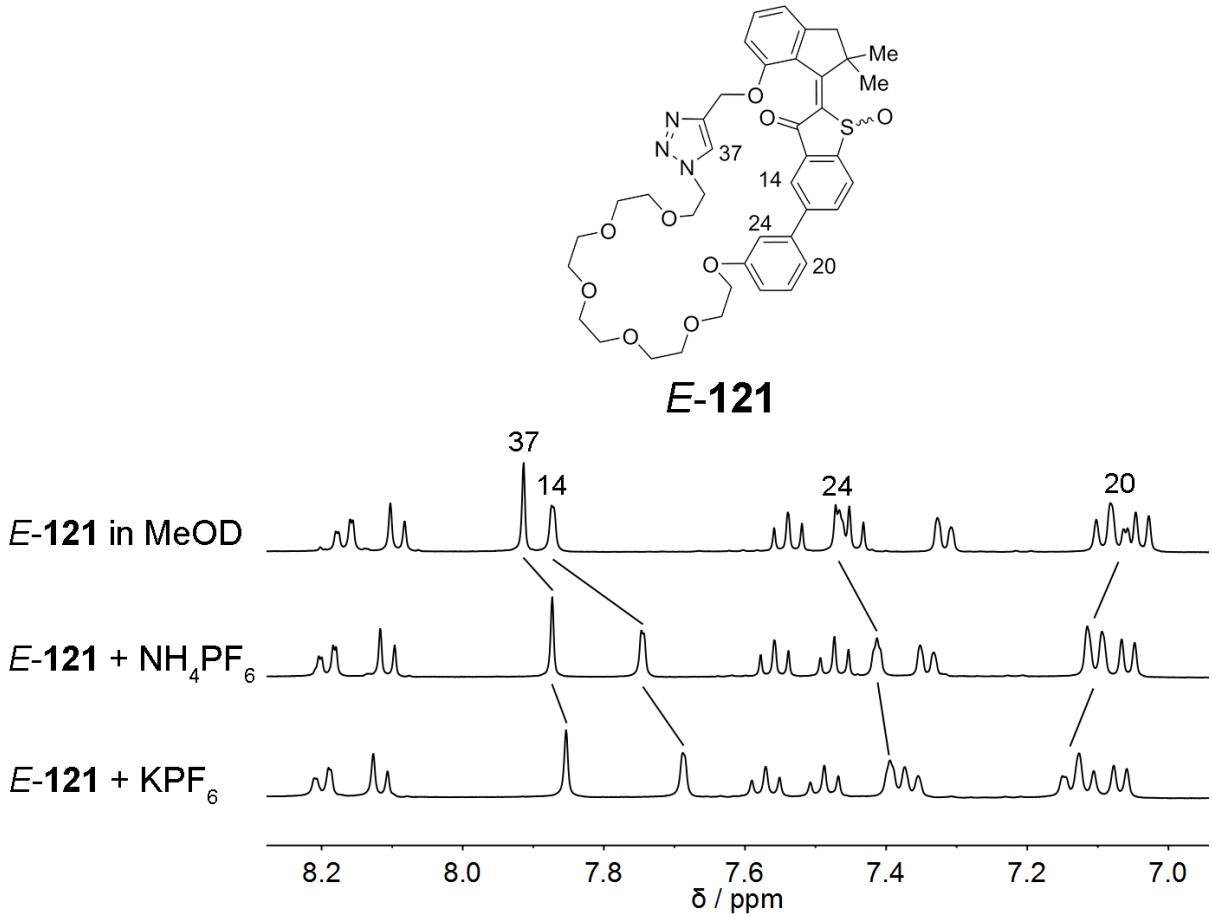

Figure 152 ^{1}H NMR spectra of the aromatic region of *E*-**121** (400 MHz, MeOD, 22 °C). Pure *E*-**121** (top). After addition of NH_4PF_6 to pure *E*-**121** (middle). After addition of KPF_6 to pure *E*-**121** (bottom). Shifts of indicative signals are highlighted.

The aromatic region of the ^{1}H spectra revealed shifts between 0.03 to 0.20 ppm compared to the pure *E*-**121** spectrum. The majority of the signals was shifted downfield within a range of 0.03 to 0.04 ppm. The strongest effect however is observed for protons 14, 24, and 37 that were shifted upfield. The section of the ^{1}H NMR spectra that shows the collective signal set of the PEG tether is shown in Figure 153.

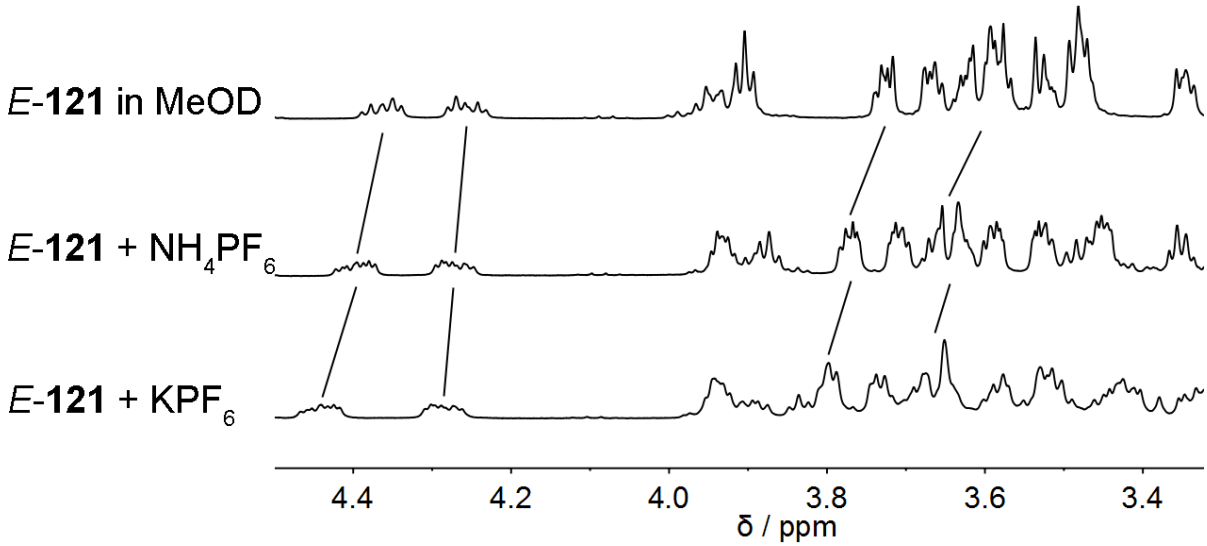

Figure 153 ^{1}H NMR spectra of the collective ethylene glycol signals of *E*-**121** (400 MHz, MeOD, 22 °C). Pure *E*-**121** (top). After addition of NH_4PF_6 to pure *E*-**121** (middle). After addition of KPF_6 to pure *E*-**121** (bottom). The solvent signal at 3.3 ppm is cut off. Proposed shifts of selected signals are highlighted but individual signals could not be traced unambiguously.

The signal changes of the PEG chain cannot be traced in full detail due to overlap. Shifts of selected methylene group protons were in the range of 0.01 to 0.07 ppm. Overall a significant shift of the ^{1}H NMR signals was observed revealing interactions between the inorganic salt and *E*-**121**. From the present data no distinct binding site can be determined. The pronounced upfield shift of selected aromatic protons can be explained by a different molecular structure in solution due to the interaction with the cations that results in shielding of the respective protons.

6.3.4 Complexation of secondary aminium ions

Organic aminium ions are commonly used as their hexafluorophosphate salts as mentioned earlier. In order to test the possible threading of the target compound **121** onto longer axles the interaction with small model compounds was investigated. To this end di-*n*-butylammonium and dibenzylammonium salts were synthesized and a general approach to the respective compounds bearing a hexafluorophosphate counterion was established (Scheme 54).

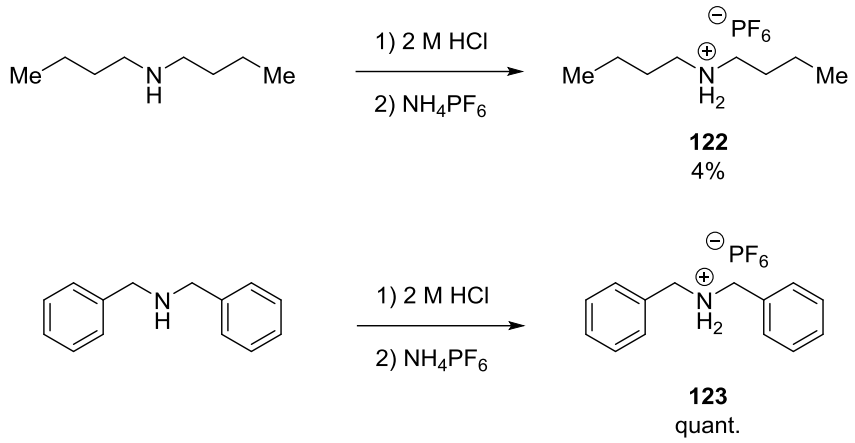

Scheme 54 General procedure for the synthesis of dialkyl and dibenzyl aminium hexafluorophosphate salts **122** and **123**.

A synthetic route that is commonly found in the literate commences with the synthesis of the ammonium chloride salts. This was realized by taking up the corresponding amine in 2 M HCl and evaporating the volatiles *in vacuo*. Next the residue was taken up in water and NH_4PF_6 was added until no further precipitation occured. This way the dibenzylammonium salt **123** was obtained quantitatively. In the case of the dialkylamminium ion no precipitation occurred upon addition of NH_4PF_6. Consequently the solution containing approximately one equivalent of NH_4PF_6 was concentrated *in vacuo* and the mixture was left to crystallize in the cold. This way sufficient amounts of **122** were obtained to conduct complexation tests and assess the binding affinity.

A solution containing *E* and *Z* configured **121** in CD_2Cl_2 was prepared and one equivalent of di-*n*-butylammonium hexafluorophosphate **122** was added. Few selected protons of *E*-**121** revealed strong shifts in the ^{1}H NMR (Figure 154). This result is similar to observations for the complexation of *E*-**121** with NH_4PF_6 or KPF_6 where the strongest interactions were found between the inorganic salt and protons at the central, aromatic part of the molecule (see also Figure 152). Interestingly the spectra indicate that *Z*-**121** does not interact strongly with **122**.

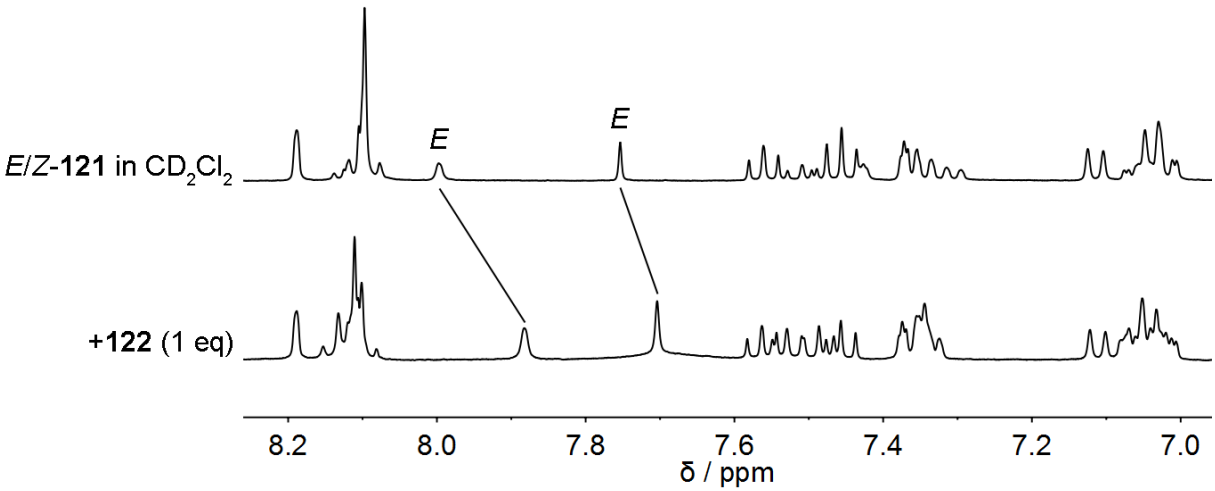

Figure 154 ^{1}H NMR spectra of the aromatic region of a mixture of *E*-**121** and *Z*-**121** (400 MHz, CD_2Cl_2, 20 °C) before (top) and after (bottom) addition of one equivalent of di-*n*-butylammonium hexafluorophosphate **122**. Strong shifts of selected *E*-**121** protons were observed. No interaction of *Z*-**121** with **122** could be identified.

In order to get more conclusive results the mixture containing *E* and *Z* configured **121** was separated on a preparative HPLC column before further experiments were conducted. In the same context a variety of conditions were tested in order to obtain a crystalline sample of either racemic mixture of *E*-**121** or *Z*-**121** to no avail. Additional attempts to crystallize the compound in the presence of selected cations were also unsuccessful.

Next, a solution of *E*-**121** in MeOD was prepared and an excess of dibenzyl ammonium salt **123** was added (Figure 155). Surprisingly, the addition had no effect on the chemical shift of ^{1}H NMR signals. This is in contrast to earlier experiments where upon addition of KPF_6 or NH_4PF_6 weak to strong shifts of the collective signal set were observed.

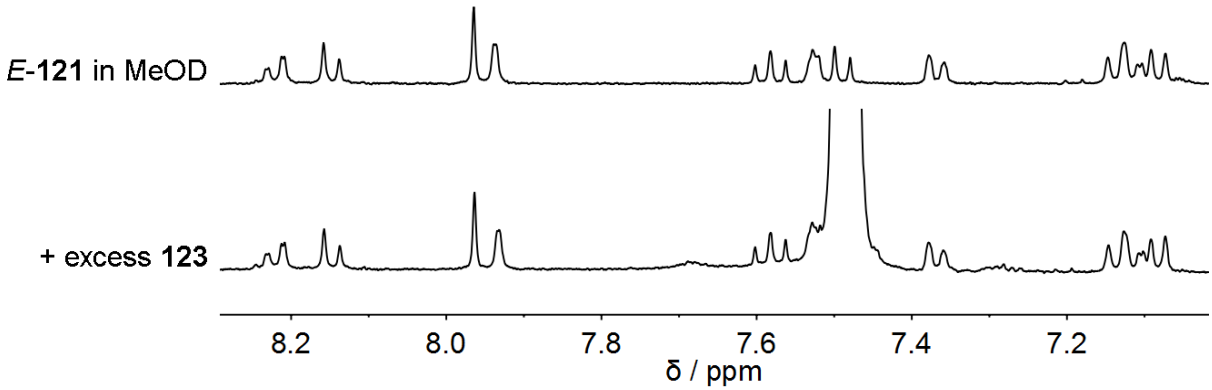

Figure 155 ^{1}H NMR spectra of a solution of *E*-**121** (400 MHz, MeOD, 20 °C) before (top) and after (bottom) addition of approximately 12 equivalents of **123**. No signal shifts upon addition of the salt were observed

The experiment was repeated using CD_2Cl_2 as solvent. Again, an excess of **123** was added. This time a very strong impact on the collective signal set was observed with individual shifts of up to 0.4 ppm (Figure 156). This shows that CD_2Cl_2 is much more favorable to promote interactions between *E*-**121** and the organic salt compared to the protic and highly polar MeOD that can block complexation sites through hydrogen bonding or act as ligand itself.

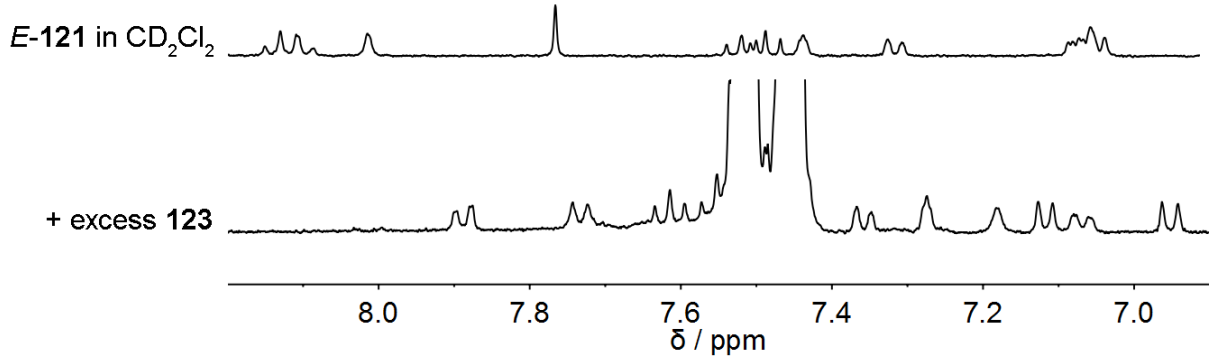

Figure 156 ^{1}H NMR spectra of a solution of *E*-**121** (CD_2Cl_2, 20 °C) before (top) and after (bottom) addition of approximately 10 equivalents of **123**. Upon addition of the salt strong upfield or downfield shifts of the collective signal set were observed.

Taken together the preliminary complexation experiments showed very promising results. However, details of the underlying interactions remained inconclusive. A shift of the collective signal set was observed in most cases and no selective binding site could be determined. In addition to the crown-ether type covalent linker several other electron-rich binding sites are present in the macrocyclic compound that can compete as a ligand in the complexation process. It also remained unclear if binding of a cation in a crown-ether type fashion was possible. In order to test this a more sophisticated approach was attempted.

6.3.5 Attempted synthesis of rotaxanes and catenanes

Based on the successful experiments with the dibenzylammonium salt **123** the use of a bifunctionalized analog was envisioned. In the case of a successful threading of macrocycle **121** onto the new compound the resulting pseudorotaxane can potentially be locked in place by attachment of appropriate bulky stopper molecules. This way separation and in depth analysis of the interlocked molecule would be possible. A schematic illustration of such a rotaxane synthesis is shown in Figure 157. Another possibility to construct mechanically interlocked molecules is realized by the use of an elongated axle. After threading of the macrocycle functionalized end groups can be fused by e.g. ring-closing metathesis (RCM) to form a catenane.

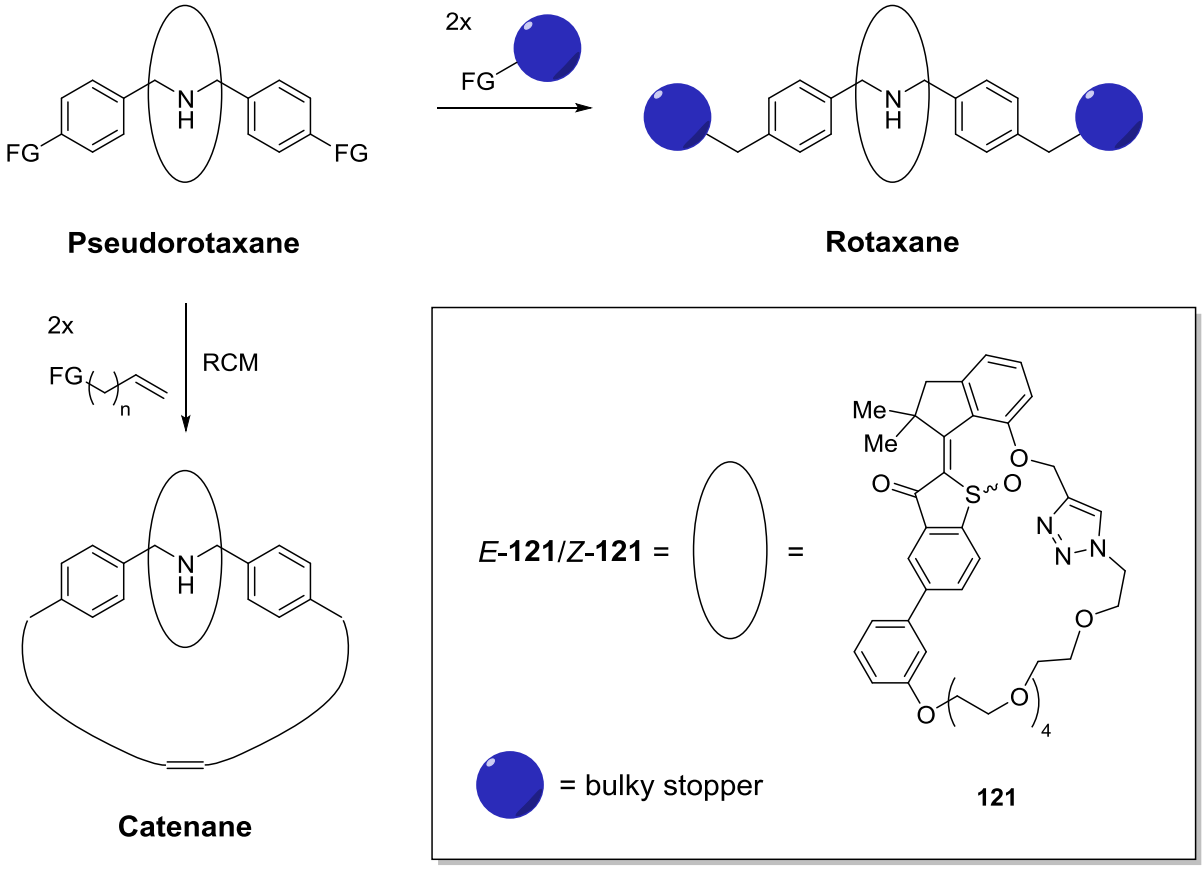

Figure 157 Potential synthesis of mechanically interlocked compounds. The macrocycle **121** (only the *Z* isomer is shown) is threaded on a bifunctionalized dibenzylamine precursor forming a pseudorotaxane (top left). Introduction of bulky stopper groups forms a rotaxane (top right). Elongation of the axle and fusing of the ring by e.g. ring-closing metathesis (RCM) can be used to construct catenanes.

Due to the complexity of macrocyclic compound **121** mild conditions were preferred for the fixation of the axles. This is commonly achieved by 1,3-dipolar cycloadditions or olefin

metathesis. A possible axle precursor for further functionalization is 4,4'-dihydroxydibenzylamine **124**. The compound was readily synthesized in one step following a literature procedure (Scheme 55).[89] However, attempts to further functionalize the molecule using either di-*tert*-butyl dicarbonate or propargyl bromide did not succeed in distinguishing between the nucleophilic (hydroxyl or amine) reaction sites and instead a mixture of products was obtained in both cases. This includes the triple functionalized molecule as well as hydroxyl and amine double substituted compounds as major byproducts when only one equivalent of either reactant was used. As a result this approach was not further pursued.

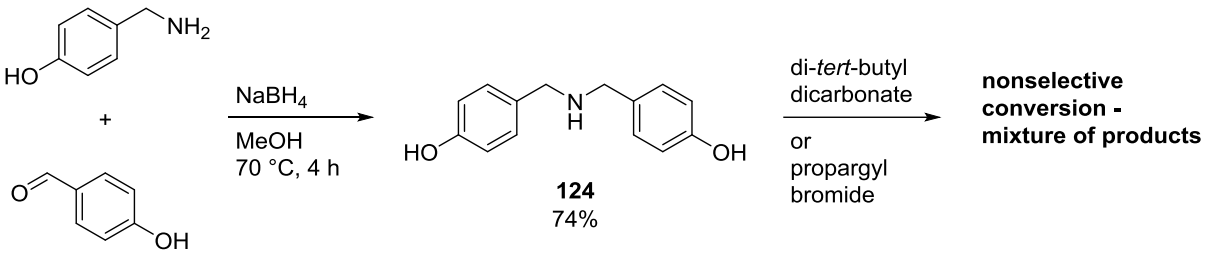

Scheme 55 Synthesis of the axle precursor **124**. Further functionalization with either di-*tert*-butyl dicarbonate or propargyl bromide was nonselective and gave a mixture of functionalized products.

A very similar approach was realized with the synthesis of literature known bisbenzylalcohol **127** (Scheme 56).[90] Contrary to the preparation of **124** the reported procedure starts with imine synthesis in a separate condensation step before reduction to the secondary amine. Applying the procedure for the synthesis of **124** allowed to shorten this to a single step that furnished intermediate **125** in a very good yield of 89%. Next, the Boc protecting group was readily introduced, which furnished **126** almost quantitatively. Subsequent reduction of the methyl ester gave diol **127** in 75% yield. Overall the synthesis provides a straightforward route to an axle building block that can be functionalized further in a variety of ways.

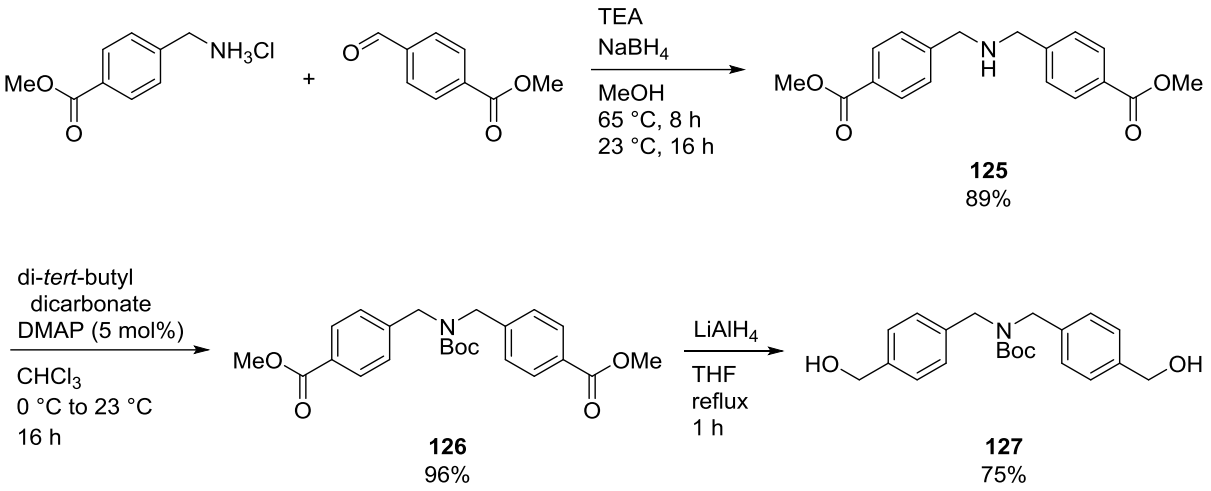

Scheme 56 Synthesis of diol **127** in 64% yield over three steps. Reductive amination afforded dibenzylamine **125**. The Boc protecting group was introduced to give **126**. Reduction with $LiAlH_4$ completed the synthesis of **127** with 75% yield.

A possible way to attach bulky ends to the axle is realized by 1,3-dipolar cycloaddition of the respective azide and alkyne functionalized compounds. Reaction of **127** with propargyl bromide gave dialkyne **128** in very good yields, which was followed by straightforward deprotection of the amine using trifluoroacetic acid (Scheme 57). Next, the organic ammonium hexafluorophosphate salt **129** was prepared following the general procedure described above. Hydrochloride salt formation followed by anion exchange furnished **129** in moderate yields over two steps.

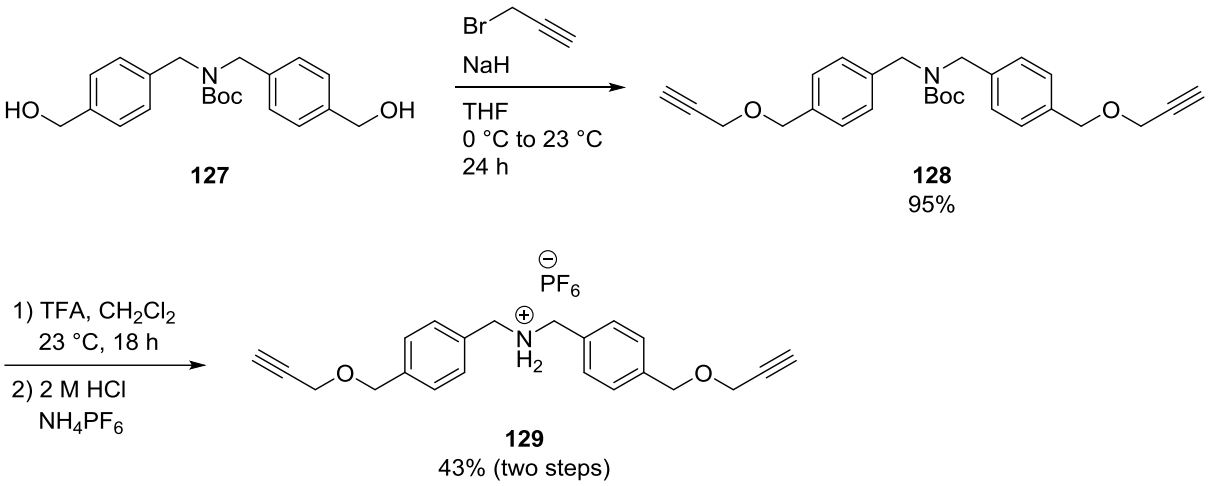

Scheme 57 Synthesis of the propargyl functionalized dibenzylammonium salt **129**. Reaction of **127** with propargyl bromide gave **128** in very good yields. Removal of the Boc protecting group using trifluoroacetic acid was followed by generation of the hydrochloride salt. Subsequent anion exchange using NH_4PF_6 gave **129** in 43% yield over two steps.

Bulky azide functionalized compounds such as **130** were readily accessible for example through substitution of 3,5-di-*tert*-butylbenzyl bromide using an azide source (Scheme 58).

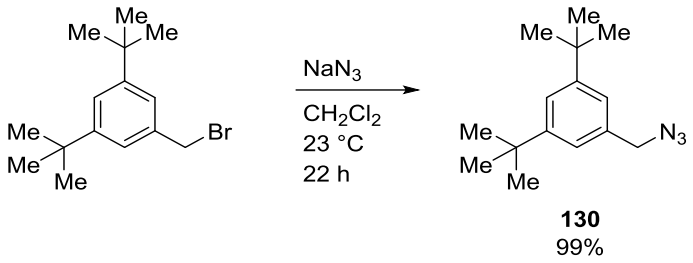

Scheme 58 Substitution of 3,5-di-*tert*-butylbenzyl bromide gave bulky azide **130**.

A modular approach to bulky azide stoppers was realized by reaction of 4-tritylphenol with a bifunctionalized PEG-type linker of variable length (Scheme 59). The comparatively low yield of 75% **131** was caused by a weighing error and can readily be improved.

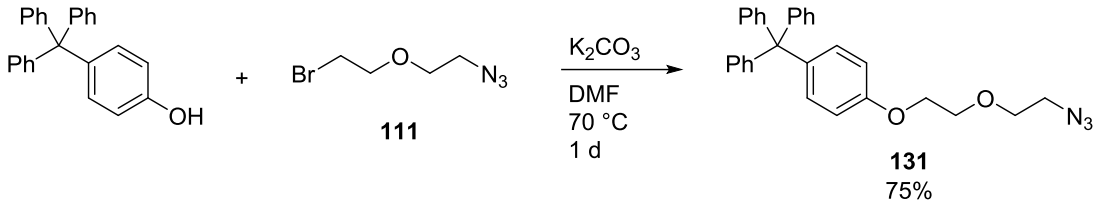

Scheme 59 Synthesis of an azide functionalized tritylphenol stopper **131** by attachment of bifunctionalized PEG-type tether **111**. The length of the tether can be modulated using a PEG substrate with additional ethylene glycol units.

The complementary setup utilized an azide functionalized axle and an alkyne stopper. The synthesis commenced from diol **127** that was chlorinated with *N*-chlorosuccinimide (NCS) leading to compound **132**, which was followed by substitution with sodium azide to give **133** in 63% yield over two steps (Scheme 60). The following deprotection and generation of the ammonium hexafluorophosphate salt proceeded similar to the synthesis of **129** and furnished diazide **134** in moderate yields.

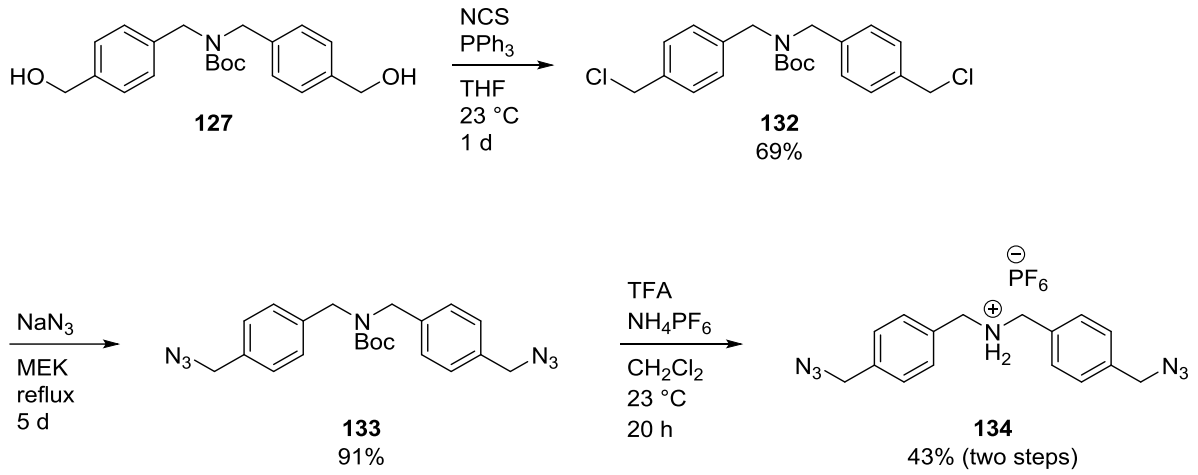

Scheme 60 Synthesis of the azide functionalized axle **134**. Chlorination of diol **127** with NCS and PPh_3 gave **132** in good yields. Substitution with sodium azide to **133** was followed by deprotection with TFA and generation of the hexafluorophosphate salt **134**.

Di-*tert*-butyl acetylenedicarboxylate **135** is a bulky alkyne-type stopper that is commonly found in the literature (Figure 158). It is available for purchase and does not require additional synthetic efforts.

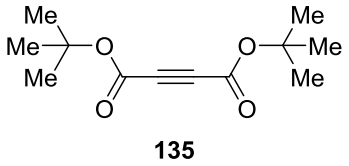

135

Figure 158 Di-*tert*-butyl acetylenedicarboxylate **135** can be used as a bulky alkyne-type stopper precursor.

A different approach that can be used to generate an interlocked molecule is realized with the functionalized axle **137** (Scheme 61). After threading of the macrocycle fusing of the alkene functionalized ends in a RCM reaction would furnish a catenane. The synthesis started from diol precursor **127** that was reacted with two equivalents of the allyl functionalized PEG tether **62** that was established earlier (see section 3.3.2). The product **136** was obtained in poor yields. Generation of the hexafluorophosphate salt gave **137** almost quantitatively, providing sufficient material for further testing.

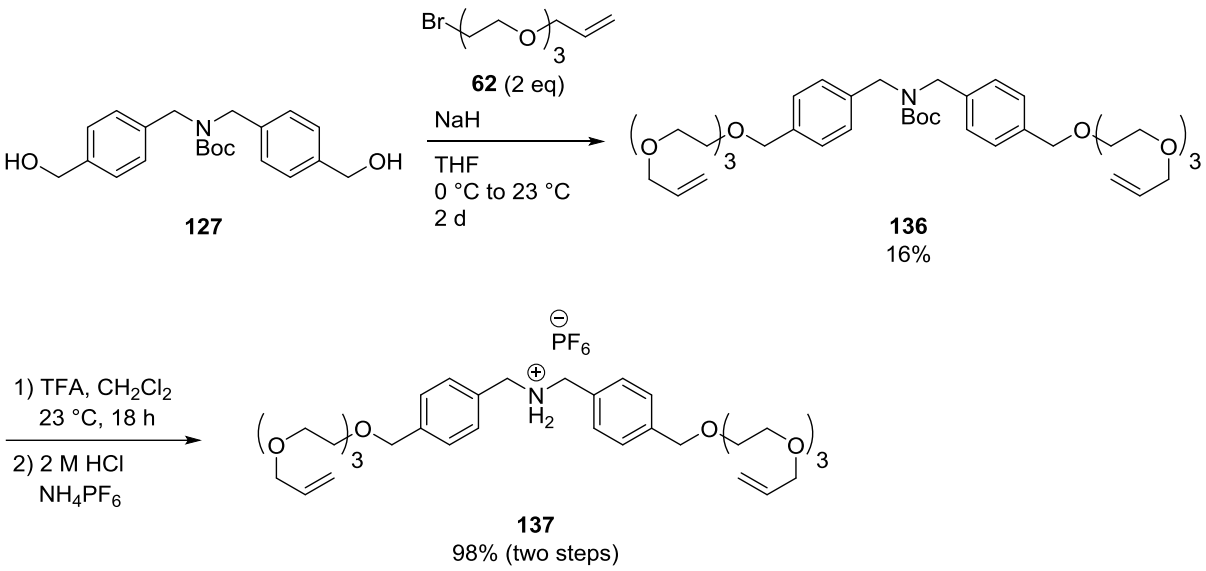

Scheme 61 Synthesis of alkene functionalized axle **137**. Conversion of diol precursor **127** using two equivalents of the functionalized PEG chain **62** furnished **136**. Deprotection followed by generation of the hexafluorophosphate salt gave **137**.

Preliminary binding studies were conducted for the two functionalized axle precursors **129** and **134**. Small amounts of *E* and *Z* configured macrocycle **121** in CD_2Cl_2 were treated with an excess of the respective ammonium salts (Figure 159). In both cases very strong shifts of the ^{1}H NMR signals of *E*/*Z*-**121** were observed. Signals could not be traced individually. This was in agreement with earlier experiments were the binding interactions of dibenzylammonium salt **123** and *E*/*Z*-**121** were assessed. The results also provided a promising basis for the synthesis of interlocked molecules.

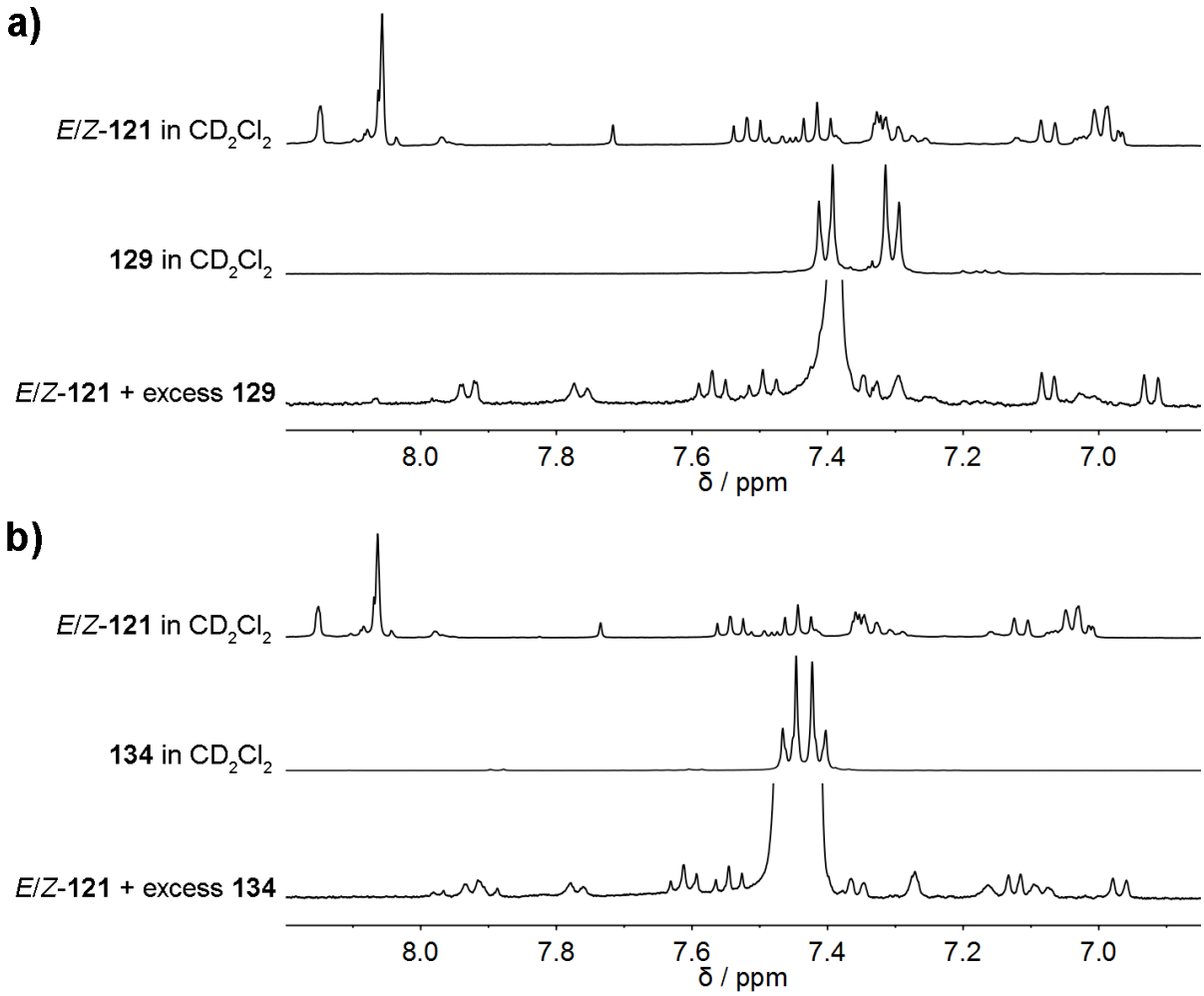

Figure 159 ^{1}H NMR spectra (400 MHz, CD_2Cl_2, 22 °C) of the aromatic region of *E*/*Z*-**121**. a) *E*/*Z*-**121** (top), axle **129** (middle) and *E*/*Z*-**121** with an excess of **129** (bottom) revealing strong shifts of the *E*/*Z*-**121** proton signals. b) *E*/*Z*-**121** (top), axle **134** (middle) and *E*/*Z*-**121** with an excess of **134** (bottom) revealing strong shifts of the *E*/*Z*-**121** proton signals.

Due to the comparatively time consuming efforts required to synthesize HTI **121** construction of the axles was first attempted in the absence of the macrocyclic compound. Complexation experiments that were described earlier showed the most promising results in CH_2Cl_2 (CD_2Cl_2) solution. First, reaction of the diazide axle **134** with acetylene stopper group **135** was attempted (Scheme 62). The tetrakis(acetonitrile)copper(I) hexafluorophosphate complex was used as copper source for the 1,3-dipolar cycloaddition. In contrast to the Cu(II)$SO_4 \cdot 5H_2O$/sodium ascorbate combination that generates the active Cu(I) species *in situ* the acetonitrile complex provides the catalyst directly in its active oxidation state. After stirring for 5 d at ambient temperatures the reaction did not show any conversion. As a result the solvent was evaporated and the mixture was heated to 55 °C in $CHCl_3$ for another 5 d. Subsequent workup did not

afford the assembled axle **138** either as ammonium salt or free amine and the reaction was not further pursued.

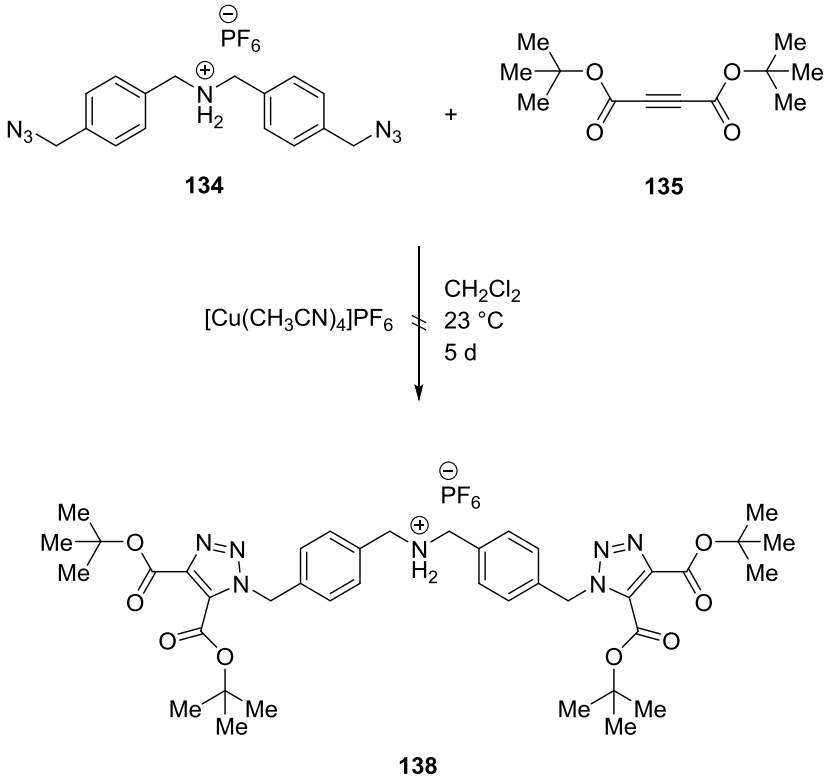

134 **135** **138**

Scheme 62 Attempted assembly of the axle **138**. Conversion of **134** with di-*tert*-butyl acetylenedicarboxylate **135** in the presence of Cu(I) did not afford the product **138** within 5 d at ambient temperatures.

Next, reaction of propargyl functionalized dibenzylamine **129** with azide stopper **130** was attempted (Scheme 63). The reaction conditions were identical to the attempted synthesis of **138**. After 5 d full conversion of the starting materials was observed and target compound **139** was obtained almost quantitatively upon work up. This stands in stark contrast to the earlier attempt towards 138 were no conversion to the desired product was observed.

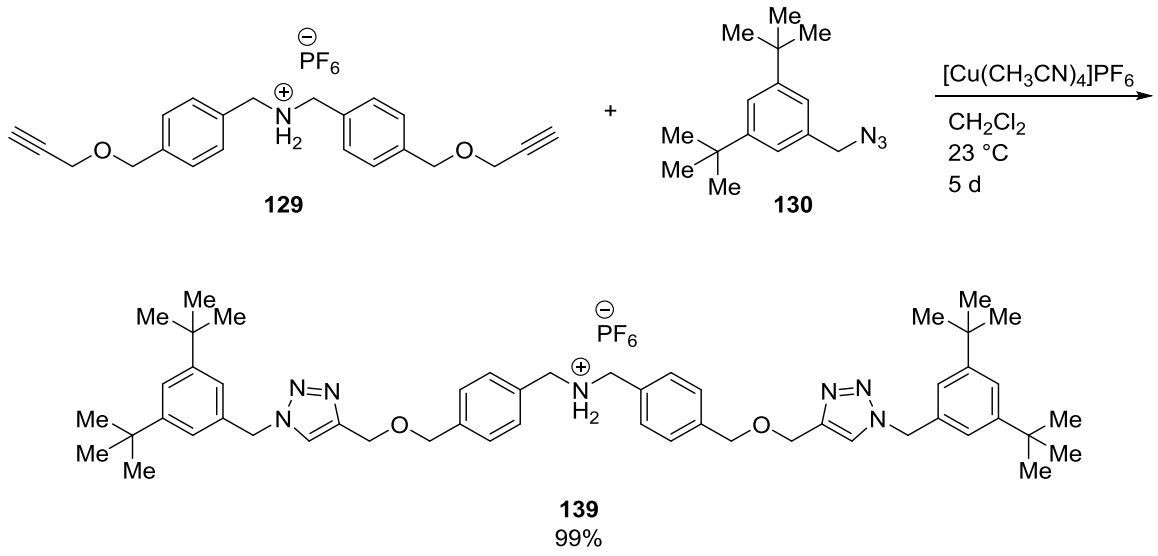

Scheme 63 Synthesis of axle **139**. Reaction of propargyl functionalized precursor **129** and azide stopper **130** furnished the target molecule **139**.

Finally, ring closing metathesis was attempted with the allyl functionalized axle **137** (Scheme 64). A second generation Grubbs catalyst was used in CH_2Cl_2 and the reaction mixture was stirred at ambient temperatures in a snap-cap vial. After 45 min of stirring built up pressure was released and the reaction was stirred for a total of 18 h. Upon workup two main products were isolated. ^{1}H NMR analysis revealed the characteristic signals of terminal allylic protons with one presumably stemming from the hydrolyzed dibenzylamine and an additional compound that could not be assigned to a structure. Because of these results and the successful synthesis of axle **140** the reaction was not further pursued.

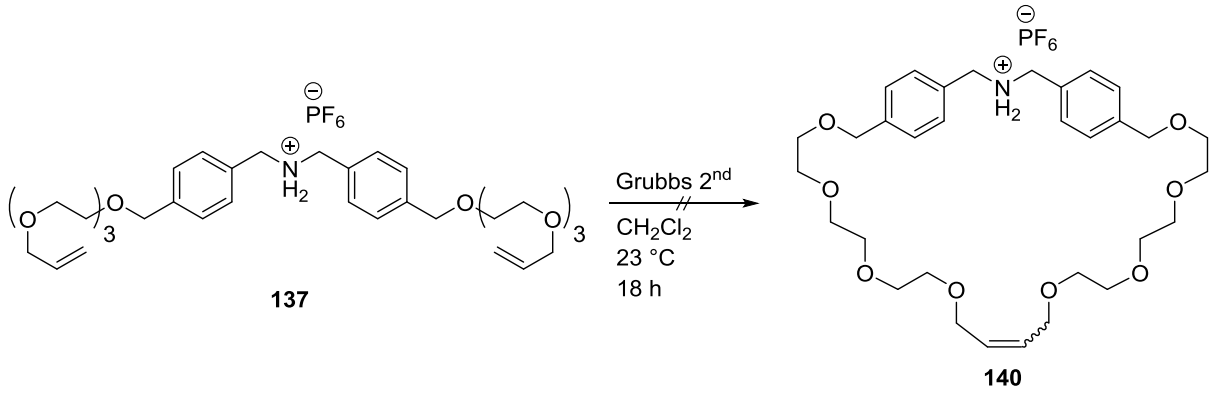

Scheme 64 Attempted synthesis of macrocyclic compound **140**. Reaction of **137** with second generation Grubbs catalyst did not afford the desired product.

Construction of a rotaxane was attempted next (Scheme 65). To this end macrocycle **121** and one equivalent of propargyl functionalized dibenzylammonium salt **129** were mixed in CH_2Cl_2

at room temperature. After 30 min two equivalents of bulky azide stopper **130** and the Cu(I) catalyst were added. The mixture was stirred for 5 d at ambient temperatures and the reaction products were purified by flash column chromatography. The macrocycle **121** and the free axle **139** were identified by ^{1}H NMR spectroscopy. No traces of the succesfully interlocked rotaxane could be identified. The reaction was repeated using overall higher concentrations with identical results.

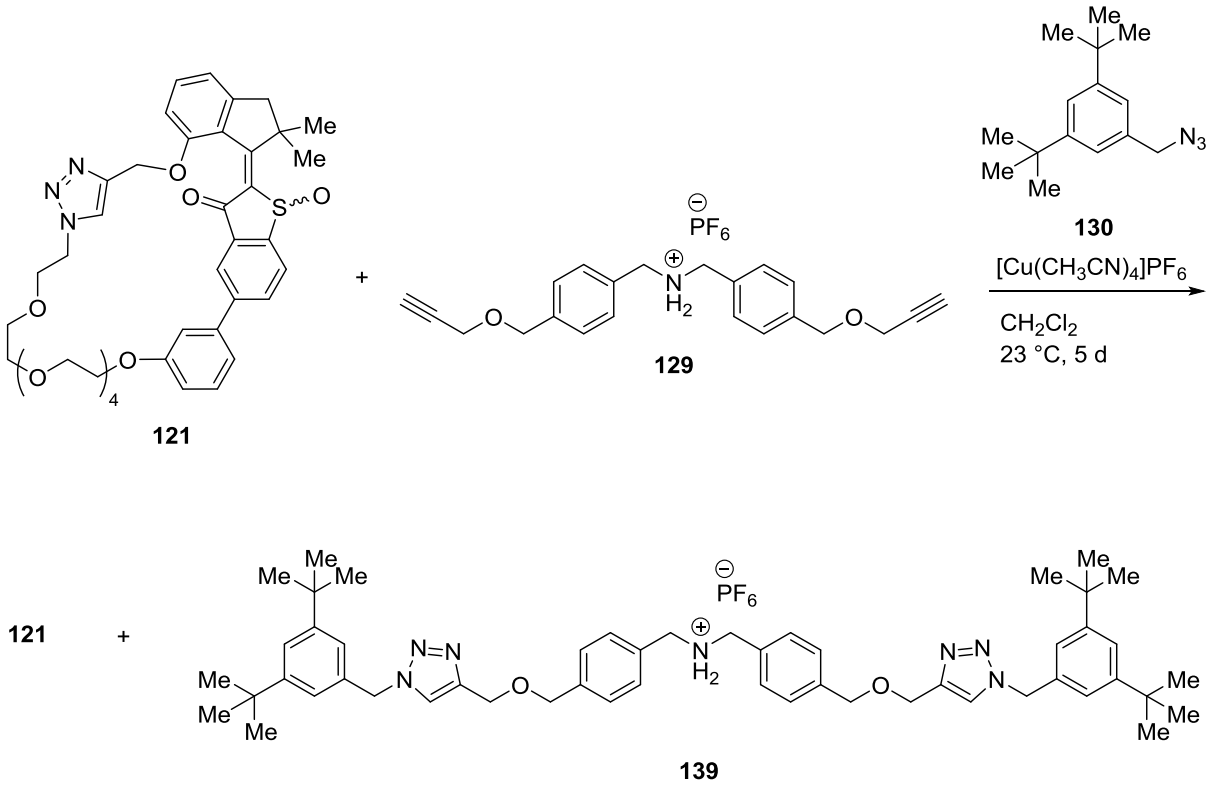

Scheme 65 Attempted construction of a rotaxane. Macrocycle **121** (mixture of *E* and *Z* configured isomers) was mixed with propargyl functionalized axle **129** (1 eq). After 30 min azide stopper **130** (2 eq) and Cu(I) containing catalyst were added. Workup after 5 d afforded macrocycle **121** and the free axle **139**.

An analogous reaction was conducted using diazide **134** and stopper **135** (Scheme 66). After stirring a CH_2Cl_2 solution, which also contained macrocycle **121** for 5 d at ambient temperatures no conversion of the starting materials was observed as judged by TLC monitoring. As a result the solvent was evaporated and the mixture was taken up in $CHCl_3$ and stirred at 50 °C for an additional 5 d. Significant amounts (60%) of the macrocycle **121** were recovered upon workup with no other isolatable products. This confirms earlier experiments were assembly of the track did not succeed under similar conditions (see Scheme 62).

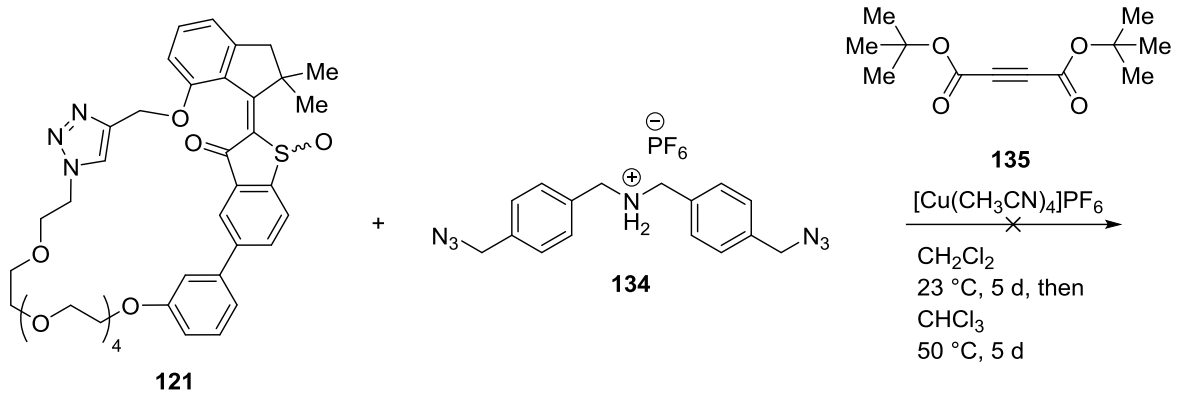

Scheme 66 Attempted construction of a rotaxane. Macrocycle **121** (mixture of *E* and *Z* configured isomers) was mixed with azide functionalized axle **134** (1 eq). After 30 min alkyne stopper **135** (2 eq) and the Cu(I) catalyst were added. After 5 d the solvent was exchanged with $CHCl_3$ and the mixture was stirred for 5 d at 50 °C. Significant amounts of macrocycle **121** were recovered upon workup but no cycloaddition products.

In summary no direct experimental evidence could be obtained that proved successful complexation of **121** and cations in either a crown-ether or rotaxane/catenane-type fashion. Still, highly promising interactions between macrocycle **121** and a variety of inorganic salts as well as organic dibenzylammonium hexafluorophosphate salts were observed. The presented work also offers a highly effective approach to a diol functionalized dibenzylamine that was functionalized further in a straightforward manner. This in combination with a general procedure for the generation of the respective hexafluorophophate salts provides a versatile basis for the construction of mechanically interlocked molecules.

Complexation results were mainly judged on the basis of proton signals of **121** in the NMR spectrum, which experience strong shifts upon addition of selected cations. The observed chemical shifts were not limited to distinct parts of the macrocycle and no selective binding mode could be determined. From these results it must be concluded that interaction of **121** with the presented cations was highly unselective as the molecule offers a variety of possible binding sites. It must also be considered that interpretation of the molecular structure of macrocycle **121** as a crown ether analog is not straightforward as the molecule exhibits a variety of rigid parts that can substantially hamper complexation. In addition to that, ^{1}H NMR experiments indicate that complexation of cations by *E* configured **121** is highly favored compared to the *Z* configured isomer. As discussed earlier the *E* configured isomer possesses the more relaxed PEG tether owing to the geometry of the central part. Because of the overall higher flexibility complexation capabilities could be significantly enhanced for this isomer. This could also

indicate that the length of the PEG-type linker is still not sufficient to allow for the threading of an extended cationic compound. Based on these results synthesis of a macrocycle with an extended PEG chain was conducted next.

6.4 HTI 149

6.4.1 Synthesis of HTI 149

Construction of HTI **149** proceeded similar to the synthesis of HTI **121** with octaethylene glycol instead of hexaethylene gycol as starting material for the covalent linker synthesis (see also Scheme 49). Again *Appel* conditions were applied in order to obtain the dibromo functionalized polyether **141** (Scheme 67a). The reaction, however, did not furnish the product. Instead the starting material and monosubstituted byproduct were obtained. In another attempt additional equivalents of tetrabromomethane were used and the reaction time was increased by one day but again no product formation was observed. This continues the trend for the reaction that reveals decreasing effectiveness when substituting PEG substrates with increasing chain lengths.

An alternative route started with tosylation of the terminal hydroxy groups to **142** and subsequent substitution with lithium bromide (Scheme 67b). The product **141** was obtained in good yields over two steps. Overall this approach was much more feasible for longer PEG substrates compared to direct bromination under *Appel* conditions as time consuming separation from reaction byproducts, in particular triphenylphosphine oxide is avoided. A drawback was the additional synthetic step that was required. Reaction of **141** sodium azide completed the synthesis of bifunctionalized linker **143**.

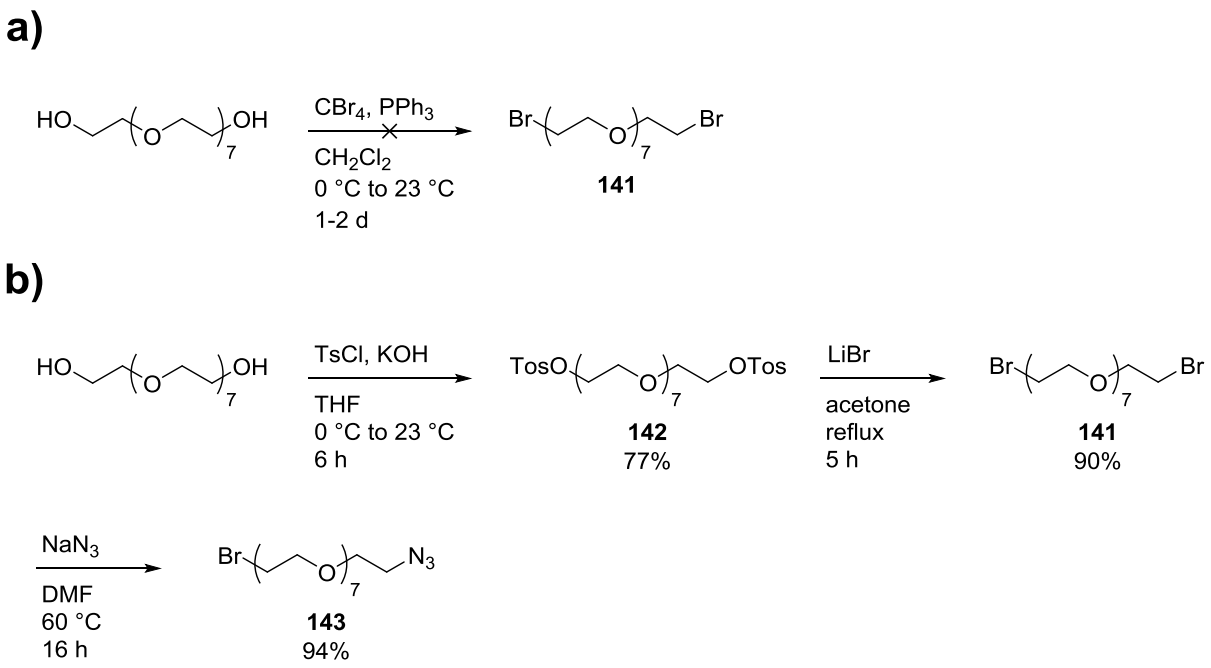

Scheme 67 Synthesis of bifunctionalized linker **143**. a) Conversion of octaethylene glycol under *Appel* conditions did not give the dibrominated product **141**. b) An alternative route via the toluenesulfonate ester **142** and reaction with lithium bromide furnished **141** over two steps. Subsequent substitution with sodium azide gave **143**.

Simultaneously another route was attempted that constructs the polyether from two functionalized tetraethylene glycol units (Scheme 68). The dibromo intermediate **144** was prepared applying *Appel* conditions. Synthesis of the complementary azide **145** was achieved via tosylation and subsequent substitution with azide. The two PEG fragments were then used to construct the bifunctionalized octaethylene glycol **143**. Due to the overall low yields and increased number of synthetic steps this approach was not pursued any further. Nevertheless this route offers an alternative for the stepwise construction of functionalized polyethers.

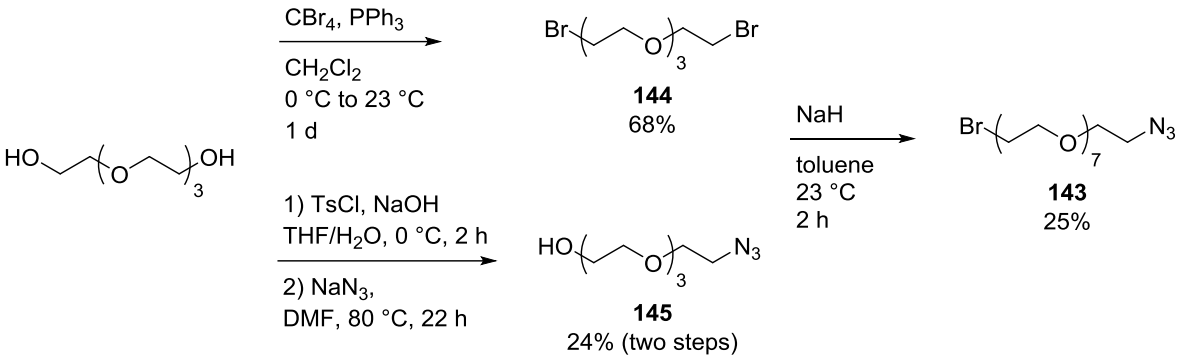

Scheme 68 Two complementary functional analogs **144** and **145** were prepared starting from tetraethylene glycol. Bifunctionalized octaethylene glycol **143** was constructed in the final step.

In the next step the PEG tether **143** was reacted with 3-hydroxyphenylboronic acid pinacol ester (Scheme 69). Building block **146** was obtained in a yield of 78%.

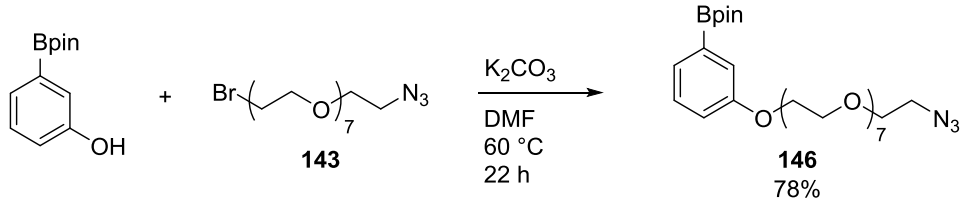

Scheme 69 Reaction of 5-hydroxyphenylboronic acid pinacol ester with functionalized octaethylene glycol **143** gave **146**.

Reaction of **146** with the established HTI fragment **75** in a copper catalyzed *Click* reaction gave triazole **147** in good yields (Scheme 70).

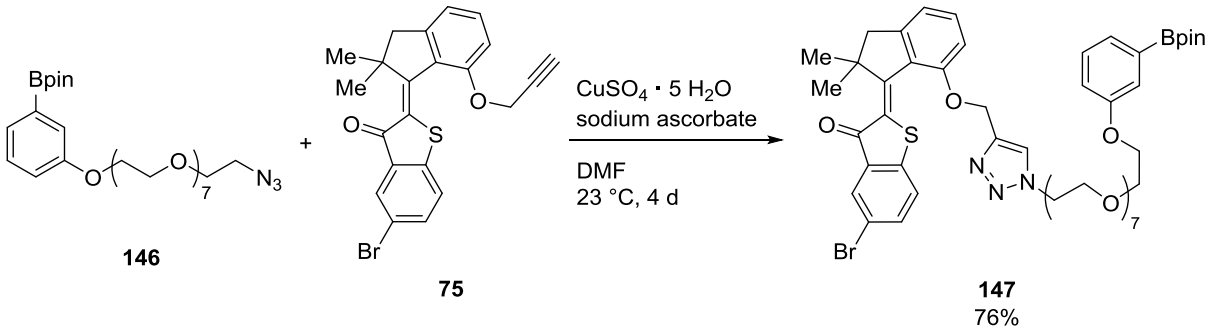

Scheme 70 Copper catalyzed 1,3-dipolar cycloaddition of boronic acid pinacol ester **146** and HTI **75**. The product **147** was obtained as a mixture of *E* and *Z* isomers. Only the *Z* configured isomer is shown.

The macrocycle was fused in an intramolecular *Suzuki-Miyaura* cross-coupling (Scheme 71). The product **148** was obtained in 50% yield.

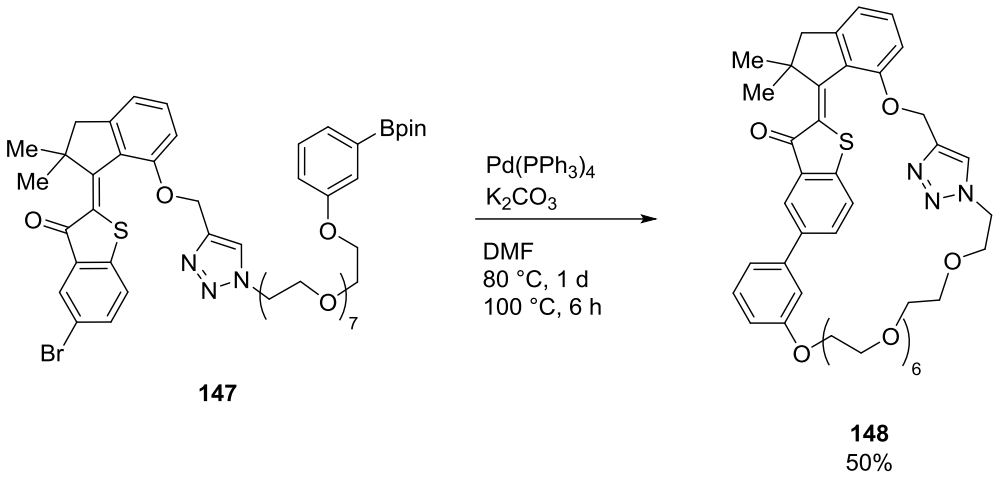

Scheme 71 Intramolecular *Suzuki* cross-coupling of **147** to **148**. Only the *Z* configured isomers are shown.

The synthesis was completed with oxidation of **148** to the corresponding sulfoxide **149** using sodium perborate tetrahydrate in acetic acid (Scheme 72). After five hours at ambient temperatures the crude product was obtained in 31% yield as a mixture of *E* and *Z* isomers.

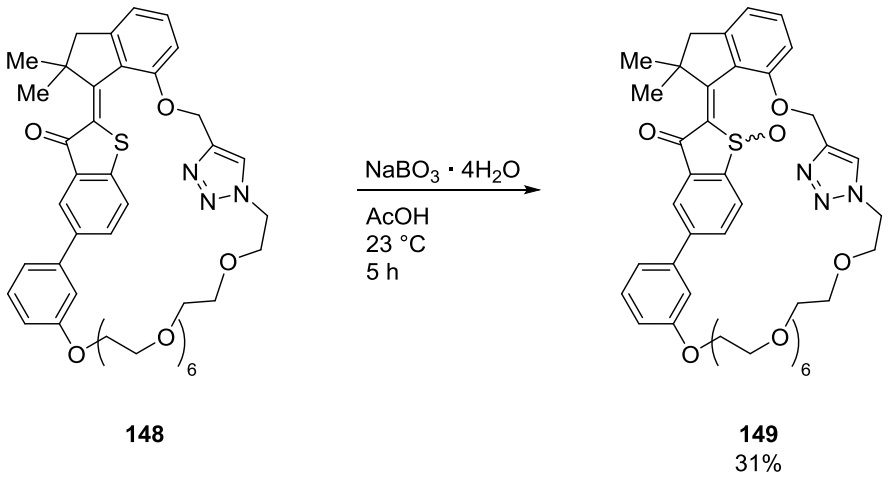

Scheme 72 Oxidation of **148** to the sulfoxide **149** using sodium perborate tetrahydrate in acetic acid. The target compound was obtained in moderate yields. Only the *Z* configured isomers are shown.

Purification on a chiral HPLC column in combination with HRMS analysis revealed a minor byproduct that was readily removed. During the separation process a strong background absorption was observed on the HPLC PDA detector. Separation of the product was also

accompanied by a huge loss of material even on repeated runs using the same sample. Identical results were obtained from separation on a reversed phase HPLC column. A possible explanation is the binding of cations by macrocycle **149** during the synthesis that results in highly polar complexes. Another indicator that supports this theory is the HRMS ESI analysis that delivered a high resolution mass peak solely for the sodium complex of **149**. As a result it was concluded that the HPLC columns and separation methods (normal and reverse phase) are not suited for the separation of the target compound. To remove possible cations a solution of **149** in toluene was stirred in the presence of the competing chelating agent [2.2.2]cryptand following a literature procedure.[74] In order to assess the decomplexation attempt ^{1}H NMR spectra of **149** before and after treatment with [2.2.2]cryptand were taken. However, no change of chemical shifts were observed and the issue remained inconclusive. Also, assignment of the observed conformers to structures with either *E* or *Z* configuration of the central double bond was not possible by 2D NMR. Similar to the previous macrocycle **121** with integrated hexaethylene glycol tether numerous attempts to obtain a crystalline sample of **149** were unsuccessful. Overall these results showed, that increasing the PEG tether length results in target compounds being in a liquid rather than a solid state at ambient temperatures.

6.4.2 Irradiation behavior at ambient temperatures

A solution of a pure isomer of **149** (racemic mixture of **149** with either *E* or *Z* configured central double bond) in CH_2Cl_2 was irradiated with light of different wavelengths (Figure 160, green line). After 10 min irradiation with 470 nm light a distinct isomerization behavior was observed (Figure 160, blue line). Continued irradiation with different wavelengths did not establish isobestic points for the individual spectra. Also, the initial pss obtained by irradiation with 470 nm could not be restored by prolonged irradiation using this wavelength. A possible explanation is the presence of additional photoactive compounds or initially complexed cations that cause this odd isomerization behavior.

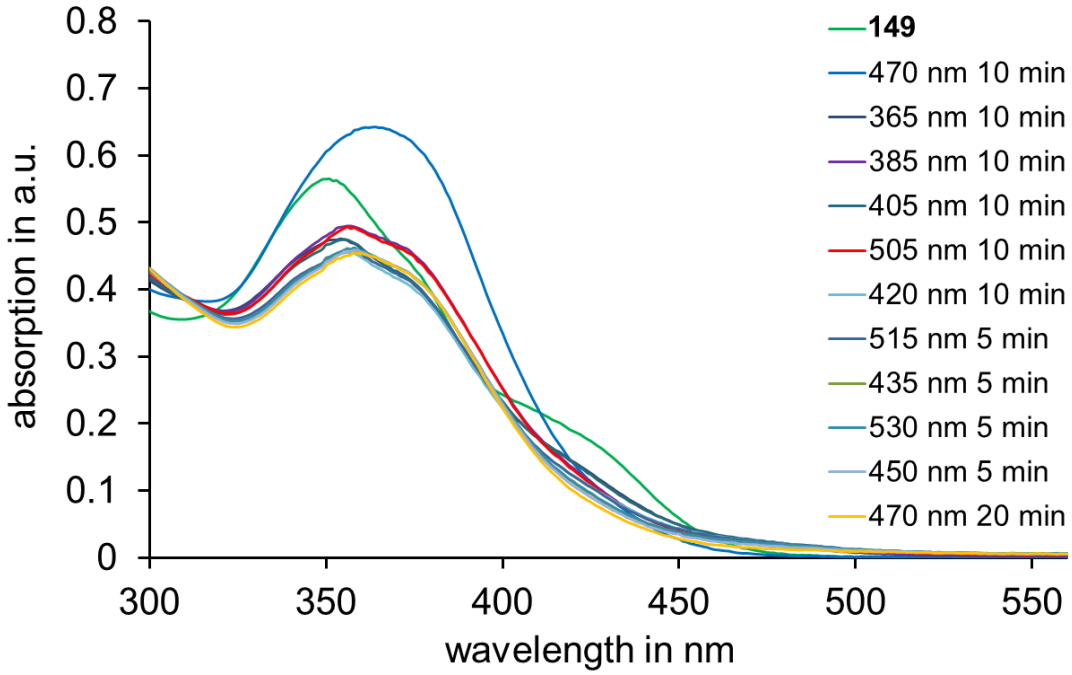

Figure 160 UV-Vis spectra of **149** (CH_2Cl_2, 23 °C) obtained after irradiation with light of different wavelengths.

The irradiation experiment was repeated using ^{1}H NMR analysis as this facilitates identification of individual isomers and possible decomposition of the sample (Figure 161).

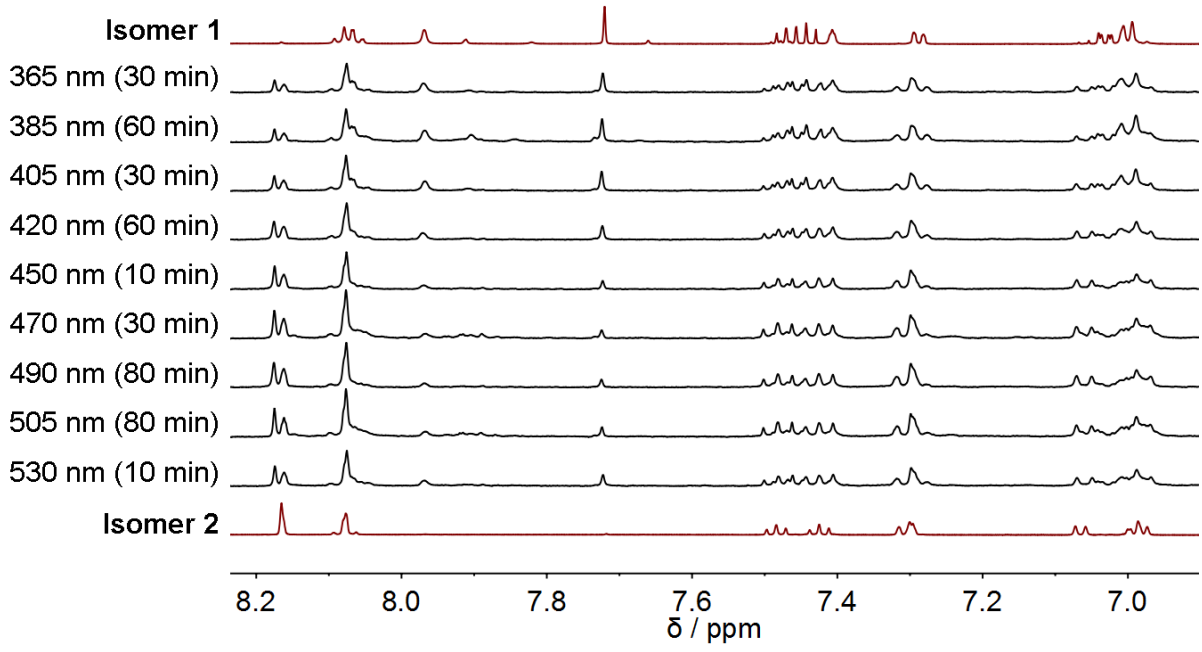

Figure 161 ^{1}H NMR spectra of pure isomers of **149** (Isomer 1 and Isomer 2, 599 MHz, CD_2Cl_2, 30 °C) and spectra obtained after irradiation with light of different wavelengths (400 MHz, 1.0 mM solution in CD_2Cl_2, 22 °C). Highest concentrations of isomer 1 (75%) were obtained from 60 min 385 nm irradiation, highest concentrations of isomer 2 (76%) after 80 min 490 nm irradiation.

The spectra revealed photoisomerization between the two isomers of **149**. Highest concentrations of up to 75% of the initial isomer were obtained from 385 nm irradiation, the second isomer was obtained in up to 76% using wavelengths between 450 nm and 490 nm. An overview of the isomer distribution is given in Table 9. Minor impurities were observed in the spectrum even after several consecutive separation steps on HPLC that could not be identified.

Table 9 Isomer distribution (*E* or *Z* configured central double bond) obtained after irradiation of **149** (1.0 mM solution in CD_2Cl_2, 22 °C) with light of different wavelengths.

wavelength [nm]	irradiation time [min]	Isomer 1	Isomer 2
365	30	44%	56%
385	60	75%	25%
405	30	55%	45%
420	60	50%	50%
450	10	25%	75%
470	30	39%	61%
490	80	24%	76%
505	80	37%	63%
530	10	57%	43%

6.4.3 Complexation attempts

Compared to the hexaethylene glycol analog **121** the new system can form a larger cavity for the complexation of cations. Different to the crown ether analogs (e.g. [24]crown-8) with an overall flexible PEG chain the macrocycle in **149** is expanded by the rigid HTI central part that could hamper coordinative binding of the oxygen atoms to the cation (Figure 162). On the other hand this could open up the possibility to bind a range of cations as the inner diameter of the macrocycle is less defined compared to [24]crown-8 ether which only allows for a highly selective binding of a few cations.

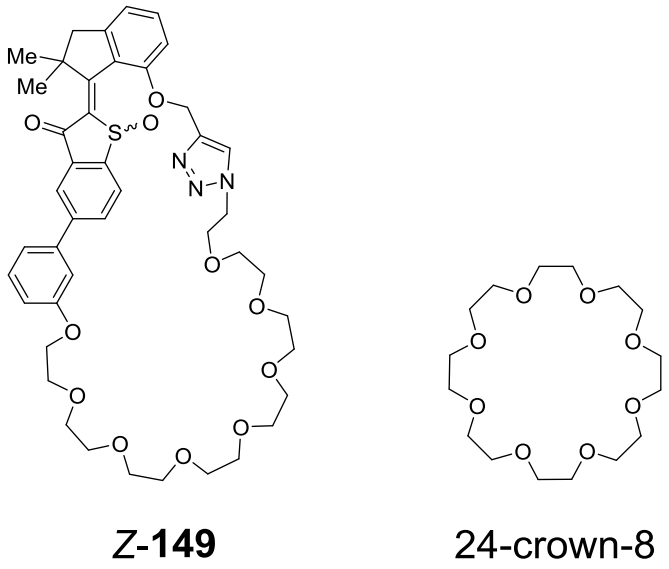

Z-**149** 24-crown-8

Figure 162 Comparison of *Z*-**149** and the crown ether analog 24-crown-8. The octaethylene glycol tether of *Z*-**149** is expanded by the rigid part of the molecule highlighting its possible enhanced flexibility.

In a first complexation attempt a pure sample of **149** (Isomer 1) in CD_2Cl_2 was mixed with an excess of NH_4PF_6. A comparison of the spectra before and after addition of the salt did not reveal changes in chemical shifts (Figure 163).

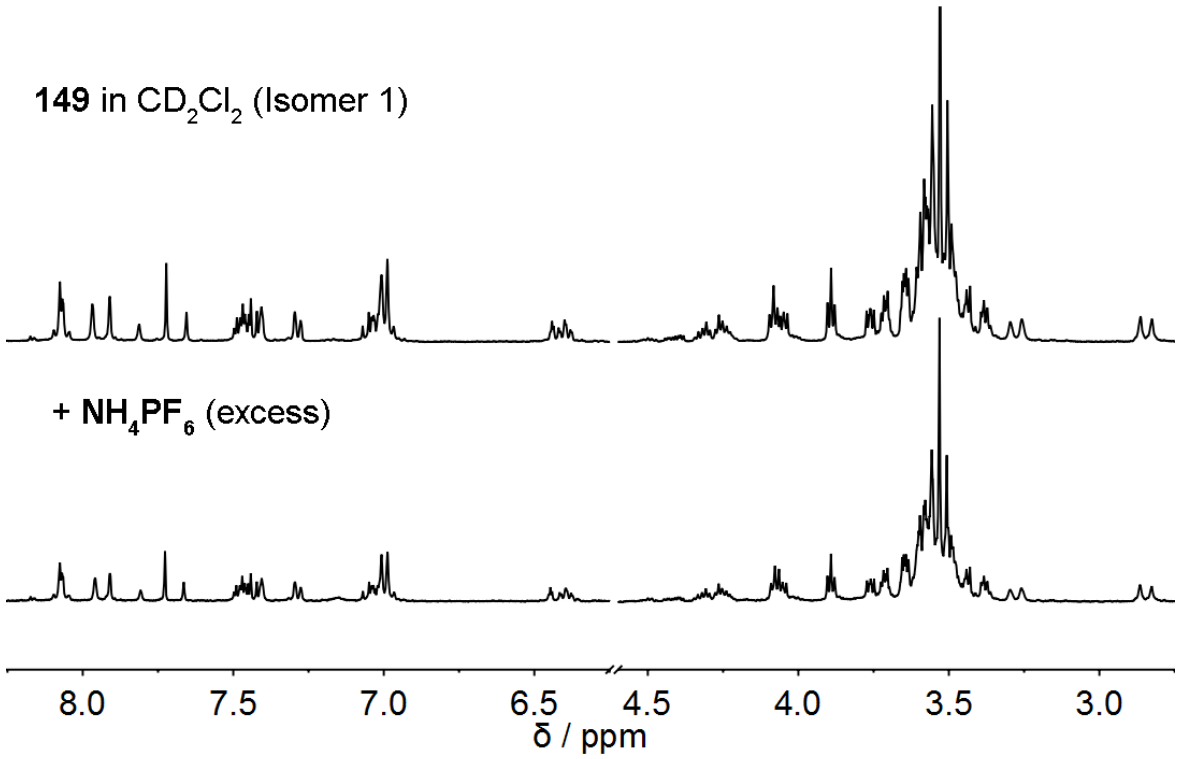

Figure 163 Selected regions of the ^{1}H NMR spectra of **149** (Isomer 1, 400 MHz, CD_2Cl_2, 22 °C) before (top) and after (bottom) addition of an excess of NH_4PF_6. The central part of the spectrum containing the solvent signal is cut out for clarity.

The experiment was repeated using MeOD as solvent (Figure 164). Again addition of an excess of NH_4PF_6 did not result in notable differences in terms of chemical shifts or splitting of signals. Minor shifts of signals (indicated in Figure 164) cannot be interpreted as distinct binding interactions given the excess (> 50 fold) in cation concentration.

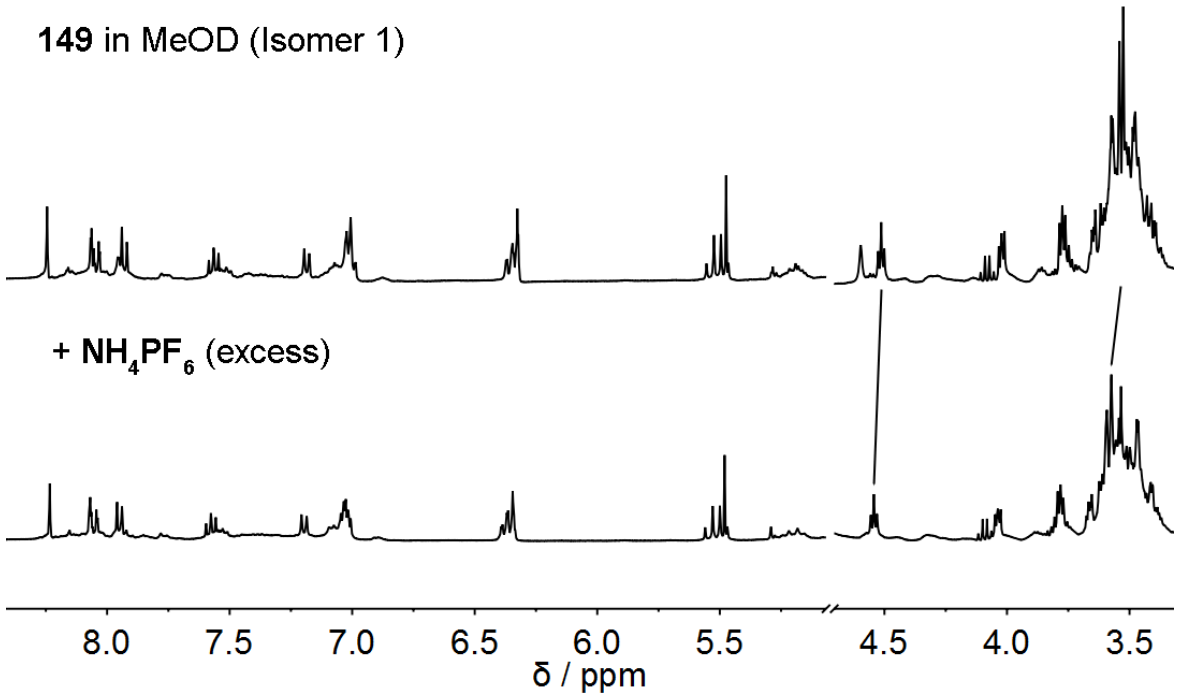

Figure 164 ^{1}H NMR spectra of **149** (Isomer 1, 400 MHz, MeOD, 22 °C) before (top) and after (bottom) addition of an excess of NH_4PF_6. The solvent signal is cut out for clarity.

Another solvent that offers good solubility for the complexation experiments is acetonitrile. A solution of **149** in MeCN-d_3 was prepared and an excess of NH_4PF_6 was added (Figure 165). Only minor shifts of selected signals were observed indicating a very weak binding interaction. Because of this KPF_6 was added to the same sample resulting in identical chemical shifts of proton signals. The solution was kept in the dark for a total of 4 d to guarantee complexation processes are in equilibrium without any observable effect (not depicted). Finally an excess of $CsCO_3$ was added (Figure 165, bottom). Changes in the spectrum stem from a slow thermal *E*/*Z* isomerization with no indication of successful binding of the cation.

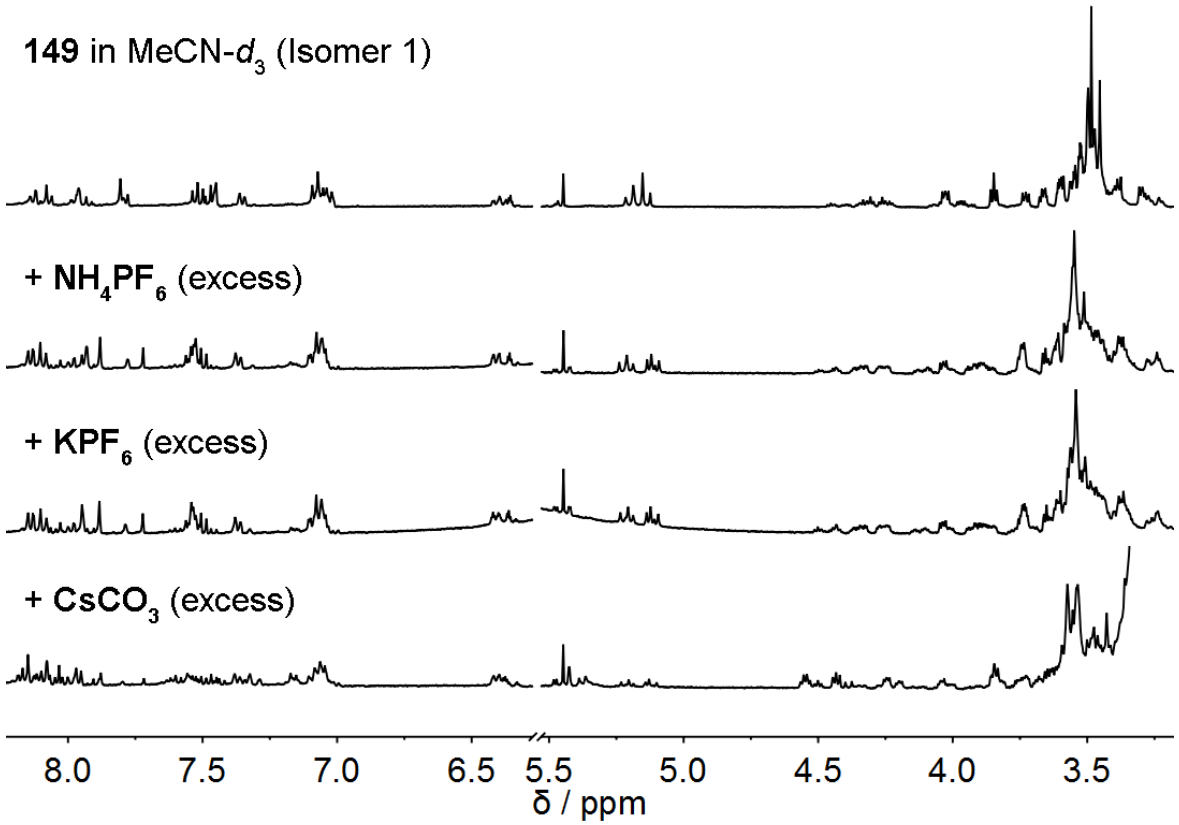

Figure 165 ^{1}H NMR spectra of **149** (Isomer 1, 400 MHz, MeCN-d_3, 22 °C) before (top) and after successive addition of an excess of NH_4PF_6 then KPF_6 then $CsCO_3$. The ammonium signal is cut out for clarity.

Overall no successful complexation was observed upon addition of NH_4^+, K^+ or Cs^+ to a solution of **149** in a variety of solvents. A possible explanation is the complexation of cations already during the synthesis of **149**. This is indicated by the odd separation behavior on HPLC where the product is found distributed over huge polarity range as well as the detection of the compound in HRMS analysis as sodium salt [**149**Na]$^+$. In this case, the added cations could not compete against the binding of sodium indicating a highly stable complex with the latter.

Another explanation would be the geometry of **149** that might not allow for a strong cation interaction. This however is contradictory to previous results from macrocycle **121** with a shorter tether that revealed binding as judged by the shift of the whole signal set in the ^{1}H NMR spectrum. It must also be noted that experiments were conducted only for one isomer of **149** (*E* or *Z* configured central double bond) and in very low concentrations as a result of the tedious purification process. Also, assessment of the complexation properties is solely based on differences in chemical shift, which cannot be interpreted as a direct measure of the actual underlying binding constants.

Decomplexation of the product before separation on a HPLC column could drastically increase the obtainable yields and improve the validity of subsequent binding studies. To this end more efficient methods for the purification of the target compound must be developed, for example by increasing the concentration of the competing chelating agent [2.2.2]cryptand in combination with longer reaction times. Another approach would be an adjusted synthesis of the target compound that avoids reagents containing certain cations, such a sodium, which can form complexes with the product or its intermediates – a task that is very difficult to realize in practice.

As mentioned earlier the construction of functional rotaxane and catenane type molecules is the primary goal of the conducted studies. With the current design of the macrocyclic compounds the envisioned interaction of the motor part with interlocked molecules is severely hampered by the triazol unit that is established during the construction of the covalent linker. Because of this the focus of future efforts is shifted into the direction of macrocycles with a solely PEG based linkers that directly attaches to the indanone rotor and aryl follower. The removal of the triazole unit also reduces the size of the rigid backbone, which greatly restricted the possible geometries of the macroyclic compounds. Overall the development of new methods to integrate a covalent tether within the target compounds would allow for the construction of more sophisticated molecular machines in the future.

7 Photocontrol of polar aromatic interactions by a bis-HTI based helical receptor

7.1 Introduction

Precise control of molecular motions is a fundamental subject of this work. From the groundbreaking development of molecular motors, that was taken one step further to controlled transmission of such motions. All these achievements are based on sophisticated interactions of photoinduced isomerizations with tailored steric interactions affecting the energy landscape of a single molecule. A first supramolecular approach was realized with integrated macrocyclic HTIs with extended ring sizes (see sections 6.3 and 6.4). Non-covalent binding of selected cations was envisioned in a crown-ether type fashion but rigidity of the HTI backbone in combination with additional binding sites did not allow for the precise determination of underlying interactions. In the following it will be demonstrated that binding interactions between a photoswitchable HTI based host and selected guests can be precisely determined and quantified.

A different, yet related type of supramolecular recognition is based on polar aromatic interactions. Parallel stacking of aromatic rings results in weak interactions that play a crucial role in many chemistry related fields such as templation and self-assembly[61,62,91] or molecular receptors[92–95]. Aromatic stacking is ubiquitous in nature enhancing the base pairing ability in DNA/RNA and enabling the non-destructive intercalation of drugs.[96,97] Four possible modes were determined for the stacking of two aromatic rings that comprise energetic minima (Figure 166).

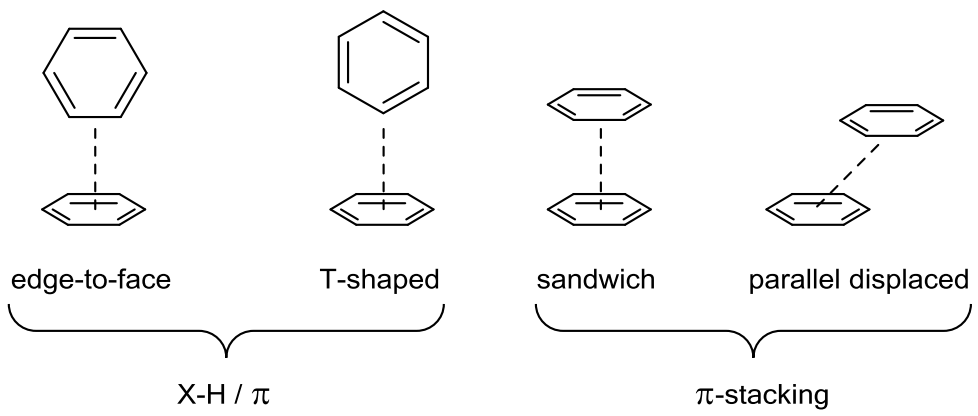

Figure 166 Calculated modes of benzene stacking that represent energetic minima.

An in depth theoretical analysis of the benzene dimer found similar binding energies for sandwich, edge-to-face and parallel displaced structures ranging from 2.4 kcal·mol^{-1} to 2.7 kcal·mol^{-1}.[98] A detailed analysis of the underlying interactions revealed no preferred stacking in the case of unsubstituted (non-polarized) hydrocarbons. Instead, the adopted geometry is a function of orientation angle and offset.[99] In this model the interaction is driven by electrostatic interactions of the π-clouds (Hunter-Sanders model) where π-systems are described as positively polarized σ-frameworks in between two clouds of negatively polarized π-electron density (Figure 167a).[100] Introduction of substituents or heteroatoms also affects interactions between neighboring π-clouds. Electron donating substituents for example increase the electron density of the π-system and therefore repulsive interactions whereas electron poor substituents reduce repulsion (Figure 167b). This theoretical approach was successfully applied to a model porphyrine compound that explains the experimentally observed off-set stacking by maximizing attractive intermolecular σ-π interactions. It was also shown in this context that the interaction of π-systems is repulsive in general as a parallel (non-offset) orientation is generally disfavored. This also excludes attractive van-der-Waals forces as the major driving force for stacking interactions as these energies are proportional to the π-overlap, which does not match the experimentally observed off-set geometries. However, van der Waals forces, solvophobic effects as well as charge-transfer modulate the magnitude of the interaction.[101]

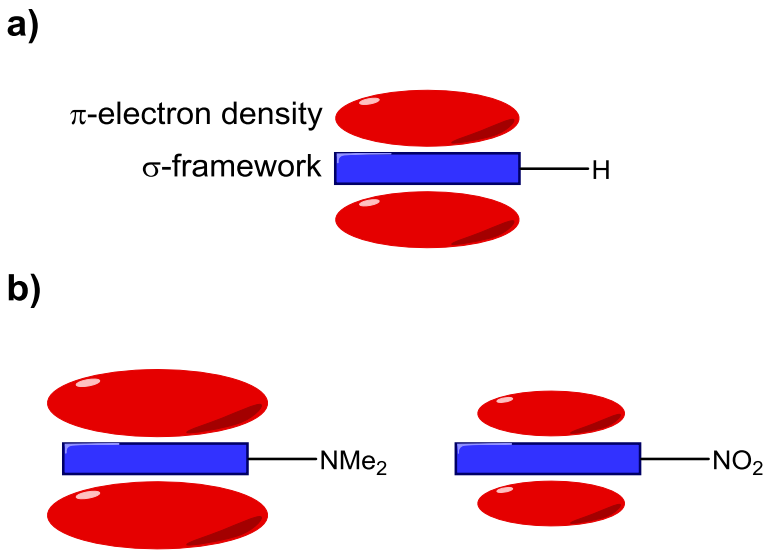

Figure 167 Schematic representation of the Hunter-Sanders model. a) A positively charged σ-framework is embedded between clouds of negatively charged π-electron density. b) Electron donating groups, (i.e. NMe_2) increase π-electron density and repulsion between two aromatic molecules. Electron withdrawing groups (i.e. NO_2) reduce electron density stabilizing the interaction.

When *Grimme* took a comprehensive look at non-covalent aromatic stacking interactions he found that there is little difference between saturated cycloalkenes and analogous aromatic systems for small molecules (< 10-15 carbon atoms).[102] Later results showed that aromaticity can even lead to a decrease in interaction strength when compared to analog polyenes with localized π systems as delocalization of π electrons in benzene shifts electron density towards the center of the ring increasing the quadrupole moment and therefore repulsion in the dimer.[103,104] Fluorination of an aromatic system however greatly alters the electrostatic potential transferring electron density from the ring center (i.e. in benzene) to the periphery (i.e. in perfluorbenzene), greatly enhancing the ability to engage in electrostatic interactions.

The electrostatic theory came under fire when theoretical studies predicted an additive effect of multiple substituents with a linear dependence of interaction energies on the number of substituents.[105] This was proven experimentally with fluorinated arenes[106] and is contrary to expectations based on the Hunter-Sanders model where interaction strength is modulated by π-polarization where additional substituents should have a decreasing effect. More recent theoretical calculations were also contradictory to the simple electrostatic model where binding strength is modulated by donating or withdrawing electron density from the π-system. Multiple studies reported that all substituted benzene dimers bound more strongly compared to the benzene dimer, irrespective of their electronic nature[107] and parallel displaced structures are stabilized stronger than their T-shaped counterparts.[108,109] Experimental results showed, that even a strong electron donor substituent like OMe increases π-stacking interactions.[110]

A revised model by *Wheeler* and *Houk* explains these finding by direct interactions of local dipoles of substituents with benzene (Figure 168a).[111] A correlation of the interaction energies and the Hammet σ_m values of 24 differently substituted benzene derivatives revealed a linear relationship, with the unsubstituted benzene dimer being an outlier. This was explained by direct dispersive interactions between the substituent and the aromatic system of the dimer counterpart. When the substituted benzene (Ar-X) is reduced to a simple hydrogen atom (H-X) the same linear relationship is observed, further proving the prevalence of direct interactions of the substituent with the neighboring aromatic ring (Figure 168b). The theory of local, direct interactions also correctly predicts that stacking interactions are additive, regardless of whether the substituents are on the same or opposite aromatic ring.[112] This is again a strong contradiction to the simple electrostatic model (Hunter-Sanders) where binding strength is modulated dominantly by donating or withdrawing electron density from the π-system.

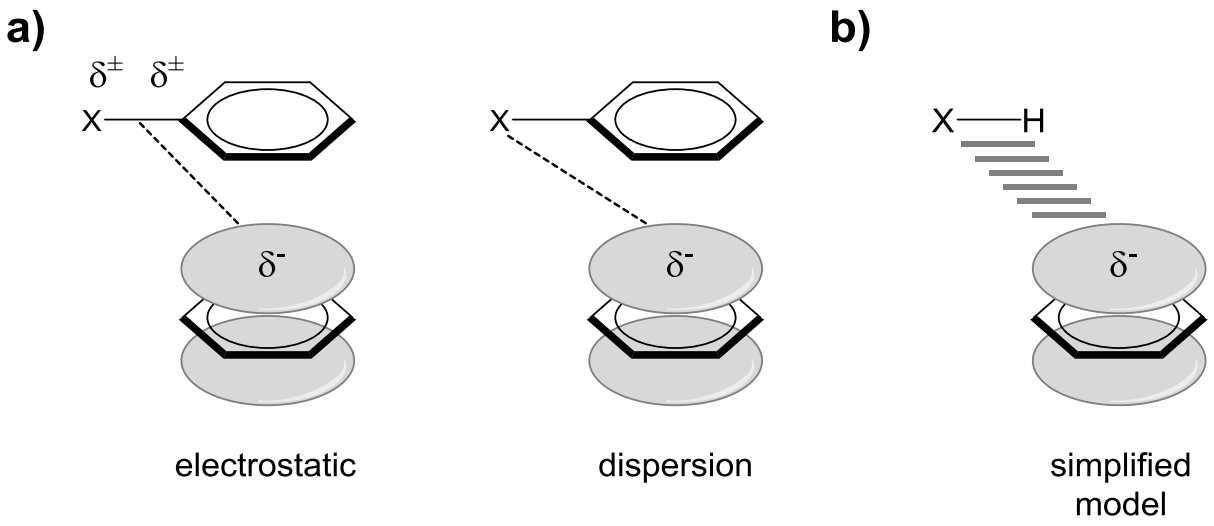

Figure 168 Schematic representation of the local, direct interaction model established by Wheeler and Houk.[104,110] a) Substituent effects arising from electrostatic and dispersive interactions. b) Generalized depiction of direct, local interactions. Replacing the substituent bearing aromatic ring with a proton results in the same trend for relative interaction energies.

In 2017 *Riwal et al.* used a Rebek amide receptor with two differents spacers to control the overlap of two aromatic platforms. When one aromatic ring was allowed to overlap with the substituent of the other, a stabilizing effect was observed, independent of the electronic nature of the substituent (Wheeler-Houk model). When this overlap was prevented by the use of a shorter linker a linear correlation of the stacking interactions with the Hammet substitution parameter σ_m was observed indicating an electrostatic influence (Hunter-Sanders model).[113] This shows, that stacking interactions are clearly a result of intermolecular distance and geometry and several aspects have to be considered to understand the underlying effects.

The electron distribution over the aromatic rings, referred to as quadrupole moment, allows the molecule to engage in a variety of polar aromatic interactions for example with cations, partial charges, dipoles or other quadrupoles. These interactions are highly selective and can be applied for molecular recognition in a field that was termed *host-guest chemistry*.[114]

When two binding units are preorganized in a way that enables "sandwich" type complexation of aromatic guest molecules an exponential increase in binding affinity is observed (Figure 169). Compounds able to form such π-systems are i.a. referred to as *molecular tweezers*.[115] Complexation via aromatic interactions is enhanced when certain prerequisites are met: 1) A rigid spacer between the complexing moieties prevents self-association. 2) The distance

between the binding sites is ~7 Å to allow for the sandwich-type stacking of aromatic systems. 3) A rigid *cis* conformation.

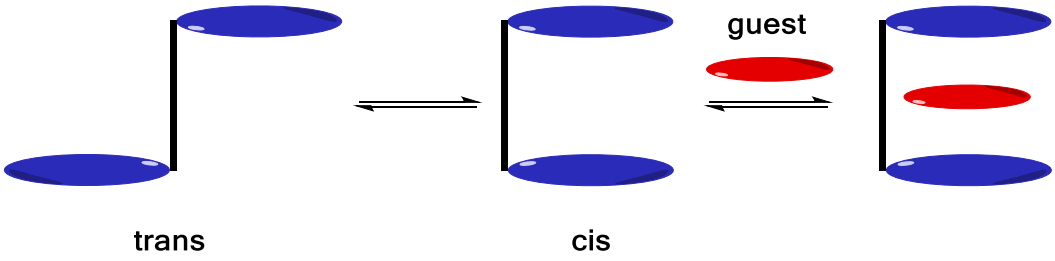

Figure 169 Model system for the formation of a "sandwich" π-system.

An early system developed by *Chen* and *Whitlock* satisfies two of these characteristics where binding caffeine moieties are fixed in a ~7 Å distance by a rigid diyne spacer (Figure 170). Experimental results clearly proved the expected exponential increase in associated binding constants. It is noteworthy, that a parallel orientation of the caffeine units is not crucial. In the example given in Figure 170 the caffeine moieties cannot close to an angle less than ~30° however, the associated binding constant with potassium 1,3-dihydroxy-2-naphthoate (DHNA) is 10^4 M^{-1} compared to $4 \cdot 10^2$ M^{-1} for the pure caffeine compound.

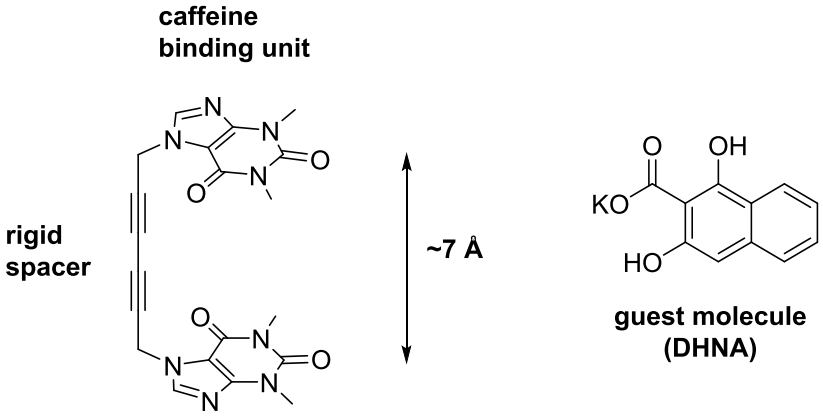

Figure 170 Example of a molecular tweezer and guest by *Chen* and *Whitlock*. Two caffeine binding units are separated by a rigid diyne spacer. A preorganized *cis* conformation is not established as the linker allows free rotation of the caffeine moieties.

Another class of tweezers established by *Klärner* also features a non-parallel orientation of two aromatic pincers (Figure 171).[116] In these compounds the requirement of a rigid *cis* configuration is met. In aqueous solution self-assembly into dimeric structures is observed that are broken when a competing guest like *N*-methylnicotinamide iodide is added. While the

differentiation of a macrocycle and a *Klärner*-type molecular tweezer become increasingly blurry the *Klärner* clip behaves more like the molecular tweezer defined by *Whitlock*. X-ray single crystal analysis even showed that upon complexation of an electron deficient guest the pincers of a bisanthracene clip are compressed reducing the distance of the endmost carbons from 10 Å to 7.6 Å.[117]

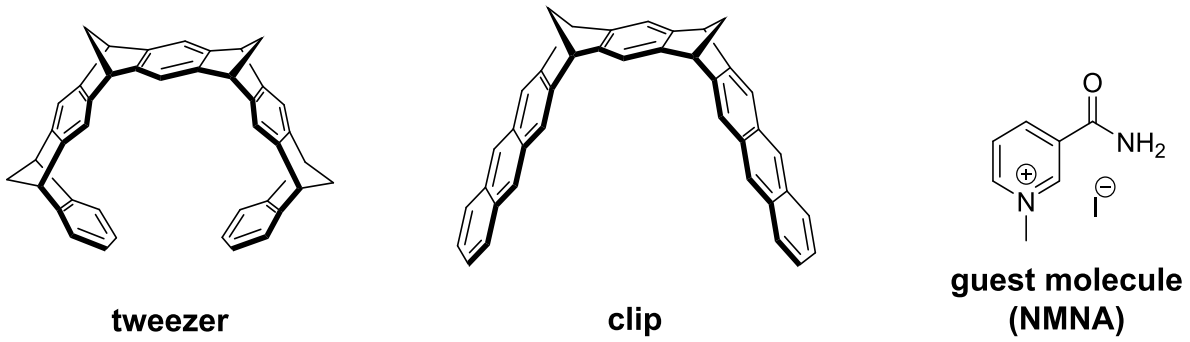

Figure 171 Representation of benzene-spaced molecular tweezer scaffolds established by *Klärner*. The tweezer bearing two anthracene units (middle) is referred to as "clip" by the group. Self-assembly in aqueous solution is overruled upon addition of *N*-methylnicotinamide iodide (NMNA).

Another system that employs a rigid spacer, which enforces *cis* configuration was developed by *Zimmermann*.[118] Here the complexing anthracene (Figure 172) or acridine moieties can rotate freely around the bond connecting them to the spacer allowing for conformational mobility in the binding process. The spacer establishes a ~7 Å distance of the binding units and a functional group within the cleft offers an additional attachment point for the modulation of binding interactions. Introduction of a carboxylic acid for example greatly enhances the stability of an adenine complex through additional hydrogen bonds.[119]

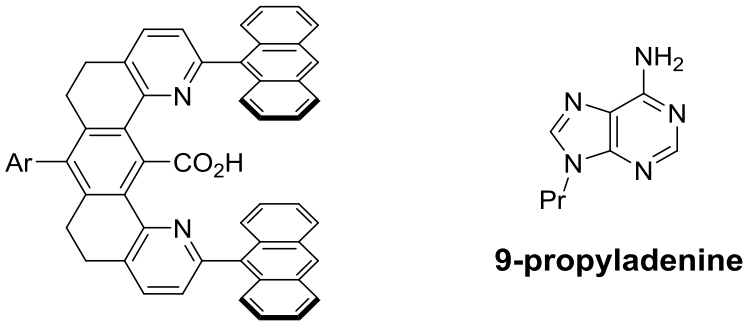

Figure 172 Example of a molecular tweezer developed by *Zimmerman*. A polycyclic spacer preorganizes two anthracene moieties in a distance of ~7 Å. Binding of an adenine analog is enhanced through additional hydrogen bonds to a carboxylic group within the cleft.

The presented systems have in common, that they offer very little direct control over the molecular recognition processes. Light as a clean, external and nonchemical stimulus for the control of supramolecular systems is of high interest.[120–123] The light induced *cis*-*trans* isomerization in azobenzenes for examples offers the possibility of significant geometrical changes.[124] *Hua* and *Flood* developed a helical foldamer that incorporates two azobenzene end groups (Scheme 73).[125] Irradiation with UV-light can be used to modulate the affinity of the receptor to chloride therefore controlling the conductivity of an electrolyte solution. In the thermodynamically favored all-*trans* conformer (Scheme 73, left) the azobenzene units are coplanar with the molecules backbone and the maximum number of π-contacts in the overlapping, helical form. Irradiation with 365 nm light generates the all-*cis* conformer, breaking coplanarity and resulting in lower affinity to chloride ions. Irradiation with 436 nm light is used to restore the all-*trans* conformer.

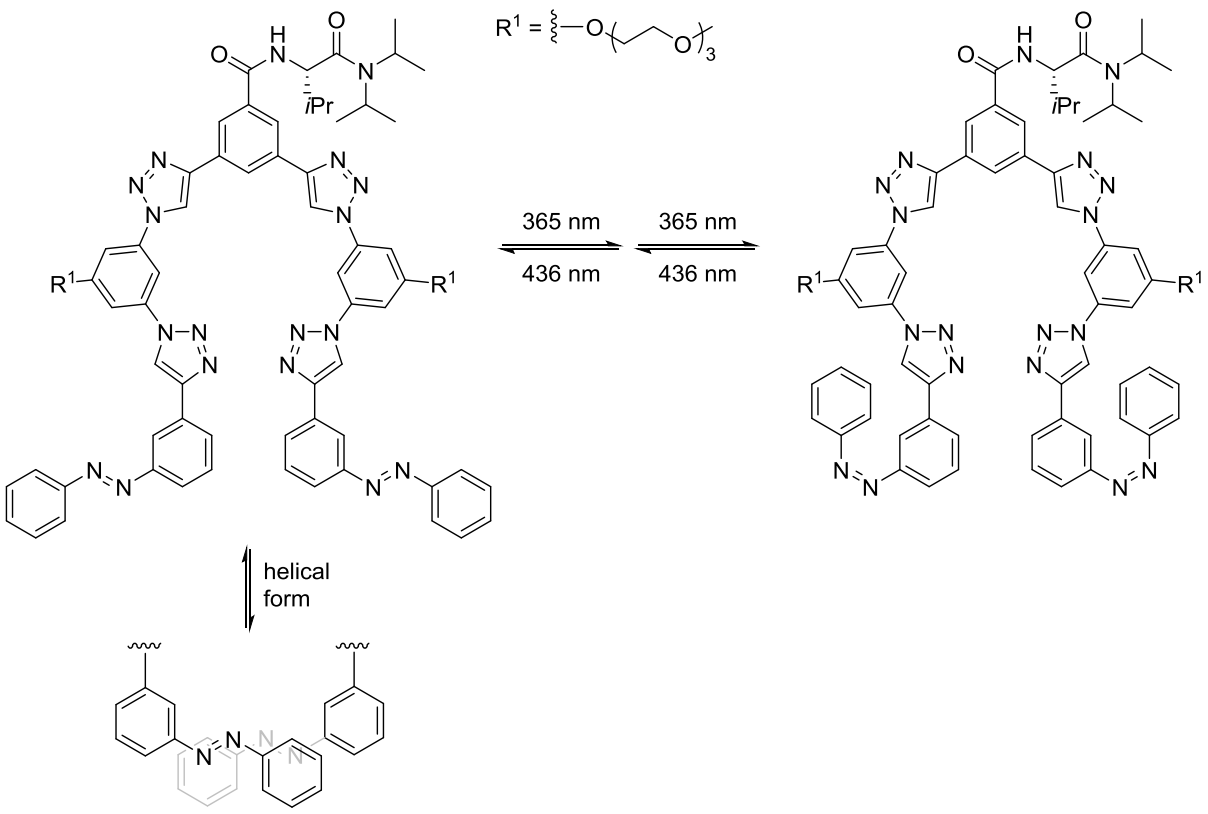

Scheme 73 Light-active foldamer developed by *Hua* and *Flood*. The all-*trans* conformer (left) stabilizes the helical form that reveals a high affinity to chloride ions in solution. The all-*cis* conformer is generated by irradiation with 365 nm light and is dominated by coil formation. Irradiation with 436 nm light restores the all-*trans* conformer.

Studies within the *Hecht* group demonstrated that incorporation of azobenze into a foldamer core allows photocontrol over helix-to-coil transitions and led to the successful development of "turn-off" helices.[126,127] A photoresponsive bis(crown ether) tweezer developed *Shinkai* et al. features an azobenzene core and uses the fast thermal relaxation of the *cis*-state to control the K^+ ion transport across a liquid membrane (Figure 173a).[128] Another azobenzene based tweezer established by *Choi et. al*. is used to modulate the receptors affinity to chloride ions (Figure 173b).[129] Cooperative binding of two urea (or thiourea) functional groups in the *cis*-state of the tweezer greatly enhances chloride ion transport across lipid and cell membranes.

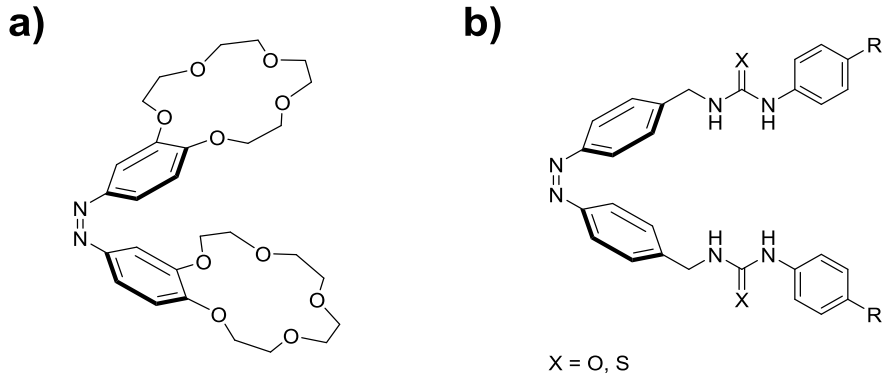

Figure 173 Examples of azobenzene based tweezers. Both receptors are depicted in the UV-light induced *cis* configuration. a) Bis(crown ether) developed by *Shinkai* et al. that selectively binds large alkali metal cations. b) Chloride anion transporter established by *Choi* et al.

The presented examples demonstrate that incorporation of photoresponsive units has huge potential for the control of molecular geometries and recognition processes. In molecular tweezers photoswitches can simultanously act as spacers to control preorganization of the binding units to actively and reversibly modulate their affinity. Common drawbacks of established systems are low thermal stabilities, photodegredation as well as the requirement of UV-light that greatly limits the application in biochemistry related fields. This places the focus on different chromophores like dithienylethenes[130,131] or HTIs that exhibit high bistabilities and provide addressability with visible light.

Bis-HTI **158** as a receptor for the photocontrolled polar aromatic interaction with electron deficient guests was developed and first synthesized by *Manuel Güntner*. Preliminary tests on a few selected, electron deficient aromatic guest molecules had already been conducted. The receptor features an asymmetric bis-HTI spacer that is connected to two biaryl pincers. Rotation of the connecting single bonds is restricted by preorganizing *n*-pentyl substituents in *ortho*

position. Upon irradiation with visible light the s-shaped planar *Z,Z* configuration is switched to a helical *E,Z* configuration that is able to bind electron deficient guests through electron-rich aniline end groups. Heating restores the *Z,Z* configuration.

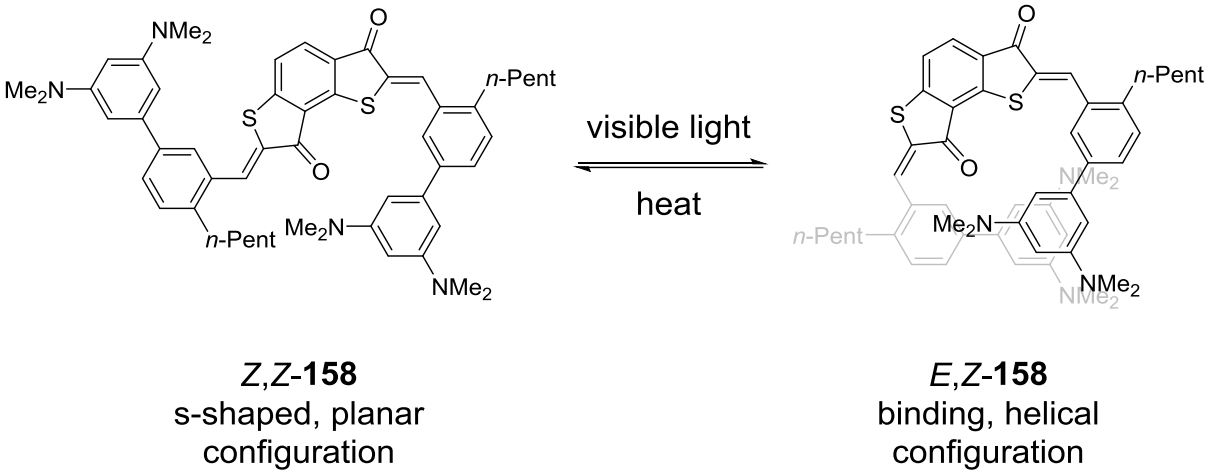

***Z*,*Z*-158**
s-shaped, planar
configuration

***E*,*Z*-158**
binding, helical
configuration

Scheme 74 Bis-HTI based molecular receptor developed by *Güntner*. Two complexing biaryl moieties are separated by an asymmetric bis-HTI spacer. Rotation around the connecting single bonds is restricted by preorganizing *n*-pentyl groups. Irradiation with visible light generates the helical *E,Z* conformer that is able to bind electron-deficient, aromatic guest through electron-rich terminal anilin groups. The non-binding *Z,Z* conformer is restored upon heating.

The aim of this work includes the revision of the synthesis, optimization of reaction conditions and increase of target compound purity. Subsequent screening of additional aromatic and electron-poor molecules should reveal suitable guests that show a high binding affinity to the receptor. Reversibility of the guest capture-and-release should be tested by multiple heating and irradiation cycles. Finally, titration experiments had to be optimized to precisely determine the binding constants. For detailed information about the development of the receptor, structures in solution and in the solid state as well as kinetic analyses see the literature.[132,133]

7.2 Synthesis of HTI 158

The synthesis started with commercially available 5-bromo-1,3-benzenediamine **150** (Scheme 75). Methylation was achieved following a literature procedure for the methylation of ethyl 3,5-diamino benzoate.[134] A suspension of $NaBH_4$ and 5-bromo-1,3-benzenediamine in THF was added to a –15 °C solution of formaldehyde (25% in H_2O) in H_2SO_4 using a Pasteur pipette with a broken off tip to ensure that the suspension does not clog the pipette. Fresh suspension

was taken up when evolution of gas upon addition decreased. Yields of **150** could be improved from 37% up to 79% using this methodology. The following palladium catalyzed *Miyaura*-Borylation of **151** with bis(pinacolato)diboron furnished **152** in excellent yields as a white solid that takes on a pinkish tone upon exposure to air.

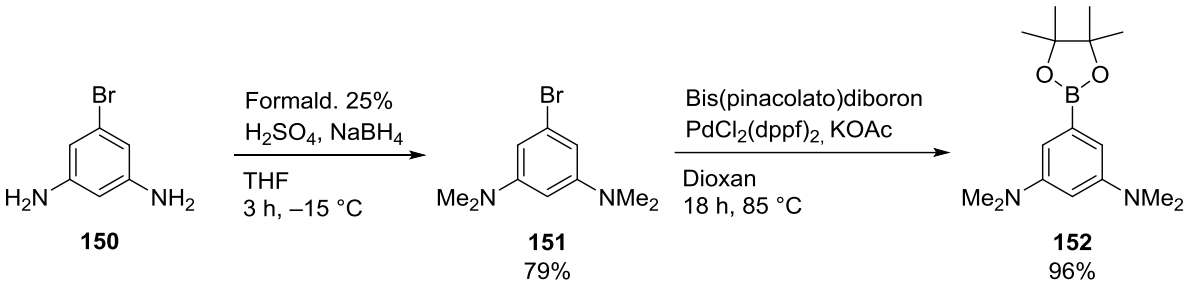

Scheme 75 Synthesis started with methylation of diamine **150** to **151**. *Miyaura*-Borylyation gave boronic acid pinacol ester **152**.

Extension of the methyl group of **153** to an *n*-pentyl chain was achieved analogously to a literature procedure (Scheme 76).[135] Subsequent electrophilic iodination of **154** *para* to the alkyl group using *Selectfluor* gave benzaldehyde **155** in excellent yields. Acetonitrile as solvent plays a crucial role in the regioselectivity of this reaction.[136] As compound **155** is prone to decomposition the crude product was used directly in the next synthetic step.

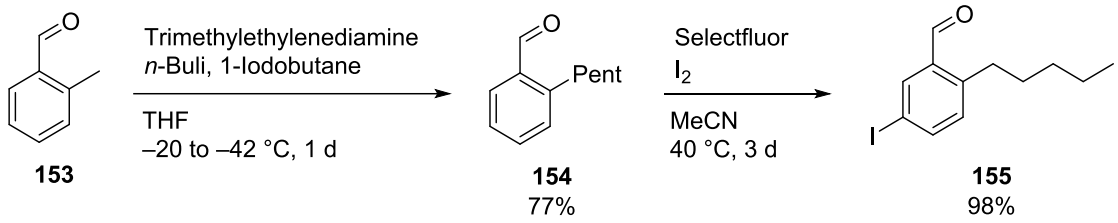

Scheme 76 The methyl group of **153** was extended to an *n*-pentyl using *n*-Buli and 1-iodobutane in the presence of trimethylenediamine. Iodination of the product **154** was achieved using *Selectfluor* and afforded **155**.

Suzuki-Miyaura coupling of building blocks **152** and **155** gave biaryl **156** in moderate yields (Scheme 77). The product was kept under an inert gas atmosphere as it slowly decomposes upon exposure to air.

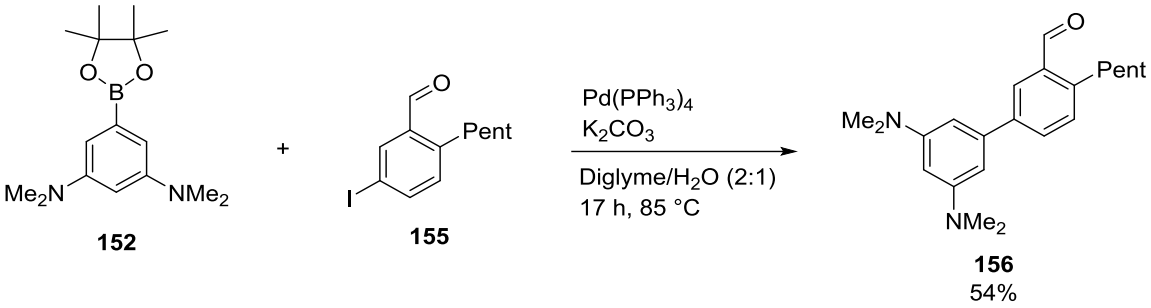

Scheme 77 Reaction of buildings blocks **152** and **155** in a *Suzuki-Miyaura* coupling afforded biaryl **156**.

Condensation of two equivalents of biaryl **156** with asymmetric bis-benzothiophenone **157** (provided by *Manuel Güntner*) furnished bis-HTI **158** exclusively with *Z,Z* configuration of the central double bonds (Scheme 78). The reaction was initiated through addition of catalytic amounts of piperidine (1 drop) to a solution of the starting materials in toluene. Increasing the temperature to 40 °C for one hour was found to be the optimal reaction condition. Still, some amounts of biaryl **156** remained unreacted and could be recovered. The product was obtained in 38% yield, however, the purity was not sufficient for further experiments and it was therefore attempted to crystallize the product in order to gain a high purity sample.

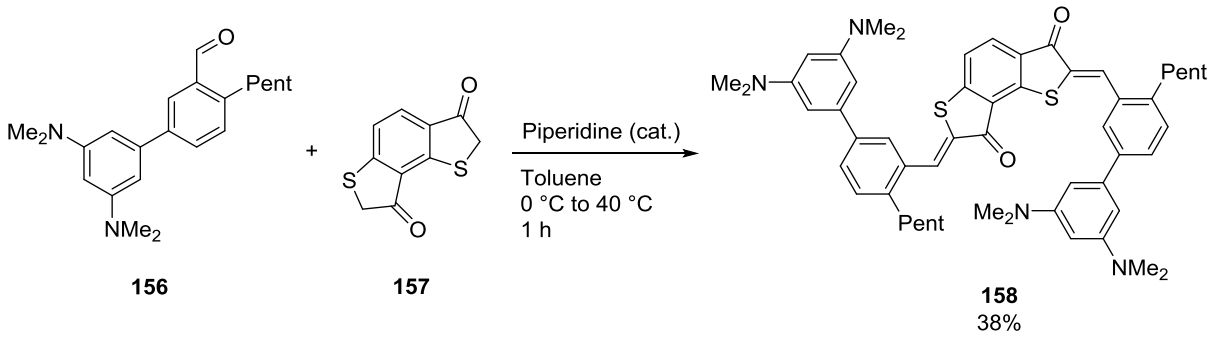

Scheme 78 Condensation of bis-benzothiophenone **157** and two equivalents of biaryl **156** using catalytic amounts of piperidine afforded the target compound **158**.

Precipitation, or ideally crystallization of a compound can occur when a solution exceeds its point of saturation. This can be achieved for example by slowly evaporating the solvent or by saturating a solution at elevated temperatures and subsequent cooling. The latter was found to be an efficient way to give bis-HTI **158** in very high purities. To this end compound **158** was suspended in *n*-heptane and carefully heated to reflux to prevent decomposition of the solid material by local overheating. Then, EtOAc was added dropwise until a clear solution was

obtained. Upon cooling compound **158** precipitated as a red powder, which was used in the following experiments.

7.3 Physical and photophysical properties of bis-HTI 158

The described synthesis provided bis-HTI **158** exclusively in its thermodynamically most stable *Z,Z* configuration. The conformation of the central double bonds as well as the adjacent single bonds in solution was unambiguously proven by comprehensive NMR studies.[133] Rotation of the single bonds connecting the biphenyl units to the asymmetric thioindigo core was effectively controlled by sterically demanding *n*-pentyl groups. As a result only one out of four possible *Z,Z*-**158** conformers was observed. Crystals suitable for single crystal crystallography could be obtained that confirmed the proposed structure.

Irradiation of a solution of *Z,Z*-**158** in toluene leads exclusively to formation of the *E,Z* isomer (Figure 174). A maximum of 94% was obtained using a wavelength of 420 nm. No other conformers (*Z,E* or *E,E*) could be detected by NMR spectroscopy proving that only one double bond is selectively addressed by irradiation. Similar to the *Z,Z* conformer, rotation of the single bonds in the *E,Z* isomeric form is controlled by the *n*-pentyl substituents. Because of this preorganization the molecule adopts a helical conformation that can effectively bind electron deficient aromatic guests by interaction with the electron rich terminal anilin groups (Figure 174a).

Prolonged heating of an *E,Z*-**158** enriched solution in toluene restored the *Z,Z* configuration in > 95% yield (no visible traces of *E,Z*-**158** in ^{1}H NMR). Kinetic analysis revealed a free activation energy of 28.2 kcal·mol^{-1} for this process, which translates to a half-life of 2.4 years at 23 °C. The irradiation/heating process to switch between maximum *Z,Z* and *E,Z* concentrations can be repeated several times. However, when this process is followed by ^{1}H NMR, minor increases in signal to noise ratio can be observed, which indicates a slow decomposition of the molecule.

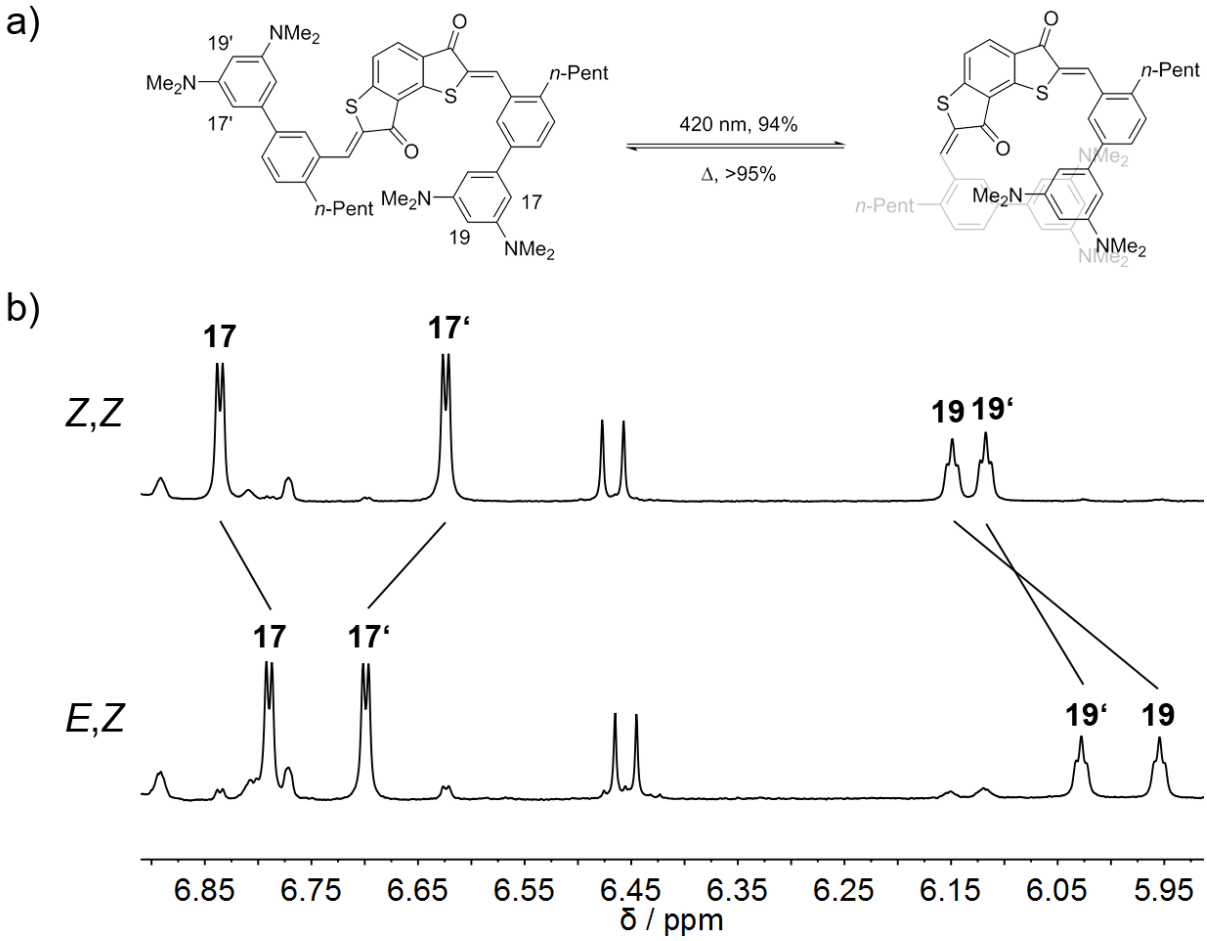

Figure 174 a) Photoisomerization of bis-HTI *Z,Z*-**158** to the *E,Z*-**158** isomer. The initial *Z,Z*-**158** isomer is quantitatively restored by heating. Indicative protons are marked with arbitrary numbers. b) ^{1}H NMR spectra of selected protons for the *Z,Z*-**158** and *E,Z*-**158** isomer.

7.4 Determination of the quantum yield of bis-HTI 158

An important property of a photoswitch is the ability to effectively convert to its isomer upon irradiation with a suitable wavelength. The amount of absorbed photons that are needed to induce such an isomerization are described by the quantum yield. The quantum yields of the photoconversions of *Z,Z*-**158** to *E,Z*-**158** and *vice versa* were calculated as the ratio of isomerized molecules to the number of absorbed photons at a certain wavelength using (*equation 10*. To calculate the number of photons absorbed during photoisomerization an experimental setup, analogous to a published version, was used.[87] Samples of *Z,Z*-**158** and *E,Z*-**158** in 2 mL of toluene with known concentrations were irradiated with 420 nm and 520 nm light, respectively. The number of absorbed photons were calculated from the absorption of the bis-HTI **158** solutions compared to a blank sample using a power photometer. UV-Vis spectra

of the samples were taken after each irradiation period and the change of absorption was plotted against time. The initial change in absorption is approximately linear as it is the results of the photoconversion of only one conformer. The slope of the fit can be used to calculate the quantum yield according to equation:

$$\Phi(\mathrm{Z} \rightarrow \mathrm{E}) = \frac{h \cdot c \cdot N_A \cdot V}{P \cdot \lambda_{\mathrm{ex}} \cdot l \cdot (\varepsilon(\mathrm{E},\mathrm{Z}) - \varepsilon(\mathrm{Z},\mathrm{Z}))} \cdot m \qquad \text{(equation 15)}$$

With h = Planck's constant $6.626 \cdot 10^{-34}$ J·s c = speed of light $2.9979 \cdot 10^{8}$ m·s^{-1}

N_A = Avogadro constant $6.022 \cdot 10^{23}$ mol^{-1} V = sample Volume

P = average absorbed power λ_{ex} = excitation wavelength

l = optical path length

$\varepsilon(E,Z)$ = molar absorption coefficient of *E*,*Z* at the excitation wavelength

$\varepsilon(Z,Z)$ = molar absorption coefficient of *Z*,*Z* at the excitation wavelength

The obtained quantum yields in toluene are 7.0%±2.0% for the *Z*,*Z*-**158** to *E*,*Z*-**158** isomerization at a wavelength of 420 nm and 0.12%±0.05% for the *E*,*Z*-**158** to *Z*,*Z*-**158** isomerization at a wavelength of 520 nm. For an in depth illustration of quantum yield determinations see section 4.5.

7.5 Screening of potential guest molecules

An important quality of a potential guest molecule is a high affinity to the receptor molecule, which is described by the binding constant *K*. Here, the binding constant is a measure for the tendency of two molecules, e.g. *E*,*Z*-**158** and guest molecule, to form a complex (denoted as *E*,*Z*-**158** ⊂ **guest**) in solution. The precise determination of binding constants requires several measurements with different concentrations and is therefore not feasible to quickly assess the binding affinity of a potential guest. In a complex the protons of *E*,*Z*-**158** in close proximity to the guest molecule should experience significant changes in their chemical environment. Even though the resulting chemical shift cannot be used to directly estimate the binding constant it can be an indicator for the interaction between the two molecules and was therefore used to quickly screen guests for their binding affinities.

The screening of some selected guests is shown in Figure 175. All tested molecules had either no impact on the chemical shift or caused a significant upfield shift. This can readily be explained by the intercalation of an aromatic guest molecule. The aromatic ring-current has a shielding effect on the terminal protons of the biphenyl units close to the binding site which resulted in the observed upfield shift. Pentafluorophenol (Figure 175, H) poses an exception to this rule but was not further investigated.

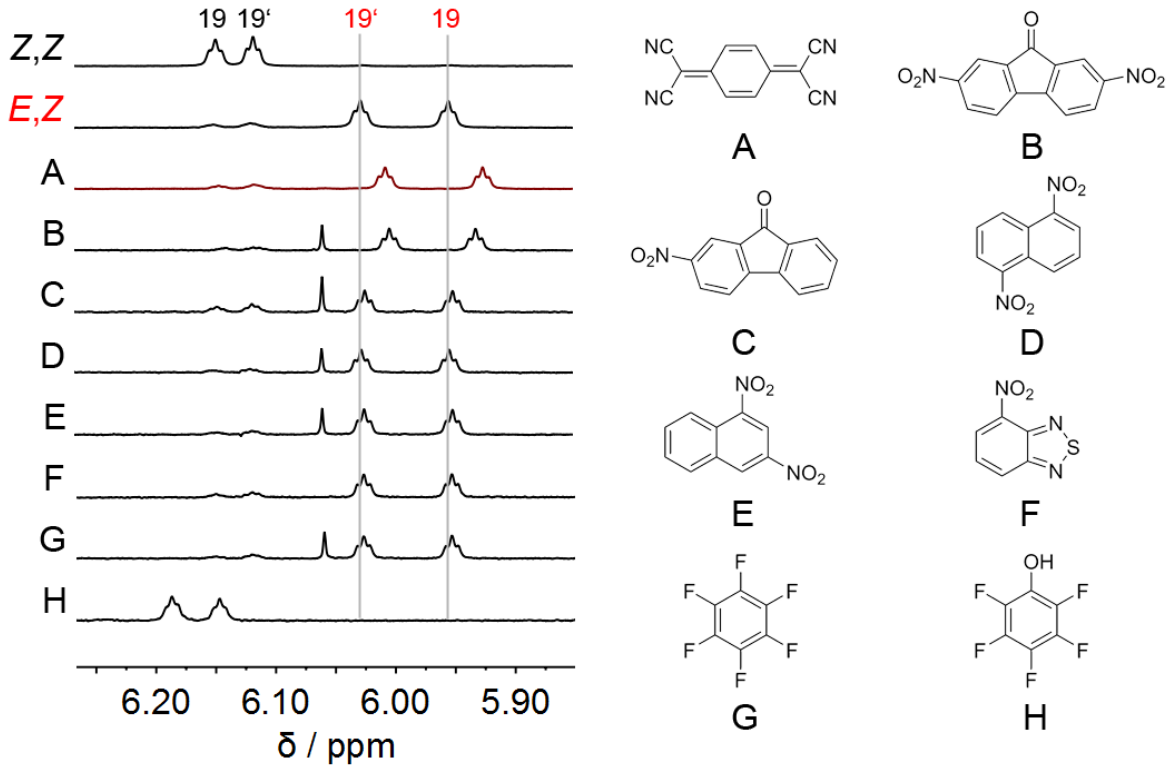

Figure 175 ^{1}H NMR screen of selected guest molecules (400 MHz, toluene-d_8, 23 °C). Shifts of indicative protons 19 and 19’ of *E*,*Z*-**158** with guest molecule (Spectra A-H) compared to the chemical shift of the pure spectrum of *E*,*Z*-**158** (indicated by grey bars) were used as a measure to estimate the binding affinity. Interactions with guest molecules A, B and H resulted in a clear deviation from the pure *E*,*Z*-**158** spectrum.

From the tested molecules that resulted in an upfield shift of indicative protons of *E*,*Z*-**158**, tetracyanoquinodimethane (TCNQ) and 2,7-dinitro-9-fluorenone showed the most promising results.

7.6 Evaluation of TCNQ as guest molecule

At the beginning of this work preliminary experiments by *Manuel Güntner* had determined a binding constant of ca. 200 $L \cdot mol^{-1}cm^{-1}$ for *E,Z*-**158** ⊂ TCNQ. Another important requirement is a low affinity of the guest to the "open" *Z,Z*-**158** isomer to guarantee effective release upon thermal *Z* to *E* isomerization. To this end conditions had to be found that could quantitatively restore the *Z,Z* isomer in a timely manner.

To test the reversibility of the photoinduced guest capture-and-release an NMR tube with a solution of bis-HTI *Z,Z*-**158** and TCNQ in toluene-d_8 was irradiated to the pss using 420 nm light (Figure 176). The sample was then wrapped in aluminum foil to protect it from ambient light and placed in an oil bath. It was found that prolonged heating up to the boiling point of toluene (111 °C) did not restore *Z,Z*-**158** in a quantitative manner. Increased temperatures were accessible when the NMR tube was tightly sealed and *parafilm* was applied. At 118 °C *Z,Z*-**158** could be fully restored within 1 d. When the temperatures exceeded 120 °C rapid decomposition of the sample was observed as significant amounts of indefinable black solids collected in the NMR tube. Below 120 °C this process was much slower but still occured after a few irradiation/heating cycles.

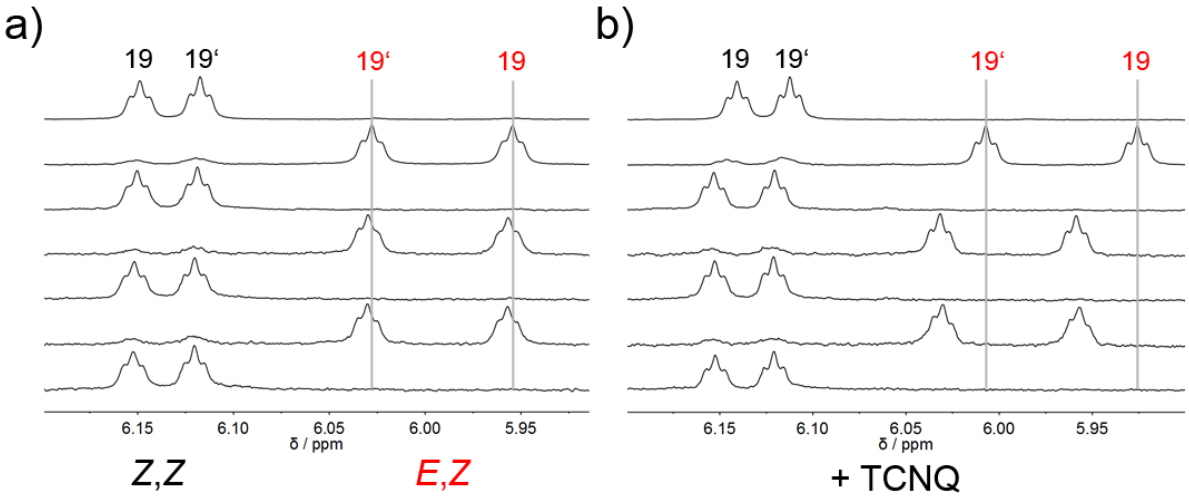

Figure 176 ^{1}H NMR (400 MHz, toluene-d_8, 22 °C) spectra of the reversible, photoinduced guest capture-and-release. A solution of *Z,Z*-**158** (^{1}H NMR signals marked with black numbers) in toluene-d_8 is repeatedly irradiated to the pss using 420 nm light to accumulate *E,Z*-**158** (^{1}H NMR signals marked with red numbers) followed by heating to 118 °C for 1 d to quantitatively restore the initial *Z,Z*-**158** isomer. a) Starting from pure *Z,Z*-**158** (no addition of guest) chemical shifts are almost fully reestablished for *E,Z*-**158** (grey bars) over several cycles. b) Starting from a solution of *Z,Z*-**158** and TCNQ initials shifts of *E,Z*-**158** ⊂ TCNQ cannot be reestablished (grey bars). The signals of *Z,Z*-**158** also reveal a minor downfield shift.

Decomposition of the samples was not visible in ^{1}H NMR by means of signals disappearing or new signals emerging. However, the initial shift of indicative host signals, caused by the intercalation of the guest molecule, could in no case be fully reestablished. Because of this TCNQ as guest molecule was discarded.

7.7 Fluorenes as guest molecules

Besides TCNQ, 2,7-dinitro-9-fluorenone showed promising results in the guest screening process. Interestingly, 2-nitrofluorenone, with only one nitro group, had a negligible impact on the chemical shift of bis-HTI *E,Z*-**158** in ^{1}H NMR. To gain further insight into the binding process different guest molecules with a nitrofluorene scaffold were screened for their binding affinities. To further increase the electron-deficiency, 9-dicyanomethylene analogs were prepared in a straightforward manner through condensation of the respective nitrofluorenones with malononitrile (Scheme 79).

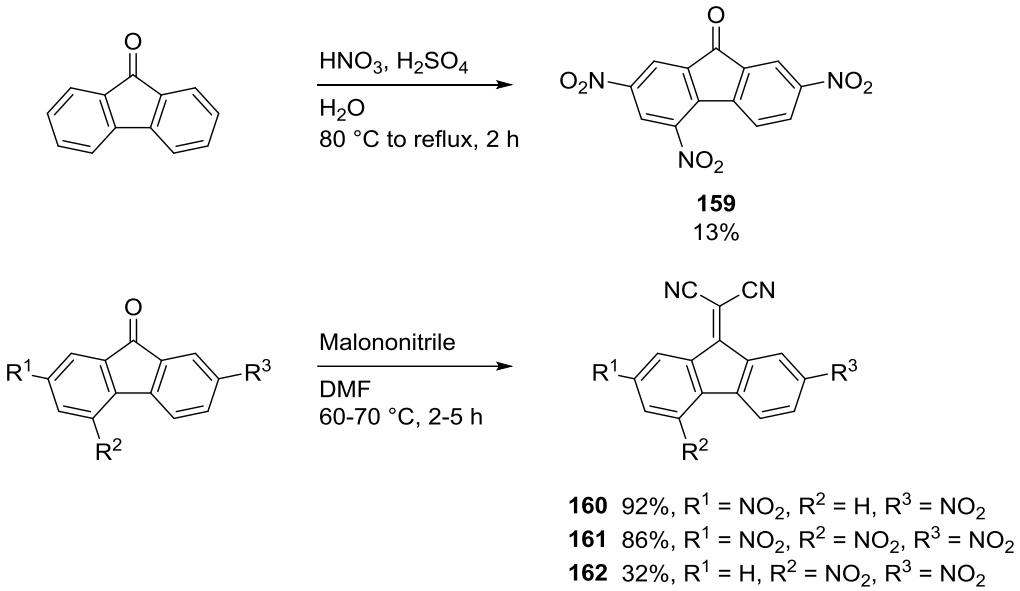

Scheme 79 Synthesis of 2,4,7-trinitro-9-fluorenone **159** and dicyanomethylene analogs **160**-**162**.

Nitration of 9-fluorenone furnished compound **159** in poor yields, most likely because of partially decomposed nitric acid, as 2,7-dinitro-9-fluorenone was obtained as a major byproduct. Condensation of the fluorenones with malononitrile at elevated temperatures in DMF gave the products in poor to very good yields.

All fluorene derivatives were screened for their binding affinity to bis-HTI *E*,*Z*-**158** (Figure 177). To this end, an *E*,*Z*-**158** solution in toluene-d_8 was treated with one equivalent of guest molecule. It showed, that the introduction of dicyanomethylene groups results in stronger upfield shifts of indicative protons compared to the analogous fluorenone compounds (Figure 177). Interestingly, compounds with a 2,5-dinitro substitution pattern revealed almost no impact on signal shifts. Addition of 9-Dicyanomethylene-2,7-dinitroflurene **160** and 9-Dicyanomethylene-2,4,7-trinitroflurene **161** resulted in the most prominent signal shifts of *E*,*Z*-**158** protons. Because fluorene **161** also showed strong interactions with the "open" *Z*,*Z*-**158** isomer (Figure 177, Spectrum 6), only compound **160** was further investigated as guest molecule.

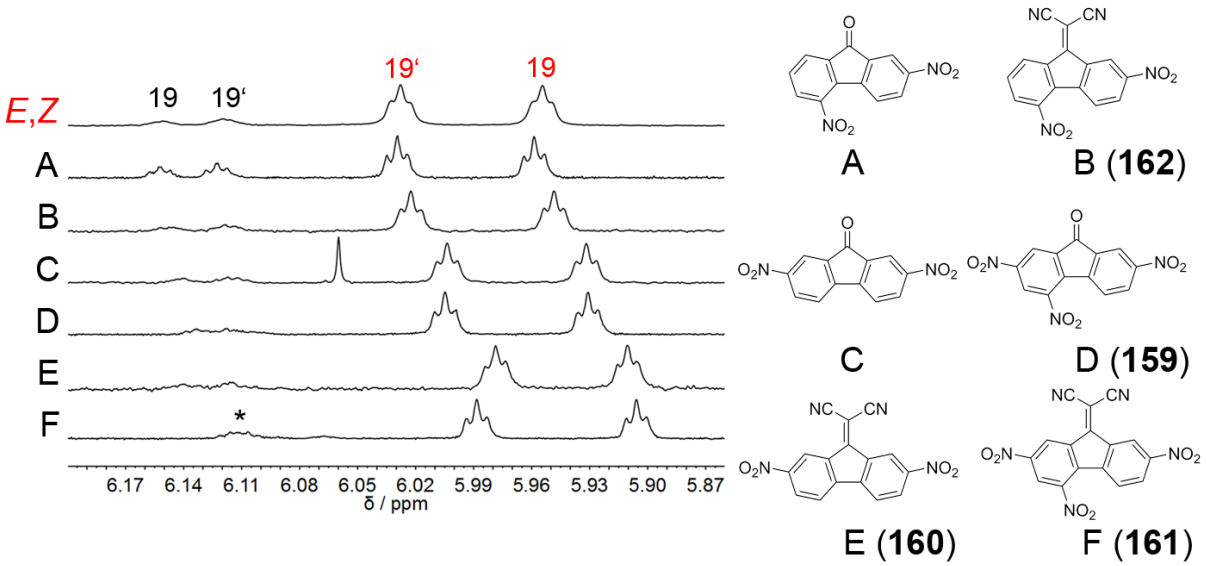

Figure 177 ^{1}H NMR spectra of an *E*,*Z* enriched solution of bis-HTI **158** in toluene-d_8. Spectra 1-6: Addition of one equivalent of guest and resulting upfield shift of indicative *E*,*Z*-**158** protons (red numbers). Spectrum 6: Proton 19 of *Z*,*Z*-**158**, marked with an asterisk, is strongly shifted upfield.

First, it was tested if fluorene **160** can be reversibly captured and released by bis-HTI **158**. Earlier experiments had shown that the *Z*,*Z*-**158** isomer can be efficiently restored at 118 °C in toluene over 1 d. Heating a solution of *E*,*Z*-**158** ⊂ **160** in toluene-d_8 to 118 °C for 3 d restored the *Z*,*Z* isomer in only 60% yield. After 3 d at 123 °C more than 80% *Z*,*Z*-**158** were obtained and after 3 d at 125 °C *Z*,*Z*-**158** was obtained quantitatively. Heating a solution of *E*,*Z*-**158** ⊂ **160** to 128 °C for several days resulted in decomposition clearly visible by indefinable black solids collecting in the NMR tube, similar to heating experiments with *E*,*Z*-**158** ⊂ TCNQ. The reversibility of the photoinduced capture-and-release was demonstrated for a total of three

cycles for two different concentrations (Figure 178) but could potentially be repeated many more times.

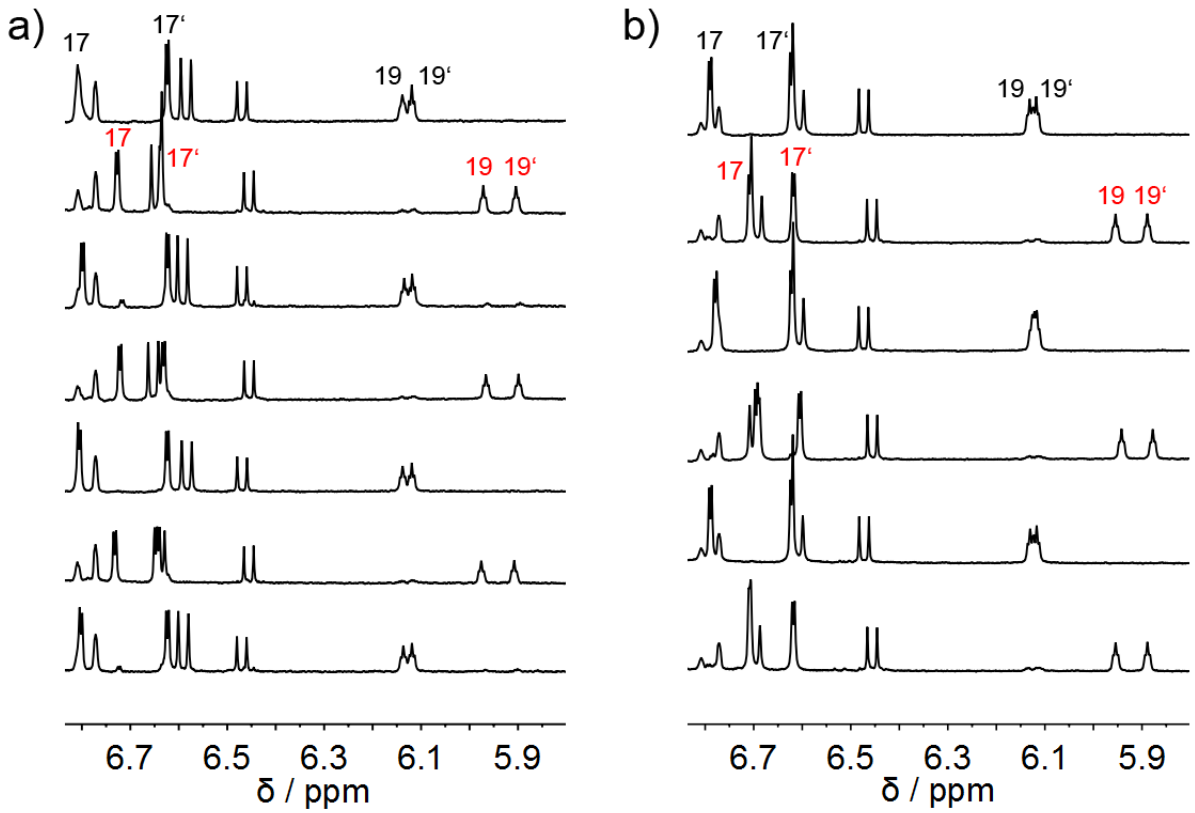

Figure 178 ^{1}H NMR (400 MHz, toluene-d_8, 22 °C) spectra of repetitive irradiation and heating of bis-HTI **158** and fluorene **160** in toluene-d_8. Starting from pure *Z,Z*-**158** (black numbers) the *E,Z*-**158** isomer (red numbers) was accumulated by irradiation with 420 nm light to the pss. Heating to 125 °C for 3 d quantitatively restored the *Z,Z*-**158** isomer. a) Cycles of a 0.4 mM solution of bis-HTI **158** and fluorene **160** b) Cycles of a 0.8 mM solution of bis-HTI **158** and fluorene **160**.

7.8 Determination of binding constants by titration experiments

Screening experiments revealed that bis-HTI **158** is able to bind dinitrofluorene **160** in its helical *E,Z* conformation. Addition of the guest to an *E,Z*-**158** enriched solution resulted in strong shifts of terminal protons of the biphenyl groups suggesting an *E,Z*-**158** ⊂ **160** complex, where the guest is located between the terminal aniline groups of the biphenyl. Incremental addition of guest to an NMR sample of *E,Z*-**158** and simultaneous determination of changes in chemical shifts provides a titration curve that approaches a point of saturation. The resulting curve can be analyzed by non-linear regression methods to give the binding constant. All host-guest titrations in this work were analyzed by uploading the data to *BindFit* at

supramolecular.org.[137] This analysis also includes the determination of the binding stoichiometry that was initially done by the *Job's method*, which would require additional experiments.

Prior to titration experiments the maximum concentration of **160** in toluene at room temperature was determined at 0.96 mM. This poses a major drawback as ^{1}H NMR experiments with an excess of guest requires a reduction of host concentration far below 0.50 mM, which quickly nears the resolution limit of 400 MHz-NMR spectrometers. As a result all titration experiments had to be performed on an 800 MHz device. To further increase the accessible concentration range two separate experiments were conducted to obtain an extended titration curve:

A first NMR tube is charged with a pure host solution with a concentration close to the resolution limit (e.g. 0.05 mM). This solution is titrated with a saturated guest solution. As addition of pure guest would decrease the initial host concentration below the resolution limit (< 0.05 mM), the added guest solution contains the same host concentration (0.05 mM) as the solution to which it is added.

If a solution of pure host is titrated with a saturated guest solution (e.g. 0.8 mM), the initial host solution would dilute the added guest, preventing maximum guest concentrations. Because of this a second titration experiment was conducted that started from a saturated guest solution (0.8 mM) that is mixed with the same, minimum amount of host as in experiment one (0.05 mM). This saturated guest solution is then diluted by titration with a pure host solution. See Figure 179 for a detailed visual representation.

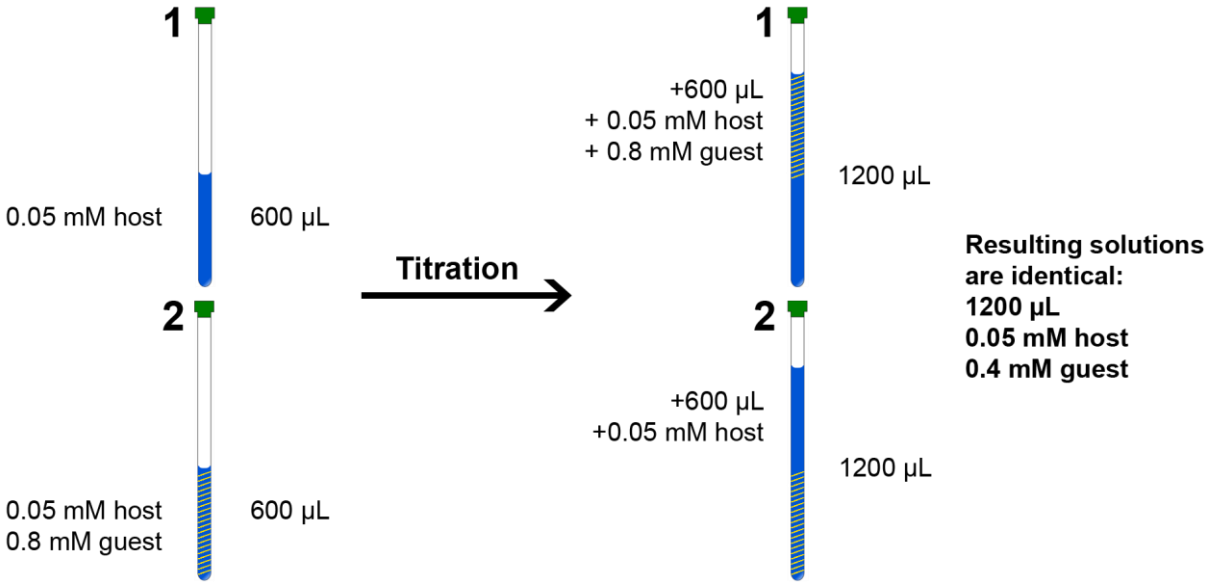

Figure 179 Visual representation of an exemplary NMR titration experiment. Mixing of the solutions is not depicted for clarity. The Host concentration (0.05 mM, indicated by a blue colored solution) is kept constant throughout the whole experiment. NMR tube 1 is initially filled with a host solution (0.05 mM) and is titrated with a concentrated guest solution (0.8 mM, indicated by orange dashes in solution) that also contains the initial host concentration (0.05 mM). NMR tube 2 is initially filled with a saturated guest solution (0.8 mM) that also contains the host (0.05 mM) and is titrated with a host solution (0.05 mM). The resulting solutions (0.05 mM host, 0.4 mM guest) are identical for tube 1 and tube 2.

This resulted in two independent titration curves. An early example is shown in Figure 180. If the experiment is conducted as shown in Figure 179 the resulting solutions, and therefore chemical shifts in the ^{1}H NMR must be identical. This serves as an internal standard that can be used to quickly estimate the quality of the conducted experiment. Clearly, this is not the case for the given example and the resulting signals are offset by 0.01 ppm. This could be explained by different concentrations in the two NMR tubes after the titration, caused by i.e. weighing errors or precipitation of a compound. In addition, the initial triplet shape of the signal is lost becoming a broad singulet. This indicates a non-established thermal equilibrium due to insufficient mixing after each titration step.

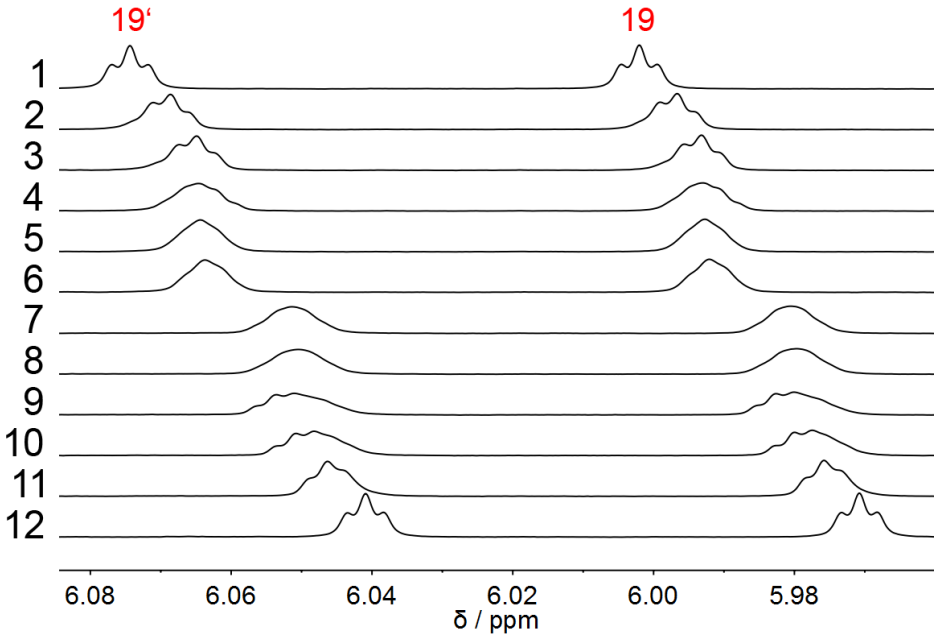

Figure 180 ^{1}H NMR spectra (800 MHz, toluene-d_8, 25 °C) acquired during titration of a solution of *E,Z*-**158** with 2,7-dinitrofluorenone. Spectrum 1 is taken from a pure host solution to which guest is added incrementally (Spectra 2-6). Spectrum 12 is taken from a host solution, saturated with guest, which is diluted by incremental addition of a host solution (spectra 11-7). Spectra 6 and 7 are the final spectra for each titration with identical compositions.

As a result an optimized experimental procedure was developed: In general sample handling after weighing on the fine scale was strictly done avoiding all ambient light. First 5.0 mL of a host solution in toluene-d_8 was prepared. From that, 2.5 mL were transferred to a vial containing the guest. Two NMR tubes were charged with 600 µL of either solution. The remaining solutions were used for the titration. After an ^{1}H NMR spectrum was taken from each NMR sample the host solution was titrated with host-guest solution and *vice versa*. Titration steps were done in 100 µL steps for a total of six steps resulting in identical solutions. The NMR tubes were carefully shaken for ca. 2 minutes after each addition and heated moderately (ca. 40 °C) using a heat gun to guarantee that an equilibrium between host and guest is established. Meanwhile it was avoided to get solution into the NMR cap to prevent spilling when opening the tube and also to minimize vaporization and concomitant precipitation of compounds in the upper half of the NMR tube.

7.9 Determination of the binding constant of bis-HTI *E,Z*-158 and 160

During the optimization process for the experimental titration procedure an optimal concentration of 0.05 mM for bis-HTI **158** was established. This concentration provided sufficient signal to noise ratio on an 800 MHz NMR device and allowed for an almost twentyfold guest concentration given the maximum concentration of 0.96 mM of **160** in toluene solution that was determined earlier. To reduce the risk of unwanted guest precipitation a concentration of 0.8 mM was used throughout the experiments. The titrations were carried out following the optimized experimental procedure. The resulting titration curves are shown in Figure 181 and Figure 182. The exact host concentration was calculated from the weighed amount of *Z,Z*-**158** and the resulting concentration of *E,Z*-**158** in the pss (ca. 94%) after irradiation with 420 nm light. The guest concentration was calculated from the exact readout of the weighed portion on the fine scale. Preparation of solutions and conduction of titration experiments was exclusively done using *Eppendorf* pipettes.

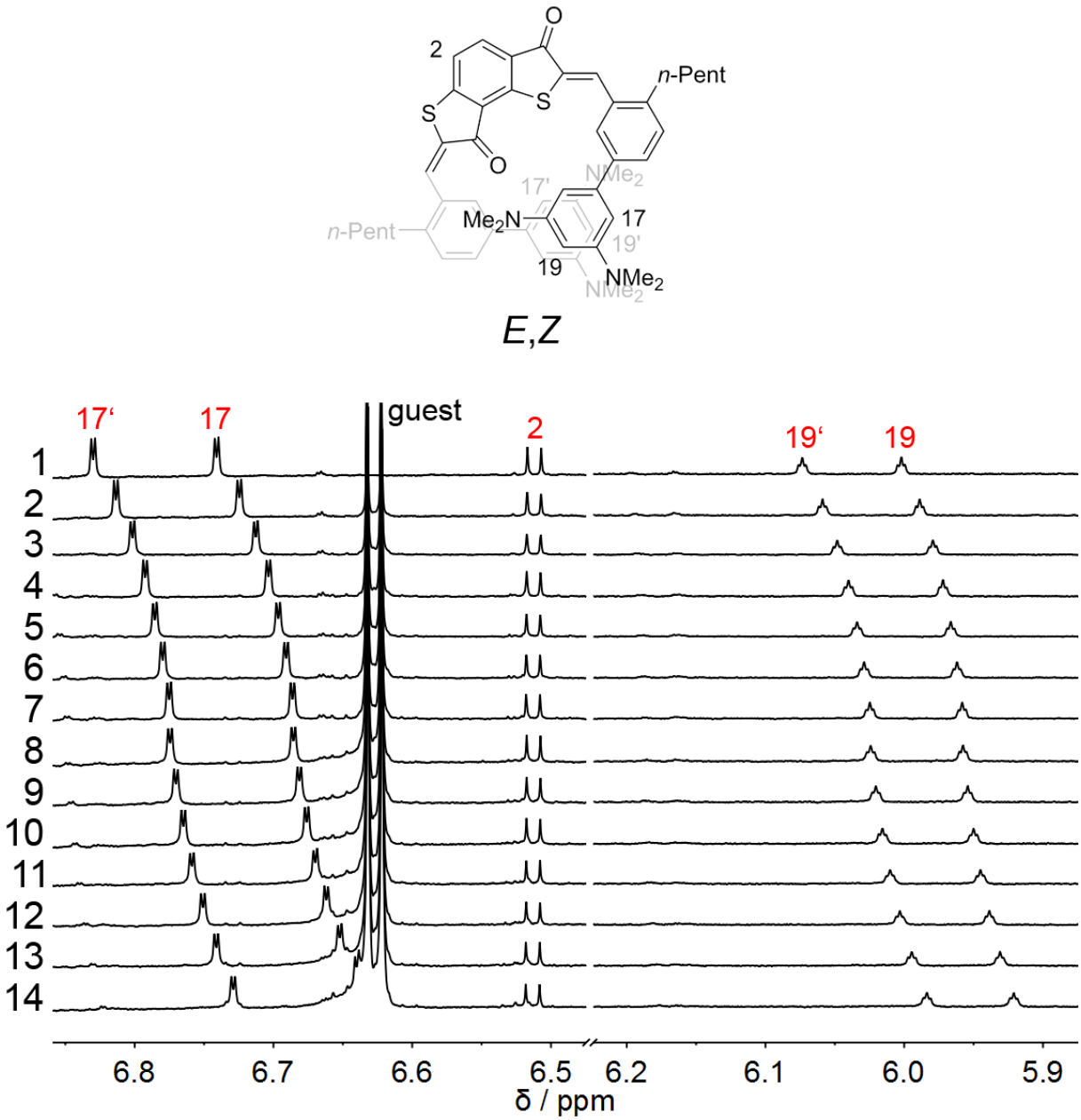

Figure 181 ^{1}H NMR spectra (800 MHz, toluene-d_8, 27 °C) acquired during the first titration of a solution of *E,Z*-**158** with 9-dicyanomethylene-2,7-dinitroflurene **160**. Spectrum 1 was taken from a 0.05 mM host solution to which a host-guest solution (0.05 mM and 0.8 mM) was added incrementally (Spectra 2-7). Spectrum 14 was taken from a host-guest solution (0.05 mM and 0.8 mM). The guest was diluted by incremental addition of a host solution (0.05 mM, spectra 13-8). Spectra 7 and 8 are the final spectra for each titration with identical compositions. The binding constant was determined to be K = 209 L·mol^{-1}cm^{-1}.

The signal shapes (doublets for protons 17 and 17' and triplets for 19 and 19') were consistent throughout the experiment. The chemical shifts of protons in the final spectra (spectra 7 and 8, Figure 182) were identical. Overall the spectra confirmed the quality of the conducted

experiment. Consequently, the titration was repeated under identical conditions (Figure 182) and the collective data were used for further analysis.

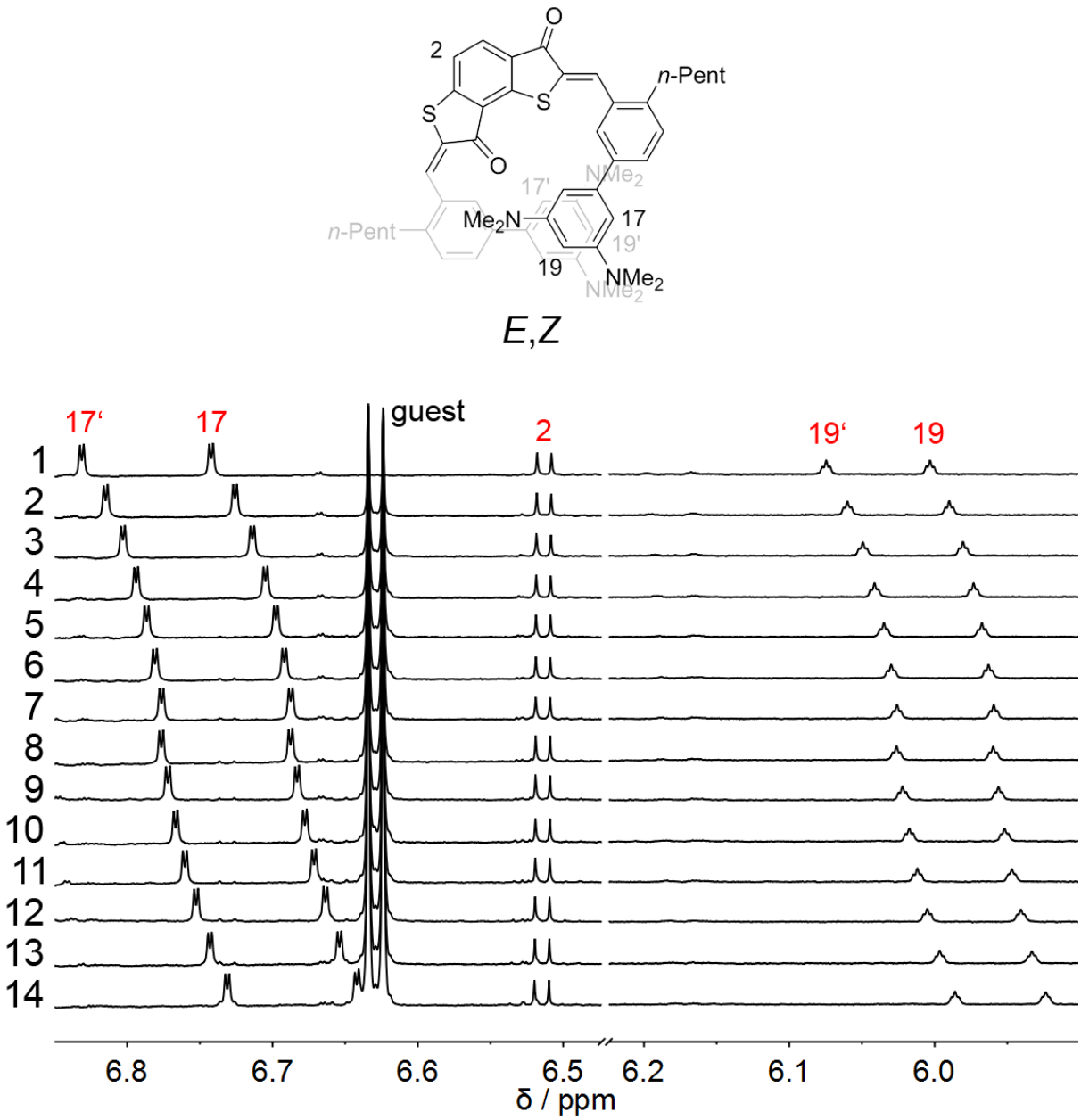

Figure 182 ^{1}H NMR spectra (800 MHz, toluene-d_8, 27 °C) acquired during the second titration of a solution of *E*,*Z*-**158** with 9-dicyanomethylene-2,7-dinitroflurene **160**. Spectrum 1 is taken from a 0.05 mM host solution to which a host-guest solution (0.05 mM and 0.8 mM) is added incrementally (Spectra 2-7). Spectrum 14 is taken from a host-guest solution (0.05 mM and 0.8 mM). The guest is diluted by incremental addition of a host solution (0.05 mM, spectra 13-8). Spectra 7 and 8 are the final spectra for each titration with identical compositions. The binding constant was determined to be K = 271 L·mol^{-1}cm^{-1}.

The chemical shifts of four different protons (17, 17', 19 and 19') of *E*,*Z*-**158** were determined for each spectrum as well as the corresponding guest concentrations. Final processing was done using the online tool *BindFit*. Here, determination of the host-guest stoichiometry is achieved by choosing between three options, i.e. 2:1, 1:1 or 1:2 host to guest ratio, and evaluation of the resulting binding constants and error values. Using an improper ratio resulted in unrealistically high or negative binding constants that varied greatly between experiments and the corresponding errors were much greater than 10%. With the correct binding stoichiometry the resulting binding constants were determined to be K = 209 $L \cdot mol^{-1}cm^{-1}$ and K = 271 $L \cdot mol^{-1}cm^{-1}$ with errors of 0.15% and 0.11%, respectively.

Table 10 Host and guest concentrations during the first titration of a solution of *E*,*Z*-**158** with 9-dicyanomethylene-2,7-dinitroflurene **160**. Shifts of indicative protons were used to determine the binding constant. A value of K = 209 $L \cdot mol^{-1}cm^{-1}$ was obtained by the *BindFit* analysis.

Host conc. [µM]	**Guest conc. [µM]**	**Proton 17' δ [ppm]**	**Proton 17 δ [ppm]**	**Proton 19' δ [ppm]**	**Proton 19 δ [ppm]**
46.55	0	6.8299	6.7410	6.0734	6.0021
46.55	124.887	6.8137	6.7248	6.0589	5.9891
46.55	218.552	6.8019	6.7127	6.0484	5.9796
46.55	291.403	6.7926	6.7035	6.0404	5.9720
46.55	349.684	6.7856	6.6964	6.0340	5.9665
46.55	397.368	6.7799	6.6910	6.0289	5.9622
46.55	437.105	6.7753	6.6863	6.0248	5.9583
46.55	437.105	6.7747	6.6856	6.0242	5.9578
46.55	476.841	6.7702	6.6815	6.0204	5.9543
46.55	524.525	6.7649	6.6761	6.0159	5.9502
46.55	582.806	6.7588	6.6700	6.0104	5.9452
46.55	655.657	6.7509	6.6621	6.0031	5.9387
46.55	749.322	6.7410	6.6525	5.9948	5.9311
46.55	874.209	6.7289	6.6401	5.9836	5.9213

Table 11 Host and guest concentrations during the second titration of a solution of *E,Z*-**158** with 9-dicyanomethylene-2,7-dinitroflurene **160**. Shifts of indicative protons were used to determine the binding constant. A value of K = 271 $L \cdot mol^{-1}cm^{-1}$ was obtained by the *BindFit* analysis.

Host conc. [µM]	Guest conc. [µM]	Proton 17' δ [ppm]	Proton 17 δ [ppm]	Proton 19' δ [ppm]	Proton 19 δ [ppm]
46.25	0	6.8311	6.7422	6.0746	6.0032
46.25	107.980	6.8146	6.7257	6.0599	5.9899
46.25	188.965	6.8029	6.7140	6.0494	5.9804
46.25	251.954	6.7938	6.7047	6.0414	5.9733
46.25	302.344	6.7866	6.6977	6.0347	5.9674
46.25	343.573	6.7808	6.6920	6.0299	5.9630
46.25	377.930	6.7765	6.6876	6.0259	5.9594
46.25	377.930	6.7766	6.6878	6.0262	5.9599
46.25	412.288	6.7721	6.6831	6.0222	5.9561
46.25	453.516	6.7668	6.6778	6.0175	5.9518
46.25	503.907	6.7604	6.6715	6.0117	5.9470
46.25	566.895	6.7526	6.6635	6.0051	5.9406
46.25	647.880	6.7429	6.6539	5.9966	5.9329
46.25	755.861	6.7312	6.6420	5.9861	5.9238

Figure 183 and Figure 184 show an excerpt of the user interface of *BindFit*. The titration data was uploaded with the required formatting using a standard *Microsoft Excel* file. After choosing a binding stoichiometry and giving an initial guess for the binding constant the fitting results could be evaluated. The titration curve of all four protons was fitted with very small maximum residuals in the range of 0.0005 ppm for the point of overlap. The residuals are very sensitive even to the smallest possible deviations of ±0.0001 ppm, which is the resolution maximum of the analytical NMR software *MestReNova*.

a)

Details

Time to fit	0.2553 s
SSR	3.7299e-6
Fitted datapoints	56
Fitted params	5

Parameters

Parameter (bounds)	Optimised	Error	Initial
K (0 → ∞)	208.87 M^{-1}	± 0.1500 %	250.00 M^{-1}

Quality of fit

Fit	RMS	Covariance
Proton 1	2.9585e-4	1.1957e-4
Proton 2	2.5386e-4	9.1594e-5
Proton 3	2.4975e-4	1.1042e-4
Proton 4	2.2819e-4	1.1403e-4
Total	**2.5808e-4**	**1.0521e-4**

Coefficients

Fit	H	HG
Proton 1	6.8299	6.1697
Proton 2	6.7410	6.0812
Proton 3	6.0734	5.4872
Proton 4	6.0021	5.4735

Back Next

b)

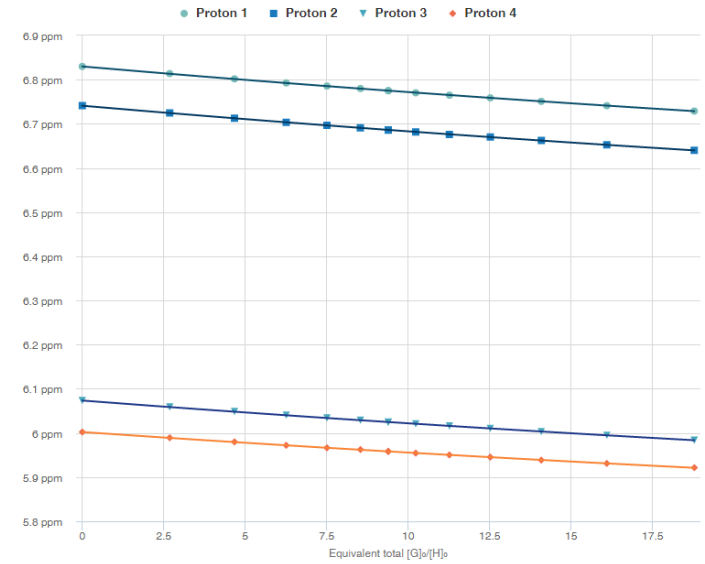

c)

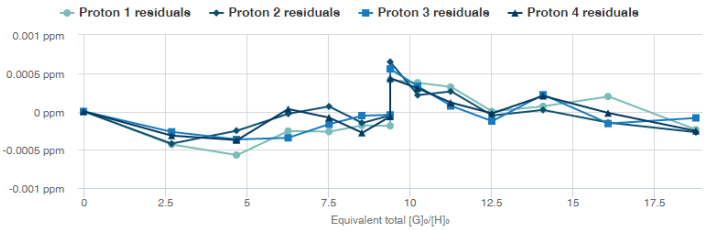

Figure 183 *BindFit* data analysis during the first titration of *E*,*Z*-**158** with compound **160** as guest using a 1:1 binding stoichiometry. a) The binding constant is determined to be K = 208.87 L·mol^{-1}cm^{-1} with an error of 0.15%. b) Plot of the chemical shifts of the four different proton signals with the fitted curve. c) Residuals obtained from the fit. The two independent titration curves show almost perfect overlap with maximum values of 0.0005 ppm.

a)

Details

Time to fit	0.2498 s
SSR	2.0781e-6
Fitted datapoints	56
Fitted params	5

Parameters

Parameter (bounds)	Optimised	Error	Initial
K (0 → ∞)	270.71 M^{-1}	± 0.1143 %	270.00 M^{-1}

Quality of fit

Fit	RMS	Covariance
Proton 1	1.8750e-4	4.9391e-5
Proton 2	1.8732e-4	4.7747e-5
Proton 3	1.9236e-4	6.8360e-5
Proton 4	2.0295e-4	9.3789e-5
Total	**1.9264e-4**	**6.0683e-5**

Coefficients

Fit	H	HG
Proton 1	6.8311	6.2367
Proton 2	6.7422	6.1471
Proton 3	6.0746	5.5470
Proton 4	6.0032	5.5291

Back Next

b)

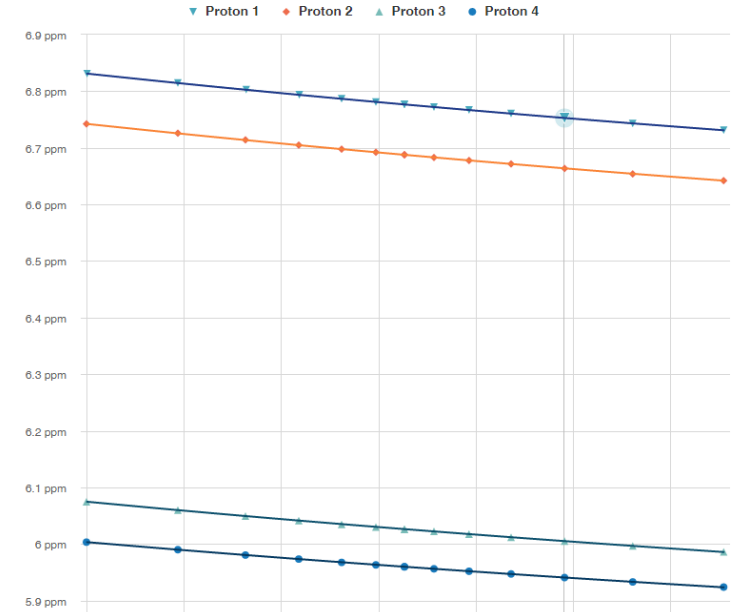

c)

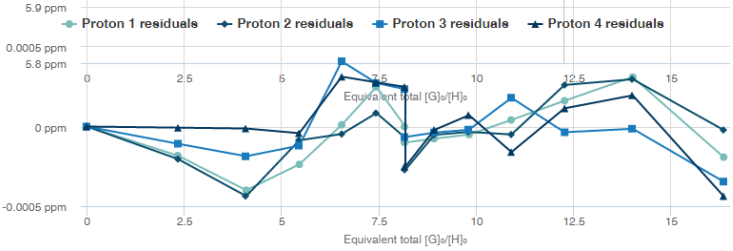

Figure 184 *BindFit* data analysis during the second titration of *E,Z*-**158** with compound **160** as guest using a 1:1 binding stoichiometry. a) The binding constant is determined to be K = 270.71 $L \cdot mol^{-1} cm^{-1}$ with an error of 0.11%. b) Plot of the chemical shifts of the four different proton signals with the fitted curve. c) Residuals obtained from the fit. The two independent titration curves show almost perfect overlap with maximum values of 0.0005 ppm. The overlap of the plots b) and c) is caused by an error in the *BindFit* user interface.

7.10 Determination of the binding constant of bis-HTI *Z,Z*-158 and 160

Having demonstrated the reversibility of the photoinduced capture-and-release of the guest and determined the binding constant of *E,Z*-**158** with compound **160**, the affinity of the "open" *Z,Z*-**158** isomer to the guest was investigated in detail. Addition of **160** to a solution of *Z,Z*-**158** in toluene revealed a weak interaction that is selective to one biphenyl unit (blue colored proton signals in Figure 185). Two independent titration experiments were carried out with identical host and guest concentrations, analogously to the titration of *E,Z*-**158** with **160**, following the optimized experimental procedure. The resulting titration curves are shown in Figure 185 and Figure 186. The signal shapes remained consistent throughout the experiments. Chemical shifts of the resulting solutions were identical for the first titration, confirming the quality of the conducted experiment. Closer inspection of the last spectrum of the second experiment, obtained from the titration of pure host with increasing amounts of guest (Figure 186, spectrum **7**) revealed a reverse trend of proton shifts (downfield shift of host proton signals compared to spectrum **6** and **8**). As the spectrum is a clear outlier the data points obtained from this single spectrum were not included in the determination of the binding constant. Three indicative protons of the interacting biphenyl unit were used to determine the binding constant. Processing was done with the *BindFit* program similar to the binding assessment of *E,Z*-**158**, which revealed a binding stoichiometry of 1:1 (Figure 187 and Figure 188). Binding constants were determined to be K = 0.13 L·mol^{-1}cm^{-1} and K = 0.14 L·mol^{-1}cm^{-1} with errors of 0.31% and 0.41%, respectively. The interaction is very small compared to the binding affinity of *E,Z*-**158** to **160** and guarantees an effective release of the guest molecule during thermal *Z* to *E* isomerization.

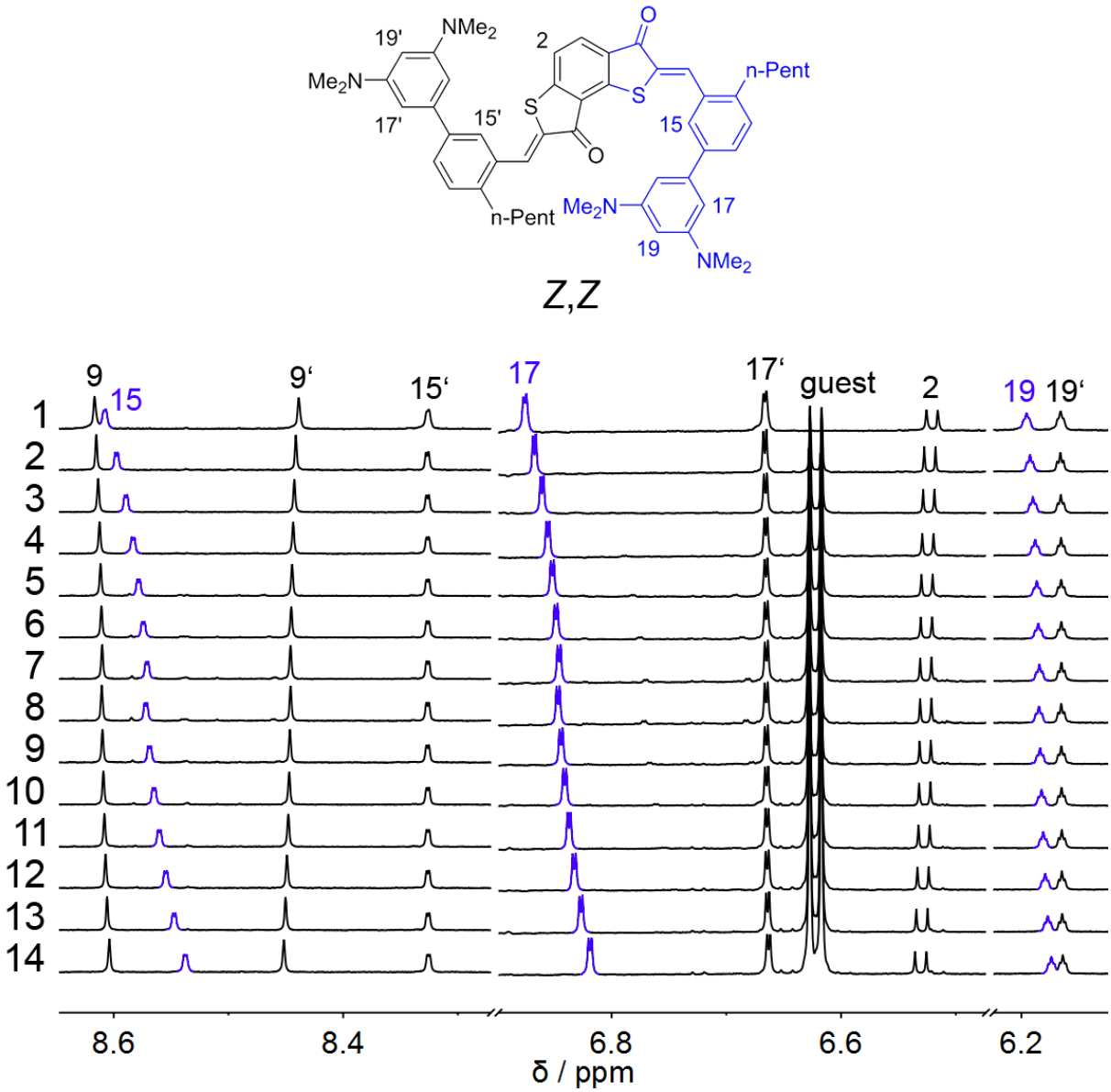

Figure 185 ^{1}H NMR spectra (800 MHz, toluene-d_8, 27 °C) acquired during the first titration of a solution of *Z*,*Z*-**158** with 9-dicyanomethylene-2,7-dinitroflurene **160**. Indicative protons of the interacting biphenyl unit are marked in blue. Spectrum 1 was taken from a 0.05 mM host solution to which a host-guest solution (0.05 mM and 0.8 mM) was added incrementally (Spectra 2-7). Spectrum 14 was taken from a host-guest solution (0.05 mM and 0.8 mM). The guest was diluted by incremental addition of a host solution (0.05 mM, spectra 13-8). Spectra 7 and 8 are the final spectra for each titration with identical compositions.

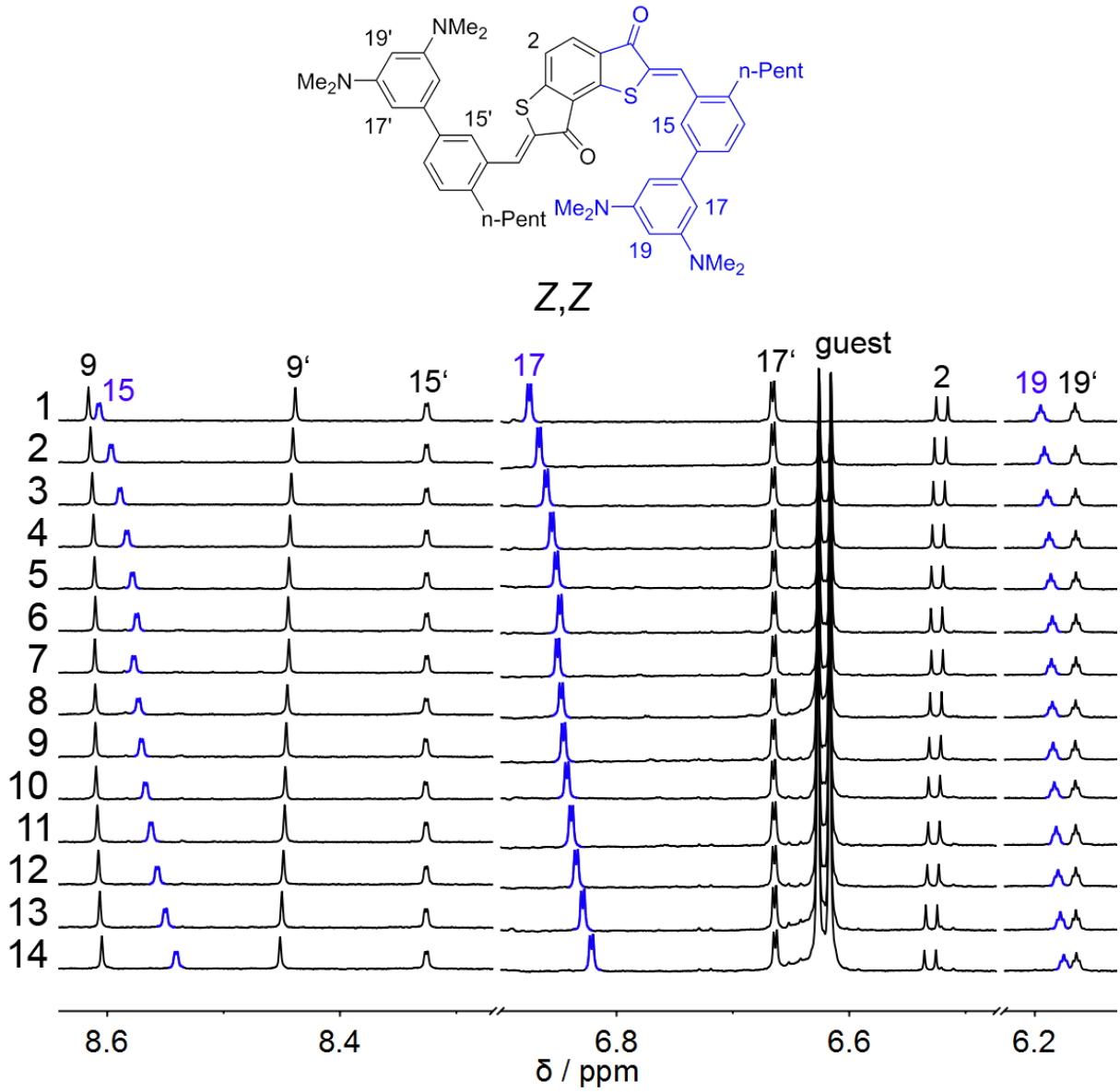

Figure 186 ^{1}H NMR spectra (800 MHz, toluene-d_8, 27 °C) acquired during the second titration of a solution of *Z*,*Z*-**158** with 9-dicyanomethylene-2,7-dinitroflurene **160**. Indicative protons of the interacting biphenyl unit are marked in blue. Spectrum 1 was taken from a 0.05 mM host solution to which a host-guest solution (0.05 mM and 0.8 mM) was added incrementally (Spectra 2-7). Spectrum 14 was taken from a host-guest solution (0.05 mM and 0.8 mM). The guest was diluted by incremental addition of a host solution (0.05 mM, spectra 13-8). A detailed analysis revealed that spectrum 7 showed a clear deviation from the titration curve and as a result was not considered for the determination of the binding constant.

Table 12 Host and guest concentrations during the first titration of a solution of *Z,Z*-**158** with 9-dicyanomethylene-2,7-dinitroflurene **160**. Shifts of indicative protons were used to determine the binding constant. A value of K = 0.13 $L \cdot mol^{-1}cm^{-1}$ was obtained by the *BindFit* analysis.

Host conc. [µM]	**Guest conc. [µM]**	**Proton 15 δ [ppm]**	**Proton 17 δ [ppm]**	**Proton 19 δ [ppm]**
50.00	0	8.6079	6.8755	6.1956
50.00	83.786	8.5975	6.8673	6.1926
50.00	146.625	8.5893	6.8607	6.1900
50.00	195.500	8.583	6.8555	6.1880
50.00	234.600	8.5783	6.8518	6.1866
50.00	266.591	8.5742	6.8484	6.1852
50.00	293.250	8.5709	6.8458	6.1844
50.00	293.250	8.572	6.8466	6.1847
50.00	319.909	8.5688	6.8441	6.1838
50.00	351.900	8.5649	6.8409	6.1825
50.00	391.000	8.5601	6.8370	6.1810
50.00	439.875	8.5546	6.8326	6.1793
50.00	502.714	8.5473	6.8267	6.1771
50.00	586.500	8.5377	6.8187	6.1739

Table 13 Host and guest concentrations during the second titration of a solution of *Z,Z*-**158** with 9-dicyanomethylene-2,7-dinitroflurene **160**. Shifts of indicative protons were used to determine the binding constant. A value of K = 0.14 $L \cdot mol^{-1}cm^{-1}$ was obtained by the *BindFit* analysis.

Host conc. [µM]	**Guest conc. [µM]**	**Proton 15 δ [ppm]**	**Proton 17 δ [ppm]**	**Proton 19 δ [ppm]**
50.00	0	8.6082	6.8753	6.1961
50.00	95.286	8.5975	6.8676	6.1929
50.00	166.750	8.5898	6.8611	6.1904
50.00	222.333	8.5840	6.8562	6.1886
50.00	266.800	8.5794	6.8527	6.1871
50.00	303.182	8.5754	6.8494	6.1860
50.00	333.500	8.5729	6.8472	6.1848
50.00	363.818	8.5706	6.8456	6.1843
50.00	400.200	8.5672	6.8427	6.1833
50.00	444.667	8.5622	6.8388	6.1817
50.00	500.250	8.5569	6.8343	6.1800
50.00	571.714	8.5500	6.8288	6.1780
50.00	667.000	8.5408	6.8214	6.1750

a)

Details

Time to fit	0.3984 s
SSR	3.0983e-6
Fitted datapoints	42
Fitted params	4

Parameters

Parameter (bounds)	Optimised	Error	Initial
K (0 → ∞)	0.13 M^{-1}	± 0.3095 %	1.00 M^{-1}

Quality of fit

Fit	RMS	Covariance
Proton 1	3.3515e-4	3.3371e-4
Proton 2	2.8551e-4	3.6946e-4
Proton 3	1.6573e-4	8.4756e-4
Total	2.7161e-4	2.4038e-4

Coefficients

Fit	H	HG
Proton 1	8.6079	7.6243
Proton 2	6.8755	6.0835
Proton 3	6.1956	5.8950

Back Next

b)

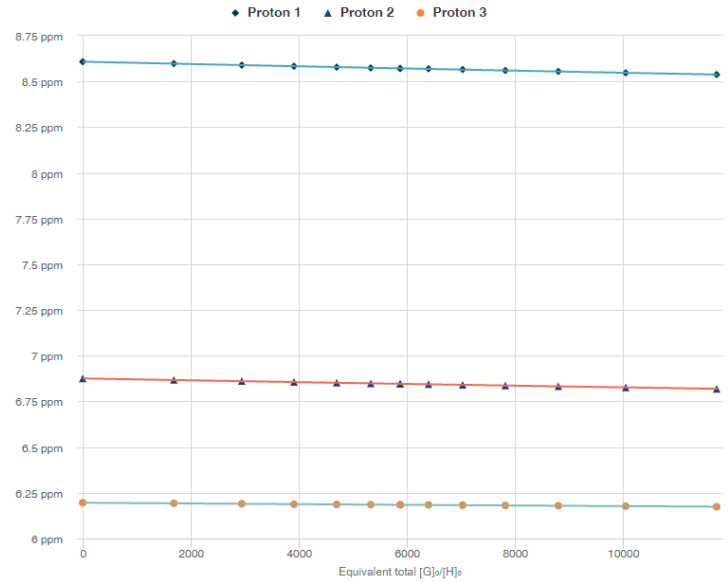

c)

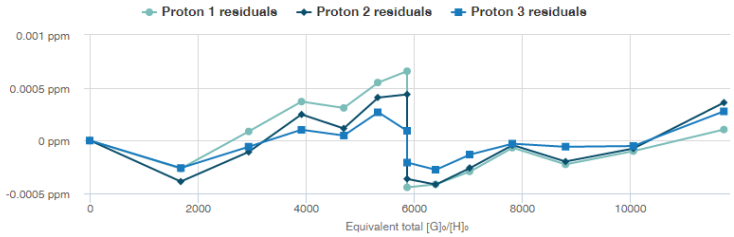

Figure 187 *BindFit* data analysis for the first titration of *Z*,*Z*-**158** with compound **160** as guest using a 1:1 binding stoichiometry. a) The binding constant is determined to be $K = 0.13\ \mathrm{L \cdot mol^{-1} cm^{-1}}$ with an error of 0.31%. b) Plot of the chemical shifts of the three different proton signals with the fitted curve. c) Residuals obtained from the fit. The two independent titration curves show almost perfect overlap with maximum values of 0.0007 ppm.

a)

Details

Time to fit	0.3924 s
SSR	4.1175e-6
Fitted datapoints	39
Fitted params	4

Parameters

Parameter (bounds)	Optimised	Error	Initial
K (0 → ∞)	0.14 M^{-1}	± 0.4061 %	0.15 M^{-1}

Quality of fit

Fit	RMS	Covariance
Proton 1	4.1690e-4	5.1348e-4
Proton 2	3.5187e-4	5.6904e-4
Proton 3	1.3824e-4	5.8692e-4
Total	3.2493e-4	3.6178e-4

Coefficients

Fit	H	HG
Proton 1	8.6082	7.8382
Proton 2	6.8753	6.2630
Proton 3	6.1961	5.9553

Back Next

b)

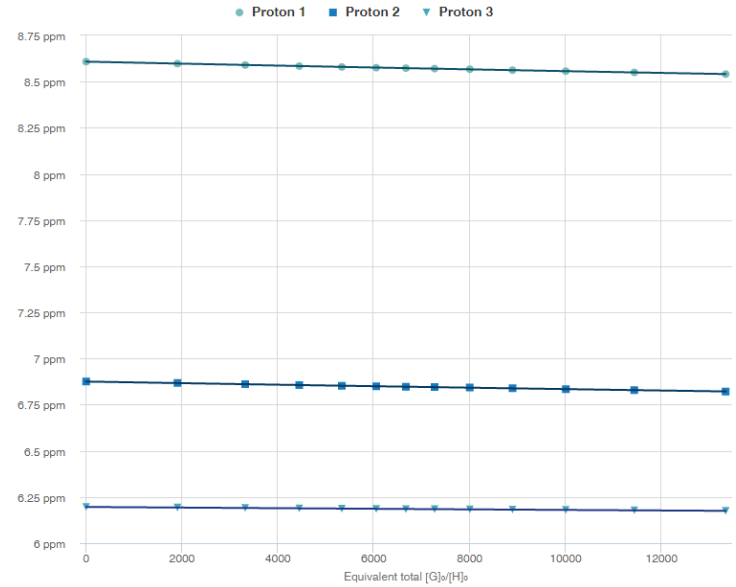

c)

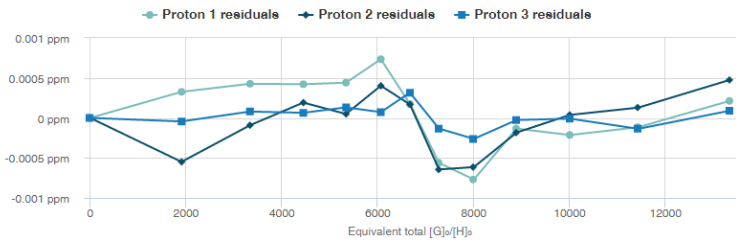

Figure 188 *BindFit* data analysis for the second titration of *Z*,*Z*-**158** with compound **160** as guest using a 1:1 binding stoichiometry. a) The binding constant is determined to be K = 0.14 L·mol^{-1}cm^{-1} with an error of 0.41%. b) Plot of the chemical shifts of the three different proton signals with the fitted curve. c) Residuals obtained from the fit. The two independent titration curves show no overlap because the signal set of one overlap spectrum was excluded. Maximum residual values are 0.0007 ppm.

7.11 Summary and conclusion

In summary it was demonstrated that the bis-HTI receptor **158** can bind electron-poor aromatic guests in its helical *E*,*Z* isomeric form. Screening experiments on a broad range of molecules indicate a high selectivity of the receptor that can effectively distinguish between regioisomers. In addition, TCNQ, 9-dicyanomethylene-2,7-dinitroflurene **160** and 9-dicyanomethylene-2,4,7-dinitroflurene **161** emerged as the most promising candidates for high binding affinities. From these TCNQ had to be discarded as the complex *E*,*Z*-**158** ⊂ TCNQ quickly decomposed at elevated temperatures, which are required for the thermal isomerization of *E*,*Z*-**158** to its non-binding *Z*,*Z* isomeric form. Because of a strong impact on the shift of *Z*,*Z*-**158** protons

compound **161** was not further investigated, which left **160** as potential guest. Due to limitations in solubility of **160** an optimized procedure for the titration experiments was developed. The optimized approach features two independent titration curves, resulting in samples of identical composition as final endpoints of both titrations. These serve as an internal quality standard that is mandatory as the limited accessible titration range renders the further analysis highly sensitive to the smallest deviations. The titration data was analyzed by the *BindFit* program in a straightforward manner. Binding constants for *E*,*Z*-**158** ⊂ **160** were determined at 240±30 $L \cdot mol^{-1}cm^{-1}$ with very small errors. The planar *Z*,*Z* isomeric form of bis-HTI **158** revealed a low affinity to the guest molecule and selectively effects one of the two biphenyl units. A binding constant of K = 0.13±0.01 $L \cdot mol^{-1}cm^{-1}$ shows, that effective release of the guest by switching from the *E*,*Z* to the *Z*,*Z* isomeric form is possible.

Taken together the efficient photocontrol of polar aromatic interactions by a bis-HTI tweezer was shown. Additional attempts to transfer chiral information from a guest to the tweezer (chirogenesis) were unsuccesful so far[132] but continue to stay in the focus as successful implementation of chiral recognition in a HTI based system would be of great interest for example in the fields of enantioselective catalysis, chiral memory, or determination of absolute configurations. More recent results on HTI based tweezers reported by *Wiedbrauk* et al. further demonstrated the feasibility of HTIs in integrated host-guest systems.[138]

In the latter work a complementary pair of tweezers was used to reversibly relocate an aromatic, electron deficient guest from one receptor to the other (Figure 189). Upon irradiation with visible light one tweezer switches from a binding "closed" configuration to a non-binding "open" form and *vice versa*. If a suitable guest is added, photoswitching of the tweezers is accompanied by its relocation from one host to the other. Light of a different wavelength can be used to reverse this process. Highly sophisticated systems like this demonstrate the great potential of HTI based molecular receptors, which opens up great prospects for future research and potential applications.

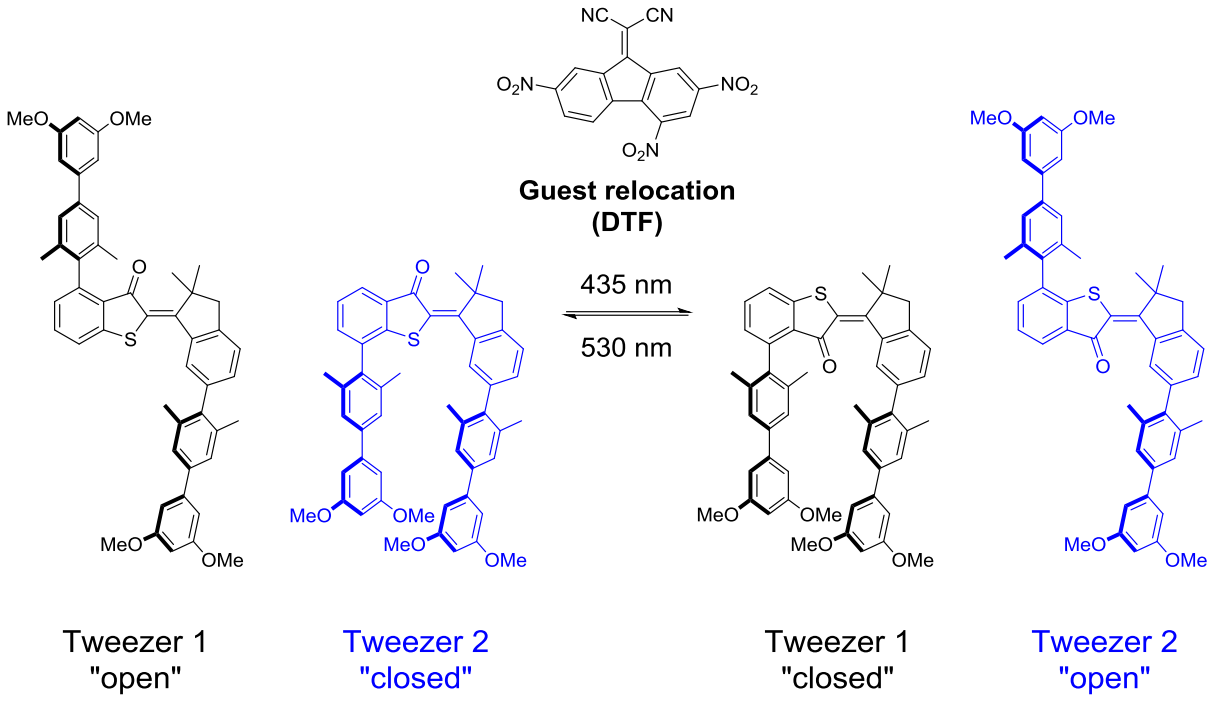

Figure 189 Simultaneous photoswitching of two complementary tweezers. In their respective *Z* configuration (left) only Tweezer 2 can bind the aromatic, electron deficient guest 9-(dicyanomethylene)-2,4,7-trinitrofluorene (DTF). Irradiation with 435 nm light generates the *E* isomeric forms (right). During this process the guest is released from Tweezer 2 and relocated to Tweezer 1. The process is reversed with 530 nm light.

8 Development of photocaged analogs of the proteasome inhibitor MG132

8.1 Introduction

The 26S Proteasome

The proteasome is an ATP-dependent multi-protein complex that hydrolyses proteins. As such it is responsible for maintaining homeostasis and plays a central role in regulatory processes. Before its discovery numerous sources reported on ring shaped 19S and 20S polypeptides with proteolytic activity. The "S" denotation refers to the Svedberg sedimentation coefficient that is commonly determined by ultracentrifugation. It was later found that these subunits belong to a larger 26S protease.[139] This "*multicatalytic proteinase complex*" discovered by *Wilk* and *Orlowski*[140] was later termed proteasome.[141] The 26S proteasome is found in the nucleus and cytoplasm of all eukaryotic cells and its formation from the 19S and 20S subunits is dependent on ATP concentration.[142]

20S core particle (CP)

Electron microscopy on the 20S particle revealed a cylindrical shape that is composed of four rings (Figure 190).[143] The structure was later refined when X-ray crystallographic data became available. It was revealed that the complex is built from a total of 14 copies of two α and β subunits where the inner two rings are composed of seven β_{1-7} units each and the two outer rings, composed of seven α_{1-7} units each.[144] The rings are tightly stacked to form an elongated cylinder with a narrow central channel that exhibits three larger cavities, two of which are located at the interface between the outer and inner rings and a third is formed by the β subunits in the center. Access to the cavities is restricted by a total of four constrictions formed by hydrophobic loops of glycine and tyrosine (part of the α-subunits) or methionine and tyrosine (part of the β-subunits) that protrude into the channel. The outer constrictions also form the more narrow bottlenecks and act as gates that allow passage only of unfolded proteins. It is also proposed that the hydrophobic interior of the channel is crucial in maintaining the unfolded shape of substrate proteins.[144] Within the 20S central chamber, three catalytic sites are provided by β_1, β_2 and β_5 subunits from each of the two rings that have trypsin-like, chymotrypsin-like and caspase-like activities and allosterically control each other.[145–147] All active sites contain an N-terminal threonine at their core, which is generated by proteolytic processing prior to assembly of the 20S particle.[148] These threonine residues provide the nucleophilic hydroxyl groups that can cleave peptide bonds in a variety of substrates.[149,150]

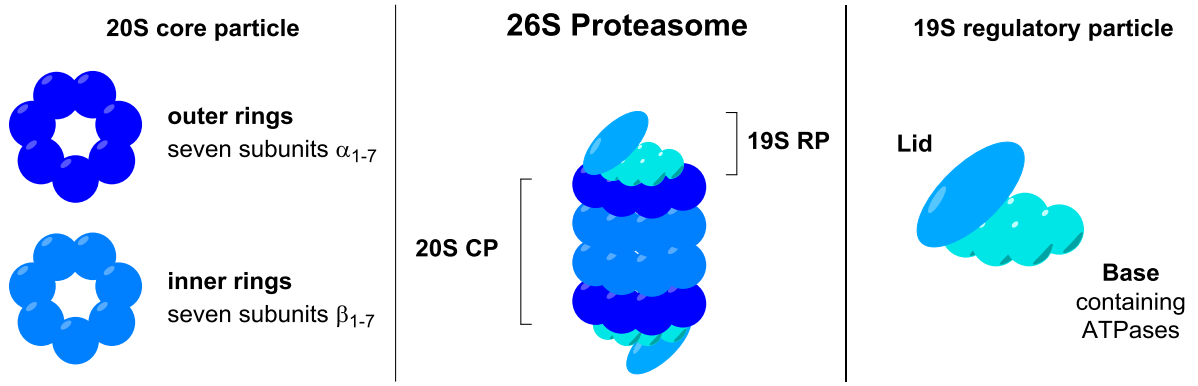

Figure 190 Model of the 26S proteasome that is composed of a 20S core particle with cylindrical shape which is capped on both sides by a 19S regulatory particle. The 20S core particle consists of four rings with seven subunits each that form a narrow channel hosting the catalytic sides. Access is restricted by the 19S regulatory particle that is formed by an ATPase containing base and a lid. The 19S RP is responsible for substrate recognition, unfolding and translocation to the 20S CP.

19S regulatory particle (RP)

The 19S regulatory particles are responsible for substrate recognition, unfolding, and translocation into the narrow core particle. Attachment of a protein substrate to one or both ends of the core particle is enabled by ATP[151] and results in a conformational change, widening the narrow constrictions of the CPs outer α-rings and allowing substrates to access the catalytic core. The regulatory particle consists of two subunits, the base and the lid (Figure 190).[152] The base contains a heterohexameric ring formed by six AAA-ATPase proteins Rpt1 to Rpt6 that loosely binds to the outer surface of the CPs α-rings.[153,154] Four additional non-ATPase proteins Rpn1, Rpn2, Rpn10 and Rpn13 complete the base complex. The lid is composed of nine non-ATPase units (Rpn3, Rpn5-9, Rpn11, Rpn12 and Sem1) with different functions. It attaches to both, the 19S and 20S particles with the Rpn6 subunit in particular connecting the ATPase- and α-rings. The structure suggests that the lid acts as a clamp that stabilizes the otherwise weakly interacting subcomplexes.[155]

Ubiquitin-proteasome pathway (UPP)

Substrate recognition and degradation by the proteasome is controlled by two fundamental elements, a polyubiquitin tag and the presence of unstructured terminal regions.[156–158] Accessibility of the disordered regions modulates affinity to the proteasome and serves as starting point for proteolysis. Only recently the Cdc48 unfoldase has been identified to play a

critical role in the ubiquitin-proteasome pathway.[159] Cdc48/p97 is an ATPase that creates flexible initiation regions in well-folded proteins in preparation for breakdown. The second factor for substrate recognition, polyubiquitination is achieved in a reaction cascade that is initiated by covalent binding of the small regulatory protein ubiquitin (Ub) to exposed lysine residues.[160] First Ub is activated by the ubiquitin-activating enzyme E1, requiring ATP (Figure **191**). The activated Ub is then transferred to a ubiquitin-conjugating enzyme E2 that covalently attaches Ub to the substrate. Selectivity is achieved by a ubiquitin ligase enzyme E3 that mediates the Ub transfer. Successive cycles of Ub activation and conjugation result in polyubiquitinated proteins that are recognized by ubiquitin-binding sites at the proteasomes 19S subunit.

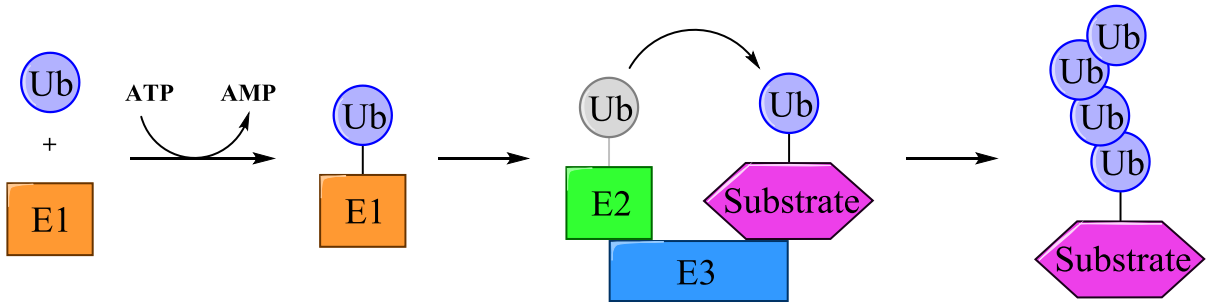

Figure 191 Substrate ubiquitination as part of the UPP. Ubiquitin (Ub) is first activated by E1 in an ATP dependent step. The activated Ub is then transferred to an ubiquitin-conjugating enzyme E2. Selectivity is achieved by a third enzyme E3 that interacts with E2 and the substrate and catalyzes bond formation between the target protein and Ub. The process is repeated several times to give polyubiquitinated substrates.

Substrate recognition by the regulatory particle takes place in two consecutive steps. An initial and reversible binding of the substrate that depends only on the presence of a Ub chain, which is followed by a second, ATP dependent step that commits the substrate to degradation.[161] A variety of ubiquitin tags qualify a substrate for degradation including monoubiquitination[162] or multiple Ub tags[163] with poly-ubiquitin chains linked through K11 or K48 (i.e. linked internally through lysine at position 11 or 48, respectively in the Ub molecule) appearing to be the favored motifs.[164,165] Results by *Thrower* et al. demonstrated that chains exceeding four ubiquitin units did not further enhance the degradation rate but increase the substrates residence time on the proteasome thus lowering its chance to escape degradation.[166] This is readily explained by the fact that substrate degradation is directly coupled to deubiquitination and a concomitant loss in affinity.[167] The regulatory particle contains several proteasomal deubiquitinating enyzmes (DUBs) with Rpn11 as the key subunit that actively release single Ub moieties for reuse prior to substrate hydrolysis.[168] After separation of the Ub chain and complete unfolding, the

substrate translocates to the core particle where it is degraded into short peptides. Upon release from the proteasome the short peptide fragments containing a mean of less than 10 residues are quickly broken down into amino acids by abundant cytosolic peptidases.[169,170]

Role in the cell cycle

Depending on the connectivity of the ubiquitin chains different outputs are generated that control cell fate in eukaryotes. As mentioned earlier K11/K48 linked ubiquitin chains are the most important signals that induce rapid protein degradation by the proteasome, which plays a critical role in signaling pathways and cell proliferation.[165] The cell-cycle is typically divided into four phases: Periods of DNA synthesis (S Phase) and Mitosis (M Phase) that are separated by gaps (G1 and G2) (Figure 192). Transition between G1/S and G2/M requires the sequential activity of cyclin dependent kinases (CDKs) that are activated by cyclins through complex formation.[171,172] Cyclins are proteins with oscillating concentrations in the cell that control the phosphorylation activity of the CDKs, which in turn trigger a multitude of cell-cycle events. The short-lived mitotic cyclin B in particular is necessary for the cell to enter and exit M Phase through interaction with CDK1, which constitutes the M Phase promoting factor (MPF).[173] Like most CDKs the MPF complex requires additional activation by a phosphatase that removes an inhibitory phosphate group to achieve its kinase activity.[172] Dissociation of cyclin B from the MPF complex enables M Phase exit.

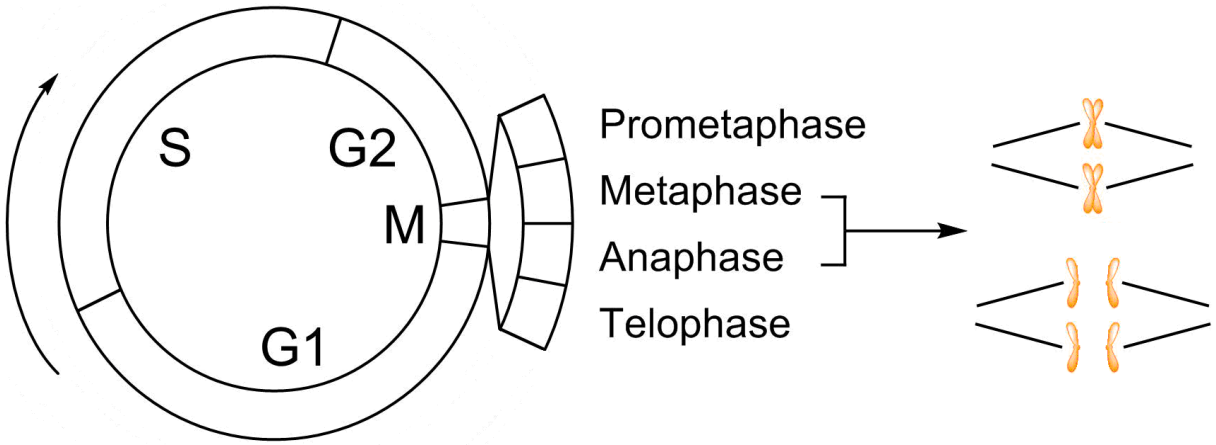

Figure 192 Stages of the cell-cycle. A short phase of mitosis (M) is followed by a growth-phase G1. Chromosomes are replicated in S phase, which is followed by a second gap phase G2 preparing the cell for mitosis. The combined G1, S, and G2 phases are called interphase. Mitosis is divided into (prophase), prometaphase, metaphase, anaphase, and telophase. Chromosomes align at the equator of the cell during metaphase and are separated in the anaphase.

The ubiquitin-proteasome-dependent degradation of cyclins during the cell-cycle is achieved by the two E3 ubiquitin ligase proteins SCF[174,175] (Skp1/Cul1/F-box protein) and APC/C[176] (Anaphase promoting complex/cyclosome).[177] While SCF plays an important role in interphase progression the APC/C complex enables transition from metaphase to anaphase during mitosis by tagging cyclin B and securin for degradation by the 26S proteasome. Securin is an inhibitor of the protease separase, which cleaves the protein complex cohesin that holds the sister chromatoids together.[178] Securin degradation therefore enables chromosomes, which are aligned on the metaphase plate, to move to opposite poles of the cell.

Proteasome inhibition and metaphase arrest

The majority of cellular proteins are degraded through the ubiquitin-proteasome pathway. This includes damaged and misfolded proteins as well as regulatory proteins that are involved in a variety of cellular and physiological functions such as cell-cycle progression, apoptosis, transcription, DNA repair, and antigen presentation. Proteasome inhibitors were initially developed to investigate the catalytic activity of the proteasome and its function within the cell before they were considered as therapeutic agents. Deregulation of the UPP is connected to a variety of diseases and it quickly emerged that inhibition of proteasome function induces apoptosis in cancer cells.[179,180] It is still unclear why malignant cells are more susceptible to cytotoxic effects of proteasome inhibition but it seems evident that highly proliferative cancer cells demand stricter control of protein balance.[181] One of the key factors associated with proteasome inhibition is the deactivation of NF-κB (nuclear factor kappa B), a protein complex that is involved in cellular stress response. Inhibition of the proteasome stabilizes its inhibitor I-κB and therefore prevents NF-κB activation and translocation to the nucleus where it triggers inflammatory responses or suppresses apoptosis.[182] This initial rationale prompted the development of the anti-cancer drug Bortezomib, which became the first proteasome inhibitor approved for clinical use in the treatment of multiple myeloma, a cancer of plasma cells (Figure **193**a). The second generation of proteasome inhibitors including Carfilzomib, Ixazomib, and Marizomib offer many benefits in terms of overcoming resistances and reduced side-effects and allow a variety of treatment options.[183]

The proteasome inhibitor MG132 (Carboxybenzyl-L-leucyl- L-leucyl- L-leucinal), a peptide-aldehyde, induces apoptosis in cancer cells through its regulating function on cancer-related protein levels (Figure 193a). This includes tumor inhibitors, transcription factors, or cell cycle proteins.[184] Another way of inducing apoptosis is through formation of reactive oxygen species

(ROS) and concomitant glutathion depletion. Transition from metaphase to anaphase is another cellular process closely related to proteasome activity. Inhibition by MG132 causes accumulation of cyclin B and increased MPF activity and arrests the cell at metaphase.[185] Experiments with non-degradable cyclins that prevent MPF inactivation have shown that MPF activity is not related to anaphase transition.[186,187] Proteolysis of cyclin B and securin by the APC/C (see cell-cycle section) on the other hand is essential and controlled by the spindle assembly checkpoint that is turned off when all chromosomes are aligned on the metaphase plate.[188] MG132 inhibition of the APC/C complex, which is part of the ubiquitin-proteasome pathway is one way to induce extended metaphase arrest that finally results in uncoordinated loss of chromatid cohesion.[189]

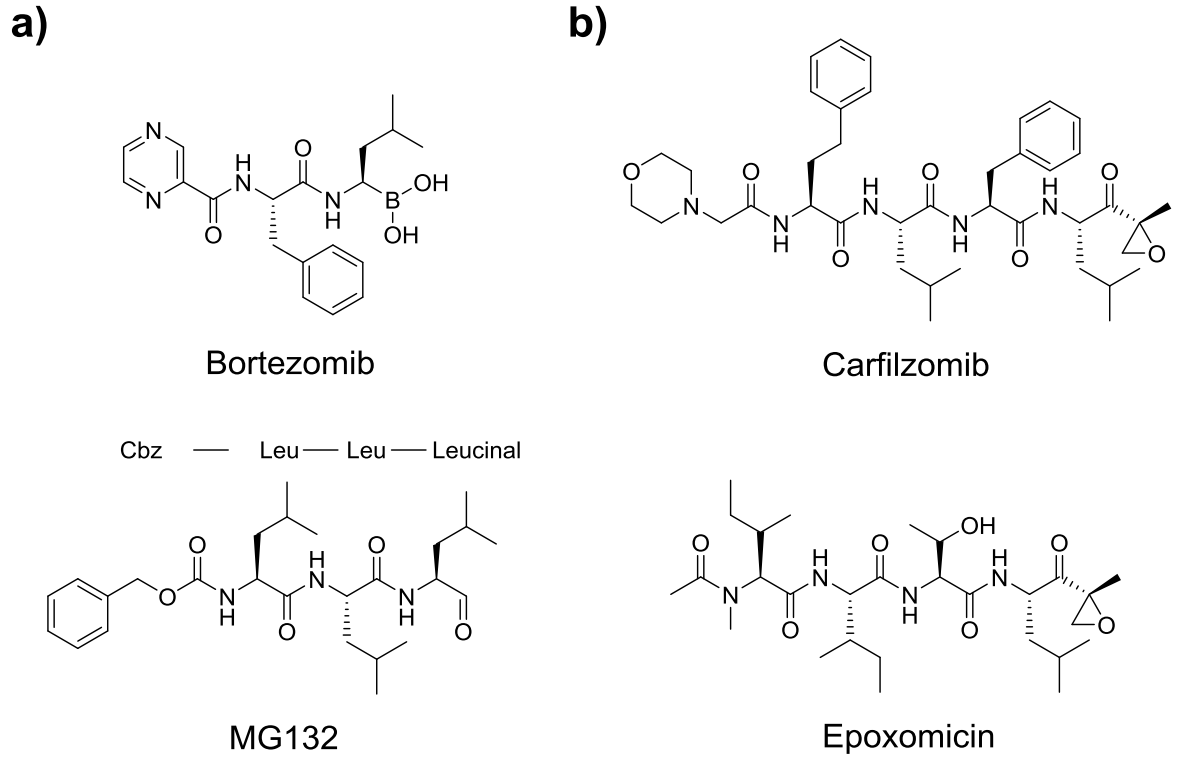

Figure 193 Exemplary proteasome inhibitors with a peptide scaffold. a) First generation, reversible proteasome inhibitors Bortezomib, approved for the treatment of multiple myeloma, and MG132 mainly used in research. b) Second generation proteasome inhibitor Carfilzomib and its natural precursor Epoxomicin bearing an α,β-epoxyketones reactive group.

Like Bortezomib and related proteasome inhibitors, MG132 covalently binds threonine at the active β-sites in the 20S core particle and effectively blocks proteolytic activity. The mechanism of inhibition is well understood und supported by a variety of crystal structural data of inhibitors in complex with the proteasome including MG132.[190,191] Reaction of the aldehyde with the

hydroxyl group of N-terminal threonine results in the formation of a hemiacetal (Scheme 80a). This covalent bond formation is reversible and mitosis continues when the inhibitor is washed out.[192]

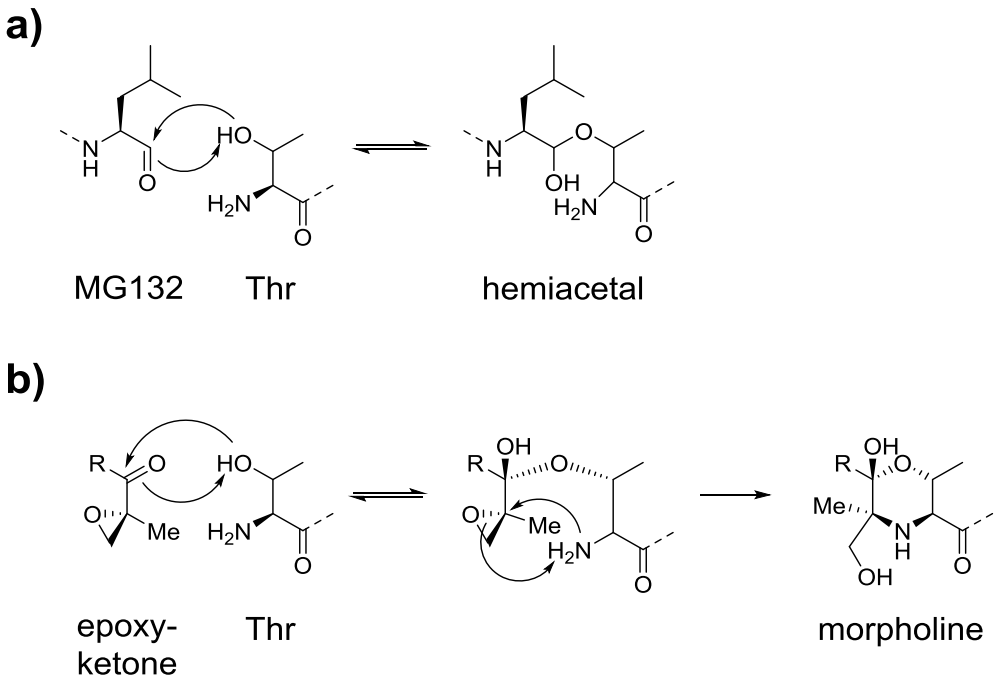

Scheme 80 Reaction mechanism of a) MG132 and b) α,β-epoxyketones with threonine at the catalytically active β-sites of the proteasome.

Studies also found that a bulky substituent at P2 (that is peptide 2 counting from the peptide aldehyde) stabilizes the hemiacetal bond by reducing its water accessibility within the pocket and hydrophobic moieties at P4 further increase binding interactions with the proteasome.[193] Second generation proteasome inhibitors like Carfilzomib, which is derived from its natural precursor Epoxomicin[194] (Figure 193b), exploit these design principles as well as the bivalent reactivity of threonine, resulting in enhanced inhibitory activity and significantly decreased side effects in clinical studies. In contrast to Bortezomib and MG132 formation of the morpholino adduct of second generation inhibitors is irreversible which can limit their applicability (Scheme 80b).

NV and NVOC as photolabile protecting groups (PPGs)

Photoremovable protecting groups (PPGs) are established as an alternative or addition to traditional protecting group chemistry. They find broad application especially in the biochemistry related fields due to the clean and non-invasive nature of the stimulus that is

required for their removal. Photochemical deprotection of such "caged" compounds occurs under mild conditions that avoids the use of additional chemical reagents and offers high spatio-temporal control. Efforts towards orthogonal deprotection of different PPGs within a single molecule have added to their versatility[195] and current research is strongly focused on red-shifted deprotection for deep-tissue penetration enabling *in vivo* applications. The incorporation of new chromophores such as BODIPY, the increase of two-photon absorption efficiency or singlet oxygen-mediated deprotection have contributed to shift uncaging wavelengths to the near-infrared region of the spectrum.[196] For this work the well-established *o*-nitrobenzyl (*o*NB) structural motif was chosen that is readily removed at $\lambda_{max} \approx 400$ nm.[197] Upon irradiation *o*NB is converted to its excited state (Scheme 81). Hydrogen transfer to the nitro group forms a ground state *aci*-nitro tautomer that irreversibly cyclizes with a decay rate that greatly depends on substitution, pH, and solvent. Ring-opening to the benzyl alcohol and subsequent formation of *o*-nitroso benzaldehyde releases the leaving group.[198,199]

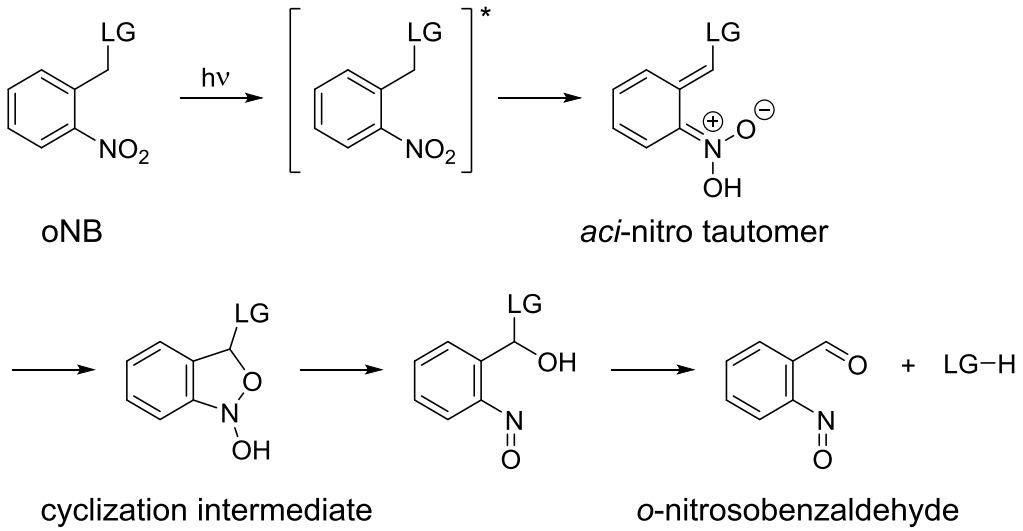

Scheme 81 General mechanism of *o*NB deprotection and release of a leaving group (LG). Irradiation converts the *o*NB molecule to the excited state, which is followed by proton transfer and formation of a ground state *aci*-nitro tautomer. Cyclization forms a dihydroisoxazol intermediate that decays in the rate determining step to nitrosobenzyl alcohol. The leaving group is then released with concomitant *o*-nitrosobenzaldehyde formation.

Most studies found the release of the product to proceed with the same rate as the decay of the *aci*-nitro intermediate but this assumption may not hold depending on pH and nature of the leaving group.[197] When *o*NB protected alcohols are uncaged ring-opening of the dihydroisoxazol cyclization intermediate forms a hemiacetal. Subsequent hydrolysis was

proven to be the rate-determining step for the release of methanol at pH < 8 and this revised mechanism might be applicable to other poor leaving groups.[200]

A variety of functional groups such as alcohols, carboxylic acids, thiols, phosphates, or amines can be protected by directly attaching them to the benzylic position. Protecting functional groups as carbonic acid derivatives is often preferred as it offers better leaving group performance and facile synthesis from the *o*NB chloroformate precursor (Scheme 82). This comes at the cost of a slower fragmentation rate with the release of CO_2 now being the rate-limiting step.[201] Drawbacks of *o*NB protection arise from the brown-colored nitrosobenzaldehyde that acts an internal light filter and quickly limits deprotection rates in higher concentrations. Side reactions of the benzaldehyde photoproduct and released amines can also result in imine formation which has to be taken into consideration.

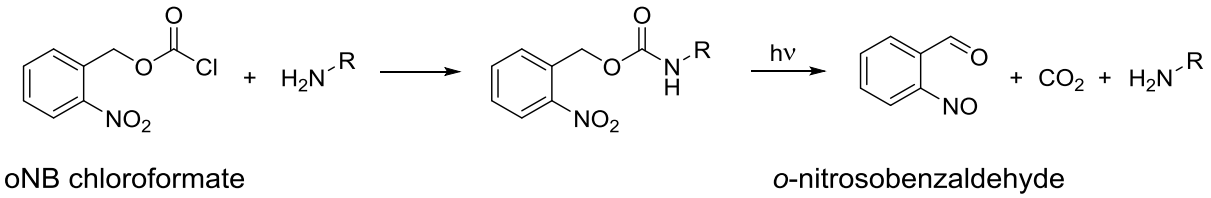

Scheme 82 Example of *o*NB amine protection starting from *o*NB chloroformate. Fragmentation and concomitant release of CO_2 is the rate limiting step. Side reactions can occur by reaction of the free amine with *o*-nitrosobenzaldehyde.

Figure 194 shows an overview of *o*NB structural analogs. A methyl substituent at the benzylic position shows minor increase in quantum efficiency[202,203] and the effect is greatly enhanced when strong electron-withdrawing groups such as CF_3 are used.[204] Introduction of a second *o*-nitro group to increase hydrogen-abstraction capacity had a comparable effect on quantum yields[205] while *o*NB analogs bearing a second *o*-nitrophenyl group at the benzylic position have also been reported to provide increased deprotection yields.[206]

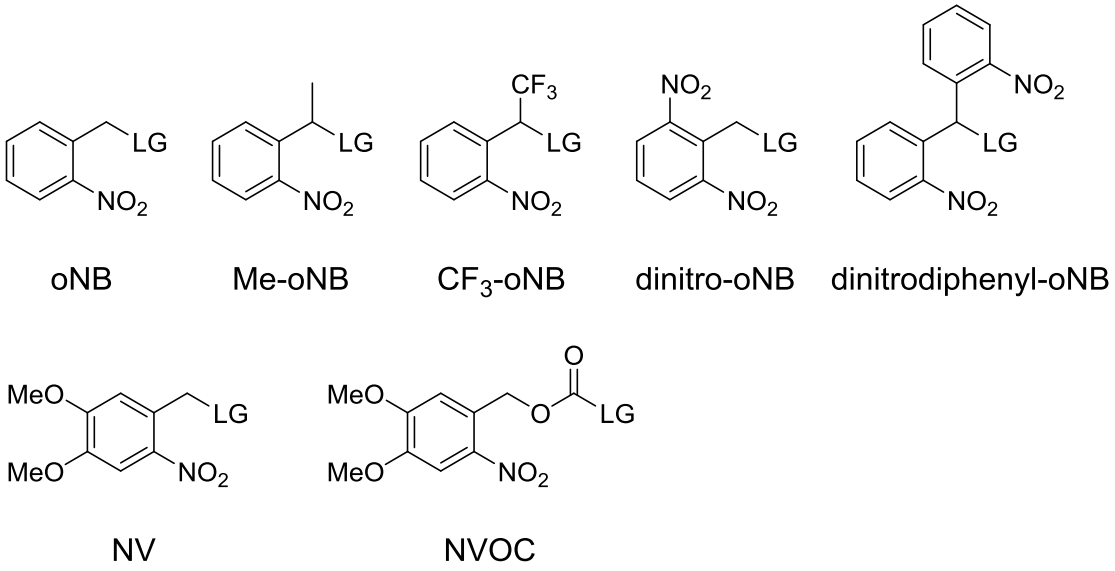

Figure 194 Structural analogs of *o*NB with enhanced performance.

Substituents at the aromatic core of *o*NB have limited impact on the absorbance and red-shifted absorptions have been reported to have an inverse effect on the quantum yield, which indicates that independent optimization of these two properties is extremely challenging.[207] *o*NB analogs bearing two methoxy groups at the aromatic core were reported early on and provide minor red-shifted absorptions with reasonable deprotection rates up to 420 nm.[208] These 6-nitroveratryl (NV) and 6-nitroveratryloxycarbonyl (NVOC) compounds are the most commonly used PPGs to date as they offer good performance and caged compounds are prepared in a straightforward manner.

Photoprotection of ketones and aldehydes is rarely seen and few have been reported that are compatible with biological systems. The coumarin analog Bhc (6-bromo-7-hydroxycoumarin-4-ylmethyl) was developed as a two-photon sensitive PPG for biological applications and Bhc-diol was successfully applied in the protection of carbonyls (Scheme 83a).[209] A related methodology that enables the use of *o*NB to protect carbonyls was reported early on (Scheme 83b)[210] and an alternative approach that releases aldehydes from NV-α-acetoxy ethers was reported decades later (Scheme 83c).[211] In this two-step approach NV esters are first prepared from small, model carboxylic acids or acid chlorides and the aldehyde oxidation state is then achieved by DIBAL-H reduction to the hemiacetal that is trapped *in situ* through addition of acetic anhydride. This use of carboxylic acids as precursors for the photorelease of the respective aldehydes was very promising for the incorporation into peptide synthesis and proved to have major impact on the herein presented work.

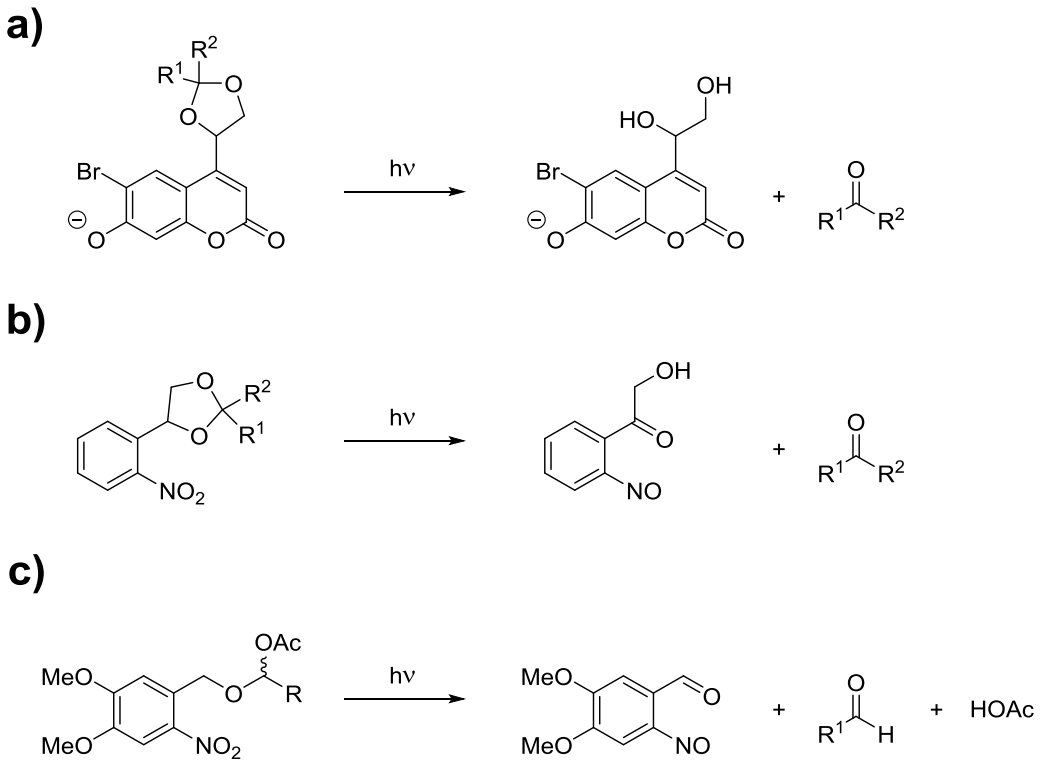

Scheme 83 Photolabile protection of carbonyls. a) Bhc-diol for 1- and 2-photon excitation.[209] b) *o*NB cage for carbonyls.[210] c) NV cage for the release of aldehydes.[211]

8.2 Photoresponsive proteasome inhibitors

A photoswitchable analog of Bortezomib has been reported by the group of *Feringa*.[212] Here an N-terminal azobenzene is used to reversible modulate the inhibitory activity. Upon irradiation the planar *trans* conformation is switched to a bent *cis* structure with increased steric repulsion at the proteasome active sites. Depending on the substitution an up to threefold change in activity is achieved (Figure 195). The group of *Abell* reported comparable results for azobenzene-containing peptidic boronate esters with a modulation of activity in the range of factor 3 to 5.[213]

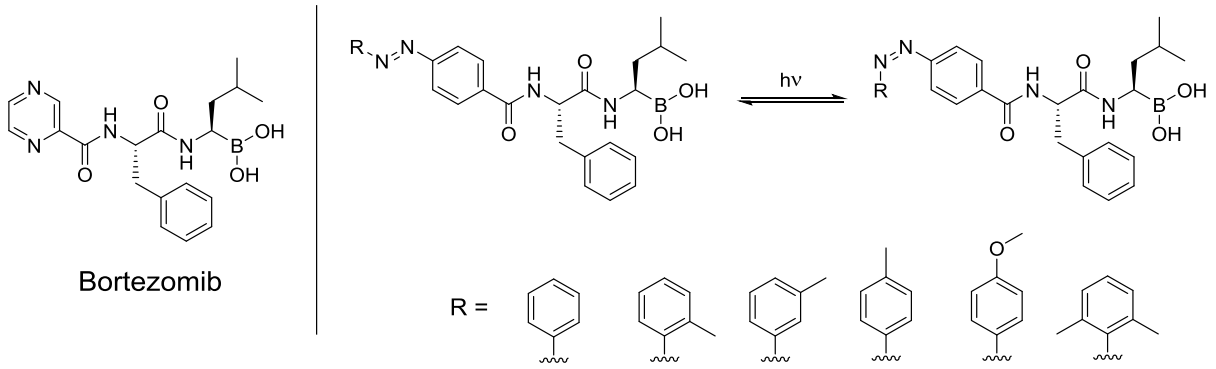

Figure 195 Photoswitchable proteasome inhibitor. An azobenzene functionalized Bortezomib analog is used to modulate its activity.

The use of PPGs to control proteasome inhibition has not been realized to date. Light induced removal of photolabile groups results in dramatic structural changes that can be used to alter interactions within the catalytically active pockets. In addition functions crucial for the inhibitors potency can be masked, which offers an on/off approach to its activity. Compared to photoswitchable control uncaging is an irreversible process. As that spatio-temporal control is limited by diffusion a once released active agent cannot be turned off.

To assess the feasibility of photocages for the control of proteasome activity, two different approaches were pursued, the substitution of a core structural element of MG132 and the photolabile protection of the aldehyde that is required for its inhibitory function (Figure 196). The release of the tripeptide fragment with an N-terminal amine from **163** has the potential to drastically alter the fit at the catalytically active site. In addition changes in polarity can be expected as free amino groups of N-terminal residues occur protonated at physiological pH. Protection of the reactive aldehyde function in **164** is straightforward and is expected to give valuable insight into the effectiveness of the uncaging process *in vivo*.

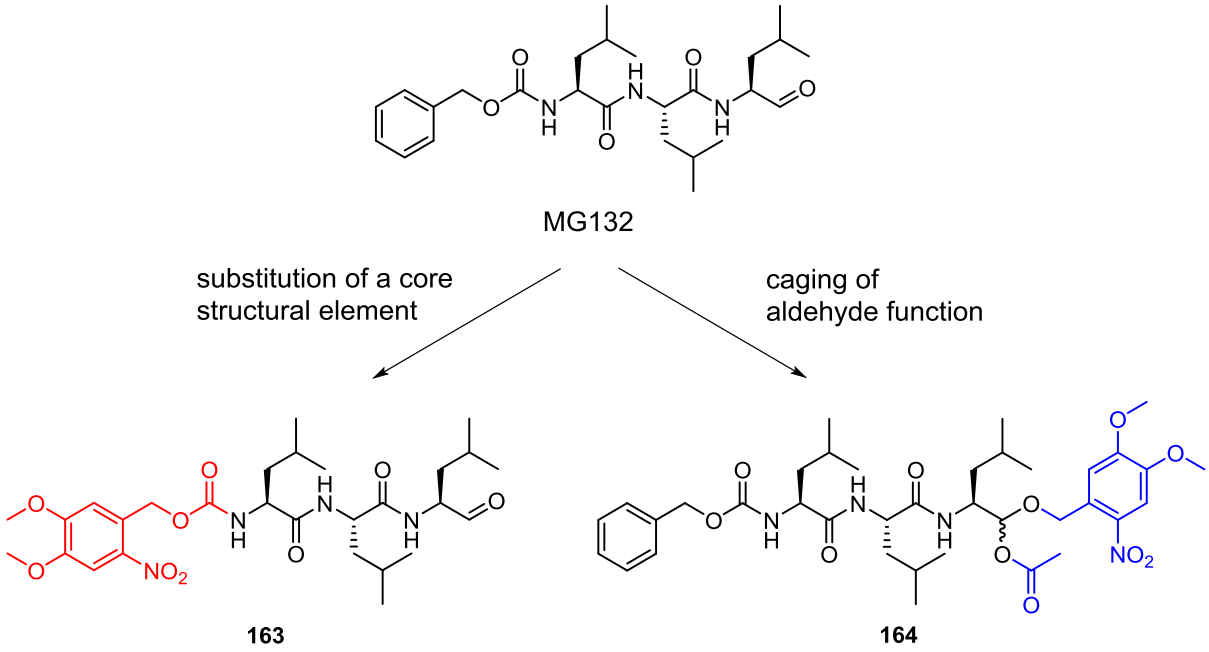

Figure 196 Different modifications of MG132 using the NV photolabile protecting group. Substitution of the carboxybenzyl group by NVOC releases the tripeptide core with free N-terminal amine upon uncaging (**163**, bottom left). Photoprotection of the aldehyde functional group by an NV hemiacetal caging methodology prevents interactions with threonine at the catalytically active sites (**164**, bottom right).

8.2.1 Synthesis of MG132 analogue 163

Tripeptide **163** was constructed from the two major building blocks **165** and **167** that are described separately in the literature.[214,215] The photoremovable nitroveratryl alcohol was introduced as chloroformate in a base promoted substitution reaction (Scheme 84). Contradictory to statements in the literature procedure 2 M NaOH did not fully dissolve L-Leucine and instead the suspension was used. The reaction afforded the product **165** with highly reproducible yields in the range of 61-63%.

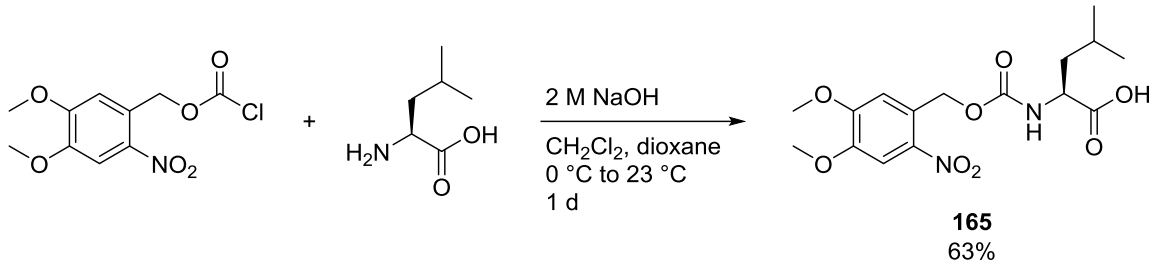

Scheme 84 Synthesis of photocaged L-Leucine **165**. Reaction of 6-nitroveratryloxycarbonyl chloride and L-Leucine using 2 M aqueous NaOH in a CH_2Cl_2:dioxane = 1:1 mixture gave **165**.

Synthesis of the dipeptide **167** commenced with a DCC/HOBt promoted coupling of *N*-Boc protected L-Leucine with L-Leucinol to **166** (Scheme 85). The reduction of the carboxylic acid to an alcohol functional group in L-Leucinol protects the C-terminus of the amino acid in the coupling reaction and serves as precursor for the late stage oxidation to the respective aldehyde. Removal of the Boc protecting group in a TFA/CH_2Cl_2 solution gave the crude product **167** that contained residual TFA, which was neutralized *in situ* in the following reaction step. To this end the reaction was estimated to proceed quantitatively and residual TFA was calculated from excess yield.

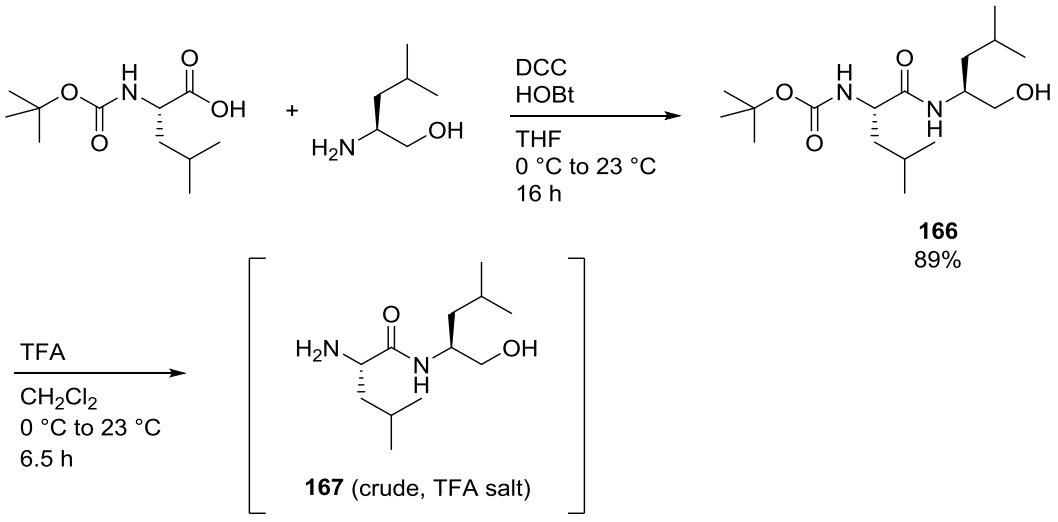

Scheme 85 Synthesis of building block **167**. Coupling of Boc-protected L-Leucine with L-Leucinol using DCC/HOBt afforded the product **166**. Removal of the Boc protecting group in a TFA:CH_2Cl_2 mixture (1:1) gave the crude dipeptide **167** as TFA salt.

The two building blocks **165** and **167** were fused in a second DCC/HOBt promoted coupling reaction (Scheme 86). Residual amounts of TFA contained in crude **167** were neutralized with additional equivalents of DIPEA. Tripeptide **168** was obtained in very good yields. The

synthesis was concluded with oxidation of the primary alcohol to the respective aldehyde using the *Dess-Martin periodane* precursor 2-iodoxybenzoic acid (IBX). Because of the potential shock sensitivity of the reagent also the stabilized formulation SIBX (45 wt. % IBX with benzoic acid and isophthalic acid) was used without any noticeable drawback. The target compound **163** was obtained in 41% yield.

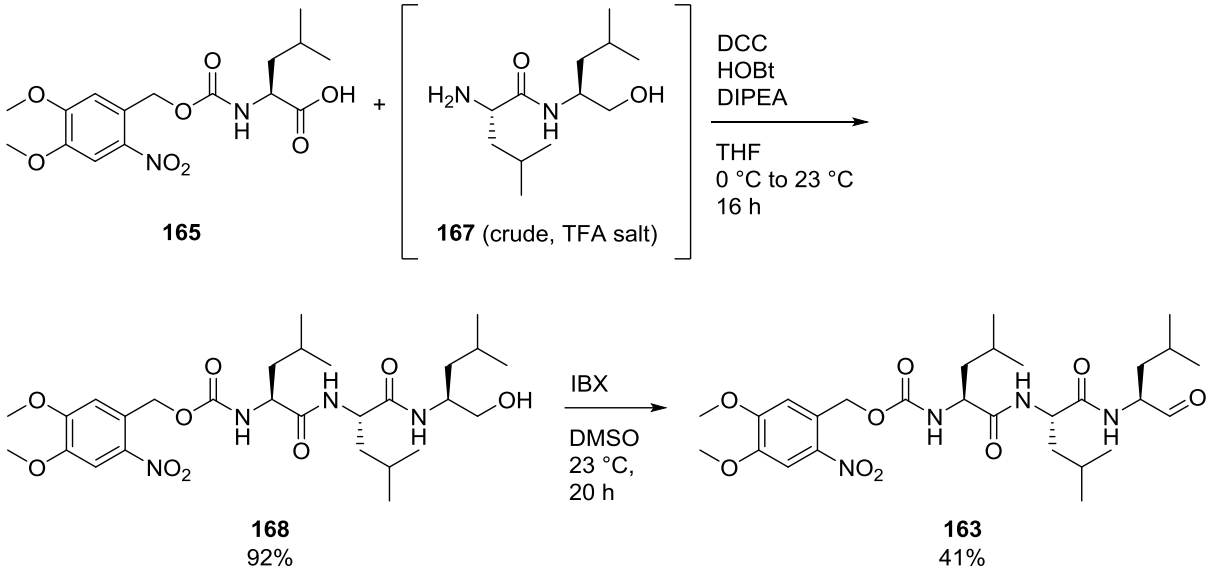

Scheme 86 Synthesis of the tripeptide aldehyde **163**. Coupling of photocaged L-Leucine **165** and crude dipeptide **167** afforded **168**. Oxidation to the aldehyde using IBX gave MG132 analog **163**.

8.2.2 Synthesis of the photocaged MG132 analog 164

Prior to the synthesis of the second analog of MG132 **164** a model compound was prepared (Scheme 87). To this point the key step that cages the aldehyde as an α-acetoxy nitroveratryl ester had only been employed on a very limited number of molecules. The model reaction was used to test the feasibility of the approach and to assess the effectiveness of the light induced uncaging process. In the first step Boc-protected L-Leucine was reacted with 6-nitroveratryl alcohol using DCC and DMAP following a literature procedure for the preparation of related compounds.[216] The product **169** was then cooled to –78 °C and the carboxyl group was reduced to the hemiacetal using DIBAL-H. The intermediate was quenched *in situ* using acetic anhydride to prevent further reduction. Subsequent workup afforded the product **170** in 18% yield.

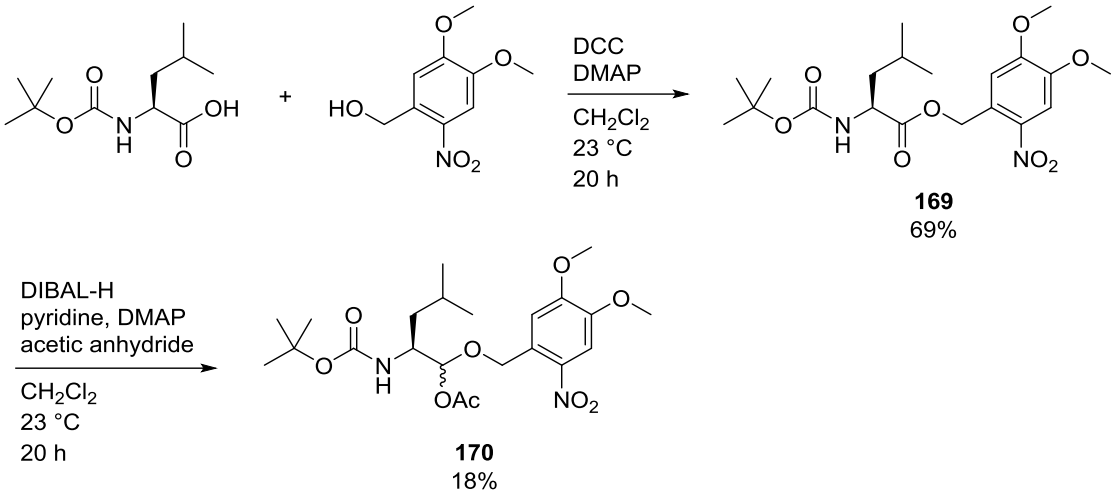

Scheme 87 Synthesis of model compound **170**. Coupling of Boc-protected L-Leucine with 6-nitroveratryl alcohol afforded ester **169**. Reduction with DIBAL-H and *in situ* trapping of the hemiacetal with acetic anhydride gave acetal **170**.

The second photocaged MG132 analog **164** was constructed from two building blocks. The N-terminal benzyloxycarbonyl group (short Z or Cbz) in the target compound simultaneously functioned as protecting group during the synthesis. According to a literature procedure commercially available *N*-Cbz-L-Leucine was reacted with L-Leucine methyl ester using PyBOP as coupling reagent.[217] Ester hydrolysis using 4 M NaOH gave dipeptide **171** in 57% yield over two steps (Scheme 88).

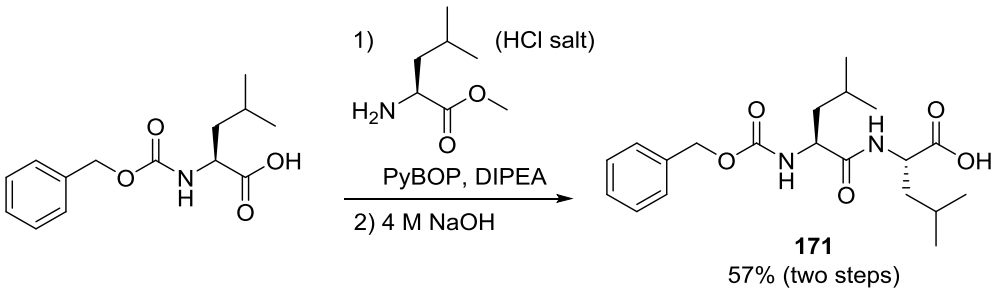

Scheme 88 Synthesis of dipeptide **171**. Coupling of *N*-Cbz-protected L-Leucine with L-Leucine methyl ester and subsequent saponification using 4 M NaOH gave **171** over two steps.

The second building block 6-nitroveratryl L-Leucine ester **169** had already been prepared in the model compound synthesis. The deprotected intermediate **172** was prepared analogously to **167** and was obtained as the crude TFA salt (Scheme 89). Coupling with dipeptide **171** was accomplished in good yields using DCC/HOBt.

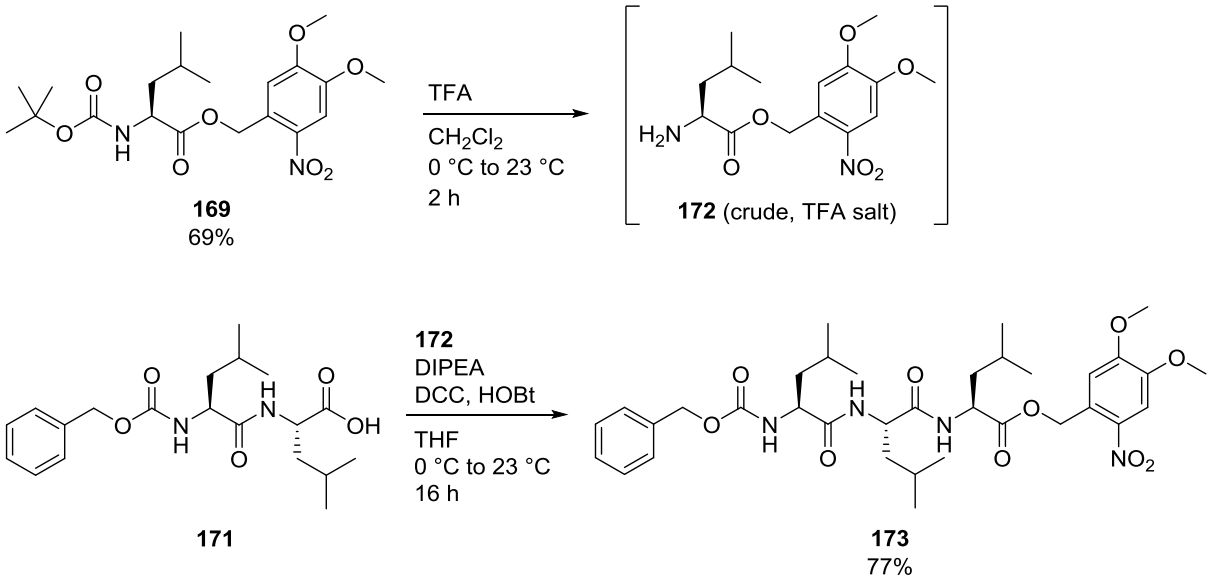

Scheme 89 Synthesis of photocaged tripeptide **173**. The Boc protecting group was removed and gave crude **172** as TFA salt. The two building blocks **171** and **172** were coupled using DCC/HOBt to give **173** in good yields.

Preparation of the caged aldehyde proceeded analogously to the synthesis of model compound **170** (Scheme 87). The nitroveratryl ester functional group was reduced to the hemiacetal at –78 °C and quenched *in situ* through addition of acetic anhydride. Upon workup caged MG132 **164** was obtained as a mixture of diastereomers (Scheme 90).

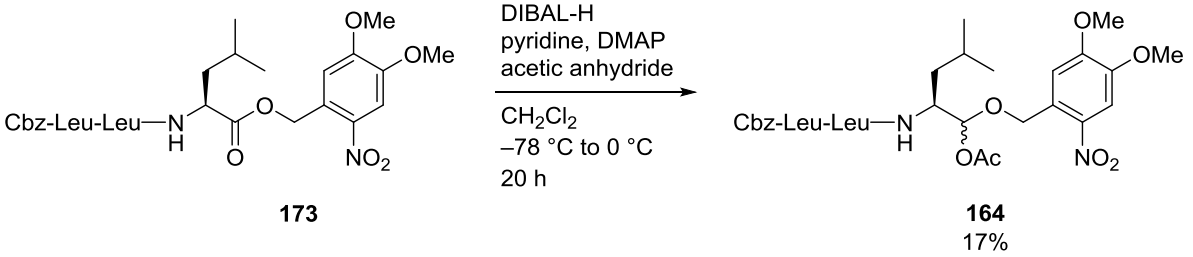

Scheme 90 Synthesis of photocaged MG132 **164**. Reduction of the nitroveratryl ester **173** using DIBAL-H and *in situ* trapping of the hemiacetal with acetic anhydride gave the target compound **164**.

The reductive acetylation of **173** provided the product **164** in 17% yield along with several byproducts. From these, only 6-nitroveratryl alcohol was identified that could be a product of partial overreduction. ^{1}H NMR analysis of other byproducts suggests structures that are closely related to tripeptide **164** but did not include precursor **173** or the free aldehyde MG132. The optimized protocol that was applied for the one-pot reduction/acetylation reaction was originally developed by *Rychnovsky* and discusses the effects of individual reagents and the importance of precise control of temperature.[218] Variations in temperature and reaction times

during repeated synthesis had no discernable effect on the obtained yields however. Due to the many factors contributing to the success of the reaction and the sufficient yield of 17% the reaction was not further optimized.

In order to test the photoinduced uncaging reaction and analyze the reaction products a second model compound **175** was synthesized (Scheme 91). Propionyl chloride was reacted with 6-nitroveratryl alcohol in the presence of TEA and DMAP to give ester **174**. The masked aldehyde was prepared analogously to previous compounds and gave **175** in very good yields, which also highlights the potential of this methodology.

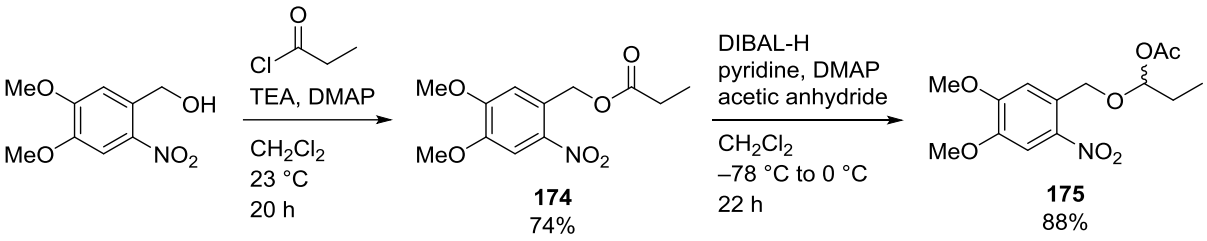

Scheme 91 Synthesis of model compound **175**. Reaction of 6-nitroveratryl alcohol with propionyl chloride gave ester **174** that was reduced to acetal **175**.

8.3 Preliminary testing

8.3.1 Irradiation of MG132 analog 163 at ambient temperatures

Prior to biological testing, photoinduced uncaging of the first MG132 analog **163** was attempted in a MeOD solution and the process was followed by ^{1}H NMR spectroscopy. After a total of 30 min irradiation with 365 nm light almost full uncaging was observed resulting in a variety of products (Figure 197). The reaction was accompanied by a distinct color change from colorless to yellow to brown.

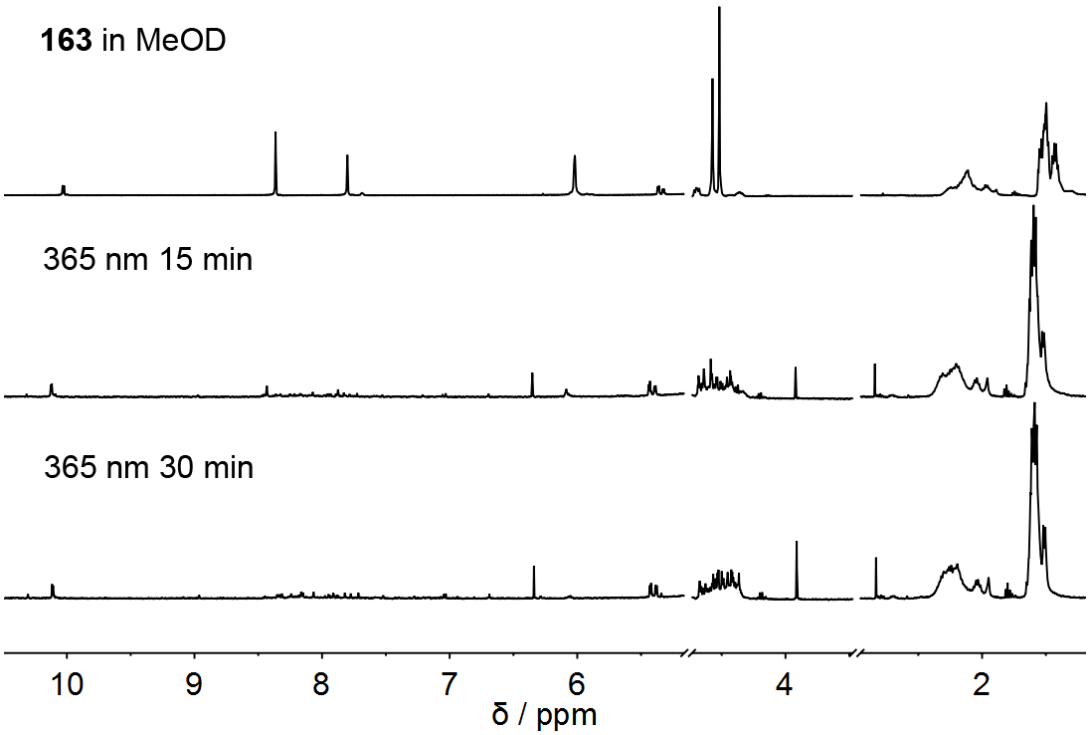

Figure 197 ^{1}H NMR spectra acquired during irradiation of **163** with 365 nm light (400 MHz, MeOD, 22 °C). Uncaging probably results in a large number of products as judged by the complexity of the resulting spectrum.

As irradiation causes the uncaging of a free amine functional group ^{1}H NMR signals were attributed to products from secondary intermolecular condensation reactions and polymerization (Scheme 92). Additional side reactions with 2-nitrosobenzaldehyde further hampered identification of photoproducts. Overall the tripeptide was effectively released upon irradiation with 365 nm light but associated side reactions of primary photoproducts could not be elucidated in detail.

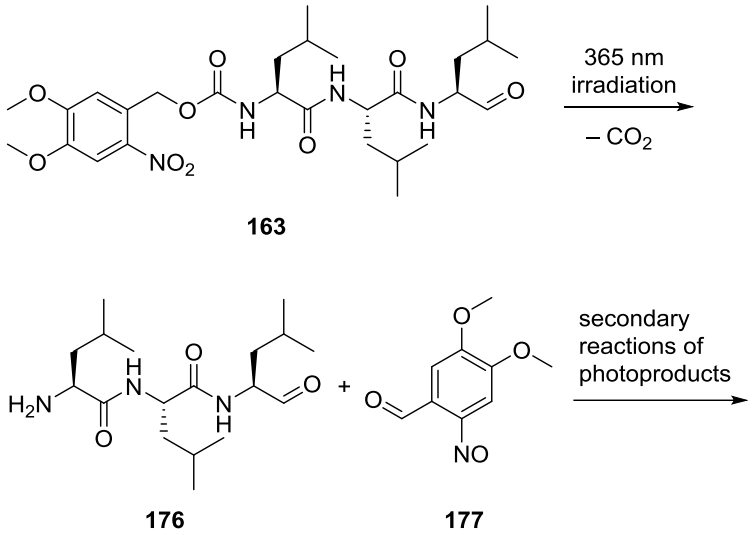

Scheme 92 Primary photoproducts of the uncaging reaction of **163** using 365 nm light. Subsequent polymerization of tripeptide **176** and possible condensation with benzaldehyde **177** would results in a variety of secondary photoproducts.

In addition to ^{1}H NMR experiments, uncaging of **163** was also attempted in water and followed by UV-Vis spectroscopy (Figure 198). Water was chosen as solvent to simulate conditions closely related to *in vivo* experiments. Irradiation with 365 nm light resulted in generation of defined photoproducts as judged by the presence of isosbestic points. The reaction was accompanied by a distinct red-shift of absorption up to 50 nm that was indicated earlier by the color change from colorless to brown during irradiation of an NMR sample. Upon prolonged irradiation (> 300 sec) decomposition of the sample was observed visible through a baseline shift and loss of isosbestic points.

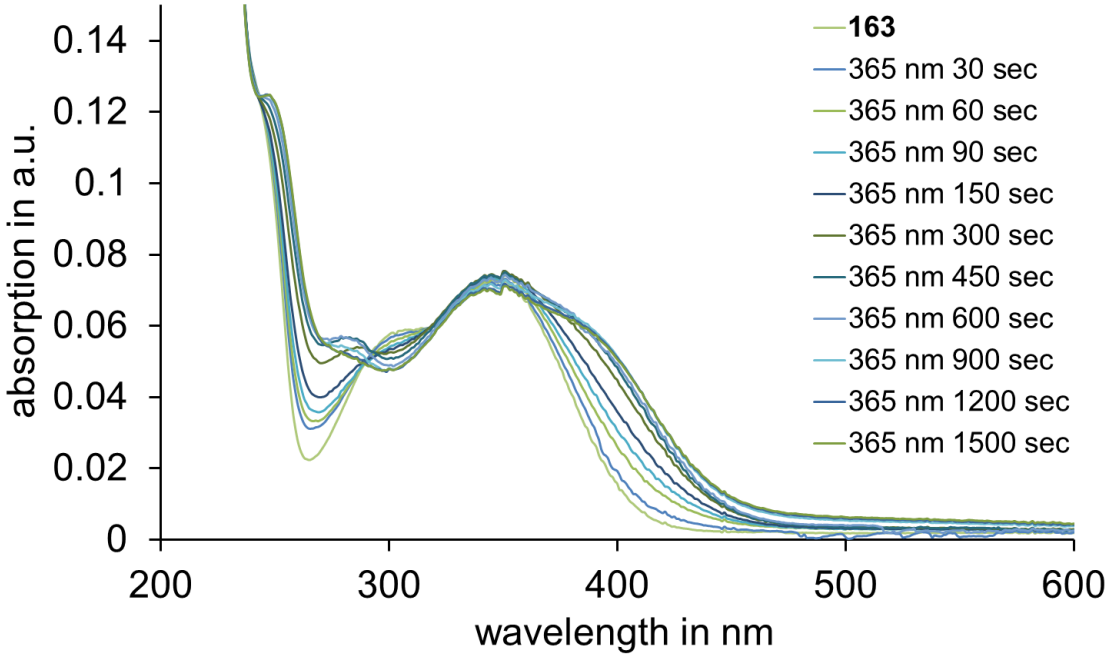

Figure 198 UV-Vis spectra of **163** (H_2O, 23 °C) acquired during irradiation with 365 nm light. Uncaging initially resulted in defined photoproducts as judged by the presence of isosbestic points. Upon prolonged irradiation (> 300 sec) decomposition of the compounds was observed.

The irradiation experiment was repeated in phenol red containing cell culture medium (Figure **199**). Irradiation with 365 nm light had only minor impact on the UV-Vis spectrum. Overall a weak baseline shift could be observed with only minor qualitative changes to the initial spectrum. From the results it was deduced that phenol red effectively prevents photoinduced uncaging of tripeptide **163** and as a result prompted the use of cell culture medium that does not contain the pH indicator dye.

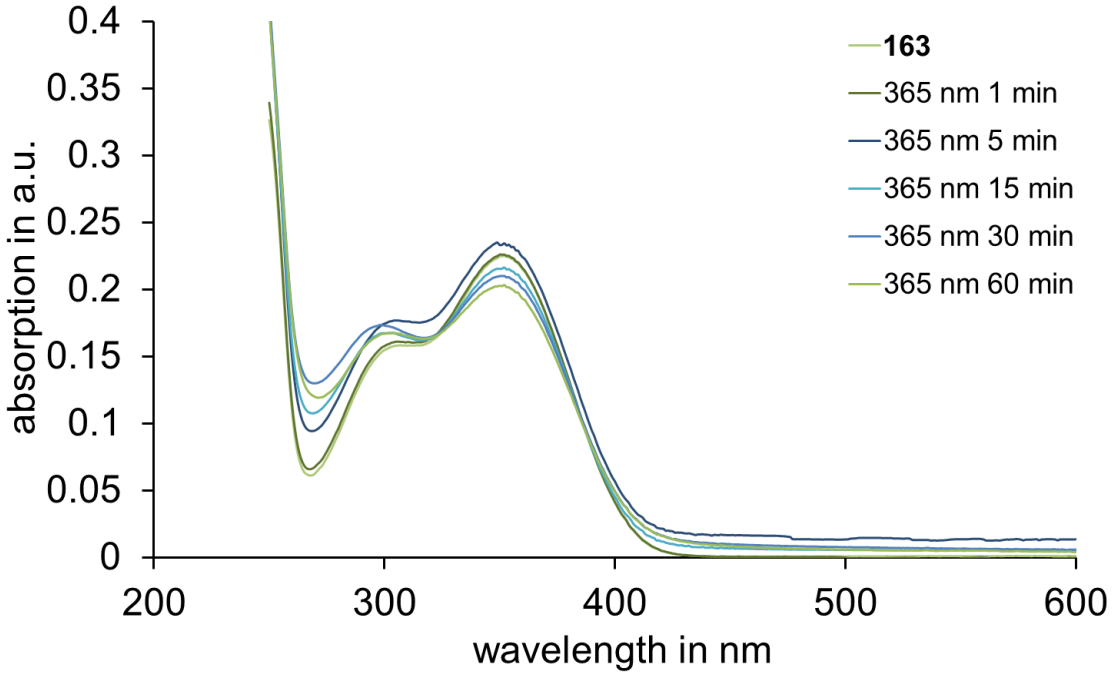

Figure 199 UV-Vis spectra of **163** (cell medium containing phenol red, 23 °C) acquired during irradiation with 365 nm light. Uncaging was effectively prevented by the pH indicator dye phenol red.

8.3.2 Irradiation of model compounds at ambient temperatures

The model compound **170** with caged aldehyde functional group was irradiated in CD_2Cl_2 and the reaction was followed by ^1H NMR spectroscopy (Figure 200). Similar to MG132 analog **163** a variety of photoproducts was observed. During the irradiation an aldehyde signal emerged that indicated the successful uncaging of this functional group. Due to the comparatively high concentration, irradiation times up to 60 min only achieved partial uncaging of the compound.

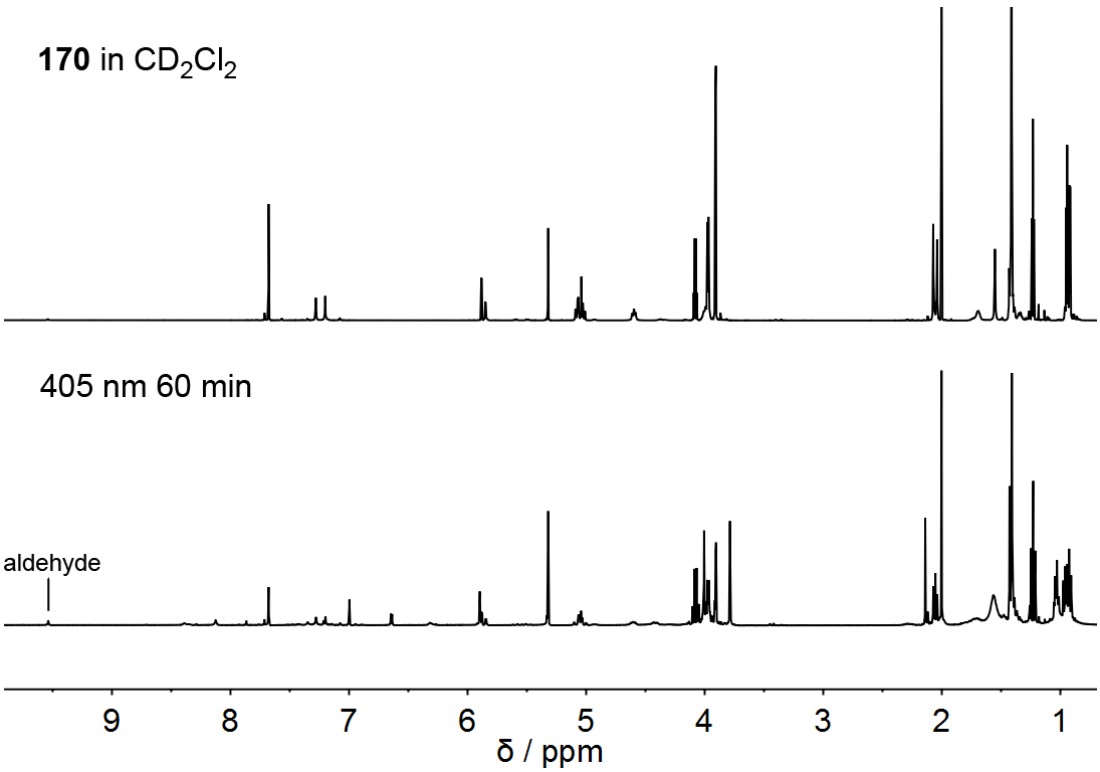

Figure 200 ^{1}H NMR spectra of **170** (400 MHz, CD_2Cl_2, 22 °C) acquired before (top) and after 60 min of 405 nm irradiation (bottom). Partial uncaging is observed accompanied by an increase in aldehyde signal intensity.

A second model compound had been prepared to assess the uncaging reaction in greater detail. The release of propanal from **175** does not interfere with the absorbance of photoproducts from the uncaged 6-nitroveratryl protecting group in the visible part of the UV-Vis spectrum. A very fast initial photoreaction resulted in a strong red-shift of absorption that decayed over the course of 60 seconds under continued irradiation (Figure 201).

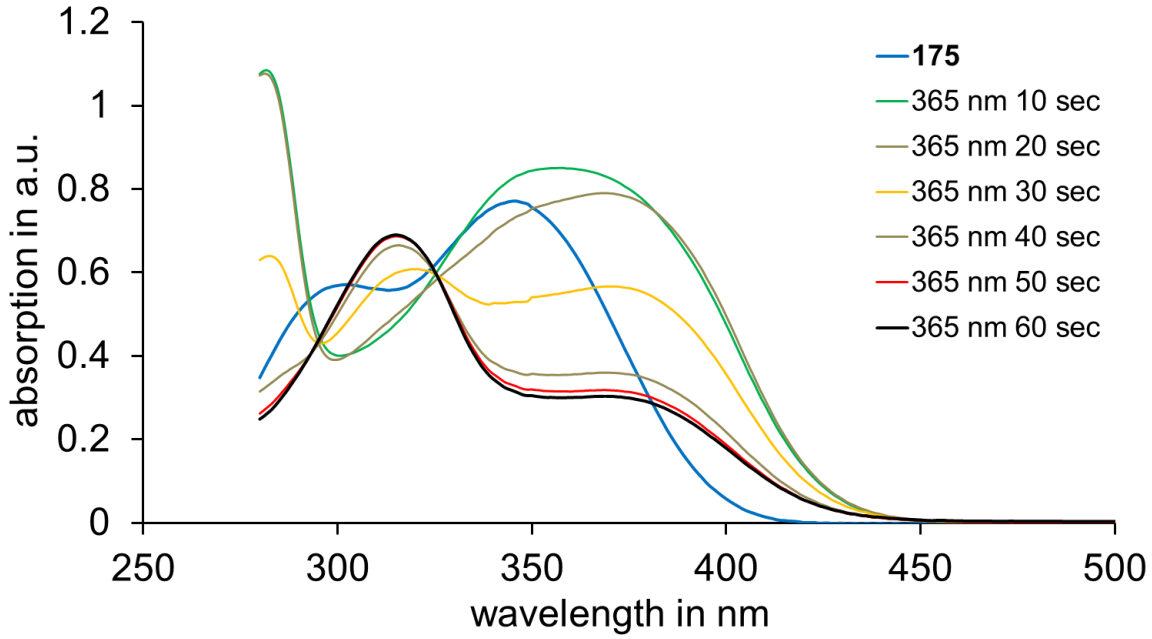

Figure 201 UV-Vis spectra of **175** ($CHCl_3$, 23 °C) acquired during irradiation with 365 nm light.

Apparently a second reaction followed the initial photoreaction that revealed defined product formation as indicated by the presence of isosbestic points (Figure 202). After a total of 300 seconds onset of a third reaction was observed that lead to a gradual increase of absorption over the acquired wavelength (Figure 202, dark blue). This is in agreement with the observed change of color from colorless to yellow to brown that was discussed earlier.

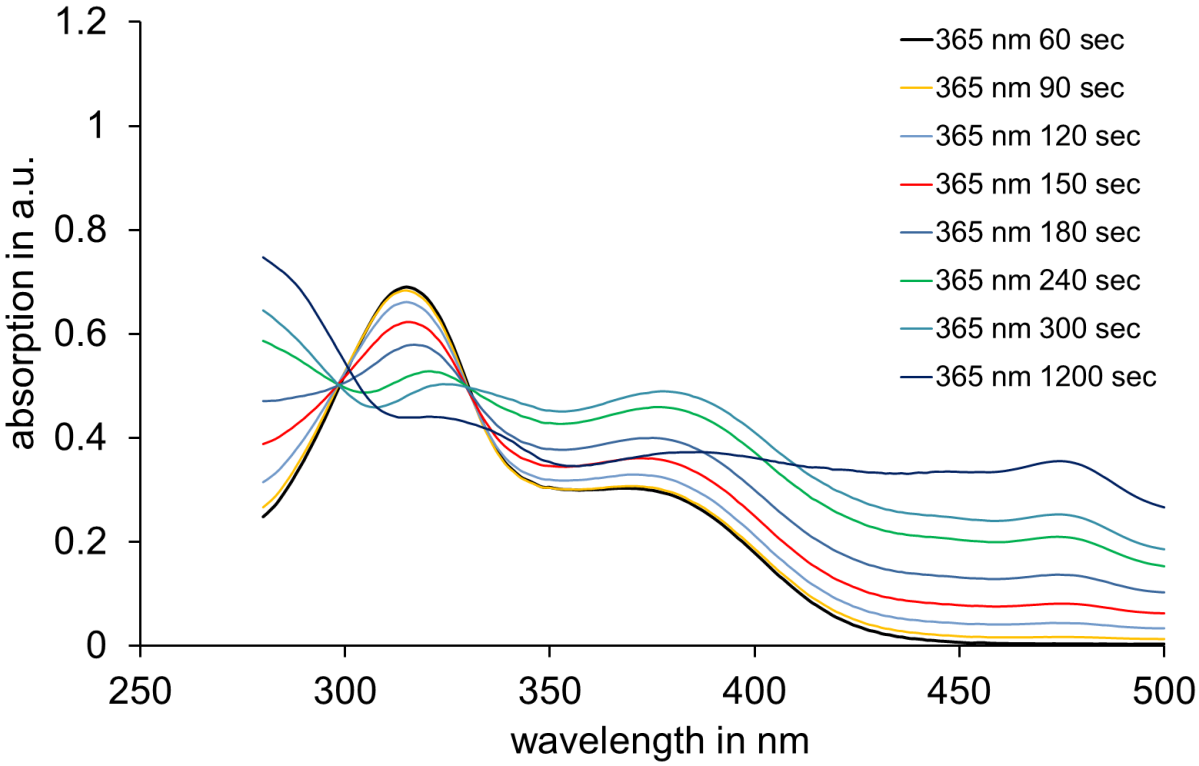

Figure 202 UV-Vis spectra of **175** ($CHCl_3$, 23 °C) acquired during irradiation with 365 nm light.

The tripeptide precursor **173** with caged acid functional group as well as caged propionic acid **174** were used in control studies. UV-Vis spectra were recorded to demonstrate successful uncaging of these compounds upon irradiation with 405 nm light. Irradiation of **173** revealed the spectral changes expected for the photodeprotection process with a strong decrease of absorption intensities at 350 nm (Figure 203).

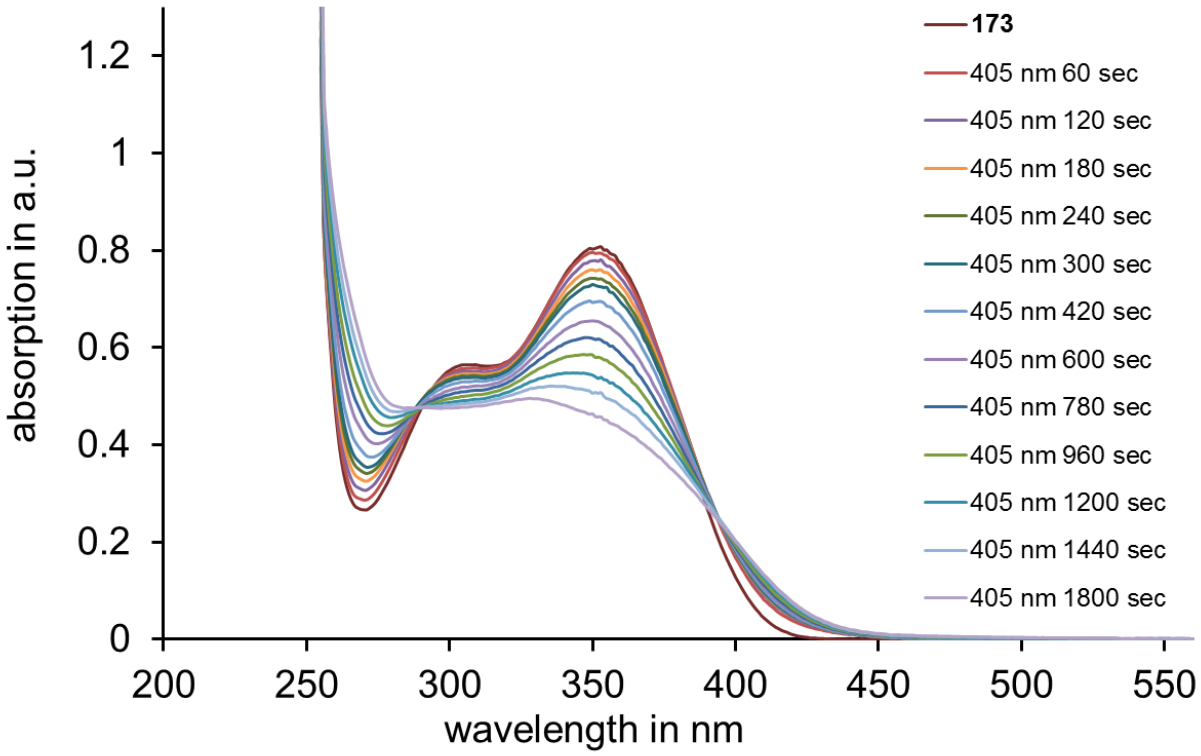

Figure 203 UV-Vis spectra of **173** (DMSO, 20 °C) acquired during irradiation with 405 nm light.

Analog behavior was observed for compound **174** (Figure 204). Upon prolonged irradiation additional side reactions were observed as judged by the absence of isosbestic points.

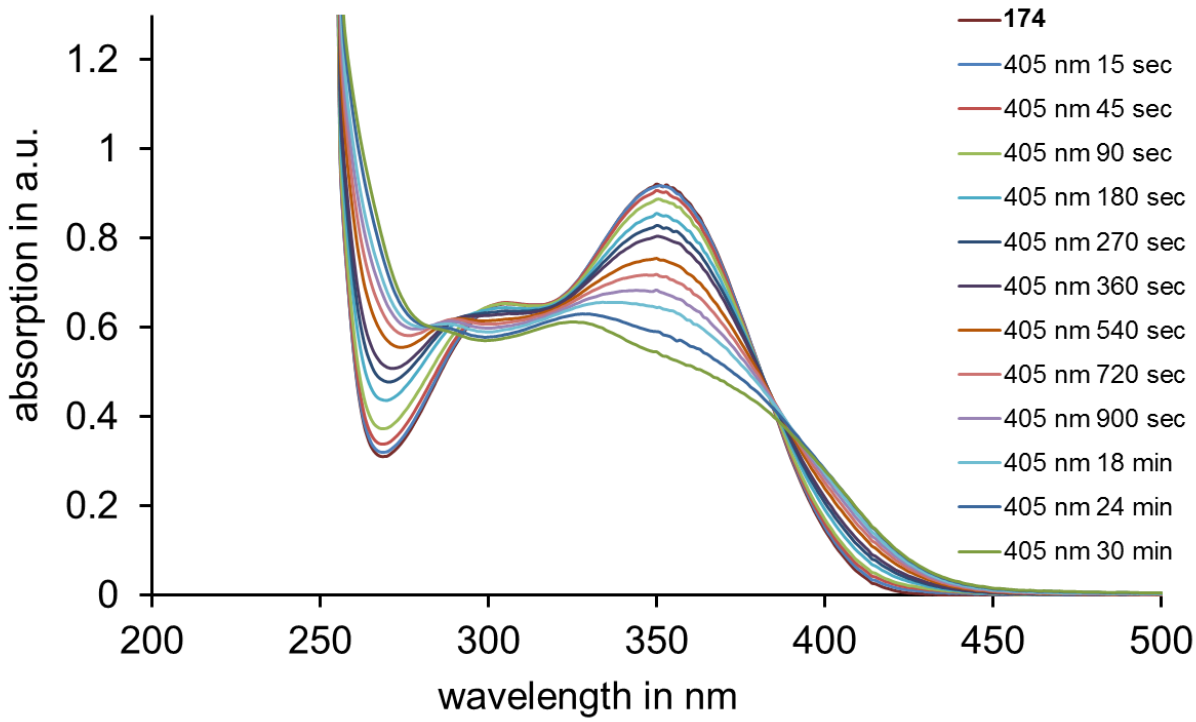

Figure 204 UV-Vis spectra of **174** (DMSO, 20 °C) acquired during irradiation with 405 nm light.

8.3.3 Irradiation of MG132 analog 164 at ambient temperatures

Caged MG132 **164** in DMSO was irradiated with 405 nm light and the process was followed by UV-Vis spectroscopy (Figure 205). The compound was released in a single photoreaction as judged by the presence of isosbestic points. No secondary reactions were observed upon prolonged irradiation. This indicates that the release of a free amine, for example from irradiation of **163**, is responsible for the observed side-reactions.

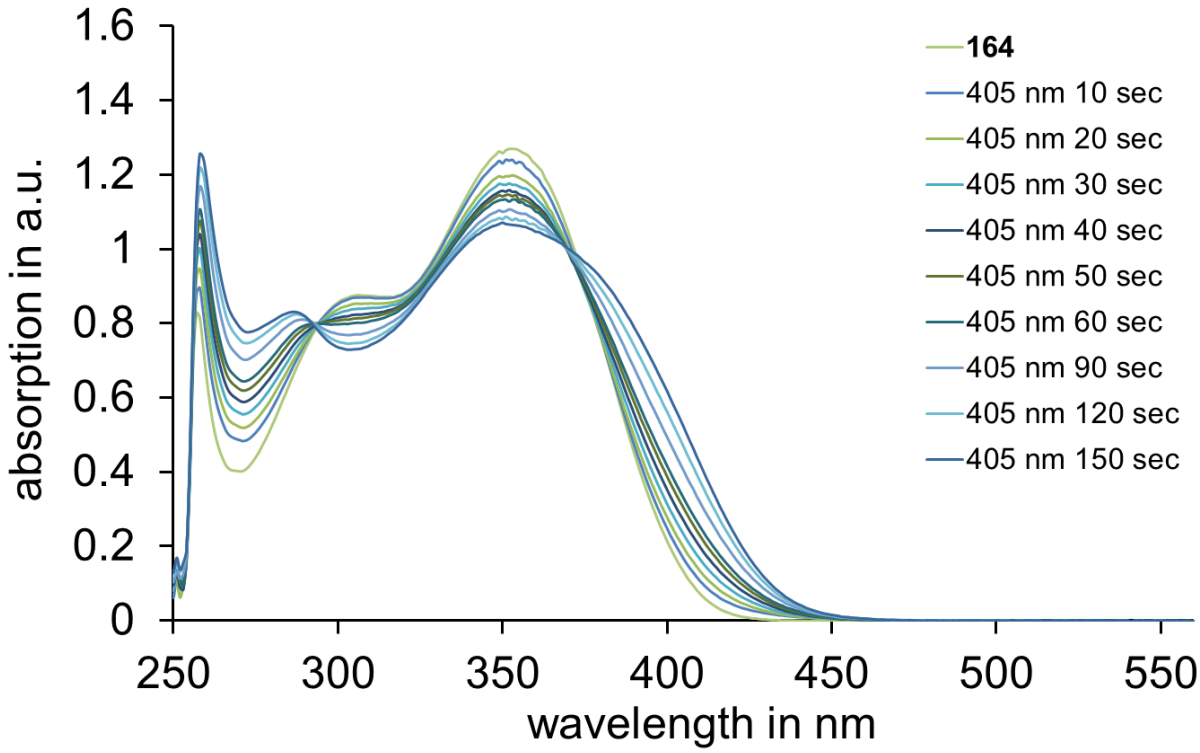

Figure 205 UV-Vis spectra of **164** (DMSO, 23 °C) acquired during irradiation with 405 nm light.

The release of MG132 from **164** was also followed by ^{1}H NMR spectroscopy (Figure 206). A solution of **164** in DMSO-d_6 was irradiated repeatedly in 1 minute intervals for a total of 10 minutes. The gradual increase of an aldehyde signal was observed that could be assigned to MG132 by direct spectral comparison (Figure 206, bottom). A second photoproduct could be assigned to the cleaved protecting group. After 10 minutes almost complete uncaging was observed resulting in a ratio of 85% MG132 to 15% **164**. Overall uncaging of **164** was highly effective using 405 nm light and resulted in mostly well-defined products with only minor amounts of byproducts.

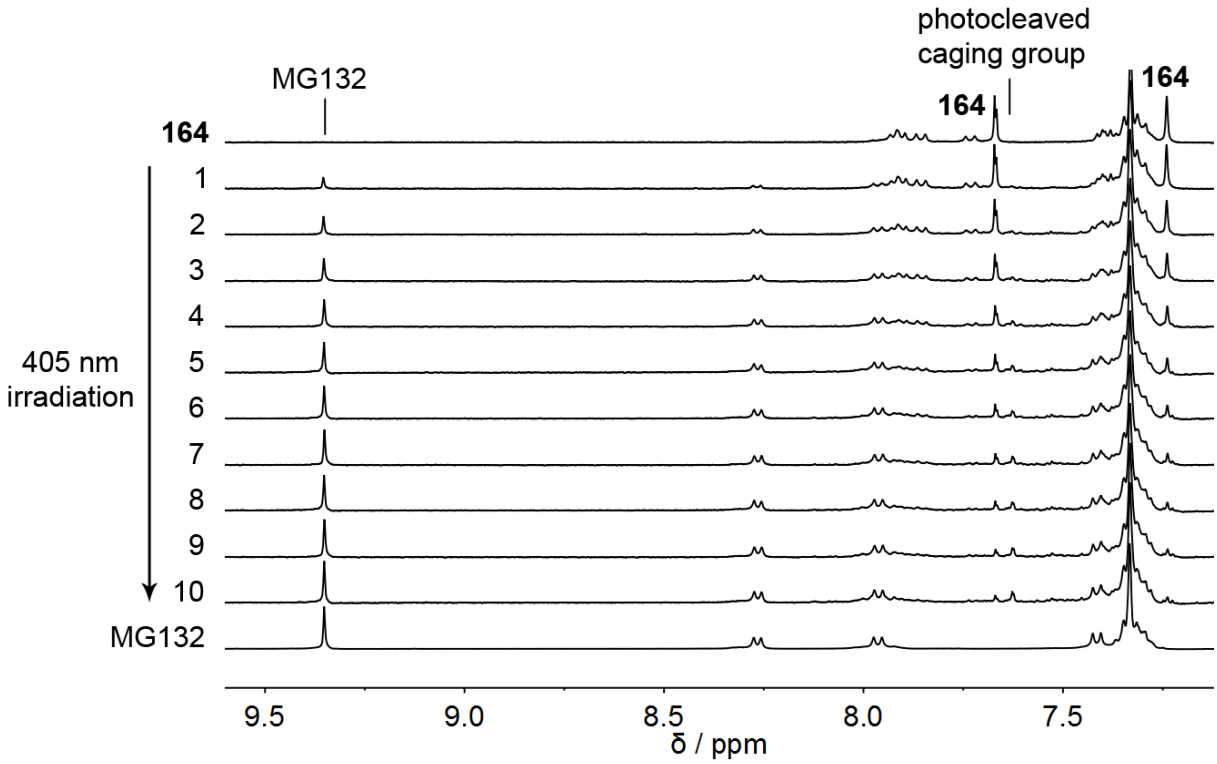

Figure 206 ^{1}H NMR spectra of **164** (400 MHz, DMSO-d_6, 22 °C) acquired during irradiation with 405 nm light. Spectra were taken in 1 min (irradiation) intervals. A spectrum of pure MG132 is shown for comparison. After a total of 10 min of 405 nm irradiation almost full uncaging was observed resulting in a ratio of 92% MG132 to 8% **164**.

8.3.4 Molar absorption coefficients and quantum yield determination

Preliminary tests were completed with the determination of the quantum yield of **164**. The experiment was conducted analog to the experimental procedure described in section 4.5. First, a UV-Vis spectrum of **164** with known concentration was taken to determine the molar absorption coefficients (Figure 207).

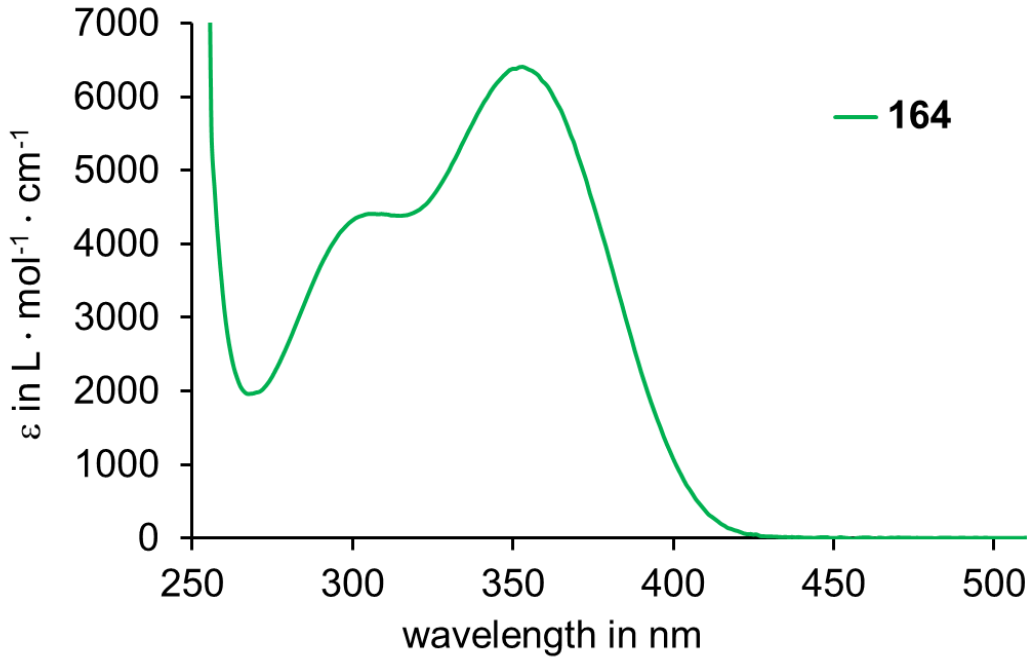

Figure 207 Molar absorption coefficients ε of **164** (139 µM, DMSO, 20 °C).

Because of potential side reactions upon prolonged irradiation a sample containing **164** in DMSO-d_6 was irradiated for a short time period (1 min) using 405 nm light and the corresponding photoconversion was determined by NMR spectroscopy (Figure 208).

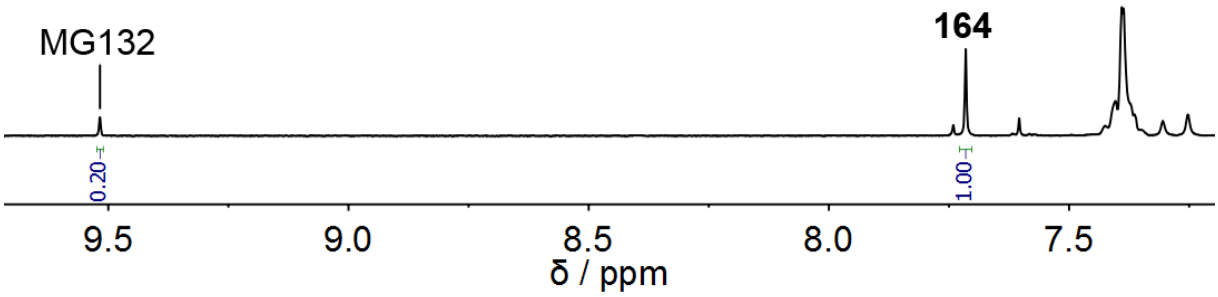

Figure 208 ^{1}H NMR spectrum of **164** (400 MHz, DMSO-d_6, 22 °C) acquired after 1 min irradiation with 405 nm light.

A portion of the NMR sample was diluted in additional DMSO and a UV-Vis spectrum was taken to obtain a reference point for the following quantum yield determination (Figure 209, blue line). After normalization to the isosbetic point at 368 nm the absorption changes during irradiation could be directly related to changes in concentration.

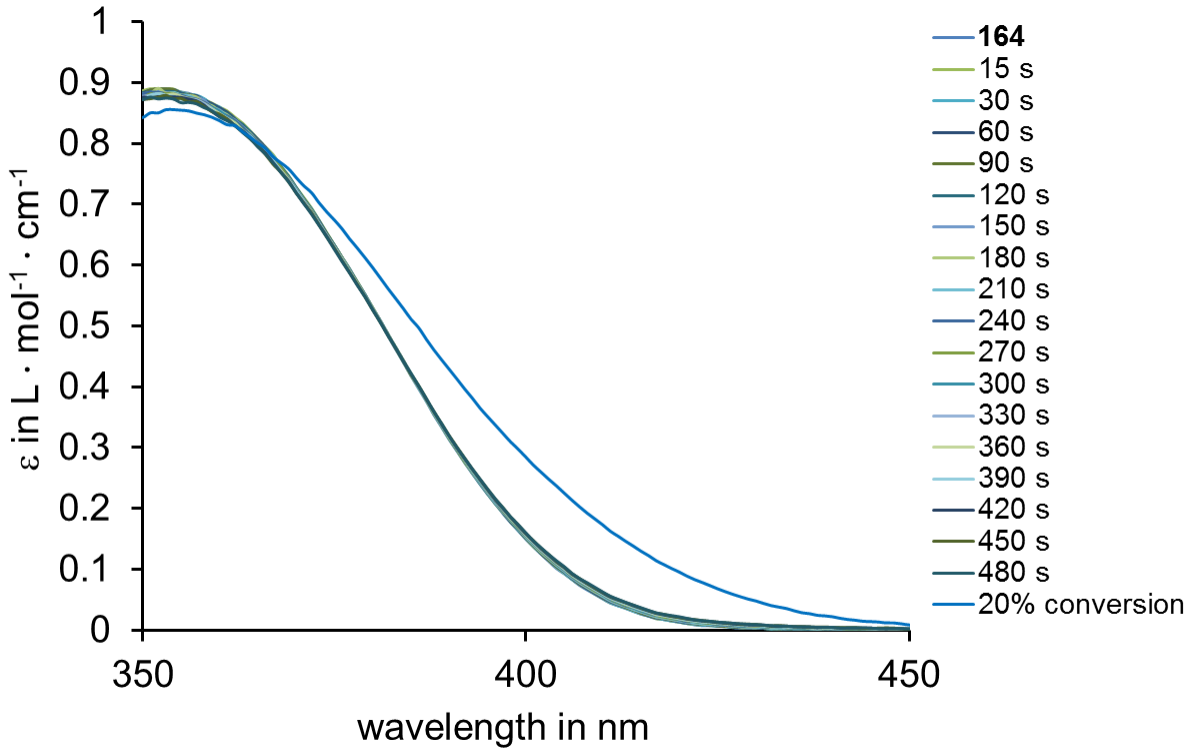

Figure 209 UV-Vis absorption spectra acquired during irradiation of a solution of **164** (139 µM, DMSO, 20 °C) with 405 nm light. A spectrum with 20% conversion was used as a reference point.

Using (equation *10)* a quantum yield of 1.0% was determined which is in very good agreement with previously reported data for the uncaging of an NV protected compound.[219]

8.4 Biological testing

All biological experiments were conducted by *Sriyash Mangal* and *Friederike Wolff* from the laboratory of *Esther Zanin* in the Department of Biology II at the LMU Munich. After preliminary testing the photocaged MG132 analogs **163** and **164** were tested *in vivo* on HeLa cells. Cells were seeded in 12-well plates and presynchronized using a double thymidine block that causes S-phase arrest, which results in more cells undergoing mitosis during the experiments. For detailed experimental procedures see the literature.[220] With this protocol the amount of cells in experimentally relevant cell division phases are greatly increased compared to interphase cells, facilitating manual counting and providing more significant results. Also, interphase cells were ignored for the counting as the experiments are not concerned with synchrony and comprehensibility of presented data is greatly enhanced. Counting of cells after fixation was done by hand using an inverted microscope or laser scanning confocal microscope.

Cells undergoing mitosis were divided into either Prometaphase/Metaphase (arrested) cells or Anaphase/Telophase (released, divided) cells and the percentage was determined by dividing through the total number of (mitotic) cells counted. For irradiation experiments well plates were placed in a self-made dark chamber and irradiated with two LEDs (365 nm or 405 nm light) that were placed ca. 1 cm above the plates. All experiment were done in pairs comparing them directly to MG132 administration under identical conditions.

First experiments were conducted with MG132 analog **163** that bears a free aldehyde functional group for effective proteasome inhibition. Modulation of the binding affinity was expected to result from uncaging of the N-terminal site and associated changes e.g. in size and polarity. For the experiments HeLa cells that express anillin-GFP and mKate2-α-tubulin were used to facilitate imaging (see experimental section for additional details). A first series of tests included washouts, addition of inhibitor in the dark and irradiation experiments (Figure 210).

Washout experiments were established to test the effectiveness of the release of cells from metaphase arrest. Two hours after inhibitor addition cells were washed by removing most of the cell medium and adding fresh medium (without inhibitor). This process was repeated a total of five times and cells were fixed after another 105 min to 120 min of incubation. Preliminary tests had already revealed that the pH indicator dye phenol red contained in fetal bovine serum (FBS) effectively prevents uncaging of **163**. As a results experiments were conducted using 0% to 10% of the serum. A significant increase of released cells was observed from 0% to 10% FBS containing medium (Figure 210, left section). Since FBS does not affect the efficiency of the washout, arrests at low concentrations are due to serum starvation. Surprisingly **163** washed out more effectively than MG132 throughout the experiments.

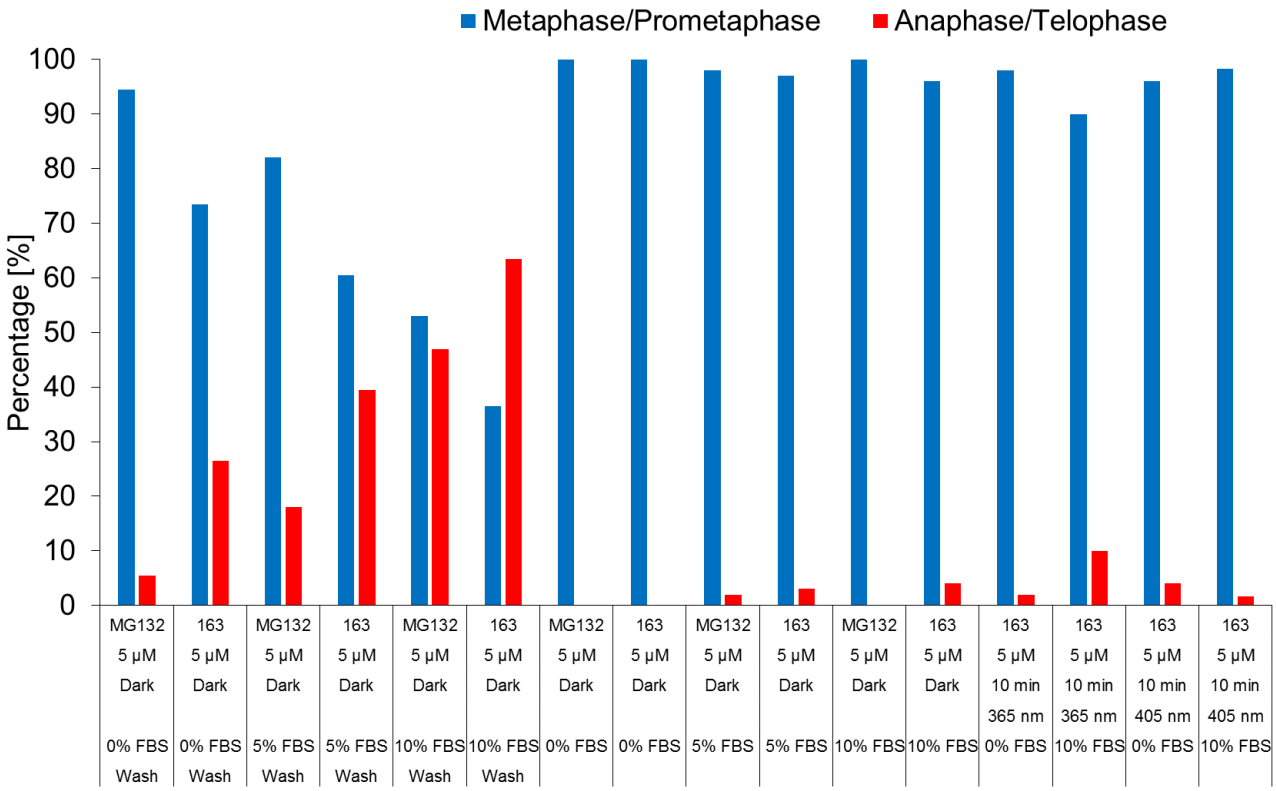

Figure 210 Results from metaphase arrest experiments using compound **163**. An inhibitor concentration (MG132 and **163**) of 5 µM was used throughout the experiments. Serum starvation reduced the efficiency of release as evidenced by washout experiments. Inhibitor **163** washed out more efficiently than MG132 and revealed an identical arrest efficiency as MG132 that is independent of FBS concentrations. Irradiation with 365 nm or 405 nm did not have a significant impact on the inhibitor performance.

Next the potency of inhibitor **163** was compared to MG132 (Figure 210, middle section). Effective inhibition using MG132 is commonly achieved using concentrations in the single-digit to low two-digit micromolar range. For the first tests a concentration of 5 µM MG132 and **163** was used and cells were fixed two hours after addition of the inhibitor. An almost quantitative metaphase arrest was observed for the caged compound **163** with minor amounts (< 5%) of released cells when increased amounts of FBS were used. The observed potency is comparable to that of MG132, which showed quantitative arrest for 0% and 10% FBS and 2% release of cells at 5% FBS. In another series of experiments the caged compound was irradiated immediately after addition to the cells using 365 nm and 405 nm light (Figure 210, right section). Again 0% and 10% FBS concentrations were tested. Irradiation with 365 nm light in 10% FBS containing medium lead to a minor increase in released cells but the underlying effects were ambiguous as uncaging of the compound is at least partly prevented by phenol red. Cells in media containing 0% FBS did not reveal a change in inhibitor potency upon irradiation

with 365 nm or 405 nm light. Overall the modulation of inhibitor potency is not significantly affected upon irradiation and associated uncaging. Also reaction conditions need to be optimized to draw precise conclusions from the experiments. Because of inconclusive performance of the compound upon irradiation and the simultaneous development of the MG132 analog **164** with caged aldehyde functionality no further *in vivo* tests were conducted with this inhibitor. Nevertheless fundamental information regarding design and conduction of experiments were gained from the tests and applied in the next experiments.

In the following examination of MG132 analog **164** was conducted *in vivo*. Different to **163** now the aldehyde functional group needed for proteasome interaction is caged in **164**. Direct comparison of MG132 and **164** in 2 µM and 5 µM concentrations demonstrated the effectiveness of this approach with MG132 showing quantitative arrest compared to only 40-50% arrest when caged compound **164** was used (Figure 211, left section). The experiments were repeated but this time cells were irradiated directly after inhibitor addition using 405 nm light for a total of 10 minutes (Figure 211, right section).

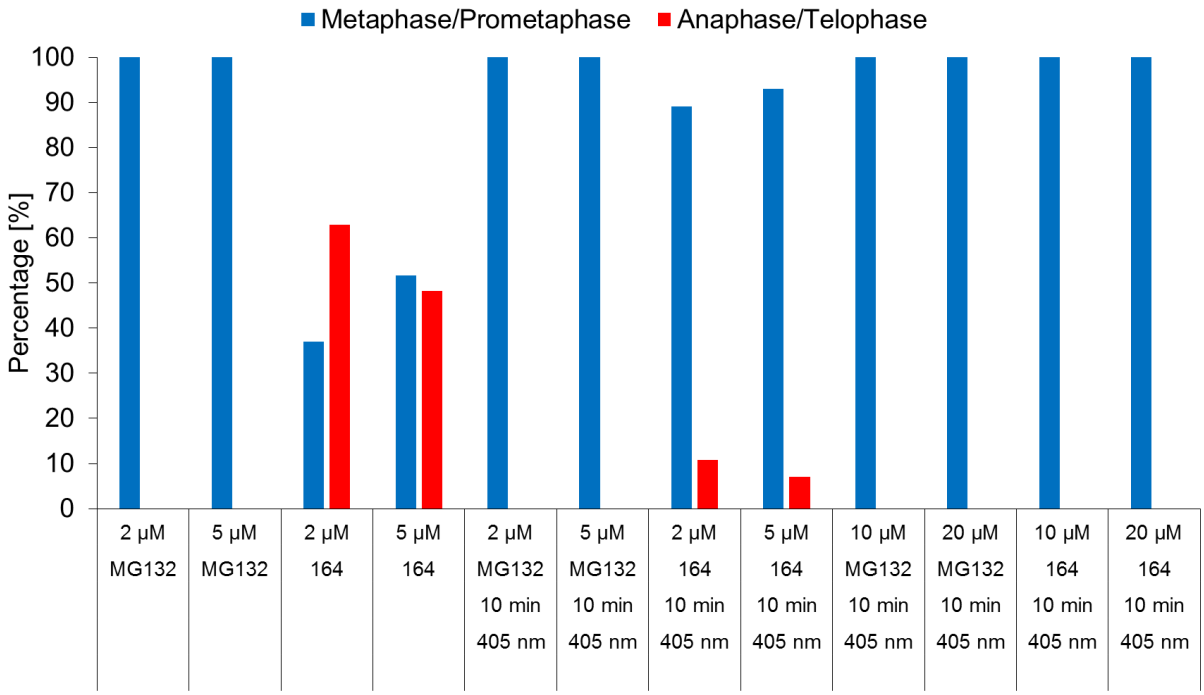

Figure 211 Results from metaphase arrest experiments using caged MG132 **164**. Inhibitor concentrations between 2 µM and 20 µm were used. Cells were unaffected by the caged compound resulting in 50-60% cell division. The active compound was released upon irradiation with 405 nm light resulting in drastically diminished amounts of proliferating cells. At lower inhibitor concentrations minor amounts of cells are still released after irradiation.

The amount of released cells was reduced significantly to 7-10% when concentrations of 2-5 µM **164** were used, revealing only slightly reduced potency compared to the quantitative arrest of the analog MG132 experiment. Increasing the concentration of **164** to 10 µm and 20 µm resulted in quantitative arrest upon 405 nm irradiation.

When cells were irradiated with 385 nm light after inhibitor addition quantitative arrest of cells was observed even at low concentrations indicating that the shorter wavelength releases the active compound more efficiently (Figure 212, left section). Washout of the uncaged inhibitor again resulted in up to 60% release, which is in the range of the analogous MG132 experiments (60-70%, Figure 212, right section). As increased energy of the 385 nm light is expected to be more harmful for cells, the majority of experiments was done using 405 nm irradiations.

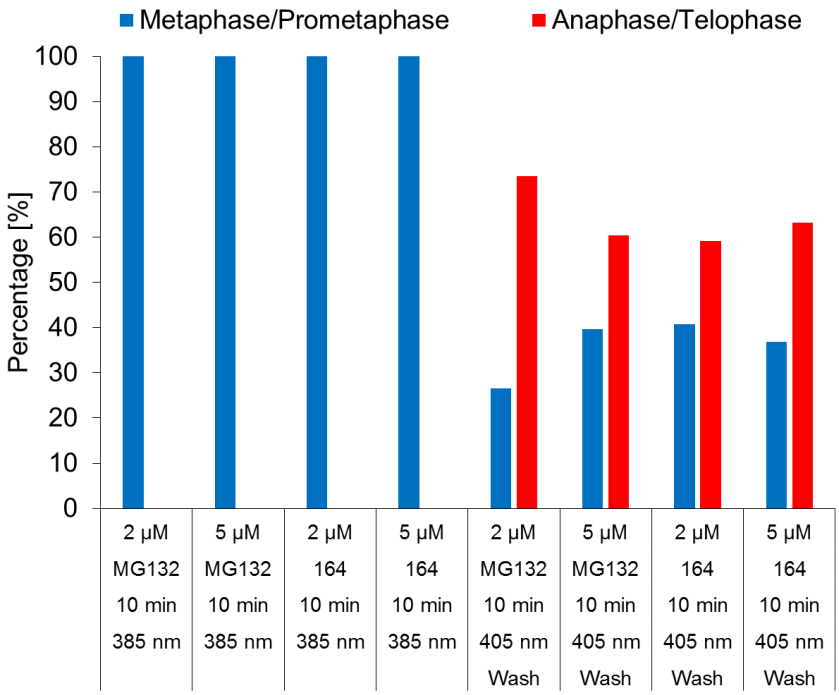

Figure 212 Results from metaphase arrest experiments using compound **164**. Inhibitor concentrations of 2 µM and 5 µm were used. The active compound was effectively released upon irradiation with 385 nm light. Washout effectiveness was comparable to MG132.

A second set of tests with overall increased concentrations of **164** (5-10 µM) was conducted (Figure 213). Direct comparison of untreated cells to cells with inactivated compound **164** further proved the caging effectiveness with comparable amounts of cells released throughout the experiments. Next, a series of irradiation experiments was conducted using **164** in 5 µM and 10 µM concentrations and 405 nm light. Irradiation times ranged from 2 min to 10 min. A constant increase of arrested cells was observed toward longer irradiation times with an overall

increased arrest when higher concentrations of **164** (10 µM compared to 5 µM) were used. The results ranged from 65% arrest using 2 µM **164** and 2 min irradiation to > 95% arrest for 5 – 10 µM concentrations and 10 min irradiation time. In a control experiment untreated cells were irradiated for 10 minutes using 405 nm light. The test resulted in 54% release of cells and safely excludes increased arrest of cells caused by irradiation damage.

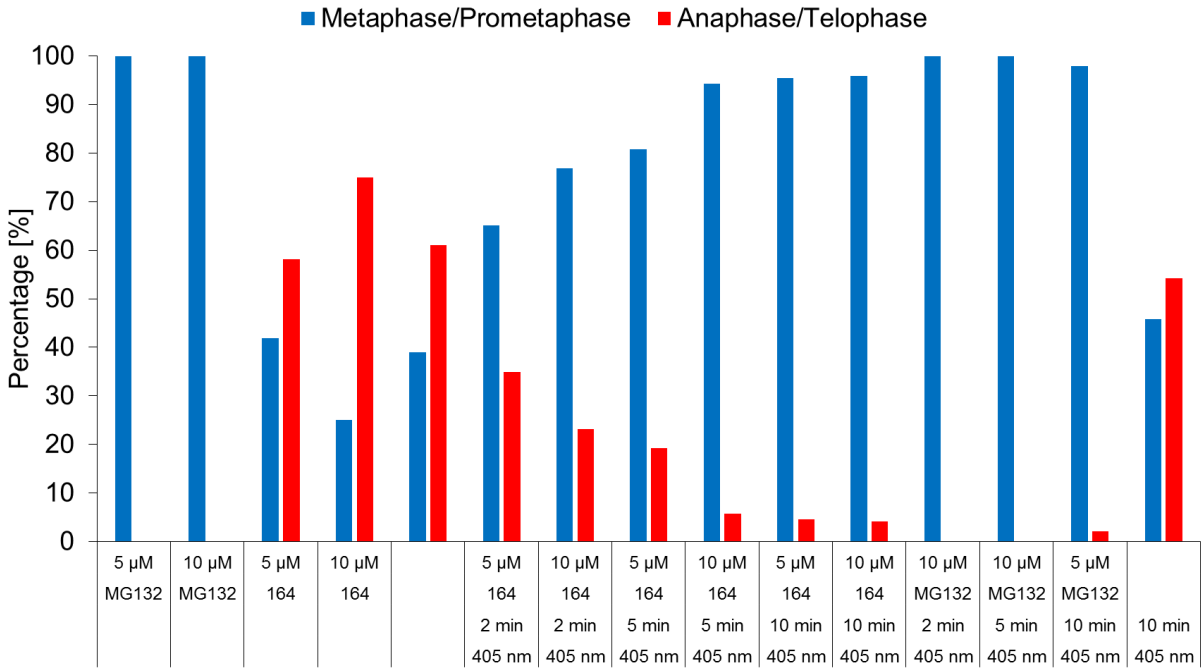

Figure 213 Results from metaphase arrest experiments with compound **164**. Inhibitor concentrations of 5 µM and 10 µm were used. Irradiation was done using 405 nm light. Cells were unaffected by the caged compound resulting in 60-75% cell division. Prolonged irradiation times and higher inhibitor concentrations resulted in significantly increased amounts of arrested cells with 65% arrest at 2 µM and 2 min irradiation to 96% arrest at 10 µM and 10 min irradiation.

At this point a new batch of compound **164** was prepared. First, the previous set of experiments shown in Figure 213 was repeated in order to get an independent confirmation of the experimental data (Figure 214). The compound wass confirmed to be inactivated by the applied caging methodology resulting in up to 75% release of cells at 10 µM concentrations. Additional experiments confirmed the increase in metaphase arrest upon prolonged irradiation and an increase in inhibitor concentrations. The results range from 60% arrest using 5 µM **164** and 5 min of 405 nm irradiation up to 98% arrest using 10 µM **164** and 10 min of 405 nm irradiation. MG132 control experiments in 5 µM and 10 µM concentrations resulted in quantitative arrest. Irradiation with 405 nm light directly after addition of MG132 had no visible effect.

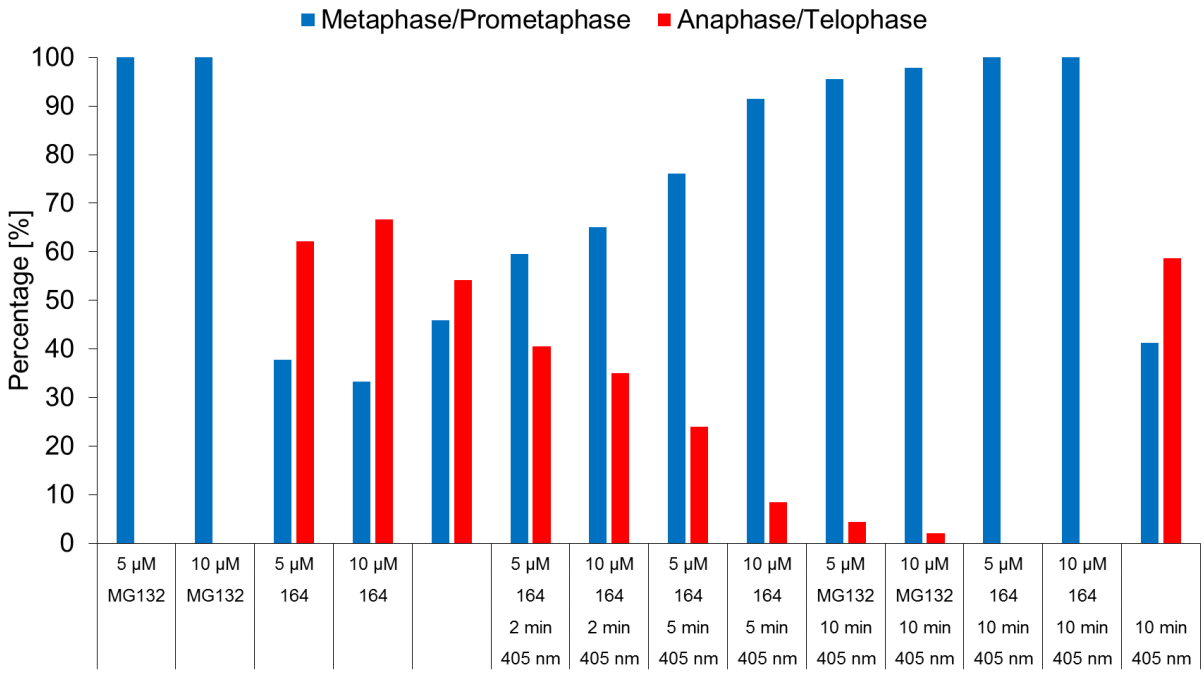

Figure 214 Replication of previous metaphase arrest experiments using a new batch of compound **164**. Inhibitor concentrations of 5 µM and 10 µm were tested. Irradiation was done using 405 nm light. Cells were unaffected by the caged compound resulting in ca. 65% cell division. Prolonged irradiation times and higher inhibitor concentrations resulted in significantly increased amounts of arrested cells with 60% arrest at 5 µM and 5 min irradiation up to 98% arrest at 10 µM and 10 min irradiation. Overall the experiment was in very good agreement with previous results.

A third batch of compound **164** was prepared and tested on cells. Inhibitor concentrations of 5 µM or 10 µM were used throughout the experiments. A 405 nm LED was employed to irradiate compounds directly after addition to the cells. Addition of the inactivated compound **164** resulted in 30-40% release of cells (Figure 215, left section). This is significantly less compared to tests on the previous cell line. However, a control experiment with untreated cells also resulted in only 36% cell division confirming a new baseline release of cells using this methodology. Washout experiments using the caged compound resulted in ca. 50% release. This was slightly more compared to the experiments with caged inhibitor and could be the result of the different timeframes for medium exchange applied in the experiments.

Irradiation of compound **164** directly after addition resulted in quantitative arrest throughout the experiments (Figure 215, middle section). This included concentrations as low as 5 µm with only 5 min irradiation. Washout of the arrested cells resulted in 40-60% release with overall more efficient release when 5 µM concentrations were used. Surprisingly release of cells that were arrested first is more effective compared to analogous washout experiments with caged

inhibitor. This could be the result of counting and presentation of data that ignore synchrony of cells – that is the amount of mitotic cells compared to interphase cells. In the current experimental setup presynchronized cells that have already entered interphase are ignored. This leads to an increased number of *release* (cells undergoing anaphase or telophase) when cells were intermittently arrested as more cells have not yet entered interphase.

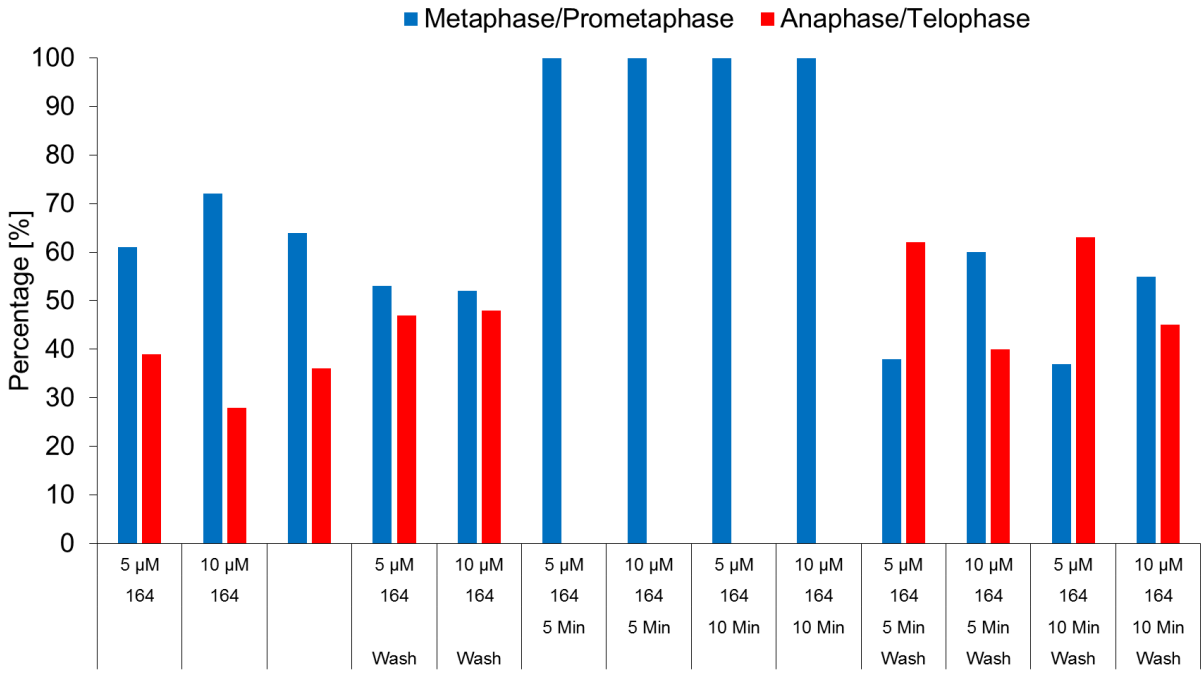

Figure 215 Results from metaphase arrest experiments using compound **164** on the new cell line. Inhibitor concentrations of 5 µM and 10 µm were used. Cells were irradiated for 5 min or 10 min using 405 nm light. Cells were unaffected by the caged compound resulting in ca. 30-40% release which is comparable to untreated cells (36% release). Irradiation after addition of **164** resulted in quantitative arrest for all applied conditions. Washout of analog experiments resulted in 40-60% release.

A series of control experiments was conducted using MG132 and untreated cells (Figure 216). Inhibitor concentrations of 5 µM or 10 µM were used and irradiation times of 5 min or 10 min with 405 nm light. Addition of MG132 to cells resulted in quantitative arrest for both concentrations. Irradiation had no impact on the potency of the inhibitor. Washout of MG132 was highly effective resulting in 55-65% release and was slightly more effective when the inhibitor was irradiated for 5 min (ca. 70%). When MG132 was irradiated for 10 min only around 30% of cells were released. This could be a result of irradiation damage or too early fixation of cells and requires further testing by repeating the experiment. Irradiation of untreated cells resulted in 44-52% release with no discernable effect of different irradiation times. This indicates that cells are not damaged by 405 nm irradiation.

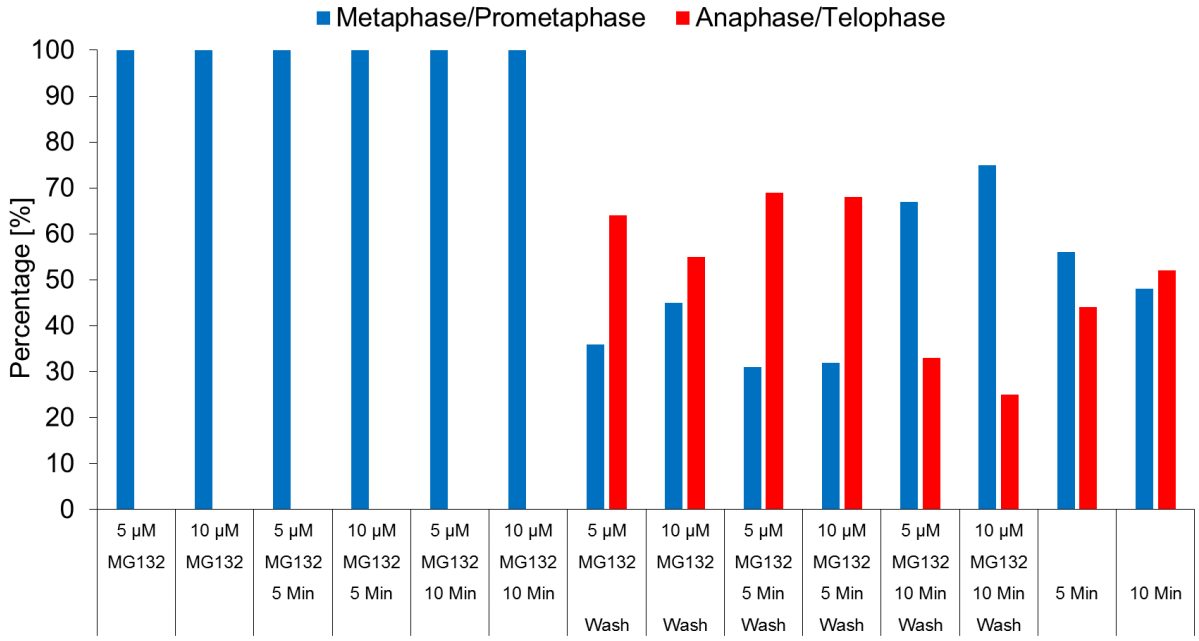

Figure 216 Results from metaphase arrest experiments using MG132 or untreated cells. Inhibitor concentrations of 5 µM and 10 µm were used. Cells were irradiated for 5 min or 10 min using 405 nm light. Addition of MG132 resulted in quantitative arrest for both concentrations and was unaffected by irradiation. Washout of MG132 was highly effective resulting in ca. 60% release with slightly increased release after 5 min irradiation. This trend is reversed after 10 min irradiation with 30% of cells dividing. Untreated cells that were irradiated for 5 min or 10 min revealed 44% and 52% release, respectively.

8.5 Summary and outlook

Two photocaged analogs of MG132 were developed and their photophysical properties were scrutinized. The α-carboxy-6-nitroveratryl moiety was implemented as a highly robust and versatile photolabile protecting group that can be effectively uncaged with UV- and visible light. The aldehyde functional group of MG132 was successfully caged in a one-pot ester reduction/acetylation reaction using DIBAL-H and acetic anhydride. Caging of aldehyde functional groups in complex molecules such as peptides has been unprecedented at the point of writing. A series of UV-Vis experiments has demonstrated that uncaging of the 6-nitroveratryl group results in multiple, consecutive reactions hampering full elucidation of the underlying photo processes and products. However, ^{1}H NMR irradiation experiments could demonstrate the effective release of the caged compounds.

Experiments with **163** on HeLa cells were used to demonstrate the effectiveness of proteasome inhibition and concomitant metaphase arrest. Modulation of inhibitor potency was insignificant when the inhibitor was uncaged with 365 nm or 405 nm light after addition to the cells. Overall the performance was very similar to MG132 that was used for control experiments. Because of the subpar performance no further tests were conducted using this compound.

In vivo experiments with inhibitor **164** demonstrated the effectiveness of the second photocaging approach, which masks the aldehyde functional group as an acetal. Proteasome inhibition is effectively prevented in this case as addition of the caged compound to cells resulted in identical amounts of release when compared to untreated cells. Uncaging, and therefore release of MG132 upon irradiation with 405 nm is highly effective resulting in comparable amounts of metaphase arrest compared to direct addition of MG132. A series of washout experiments have demonstrated to efficiently release cells from such induced arrest. Control experiments also revealed that 405 nm irradiation has no discernable effect on the cells.

Additional experiments conducted by *Friederike Wolff* gave insight into light induced apoptosis using caged inhibitor **164**. For the comprehensive data see the literature.[220] To this end cells were incubated with DMSO, MG132 and **164** and irradiated with 405 nm light for 10 min or kept in the dark. Cell viability was monitored in intervals over a total of 24 h. During this time the amount of control cells doubled. Cells treated with compound **164**, which was irradiated directly after addition decreased to 2% which is comparable to cells treated with MG132 directly. When **164** was added and kept in the dark cells continued to proliferate similar to cells treated with DMSO showing that the caged inhibitor is stable in solution. Control experiments with caged tripeptide ester **173** and caged propionic acid **174** that were exposed to light revealed similar amounts of healthy cells proving that release of the nitrosobenzaldehyde by-product has no detrimental effect on cell viability. The effectiveness of **164** uncaging compared to MG132 was further demonstrated in a dose response experiment. For both compounds the number of healthy cells started to increase when inhibitor concentrations were reduced to ~1 μM and concentrations below 10^{-2} μM had no discernable effect on cells. Overall these results establish caged MG132 anlog **164** as an effective tool to control the cell-cycle and apoptosis through irradiation.

Additional attempts at spatially resolving metaphase arrests were unsuccessful so far. Possible explanations are the high diffusibility of the inhibitor and the long incubation times that are required prior to fixation. Diffusion could be circumvented by reducing the cell medium to a

minimum or use of solid medium. Nevertheless the results offer a highly effective methodology for the caging of bioactive compounds carrying an aldehyde functional group opening up new prospects for a widespread use in related fields.

9 Experimental section

9.1 Materials and methods

Reagents and solvents were obtained from *abcr*, *Merck*, *Sigma-Aldrich* or *TCI* in the qualities *puriss.*, *p.a.*, or *purum* and used as received. Technical solvents were distilled prior to use for column chromatography and extraction on a rotary evaporator (*Heidolph Laborota* 4000 and 4001). Reactions were monitored on *Merck* Silica 60 F254 TLC plates and detection was done by irradiation with UV light (254 nm or 366 nm).

Column chromatography was performed on silica gel (*Merck*, particle size 0.040 - 0.063 mm or *ACROS*, 0.035 – 0.070 mm) and distilled technical solvents.

High Performance Liquid Chromatography (HPLC) was performed on a *Shimadzu* HPLC system consisting of a LC-20AP solvent delivery module, a CTO-20A column oven, a SPD-M20A photodiode array UV-Vis detector, and a CBM-20A system controller using a semi preparative CHIRALPAK® IC column (particle size 5 µm) from Diacel and HPLC grade solvents (EtOAc and *n*-heptane) from *Sigma-Aldrich* and *ROTH*.

^{1}H NMR and ^{13}C NMR spectra were measured on a JEOL ECX 400 (400 MHz), Bruker AVANCE III HD 400 (400 MHz), Varian VNMRS 400 (400 MHz), Varian VNMRS 600 (600 MHz), or Bruker AVANCE III HD 800 (800 MHz) NMR spectrometer. Deuterated solvents were obtained from *Cambridge Isotope Laboratories* and used without further purification. Chemical shifts (δ) are given relative to tetramethylsilane as external standard. Residual solvent signals in the ^{1}H and ^{13}C NMR spectra were used as internal reference. $CDCl_3$: δ_H = 7.260 ppm, δ_C = 77.160 ppm; CD_2Cl_2: δ_H = 5.320 ppm, δ_C = 54.000 ppm. Resonance multiplicity is indicated as s (singlet), d (doublet), t (triplet), q (quartet), and m (multiplet). Chemical shifts are given in parts per million (ppm) on the delta scale (δ) and the coupling constant values (J) are in hertz (Hz). Signal assignments are given in the experimental part with the arbitrary numbering indicated.

Electron Impact (EI) mass spectra were measured on a *Finnigan MAT95Q* or on a *Finnigan MAT90* mass spectrometer.

Infrared spectra were recorded on a *Perkin Elmer Spectrum BX-FT-IR* instrument equipped with a *Smith DuraSamplIR II* ATR-device. Transmittance values are qualitatively described by wavenumber (cm^{-1}) as very strong (vs), strong (s), medium (m), and weak (w).

UV-Vis absorption spectra were measured on a *Varian Cary 5000* spectrophotometer. The spectra were recorded in a quartz cuvette (1 cm). Spectral grade solvents were obtained from *VWR* and *Merck*. Absorption wavelengths (λ) are reported in nm and the molar absorption coefficients (ε) $L \cdot mol^{-1} \cdot cm^{-1}$.

Electronic circular dichroism (ECD) spectra were measured on a *Jasco J-810 Spectropolarimeter*.

Melting points (M.p.) were measured on a *Stuart* SMP10 *melting point* apparatus in open capillaries and are not corrected.

Photoisomerization experiments: Continuous irradiation of the solutions was conducted in NMR tubes in CD_2Cl_2 and CD_2Cl_2/CS_2 (4:1). Irradiations at 23 °C were conducted using LEDs from Roithner Lasertechnik GmbH (365 nm, 385 nm, 405 nm, 420 nm, 435 nm, 450 nm, 470 nm, 490 nm, 505 nm, 515 nm, and 530 nm). For low temperature studies a *Prizmatix UHP-T-450-DI LED* (450 nm) was used as light source and the light beam was guided by a fiber-optic cable from Thorlabs (FT1500UMT, 0.39 NA, 1500 µm, one SMA, one blank end) and pointed directly into the NMR tube during NMR measurements.

Low temperature CD spectra: were measured in CH_2Cl_2 and CH_2Cl_2/DMF = 6/4 at –105 °C on a *Jasco J-810 Spectropolarimeter* with an *Oxford DN 1704* optical cryostat controlled by an *Oxford ITC 4* device. The spectra were recorded in a quartz cuvette (1 cm).

9.2 Synthesis of compounds

Compound 51

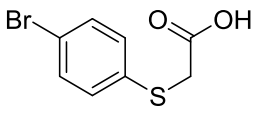

[247.106]

$C_8H_7BrO_2S$

To a solution of 4-bromothiophenol (5.00 g, 26.4 mmol, 1.0 eq) in acetone (50 mL) was added bromoacetic acid (4.04 g, 29.1 mmol, 1.1 eq) and K_2CO_3 (11.0 g, 79.3 mmol, 3.0 eq) and the reaction mixture was stirred at 23 °C for 1 d. The resulting suspension was transferred to a separatory funnel charged with an aqueous 2 M HCl solution and the aqueous phase was extracted with EtOAc. The combined organic phases were washed with brine, dried over Na_2SO_4 and the solvent was removed *in vacuo* to give the crude compound **51** (5.81 g, 23.5 mmol, 89%) as colorless crystals that was used in the next synthetic step without further purification.

^{1}H NMR (400 MHz, CD_2Cl_2, 22 °C) δ = 7.40 – 7.35 (m, 2H), 7.24 – 7.19 (m, 2H), 3.60 (s, 2H).

Compound 52

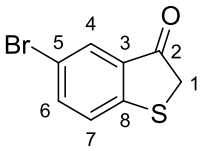

[229.091]

C_8H_5BrOS

2-((4-Bromophenyl)thio)acetic acid (1.60 g, 6.47 mmol, 1.0 eq) was dissolved in thionyl chloride (4.23 mL, 58.3 mmol, 9.0 eq) and heated for 3 h under reflux (85 °C). Excess thionyl chloride was removed *in vacuo* and the crude acid chloride was dissolved in $(CH_2Cl)_2$ (10 mL). The stirring solution was cooled to 0 °C in an ice bath and aluminum chloride (2.59 g, 19.4 mmol, 3.0 eq) was added. The reaction mixture was allowed to warm to 23 °C and stirred for 3 h before it was poured into a separatory funnel charged with ice/aqueous 2 M HCl (100 mL). The aqueous phase was extracted with CH_2Cl_2 (3 × 60 mL), the combined organic phases were dried over Na_2SO_4 and the solvent was removed *in vacuo* to give compound **52**

(1.45 g, 6.33 mmol, 98%) as a brown solid that was used in the next synthetic step without further purification.

^{1}H NMR (400 MHz, CD_2Cl_2) δ = 7.86 (dd, *J* = 2.1, 0.5 Hz, 1H, H-C(4)), 7.65 (dd, *J* = 8.4, 2.1 Hz, 1H, H-C(6)), 7.35 (dd, *J* = 8.4, 0.5 Hz, 1H, H-C(7)), 3.84 (s, 2H, H-C(1)).

^{13}C NMR (150 MHz, CD_2Cl_2) δ = 198.89 (C-2), 153.58 (C-8), 138.70 (C-6), 133.32 (C-3), 129.57 (C-4), 126.57 (C-7), 118.79 (C-5), 40.50 (C-1).

HR-MS (EI^+), $[M]^+$ calc. for $[C_8H_5BrOS]^+$: 227.9245, found: 227.9226.

Compound 53

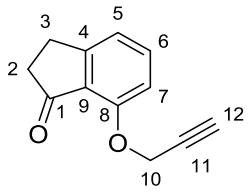

[186.210]

$C_{12}H_{10}O_2$

To a solution of 7-Hydroxy-1-indanone (1.00 g, 6.75 mmol, 1.0 eq) in DMF (45.0 mL) was added propargyl bromide (80% in toluene, 1.00 g, 6.75 mmol, 1.0 eq) and K_2CO_3 (3.73 g, 27.0 mmol, 4.0 eq) and the reaction mixture was stirred for 6 h at 70 °C. The crude product was transferred to a separatory funnel charged with water (100 mL) and the aqueous phase was extracted with EtOAc (3 × 100 mL). The combined organic phases were washed with an excess of water (until residual DMF was removed as judged by the disappearance of DMF streaks in the aqueous phase) and brine (2 × 100 mL), dried over Na_2SO_4 and the solvent was removed *in vacuo* to give compound **53** (1.20 g, 6.44 mmol, 95%) as a colorless solid.

^{1}H NMR (400 MHz, $CDCl_3$, 25 °C) δ = 7.53 (dd, *J* = 8.2, 7.6 Hz, 1H, H-C(6)), 7.09 (dd, *J* = 7.6, 0.9 Hz, 1H, H-C(5)), 6.91 (dd, *J* = 8.2, 0.8 Hz, 1H, H-C(7)), 4.84 (d, *J* = 2.4 Hz, 2H, H-C(10)), 3.10 – 3.04 (m, 2H, H-C(2)), 2.64 – 2.58 (m, 3H, H-C(3) and H-C(12)).

^{13}C NMR (101 MHz, CD_2Cl_2, 25 °C) δ = 204.31 (C-1), 158.68 (C-4), 156.10 (C-8), 136.41 (C-6), 126.32 (C-9), 120.08 (C-5), 111.28 (C-7), 78.56 (C-11), 76.46 (C-12), 56.71 (C-10), 37.31 (C-3), 26.07 (C-2).

HR-MS (EI^+), $[M-H]^+$ calc. for $[C_{12}H_9O_2]^+$: 185.0603, found: 185.0597.

Compound 55

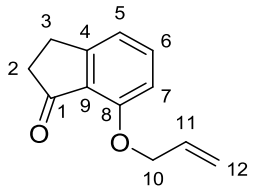

[188.226]

$C_{12}H_{12}O_2$

To a solution of 7-Hydroxy-1-indanone (50.0 g, 337 µmol, 1.0 eq) in DMF (2.25 mL) was added allyl bromide (40.8 mg, 337 µmol, 1.0 eq) and K_2CO_3 (187 mg, 1.35 mmol, 4.0 eq) and the reaction mixture was stirred for 5 h at 70 °C. The crude product was transferred to a separatory funnel charged with water and the aqueous phase was extracted with EtOAc. The combined organic phases were washed with an excess of water (until residual DMF was removed as judged by the disappearance of DMF streaks in the aqueous phase) and brine, dried over Na_2SO_4 and the solvent was removed *in vacuo* to give compound **55** (42.0 mg, 223 µmol, 66%) as a colorless solid.

^{1}H NMR (400 MHz, CD_2Cl_2, 27 °C) δ = 7.49 (dd, *J* = 8.2, 7.6 Hz, 1H, H-C(6)), 7.02 (dd, *J* = 7.6, 0.9 Hz, 1H, H-C(5)), 6.77 (dd, *J* = 8.2, 0.8 Hz, 1H, H-C(7)), 6.09 (ddt, *J* = 17.2, 10.5, 5.0 Hz, 1H, H-C(11)), 5.52 (dq, *J* = 10.6, 1.5 Hz, 1H, H-C(12)), 5.32 (dq, *J* = 17.2, 1.5 Hz, 1H, H-C(12)), 4.65 (dt, *J* = 5.0, 1.6 Hz, 2H, H-C(10)), 3.09 – 3.04 (m, 2H, H-C(3)), 2.63 – 2.56 (m, 2H, H-C(2)).

^{13}C NMR (101 MHz, CD_2Cl_2, 27 °C) δ = 204.37 (C-1), 158.55 (C-4), 157.48 (C-8), 136.51 (C-6), 133.28 (C-11), 126.04 (C-9), 119.13 (C-5), 118.11 (C-12), 110.69 (C-7), 69.53 (C-10), 37.33 (C-2), 26.04 (C-3).

HR-MS (EI^+) calc. [$C_{12}H_{12}O_2^+$]: 188.0837, found: 188.0831.

Compound 56

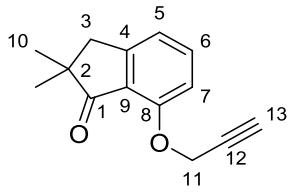

[214.264]

$C_{14}H_{14}O_2$

Compound **53** (1.20 g, 6.44 mmol, 1.0 eq) was dissolved in DMF (12.9 mL) and cooled to 0 °C, then sodium hydride (60% dispersion in mineral oil, 644 mg, 16.1 mmol, 2.5 eq) and methyl iodide (2.25 g, 16.1 mmol, 2.5 eq) were added. After stirring for 2 h at 23 °C a saturated NH_4Cl solution (50 mL) was added and the aqueous phase was extracted with EtOAc (3 × 50 mL). The combined organic phases were washed with an excess of water (until residual DMF was removed as judged by the disappearance of DMF streaks in the aqueous phase) and brine (2 × 50 mL), dried over Na_2SO_4 and the solvent was removed *in vacuo*. The crude product was purified by flash column chromatography (SiO_2, *i*-Hex:EtOAc = 9:1) to give compound **56** (1.09 mg, 5.08 mmol, 79%) as a colorless liquid that slowly gives colorless crystals.

m.p.: 104 °C

^{1}H NMR (400 MHz, $CDCl_3$) δ = 7.53 (dd, *J* = 8.2, 7.6 Hz, 1H, H-C(6)), 7.03 – 7.00 (m, 1H, H-C(5)), 6.96 (dd, *J* = 8.2, 0.8 Hz, 1H, H-C(7)), 4.86 (d, *J* = 2.4 Hz, 2H, H-C(11)), 2.95 (m, 2H, H-C(3)), 2.52 (t, *J* = 2.4 Hz, 1H, H-C(13)), 1.22 (s, 6H, H-C(10)).

^{13}C NMR (101 MHz, $CDCl_3$) δ = 208.82 (C-1), 156.33 (C-8), 154.97 (C-4), 136.23 (C-6), 124.16 (C-9), 119.55 (C-5), 111.22 (C-7), 78.16 (C-12), 76.47 (C-13), 56.48 (C-11), 45.75 (C-2), 42.75 (C-3), 25.60 (C-10).

IR: $\tilde{\nu}$ = 3194m, 2926w, 2206w, 2112w, 1996vw, 1963vw, 1697s, 1600m, 1590m, 1481m, 1445w, 1376w, 1298w, 1278m, 1236m, 1202w, 1181w, 1080w, 1066s, 1012w, 992m, 934m, 914w, 866w, 849w, 790w, 776s, 729m, 693m, 681m.

HR-MS (EI$^+$), $[M]^+$ calc. for $[C_{14}H_{14}O_2]^+$: 214.0994, found: 214.0987.

Compound 57

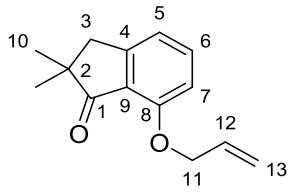

[216.280]

$C_{14}H_{16}O_2$

Compound **55** (41.0 mg, 218 µmol, 1.0 eq) was dissolved in DMF (436 µL) and cooled to 0 °C, then sodium hydride (60% dispersion in mineral oil, 13.1 mg, 545 µmol, 2.5 eq) and methyl iodide (77.3 mg, 545 µmol, 2.5 eq) were added. After stirring for 2 h at 23 °C a saturated NH_4Cl solution was added and the aqueous phase was extracted with EtOAc. The combined organic phases were washed with an excess of water (until residual DMF was removed as judged by the disappearance of DMF streaks in the aqueous phase) and brine, dried over Na_2SO_4 and the solvent was removed *in vacuo*. The crude product was purified by flash column chromatography (SiO_2, *i*-Hex:EtOAc = 9:1) to give compound **57** (39.0 mg, 180 µmol, 83%) as a pale yellow oil.

^{1}H NMR (400 MHz, CD_2Cl_2, 27 °C) δ = 7.50 (dd, *J* = 8.2, 7.5 Hz, 1H, H-C(6)), 7.00 – 6.95 (m, 1H, H-C(5)), 6.78 (dd, *J* = 8.2, 0.8 Hz, 1H, H-C(7)), 6.10 (ddt, *J* = 17.2, 10.6, 5.0 Hz, 1H, H-C(12)), 5.55 (dq, *J* = 17.2, 1.7 Hz, 1H, H-C(13)), 5.32 (dq, *J* = 10.6, 1.5 Hz, 1H, H-C(13)), 4.65 (dt, *J* = 5.0, 1.7 Hz, 2H, H-C(11)), 2.93 (s, *J* = 0.8 Hz, 2H, H-C(3)), 1.18 (s, 6H, H-C(10)).

^{13}C NMR (101 MHz, CD_2Cl_2, 27 °C) δ = 208.76 (C-1), 157.89 (C-8), 155.35 (C-4), 136.66 (C-6), 133.26 (C-12), 124.12 (C-9), 119.09 (C-5), 118.02 (C-13), 110.79 (C-7), 69.49 (C-11), 45.89 (C-2), 42.96 (C-3), 25.76 (C-10).

HR-MS (EI^+) calc. [$C_{14}H_{16}O_2^+$]: 216.1150, found: 216.1146.

Compound 58

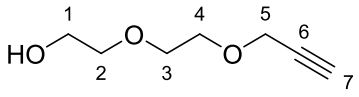

[144.170]

$C_7H_{12}O_3$

A stirring solution of potassium *tert*-butoxide (1.02 g, 9.10 mmol, 1.01 eq) in THF (25.0 mL) was cooled to 0 °C and diethylene glycol (1.91 g, 18.0 mmol, 2.0 eq) was added dropwise. The suspension was allowed to warm to 23 °C and stirred for 30 min before a solution of propargyl bromide (80% in toluene, 1.34 g, 9.00 mmol, 1.0 eq) in THF (5.0 mL) was added dropwise. After stirring for 18 h the reaction mixture was filtered and the solvent was removed *in vacuo*. After flash column chromatography (SiO_2, EtOAc) compound **58** (1.05 g, 7.27 mmol, 81%) was obtained as a colorless liquid.

^{1}H NMR (400 MHz, $CDCl_3$, 20 °C) δ = 4.21 (d, *J* = 2.4 Hz, 2H), 3.77 – 3.73 (m, 2H), 3.71 (s, 4H), 3.63 – 3.59 (m, 2H), 2.44 (t, *J* = 2.4 Hz, 1H).

Compound 59

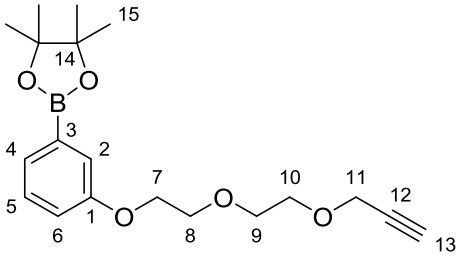

[346.230]

$C_{19}H_{27}BO_5$

K_2CO_3 (1.32 g, 9.52 mmol, 4.0 eq) was added to a solution of compound **60** (493 mg, 2.38 mmol, 1.0 eq) and 3-hydroxyphenylboronic acid pinacol ester (524 mg, 2.38 mmol, 1.0 eq) in DMF (15.0 mL) and the mixture was stirred at 70 °C for 18 h. The reaction mixture was partitioned between EtOAc and saturated aqueous $NaHCO_3$ and extracted with additional EtOAc. The combined organic phases were dried over Na_2SO_4, filtered and the solvent was removed *in vacuo* to give compound **59** in quantitative yields as a brown liquid that was used in the next synthetic step without further purification. A pure sample of compound **59** was

obtained after purification of a portion of the product by flash column chromatography (SiO_2, *i*-Hex:EtOAc = 8:2) as colorless crystals.

The boron bearing carbon atom was not observed due to quadrupolar relaxation.

^{1}H NMR (400 MHz, $CDCl_3$, 27 °C) δ = 7.39 (d, *J* = 7.2 Hz, 1H), 7.34 (dd, *J* = 2.8, 0.8 Hz, 1H, H-C(2)), 7.30 – 7.26 (m, 1H, H-C(5)), 7.03 (ddd, *J* = 8.1, 2.7, 1.1 Hz, 1H), 4.22 (d, *J* = 2.2 Hz, 2H, H-C(11)), 4.19 – 4.15 (m, 2H, H-C(7)), 3.88 – 3.84 (m, 2H, H-C(8)), 3.78 – 3.74 (m, 2H, H-C(9)), 3.72 (ddd, *J* = 6.1, 3.1, 1.3 Hz, 2H, H-C(10)), 2.43 (t, *J* = 2.3 Hz, 1H, H-C(13)), 1.34 (s, 12H, H-C(15)).

^{1}H NMR (101 MHz, $CDCl_3$, 27 °C) δ = 158.37 (C-1), 129.07 (C-5), 127.51 (C-4 or C-6), 119.83 (C-2), 118.63 (C-4 or C-6), 83.96 (C-14), 79.81 (C-12), 74.68 (C-13), 70.80 (C-9), 69.99 (C-8), 69.34 (C-10), 67.58 (C-7), 58.60 (C-11), 25.02 (C-15).

HR-MS (ESI$^+$), $[M+NH_4]^+$ calc. for $[C_{19}H_{15}BrO_2S]^+$: 364.2295, found: 364.2286.

Compound 60

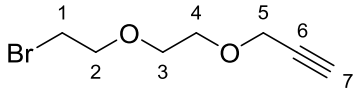

[207.067]

$C_7H_{11}BrO_2$

A stirring solution of compound **58** (500 mg, 3.47 mmol, 1.0 eq) and CBr_4 (1.27 g, 3.81 mmol, 1.1 eq) in CH_2Cl_2 (5.34 mL) was cooled to 0 °C and PPh_3 (1.00 g, 3.81 mmol, 1.1 eq) was added slowly. The solution was allowed to warm to 23 °C and stirred for 1 d. The solvent was removed *in vacuo* and the crude product was purified by flash column chromatography (SiO_2, *i*-Hex:EtOAc = 6:4 → 1:1) to give compound **60** (596 mg, 2.88 mmol, 83%) as a colorless liquid.

^{1}H NMR (400 MHz, $CDCl_3$, 20 °C) δ = 4.22 (d, *J* = 2.5 Hz, 2H, H-C(5)), 3.81 (t, *J* = 6.4 Hz, 2H, H-C(2)), 3.71 (s, 4H, H-C(3) and H-C(4)), 3.48 (t, *J* = 6.3 Hz, 2H, H-C(1)), 2.44 (t, *J* = 2.5 Hz, 1H, H-C(7)).

Compound 61

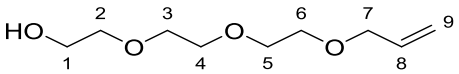

[190.239]

$C_9H_{18}O_4$

A stirring solution of potassium *tert*-butoxide (1.02 g, 9.10 mmol, 1.01 eq) in THF (25.0 mL) was cooled to 0 °C and triethylene glycol (2.70 g, 18.0 mmol, 2.0 eq) was added dropwise. The suspension was allowed to warm to 23 °C and stirred for 30 min before a solution of allyl bromide (1.09 g, 9.00 mmol, 1.0 eq) in THF (5.0 mL) was added dropwise. After stirring for 1 d the reaction mixture was filtered and the solvent was removed *in vacuo*. After flash column chromatography (SiO_2, EtOAc) compound **61** (1.10 g, 5.78 mmol, 64%) was obtained as a colorless liquid.

Due to overlapping proton signals carbon atoms could only be partially assigned.

^{1}H NMR (400 MHz, CD_2Cl_2, 27 °C) δ = 5.92 (ddt, *J* = 17.2, 10.4, 5.6 Hz, 1H, H-C(8)), 5.27 (dq, *J* = 17.3, 1.7 Hz, 1H, H-C-(9)), 5.16 (dq, *J* = 10.4, 1.5 Hz, 1H, H-C-(9)), 3.99 (dt, *J* = 5.6, 1.5 Hz, 2H, H-C(7)), 3.69 – 3.54 (m, 12H, H-C(1,2,3,4,5,6)), 2.42 (d, *J* = 5.7 Hz, 1H, *H*O-C(1)).

^{13}C NMR (101 MHz, CD_2Cl_2, 27 °C) δ = 135.57 (C-8), 117.04 (C-9), 73.05, 72.58 (C-7), 71.11, 71.09, 70.89, 70.07 (C-6), 62.21.

HR-MS (EI), [M+H]: 191.1283 for [$C_9H_{19}O_4$]; found: 191.1279.

HR-MS (EI), [M+NH_4]: 208.1549 for [$C_9H_{22}O_4N$]; found: 208.1544.

Compound 62

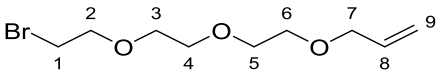

[253.136]

$C_9H_{17}BrO_3$

A stirring solution of compound **61** (819 mg, 4.31 mmol, 1.0 eq) and CBr_4 (1.57 g, 4.74 mmol, 1.1 eq) in CH_2Cl_2 (6.62 mL) was cooled to 0 °C and PPh_3 (1.24 g, 4.74 mmol, 1.1 eq) was added slowly. The solution was allowed to warm to 23 °C and stirred for 1 d. The solvent was removed *in vacuo* and the crude product was purified by flash column chromatography (SiO_2, *i*-Hex:EtOAc = 7:3) to give compound **62** (966 mg, 3.82 mmol, 89%) as a colorless liquid.

Due to overlapping proton signals carbon atoms could only be partially assigned.

^{1}H NMR (400 MHz, CD_2Cl_2, 27 °C) δ = 5.92 (ddt, *J* = 17.2, 10.4, 5.6 Hz, 1H, H-C(8)), 5.27 (dq, *J* = 17.3, 1.7 Hz, 1H, H-C-(9)), 5.16 (dq, *J* = 10.4, 1.5 Hz, 1H, H-C-(9)), 3.99 (dt, *J* = 5.6, 1.5 Hz, 2H, H-C(7)), 3.69 – 3.54 (m, 12H, H-C(1,2,3,4,5,6)), 2.42 (d, *J* = 5.7 Hz, 1H, *H*O-C(1)).

^{13}C NMR (101 MHz, CD_2Cl_2, 27 °C) δ = 135.57 (C-8), 117.04 (C-9), 73.05, 72.58 (C-7), 71.11, 71.09, 70.89, 70.07 (C-6), 62.21.

HR-MS (EI), [M+NH_4]: *m/z* calc.: 270.0705 for [$C_9H_{21}BrNO_3$]; found: 270.0700.

Compound 63

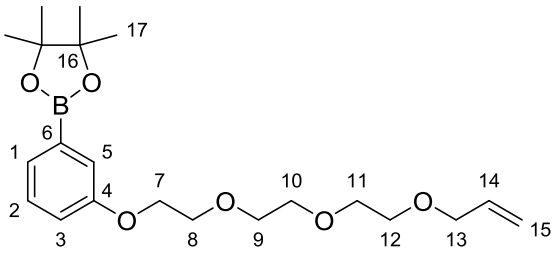

[392.299]

$C_{21}H_{33}BO_6$

Compound **62** (51.5 mg, 203 µmol, 1.0 eq) was dissolved in DMF (1.36 mL), then 3-hydroxyphenylboronic acid pinacol ester (44.8 mg, 203 µmol, 1.0 eq) and K_2CO_3 (112 mg, 814 µmol, 4.0 eq) were added. The reaction mixture was heated for 1 d at 60 °C before it was transferred to a separatory funnel charged with a saturated $NaHCO_3$ solution. The aqueous

phase was extracted with EtOAc. The combined organic phases were washed with an excess of water (until residual DMF was removed as judged by the disappearance of DMF streaks in the aqueous phase) and brine, dried over Na_2SO_4 and the solvent was evaporated *in vacuo*. Compound **63** (57.0 mg, 145 µmol, 71%) was obtained as a highly viscous yellow to brown oil that was used in the next synthetic step without further purification.

^{1}H NMR (599 MHz, CD_2Cl_2, 27 °C) δ = 7.35 – 7.32 (m, 1H, H-C(1) or H-C(3)), 7.30 – 7.28 (m, 2H, H-C(2), H-C(5)), 7.03 – 7.00 (m, 1H, H-C(1) or H-C(3)), 5.96 – 5.87 (m, 1H, H-C(14)), 5.29 – 5.23 (m, 1H, H-C(15)), 5.16 (ddt, *J* = 10.4, 1.9, 1.2 Hz, 1H, H-C(15)), 4.16 – 4.11 (m, 2H, H-C(7)), 4.01 – 3.98 (m, 2H, H-C(13)), 3.83 – 3.80 (m, 2H, H-C(8)), 3.70 – 3.67 (m, 2H, H-C(9)), 3.65 – 3.60 (m, 4H, H-C(10), H-C(11)), 3.57 (m, 2H, H-C(12)), 1.32 (dd, *J* = 3.8, 1.2 Hz, 12H, H-C(17)).

^{13}C NMR (151 MHz, CD_2Cl_2, 27 °C) δ = 158.82 (C-4), 135.55 (C-14), 129.47 (C-2), 127.67 (C-1 or C-3), 120.07 (C-5), 118.65 (C-1 or C-3), 117.98 (C-6), 117.04 (C-15), 84.39 (C-16), 72.55 (C-13), 71.29 (C-9), 71.10 (2C, C-10, C-11), 70.24 (C-8), 70.05 (C-12), 67.96 (C-7), 25.20 (C-17).

HR-MS (EI), [M+H]: *m/z* calc.: 392.2370 for [$C_{21}H_{33}BO_6$]; found: 392.2373.

Compound 71

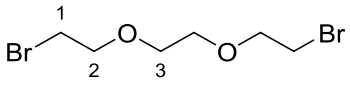

[275.968]

$C_6H_{12}Br_2O_2$

Triethylene glycol (1.50 g, 9.99 mmol, 1.0 eq) and CBr_4 (7.29 g, 22.0 mmol, 2.2 eq) were dissolved in THF (15.4 mL) and cooled to 0 °C. After addition of triphenylphosphine (5.50 g, 21.0 mmol, 2.1 eq) the reaction mixture was allowed to warm to 23 °C and stirred for 6 h. The solvent was removed *in vacuo* and the crude product was purified by flash column chromatography (SiO_2, *i*-Hex:EtOAc = 3:1) to give compound **71** (2.17 g, 7.86 mmol, 79%) as a colorless liquid.

^{1}H NMR (400 MHz, CD_2Cl_2) δ = 3.80 (t, *J* = 6.0 Hz, 4H, H-C(2)), 3.65 (s, 4H, H-C(3)), 3.49 (t, *J* = 6.0 Hz, 4H, H-C(1)).

^{13}C NMR (101 MHz, CD_2Cl_2) δ = 71.71 (C-2), 70.98 (C-3), 31.43 (C-1).

Compound 72

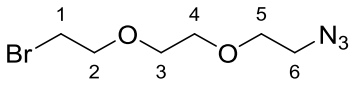

[238.085]

$C_6H_{12}BrN_3O_2$

Compound **71** (2.06 g, 7.46 mmol, 1.0 eq) was dissvoled in DMF (5 mL) and sodium azide (288 mg, 4.42 mmol, 0.6 eq) was added. The reaction mixture was stirred at 60 °C for 20 h. The crude product was transferred to a separatory funnel charged with water (100 mL) and the aqueous phase was extracted with EtOAc (3 × 50 mL). The combined organic phases were washed with an excess of water (until residual DMF was removed as judged by the disappearance of DMF streaks in the aqueous phase) and brine (1 × 50 mL), dried over Na_2SO_4 and the solvent was removed *in vacuo*. The crude product was purified by flash column chromatography (SiO_2, *i*-Hex:EtOAc = 9:1) to give compound **72** (531 mg, 2.23 mmol, 30%, 50% brsm.) as a colorless liquid (at the same time 685 mg, 2.48 mmol of starting material could be recovered).

^{1}H NMR (400 MHz, CD_2Cl_2) δ = 3.79 (t, *J* = 6.0 Hz, 2H, H-C(2)), 3.68 – 3.61 (m, 6H, H-C(3), H-C(4), H-C(5)), 3.48 (t, *J* = 6.0 Hz, 2H, H-C(1)), 3.37 (t, *J* = 5.0 Hz, 2H, H-C(6)).

^{13}C NMR (101 MHz, CD_2Cl_2) δ = 71.67 (C-2), 71.08 (C-4), 71.00 (C-3), 70.50 (C-5), 51.33 (C-6), 31.40 (C-1).

Compound 73

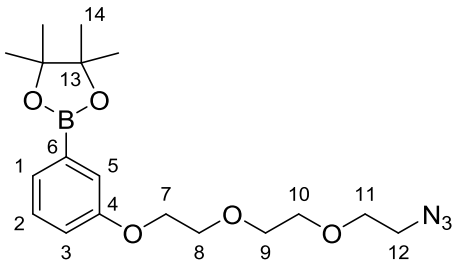

[377.,248]

$C_{18}H_{28}BN_3O_5$

Compound **72** (464 mg, 1.95 mmol, 1.0 eq) was dissolved in DMF (13 mL), then 3-hydroxyphenylboronic acid pinacol ester (429 mg, 1.95 mmol, 1.0 eq) and K_2CO_3 (1.08 g, 7.80 mmol, 4.0 eq) were added. The reaction mixture was heated for 1 d at 60 °C before it was transferred to a separatory funnel charged with a saturated $NaHCO_3$ solution (50 mL). The aqueous phase was extracted with EtOAc (3 × 50 mL). The combined organic phases were washed with an excess of water (until residual DMF was removed as judged by the disappearance of DMF streaks in the aqueous phase) and brine (1 × 50 mL), dried over Na_2SO_4 and the solvent was evaporated *in vacuo*. Compound **7** (648 mg, 1.72 mmol, 88%) was obtained as a yellow to brown oil that was used in the next synthetic step without further purification.

^{1}H NMR (599 MHz, $CDCl_3$) δ = 7.39 (dt, *J* = 7.2, 1.0 Hz, 1H, H-C(1) or H-C(3)), 7.34 (dd, *J* = 2.8, 0.9 Hz, 1H, H-C(5)), 7.30 – 7.26 (m, 1H, H-C(2)), 7.03 (ddd, *J* = 8.2, 2.8, 1.1 Hz, 1H, H-C(1) or H-C(3)), 4.18 – 4.14 (m, 2H, H-C(7)), 3.88 – 3.85 (m, 2H, H-C(8)), 3.76 – 3.73 (m, 2H, H-C(9)), 3.70 – 3.67 (m, 4H, H-C(10), H-C(11)), 3.42 – 3.36 (m, 2H, H-C(12)), 1.34 (s, 12H, H-C(14)).

^{13}C NMR (151 MHz, $CDCl_3$) δ = 158.36 (C-4), 130.36 (C-6), 129.08 (C-2), 127.50 (C-1 or C-3), 119.76 (C-5), 118.63 (C-1 or C-3), 83.97 (C-13), 71.05 (C-9), 70.90 (C-10), 70.22 (C-11), 70.05 (C-8), 67.55 (C-7), 50.84 (C-12), 25.01 (C-14).

HR-MS (EI^+) calc. [$C_{18}H_{28}BN_3O_5^+$]: 377.2122, found: 377.2117.

Compound 75

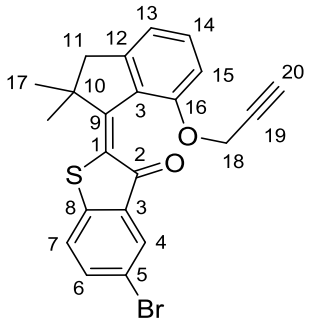

[425.340]

$C_{22}H_{17}BrO_2S$

Indanone **56** (450 mg, 2.10 mmol, 1.0 eq) and benzothiophenone **52** (529 mg, 2.31 mmol, 1.1 eq) were dissolved in CH_2Cl_2 (500 µL each) in two separate Schlenk flasks and cooled to 0 °C on an ice bath. BCl_3 (2.31 mL, 1 M in toluene, 2.31 mmol, 1.1 eq) was added to the flask

containing compound **52** and the suspension was immediately taken up in a syringe and added to the solution containing indanone **56**. After stirring for 20 min at 23 °C the reaction was stopped by addition of water (5 mL). The reaction mixture was transferred to a separatory funnel charged with a saturated NH_4Cl solution (50 mL). The aqueous phase was extracted with CH_2Cl_2 (3 × 50 mL), the combined organic phases were washed with brine (1 × 50 mL), dried over Na_2SO_4 and the solvent was evaporated *in vacuo*. The crude product was purified by flash column chromatography (SiO_2, *i*-Hex:EtOAc = 24:1) to give to give compound **75** (470 mg, 1.10 mmol, *E* isomer:*Z* isomer 3:1, 53%) as a red solid.

m.p.: 75 °C

***E* isomer**:

^{1}H NMR (600 MHz, $CDCl_3$) δ = 8.01 (dd, *J* = 2.1, 0.5 Hz, 1H, H-C(4)), 7.60 – 7.57 (m, 1H, H-C(6)), 7.35 – 7.31 (m, 2H, H-C(7) and H-C(14)), 6.92 (d, *J* = 7.4 Hz, 1H, H-C(13)), 6.86 (dd, *J* = 8.3, 0.8 Hz, 1H, H-C(15)), 4.74 (m, 2H, H-C(18)), 3.17 (d, *J* = 15.3 Hz, 1H, H-C(11)), 2.76 (d, *J* = 15.2 Hz, 1H, H-C(11)), 2.42 (t, *J* = 2.4 Hz, 1H, H-C(20)), 1.67 (s, 3H, H-C(17)), 1.22 (s, 3H, H-C(17)).

^{13}C NMR (150 MHz, $CDCl_3$) δ = 186.04 (C-2), 157.59 (C-9), 156.88 (C-16), 149.59 (C-12), 142.70 (C-8), 136.33 (C-6), 134.00 (C-3 or C-5), 132.33 (C-14), 129.29 (C-4), 128.52 (C-3), 124.67 (C-7), 118.40 (C-3 or C-5), 117.90 (C-13), 110.54 (C-15), 78.84 (C-19), 75.62 (C-20), 56.30 (C-18), 50.83 (evtl. C-10), 49.38 (C-11), 26.65 (C-17), 26.48, 26.12 (C-17). C-1 could not be assigned.

IR: $\tilde{\nu}$ = 3294w, 2957w, 2923w, 2176w, 2135w, 1926vw, 1661m, 1580s, 1528m, 1473m, 1444s, 1407m, 1363w, 1294m, 1272s, 1248s, 1216m, 1188m, 1081s, 1063s, 1046s, 1002m, 952m, 893w, 849w, 809s, 770s, 746s, 666m.

HR-MS (EI^+) calc. [$C_{22}H_{17}BrO_2S^+$]: 424.0133, found: 424.0125.

Compound 76

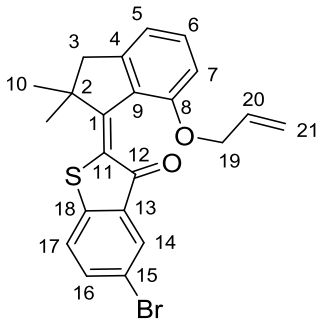

[427.356]

$C_{22}H_{19}BrO_2S$

Indanone **57** (429 mg, 1.98 mmol, 1.0 eq) and benzothiophenone **52** (500 mg, 2.18 mmol, 1.1 eq) were dissolved in CH_2Cl_2 (2.0 mL each) in two separate Schlenk flasks and cooled to 0 °C on an ice bath. BCl_3 (2.18 mL, 1 M in toluene, 2.18 mmol, 1.1 eq) was added to the flask containing compound **52** and the suspension was immediately taken up in a syringe and added to the solution containing indanone **57**. After stirring for 20 min at 23 °C the reaction was stopped by addition of water. The reaction mixture was transferred to a separatory funnel charged with a saturated NH_4Cl solution (50 mL). The aqueous phase was extracted with CH_2Cl_2, the combined organic phases were dried over Na_2SO_4 and the solvent was evaporated *in vacuo*. The crude product was purified by flash column chromatography (SiO_2, *i*-Hex:EtOAc = 19:1) to give to give compound **76** (239 mg, 559 µmol, *E* isomer:*Z* isomer 3:1, 28%) as a red solid.

***E* isomer**:

^{1}H NMR (599 MHz, CD_2Cl_2, 27 °C) δ = 7.91 (dd, *J* = 2.1, 0.5 Hz, 1H, H-C(14)), 7.62 (dd, *J* = 8.4, 2.0 Hz, 1H, H-C(16)), 7.38 (dd, *J* = 8.3, 0.5 Hz, 1H, H-C(17)), 7.34 (dd, *J* = 8.3, 7.4 Hz, 1H, H-C(6)), 6.91 (dt, *J* = 7.3, 0.9 Hz, 1H, H-C(5)), 6.78 (dd, *J* = 8.3, 0.8 Hz, 1H, H-C(7)), 5.95 – 5.88 (m, 1H, H-C(20)), 5.29 – 5.24 (m, 1H, H-C(21)), 5.13 (dq, *J* = 10.5, 1.4 Hz, 1H, H-C(21)), 4.66 – 4.60 (m, 1H, H-C(19)), 4.56 (dd, *J* = 12.4, 5.6 Hz, 1H, H-C(19)), 3.18 (d, *J* = 15.3 Hz, 1H, H-C(3)), 2.78 (d, *J* = 15.3 Hz, 1H, H-C(3)), 1.68 (s, 3H, H-C(10)), 1.21 (s, 3H, H-C(10)).

^{13}C NMR (151 MHz, CD_2Cl_2, 27 °C) δ = 185.70 (C-12), 158.33 (C-1), 158.18 (C-8), 150.03 (C-4), 143.10 (C-18), 136.73 (C-16), 134.38 (C-13), 133.92 (C-20), 132.76 (C-6), 129.27 (C-14), 128.71 (C-9), 125.55 (C-11), 125.31 (C-17), 118.82 (C-15), 117.97 (C-21), 117.37 (C-5), 110.42 (C-7), 69.47 (C-19), 51.23 (C-2), 49.72 (C-3), 26.85 (C-10), 26.32 (C-10).

HR-MS (EI^+) calc. [$C_{22}H_{17}BrO_2S^+$]: 426.0289, found: 426.0274.

Compound 77

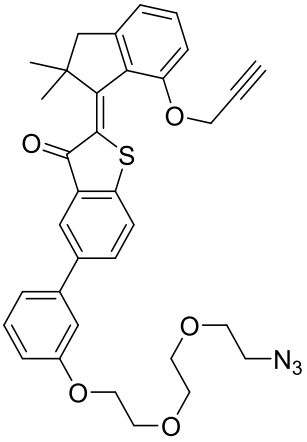

[595.714]

$C_{34}H_{33}N_3O_5S$

Compound **73** (18 mg, 47 µmol, 1.0 eq) and compound **75** (20 mg, 47 µmol, 1.0 eq) were added to a suspension of PEPPSI™-*i*Pr (4.5 mg, 2.4 µmol, 2 mol%) and K_2CO_3 (19 mg, 0.14 mmol, 3.0 eq) in H_2O/Dioxan (100 µL/500 µL). The reaction mixture was heated for 16 h at 60 °C before it was transferred to a separatory funnel charged with a saturated NH_4Cl solution. The aqueous phase was extracted with EtOAc. The combined organic phases were washed with water and brine, dried over Na_2SO_4 and the solvent was evaporated *in vacuo*. After purification by flash column chromatography (SiO_2, *i*-Hex:EtOAc = 3:1) compound **77** (2.7 mg, 4.5 µmol, 9%) was obtained as a red solid.

^{1}H NMR (599 MHz, $CDCl_3$, 27 °C) δ = 8.12 (dd, *J* = 2.0, 0.7 Hz, 1H), 7.76 (dd, *J* = 8.2, 1.9 Hz, 1H), 7.51 (dd, *J* = 8.2, 0.6 Hz, 1H), 7.36 (t, *J* = 7.9 Hz, 1H), 7.24 – 7.22 (m, 1H), 6.94 – 6.91 (m, 1H), 4.23 – 4.20 (m, 2H), 3.93 – 3.90 (m, 2H), 3.79 – 3.76 (m, 2H), 3.72 – 3.68 (m, 4H), 3.41 – 3.38 (m, 2H), 3.19 (d, *J* = 15.2 Hz, 1H), 2.77 (d, *J* = 15.2 Hz, 1H), 2.36 (t, *J* = 2.4 Hz, 1H), 1.70 (s, 3H), 1.25 (s, 3H).

HR-MS (EI), [M+H]: *m/z* calc.: 595.2141 for [$C_{34}H_{33}N_3O_5S$]; found: 595.2132.

Compound 79

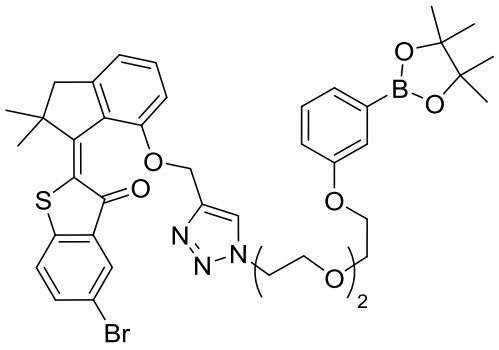

[802.588]

$C_{40}H_{45}BBrN_3O_7S$

Compound **75** (277 mg, 651 µmol, 1.0 eq) and compound **73** (246 mg, 651 µmol, 1.0 eq) were dissolved in DMF (3.0 mL), then sodium ascorbate (12.9 mg, 65.1 µmol, 10 mol%) and $CuSO_4 \cdot 5H_2O$ (3.3 mg, 13.0 µmol, 2 mol%) were added. The reaction mixture was stirred at 23 °C for 1 d before it was transferred to a separatory funnel charged with a saturated NH_4Cl solution (50 mL). The aqueous phase was extracted with EtOAc (3 × 50 mL), the combined organic phases were washed with an excess of water (until residual DMF was removed as judged by the disappearance of DMF streaks in the aqueous phase) and brine (1 × 50 mL), dried over Na_2SO_4 and the solvent was evaporated *in vacuo*. After purification by flash column chromatography (SiO_2, CH_2Cl_2 → CH_2Cl_2:MeOH = 19:1) compound **79** (515 mg, 642 µmol, 99%) was obtained as a red oil that was used in the next synthetic step without further purification.

HR-MS (EI^+) calc. [$C_{40}H_{45}BBrN_3O_7S^+$]: 801.2255, found: 801.2248.

Compound 80

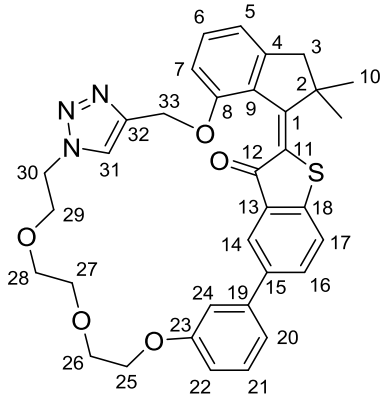

[595.714]

$C_{34}H_{33}N_3O_5S$

Compound **79** (156 mg, 198 µmol, 1.0 eq) was dissolved in DMF (10 mL), then K_2CO_3 (82 mg, 593 µmol, 3.0 eq), $Pd(PPh_3)_4$ (11.4 mg, 9.9 µmol, 5 mol%) and five drops of water were added. The reaction mixture was stirred at 85 °C for 4 h before the reaction was stopped by addition of a saturated NH_4Cl solution (5 mL) and the suspension was transferred to a separatory funnel. Additional saturated NH_4Cl solution (45 mL) was added and the aqueous phase was extracted with EtOAc (3 × 50 mL). The combined organic phases were washed with an excess of water (until residual DMF was removed as judged by the disappearance of DMF streaks in the aqueous phase) and brine (1 × 50 mL), dried over Na_2SO_4 and the solvent was evaporated *in vacuo*. After purification by flash column chromatography (SiO_2, *i*-Hex:EtOAc = 3:7 → 1:9) compound **80** (40 mg, 67 µmol, *E* isomer:*Z* isomer 9:1, 34%) was obtained as a yellow to orange solid.

***E* isomer**:

m.p.: 196 °C

^{1}H NMR (599 MHz, CD_2Cl_2) δ = 8.01 (d, *J* = 1.9 Hz, 1H, H-C(14)), 7.99 (s, 1H, H-C(31)), 7.84 (dd, *J* = 8.2, 2.0 Hz, 1H, H-C(16)), 7.54 (dd, *J* = 8.2, 0.6 Hz, 1H, H-C(17)), 7.44 (t, *J* = 2.1 Hz, 1H, H-C(24)), 7.41 – 7.37 (m, 1H, H-C(21)), 7.35 (dd, *J* = 8.3, 7.4 Hz, 1H, H-C(6)), 7.24 (ddd, *J* = 7.7, 1.7, 0.9 Hz, 1H, H-C(20)), 6.96 – 6.93 (m, 2H, H-C(5), H-C(22)), 6.91 (d, *J* = 8.3 Hz, 1H, H-C(7)), 5.27 (d, *J* = 11.7 Hz, 1H, H-C(33)), 5.19 (d, *J* = 11.8 Hz, 1H, H-C(33)), 4.42 – 4.34 (m, 1H, H-C(25)), 4.28 (m, *J* = 11.7, 4.8, 2.4 Hz, 1H, H-C(25)), 4.21 (ddd, *J* = 14.2, 6.1, 4.4 Hz, 1H, H-C(30)), 3.97 (ddd, *J* = 14.1, 6.9, 4.4 Hz, 1H, H-C(30)), 3.90 (ddd, *J* = 11.6, 6.4, 2.6 Hz, 1H, H-C(26)), 3.83 (ddd, *J* = 11.5, 5.8, 2.6 Hz, 1H, H-C(26)), 3.69 – 3.65 (m, 2H, H-C(27)), 3.63 (ddd, *J* = 12.7, 6.3, 4.4 Hz, 2H, H-C(29)), 3.58 (ddd, *J* = 11.2, 4.6, 3.1 Hz, 1H, H-

C(28)), 3.51 (ddd, *J* = 11.2, 5.7, 3.9 Hz, 1H, H-C(28)), 3.19 (d, *J* = 15.3 Hz, 1H, H-C(3)), 2.79 (d, *J* = 15.3 Hz, 1H, H-C(3)), 1.70 (s, 3H, H-C(10)), 1.22 (s, 3H, H-C(10)).

^{13}C NMR (151 MHz, CD_2Cl_2) δ = 187.02 (C-12), 160.15 (C-23), 157.83 (C-1), 157.77 (C-8), 150.21 (C-4), 143.79 (C-32), 143.64 (C-18), 141.52 (C-19), 137.87 (C-15), 133.07 (C-13), 132.90 (C-16), 132.68 (C-6), 130.55 (C-21), 128.67 (C-9), 126.36 (C-11), 125.49 (C-31), 124.32 (C-14), 124.30 (C-17), 119.80 (C-20), 117.58 (C-7), 114.87 (C-22), 114.62 (C-24), 110.29 (C-5), 71.58 (C-28), 71.28 (C-27), 70.37 (C-26), 69.96 (C-29), 68.50 (C-25), 62.41 (C-33), 51.42 (C-2), 50.68 (C-30), 49.78 (C-3), 26.98 (C-10), 26.28 (C-10).

IR: $\tilde{\nu}$ = 2955w, 2928w, 2860w, 1667m, 1604m, 1579m, 1544m, 1466m, 1385w, 1325m, 1302m, 1273s, 1223m, 1210m, 1181m, 1130m, 1083s, 1048s, 999m, 977w, 943m, 895w, 828s, 801w, 776s, 749m, 710m, 699w, 669w.

HR-MS (EI^+) calc. [$C_{34}H_{33}N_3O_5S^+$]: 595.2141, found: 595.2131.

Compound 81

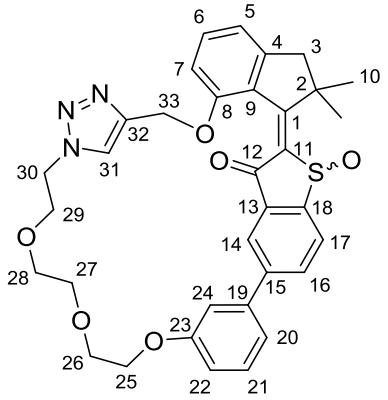

[611.713]

$C_{34}H_{33}N_3O_6S$

Compound **80** (28.8 mg, 48.3 µmol, 1.0 eq) was dissolved in acetic acid (3.00 mL) and $NaBO_2(OH)_2$ (29.8 mg, 193 µmol, 4.0 eq) was added. The reaction mixture was stirred at 23 °C for 4 h before it was transferred dropwise to a separatory funnel charged with a saturated $NaHCO_3$ solution (50 mL). The aqueous phase was extracted with EtOAc (3 × 50 mL), the combined organic phases were washed brine (1 × 50 mL), dried over Na_2SO_4 and the solvent was evaporated *in vacuo*. After purification by flash column chromatography (SiO_2, EtOAc) compound **81** (24 mg, 39 µmol, pure *E* isomer, 81%) was obtained as a yellow solid. (*R*) and (*S*) configured E isomers were separated on a CHIRALPAK® IC column from Diacel (*n*-heptane/EtOAc = 65/35, at 30 °C). (*R*) and (*S*) configured Z isomers were separated on a CHIRALPAK® IC column from Diacel (*n*-heptane/EtOAc = 30/70, at 30 °C) after irradiation of a solution of E isomer with 450 nm or 470 nm LED to the pss.

***E*-(*S*)-*P* isomer**:

m.p.: 184 - 187 °C

^{1}H NMR (599 MHz, CD_2Cl_2) δ = 8.11 (m, 1H, H-C(14)), 8.09 (m, 2H, H-C(16), H-C(17)), 7.92 (s, 1H, H-C(31)), 7.52 (t, *J* = 2.0 Hz, 1H, H-C(24)), 7.43 (m, 2H, H-C(6), H-C(21)), 7.29 (ddt, *J* = 7.7, 1.8, 0.9 Hz, 1H, H-C(20)), 7.01 (ddt, *J* = 8.2, 2.5, 0.9 Hz, 1H, H-C(22)), 6.98 (ddd, *J* = 7.5, 1.4, 0.8 Hz, 1H, H-C(5)), 6.95 (dd, *J* = 8.4, 0.9 Hz, 1H, H-C(7)), 5.29 (d, *J* = 12.1 Hz, 1H, H-C(33)), 5.19 (dd, *J* = 12.2, 0.8 Hz, 1H, H-C(33)), 4.37 (ddd, *J* = 11.1, 5.9, 2.6 Hz, 1H, H-C(25)), 4.26 (m, 2H, H-C(25), H-C(30)), 4.13 – 4.09 (m, 1H, H-C(30)), 3.90 – 3.85 (m, 1H, H-C(26)), 3.85 – 3.81 (m, 1H, H-C(26)), 3.76 (ddd, *J* = 10.8, 6.6, 4.4 Hz, 1H, H-C(29)), 3.72 – 3.66 (m, 3H, H-C(27), H-C(29)), 3.61 (ddd, *J* = 11.2, 4.9, 3.4 Hz, 1H, H-C(28)), 3.54 (ddd, *J* =

11.1, 5.3, 4.0 Hz, 1H, H-C(28)), 3.26 (d, *J* = 15.1 Hz, 1H, H-C(3)), 2.84 (d, *J* = 15.1 Hz, 1H, H-C(3')), 1.97 (s, 3H, H-C(10)), 1.39 (s, 3H, H-C(10')).

^{13}C NMR (151 MHz, CD_2Cl_2) δ = 183.18 (C-12), 170.14 (C-1), 160.14 (C-23), 158.34 (C-8), 151.40 (C-4), 148.24 (C-18), 145.41 (C-15), 143.49 (C-32), 140.75 (C-19), 140.54 (C-11), 136.56 (C-13), 134.72 (C-6 or C-21), 133.95 (C-16 or C-17), 130.74 (C-6 or C-21), 128.10 (C-9), 127.79 (C-16 or C-17), 125.08 (C-31), 123.58 (C-14), 120.30 (C-20), 117.90 (C-5), 115.52 (2C, C-22 and C-24), 110.71 (C-7), 71.45 (C-28), 71.27 (C-27), 70.26 (C-26), 69.87 (C-29), 68.48, (C-25), 62.62 (C-33), 53.28 (C-2), 50.74 (C-30), 50.21 (C-3), 28.54 (C-10'), 26.50 (C-10).

^{1}H NMR (599 MHz, THF-d_8) δ = 8.21 (d, *J* = 1.8 Hz, 1H, H-C(14)), 8.13 (dd, *J* = 8.1, 1.8 Hz, 1H, H-C(16)), 8.09 (d, *J* = 8.1 Hz, 1H, H-C(17)), 8.00 (s, 1H, H-C(31)), 7.65 (t, *J* = 2.1 Hz, 1H, H-C(24)), 7.41 – 7.35 (m, 2H, H-C(6) and H-C(21)), 7.30 (ddd, *J* = 7.7, 1.9, 1.0 Hz, 1H, H-C(20)), 7.04 (d, *J* = 8.3 Hz, 1H, H-C(7)), 6.99 (ddd, *J* = 8.2, 2.5, 0.9 Hz, 1H, H-C(22)), 6.91 (d, *J* = 7.3 Hz, 1H, H-C(5)), 5.23 (d, *J* = 12.2 Hz, 1H, H-C(33)), 5.17 (d, *J* = 12.1 Hz, 1H, H-C(33)), 4.35 (ddd, *J* = 11.5, 5.5, 3.4 Hz, 1H, H-C(25)), 4.30 – 4.22 (m, 2H, H-C(25) and H-C(30)), 4.21 – 4.15 (m, 1H, H-C(30)), 3.85 – 3.79 (m, 2H, H-C(26)), 3.77 (ddd, *J* = 11.0, 6.6, 5.0 Hz, 1H, H-C(29)), 3.72 – 3.66 (m, 1H, H-C(29)), 3.64 (t, *J* = 4.6 Hz, 2H, H-C(27)), 3.61 – 3.55 (m, 1H, H-C(28)), 3.52 (dt, *J* = 11.2, 4.8 Hz, 1H, H-C(28)), 3.22 (d, *J* = 14.9 Hz, 1H, H-C(3)), 2.80 (d, *J* = 14.9 Hz, 1H, H-C(3)), 1.97 (s, 3H, H-C(10)), 1.37 (s, 3H, H-C(10)).

^{13}C NMR (151 MHz, THF-d_8) δ = 182.95 (C-12), 168.68 (C-1), 161.10 (C-23), 159.30 (C-8), 151.14 (C-4), 149.66 (C-18), 145.80 (C-15), 143.88 (C-32), 142.31 (C-11), 141.56 (C-19), 137.47 (C-13), 134.53 (C-6), 134.01 (C-16), 130.88 (C-21), 128.93 (C-9), 128.12 (C-17), 125.44 (C-31), 124.10 (C-14), 120.53 (C-20), 117.73 (C-5), 115.98 (C-24), 115.82 (C-22), 111.40 (C-7), 72.00 (C-27), 71.69 (C-28), 70.82 (C-26), 70.57 (C-29), 69.08 (C-25), 63.03 (C-33), 53.22 (C-2), 50.75 (C-30), 50.60 (C-3), 28.67 (C-10), 26.57 (C-10).

IR: $\tilde{\nu}$ = 2916m, 2849w, 1678m, 1582m, 1571m, 1552m, 1455m, 1437w, 1410w, 1383w, 1362w, 1324w, 1303m, 1275m, 1229m, 1211m, 1183m, 1175m, 1127m, 1117m, 1089m, 1082m, 1071m, 1051vs, 997m, 986m, 944m, 913m, 896m, 831m, 813m, 801w, 775vs, 752s, 735m, 716s, 694m, 679w, 663m.

HR-MS (EI^+) calc. [$C_{34}H_{33}N_3O_6S^+$]: 611.2090, found: 611.2091.

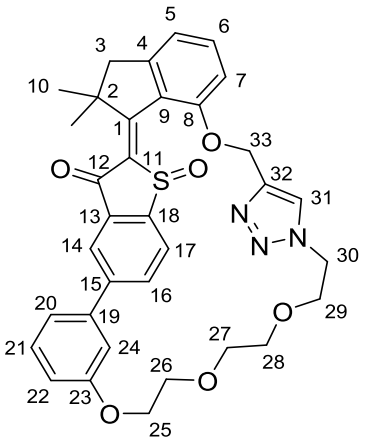

***Z*-(*S*)-*P* isomer**:

^{1}H NMR (599 MHz, CD_2Cl_2) δ = 8.10 (dd, *J* = 1.7, 0.8 Hz, 1H, H-C(14)), 8.04 (dd, *J* = 8.0, 1.7 Hz, 1H, H-C(16)), 8.00 (dd, *J* = 7.9, 0.6 Hz, 1H, H-C(17)), 7.67 (t, *J* = 2.1 Hz, 1H, H-C(24)), 7.62 (s, 1H, H-C(23)), 7.59 (dd, *J* = 8.2, 7.4 Hz, 1H, H-C(6)), 7.38 – 7.35 (m, 1H, H-C(21)), 7.29 (ddt, *J* = 7.5, 1.6, 0.9 Hz, 1H, H-C(20)), 7.06 (d, *J* = 7.6 Hz, 1H, H-C(5)), 7.04 (d, *J* = 8.3 Hz, 1H, H-C(7)), 6.99 – 6.96 (m, 1H, H-C(22)), 5.47 (d, *J* = 10.7 Hz, 1H, H-C(33)), 5.32 (d, *J* =10.7 Hz, 1H, H-C(33)), 4.46 (ddd, *J* = 13.8, 7.0, 1.9 Hz, 1H, H-C(25)), 4.41 – 4.30 (m, 3H, H-C(25), H-C(30)), 3.79 (ddd, *J* = 11.5, 5.2, 1.9 Hz, 1H, H-C(26)), 3.72 (ddd, *J* = 11.4, 7.0, 2.0 Hz, 1H, H-C(26)), 3.56 (ddd, *J* = 10.4, 6.8, 3.7 Hz, 1H, H-C(27)), 3.45 – 3.41 (m, 1H, H-C(27)), 3.34 – 3.29 (m, 1H, H-C(28)), 3.29 – 3.23 (m, 2H, H-C(3'), H-C(29)), 3.20 – 3.14 (m, 2H, H-C(28), H-C(29)), 2.90 (d, *J* = 15.8 Hz, 1H, H-C(3)), 1.62 (s, 3H, H-C(10')), 1.50 (s, 3H, H-C(10)).

^{13}C NMR (151 MHz, CD_2Cl_2) δ = 183.84 (C-12), 173.24 (C-1), 160.01 (C-23), 156.57 (C-8), 152.42 (C-4), 147.55 (C-18), 146.21 (C-15), 142.60 (C-32), 141.66 (C-11), 140.55 (C-19), 135.83 (C-13), 135.42 (C-6), 134.33 (C-16), 129.78 (C-21), 126.65 (C-17), 126.27 (C-9), 124.21 (C-31), 123.50 (C-14), 119.55 (C-20), 118.25 (C-5), 117.96 (C-22), 115.49 (C-24), 110.14 (C-7), 72.15 (C-26), 70.75 (C-28), 69.80 (C-27), 69.65 (C-25), 69.31 (C-29), 62.88 (C-33), 52.87 (C-2), 50.70 (C-3), 48.90 (C-30), 26.91 (C-10), 25.09 (C-10').

HR-MS (EI^+) calc. [$C_{34}H_{33}N_3O_6S^+$]: 611.2090, found: 611.2091.

Compound 84

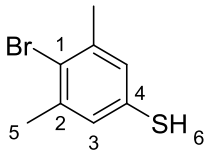

[217.124]

C_8H_9BrS

Compound **87** (1.18 g, 4.09 mmol, 1.0 eq) and potassium methoxide (290 mg, 4.14 mmol, 1.01 eq) in methanol (10 mL) were heated under reflux for 1 d. The crude product was transferred to a separatory funnel charged with a saturated aqueous NH_4Cl solution and the aqueous phase was extracted with EtOAc. The combined organic phases were washed with brine, dried over Na_2SO_4 and the solvent was removed *in vacuo*. The crude product was purified by flash column chromatography (SiO_2, *i*-Hex) to give compound **84** (778 mg, 3.58 mmol, 88%) as a colorless liquid. The disulfide dimer was observed as a minor byproduct.

^{1}H NMR (400 MHz, CD_2Cl_2, 25 °C) δ = 7.01 (t, *J* = 0.7 Hz, 2H, H-C(3)), 3.45 (s, 1H, SH)), 2.35 (d, *J* = 0.7 Hz, 6H, H-C(5)).

^{13}C NMR (101 MHz, CD_2Cl_2, 25 °C) δ = 139.65 (C-2), 129.74 (C-4), 129.29 (C-3), 125.11 (C-1), 23.99 (C-5).

HR-MS (EI): *m/z* calc.: 214.9530 for [C_8H_8BrS]; found: 214.9515.

Compound 86

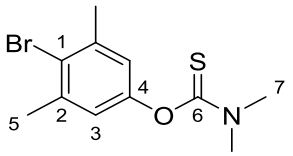

[288.203]

$C_{11}H_{14}BrNOS$

4-Bromo-3,5-dimethylphenol (1.00 g, 4.97 mmol, 1.0 eq), dimethylthiocarbamoyl chloride (768 mg, 6.22 mmol, 1.25 eq), 4-dimethylaminopyridine (608 mg, 4.97 mmol, 1.0 eq) and triethylamine (1.01 g, 9.95 mmol, 2.0 eq) were dissolved in dioxane (20 mL) and stirred under reflux for 20 h. The crude product was transferred to a separatory funnel charged with a

saturated aqueous NH_4Cl solution and the resulting aqueous phase was extracted with EtOAc. The combined organic phases were washed with brine, dried over Na_2SO_4, and the solvent was removed *in vacuo*. The crude product was purified by flash column chromatography (SiO_2, *i*-Hex:EtOAc, 19:1) to give compound **86** (1.38 g, 4.79 mmol, 96%) as colorless crystals.

^{1}H NMR (400 MHz, CD_2Cl_2, 27 °C) δ = 6.82 (dd, *J* = 1.4, 0.7 Hz, 2H, H-C(3)), 3.41 (s, 3H, H-C(7)), 3.30 (s, 3H, H-C(7)), 2.41 (t, *J* = 0.7 Hz, 6H, H-C(5)).

^{13}C NMR (101 MHz, CD_2Cl_2, 27 °C) δ = 187.92 (C-6), 153.15 (C-4), 139.69 (C-2), 124.43 (C-1), 122.99 (C-3), 43.65 (C-7), 39.12 (C-7), 24.24 (C-5).

HR-MS (EI): *m/z* calc.: 286.9979 for [$C_{11}H_{14}BrNOS$]; found: 286.9972.

Compound 87

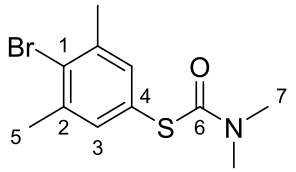

[288.203]

$C_{11}H_{14}BrNOS$

Compound **86** (1.38 g, 4.79 mmol) in tetradecane (10 mL) was heated under reflux for 5 h using a sand bath. The reaction mixture was allowed to cool to room temperature and directly subjected to flash column chromatography (SiO_2, *i*-Hex:EtOAc = 9:1) to give compound **87** (1.19 g, 4.79 mmol, 86%) as a brown solid.

^{1}H NMR (400 MHz, CD_2Cl_2, 27 °C) δ = 7.20 (t, *J* = 0.7 Hz, 2H, H-C(3)), 3.01 (m, 6H, H-C(7)), 2.42 (d, *J* = 0.7 Hz, 6H, H-C(5)).

^{13}C NMR (101 MHz, CD_2Cl_2, 27 °C) δ = 166.52 (C-6), 139.51 (C-2), 135.61 (C-3), 129.46 (C-1), 127.92 (C-4), 37.29 (C-7), 24.08 (C-5).

HR-MS (EI): *m/z* calc.: 286.9979 for [$C_{11}H_{14}BrNOS$]; found: 286.9973.

Compound 89

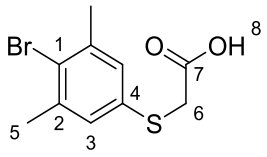

[275.160]

$C_{10}H_{11}BrO_2S$

Compound **84** (778 mg, 3.58 mmol, 1.0 eq) was dissolved in acetone (10 mL). Bromoacetic acid (548 mg, 3.94 mmol, 1.1 eq) and K_2CO_3 (1.49 g, 10.7 mmol, 3.0 eq) were added and the reaction mixture was stirred at room temperature for 18 h. The resulting suspension was transferred to a separatory funnel charged with an aqueous 2 M HCl solution and the aqueous phase was extracted with EtOAc. The combined organic phases were washed with brine, dried over Na_2SO_4 and the solvent was removed *in vacuo* to give compound **89** (844 mg, 3.07 mmol, 86%) as colorless crystals.

^{1}H NMR (400 MHz, CD_2Cl_2, 25 °C) δ = 7.13 (dd, *J* = 1.3, 0.7 Hz, 2H, H-C(3)), 3.67 (s, 2H, H-C(6)), 2.38 (d, *J* = 0.7 Hz, 6H, H-C(5)).

^{13}C NMR (101 MHz, CD_2Cl_2, 25 °C) δ = 174.29 (C-7), 139.82 (C-2), 133.35 (C-4), 129.92 (C-3), 127.04 (C-1), 36.79 (C-6), 24.11 (C-5).

HR-MS (EI): *m/z* calc.: 273.9663 for [$C_{10}H_{11}BrO_2S$]; found: 273.9663.

Compound 90

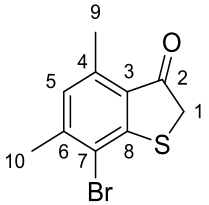

[257.145]

$C_{10}H_9BrOS$

Compound **89** (837 mg, 3.04 mmol, 1.0 eq) was dissolved in thionyl chloride (1.99 mL, 27.4 mmol, 9.0 eq) and heated for 1.5 h under reflux (85 °C). Excess thionyl chloride was removed *in vacuo* and the crude acid chloride was dissolved in $(CH_2Cl)_2$ (5.0 mL). The stirring

solution was cooled to 0 °C on an ice bath and aluminum chloride (1.22 g, 9.13 mmol, 3.0 eq) was added. The reaction mixture was allowed to warm to 23 °C and stirred for 2 h before it was poured into a separatory funnel charged with ice/aqueous 2 M HCl. The aqueous phase was extracted with CH_2Cl_2, the combined organic phases were dried over Na_2SO_4 and the solvent was removed *in vacuo* to give compound **90** (688 mg, 2.68 mmol, 88%) as a red solid. The crude product can be further purified by flash column chromatography (SiO_2, *i*-Hex:EtOAc = 49:1 → 19:1) with siginificantly decreased yield due to decomposition to give compound **90** (259 mg, 1.01 mmol, 33%) as a purple solid.

^{1}H NMR (400 MHz, CD_2Cl_2, 25 °C) δ = 6.89 (p, *J* = 0.8 Hz, 1H, H-C(5)), 3.80 (s, 2H, H-C(1)), 2.53 (d, *J* = 0.8 Hz, 3H, H-C(9)), 2.43 (s, 3H, H-C(10)).

^{13}C NMR (101 MHz, CD_2Cl_2, 25 °C) δ = 200.61 (C-2), 157.32 (C-8), 145.88 (C-4 or C-6), 140.58 (C-4 or C-6), 130.35 (C-5), 128.88 (C-3), 118.07 (C-7), 41.25 (C-1), 23.32 (C-10), 18.63 (C-9).

HR-MS (EI): *m/z* calc.: 255.9558 for [$C_{10}H_9BrOS$]; found: 255.9548.

Compound 91

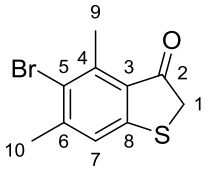

[257.145]

$C_{10}H_9BrOS$

Compound **89** (530 mg, 1.93 mmol, 1.0 eq) was dissolved in thionyl chloride (1.26 mL, 17.3 mmol, 9.0 eq) and heated under reflux for 1.5 h. The volatiles were removed *in vacuo* and the residue was taken up in 1,2-dichloroethane (5.0 mL). The solution was cooled to 0 °C and $AlCl_3$ (270 mg, 2.02 mmol, 1.05 eq) was added. The suspension was stirred for 30 min at 0 °C before the ice bath was removed. The reaction mixture was stirred for another 30 min at 23 °C before it was transferred to a separatory funnel that was charged with a H_2O-ice / 2 M aqueous HCl mixture. The aqueous phase was extracted with CH_2Cl_2. The combined organic phases were dried over Na_2SO_4 and the solvent was removed *in vacuo* to give compound **7** (492 mg, 1.91 mmol, 99%) as a deep red solid.

^{1}H NMR (400 MHz, CD_2Cl_2) δ = 7.19 (s, 1H, H-C(7)), 3.79 (s, 2H, H-C(1)), 2.74 (s, 3H, H-C(9)), 2.46 (s, 3H, H-C(10)).

^{13}C NMR (101 MHz, CD_2Cl_2) δ = 200.09 (C-2), 154.71 (C-8), 146.48 (C-4), 141.89 (C-6), 127.69 (C-3), 126.05 (C-5), 124.22 (C-7), 40.42 (C-1), 25.41 (C-10), 17.98 (C-9).

HR-MS (EI): *m/z* calc.: 255.9558 for [$C_{10}H_9BrOS$]; found: 255.9563.

Compound 92

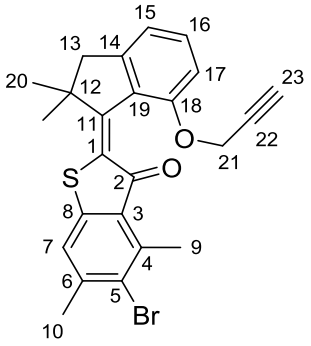

[453.394]

$C_{24}H_{21}BrO_2S$

In a Schlenk flask compound **91** (534 mg, 2.08 mmol, 1.1 eq) was dissolved in CH_2Cl_2 (3.0 mL) and cooled to –78 °C. BCl_3 (1.98 mL, 1.98 mmol, 1 M in toluene, 1.05 eq) was added and the cold reaction mixture was immediately transferred to a second Schlenk flask containing a 0 °C cold solution of compound **56** (405 mg, 1.89 mmol, 1.0 eq) in CH_2Cl_2 (3.0 mL). After stirring for 40 min at room temperature the reaction was stopped by addition of a saturated aqueous NH_4Cl solution. The mixture was transferred to a separatory funnel charged with a saturated aqueous NH_4Cl solution. The aqueous phase was extracted with CH_2Cl_2. The combined organic phases were dried over Na_2SO_4 and the solvent was removed *in vacuo*. The crude product was purified by flash column chromatography (SiO_2, *i*-Hex:EtOAc = 49:1 → 19:1) to give compound **92** (523 mg, 1.15 mmol, mixture of *E* and *Z* isomer, 61%) as an orange solid.

***E* isomer**

^{1}H NMR (599 MHz, CD_2Cl_2, 27 °C) δ = 7.33 (dd, *J* = 8.3, 7.4 Hz, 1H, H-C(16)), 7.23 – 7.22 (m, 1H, H-C(7)), 6.94 (dd, *J* = 7.4, 1.0 Hz, 1H, H-C(15)), 6.86 (dd, *J* = 8.3, 0.8 Hz, 1H, H-C(17)), 4.71 (d, *J* = 2.4 Hz, 2H, H-C(21)), 3.17 (d, *J* = 15.4 Hz, 1H, H-C(13)), 2.87 (d, *J* = 0.5

Hz, 3H, H-C(9)), 2.75 (d, *J* = 15.4 Hz, 1H, H-C(13)), 2.49 (d, *J* = 0.7 Hz, 3H, H-C(10)), 2.47 (t, *J* = 2.4 Hz, 1H, H-C(23)), 1.66 (s, 3H, H-C(20)), 1.18 (s, 3H, H-C(20)).

^{13}C NMR (101 MHz, CD_2Cl_2) δ = 188.03 (C-2), 156.66 (C-18), 155.28 (C-11), 149.63 (C-14), 144.42 (C-4 or C-6), 144.01 (C-1 or C-8), 141.03 (C-4 or C-6), 131.98 (C-16), 129.08 (C-19), 128.84 (C-3), 126.60 (C-1 or C-8), 126.27 (C-5), 123.00 (C-7), 118.21 (C-15), 110.39 (C-17), 78.98 (C-22), 75.72 (C-23), 56.29 (C-21), 50.95 (C-12), 49.71 (C-13), 26.84 (C-20), 26.05 (C-20), 25.35 (C-10), 18.40 (C-9).

HR-MS (EI): *m/z* calc. [M + Na]: 475.0343 for [$C_{24}H_{21}BrNaO_2S$]; found: 475.0338.

Compound 93

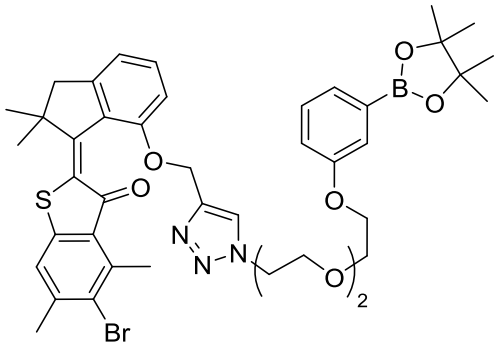

[830.642]

$C_{42}H_{49}BBrN_3O_7S$

Compound **92** (300 mg, 662 µmol, 1.0 eq) and compound **73** (262 mg, 695 µmol, 1.05 eq) were dissolved in DMF (2.8 mL), then sodium ascorbate (13.1 mg, 66.2 µmol, 10 mol%) and $CuSO_4 \cdot 5H_2O$ (3.3 mg, 13.2 µmol, 2 mol%) were added. The reaction mixture was stirred at 23 °C for 1 d before it was transferred to a separatory funnel charged with a saturated aqueous NH_4Cl solution. The aqueous phase was extracted with EtOAc, the combined organic phases were washed with an excess of water (until residual DMF was removed as judged by the disappearance of DMF streaks in the aqueous phase) and brine, dried over Na_2SO_4 and the solvent was evaporated *in vacuo*. After purification by flash column chromatography (SiO_2, CH_2Cl_2 → CH_2Cl_2:MeOH = 25:1) compound **93** (463 mg, 557 µmol, 84%) was obtained as a red oil that was used in the next synthetic step without further purification.

HR-MS (EI^+) calc. [$C_{42}H_{50}BBrN_3O_7S^+$]: 830.2646, found: 830.2635.

Compound 94

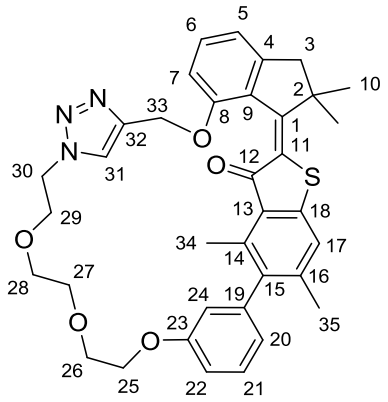

[623.768]

$C_{36}H_{37}N_3O_5S$

Compound **93** (460 mg, 554 µmol, 1.0 eq) was dissolved in DMF (5.0 mL), then K_2CO_3 (230 mg, 1.66 mmol, 3.0 eq), $Pd(PPh_3)_4$ (32.0 mg, 27.7 µmol, 5 mol%) and one drop of water were added. The reaction mixture was stirred at 80 °C for 10 h before the reaction was stopped by addition of a saturated aqueous NH_4Cl solution. The aqueous phase was extracted with EtOAc, the combined organic phases were washed with an excess of water (until residual DMF was removed as judged by the disappearance of DMF streaks in the aqueous phase) and brine, dried over Na_2SO_4 and the solvent was evaporated *in vacuo*. After purification by flash column chromatography (SiO_2, *i*-Hex:EtOAc = 1:1) compound **94** (80.3 mg, 129 µmol, mixture of *E* and *Z* isomers, 23%) was obtained as an orange solid.

***E* isomer**

C-11 and C-18 could not be assigned

^{1}H NMR (599 MHz, CD_2Cl_2, 27 °C) δ = 7.55 (s, 1H, H-C(31)), 7.37 (t, *J* = 7.9 Hz, 1H, H-C(21)), 7.34 – 7.31 (m, 1H, H-C(6)), 7.21 (s, 1H, H-C(17)), 6.96 – 6.91 (m, 3H, H-C(5), H-C(7) and H-C(22)), 6.82 (t, *J* = 2.0 Hz, 1H, H-C(24)), 6.74 (d, *J* = 7.5 Hz, 1H, H-C(20)), 5.27 – 5.24 (m, 1H, H-C(33)), 5.17 (d, *J* = 11.9 Hz, 1H, H-C(33)), 4.44 – 4.39 (m, 1H, H-C(30)), 4.31 – 4.21 (m, 3H, H-C(25) and H-C(30)), 3.83 – 3.80 (m, 3H, H-C(26) and H-C(29)), 3.80 – 3.74 (m, 1H, H-C(26)), 3.64 – 3.61 (m, 2H, H-C(27)), 3.58 – 3.56 (m, 2H, H-C(28)), 3.20 – 3.16 (m, 1H, H-C(3)), 2.75 (d, *J* = 15.3 Hz, 1H, H-C(3)), 2.31 (s, 3H, H-C(34)), 2.11 (s, 3H, H-C(35)), 1.68 (s, 3H, H-C(10)), 1.19 (s, 3H, H-C(10)).

^{13}C NMR (151 MHz, CD_2Cl_2, 27 °C) δ = 188.29 (C-12), 159.71 (C-23), 157.85 (C-8), 155.17 (C-1), 149.54 (C-4), 144.41 (C-32), 143.15 (C-14 or C-16), 141.67 (C-19), 140.22 (C-15),

138.80 (C-14 or C-16), 132.05 (C-6), 130.25 (C-21), 129.37 (C-9), 127.47 (C-13), 124.08 (C-31), 122.78 (C-20), 122.27 (C-17), 118.12 (C-24), 117.70 (C-5), 114.40 (C-22), 110.43 (C-7), 71.70 (C-27), 71.18 (C-28), 70.32 (C-26), 69.89 (C-29), 68.85 (C-25), 62.79 (C-33), 51.34 (C-2), 50.70 (C-30), 49.88 (C-3), 26.97 (C-10), 26.24 (C-10), 22.19 (C-35), 16.13 (C-34).

HR-MS (EI^+) calc. [$C_{40}H_{45}N_3O_8S^+$]: 623.2454, found: 623.2457.

Compound 95

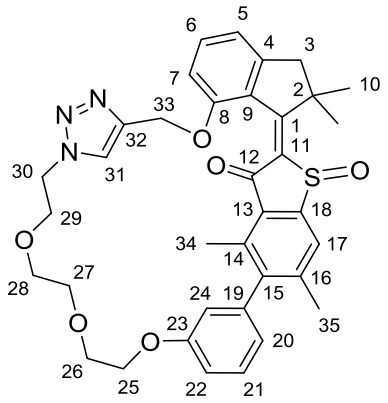

[639.767]

$C_{36}H_{37}N_3O_6S$

Compound **94** (68.0 mg, 109 µmol, 1.0 eq) was dissolved in acetic acid (5.0 mL) and sodium perborate tetrahydrate (67.1 mg, 436 µmol, 4.0 eq) was added. The reaction mixture was stirred at room temperature for 4 h before it was transferred dropwise to a separatory funnel charged with a saturated aqueous $NaHCO_3$ solution. The aqueous phase was extracted with CH_2Cl_2. The combined organic phases were washed with brine, dried over Na_2SO_4 and the solvent was removed *in vacuo*. The crude product was purified by flash column chromatography (SiO_2, EtOAc) to give compound **95** (55.5 mg, 86.8 µmol, mixture of *E* and *Z* isomers, 80%) as a yellow solid.

***E* isomer**

^{1}H NMR (599 MHz, CD_2Cl_2) δ = 7.77 (s, 1H, H-C(17)), 7.56 (s, 1H, H-C(31)), 7.44 (t, *J* = 7.8 Hz, 1H, H-C(6)), 7.40 (t, *J* = 7.9 Hz, 1H, H-C(21)), 7.06 (d, *J* = 8.3 Hz, 1H, H-C(7)), 6.98 (d, *J* = 7.3 Hz, 1H, H-C(5)), 6.96 (ddd, *J* = 8.4, 2.6, 0.8 Hz, 1H, H-C(22)), 6.88 (dd, *J* = 2.6, 1.5 Hz, 1H, H-C(24)), 6.74 (dt, *J* = 7.4, 1.1 Hz, 1H, H-C(20)), 5.24 (d, *J* = 12.1 Hz, 1H, H-C(33)), 5.15 (d, *J* = 12.1 Hz, 1H, H-C(33')), 4.38 (t, *J* = 5.9 Hz, 2H, H-C(30)), 4.29 – 4.25 (m, 2H, H-

C(25)), 3.86 – 3.77 (m, 4H, H-C(26), H-C(29)), 3.66 – 3.62 (m, 2H, H-C(27) or H-C(28)), 3.60 – 3.55 (m, 2H, H-C(27) or H-C(28)), 3.27 (d, *J* = 15.1 Hz, 1H, H-C(3)), 2.82 (d, *J* = 15.0 Hz, 1H, H-C(3')), 2.36 (s, 3H, H-C(34)), 2.23 (s, 3H, H-C(35)), 1.95 (s, 3H, H-C(10)), 1.37 (s, 3H, H-C(10')).

^{13}C NMR (151 MHz, CD_2Cl_2) δ = 184.51 (C-12), 168.12 (C-1), 159.90 (C-23), 158.49 (C-8), 150.74 (C-4), 149.68 (C-18), 147.30 (C-15), 144.50 (C-14), 143.76 (C-32), 140.96 (C-19), 140.69 (C-11), 138.72 (C-16), 134.20 (C-6), 130.86 (C-13), 130.45 (C-21), 128.66 (C-9), 125.47 (C-17), 124.32 (C-31), 121.77 (C-20), 118.07 (C-5), 116.89 (C-24), 114.64 (C-22), 111.05 (C-7), 71.75 (C-27 or C-28), 71.22 (C-27 or C-28), 70.27 (C-26 or C-29), 70.00 (C-26 or C-29), 68.46 (C-25), 62.92 (C-33), 53.06 (C-2), 50.76 (C-30), 50.28 (C-3), 28.45 (C-10'), 26.45 (C-10), 22.31 (C-35), 16.63 (C-34).

***Z* isomer**

^{1}H NMR (599 MHz, CD_2Cl_2) δ = 7.64 (s, 1H, H-C(17)), 7.61 (s, 1H, H-C(31)), 7.56 (dd, *J* = 8.2, 7.5 Hz, 1H, H-C(6)), 7.36 (dd, *J* = 8.3, 7.3 Hz, 1H, H-C(21)), 7.16 (dd, *J* = 2.7, 1.5 Hz, 1H, H-C(24)), 7.03 (m, 2H, H-C(5) and H-C(7)), 6.94 (ddd, *J* = 8.3, 2.6, 1.0 Hz, 1H, H-C(22)), 6.81 (dt, *J* = 7.3, 1.2 Hz, 1H, H-C(20)), 5.49 (d, *J* = 10.8 Hz, 1H, H-C(33)), 5.34 (d, *J* = 10.8 Hz, 1H, H-C(33)), 4.45 (ddd, *J* = 13.6, 8.4, 6.1 Hz, 1H, H-C(30)), 4.39 – 4.34 (m, 1H, H-C(30)), 4.31 (ddd, *J* = 13.8, 5.5, 3.3 Hz, 1H, H-C(25)), 4.25 (ddd, *J* = 13.9, 4.5, 2.9 Hz, 1H, H-C(25)), 3.72 – 3.70 (m, 2H, H-C(26)), 3.50 (td, *J* = 5.7, 5.2, 3.7 Hz, 2H, H-C(27)), 3.45 (ddd, *J* = 9.7, 8.4, 6.1 Hz, 1H, H-C(29)), 3.30 (ddd, *J* = 10.9, 5.2, 3.7 Hz, 1H, H-C(28)), 3.28 – 3.20 (m, 3H, H-C(3), H-C(28) and H-C(29)), 2.86 (d, *J* = 15.8 Hz, 1H, H-C(3')), 2.48 (s, 3H, H-C(34)), 2.16 (s, 3H, H-C(35)), 1.58 (s, 3H, H-C(10)), 1.51 (s, 3H, H-C(10')).

^{13}C NMR (151 MHz, CD_2Cl_2) δ = 186.02 (C-12), 170.76 (C-1), 160.63 (C-23), 156.78 (C-8), 152.27 (C-4), 150.11 (C-18), 147.78 (C-15), 145.11 (C-16), 143.49 (C-32), 143.23 (C-11), 140.73 (C-19), 138.59 (C-14), 135.34 (C-6), 130.99 (C-13), 130.15 (C-21), 126.79 (C-9), 124.94 (C-17), 124.56 (C-31), 121.39 (C-20), 118.66 (C-5), 117.53 (C-22), 116.52 (C-24), 110.33 (C-7), 72.48 (C-26), 71.17 (C-28), 70.63 (C-25), 70.52 (C-27), 70.05 (C-29), 63.59 (C-33), 53.01 (C-2), 51.22 (C-3), 49.70 (C-30), 27.85 (C-10), 25.75 (C-10), 22.38 (C-35), 16.68 (C-34).

HR-MS (EI^+) calc. [$C_{36}H_{37}N_3O_6S^+$]: 639.2403, found: 639.2413.

Compound 96

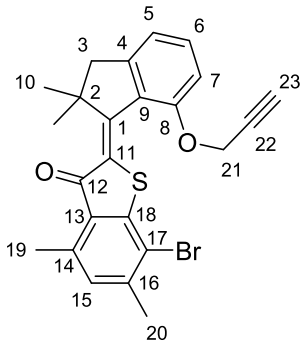

[453.394]

$C_{24}H_{21}BrO_2S$

Benzothiophenone **90** (259 mg, 1.13 mmol, 1.1 eq) was dissolved in CH_2Cl_2 (2.0 mL) and cooled to –78 °C. BCl_3 (1.08 mL, 1 M in toluene, 1.08 mmol, 1.05 eq) was added and the suspension was immediately taken up in a syringe and added to a stirring 0 °C solution of indanone **56** (220 mg, 1.03 mmol, 1.0 eq) in CH_2Cl_2 (2.0 mL). After stirring for 10 min at 0 °C the reaction was stopped by addition of a saturated NH_4Cl solution. The mixture was transferred to a separatory funnel charged with additional saturated NH_4Cl solution. The aqueous phase was extracted with CH_2Cl_2, the combined organic phases were dried over Na_2SO_4 and the solvent was evaporated *in vacuo*. The crude product was purified by flash column chromatography (SiO_2, *i*-Hex:EtOAc = 49:1 → 9:1) to give to give compound **96** (232 mg, 512 µmol, 50%) as an orange solid that readily crystallizes from a saturated EtOAc solution.

***E* isomer**

^{1}H NMR (599 MHz, CD_2Cl_2, 27 °C) δ = 7.33 (dd, *J* = 8.2, 7.4 Hz, 1H, H-C(6)), 6.94 (dd, *J* = 7.4, 0.9 Hz, 1H, H-C(5)), 6.94 – 6.93 (m, 1H, H-C(15)), 6.86 – 6.84 (m, 1H, H-C(7)), 4.71 (d, *J* = 2.4 Hz, 2H, H-C(21)), 3.18 (d, *J* = 15.3 Hz, 1H, H-C(3)), 2.77 (d, *J* = 15.3 Hz, 1H, H-C(3)), 2.66 (d, *J* = 0.8 Hz, 3H, H-C(19)), 2.46 – 2.44 (m, 4H, H-C(20) and H-C(23)), 1.71 (s, 3H, H-C(10)), 1.22 (d, *J* = 1.8 Hz, 3H, H-C(10)).

^{13}C NMR (151 MHz, CD_2Cl_2, 27 °C) δ = 188.43 (C-12), 156.92 (C-8), 155.77 (C-1), 149.78 (C-4), 147.06 (C-18), 143.70 (C-14 or C-16), 139.78 (C-14 or C-16), 132.11 (C-6), 130.33 (C-15), 129.92 (C-13), 129.11 (C-9), 127.45 (C-11), 118.19 (C-5), 116.76 (C-17), 110.38 (C-7), 79.03 (C-22), 75.63 (C-23), 56.33 (C-21), 51.10 (C-2), 49.75 (C-3), 26.94 (C-10), 26.17 (C-10), 23.22 (C-20), 18.83 (C-19).

HR-MS (EI): *m/z* calc.: 452.0446 for [$C_{24}H_{21}BrO_2S$]; found: 452.0450.

Compound 97

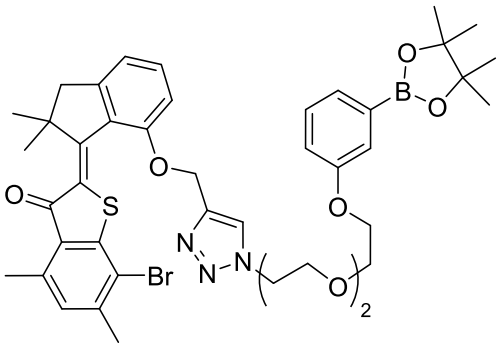

[830.642]

$C_{42}H_{49}BBrN_3O_7S$

Compound **96** (152 mg, 335 µmol, 1.0 eq) and compound **73** (133 mg, 352 µmol, 1.05 eq) were dissolved in DMF (1.6 mL), then sodium ascorbate (6.6 mg, 34 µmol, 10 mol%) and $CuSO_4 \cdot 5H_2O$ (1.7 mg, 6.7 µmol, 2 mol%) were added. The reaction mixture was stirred at 23 °C for 3 d before it was transferred to a separatory funnel charged with a saturated NH_4Cl solution. The aqueous phase was extracted with EtOAc, the combined organic phases were washed with an excess of water (until residual DMF was removed as judged by the disappearance of DMF streaks in the aqueous phase) and brine, dried over Na_2SO_4 and the solvent was evaporated *in vacuo*. After purification by flash column chromatography (SiO_2, CH_2Cl_2:MeOH = 49:1 → 19:1) compound **97** (250 mg, 301 µmol, 90%) was obtained as a red oil that was used in the next synthetic step without further purification.

HR-MS (EI^+) calc. [$C_{40}H_{45}BBrN_3O_7S^+$]: 829.2568, found: 829.2552.

Compound 98

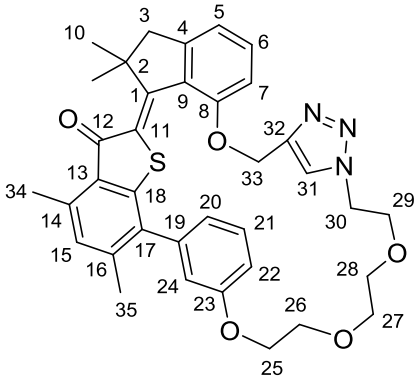

[623.768]

$C_{36}H_{37}N_3O_5S$

Compound **97** (250 mg, 301 µmol, 1.0 eq) was dissolved in DMF (11 mL), then K_2CO_3 (125 mg, 903 µmol, 3.0 eq), $Pd(PPh_3)_4$ (17.4 mg, 15.0 µmol, 5 mol%) and two drops of water were added. The reaction mixture was stirred at 85 °C for 20 h before the reaction was stopped by addition of a saturated NH_4Cl solution and the suspension was transferred to a separatory funnel. Additional saturated NH_4Cl solution was added and the aqueous phase was extracted with EtOAc. The combined organic phases were washed with an excess of water (until residual DMF was removed as judged by the disappearance of DMF streaks in the aqueous phase) and brine, dried over Na_2SO_4 and the solvent was evaporated *in vacuo*. After purification by flash column chromatography (SiO_2, *i*-Hex:EtOAc = 4:6 → 1:9) compound **98** (80.4 mg, 129 µmol, 43%) was obtained as a red oil.

HR-MS (EI^+) calc. [$C_{40}H_{45}BBrN_3O_7S^+$]: 623.2454, found: 623.2455.

Compound 99

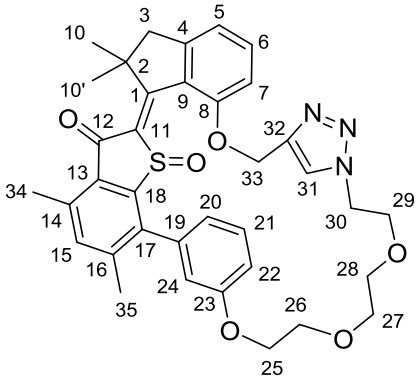

[639.767]

$C_{36}H_{37}N_3O_6S$

Compound **98** (80.0 mg, 134 µmol, 1.0 eq) was dissolved in acetic acid (10.0 mL) and $NaBO_2(OH)_2$ (82.6 mg, 537 µmol, 4.0 eq) was added. The reaction mixture was stirred at 23 °C for 5 h before it was transferred dropwise to a separatory funnel charged with a saturated $NaHCO_3$ solution. The aqueous phase was extracted with CH_2Cl_2, the combined organic phases were washed brine, dried over Na_2SO_4 and the solvent was evaporated *in vacuo*. After purification by flash column chromatography (SiO_2, CH_2Cl_2:MeOH = 49:1 → 19:1) and (SiO_2, *i*-Hex:EtOAc = 4:6 → EtOAc) and preparative HPLC (SiO_2, heptane:EtOAc = 8:2) compound **99** (6.0 mg, 9.4 µmol, 7%) was obtained as a yellow solid.

***E*-(*S*)-*P* isomer**:

^{1}H NMR (599 MHz, CD_2Cl_2, 27 °C) δ = 7.46 (dd, *J* = 8.2, 7.4 Hz, 1H, H-C(6)), 7.44 (dd, *J* = 8.4, 7.4 Hz, 1H, H-C(21)), 7.37 (s, 1H, H-C(31)), 7.29 (m, 1H, H-C(15)), 7.27 (dd, *J* = 2.5, 1.5 Hz, 1H, H-C(24)), 7.05 (ddd, *J* = 8.3, 2.5, 1.0 Hz, 1H, H-C(22)), 7.01 (dt, *J* = 7.4, 1.3 Hz, 1H, H-C(20)), 6.99 (d, *J* = 7.4 Hz, 1H, H-C(5)), 6.93 (d, *J* = 8.3 Hz, 1H, H-C(7)), 5.36 – 5.33 (m, 1H, H-C(33)), 5.14 (dd, *J* = 11.8, 0.9 Hz, 1H, H-C(33)), 4.36 (ddd, *J* = 14.0, 6.4, 4.7 Hz, 1H, H-C(30)), 4.29 (td, *J* = 4.3, 1.7 Hz, 2H, H-C(25)), 3.80 – 3.76 (m, 1H, H-C(26)), 3.76 – 3.71 (m, 1H, H-C(30)), 3.68 (dt, *J* = 11.1, 4.2 Hz, 1H, H-C(26)), 3.63 (ddd, *J* = 10.5, 5.2, 1.7 Hz, 1H, H-C(29)), 3.61 – 3.54 (m, 4H, H-C(27), H-C(28) and H-C(29)), 3.50 – 3.46 (m, 1H, H-C(28)), 3.25 (d, *J* = 14.9 Hz, 1H, H-C(3)), 2.77 (d, *J* = 14.9 Hz, 1H, H-C(3)), 2.36 (s, 3H, H-C(34)), 2.26 (s, 3H, H-C(35)), 1.78 (s, 3H, H-C(10)), 1.24 (s, 3H, H-C(10)).

^{13}C NMR (101 MHz, CD_2Cl_2) δ = 185.12 (C-12), 168.38 (C-1), 159.57 (C-23), 157.77 (C-8), 150.98 (C-4), 148.68 (C-18), 144.81 (C-32), 143.93 (C-14 or C-16), 140.62 (C-11), 139.91 (C-17), 139.51 (C-14 or C-16), 137.16 (C-19), 136.75 (C-15), 134.33 (C-6), 131.06 (C-13), 130.12

(C-21), 129.92 (C-9), 123.30 (C-31), 122.28 (C-20), 120.16 (C-24), 118.50 (C-5), 118.45 (C-22), 111.63 (C-7), 71.72 (C-27), 71.21 (C-28), 70.45 (C-26), 70.43 (C-25), 69.37 (C-29), 64.64 (C-33), 53.56 (C-2), 50.54 (C-3), 50.43 (C-30), 27.88 (C-10), 26.59 (C-10), 20.69 (C-35), 18.75 (C-34).

HR-MS (EI^+) calc. [$C_{36}H_{37}N_3O_6S^+$]: 639.2403, found: 639.2389.

Compound 100

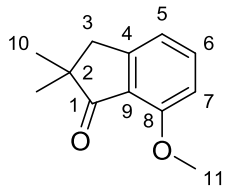

[190.242]

$C_{12}H_{14}O_2$

A stirring solution of 7-methoxy-1-indanone (1.00 g, 6.17 mmol, 1.0 eq) in DMF (12.4 mL) was cooled to 0 °C and sodium hydride (60% dispersion in mineral oil, 616 mg, 15.4 mmol, 2.5 eq) was added. After 20 min iodomethane (2.19 g, 15.4 mmol, 2.5 eq) was added dropwise over 30 min and the reaction mixture was vigorously stirred for 2 h at 0 °C. The reaction was stopped by addition of saturated ammonium chloride solution. The aqueous phase was extracted with EtOAc. The combined organic phases were washed with an excess of water and brine, dried over Na_2SO_4, filtered and the solvent was removed *in vacuo*. After flash column chromatography (SiO_2, *i*-Hex/EtOAc 24:1) compound **100** (1.14 g, 5.99 mmol, 97%) was obtained as an orange liquid that crystallizes under high vacuum to give a pale orange solid.

^{1}H NMR (400 MHz, CD_2Cl_2, 25 °C) δ = 7.53 (dd, *J* = 8.2, 7.5 Hz, 1H, H-C(6)), 6.98 (ddt, *J* = 7.5, 0.9, 0.9 Hz, 1H, H-C(5)), 6.80 (dd, *J* = 8.3, 0.8 Hz, 1H, H-C(7)), 3.91 (s, 3H, H-C(11)), 2.93 (t, *J* = 0.9 Hz, 2H, H-C(3)), 1.17 (s, 6H, H-C(10)).

^{13}C NMR (101 MHz, CD_2Cl_2, 25 °C) δ = 208.97 (C-1), 158.96 (C-8), 155.36 (C-4), 136.82 (C-6), 123.81 (C-9), 118.92 (C-5), 109.47 (C-7), 56.11 (C-11), 45.90 (C-2), 42.95 (C-3), 25.73 (C-10).

HR-MS (EI^+), $[M]^+$ calc. for $[C_{12}H_{14}O_2]^+$: 190.0994, found:190.0986.

Compound 101

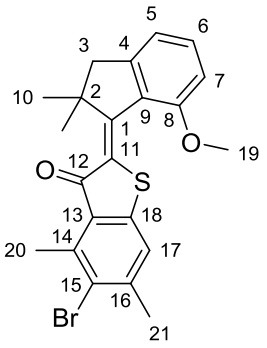

[429.372]

$C_{22}H_{21}BrO_2S$

In a Schlenk flask compound **91** (149 mg, 578 µmol, 1.1 eq) was dissolved in CH_2Cl_2 (1.0 mL) and cooled to –78 °C. BCl_3 (552 µL, 552 µmol, 1 m in toluene, 1.05 eq) was added and the cold reaction mixture was immediately transferred to a second Schlenk flask containing a 0 °C cold solution of compound **100** (100 mg, 526 µmol, 1.0 eq) in CH_2Cl_2 (1.0 mL). After stirring for 30 min at 0 °C the reaction was stopped by addition of a saturated aqueous NH_4Cl solution. The aqueous phase was extracted with CH_2Cl_2. The combined organic phases were dried over Na_2SO_4 and the solvent was removed *in vacuo*. The crude product was purified by flash column chromatography (SiO_2, *i*-Hex → *i*-Hex:EtOAc = 49:1) to give compound **101** (113 mg, 263 µmol, mixture of *E* and *Z* isomer, 50%) as an orange oil that crystallizes from EtOAc as orange needles.

^{1}H NMR (400 MHz, CD_2Cl_2, 25 °C) δ = 7.32 (dd, *J* = 8.3, 7.3 Hz, 1H, H-C(6)), 7.23 – 7.22 (m, 1H, H-C(17)), 6.89 (ddt, *J* = 7.3, 0.9, 0.9 Hz, 1H, H-C(5)), 6.77 (d, *J* = 8.2 Hz, 1H, H-C(7)), 3.82 (s, 3H, H-C(19)), 3.17 (d, *J* = 15.4 Hz, 1H, H-C(3)), 2.85 (d, *J* = 0.6 Hz, 3H, H-C(20)), 2.75 (d, *J* = 15.4 Hz, 1H, H-C(3)), 2.49 (d, *J* = 0.8 Hz, 3H, H-C(21)), 1.66 (s, 3H, H-C(10)), 1.17 (s, 3H, H-C(10)).

^{13}C NMR (101 MHz, CD_2Cl_2, 25 °C) δ = 188.15 (C-12), 158.48 (C-8), 155.67 (C-1), 149.41 (C-4), 144.28 (C-16), 143.89 (C-11 or C-18), 140.64 (C-14), 132.20 (C-6), 128.98 (C-13), 128.63 (C-9), 126.18 (C-15), 126.09 (C-11 or C-18), 123.04 (C-17), 117.26 (C-5), 109.24 (C-7), 55.30 (C-19), 50.75 (C-2), 49.71 (C-3), 26.84 (C-10), 26.02 (C-10), 25.33 (C-21), 18.10 (C-20).

HR-MS (EI^+), $[M]^+$ calc. for $[C_{22}H_{21}BrO_2S]^+$: 428.0446, found: 428.0409.

Compound 102

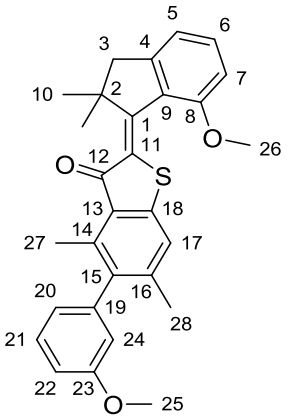

[456.600]

$C_{29}H_{28}O_3S$

To a stirring solution of compound **101** (67.6 mg, 157 µmol, 1.0 eq) in DMF (1.0 mL) was added 3-methoxyphenylboronic acid pinacol ester (39.4 µL, 40.5 mg, 173 µmol, 1.1 eq), $Pd(PPh_3)_4$ (9.1 mg, 7.87 µmol, 5 mol%), K_2CO_3 (65.3 mg, 472 µmol, 3.0 eq) and a drop of water. The reaction mixture was stirred at 85 °C for 16 h before it was transferred to a separatory funnel charged with a satureated aqueous NH_4Cl solution. The aqueous phase was extracted with EtOAc. The combined organic phases were washed with water and brine, dried over Na_2SO_4, filtered and the solvent was evaporated *in vacuo*. The crude product was purified by flash column chromatography (SiO_2, *i*-Hex:EtOAc = 49:1 → 19:1) to give compound **102** (29.8 mg, 65.3 µmol, mixture of *E* and *Z* isomer, 41% (94%), 37.9 mg of starting material could be recovered) as an orange solid.

***Z* isomer**

^{1}H NMR (400 MHz, CD_2Cl_2, 25 °C) δ = 7.41 – 7.34 (m, 2H, H-C(6) and H-C(21)), 7.12 – 7.10 (m, 1H, H-C(17)), 6.93 – 6.89 (m, 2H, H-C(5) and H-C(22)), 6.83 (dd, *J* = 8.3, 0.9 Hz, 1H, H-C(7)), 6.74 – 6.70 (m, 1H, H-C(20)), 6.68 (dd, *J* = 2.6, 1.5 Hz, 1H, H-C(24)), 3.97 (s, 3H, H-C(26)), 3.81 (s, 3H, H-C(25)), 2.95 (s, 2H, H-C(3)), 2.36 (d, *J* = 0.5 Hz, 3H, H-C(27)), 2.06 (d, *J* = 0.7 Hz, 3H, H-C(28)), 1.51 (s, 6H, H-C(10)).

^{13}C NMR (101 MHz, CD_2Cl_2, 25 °C) δ = 191.37 (C-12), 160.47 (C-23), 160.07 (C-1), 156.68 (C-8), 150.35 (C-4), 146.23 (C-11 or C-18), 143.59 (C-14 or C-16), 141.82 (C-19), 139.95 (C-15), 138.58 (C-14 or C-16), 133.42 (C-6), 130.15 (C-21), 129.91 (C-11 or C-18), 128.40 (C-9), 128.00 (C-13), 122.36 (C-20), 121.65 (C-17), 117.72 (C-5), 115.58 (C-24), 112.93 (C-22),

109.71 (C-7), 55.74 (C-25), 55.06 (C-26), 51.55 (C-2 and C-3), 27.07 (C-10), 22.21 (C-28), 16.21 (C-27).

***E* isomer**

Broadening/splitting of signals is observed for protons/carbons in close proximity to methoxy group H-C(25).

^{1}H NMR (400 MHz, CD_2Cl_2, 25 °C) δ = 7.40 – 7.35 (m, 1H, H-C(21)), 7.31 (dd, *J* = 8.3, 7.4 Hz, 1H, H-C(6)), 7.23 – 7.20 (m, 1H, H-C(17)), 6.92 (ddd, *J* = 8.4, 2.6, 1.0 Hz, 1H, H-C(22)), 6.89 (dq, *J* = 7.4, 0.9 Hz, 1H, H-C(5)), 6.78 – 6.74 (m, 1H, H-C(7)), 6.74 – 6.68 (m, 2H, H-C(20) and H-C(24)), 3.83 – 3.80 (m, 6H, H-C(24) and H-C(25)), 3.18 (d, *J* = 15.5 Hz, 1H, H-C(3)), 2.75 (d, *J* = 15.4 Hz, 1H, H-C(3)), 2.42 (s, 3H, H-C(20)), 2.09 (d, *J* = 0.7 Hz, 3H, H-C(21)), 1.68 (s, 3H, H-C(10)), 1.19 (s, 3H, H-C(10)).

^{13}C NMR (101 MHz, CD_2Cl_2, 25 °C) δ = 189.29 (C-12), 160.45 (C-23), 158.48 (C-8), 154.57 (C-1), 149.21 (C-4), 143.90 (C-11 or C-18), 143.13 (C-14 or C-16), 141.86 (C-19), 140.33 (C-15), 138.73 (C-14 or C-16), 131.91 (C-6), 130.22 (C-21), 130.12 (C-21), 128.79 (C-9), 127.85 (C-13), 126.49 (C-11 or C-18), 122.40 (C-20), 122.27 (C-20), 122.15 (C-17), 117.21 (C-5), 115.67 (C-24), 115.52 (C-24), 113.03 (C-22), 112.77 (C-22), 109.20 (C-7), 55.75 (C-24), 55.31 (C-25), 50.68 (C-2), 49.74 (C-3), 26.92 (C-10), 26.00 (C-10), 22.16 (C-21), 16.13 (C-20).

HR-MS (EI^+), $[M]^+$ calc. for $[C_{29}H_{28}O_3S]^+$: 456.1759, found: 456.1749.

Compound 103

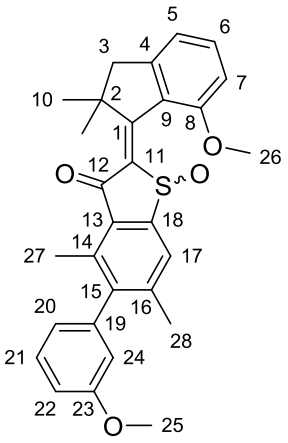

[472.599]

$C_{29}H_{28}O_4S$

Compound **102** (30.0 mg, 65.7 µmol, 1.0 eq) was dissolved in acetic acid (2.0 mL) and sodium perborate tetrahydrate (40.4 mg, 263 µmol, 4.0 eq) was added. The reaction mixture was stirred at room temperature for 5 h before it was transferred dropwise to a separatory funnel charged with a saturated aqueous $NaHCO_3$ solution. The aqueous phase was extracted with EtOAc. The combined organic phases were washed with brine, dried over Na_2SO_4 and the solvent was removed *in vacuo*. The crude product was purified by flash column chromatography (SiO_2, *i*-Hex:EtOAc = 9:1 → 1:1) to give compound **103** (14.8 mg, 31.3 µmol, mixture of *E* and *Z* isomer, 48%) as an orange solid.

***E* isomer**

^{1}H NMR (599 MHz, CD_2Cl_2, 27 °C) δ = 7.79 (s, 1H, H-C(17)), 7.44 – 7.39 (m, 2H, H-C(6) and H-C(21)), 6.98 – 6.94 (m, 2H, H-C(5) and H-C(22)), 6.78 (d, *J* = 8.2 Hz, 1H, H-C(7)), 6.73 (ddt, *J* = 10.9, 7.5, 1.2 Hz, 1H, H-C(20)), 6.69 (ddd, *J* = 11.1, 2.7, 1.5 Hz, 1H, H-C(24)), 3.83 (dd, *J* = 10.8, 1.0 Hz, 3H, H-C(25)), 3.80 (d, *J* = 2.1 Hz, 3H, H-C(26)), 3.26 (d, *J* = 15.1 Hz, 1H, H-C(3)), 2.82 (d, *J* = 15.0 Hz, 1H, H-C(3)), 2.47 (s, 3H, H-C(27)), 2.21 (s, 3H, H-C(28)), 1.95 (s, 3H, H-C(10)), 1.37 (s, 3H, H-C(10)).

^{13}C NMR (151 MHz, CD_2Cl_2, 27 °C) δ = 184.84 (C-12), 167.38 (C-1), 160.65 (C-23), 160.63 (C-23), 159.06 (C-8), 150.56 (C-4), 149.62 (C-18), 147.39 (C-15), 144.66 (C-14 or C-16), 144.65 (C-14 or C-16), 141.06 (C-19), 138.13 (C-14 or C-16), 134.13 (C-6), 131.38 (C-13), 130.51 (C-21), 130.48 (C-21), 128.07 (C-9), 125.55 (C-17), 121.54 (C-20), 121.49 (C-20), 117.54 (C-5), 114.99 (C-24), 114.86 (C-24), 113.37 (C-22), 113.19 (C-22), 109.37 (C-7), 55.80

(C-25), 55.78 (C-25), 55.45 (C-26), 52.60 (C-2), 50.18 (C-3), 28.51 (C-10), 26.28 (C-10), 22.29 (C-28), 22.28 (C-28), 16.47 (C-27). C-11 could not be assigned

***Z* isomer**

Mixture of diastereomeric atropisomers (1:1), two sets of signals are observed only for protons and carbons close to the biaryl axis. Assignments of signals to a specific atropisomer was not possible.

^{1}H NMR (599 MHz, CD_2Cl_2, 27 °C) δ = 7.73 (s, 1H, H-C(17)), 7.50 (t, *J* = 7.9 Hz, 1H, H-C(6)), 7.41 (td, *J* = 7.9, 3.1 Hz, 1H, H-C(21)), 6.98 – 6.94 (m, 2H, H-C(5) and H-C(22)), 6.89 (d, *J* = 8.3 Hz, 1H, H-C(7)), 6.72 (ddt, *J* = 8.8, 7.2, 1.2 Hz, 1H, H-C(20)), 6.68 (ddd, *J* = 10.3, 2.6, 1.5 Hz, 1H, H-C(24)), 4.09 (s, 3H, H-C(26)), 3.82 (d, *J* = 6.2 Hz, 3H, H-C(25)), 3.17 (d, *J* = 15.7 Hz, 1H, H-C(3)), 2.84 (d, *J* = 15.7 Hz, 1H, H-C(3)), 2.44 (s, 3H, H-C(27)), 2.19 (s, 3H, H-C(28)), 1.52 (s, 6H, H-C(10)).

^{13}C NMR (151 MHz, CD_2Cl_2, 27 °C) δ = 186.96 (C-12), 167.62 (C-1), 160.63 (C-23), 160.63 (C-23), 157.84 (C-8), 151.37 (C-4), 150.98 (C-11 or C-18), 150.96 (C-11 or C-18), 146.82 (C-15), 145.10 (C-14 or C-16), 144.45 (C-11 or C-18), 141.06 (C-19), 137.91 (C-14 or C-16), 137.89 (C-14 or C-16), 135.08 (C-6), 131.76 (C-13), 131.74 (C-13), 130.48 (C-21), 130.45 (C-21), 125.96 (C-9), 124.93 (C-17), 121.59 (C-20), 121.54 (C-20), 117.98 (C-5), 114.98 (C-24), 114.80 (C-24), 113.41 (C-22), 113.29 (C-22), 109.42 (C-7), 55.79 (C-25), 55.36 (C-26), 52.03 (C-2), 52.02 (C-2), 50.93 (C-3), 28.60 (C-10), 25.86 (C-10), 22.37 (C-28), 22.36 (C-28), 16.65 (C-27), 16.64 (C-27).

HR-MS (EI^+), $[M]^+$ calc. for $[C_{29}H_{28}O_4S]^+$: 472.1708, found: 472.1706.

Compound 104

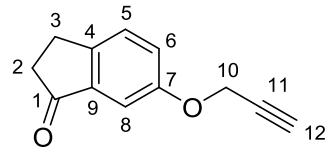

[186.210]

$C_{12}H_{10}O_2$

To a stirring solution of 6-hydroxy indanone (1.00 g, 6.75 mmol, 1.0 eq) in DMF (45 mL) was added propargyl bromide (80 wt. % in toluene, 1.00 g, 1.0 eq) and K_2CO_3 (3.73 g, 27.0 mmol, 4.0 eq). The reaction mixture was stirred at 70 °C for 5 h. The reaction was stopped by addition

of water and extracted with EtOAc. The combined organic phases were washed with an excess of water and brine, dried over Na_2SO_4 and the solvent was evaporated *in vacuo*. After purification by flash column chromatography (SiO_2, *i*-Hex:EtOAc = 8:2) compound **104** was obtained as a yellow oil that crystallized under high vacuum (1.05 g, 5.64 mmol, 84%).

m.p.: 63 – 64 °C

^{1}H NMR (400 MHz, CD_2Cl_2, 25 °C) δ = 7.44 – 7.40 (m, 1H, H-C(5)), 7.26 – 7.21 (m, 2H, H-C(6) and H-C(8)), 4.74 (d, *J* = 2.4 Hz, 2H, H-C(10)), 3.10 – 3.04 (m, 2H, H-C(2)), 2.70 – 2.65 (m, 2H, H-C(3)), 2.59 (t, *J* = 2.4 Hz, 1H, H-C(12)).

^{13}C NMR (101 MHz, CD_2Cl_2, 25 °C) δ = 206.79 (C-1), 157.71 (C-7), 149.31 (C-9), 138.82 (C-4), 128.20 (C-5), 124.49 (C-6), 106.85 (C-8), 78.71 (C-11), 76.14 (C-12), 56.67 (C-10), 37.50 (C-3), 25.65 (C-2).

IR: $\tilde{\nu}$ = 3246 (w), 2924 (w), 2361 (w), 2114 (w), 1691 (s), 1613 (w), 1486 (m), 1444 (m), 1398 (w), 1278 (s), 1242 (m), 1212 (m), 1167 (m), 1020 (s), 925 (m), 904 (m), 882 (m), 830 (s), 770 (w), 697 (s).

HR-MS (EI^+), $[M]^+$ calc. for $[C_{12}H_{10}O_2]^{+\cdot}$ 186.0681, found: 186.0675.

Compound 105

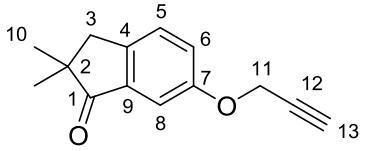

[214.264]

$C_{14}H_{14}O_2$

A stirring solution of compound **104** (1.05 g, 5.64 mmol, 1.0 eq) in DMF (15 mL) was cooled to 0 °C and sodium hydride (60% dispersion in mineral oil, 564 mg, 14.1 mmol, 2.5 eq) was added. After 15 min iodomethane (2.00 g, 14.1 mmol, 2.5 eq) was added dropwise addition of nd the reaction mixture was stirred for 1 h at 0 °C. The reaction was stopped by addition of saturated ammonium chloride solution. The aqueous phase was extracted with EtOAc. The combined organic phases were washed with an excess of water and brine, dried over Na_2SO_4, filtered and the solvent was removed *in vacuo*. After flash column chromatography (SiO_2, *i*-Hex:EtOAc = 19:1) compound **105** (831 mg, 3.88 mmol, 69%) was obtained as a yellow oil.

^{1}H NMR (400 MHz, CD_2Cl_2, 25 °C) δ = 7.39 – 7.35 (m, 1H, H-C(5)), 7.27 – 7.22 (m, 2H, H-C(6) and H-C(8)), 4.74 (d, *J* = 2.4 Hz, 2H, H-C(11)), 2.93 (d, *J* = 0.9 Hz, 2H, H-C(3)), 2.59 (t, *J* = 2.4 Hz, 1H, H-C(13)), 1.20 (s, 6H, H-C(10)).

^{13}C NMR (101 MHz, CD_2Cl_2, 25 °C) δ = 211.33 (C-1), 157.83 (C-7), 146.37 (C-4), 137.05 (C-9), 128.19 (C-5), 124.76 (C-6), 107.48 (C-8), 78.75 (C-12), 76.14 (C-13), 56.66 (C-11), 46.76 (C-2), 42.62 (C-3), 25.61 (C-10).

HR-MS (EI$^+$), $[M]^+$ calc. for $[C_{14}H_{14}O_2]^+$: 214.0994, found: 214.0986.

Compound 106

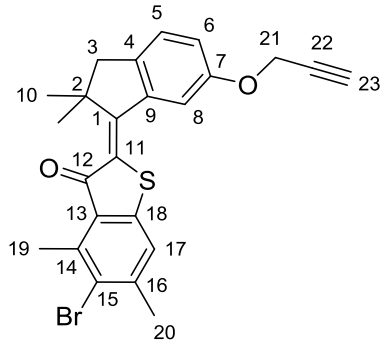

[453.394]

$C_{24}H_{21}BrO_2S$

Indanone **105** (401 mg, 1.87 mmol, 1.0 eq) and benzothiophenone **91** (530 mg, 2.06 mmol, 1.1 eq) were dissolved in CH_2Cl_2 (1.5 mL each) in two separate Schlenk flasks. The Schlenk flask containing benzothiophenone **91** was cooled to –78 °C in a dry-ice/acetone bath and the Schlenk flask containing indanone **105** was cooled to 0 °C on an ice bath. BCl_3 (1.97 mL, 1 M in toluene, 1.97 mmol, 1.1 eq) was added to the flask containing benzothiophenone **91** and the mixture was immediately taken up in a syringe and added to the solution containing indanone **105**. After stirring for 30 min at 23 °C the reaction was stopped by addition of a saturated NH_4Cl solution (5 mL). The reaction mixture was transferred to a separatory funnel charged with a saturated NH_4Cl solution (50 mL). The aqueous phase was extracted with CH_2Cl_2 (3 x 50 mL), the combined organic phases were washed with brine (1 x 50 mL), dried over Na_2SO_4 and the solvent was removed *in vacuo*. The crude product was purified by flash column chromatography (SiO_2, *i*-Hex:EtOAc = 49:1 → 9:1) to give compound **106** (445 mg, 981 µmol, *E* isomer : *Z* isomer 7:3, 52%) as a red oil.

***Z* isomer**

Carbons C-11 and C-18 could not be unambiguously assigned due to the substitution pattern and *E*/*Z* isomeric mixture.

^{1}H NMR (400 MHz, CD_2Cl_2, 25 °C) δ = 7.68 (d, *J* = 2.3 Hz, 1H, H-C(8)), 7.24 (dtd, *J* = 8.4, 0.9, 0.5 Hz, 1H, H-C(5)), 7.22 – 7.21 (m, 1H, H-C(17)), 7.05 (dd, *J* = 8.4, 2.3 Hz, 1H, H-C(6)), 4.78 (d, *J* = 2.4 Hz, 2H, H-C(21)), 3.01 (s, 2H, H-C(3)), 2.85 (s, 3H, H-C(19)), 2.63 (t, *J* = 2.4 Hz, 1H, H-C(23)), 2.49 (s, 3H, H-C(20)), 1.61 (s, 6H, H-C(10)).

^{13}C NMR (101 MHz, CD_2Cl_2, 25 °C) δ = 188.35 (C-12), 162.70 (C-1), 157.40 (C-7), 145.18 (C-14), 143.46 (C-4), 141.85 (C-9), 141.63 (C-16), 128.49 (C-13), 126.80 (C-15), 126.40 (C-5), 122.95 (C-17), 119.35 (C-6), 113.86 (C-8), 79.08 (C-22), 76.11 (C-23), 56.87 (C-21), 51.05 (C-3), 49.67 (C-2), 25.88 (C-10), 25.47 (C-20), 18.28 (C-19).

***E* isomer**

^{1}H NMR (400 MHz, CD_2Cl_2, 25 °C) δ = 8.54 (d, *J* = 2.5 Hz, 1H, H-C(8)), 7.22 – 7.21 (m, 1H, H-C(17)), 7.21 – 7.19 (m, 1H, H-C(5)), 7.02 (dd, *J* = 8.9, 2.4 Hz, 1H, H-C(6)), 4.75 (d, *J* = 2.4 Hz, 2H, H-C(21)), 2.94 – 2.93 (m, 2H, H-C(3)), 2.88 (s, 3H, H-C(19)), 2.59 (t, *J* = 2.4 Hz, 1H, H-C(23)), 2.49 (s, 3H, H-C(20)), 1.50 (s, 6H, H-C(10)).

HR-MS (EI$^+$), $[M]^+$ calc. for $[C_{24}H_{21}BrO_2S]^+$: 452.0440, found: 452.0434.

Compound 107

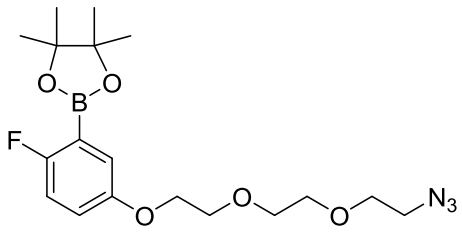

[395.238]

$C_{18}H_{27}BFN_3O_5$

Compound **72** (439 mg, 1.85 mmol, 1.0 eq) was dissolved in DMF (13 mL), then 4-fluoro-3-(4,4,5,5-tetramethyl-1,3,2-dioxaborolan-2-yl)phenol (438 mg, 1.84 mmol, 1.0 eq) and K_2CO_3 (1.02 g, 7.36 mmol, 4.0 eq) were added. The reaction mixture was heated for 15 h at 60 °C before it was transferred to a separatory funnel charged with a saturated $NaHCO_3$ solution

(50 mL). The aqueous phase was extracted with EtOAc (3 x 50 mL). The combined organic phases were washed with an excess of water (until residual DMF was removed as judged by the disappearance of DMF streaks in the aqueous phase) and brine (1 x 50 mL), dried over Na_2SO_4 and the solvent was removed *in vacuo*. Compound **107** (535 mg, 1.35 mmol, 74%) was obtained as a brown oil that was used in the next synthetic step without further purification.

HR-MS (EI^+), $[M]^+$ calc. for $[C_{18}H_{27}BFN_3O_5]^+$: 395.2028, found: 395.2021.

Compound 108

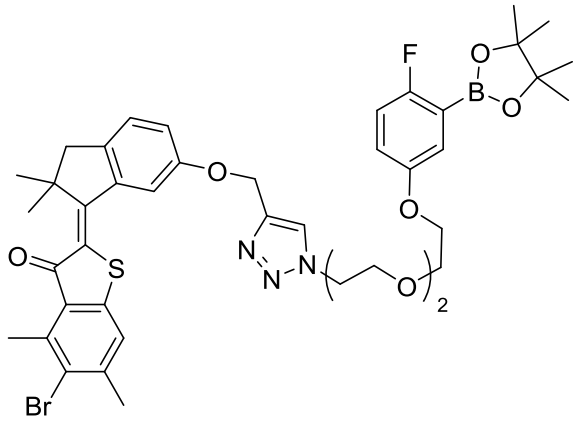

[848.632]

$C_{42}H_{48}BBrFN_3O_7S$

Compound **106** (445 mg, 981 µmol, 1.0 eq) and compound **107** (388 mg, 981 µmol, 1.0 eq) were dissolved in DMF (6 mL), then $CuSO_4 \cdot 5H_2O$ (4.9 mg, 20 µmol, 2 mol%) and sodium ascorbate (19.4 mg, 98.2 µmol, 10 mol%) were added. The reaction mixture was stirred at 23 °C for 20 h before it was poured into a separatory funnel charged with a saturated NH_4Cl solution (50 mL). The aqueous phase was extracted with EtOAc (3 x 50 mL), the combined organic phases were washed with an excess of water (until residual DMF was removed as judged by the disappearance of DMF streaks in the aqueous phase) and brine (1 x 50 mL), dried over Na_2SO_4 and the solvent was removed *in vacuo*. After purification by flash column chromatography (SiO_2, CH_2Cl_2 → CH_2Cl_2:MeOH = 97:3) compound **108** (756 mg, 891 µmol, 91%) was obtained as a red oil that was used in the next synthetic step without further purification.

Compound 109

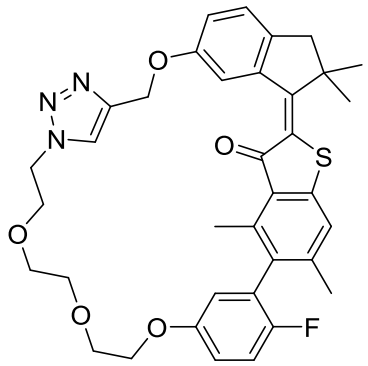

[641.758]

$C_{36}H_{36}FN_3O_5S$

Compound **108** (756 mg, 891 µmol, 1.0 eq) was dissolved in DMF (40 mL), then K_2CO_3 (369 mg, 2.67 mmol, 3.0 eq), $Pd(PPh_3)_4$ (51.5 mg, 44.5 µmol, 5 mol%) and five drops of water were added. The reaction mixture was stirred at 85 °C for 20 h before the reaction was stopped by addition of a saturated NH_4Cl solution (5 mL). The suspension was transferred to a separatory funnel charged with additional saturated NH_4Cl solution (50 mL) and the aqueous phase was extracted with EtOAc (3 x 50 mL). The combined organic phases were washed with an excess of water (until residual DMF was removed as judged by the disappearance of DMF streaks in the aqueous phase) and brine (1 x 50 mL), dried over Na_2SO_4 and the solvent was removed *in vacuo*. After purification by flash column chromatography (SiO_2, CH_2Cl_2 → CH_2Cl_2:MeOH = 19:1) then (SiO_2, *i*-Hex:EtOAc = 6:4 → 1:9) compound **109** (34.5 mg, 53.8 µmol, 6%) was obtained as an orange oil that was used in the next synthetic step without further purification.

Compound 110

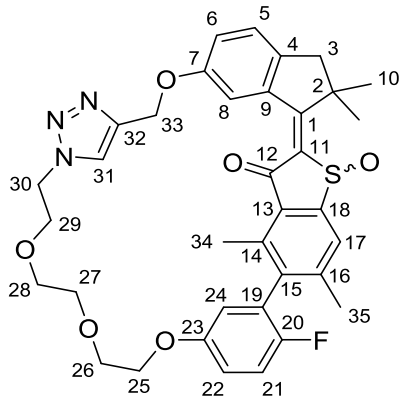

[657.757]

$C_{36}H_{36}FN_3O_6S$

Compound **109** (34.5 mg, 53.8 µmol, 1.0 eq) was dissolved in acetic acid (5.00 mL) and sodium perborate tetrahydrate (33.1 mg, 215 µmol, 4.0 eq) was added. The reaction mixture was stirred at 23 °C for 4 h before it was transferred dropwise to a separatory funnel charged with a saturated $NaHCO_3$ solution (50 mL). The aqueous phase was extracted with EtOAc (3 x 50 mL), the combined organic phases were washed with brine (1 x 50 mL), dried over Na_2SO_4 and the solvent was removed *in vacuo*. After purification by flash column chromatography (SiO_2, CH_2Cl_2 → CH_2Cl_2:MeOH = 19:1) compound **110** (21.3 mg, 32.4 µmol, 60%) was obtained as a yellow solid. Further purification via preparative HPLC (SiO_2 column from Diacel, *n*-heptane:EtOAc = 30:70, 30 °C) gave compound **110** (7.00 mg, 10.6 µmol, 20%) as a yellow solid. Crystals suitable for single crystal X-ray analysis were either obtained from a CH_2Cl_2 solution overlayed with EtOAc (E1) or an EtOAc solution overlayed with *n*-heptane (Z and E2) that was allowed to slowly evaporate at 23 °C.

***E*1 isomer**

C-11, C-12, C-18, C-20, and C-32 could not be assigned.

^{1}H NMR (800 MHz, CD_2Cl_2, 25 °C) δ = 7.97 (s, 1H, H-C(31)), 7.87 (q, *J* = 0.7 Hz, 1H, H-C(17)), 7.86 (d, *J* = 2.5 Hz, 1H, H-C(8)), 7.31 (dp, *J* = 8.3, 0.5 Hz, 1H, H-C(5)), 7.18 (t, *J* = 8.8 Hz, 1H, H-C(21)), 7.13 (dd, *J* = 8.3, 2.5 Hz, 1H, H-C(6)), 7.01 (ddd, *J* = 9.0, 4.0, 3.1 Hz, 1H, H-C(22)), 6.78 (dd, *J* = 5.7, 3.1 Hz, 1H, H-C(24)), 5.23 (d, *J* = 12.6 Hz, 1H, H-C(33)), 5.21 (d, *J* = 12.6 Hz, 1H, H-C(33)), 4.55 – 4.52 (m, 2H, H-C(30)), 4.29 (ddd, *J* = 11.6, 6.2, 4.2 Hz, 1H, H-C(25)), 4.18 (ddd, *J* = 11.6, 5.5, 4.2 Hz, 1H, H-C(25)), 3.92 – 3.88 (m, 1H, H-C(29)), 3.87 – 3.84 (m, 1H, H-C(29)), 3.81 – 3.75 (m, 2H, H-C(26)), 3.65 – 3.60 (m, 2H, H-C(27)), 3.60 –

3.55 (m, 2H, H-C(28)), 3.22 (d, *J* = 14.9 Hz, 1H, H-C(3)), 2.84 (d, *J* = 14.9 Hz, 1H, H-C(3)), 2.60 (s, 3H, H-C(34)), 2.36 (s, 3H, H-C(35)), 1.95 (s, 3H, H-C(10)), 1.48 (s, 3H, H-C(10)).

^{13}C NMR (201 MHz, CD_2Cl_2, 25 °C) δ = 174.15 (C-1), 156.55 (C-7), 155.17 (C-23), 149.91, 145.66 (C-14 or C-16), 143.35 (C-32), 143.05 (C-4), 141.08 (C-15), 139.43 (C-14 or C-16), 139.16, 138.43 (C-9), 130.16 (C-13), 125.86 (C-5), 124.76 (C-17), 124.15 (C-31), 121.98 (C-6), 117.53 (C-22), 116.94 (C-24), 116.65 (C-21), 113.93 (C-8), 70.47 (C-28), 70.36 (C-27), 69.68 (C-26), 69.58 (C-29), 68.32 (C-25), 62.23 (C-33), 52.15 (C-2), 50.50 (C-30), 49.12 (C-3), 28.84 (C-10), 25.79 (C-10), 21.19 (C-35), 16.54 (C-34).

HR-MS (EI$^+$), $[M]^+$ calc. for $[C_{36}H_{36}FN_3O_6S]^+$: 657.2309, found: 657.2291.

Compound 111

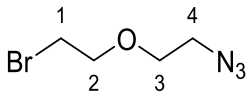

[194.032]

$C_4H_8BrN_3O$

A solution of bis(2-bromoethyl) ether (2.00 g, 8.62 mmol, 1.0 eq) in DMF (10.0 mL) was colled to 0 °C and sodium azide (561 mg, 8.62 mmol, 1.0 eq) was added. The mixture was stirred at 60 °C for 1 d before it was transferred to a separatory funnel charged with water. The aqueous phase was extracted with EtOAc. The combined organic phases were washed with an excess of water and brine, dried over Na_2SO_4, filtered and the solvent was removed *in vacuo*. After flash column chromatography (SiO_2, *i*-Hex → *i*-Hex/EtOAc = 19/1) compound **111** (790 mg, 4.07 mmol, 47%) was obtained as a colorless liquid.

^{1}H NMR (400 MHz, CD_2Cl_2, 25 °C) δ = 3.81 (t, *J* = 6.0 Hz, 2H, H-C(2)), 3.70 – 3.66 (m, 2H, H-C(3)), 3.49 (t, *J* = 6.0 Hz, 2H, H-C(1)), 3.39 (t, *J* = 5.0 Hz, 2H, H-C(4)).

^{13}C NMR (101 MHz, CD_2Cl_2, 25 °C) δ = 71.63 (C-2), 70.41 (C-3), 51.33 (C-4), 31.07 (C-1).

Compound 112

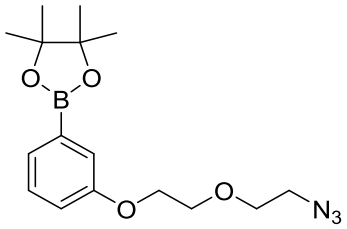

[333.195]

$C_{16}H_{24}BN_3O_4$

Compound **111** (635 mg, 2.89 mmol, 1.0 eq) was dissolved in DMF (10.0 mL), then 3-hydroxyphenylboronic acid pinacol ester (560 mg, 2.89 mmol, 1.0 eq) and K_2CO_3 (1.60 g, 11.5 mmol, 4.0 eq) were added. The reaction mixture was heated for 19 h at 60 °C before it was transferred to a separatory funnel charged with a saturated $NaHCO_3$ solution. The aqueous phase was extracted with EtOAc. The combined organic phases were washed with an excess of water (until residual DMF was removed as judged by the disappearance of DMF streaks in the aqueous phase) and brine, dried over Na_2SO_4 and the solvent was evaporated *in vacuo*. Compound **112** (920 mg, 2.76 mmol, 96%) was obtained as a brown oil that was used in the next synthetic step without further purification.

^{1}H NMR (400 MHz, CD_2Cl_2, 22 °C) δ = 7.36 – 7.26 (m, 3H), 7.01 (ddd, *J* = 8.1, 2.7, 1.3 Hz, 1H), 4.16 – 4.13 (m, 2H), 3.87 – 3.82 (m, 2H), 3.73 (dd, *J* = 5.6, 4.5 Hz, 2H), 3.40 (m, 2H), 1.33 (s, 12H).

Compound 113

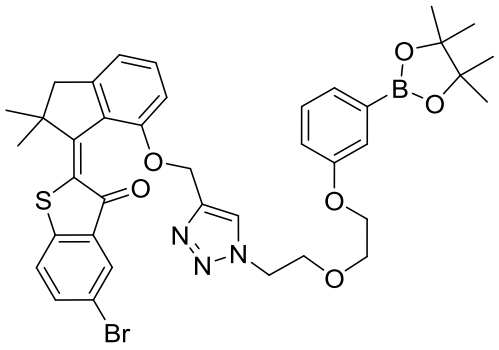

[758.535]

$C_{38}H_{41}BBrN_3O_6S$

Compound **112** (86.2 mg, 259 µmol, 1.1 eq) and compound **75** (100 mg, 235 µmol, 1.0 eq) were dissolved in DMF (1.0 mL), then sodium ascorbate (4.7 mg, 24 µmol, 10 mol%) and $CuSO_4 \cdot 5H_2O$ (1.2 mg, 4.7 µmol, 2 mol%) were added. The reaction mixture was stirred at 23 °C for 1 d before it was transferred to a separatory funnel charged with a saturated NH_4Cl solution. The aqueous phase was extracted with EtOAc, the combined organic phases were washed with an excess of water (until residual DMF was removed as judged by the disappearance of DMF streaks in the aqueous phase) and brine, dried over Na_2SO_4 and the solvent was evaporated *in vacuo*. After purification by flash column chromatography (SiO_2, CH_2Cl_2 → CH_2Cl_2:MeOH = 97:3) compound **113** (156 mg, 206 µmol, 87%) was obtained as a red solid that was used in the next synthetic step without further purification.

HR-MS (ESI$^+$) $[M+H]^+$ calc. [$C_{38}H_{42}BBrN_3O_6S^+$]: 758.2071, found: 758.2079.

Compound 114

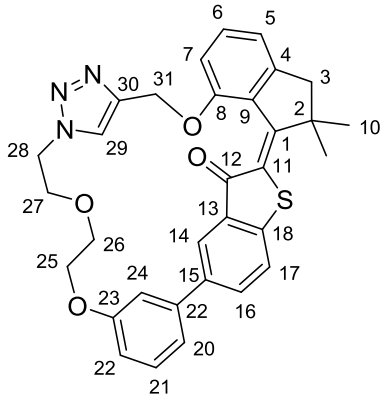

[551.661]

$C_{32}H_{29}N_3O_4S$

Compound **113** (155 mg, 204 µmol, 1.0 eq) was dissolved in DMF (12 mL), then K_2CO_3 (85 mg, 613 µmol, 3.0 eq), $Pd(PPh_3)_4$ (11.8 mg, 10.2 µmol, 5 mol%) and five drops of water were added. The reaction mixture was stirred at 90 °C for 1 d before the reaction was stopped by addition of a saturated NH_4Cl solution and the suspension was transferred to a separatory funnel. Additional saturated NH_4Cl solution was added and the aqueous phase was extracted with EtOAc. The combined organic phases were washed with an excess of water (until residual DMF was removed as judged by the disappearance of DMF streaks in the aqueous phase) and brine, dried over Na_2SO_4 and the solvent was evaporated *in vacuo*. After purification by flash column chromatography (SiO_2, *i*-Hex:EtOAc = 2:8) compound **114** (63.0 mg, 114 µmol, 56%) was obtained as an orange solid.

***E*-(*S*)-*P* isomer**:

^{1}H NMR (599 MHz, CD_2Cl_2, 27 °C) δ = 8.21 (d, *J* = 2.0 Hz, 1H, H-C(14)), 7.92 (s, 1H, H-C(29)), 7.89 (t, *J* = 2.1 Hz, 1H, H-C(24)), 7.86 (dd, *J* = 8.2, 2.0 Hz, 1H, H-C(16)), 7.56 (d, *J* = 8.2 Hz, 1H, H-C(17)), 7.41 (dd, *J* = 8.3, 7.3 Hz, 1H, H-C(6)), 7.34 (t, *J* = 7.9 Hz, 1H, H-C(21)), 7.26 (dt, *J* = 7.7, 1.2 Hz, 1H, H-C(20)), 7.01 (d, *J* = 8.3 Hz, 1H, H-C(7)), 6.95 (d, *J* = 7.3 Hz, 1H, H-C(5)), 6.93 (ddd, *J* = 8.1, 2.5, 0.9 Hz, 1H, H-C(22)), 5.34 (d, *J* = 10.9 Hz, 1H, H-C(31)), 5.28 (d, *J* = 10.9 Hz, 1H, H-C(31)), 4.62 (ddd, *J* = 14.0, 8.6, 1.7 Hz, 1H, H-C(25)), 4.48 (ddd, *J* = 14.5, 3.5, 2.0 Hz, 1H, H-C(28)), 4.31 (ddd, *J* = 14.0, 4.0, 1.9 Hz, 1H, H-C(25)), 3.93 (ddd, *J* = 14.5, 9.3, 3.2 Hz, 1H, H-C(28)), 3.87 (ddd, *J* = 11.2, 4.0, 1.7 Hz, 1H, H-C(26)), 3.76 – 3.69 (m, 3H, H-C(26) and H-C(27)), 3.19 (d, *J* = 15.4 Hz, 1H, H-C(3)), 2.80 (d, *J* = 15.4 Hz, 1H, H-C(3)), 1.70 (s, 3H, H-C(10)), 1.22 (s, 3H, H-C(10)).

^{13}C NMR (151 MHz, CD_2Cl_2, 27 °C) δ = 186.50 (C-12), 160.89 (C-23), 158.40 (C-8), 158.09 (C-1), 149.92 (C-4), 143.84 (C-18 or C-30), 143.82 (C-18 or C-30), 141.02 (C-22), 138.33 (C-15), 133.18 (C-13 or C-16), 133.16 (C-13 or C-16), 132.81 (C-6), 130.31 (C-21), 128.76 (C-11), 125.68 (C-29), 125.64 (C-29), 124.43 (C-17), 123.79 (C-14), 119.43 (C-20), 117.68 (C-22), 117.64 (C-5), 113.36 (C-24), 109.98 (C-7), 73.14 (C-26), 70.64 (C-27), 69.31 (C-25), 62.13 (C-31), 51.42 (C-28), 51.31 (C-2), 49.68 (C-3), 26.98 (C-10), 26.59 (C-10).

HR-MS (ESI): *m/z* calc.: 552.1957 for [$C_{32}H_{29}N_3O_4S$]; found: 552.1950.

Compound 115

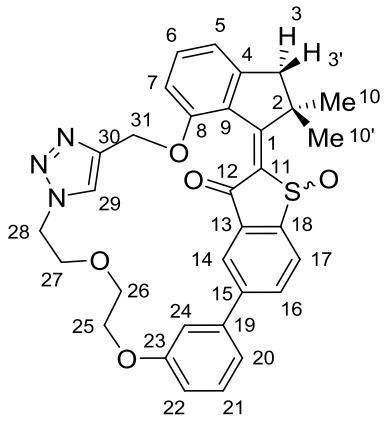

[567.660]

$C_{32}H_{29}N_3O_5S$

Compound **114** (55.0 mg, 99.7 µmol, 1.0 eq) was dissolved in acetic acid (6.0 mL) and $NaBO_2(OH)_2$ (61.4 mg, 399 µmol, 4.0 eq) was added. The reaction mixture was stirred at 23 °C for 5 h before it was transferred dropwise to a separatory funnel charged with a saturated $NaHCO_3$ solution. The aqueous phase was extracted with EtOAc, the combined organic phases were washed brine, dried over Na_2SO_4 and the solvent was evaporated *in vacuo*. After purification by flash column chromatography (SiO_2, *i*-Hex:EtOAc = 2:8) compound **115** (23 mg, 40.5 µmol, 41%) was obtained as a yellow solid.

***E*-(*S*)-*P* isomer**:

^{1}H NMR (599 MHz, CD_2Cl_2, 27 °C) δ = 8.28 (s, 1H, H-C(14)), 8.13 – 8.09 (m, 2H, H-C(16) and H-C(17)), 7.90 (s, 1H, H-C(29)), 7.79 (t, *J* = 2.0 Hz, 1H, H-C(24)), 7.50 (dd, *J* = 8.3, 7.4 Hz, 1H, H-C(6)), 7.39 (t, *J* = 7.9 Hz, 1H, H-C(21)), 7.29 (dt, *J* = 7.6, 1.3 Hz, 1H, H-C(20)), 7.07 (d, *J* = 8.3 Hz, 1H, H-C(7)), 7.03 – 6.99 (m, 2H, H-C(5) and H-C(22)), 5.34 – 5.31 (m, 1H, H-C(31)), 5.29 (d, *J* = 11.7 Hz, 1H, H-C(31)), 4.57 (ddd, *J* = 13.8, 7.7, 2.3 Hz, 1H, H-

C(25)), 4.48 (ddd, *J* = 14.6, 4.3, 2.3 Hz, 1H, H-C(28)), 4.32 (ddd, *J* = 13.7, 4.7, 2.4 Hz, 1H, H-C(25)), 4.11 – 4.04 (m, 1H, H-C(28)), 3.85 (ddd, *J* = 10.9, 4.8, 2.3 Hz, 1H, H-C(26)), 3.80 – 3.70 (m, 3H, H-C(26) and H-C(27)), 3.27 (d, *J* = 15.2 Hz, 1H, H-C(3')), 2.87 (d, *J* = 15.2 Hz, 1H, H-C(3)), 1.98 (s, 3H, H-C(10')), 1.39 (s, 3H, H-C(10)).

^{13}C NMR (151 MHz, CD_2Cl_2, 27 °C) δ = 182.95 (C-12), 170.98 (C-1), 160.86 (C-23), 158.98 (C-8), 151.17 (C-4), 148.06 (C-18), 146.00 (C-15), 143.66 (C-30), 140.25 (C-22), 139.19 (C-11), 136.55 (C-13), 134.93 (C-6), 134.24 (C-16), 130.60 (C-21), 128.20 (C-9 and C-17)), 125.10 (C-29), 123.01 (C-14), 120.30 (C-20), 118.95 (C-22), 117.94 (C-5), 113.86 (C-24), 110.40 (C-7), 72.49 (C-26), 70.49 (C-27), 69.22 (C-25), 62.50 (C-31), 53.08 (C-2), 51.16 (C-28), 50.04 (C-3), 28.57 (C-10), 26.60 (C-10').

HR-MS (ESI) [M+H]: *m/z* calc.: 568.1906 for [$C_{32}H_{29}N_3O_5S^+$]; found: 568.1901.

Compound 116

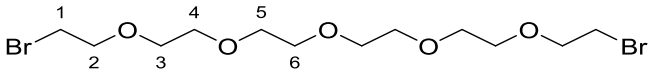

[408.127]

$C_{12}H_{24}Br_2O_5$

Hexaethylene glycol (1.41 g, 5.00 mmol, 1.0 eq) and CBr_4 (3.65 g, 11.0 mmol, 2.2 eq) were dissolved in CH_2Cl_2 (8.0 mL) and cooled to 0 °C. After addition of triphenylphosphine (2.75 g, 10.5 mmol, 2.1 eq) the reaction mixture was allowed to warm to 23 °C and stirred for 1 d. The solvent was removed *in vacuo* and the crude product was purified by flash column chromatography (SiO_2, *i*-Hex:EtOAc = 1:1 → 2:3) and (SiO_2, CH_2Cl_2 → CH_2Cl_2:MeOH = 49:1) to give compound **116** (740 mg, 1.81 mmol, 36%) as a colorless liquid.

^{1}H NMR (400 MHz, CD_2Cl_2, 25 °C) δ = 3.79 (t, *J* = 6.1 Hz, 4H, H-C(2)), 3.64 (ddd, *J* = 5.6, 3.0, 1.3 Hz, 4H), 3.62 – 3.58 (m, 12H), 3.49 (t, *J* = 6.1 Hz, 4H, H-C(1)).

^{13}C NMR (101 MHz, CD_2Cl_2, 25 °C) δ = 71.68 (C-2), 71.14, 71.07, 71.03, 31.41 (C-1).

Compound 117

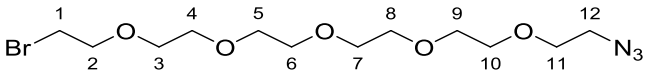

[370.244]

$C_{12}H_{24}BrN_3O_5$

Compound **116** (438 mg, 1.07 mmol, 1.0 eq) was dissvoled in DMF (1.0 mL) and sodium azide (69.8 mg, 1.07 mmol, 1.0 eq) was added. The reaction mixture was stirred at 60 °C for 5 h. The crude product was transferred to a separatory funnel charged with a saturated NH_4Cl solution and the aqueous phase was extracted with EtOAc. The combined organic phases were washed with an excess of water (until residual DMF was removed as judged by the disappearance of DMF streaks in the aqueous phase) and brine, dried over Na_2SO_4 and the solvent was removed *in vacuo*. The crude product was purified by flash column chromatography (SiO_2, *i*-Hex:EtOAc = 1:1) to give compound **117** (213 mg, 575 µmol, 54%) as a colorless liquid.

^{1}H NMR (400 MHz, CD_2Cl_2, 22 °C) δ = 3.79 (t, *J* = 6.1 Hz, 2H, H-C(2)), 3.67 – 3.57 (m, 18H, H-C(3) to H-C(11)), 3.49 (t, *J* = 6.1 Hz, 2H, H-C(1)), 3.38 (t, *J* = 5.0 Hz, 2H, H-C(12)).

Compound 118

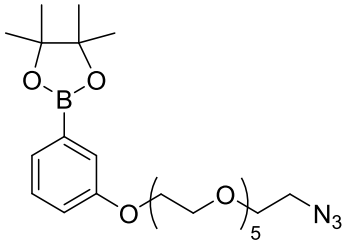

[509.407]

$C_{24}H_{40}BN_3O_8$

Compound **117** (213 mg, 575 µmol, 1.0 eq) was dissolved in DMF (2.0 mL), then 3-hydroxyphenylboronic acid pinacol ester (139 mg, 633 µmol, 1.1 eq) and K_2CO_3 (318 mg, 2.30 mmol, 4.0 eq) were added. The reaction mixture was heated for 22 h at 60 °C before it was transferred to a separatory funnel charged with a saturated NH_4Cl solution. The aqueous phase was extracted with EtOAc. The combined organic phases were washed with an excess of water (until residual DMF was removed as judged by the disappearance of DMF streaks in the aqueous phase) and brine, dried over Na_2SO_4 and the solvent was evaporated *in vacuo*.

Compound **118** (228 mg, 448 µmol, 78%) was obtained as a brown oil that was used in the next synthetic step without further purification.

HR-MS (EI^+) calc. [$C_{24}H_{40}BN_3O_8^+$]: 509.2908, found: 509.2898.

Compound 119

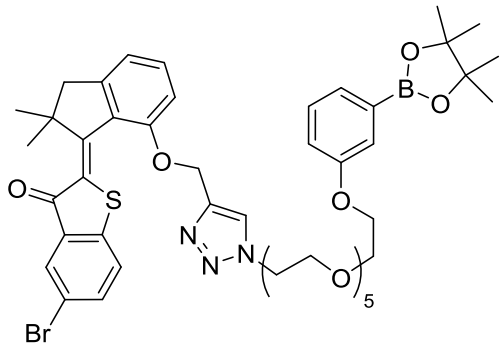

[934.747]

$C_{46}H_{57}BBrN_3O_{10}S$

Compound **75** (80.0 mg, 188 µmol, 1.0 eq) and compound **118** (105 mg, 207 µmol, 1.1 eq) were dissolved in DMF (1.0 mL), then sodium ascorbate (3.7 mg, 19 µmol, 10 mol%) and $CuSO_4 \cdot 5H_2O$ (0.9 mg, 3.8 µmol, 2 mol%) were added. The reaction mixture was stirred at 23 °C for 3 d before it was transferred to a separatory funnel charged with a saturated NH_4Cl solution. The aqueous phase was extracted with EtOAc, the combined organic phases were washed with an excess of water (until residual DMF was removed as judged by the disappearance of DMF streaks in the aqueous phase) and brine, dried over Na_2SO_4 and the solvent was evaporated *in vacuo*. After purification by flash column chromatography (SiO_2, CH_2Cl_2 → CH_2Cl_2:MeOH = 19:1) compound **119** (162 mg, 173 µmol, 92%) was obtained as a red oil that was used in the next synthetic step without further purification.

HR-MS (EI^+) calc. [$C_{40}H_{45}BBrN_3O_7S^+$]: 933.3041, found: 933.3036.

Compound 120

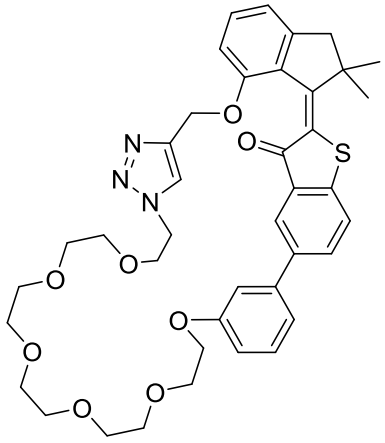

[727.873]

$C_{40}H_{45}N_3O_8S$

Compound **119** (296 mg, 317 µmol, 1.0 eq) was dissolved in DMF (25 mL), then K_2CO_3 (131 mg, 950 µmol, 3.0 eq), $Pd(PPh_3)_4$ (18.3 mg, 15.8 µmol, 5 mol%) and ten drops of water were added. The reaction mixture was stirred at 80 °C for 1 d before the reaction was stopped by addition of a saturated NH_4Cl solution and the suspension was transferred to a separatory funnel. Additional saturated NH_4Cl solution was added and the aqueous phase was extracted with EtOAc. The combined organic phases were washed with an excess of water (until residual DMF was removed as judged by the disappearance of DMF streaks in the aqueous phase) and brine, dried over Na_2SO_4 and the solvent was evaporated *in vacuo*. After purification by flash column chromatography (SiO_2, CH_2Cl_2:MeOH = 99:1) compound **120** (89.0 mg, 122 µmol, 39%) was obtained as an orange oil that was used in the next synthetic step without further purification.

HR-MS (EI^+) calc. [$C_{40}H_{45}N_3O_8S^+$]: 727.2927, found: 727.2912.

Compound 121

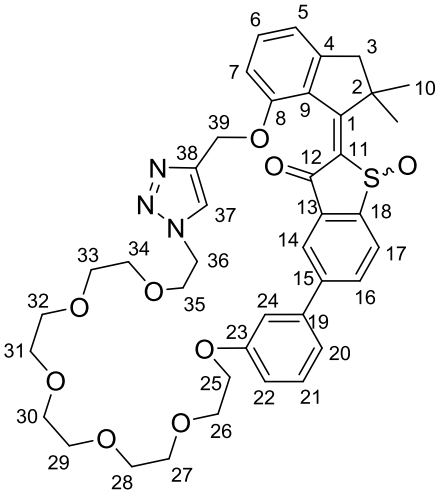

[743.872]

$C_{40}H_{45}N_3O_9S$

Compound **120** (89.0 mg, 122 µmol, 1.0 eq) was dissolved in acetic acid (3.0 mL) and $NaBO_2(OH)_2$ (75.3 mg, 489 µmol, 4.0 eq) was added. The reaction mixture was stirred at 23 °C for 3 h before it was transferred dropwise to a separatory funnel charged with a saturated $NaHCO_3$ solution. The aqueous phase was extracted with CH_2Cl_2, the combined organic phases were washed brine, dried over Na_2SO_4 and the solvent was evaporated *in vacuo*. After purification by flash column chromatography (SiO_2, CH_2Cl_2 → CH_2Cl_2:MeOH = 24:1) compound **121** (62.7 mg, 84.3 µmol, 69%) was obtained as a yellow solid.

***Z* isomer**

Atoms with numbers 29 to 34 could not be unambiguously assigned due to overlapping signals

^{1}H NMR (800 MHz, CD_2Cl_2, 25 °C) δ = 8.15 (d, *J* = 1.6 Hz, 1H, H-C(14)), 8.07 (dd, *J* = 8.0, 1.7 Hz, 1H, H-C(16)), 8.06 – 8.05 (m, 2H, H-C(17) and H-C(37)), 7.52 (dd, *J* = 8.4, 7.4 Hz, 1H, H-C(6)), 7.42 (t, *J* = 7.9 Hz, 1H, H-C(21)), 7.34 (t, *J* = 2.0 Hz, 1H, H-C(24)), 7.31 (dt, *J* = 7.7, 1.2 Hz, 1H, H-C(20)), 7.08 (d, *J* = 8.3 Hz, 1H, H-C(7)), 7.00 (d, *J* = 7.4 Hz, 1H, H-C(5)), 6.98 (ddd, *J* = 8.2, 2.5, 0.9 Hz, 1H, H-C(22)), 5.50 (s, 2H, H-C(39)), 4.52 – 4.45 (m, 2H, H-C(36)), 4.28 – 4.23 (m, 2H, H-C(25)), 3.84 (t, *J* = 4.7 Hz, 2H, H-C(26)), 3.78 – 3.72 (m, 2H, H-C(35)), 3.69 – 3.66 (m, 2H, H-C(27)), 3.61 – 3.58 (m, 2H, H-C(28)), 3.56 – 3.54 (m, 2H), 3.53 – 3.51 (m, 2H), 3.51 – 3.47 (m, 4H), 3.41 – 3.33 (m, 4H), 3.19 (d, *J* = 15.9 Hz, 1H, H-C(3)), 2.87 (d, *J* = 15.9 Hz, 1H, H-C(3)), 1.54 (s, 3H, H-C(10)), 1.53 (s, 3H, H-C(10)).

^{13}C NMR (201 MHz, CD_2Cl_2, 25 °C) δ = 184.92 (C-12), 170.93 (C-1), 160.13 (C-23), 156.92 (C-8), 152.27 (C-4), 149.34 (C-18), 145.45 (C-15), 143.64 (C-11), 143.23 (C-38), 140.95 (C-19), 136.87 (C-13), 135.61 (C-6), 134.69 (C-16), 130.67 (C-21), 127.27 (C-17), 126.13 (C-9), 125.51 (C-37), 123.10 (C-14), 120.33 (C-20), 118.50 (C-5), 115.38 (C-22), 115.20 (C-24), 110.78 (C-7), 71.46 (C-27), 71.11 (C-28), 71.04, 71.00, 70.91, 70.88, 70.72, 70.26 (C-26), 69.90 (C-35), 68.54 (C-25), 63.01 (C-39), 52.69 (C-2), 51.02 (C-3), 50.86 (C-36), 28.40 (C-10), 25.76 (C-10).

***E* isomer**:

^{1}H NMR (599 MHz, CD_2Cl_2, 27 °C) δ = 8.09 (d, *J* = 8.1 Hz, 1H), 8.05 (dd, *J* = 8.0, 1.7 Hz, 1H), 7.97 (d, *J* = 1.8 Hz, 1H), 7.71 (s, 1H), 7.47 (dd, *J* = 8.3, 7.4 Hz, 1H), 7.44 (t, *J* = 7.9 Hz, 1H), 7.39 (t, *J* = 2.1 Hz, 1H), 7.27 (dt, *J* = 7.7, 1.0 Hz, 1H), 7.04 – 6.99 (m, 3H), 5.26 (d, *J* = 11.7 Hz, 1H), 5.16 (d, *J* = 11.7 Hz, 1H), 4.34 – 4.29 (m, 1H), 4.28 – 4.23 (m, 1H), 4.11 – 4.05 (m, 2H), 3.89 (t, *J* = 4.6 Hz, 2H), 3.72 – 3.69 (m, 2H), 3.65 – 3.62 (m, 2H), 3.61 – 3.53 (m, 8H), 3.53 – 3.47 (m, 4H), 3.42 (t, *J* = 4.8 Hz, 2H), 3.28 (d, *J* = 15.0 Hz, 1H), 2.85 (d, *J* = 15.1 Hz, 1H), 1.96 (s, 3H), 1.38 (s, 3H).

^{13}C NMR (101 MHz, CD_2Cl_2, 22 °C) δ = 183.04, 171.37, 170.03, 160.18, 158.53, 151.26, 148.12, 145.67, 143.41, 140.96, 140.42, 136.48, 134.73, 134.18, 130.73, 128.33, 127.73, 124.79, 123.55, 120.48, 118.02, 115.46, 114.45, 110.93, 71.38, 71.20, 71.16, 71.08, 71.03, 70.91, 70.27, 69.58, 68.49, 62.79, 60.78, 53.24, 50.30, 50.22, 28.50, 26.48, 21.34, 14.54.

HR-MS (EI$^+$) calc. [$C_{40}H_{45}N_3O_8S^+$]: 743.2877, found: 743.2870.

Compound 125

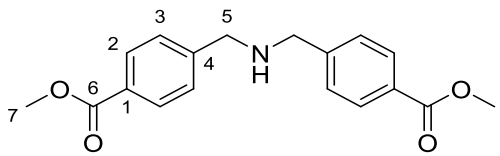

[313.353]

$C_{18}H_{19}NO_4$

Methyl 4-(aminomethyl)benzoate hydrochloride (2.46 g, 12.2 mmol, 1.0 eq) in methanol was treated with TEA (1.23 g, 12.2 mmol, 1.0 eq). Methyl 4-formylbenzoate (2.00 g, 12.2 mmol, 1.0 eq) was added and the suspension was stirred at 65 °C for 7.5 h. $NaBH_4$ (1.38 g, 36.5 mmol)

was added in four portions over 1 h and the reaction mixture was stirred at 23 °C for 16 h before water was added. The aqueous phase was extracted with CH_2Cl_2. The organic phases were combined and the solvent removed *in vacuo* to obtain compound **125** (3.41 g, 10.9 mmol, 89%) as a colorless solid.

^{1}H NMR (400 MHz, CD_2Cl_2, 25 °C) δ = 8.00 – 7.96 (m, 4H, H-C(2)), 7.46 – 7.42 (m, 4H, H-C(3)), 3.88 (s, 6H, H-C(7)), 3.86 (s, 4H, H-C(5)).

^{13}C NMR (101 MHz, CD_2Cl_2, 25 °C) δ = 167.35 (C-6), 146.40 (C-4), 130.06 (C-2), 129.53 (C-1), 128.53 (C-3), 53.32 (C-5), 52.44 (C-7).

HR-MS (EI$^+$), $[M–H]^+$ calc. for $[C_{18}H_{18}NO_4]^+$: 312.1236, found: 312.1235.

Compound 126

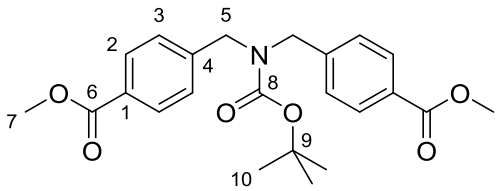

[413.470]

$C_{23}H_{27}NO_6$

Di-*tert*-butyl dicarbonate (2.38 g, 10.9 mmol, 1.0 eq) and DMAP (66.5 mg, 544 µmol, 5 mol%) were added to a solution of compound **125** (3.41 g, 10.9 mmol, 1.0 eq) in chloroform (100 mL) at 0 °C. After stirring at 23 °C for 16 h the organic phase was washed with 2 M HCl and water. The solvent was removed *in vacuo* to obtain compound **126** (4.30 g, 10.4 mmol, 96%) as a colorless oil.

^{1}H NMR (400 MHz, CD_2Cl_2, 25 °C) δ = 7.99 – 7.95 (m, 4H, H-C(2)), 7.28 (s, 4H, H-C(3)), 4.53 – 4.37 (m, 4H, H-C(5)), 3.88 (s, 6H, H-C(7)), 1.45 (s, 9H, H-C(10)).

^{13}C NMR (101 MHz, CD_2Cl_2, 25 °C) δ = 167.20 (C-6), 156.23 (C-8), 144.00 (C-4), 130.24 (C-2), 129.86 (C-1), 128.15 (C-3), 127.80 (C-3), 80.92 (C-9), 52.50 (C-7), 50.46 (C-5), 50.17 (C-5), 28.61 (C-10).

HR-MS (ESI$^+$), $[(M–Boc)+H]^+$ calc. for $[C_{18}H_{20}NO_4]^+$: 314.1392, found: 314.1385.

Compound 127

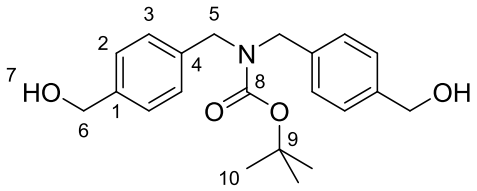

[357.450]

$C_{21}H_{27}NO_4$

Compound **126** (3.19 g, 7.72 mmol, 1.0 eq) in THF (100 mL) was heated to reflux under nitrogen. $LiAlH_4$ solution (2.4 M in THF, 12.9 mL, 30.9 mmol, 4.0 eq) was added dropwise over 30 min. After another 30 min the reaction mixture was cooled to 23 °C and the reaction was stopped by addition of water. 2 M HCl was added until a pH of 3 was reached and the solvent was removed *in vacuo*. The remaining aqueous phase was extracted with CH_2Cl_2. The combined organic phases were dried over Na_2SO_4, filtered and the solvent was evaporated *in vacuo* to obtain compound **127** (2.08 g, 5.82 mmol, 75%) as an oil.

^{1}H NMR (400 MHz, CD_2Cl_2, 25 °C) δ = 7.31 (d, *J* = 8.1 Hz, 4H, H-C(2)), 7.19 (d, *J* = 7.7 Hz, 4H, H-C(3)), 4.65 (d, *J* = 5.4 Hz, 4H, H-C(6)), 4.42 – 4.31 (m, 4H, H-C(5)), 1.78 (t, *J* = 5.8 Hz, 2H, H-O(7)), 1.48 (s, 9H, H-C(10)).

^{13}C NMR (101 MHz, CD_2Cl_2, 25 °C) δ = 156.32 (C-8), 140.72 (C-1), 138.10 (C-4), 128.25 (C-3), 127.63 (C-2), 80.41 (C-9), 65.39 (C-6), 49.47 (C-5), 28.70 (C-10).

HR-MS (ESI$^+$), $[M+H]^+$ calc. for $[C_{21}H_{28}NO_4]^+$: 358.2018, found: 358.2017.

Compound 128

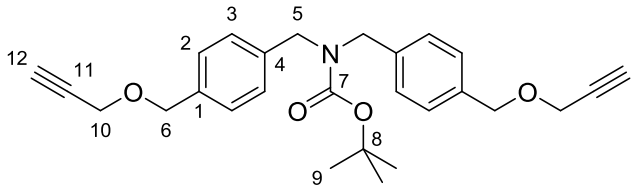

[433.548]

$C_{27}H_{31}NO_4$

A stirring solution of compound **127** (500 mg, 1.40 mmol, 1.0 eq) in THF (10 mL) was cooled to 0 °C and sodium hydride (60% dispersion in mineral oil, 134 mg, 3.36 mmol, 2.4 eq) was

added. After 30 min propargyl bromide (80% in toluene, 499 mg, 3.36 mmol, 2.4 eq) was added and the reaction mixture was stirred at 23 °C for 24 h. The reaction was stopped by addition of water and the aqueous phase was extracted with CH_2Cl_2. The combined organic phases were washed with brine, dried over Na_2SO_4, filtered and the solvent was evaporated *in vacuo* to obtain compound **128** (578 mg, 1.33 mmol, 95%) as a yellow oil.

^{1}H NMR (599 MHz, CD_2Cl_2, 30 °C) δ = 7.33 – 7.28 (m, 4H, H-C(2)), 7.20 (s, 4H, H-C(3)), 4.57 (s, 4H, H-C(6)), 4.42 – 4.30 (m, 4H, H-C(5)), 4.17 (d, *J* = 2.4 Hz, 4H, H-C(10)), 2.51 (t, *J* = 2.4 Hz, 2H, H-C(12)), 1.47 (s, 9H, H-C(9)).

^{13}C NMR (151 MHz, CD_2Cl_2, 30 °C) δ = 156.34 (C-7), 138.50 (C-4), 137.07 (C-1), 128.78 (C-2), 128.39 (C-3), 128.07 (C-3), 80.43 (C-8), 80.33 (C-11), 74.81 (C-12), 71.85 (C-6), 57.68 (C-10), 49.86 (C-5), 49.44 (C-5), 28.70 (C-9).

HR-MS (ESI$^+$), $[M+H]^+$ calc. for $[C_{27}H_{32}NO_4]^+$: 434.2331, found: 434.2329.

Compound 129

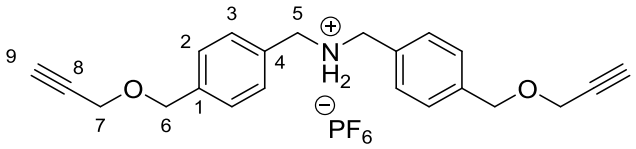

[479.403]

$C_{22}H_{24}F_6NO_2P$

A solution of compound **128** (576 mg, 1.33 mmol, 1.0 eq) in CH_2Cl_2 (10.0 mL) and trifluoroacetic acid (2.0 mL) was stirred for 20 h at 23 °C. The solvent was evaporated *in vacuo* and the crude product was partitioned between 2 M NaOH and CH_2Cl_2. The aqueous phase was extracted with additional CH_2Cl_2 and the combined organic phases were dried over Na_2SO_4, filtered and the solvent was removed *in vacuo*. The resulting oil was diluted with an excess of 2 M HCl, sonicated and the aqueous phase was evaporated *in vacuo*. The remaining solid was taken up in water and ammonium hexafluorophosphate (217 mg, 1.33 mmol, 1.0 eq) was added. The suspension was extracted with CH_2Cl_2. The combined organic phases were dried over Na_2SO_4, filtered and the solvent was evaporated *in vacuo* to give compound **129** (277 mg, 578 µmol, 43%) as a pearl white solid.

^{1}H NMR (599 MHz, CD_2Cl_2, 30 °C) δ = 7.40 (d, *J* = 8.0 Hz, 4H, H-C(3)), 7.34 (d, *J* = 7.9 Hz, 4H, H-C(2)), 4.56 (s, 4H, H-C(6)), 4.20 (d, *J* = 2.4 Hz, 4H, H-C(7)), 4.01 (s, 4H), 2.54 (t, *J* = 2.4 Hz, 2H, H-C(9)).

^{13}C NMR (151 MHz, CD_2Cl_2, 30 °C) δ = 139.14 (C-1), 133.26 (C-4), 130.18 (C-3), 129.13 (C-2), 80.12 (C-8), 75.14 (C-9), 71.72 (C-6), 58.08 (C-7), 51.93 (C-5), 30.26.

HR-MS (ESI$^+$), $[(M–PF_6)+H]^+$ calc. for $[C_{22}H_{24}NO_2]^+$: 334.1807, found: 334.1797.

HR-MS (ESI$^–$), $[(M+PF_6)+H]^–$ calc. for $[C_{22}H_{24}F_{12}NO_2P_2]^–$: 624.1091, found: 624.1096.

Compound 130

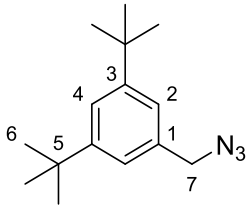

[245.370]

$C_{15}H_{23}N_3$

3,5-Di-*tert*-butylbenzyl bromide (500 mg, 1.77 mmol, 1.0 eq) and sodium azide (344 mg, 5.30 mmol, 3.0 eq) in CH_2Cl_2 were stirred at 23 °C for 22 h. The reaction mixture was partitioned between EtOAc and water and extracted with additional EtOAc. The combined organic phases were washed with water and brine, dried over Na_2SO_4, filtered and the solvent was evaporated *in vacuo* to give compound **130** (428 mg, 1.74 mmol, 99%) as a pale yellow liquid.

^{1}H NMR (400 MHz, CD_2Cl_2, 25 °C) δ = 7.41 (t, *J* = 1.8 Hz, 1H, H-C(4)), 7.15 (d, *J* = 1.8 Hz, 2H, H-C(2)), 4.33 (s, 2H, H-C(7)), 1.33 (s, 18H, H-C(6)).

^{13}C NMR (101 MHz, CD_2Cl_2, 25 °C) δ = 151.99 (C-3), 135.26 (C-1), 123.04 (C-2), 122.83 (C-4), 56.01 (C-7), 35.30 (C-5), 31.70 (C-6).

HR-MS (EI$^+$), $[M]^+$ calc. for $[C_{15}H_{23}N_3]^+$: 245.1892, found: 245.1884.

Compound 131

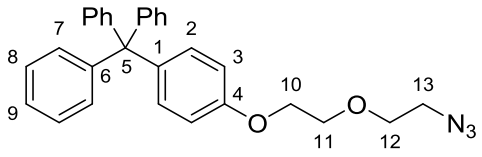

[449.554]

$C_{29}H_{27}N_3O_2$

To a stirring solution of 4-tritylphenol (1.48 g, 4.40 mmol, 1.09 eq) and compound **111** (781 mg, 4.03 mmol, 1.0 eq) in DMF (4.5 mL) was added K_2CO_3 (1.83 g, 13.2 mmol, 3.28 eq). The mixture was heated at 70 °C for 1 d before it was transferred to a separatory funnel charged with a saturated NH_4Cl solution. The aqueous phase was extracted with EtOAc. The combined organic phases were washed with an excess of water (until residual DMF was removed as judged by the disappearance of DMF streaks in the aqueous phase) and brine, dried over Na_2SO_4 and the solvent was removed *in vacuo*. The crude product was purified by flash column chromatography (SiO_2, *i*-Hex:EtOAc = 19:1) to give compound **131** (1.48 g, 3.29 mmol, 75%) as a colorless solid.

^{1}H NMR (400 MHz, CD_2Cl_2, 25 °C) δ = 7.29 – 7.16 (m, 15H, H-C(7) to H-C(9)), 7.15 – 7.10 (m, 2H, H-C(2)), 6.82 – 6.78 (m, 2H, H-C(3)), 4.12 – 4.08 (m, 2H, H-C(10)), 3.85 – 3.81 (m, 2H, H-C(11)), 3.73 – 3.70 (m, 2H, H-C(12)), 3.39 (t, *J* = 5.0 Hz, 2H, H-C(13)).

^{13}C NMR (101 MHz, CD_2Cl_2, 25 °C) δ = 157.29 (C-4), 147.69 (C-6), 139.83 (C-1), 132.63 (C-2), 131.51 (C-7), 128.02 (C-8), 126.35 (C-9), 113.90 (C-3), 70.67 (C-12), 70.26 (C-11), 67.97 (C-10), 64.89 (C-5), 51.37 (C-13).

HR-MS (ESI$^+$), $[M+NH_4]^+$ calc. for $[C_{29}H_{31}N_4O_2]^+$: 467.2447, found: 467.2447.

Compound 132

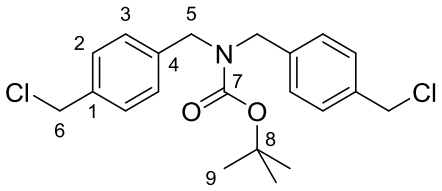

[394.336]

$C_{21}H_{25}Cl_2NO_2$

A solution of *N*-chlorosuccinimide (747 mg, 5.60 mmol, 4.0 eq) in THF (25 mL) was added to a stirring solution of triphenylphosphine (1.28 g, 4.90 mmol, 3.5 eq) in THF (25 mL). After 45 min compound **127** (500 mg, 1.40 mmol, 1.0 eq) in THF (2.0 mL) was added and the reaction mixture was stirred for 1 d at 23 °C. The solvent was evaporated *in vacuo* and after purification by flash column chromatography (SiO_2, *i*-Hex:EtOAc = 9:1) compound **132** (381 mg, 966 µmol, 69%) was obtained as a pale yellow oil.

^{1}H NMR (599 MHz, CD_2Cl_2, 30 °C) δ = 7.37 – 7.34 (m, 4H, H-C(2)), 7.21 (s, 4H, H-C(3)), 4.60 (s, 4H, H-C(6)), 4.43 – 4.32 (m, 4H, H-C(5)), 1.47 (s, 9H, H-C(9)).

^{13}C NMR (151 MHz, CD_2Cl_2, 30 °C) δ = 156.29 (C-7), 139.19 (C-4), 137.17 (C-1), 129.36 (C-2), 128.66 (C-3), 128.36 (C-3), 80.60 (C-8), 49.98 (C-5), 49.54 (C-5), 46.72 (C-6), 28.68 (C-9).

HR-MS (ESI$^+$), $[(M–tBu)+H]^+$ calc. for $[C_{17}H_{18}Cl_2NO_2]^+$: 338.0715, found: 338.0711.

Compound 133

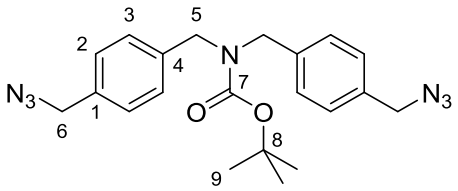

[407.478]

$C_{21}H_{25}N_7O_2$

Sodium azide (311 mg, 4.78 mmol, 5.0 eq) was added to a solution of compound **132** (377 mg, 1.05 mmol, 1.0 eq) in butanone (5.0 mL) and the reaction mixture was heated under reflux for 5 d. The solvent was removed *in vacuo* and the residue was taken up in chloroform. After

filtration the solvent was again removed *in vacuo* to give compound **133** (393 mg, 964 µmol, 91%) as a brown oil.

^{1}H NMR (400 MHz, CD_2Cl_2, 25 °C) δ = 7.31 – 7.26 (m, 4H, H-C(2)), 7.26 – 7.20 (m, 4H, H-C(3)), 4.45 – 4.35 (m, 4H, H-C(5)), 4.34 (s, 4H, H-C(6)), 1.47 (s, 9H, H-C(9)).

^{13}C NMR (101 MHz, CD_2Cl_2, 25 °C) δ = 156.30 (C-7), 139.01 (C-4), 135.05 (C-1), 128.97 (C-4), 128.67 (C-3), 128.45 (C-3), 80.57 (C-8), 55.05 (C-6), 50.05 (C-5), 49.73 (C-5), 28.67 (C-9).

HR-MS (ESI$^+$), $[(M–tBu)+H]^+$ calc. for $[C_{17}H_{18}N_7O_2]^+$: 352.1522, found: 352.1518.

Compound 134

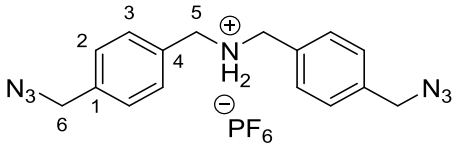

[453.333]

$C_{16}H_{18}F_6N_7P$

A solution of compound **133** (390 mg, 957 µmol, 1.0 eq) in CH_2Cl_2 (10.0 mL) and trifluoroacetic acid (2.0 mL) was stirred for 20 h at 23 °C. The solvent was evaporated *in vacuo* and the crude product was partitioned between 2 M NaOH and CH_2Cl_2. The aqueous phase was extracted with additional CH_2Cl_2 and the combined organic phases were dried over Na_2SO_4, filtered and the solvent was removed *in vacuo*. The crude product was diluted with an excess of 2 M HCl, sonicated and the aqueous phase was evaporated *in vacuo*. The remaining solid was taken up in water and ammonium hexafluorophosphate (156 mg, 957 mmol, 1.0 eq) was added. The suspension was extracted with CH_2Cl_2. The combined organic phases were dried over Na_2SO_4, filtered and the solvent was evaporated *in vacuo* to give compound **134** (260 mg, 574 µmol, 60%) as a colorless solid.

^{1}H NMR (400 MHz, CD_2Cl_2, 25 °C) δ = 7.45 – 7.41 (m, 4H, H-C(3)), 7.41 – 7.37 (m, 4H, H-C(2)), 4.37 (s, 4H, H-C(6)), 4.11 (s, 4H, H-C(5)).

^{13}C NMR (101 MHz, CD_2Cl_2, 25 °C) δ = 138.21 (C-1), 131.00 (C-4), 130.73 (C-3), 129.64 (C-2), 54.69 (C-6), 51.53 (C-5).

HR-MS (ESI$^+$), $[(M–PF_6)+H]^+$ calc. for $[C_{16}H_{18}N_7]^+$: 308.1624, found: 308.1615.

HR-MS (ESI$^-$), $[(M+PF_6)+H]^-$ calc. for $[C_{16}H_{18}F_{12}N_7P_2]^-$: 598.0907, found: 598.0916.

Compound 136

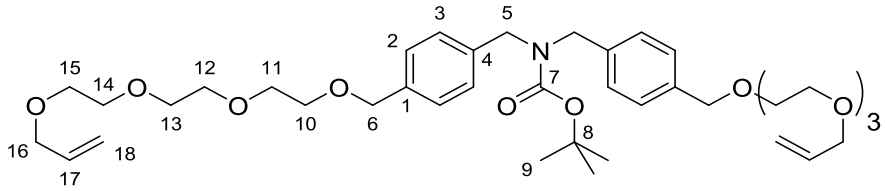

[701.898]

$C_{39}H_{59}NO_{10}$

A stirring solution of compound **127** (252 mg, 705 µmol, 1.0 eq) in THF (5.0 mL) was cooled to 0 °C and sodium hydride (60% dispersion in mineral oil, 59.2 mg, 1.48 mmol, 2.1 eq) was added. After 30 min compound **62** (366 mg, 1.45 mmol, 2.05 eq) was added and the reaction mixture was stirred at 23 °C for 48 h. The reaction was stopped by addition of water and the aqueous phase was extracted with CH_2Cl_2. The combined organic phases were washed with brine, dried over Na_2SO_4, filtered and the solvent was evaporated *in vacuo*. After flash column chromatography (SiO_2, CH_2Cl_2:MeOH = 99:1) compound **136** (78.8 mg, 112 µmol, 16%) was obtained as a colorless oil.

^{1}H NMR (400 MHz, CD_2Cl_2, 25 °C) δ = 7.33 – 7.28 (m, 4H, H-C(2)), 7.20 (d, *J* = 7.7 Hz, 4H, H-C(3)), 5.91 (ddt, *J* = 17.2, 10.4, 5.6 Hz, 2H, H-C(17)), 5.29 – 5.23 (m, 2H, H-C(18)), 5.18 – 5.13 (m, 2H, H-C(18)), 4.52 (s, 4H, H-C(6)), 4.41 – 4.29 (m, 4H, H-C(5)), 3.99 (dt, *J* = 5.6, 1.5 Hz, 4H, H-C(16)), 3.66 – 3.54 (m, 24H, H-C(10) to H-C(15)), 1.47 (s, 9H, H-C(9)).

^{13}C NMR (101 MHz, CD_2Cl_2, 25 °C) δ = 156.34 (C-7), 138.13 (C-4), 138.06 (C-1), 135.63 (C-17), 128.47 (C-2), 128.31 (C-3), 128.03 (C-3), 116.94 (C-18), 80.35 (C-8), 73.42 (C-6), 72.56 (C-16), 71.14 (C-11 to C-14), 71.11 (C-11 to C-14), 70.24 (C-10), 70.12 (C-15), 49.68 (C-5), 49.26 (C-5), 28.70 (C-9).

HR-MS (ESI$^+$), $[M+NH_4]^+$ calc. for $[C_{39}H_{63}N_2O_{10}]^+$: 719.4483, found: 719.4478.

Compound 137

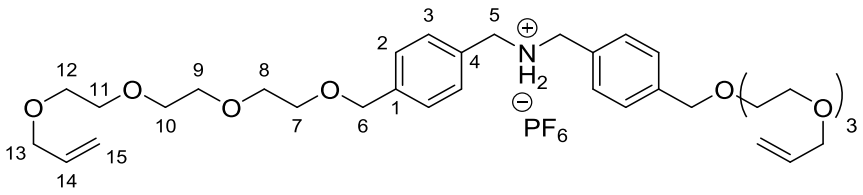

[747.753]

$C_{34}H_{52}F_6NO_8P$

A solution of compound **136** (73.0 mg, 104 µmol, 1.0 eq) in CH_2Cl_2 (10.0 mL) and trifluoroacetic acid (1.5 mL) was stirred for 18 h at 23 °C. The solvent was evaporated *in vacuo* and the crude product was partitioned between 2 M NaOH and CH_2Cl_2. The aqueous phase was extracted with additional CH_2Cl_2 and the combined organic phases were dried over Na_2SO_4, filtered and the solvent was removed *in vacuo*. The crude product was diluted with an excess of 2 M HCl and the aqueous phase was evaporated *in vacuo*. The resulting liquid was taken up in water and ammonium hexafluorophosphate (17.0 mg, 104 µmol, 1.0 eq) in water (1.0 mL) was added dropwise. The suspension was extracted with CH_2Cl_2. The combined organic phases were dried over Na_2SO_4, filtered and the solvent was evaporated *in vacuo* to give compound **137** (75.9 mg, 102 µmol, 98%) as a yellow oil.

^{1}H NMR (599 MHz, CD_2Cl_2, 30 °C) δ = 7.39 (d, *J* = 8.2 Hz, 4H, H-C(2)), 7.34 (d, *J* = 8.1 Hz, 4H, H-C(3)), 5.86 (ddt, *J* = 17.3, 10.4, 5.9 Hz, 2H, H-C(14)), 5.27 – 5.23 (m, 2H, H-C(15)), 5.21 – 5.18 (m, 2H, H-C(15)), 4.55 (s, 4H, H-C(6)), 4.03 (s, 4H, H-C(5)), 3.94 (dt, *J* = 5.9, 1.3 Hz, 4H, H-C(13)), 3.67 – 3.64 (m, 4H, H-C(7)), 3.59 – 3.56 (m, 4H, H-C(8)), 3.51 – 3.48 (m, 8H, H-C(9) and H-C(12)), 3.45 – 3.43 (m, 8H, H-C(10) and H-C(11)).

^{13}C NMR (151 MHz, CD_2Cl_2, 30 °C) δ = 140.20 (C-1), 134.86 (C-14), 131.05 (C-4), 130.49 (C-3), 129.06 (C-2), 118.37 (C-15), 73.41 (C-6), 72.81 (C-13), 71.11 (C-8), 71.06 (C-9), 71.00 (C-10 or C-11), 70.99 (C-10 or C-11), 70.49 (C-7), 69.78 (C-12), 52.32 (C-5).

HR-MS (ESI^+), $[(M–PF_6)+H]^+$ calc. for $[C_{34}H_{52}NO_8]^+$: 602.3693, found: 602.3688.

Compound 139

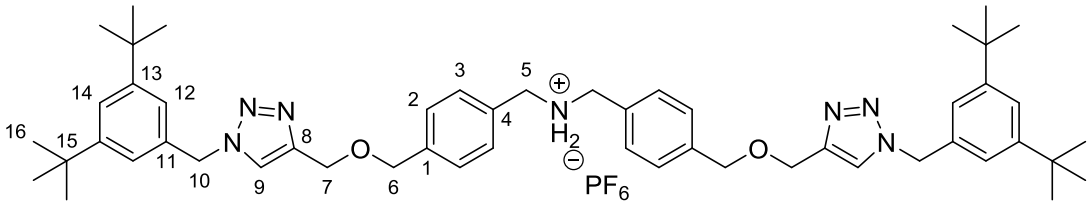

[970.143]

$C_{52}H_{70}F_6N_7O_2P$

A mixture of compound **129** (20.0 mg, 41.7 µmol, 1.0 eq), compound **130** (20.5 mg, 83.4 µmol, 2.0 eq) and $[Cu(CH_3CN)_4]PF_6$ (31.1 mg, 83.4 µmol, 2.0 eq) in CH_2Cl_2 (1.0 mL) was stirred for 5 d at 23 °C. Water was added and the aqueous phase was extracted with CH_2Cl_2. The combined organic phases were washed with brine, dried over Na_2SO_4, filtered and the solvent was evaporated *in vacuo*. After flash column chromatography (SiO_2, CH_2Cl_2:MeOH = 25:1) compound **139** (40.0 mg, 41.2 µmol, 99%) was obtained as a colorless oil.

^{1}H NMR (400 MHz, CD_2Cl_2, 25 °C) δ = 7.51 (s, 2H, H-C(9)), 7.43 (t, *J* = 1.8 Hz, 2H, H-C(14)), 7.33 – 7.29 (m, 4H, H-C(3)), 7.29 – 7.26 (m, 4H, H-C(2)), 7.13 (d, *J* = 1.9 Hz, 4H, H-C(12)), 5.49 (s, 4H, H-C(10)), 4.62 (s, 4H, H-C(7)), 4.53 (s, 4H, H-C(6)), 3.77 (s, 4H, H-C(5)), 1.30 (s, 36H, H-C(16)).

^{13}C NMR (101 MHz, CD_2Cl_2, 25 °C) δ = 152.32 (C-13), 145.85 (C-8), 140.71 (C-4), 137.25 (C-1), 134.66 (C-11), 128.63 (C-3), 128.43 (C-2), 123.27 (C-14), 123.02 (C-9), 122.97 (C-12), 72.57 (C-6), 64.14 (C-7), 55.19 (C-10), 53.35 (C-5), 35.32 (C-15), 31.67 (C-16).

HR-MS (ESI$^+$), $[(M–PF_6)+H]^+$ calc. for $[C_{52}H_{70}N_7O_2]^+$: 824.5586, found: 824.5598.

Compound 141

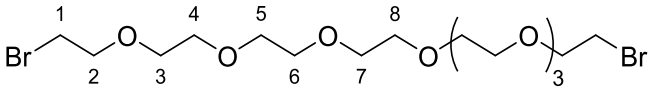

[496.233]

$C_{16}H_{32}Br_2O_7$

Compound **142** (991 mg, 1.46 mmol, 1.0 eq) and lithium bromide (634 mg, 7.30 mmol, 5.0 eq) in acetone (10.0 mL) were heated under reflux for 5 h. The solvent was removed *in vacuo* and

the crude product was purified by flash column chromatography (SiO_2, EtOAc) to give compound **141** (653 mg, 1.32 mmol, 90%) as a colorless oil.

^{1}H NMR (400 MHz, CD_2Cl_2, 25 °C) δ = 3.79 (t, *J* = 6.1 Hz, 4H, H-C(2)), 3.66 – 3.59 (m, 24H, H-C(3) to H-C(8)), 3.49 (t, *J* = 6.1 Hz, 4H, H-C(1)).

^{13}C NMR (101 MHz, CD_2Cl_2, 25 °C) δ = 71.69 (C-2), 71.14, 71.09, 71.08, 71.04, 31.42 (C-1).

Compound 142

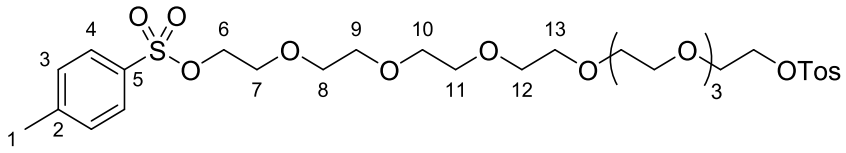

[678.805]

$C_{30}H_{46}O_{13}S_2$

A stirring solution of octaethylene glycol (700 mg, 1.89 mmol, 1.0 eq) and tosyl chloride (771 mg, 4.04 mmol, 2.14 eq) in THF (11.5 mL) was cooled to 0 °C. Solution of KOH (500 mg, 8.91 mmol, 4.71 eq) in water (1.5 mL) was added dropwise over 15 min. The reaction was allowed to warm to 23 °C and stirred for 5.5 h. Then the reaction mixture was transferred to a separatory funnel charged with a saturated NH_4Cl solution. The aqueous phase was extracted with CH_2Cl_2 and the combined organic phases were dried over Na_2SO_4. Removing the solvent *in vacuo* yielded compound **142** (992 mg, 1.46 mmol, 77%) as a colorless oil.

^{1}H NMR (400 MHz, CD_2Cl_2, 25 °C) δ = 7.80 – 7.76 (m, 4H, H-C(4)), 7.39 – 7.35 (m, 4H, H-C(3)), 4.14 – 4.10 (m, 4H, H-C(6)), 3.66 – 3.63 (m, 4H, H-C(7)), 3.58 – 3.56 (m, 16H, H-C(10) to H-C(13)), 3.54 (s, 8H, H-C(8) and H-C(9)), 2.45 (s, 6H, H-C(1)).

^{13}C NMR (101 MHz, CD_2Cl_2, 25 °C) δ = 145.65 (C-2), 133.48 (C-5), 130.43 (C-3), 128.43 (C-4), 71.21, 71.10, 71.05, 71.03, 70.95, 70.06 (C-6), 69.15 (C-7), 21.94 (C-1).

Compound 143

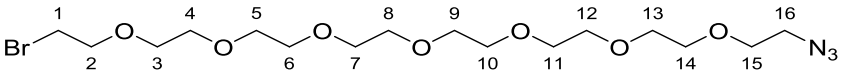

[458.350]

$C_{16}H_{32}BrN_3O_7$

A stirring solution of compound **141** (648 mg, 1.32 mmol, 1.0 eq) and sodium azide (84.8 mg, 1.31 mmol, 1.0 eq) in DMF (2.0 mL) were heated to 60 °C for 16 h. The solvent was removed *in vacuo* and the crude product was purified by flash column chromatography (SiO_2, CH_2Cl_2 → CH_2Cl_2:MeOH = 47:3) to give compound **143** (563 mg, 1.23 mmol, 94%) as a colorless oil.

^{1}H NMR (599 MHz, CD_2Cl_2, 27 °C) δ = 3.79 (td, *J* = 6.1, 0.8 Hz, 2H, H-C(2)), 3.66 – 3.58 (m, 26H, H-C(3) to H-C(15)), 3.49 (t, *J* = 6.1 Hz, 2H, H-C(1)), 3.38 (t, *J* = 5.1 Hz, 2H, H-C(16)).

^{13}C NMR (151 MHz, CD_2Cl_2, 27 °C) δ = 71.68 (C-2), 71.17, 71.14, 71.13, 71.08, 71.08, 71.07, 71.03, 71.03, 70.44 (C-15), 51.37 (C-16), 31.42 (C-1).

Compound 144

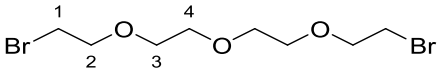

[320.02]

$C_8H_{16}Br_2O_3$

A stirring solution of tetraethylene glycol (2.40 g, 16.0 mmol, 1.0 eq) and tetrabromomethane (11.7 g, 35.2 mmol, 2.2 eq) in CH_2Cl_2 (22.0 mL) was cooled to 0 °C. Triphenylphosphine (8.81 g, 33.6 mmol, 2.1 eq) was added in portions over 20 min. The reaction was allowed to warm to 23 °C and stirred for 20 h. Then the reaction mixture was transferred to a separatory funnel charged with a saturated NH_4Cl solution. The aqueous phase was extracted with CH_2Cl_2 and the combined organic phases were dried over Na_2SO_4. The solvent was removed *in vacuo* and the crude product was purified by flash column chromatography (SiO_2, *i*-Hex:EtOAc = 3:1) to give compound **143** (563 mg, 1.23 mmol, 94%) as a colorless oil.

^{1}H NMR (400 MHz, CD_2Cl_2, 25 °C) δ = 3.79 (t, *J* = 6.0 Hz, 4H, H-C(2)), 3.66 – 3.59 (m, 8H, H-C(3) and H-C(4)), 3.49 (t, *J* = 6.1 Hz, 4H, H-C(1)).

Compound 145

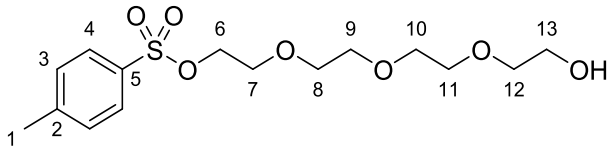

[348.41]

$C_{15}H_{24}O_7S$

To a stirring solution of tetraethylene glycol (4.74 g, 31.6 mmol, 3.0 eq) in THF (6.0 mL) was added a solution of NaOH (400 mg, 10.5 mmol, 1.0 eq) in water (4.0 mL). The mixture was cooled to 0 °C and a solution of 4-toluenesulfonyl chloride (2.00 g, 10.5 mmol, 1.0 eq) in THF (10.0 mL) was added dropwise over 2 h under vigoros stirring. The reaction mixture was transferred to a separatory funnel charged with a saturated NH_4Cl solution. The aqueous phase was extracted with CH_2Cl_2 and the combined organic phases were dried over Na_2SO_4. The solvent was removed *in vacuo* and the crude product **143** (563 mg, 1.23 mmol, 94%) was obtained as a colorless liquid.

^{1}H NMR (400 MHz, CD_2Cl_2, 25 °C) δ = 7.81 – 7.75 (m, 2H, H-C(4)), 7.37 (dd, *J* = 8.3, 2.8 Hz, 2H, H-C(3)), 4.15 – 4.09 (m, 2H, H-C(13)), 3.67 – 3.51 (m, 14H, H-C(6-12)), 2.44 (s, 3H, H-C(1)), 1.82 (s, 1H, H-O).

Compound 146

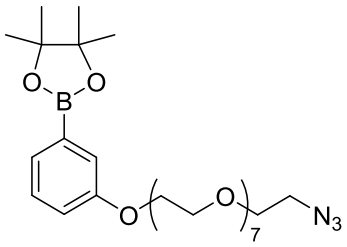

[597.513]

$C_{28}H_{48}BN_3O_{10}$

Compound **143** (213 mg, 575 µmol, 1.0 eq) was dissolved in DMF (2.0 mL), then 3-hydroxyphenylboronic acid pinacol ester (139 mg, 633 µmol, 1.1 eq) and K_2CO_3 (318 mg, 2.30 mmol, 4.0 eq) were added. The reaction mixture was heated for 22 h at 60 °C before it was transferred to a separatory funnel charged with a saturated NH_4Cl solution. The aqueous phase was extracted with EtOAc. The combined organic phases were washed with an excess of water

(until residual DMF was removed as judged by the disappearance of DMF streaks in the aqueous phase) and brine, dried over Na_2SO_4 and the solvent was evaporated *in vacuo*. Compound **146** (228 mg, 448 µmol, 78%) was obtained as a brown oil that was used in the next synthetic step without further purification.

^{1}H NMR (400 MHz, CD_2Cl_2, 22 °C) δ = 7.35 – 7.25 (m, 3H), 7.01 (ddd, *J* = 8.0, 2.7, 1.3 Hz, 1H), 4.15 – 4.12 (m, 2H), 3.81 (ddd, *J* = 6.1, 3.3, 1.4 Hz, 2H), 3.70 – 3.55 (m, 26H), 3.38 (t, *J* = 5.0 Hz, 2H), 1.32 (d, *J* = 1.3 Hz, 12H).

Compound 147

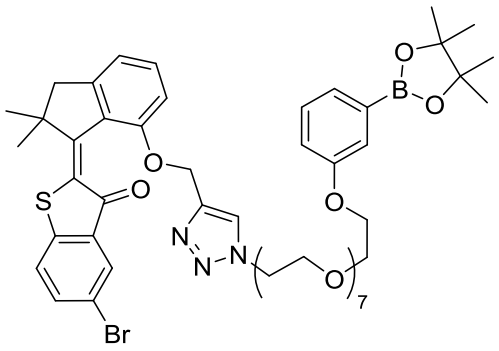

[1022.853]

$C_{50}H_{65}BBrN_3O_{12}S$

Compound **146** (783 mg, 1.31 µmol, 1.1 eq) and compound **75** (507 mg, 1.19 mmol, 1.0 eq) were dissolved in DMF (8.0 mL), then sodium ascorbate (23.6 mg, 119 µmol, 10 mol%) and $CuSO_4 \cdot 5H_2O$ (6.0 mg, 24 µmol, 2 mol%) were added. The reaction mixture was stirred at 23 °C for 4 d before the solvent was removed *in vacuo*. After purification by flash column chromatography (SiO_2, CH_2Cl_2 → CH_2Cl_2:MeOH = 24:1) compound **147** (926 mg, 910 µmol, 76%) was obtained as a red solid that was used in the next synthetic step without further purification.

Compound 148

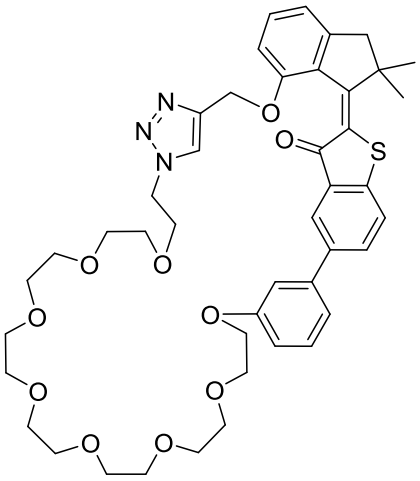

[815.979]

$C_{44}H_{53}N_3O_{10}S$

Compound **147** (926 mg, 906 µmol, 1.0 eq) was dissolved in DMF (45 mL), then K_2CO_3 (375 mg, 2.72 mmol, 3.0 eq) and $Pd(PPh_3)_4$ (52.3 mg, 45.3 µmol, 5 mol%) were added. The reaction mixture was stirred at 80 °C for 24 h and 20 drops of water were added. After 6 h at 100 °C the reaction was stopped by addition of a saturated aqueous NH_4Cl solution. The aqueous phase was extracted with EtOAc, the combined organic phases were washed with an excess of water (until residual DMF was removed as judged by the disappearance of DMF streaks in the aqueous phase) and brine, dried over Na_2SO_4 and the solvent was evaporated *in vacuo*. After purification by flash column chromatography (SiO_2, CH_2Cl_2 → CH_2Cl_2:MeOH = 9:1) compound **148** (370 mg, 451 µmol, 50%) was obtained as an orange solid that was used in the next synthetic step without further purification.

HR-MS (ESI^+) calc. for [M+H] [$C_{40}H_{46}N_3O_8S^+$]: 816.3530, found: 816.3527.

Compound 149

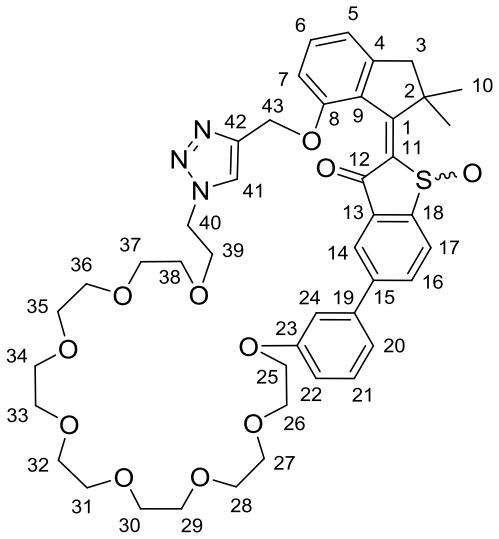

[831.978]

$C_{44}H_{53}N_3O_{11}S$

Compound **148** (367 mg, 451 µmol, 1.0 eq) was dissolved in acetic acid (30 mL) and $NaBO_2(OH)_2$ (277 mg, 1.80 mmol, 4.0 eq) was added. The reaction mixture was stirred at 23 °C for 5 h before it was transferred dropwise to a separatory funnel charged with a saturated $NaHCO_3$ solution. The aqueous phase was extracted with CH_2Cl_2, the combined organic phases were washed brine, dried over Na_2SO_4 and the solvent was evaporated *in vacuo*. After purification by flash column chromatography (SiO_2, CH_2Cl_2 → CH_2Cl_2:MeOH = 9:1) compound **149** (116 mg, 139 µmol, 31%) was obtained as a yellow solid.

Isomer 1

^{1}H NMR (599 MHz, CD_2Cl_2, 30 °C) δ = 8.08 (d, *J* = 8.1 Hz, 1H, H-C(17)), 8.06 (dd, *J* = 8.1, 1.7 Hz, 1H H-C(16)), 7.97 (s, 1H, H-C(14)), 7.72 (s, 1H, H-C(41)), 7.47 (dd, *J* = 8.5, 7.6 Hz, 1H, H-C(6)), 7.46 – 7.43 (m, 1H, H-C(21)), 7.41 (t, *J* = 2.2 Hz, 1H, H-C(24)), 7.29 (ddd, *J* = 7.5, 1.6, 0.8 Hz, 1H, H-C(20)), 7.03 (ddd, *J* = 8.3, 2.5, 0.8 Hz, 1H, H-C(22)), 7.01 – 6.99 (m, 2H, H-C(5) and H-C(7)), 5.27 (d, *J* = 11.8 Hz, 1H, H-C(43)), 5.18 (d, *J* = 11.6 Hz, 1H, H-C(43)), 4.32 (dt, *J* = 9.9, 4.8 Hz, 1H, H-C(25)), 4.28 – 4.23 (m, 1H, H-C(25)), 4.09 (t, *J* = 5.3 Hz, 2H, H-C(40)), 3.89 (t, *J* = 4.7 Hz, 2H, H-C(26)), 3.73 – 3.70 (m, 2H, H-C(27)), 3.66 – 3.64 (m, 2H, H-C(28)), 3.61 (ddt, *J* = 5.2, 3.2, 1.8 Hz, 2H, H-C(29) to H-C(39)), 3.59 – 3.50 (m, 14H, H-C(29) to H-C(39)), 3.49 (dq, *J* = 6.1, 1.8 Hz, 2H, H-C(29) to H-C(39)), 3.45 (dt, *J* = 5.2, 3.5 Hz, 2H, H-C(29) to H-C(39)), 3.39 (ddd, *J* = 6.7, 5.2, 3.6 Hz, 2H, H-C(29) to H-C(39)),

3.28 (d, *J* = 15.1 Hz, 1H, H-C(3)), 2.85 (d, *J* = 15.1 Hz, 1H, H-C(3)), 1.96 (s, 3H, H-C(10)), 1.38 (s, 3H, H-C(10)).

^{13}C NMR (201 MHz, CD_2Cl_2, 25 °C) δ = 183.05 (C-12), 170.03 (C-1), 160.19 (C-23), 158.53 (C-8), 151.26 (C-4), 148.07 (C-18), 145.65 (C-15),143.48 (C-42), 140.88 (C-19), 136.50 (C-13), 134.64 (C-6), 134.13 (C-16), 130.70 (C-21), 128.57 (C-9), 127.74 (C-17), 124.89 (C-41), 123.67 (C-14), 120.52 (C-20), 118.04 (C-5 oder C-7), 115.54 (C-22), 114.33 (C-24), 110.95 (C-5 or C-7), 71.34 (C-27), 71.19 (C-28), 71.14 (C-29 to C-39), 71.09 (C-29 to C-39), 71.04 (C-29 to C-39), 71.01 (C-29 to C-39), 70.98 (C-29 to C-39), 70.96 (C-29 to C-39), 70.91 (C-29 to C-39), 70.85 (C-29 to C-39), 70.79 (C-29 to C-39), 70.20 (C-26), 68.34 (C-25), 62.93 (C-43), 53.24 (C-2), 50.39 (C-40), 50.26 (C-3), 28.52 (C-10), 26.49 (C-10). C-11 could not be assigned

HR-MS (ESI$^+$) calc. for [M+H] [$C_{44}H_{53}N_3NaO_{11}S^+$]: 854.3299, found: 854.3290.

Isomer 2

^{1}H NMR (599 MHz, CD_2Cl_2, 30 °C) δ = 8.17 – 8.15 (m, 2H, H-C(14) and H-C(41)), 8.10 – 8.06 (m, 2H, H-C(16) and H-C(17)), 7.48 (t, *J* = 7.9 Hz, 1H, H-C(6)), 7.42 (t, *J* = 7.9 Hz, 1H, H-C(21)), 7.32 – 7.29 (m, 2H, H-C(24) and H-C(20)), 7.06 (d, *J* = 8.4 Hz, 1H, H-C(7)), 7.00 – 6.97 (m, 2H, H-C(5) and H-C(22)), 5.54 (s, 2H, H-C(43)), 4.55 – 4.46 (m, 2H, H-C(40)), 4.25 – 4.22 (m, 2H, H-C(25)), 3.87 (dd, *J* = 5.5, 3.9 Hz, 2H, H-C(26)), 3.80 (ddt, *J* = 15.7, 10.2, 5.3 Hz, 2H, H-C(39)), 3.70 (dd, *J* = 5.8, 3.1 Hz, 2H, H-C(27)), 3.63 (dd, *J* = 5.8, 3.2 Hz, 2H, H-C(28)), 3.61 – 3.44 (m, 20H, H-C(29) to H-C(38)), 3.18 (d, *J* = 15.9 Hz, 1H, H-C(3)), 2.86 (d, *J* = 15.9 Hz, 1H, H-C(3)), 1.54 – 1.53 (m, 6H, H-C(10)).

^{13}C NMR (201 MHz, CD_2Cl_2, 25 °C) δ = 185.08 (C-12), 170.84 (C-1), 160.05 (C-23), 156.81 (C-8), 152.25 (C-4), 149.42 (C-18), 145.40 (C-15), 143.43 (C-42), 140.99 (C-19), 136.94 (C-13), 135.58 (C-6), 134.74 (C-16 or C-17), 130.76 (C-21), 127.32 (C-16 or C-17), 126.07 (C-9), 125.70 (C-41), 123.11 (C-14), 120.38 (C-20), 118.40 (C-5), 115.01 (C-22), 114.67 (C-24), 111.01 (C-7), 71.42 (C-27), 71.21 (C-28), 71.19 (C-29 to C-38), 71.09 (C-29 to C-38), 71.04 (C-29 to C-38), 71.01 (C-29 to C-38), 70.98 (C-29 to C-38), 70.23 (C-26), 69.88 (C-39), 68.40 (C-25), 62.90 (C-43), 52.74 (C-2), 51.04 (C-40), 50.89 (C-3), 28.46 (C-10), 25.76 (C-10). C-11 could not be assigned

HR-MS (ESI$^+$) calc. for [M+H] [$C_{44}H_{53}N_3NaO_{11}S^+$]: 854.3299, found: 854.3291.

Compound 151

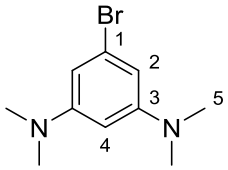

[243.148]

$C_{10}H_{15}BrN_2$

An excess of $NaBH_4$ (2.00 g, 52.9 mmol, ca. 20 eq) was added to a solution of 5-bromobenzene-1,3-diamine (500 mg, 2.67 mmol, 1.0 eq) in THF (21.0 mL). The mixture was stirred vigorously to obtain a homogenous suspension. In another flask formaldehyde (25 wt. % in water, 9.05 mL) and 3 M H_2SO_4 (15.0 mL) were cooled to –15 °C using an ice/sodium chloride cooling bath and the suspension containing 5-Bromobenzene-1,3-diamine was added dropwise using a glass pasteur pipette with a broken off tip. The reaction mixture was allowed to warm to 23 °C and stirred for 3 h. The suspension was diluted with THF (21.0 mL) and NaOH (33% w/w) was added until a pH of 10 was reached. Water (60 mL) was added and the mixture was extracted with EtOAc. The combined organic phases were washed with brine, dried over Na_2SO_4, filtered and the solvent was removed *in vacuo*. After purification by flash column chromatography (SiO_2, *i*-Hex:EtOAc = 19:1) compound **151** (512 mg, 2.11 mmol, 79%) was obtained as a brown liquid.

^{1}H NMR (200 MHz, $CDCl_3$, 23 °C) δ = 6.28 (d, *J* = 2.2 Hz, 2H, H-C(2)), 5.90 (t, *J* = 2.2 Hz, 1H, H-C(4)), 2.93 (s, 12H, H-C(5)).

Compound 152

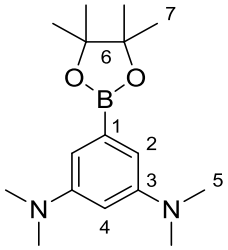

[290.214]

$C_{16}H_{27}BN_2O_2$

Compound **151** (512 mg, 2.11 mmol, 1.0 eq), 4,4,4',4',5,5,5',5'-octamethyl-2,2'-bi-(1,3,2-dioxaborolane) (802 mg, 3.16 mmol, 1.5 eq), KOAc (620 mg, 6.32 mmol, 3.0 eq) and

Pd(dppf)Cl_2 (172 mg, 0.21 mmol, 10 mol%) were dissolved in dioxane (18.4 mL) and stirred for 16 h at 85 °C. The reaction was quenched with a saturated NH_4Cl-solution (50 mL) and the mixture was extracted with EtOAc (3 x 50 mL). The combined organic phases were dried over Na_2SO_4, filtered and the solvent was removed in vacuo. The crude product was purified by flash column chromatography (SiO_2, i-Hex:EtOAc = 85:15) yielding compound **152** (587 mg, 2.02 mmol, 96%) as a colorless solid that slowly turns pale pink.

^{1}H NMR (200 MHz, $CDCl_3$, 23 °C) δ = 6.66 (d, *J* = 2.3 Hz, 2H, H-C(2)), 6.24 (t, *J* = 2.3 Hz, 1H, H-C(4)), 2.95 (s, 12H, H-C(5)), 1.33 (s, 12H, H-C(7)).

Compound 154

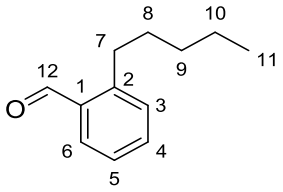

[176.259]

$C_{12}H_{16}O$

N^1,N^1,N^2-trimethylethylene-1,2-diamine (579 µL, 455 mg, 4.45 mmol, 1.07 eq) was dissolved in THF (11.0 mL). *n*-BuLi (1.71 mL, 4.29 mmol, 2.5 M in *n*-Hexan, 1.03 eq) was added at –20 °C and the solution was stirred for 15 min. 2-Methylbenzaldehyde (481 µL, 500 mg, 4.16 mmol, 1.0 eq) was dissolved in THF (2 mL), added to the reaction mixture and stirred for 15 min. *n*-BuLi (4.99 mL, 12.5 mmol, 2.5 M in *n*-Hexan, 3.0 eq) was added dropwise at –20 °C and stirred for 1.5 h. The solution was cooled down to –42 °C and iodobutane (2.84 mL, 4.59 g, 25.0 mmol, 6.0 eq) was added. After stirring for 1 d at 23 °C, the reaction was quenched with a saturated NH_4Cl-solution (50 mL) and extracted with EtOAc (3 x 50 mL). The combined organic phases were dried over Na_2SO_4, filtered and the solvent was removed *in vacuo*. The crude product was purified by flash column chromatography (SiO_2, *i*-Hex) yielding compound **154** (564 mg, 3.20 mmol, 77%) as a colourless oil.

^{1}H NMR (200 MHz, $CDCl_3$, 23 °C) δ = 10.30 (s, 1H), 7.83 (dd, *J* = 7.6, 1.6 Hz, 1H), 7.50 (td, *J* = 7.5, 1.6 Hz, 1H), 7.37 (dd, *J* = 7.5, 1.4 Hz, 1H), 7.32 – 7.20 (m, 1H), 3.08 – 2.94 (m, 2H), 1.71 – 1.51 (m, 2H), 1.36 (dq, *J* = 7.2, 3.8 Hz, 4H), 0.98 – 0.82 (m, 3H).

Compound 155

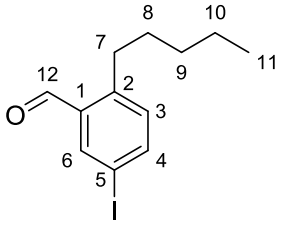

[302.155]

$C_{12}H_{15}IO$

Compound **154** (564 mg, 3.20 mmol, 1.0 eq), I_2 (812 mg, 3.20 mmol, 1.0 eq) and selectfluor (1-chloromethyl-4-fluoro-1,4-diazoniabicyclo[2.2.2]octane bis(tetrafluoro-borate)) (1.13 g, 3.20 mmol, 1.0 eq) were dissolved in acetonitrile (7.4 mL) and stirred for 3 d at 40 °C. The reaction was stopped by addition of a saturated NH_4Cl-solution (50 mL) and extracted with EtOAc (3 x 50 mL). The combined organic phases were washed with sodium bisulfite solution (2 x 30 mL) and brine (2 x 50 mL), dried over Na_2SO_4, filtered and the solvent was removed *in vacuo* yielding crude compound **155** (944 mg, 3.12 mmol, 98%) as a brownish oil. Because of its high tendency to decompose the product was used without further purification in the next synthetic step.

^{1}H NMR (400 MHz, $CDCl_3$, 22 °C) δ = 10.19 (d, *J* = 2.1 Hz, 1H, H-C(12)), 8.12 (d, *J* = 2.0 Hz, 1H, H-C(6)), 7.79 (dd, *J* = 8.1, 2.0 Hz, 1H, H-C(4)), 7.02 (d, *J* = 8.1 Hz, 1H, H-C(3)), 2.98 – 2.91 (m, 2H, H-C(7)), 1.63 – 1.52 (m, 2H, H-C(8)), 1.37 – 1.29 (m, 4H, H-C(9) and H-C(10)), 0.92 – 0.84 (m, 3H, H-C(11)).

^{13}C NMR (101 MHz, $CDCl_3$, 22 °C) δ = 190.69 (C-12), 145.37 (C-2), 142.51 (C-4), 139.65 (C-6), 135.32 (C-1), 133.02 (C-3), 32.13 (C-8), 32.04 (C-7), 31.68 (C-9 or C-10), 22.59 (C-9 or C-10), 14.11 (C-11).

Compound 156

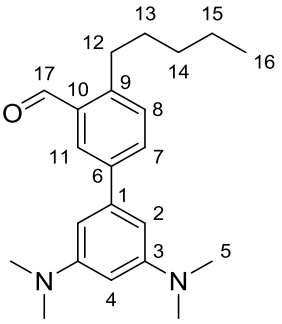

[338.495]

$C_{22}H_{30}N_2O$

Compound **152** (587 mg, 2.02 mmol, 1.0 eq), **155** (611 mg, 2.02 mmol, 1.0 eq), K_2CO_3 (839 mg, 6.07 mmol, 3.0 eq) and $Pd(PPh_3)_4$ (70.1 mg, 60.7 µmol, 3 mol%) were dissolved in diglyme/H_2O (2:1, 16.2 mL). The reaction mixture was stirred for 1 d at 85 °C. The reaction was stopped by addition of a saturated NH_4Cl-solution (50 mL) and extracted with EtOAc (3 x 50 mL). The combined organic phases were washed with water (2 x 50 mL) and brine (2 x 50 mL), dried over Na_2SO_4, filtered and the solvent was removed *in vacuo*. The crude product was purified by flash column chromatography (SiO_2, *i*-Hex:EtOAc = 19:1) yielding compound **156** (368 mg, 1.09 mmol, 54%) as a yellow oil.

^{1}H NMR (200 MHz, $CDCl_3$, 23 °C) δ = 10.35 (s, 1H, H-C(17)), 8.06 (d, *J* = 2.1 Hz, 1H, H-C(11)), 7.74 (dd, *J* = 7.9, 2.1 Hz, 1H, H-C(7)), 7.31 (d, *J* = 7.9 Hz, 1H, H-C(8)), 6.37 (d, *J* = 2.2 Hz, 2H, H-C(2)), 6.12 (t, *J* = 2.2 Hz, 1H, H-C(4)), 3.10 – 2.95 (m, 14H, H-C(5) and H-C(12)), 1.75 – 1.57 (m, 2H, H-C(13)), 1.46 – 1.32 (m, 4H, H-C(14) and H-C(15)), 0.98 – 0.85 (m, 3H, H-C(16)).

Compound 158

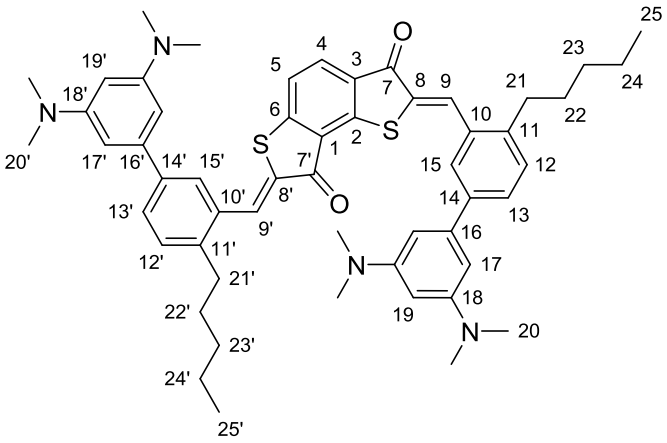

[863.236]

$C_{54}H_{62}N_4O_2S_2$

Compound **156** (100 mg, 295 µmol, 2.0 eq) and bis-benzothiophenone **157** (34 mg, 148 µmol, 1.0 eq, provided by *Manuel Güntner*) were dissolved in toluene (1.2 mL). One drop of piperidine was added and the solution was stirred at 23 °C for 2 h followed by 1 h at 40 °C before the reaction was stopped by addition of a saturated NH_4Cl-solution (50 mL). The mixture was extracted with EtOAc (3 x 50 mL). The combined organic phases were washed with brine (2 x 50 mL), dried over Na_2SO_4, filtered and the solvent was removed in vacuo. The crude product was purified by flash column chromatography (SiO_2, *i*-Hex:EtOAc = 8:2) to give 49 mg of compound **158**. 22 mg (65.0 µmol) of compound **156** could be recovered. The crude product was suspended in heptane and heated under reflux. EtOAc was added dropwise until a clear solution was obtained. Compound **158** precipitated as a red solid upon cooling (26 mg, 42% based on recovered **156**).

^{1}H NMR (800 MHz, toluene-d_8, 25 °C) δ = 8.57 – 8.56 (m, 2H, H-C(9) and H-C(15)), 8.38 (s, 1H, H-C(9')), 8.28 (d, *J* = 1.8 Hz, 1H, H-C(15')), 7.68 (dd, *J* = 7.8, 1.8 Hz, 1H, H-C(13)), 7.65 – 7.63 (m, 2H, H-C(4) and H-C(13')), 7.14 – 7.12 (m, 2H, H-C(12) and H-C(12')), 6.83 (d, *J* = 2.1 Hz, 2H, H-C(17)), 6.62 (d, *J* = 2.1 Hz, 2H, H-C(17')), 6.48 (d, *J* = 7.9 Hz, 1H, H-C(5)), 6.15 (t, *J* = 2.2 Hz, 1H, H-C(19)), 6.11 (t, *J* = 2.2 Hz, 1H, H-C(19')), 2.97 (s, 12H, H-C(20)), 2.79 (s, 12H, H-C(20')), 2.72 – 2.68 (m, 4H, H-C(21) and H-C(21')), 1.63 – 1.56 (m, 4H, H-C(22) and H-C(22')), 1.36 – 1.24 (m, 8H, H-C(23), H-C(23'), H-C(24) and H-C(24')), 0.92 – 0.85 (m, 6H, H-C(25) and H-C(25')).

^{13}C NMR (201 MHz, toluene-d_8, 25 °C) δ = 185.67 (C-7'), 185.32 (C-7), 153.83 (C-2 or C-6), 152.24 (C-18), 152.14 (C-18'), 148.05 (C-2 or C-6), 142.95 (C-11'), 142.83 (C-11), 142.28 (C-

14 or C-14'), 142.01 (C-14 or C-14'), 141.91 (C-16'), 141.51 (C-16), 132.91 (C-10 or C-10'), 132.71 (C-10 or C-10'), 132.42 (C-9), 132.19 (C-8), 131.50 (C-9'), 131.37 (C-8'), 131.15 (C-4), 130.40 (C-12 or C-12'), 130.32 (C-12 or C-12'), 129.49 (C-1 or C-3), 129.27 (C-13'), 128.78 (C-13), 128.53 (C-15), 128.04 (C-15'), 125.27 (C-1 or C-3), 119.74 (C-5), 101.90 (C17 and C17'), 97.20 (C-19), 97.10 (C-19'), 40.54 (C-20), 40.25 (C-20'), 33.34 (C-21 or C-21'), 33.17 (C-21 or C-21'), 31.79 (C-23 or C-23'), 31.63 (C-22 or C-22'), 31.57 (C-23 or C-23'), 31.50 (C-22 or C-22')), 22.56 (C-24 or C-24'), 22.54 (C-24 or C-24'), 13.95 (C-25 or C-25'), 13.88 (C-25 or C-25').

HR-MS (EI^+), $[M]^+$ calc. for $[C_{54}H_{62}N_4O_2S_2]^+$: 862.4314, found: 862.4307.

Compound 159

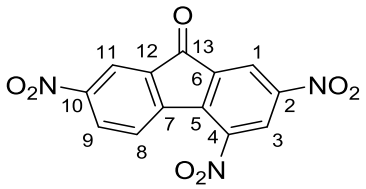

[315.197]

$C_{13}H_5N_3O_7$

In an ice cooled 50 mL round-bottom flask nitric acid (95%, 112 mmol, 4.67 mL, 11.2 eq) was slowly treated with sulfuric acid (95 – 98%, 90.0 mmol, 4.88 mL, 9.0 eq). In a 100 mL round-bottom flask 9-fluorenone (1.80 g, 10.0 mmol, 1.0 eq) in 2 mL H_2O was heated to 80 °C. The sulphonitric acid was added dropwise and the mixture was stirred at reflux for 2 h. The reaction was quenched with 40 mL H_2O and the precipitate was filtered off, washed with 2 M NaOH (2 x 20 mL) and an excess of water. The crude product (a mixture of 2,7-dinitro-9*H*-fluoren-9-one and 2,4,7-dinitro-9*H*-fluoren-9-one) was purified by flash column chromatography (*i*-Hex/EtOAc 85/15) yielding **159** (410 mg, 1.30 mmol, 13%) as a pale yellow solid.

^{1}H NMR (400 MHz, $CDCl_3$) δ = 9.03 (d, *J* = 2.0 Hz, 1H, H-C(3)), 8.83 (d, *J* = 2.1 Hz, 1H, H-C(1)), 8.68 (d, *J* = 2.3 Hz, 1H, H-C(11)), 8.58 (dd, *J* = 8.6, 2.3 Hz, 1H, H-C(9)), 8.37 (d, *J* = 8.6 Hz, 1H, H-C(8)).

^{13}C NMR (101 MHz, $CDCl_3$) δ = 186.08 (C-13), 150.46 (C-10 or C-12), 149.38 (C-2 or C-4 or C-6), 145.28 (C-2 or C-4 or C-6), 143.49 (C-7), 139.62 (C-5), 138.56 (C-2 or C-4 or C-6), 136.45 (C-10 or C-12), 130.91 (C-9), 128.34 (C-8), 125.98 (C-3), 123.15 (C-1), 120.35 (C-11)

HR-MS (EI^+), [M] calc. for [$C_{13}H_5N_3O_7$]: 315.0127, found: 315.0126.

Compound 160

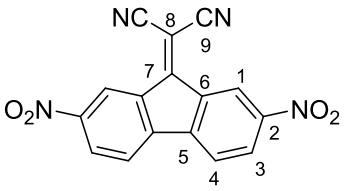

[318.248]

$C_{16}H_6N_4O_4$

In a 100 mL round-bottom flask 2,7-dinitro-9*H*-fluoren-9-one (1.00 g, 3.70 mmol, 1.0 eq) was dissolved in DMF at 70 °C. Malonitrile (626 mg, 9.47 mmol, 2.56 eq) was added and the mixture was stirred for 2.5 h at 70 °C. The product was filtered off and washed with DMF (1 mL) and an excess of EtOH. Compound **160** (1.08 g, 3.40 mmol, 92%) was obtained as a yellow solid.

^{1}H NMR (800 MHz, CD_2Cl_2) δ = 9.32 (dd, *J* = 2.0, 0.6 Hz, 2H, H-C(1)), 8.54 (dd, *J* = 8.3, 1.9 Hz, 2H, H-C(3)), 7.97 (dd, *J* = 8.3, 0.5 Hz, 2H, H-C(4)).

^{13}C NMR (201 MHz, CD_2Cl_2) δ = 157.16 (C-7), 149.92 (C-6), 145.48 (C-5), 136.25 (C-2), 130.60 (C-3), 123.35 (C-4), 122.50 (C-1), 112.64 (C-9), 81.91 (C-8).

HR-MS (ESI^-), [M] calc. for [$C_{16}H_6N_4O_4$]: 318.0389, found: 318.0394.

Compound 161

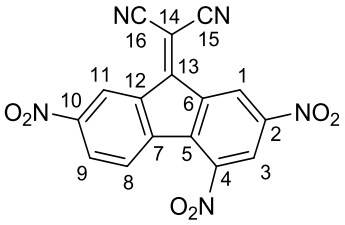

[363.245]

$C_{16}H_5N_5O_6$

In a 50 mL round-bottom compound **159** (100 mg, 317 µmol, 1.0 eq) was dissolved in DMF at 60 °C. Malonitrile (46 mg, 0.70 mmol, 2.2 eq) was added and the mixture was stirred for 2 h at 60 °C. Then 2-propanol (2 mL) was added and the reaction mixture was stored overnight at

0 °C. The crude product was filtered off and washed with an excess of EtOH. Compound **161** (99 mg, 0.27 mmol, 86%) was obtained as a green to yellow solid.

^{1}H NMR (800 MHz, CD_2Cl_2) δ = 9.64 (d, *J* = 1.9 Hz, 1H, H-C(1)), 9.45 (dd, *J* = 2.1, 0.5 Hz, 1H, H-C(11)), 8.95 (d, *J* = 1.9 Hz, 1H, H-C(3)), 8.56 (dd, *J* = 8.7, 2.1 Hz, 1H, H-C(9)), 8.23 (dd, *J* = 8.7, 0.5 Hz, 1H, H-C(8)).

^{13}C NMR (201 MHz, CD_2Cl_2) δ = 154.52 (C-11), 150.41 (C-10 or C-12), 149.07 (C-2 or C-4 or C-6), 146.06 (C-2 or C-4 or C-6), 140.96 (C-7), 139.06 (C-2 or C-4 or C-6), 137.24 (C-5), 136.96 (C-10 or C-12), 130.73 (C-9), 128.19 (C-8), 125.57 (C-3), 124.81 (C-1), 122.17 (C-11), 112.45 (C-15 or C-16), 112.30 (C-15 or C-16), 83.75 (C-12).

HR-MS (ESI^-), [M] calc. for [$C_{16}H_5N_5O_6$]: 363.0240, found: 363.0246.

Compound 162

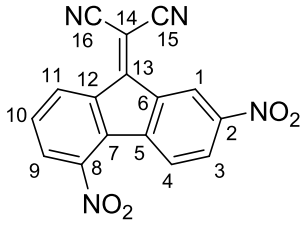

[318.248]

$C_{16}H_6N_4O_4$

In a 50 mL round-bottom flask 2,5-dinitro-9*H*-fluoren-9-one (50 mg, 185 µmol, 1.0 eq) was dissolved in DMF at 65 °C. Malonitrile (27 mg, 0.41 mmol, 2.2 eq) was added and the mixture was stirred for 5 h at 65 °C. The reaction mixture was stored at 0 °C overnight. The crude product was filtered off and washed with DMF (1 mL) and an excess of EtOH. Compound **162** (19 mg, 60 µmol, 32%) was obtained as an orange solid.

^{1}H NMR (800 MHz, CD_2Cl_2) δ = 9.37 (dd, *J* = 2.1, 0.5 Hz, 1H, H-C(1)), 8.84 (dd, *J* = 7.9, 0.9 Hz, 1H, H-C(11)), 8.46 (dd, *J* = 8.6, 2.1 Hz, 1H, H-C(3)), 8.09 (dd, *J* = 8.6, 0.5 Hz, 1H, H-C(4)), 8.08 (dd, *J* = 8.2, 0.9 Hz, 1H, H-C(9)), 7.71 (t, *J* = 8.0 Hz, 1H, H-C(10)).

^{13}C NMR (201 MHz, CD_2Cl2) δ 156.75 (C-13), 149.49 (C-2 or C-6), 146.63 (C-8 or C-12), 143.12 (C-5), 137.90 (C-8 or C-12), 136.03 (C-2 or C-6), 132.57 (C-7), 132.15 (C-10), 130.95 (C-11), 130.44 (C-9), 130.32 (C-3), 126.73 (C-4), 121.85 (C-1), 113.01 (C-15 or C-16), 112.90 (C-15 or C-16), 81.39 (C-14).

IR: 3087.0 (vw), 1606.0 (w), 1569.9 (w), 1530.9 (m), 1518.1 (s), 1455.7 (w), 1360.6 (m), 1348.1 (s), 1311.6 (m), 1288.1 (w), 1177.5 (w), 1089.0 (w), 905.8 (w), 856.8 (m), 844.2 (m), 814.2 (w), 765.9 (m), 737.7 (m), 725.5 (s).

HR-MS (ESI^-), [M] calc. for [$C_{16}H_5N_5O_6$]: 318.0389, found: 318.0394.

EA calc.: C: 60.39; H, 1.90; N, 17.61; found: C: 60.25; H: 2.15; N: 17.34.

Compound 163

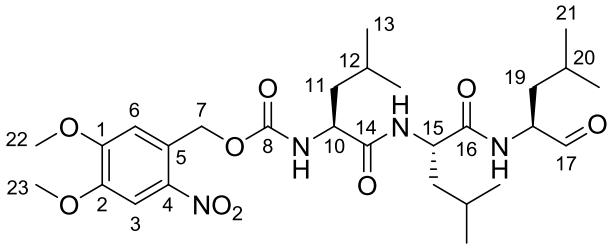

[580.679]

$C_{28}H_{44}N_4O_9$

NVOC-Leu-Leu-Leucinol **168** (364 mg, 625 µmol, 1.0 eq) in DMSO (4.4 mL) was treated with IBX (350 mg, 1.25 mmol, 2.0 eq) and stirred for 20 h at 23 °C. The reaction mixture was transferred to a separatory funnel that was charged with saturated $NaHCO_3$ and extracted with EtOAc. The combined organic phases were washed with brine, dried over Na_2SO_4, filtered and the solvent was evaporated *in vacuo*. After flash column chromatography (SiO_2, *i*-Hex:EtOAc = 3:2) compound **163** (149 mg, 257 µmol, 41%) was obtained as an off-white solid.

Attribution of NMR signals was not possible due to overlap and missing 2D signals.

^{1}H NMR (599 MHz, CD_3OD) δ = 7.73 (s, 1H, H-C(3)), 7.08 (s, 1H, H-C(6)), 5.66 (d, *J* = 15.3 Hz, 1H), 5.52 (d, *J* = 15.0 Hz, 1H), 4.87 (d, *J* = 8.5 Hz, 1H, H-C(15)), 4.40 (td, *J* = 9.1, 5.5 Hz, 1H, H-C(10)), 4.03 (s, 3H, H-C(22)), 3.96 (s, 3H, H-C(23)), 1.78 – 1.71 (m, 1H, H-C(12)), 1.66 (ddd, *J* = 13.7, 8.2, 5.5 Hz, 1H, H-C(11)), 1.61 – 1.52 (m, 3H, H-C(11)), 1.42 (d, *J* = 1.6 Hz, 9H), 0.97 (dd, *J* = 6.5, 1.9 Hz, 6H, H-C(13)).

^{13}C NMR (151 MHz, CD_3OD, 27 °C) δ = 173.38 (C-8), 155.70 (C-14), 154.01 (C-1), 148.27 (C-2), 139.66 (C-4 or C-5), 127.47 (C-4 or C-5)), 109.99 (C-6), 108.28 (C-3), 80.20, 63.96, 56.79, 56.56, 52.49, 41.59 (C-11), 28.45, 25.04 (C-12), 23.00 (C-13), 22.00 (C-13).

HR-MS (ESI^+), [M] calc. for [$C_{28}H_{45}N_4O_9$]: 581.3187, found: 581.3191.

Compound 164

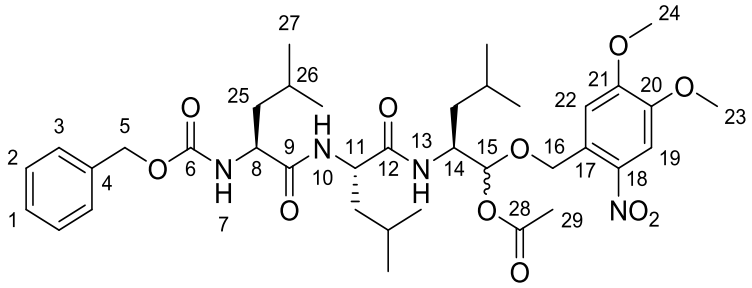

[730.856]

$C_{37}H_{54}N_4O_{11}$

Compound **173** (222 mg, 323 mmol, 1.0 eq) in CH_2Cl_2 (2.0 mL) was cooled to –78 °C and DIBAL-H (1 M in hexanes, 646 µL, 646 µmol, 2.0 eq) was added dropwise. 45 min after complete addition pyridine (76.7 mg, 970 µmol, 3.0 eq), DMAP solution (26.0 mg, 213 µmol, 0.66 eq in 1.0 mL CH_2Cl_2) and acetic anhydride (198 mg, 1.94 mmol, 6.0 eq) were added. The reaction mixture was stirred for another 20 h at –78 °C before it was warmed to 0 °C. After another 35 min the reaction was stopped by addition of saturated ammonium chloride solution and saturated Rochelle salt solution. The mixture was stirred for 50 min at 23 °C and then extracted with CH_2Cl_2. The combined organic phases were washed with ice cold 1 M potassium bisulfate solution, saturated sodium bicarbonate solution and brine. The organic phase was dried over Na_2SO_4, filtered and the solvent was evaporated *in vacuo*. After flash column chromatography (SiO_2, *i*-Hex:EtOac = 3:1) compound **164** (mixture of diastereomers (6:4), 40 mg, 54.7 µmol, 17%) was obtained as an off-white solid.

NMR stereomeric mixture 6:4

^{1}H NMR (800 MHz, CD_2Cl_2, 27 °C) δ = 7.68 (s, 1H, H-C(19)), 7.38 – 7.31 (m, 5H, H-C(1) to H-C(3)), 7.27 (s, 1H, H-C(22)), 7.21 (s, 1H, H-C(22)), 6.32 – 6.25 (m, 2H, H-N(10) and H-N(13)), 5.90 (d, *J* = 3.6 Hz, 1H, H-C(15)), 5.87 (d, *J* = 3.2 Hz, 1H, H-C(15)), 5.15 – 4.98 (m, 5H, H-C(5), H-N(7) and H-C(16)), 4.36 – 4.29 (m, 2H, H-C(11) and H-C(14)), 4.10 – 4.03 (m, 1H, H-C(8)), 3.99 (s, 3H, H-C(24)), 3.91 (s, 2H, H-C(23)), 3.90 (s, 1H, H-C(24)), 2.09 (s, 1H, H-C(29)), 2.05 (s, 2H, H-C(29)), 1.73 – 1.40 (m, 9H, H-C(25) and H-C(26)), 0.95 – 0.83 (m, 18H, H-C(27)).

^{13}C NMR (201 MHz, CD_2Cl_2, 27 °C) δ = 172.52 (C-9), 171.97 (C-12), 171.15 (C-28), 154.52 (C-21), 154.39 (C-21), 148.63 (C-20), 139.94 (C-18), 136.88 (C-4), 129.49 (C-17), 129.09 (C-2), 128.80 (C-1), 128.53 (C-3), 128.50 (C-3), 110.75 (C-22), 110.68 (C-22), 108.60 (C-19),

108.49 (C-19), 97.93 (C-15), 97.82 (C-15), 69.38 (C-16), 69.14 (C-16), 67.67 (C-5), 57.02 (C-24), 56.94 (C-24), 56.84 (C-23), 56.81 (C-23), 52.59 (C-11 or C-14), 52.48 (C-11 or C-14), 50.37 (C-11 or C-14), 50.12 (C-11 or C-14), 41.66 (C-25), 41.06 (C-25), 40.93 (C-25), 39.06 (C-25), 39.01 (C-25), 25.32 (C-26), 25.28 (C-26), 25.11 (C-26), 25.01 (C-26), 23.87 (C-27), 23.76 (C-27), 23.26 (C-27), 23.23 (C-27), 23.11 (C-27), 22.26 (C-27), 22.13 (C-27), 22.09 (C-27), 22.00 (C-27), 21.91 (C-27), 21.38 (C-29).

HR-MS (ESI$^+$), $[M+NH_4]^+$ calc. for $[C_{35}H_{54}N_5O_{10}]$: 748.4127 found: 748.4134.

Compound 165

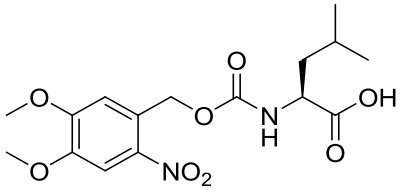

[370.358]

$C_{16}H_{22}N_2O_8$

Leucin (131 mg, 1.00 mmol, 1.0 eq) was suspended in aqueous 2 M NaOH (0.50 mL) and cooled to 0 °C. A solution of 4,5-dimethoxy-2-nitrobenzyl chloroformate (331 mg, 1.20 mmol, 1.2 eq) in dioxane/CH_2Cl_2 (0.50 mL/2.0 mL) and additional 2 M NaOH (0.55 mL) were added alternatingly in a total of ten portions each. The mixture was allowed to warm to 23 °C and stirred for 1 d before it was transferred to a separatory funnel charged with water. The organic layer was removed and the aqueous layer was acidified with aqueous 5 M HCl. After extraction of with EtOAc the combined organic phases were dried over Na_2SO_4, filtered and the solvent was evaporated *in vacuo*. After flash column chromatography (SiO_2, CH_2Cl_2:MeOH = 97:3) compound **165** (232 mg, 626 mmol, 63%) was obtained as a yellow solid.

^{1}H NMR (200 MHz, $CDCl_3$, 23 °C) δ = 7.71 (s, 1H), 6.99 (s, 1H), 5.66 – 5.42 (m, 2H), 5.28 (d, *J* = 8.7 Hz, 1H), 4.49 – 4.32 (m, 1H), 3.97 (s, 3H), 3.95 (s, 3H), 1.66 (m, 3H), 0.97 (d, *J* = 5.9 Hz, 6H).

Compound 166

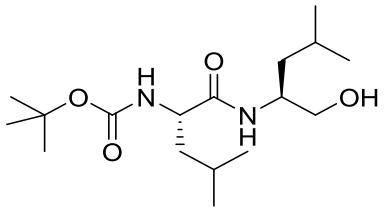

[330.469]

$C_{17}H_{34}N_2O_4$

Boc-Leu-OH (1.16 g, 5.00 mmol, 1.0 eq) in THF (10.0 mL) was cooled to 0 °C, then HOBt · H_2O (842 mg, 5.5 mmol, 1.1 eq) and DCC (1.13 g, 5.5 mmol, 1.1 eq) were added. Leucinol (586 mg, 5.0 mmol, 1.0 eq) was added dropwise and the solution was allowed to warm to 23 °C. After stirring for 1 d the reaction mixture was transferred to a separatory funnel that was charged with 10% citric acid and extracted with EtOAc. The combined organic phases were washed with saturated $NaHCO_3$ solution and brine, dried over Na_2SO_4, filtered and the solvent was evaporated *in vacuo*. After flash column chromatography (SiO_2, CH_2Cl_2:MeOH = 98:2) compound **166** (747 mg, 2.26 mmol, 45%) was obtained as a colorless solid. Further purification by recrystallization from heptane/EtOH afforded compound **116** (386 mg, 1.17 mmol, 23%) as a cottonlike, colorless solid.

^{1}H NMR (400 MHz, CD_2Cl_2, 22 °C) δ = 6.19 (d, *J* = 8.4 Hz, 1H), 4.96 (d, *J* = 6.8 Hz, 1H), 4.04 – 3.92 (m, 2H), 3.60 (ddd, *J* = 11.1, 6.8, 3.7 Hz, 1H), 3.44 (dd, *J* = 11.0, 5.5 Hz, 1H), 2.72 (dd, *J* = 6.8, 5.1 Hz, 1H), 1.68 – 1.55 (m, 2H), 1.43 (s, 11H), 0.92 (ddd, *J* = 13.2, 8.2, 6.5 Hz, 12H).

Compound 168

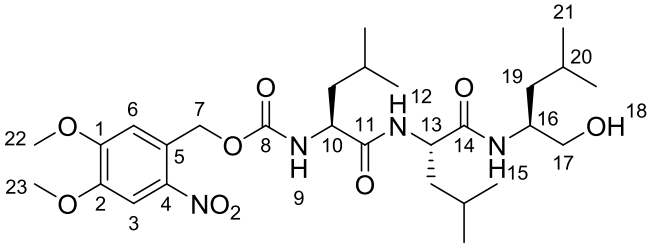

[582.695]

$C_{28}H_{46}N_4O_9$

NVOC-Leu (100 mg, 270 µmol, 1.0 eq) in THF (2.2 mL) was cooled to 0 °C, then HOBt · H_2O (45.5 mg, 297 µmol, 1.1 eq) and DCC (61.3 mg, 297 µmol, 1.1 eq) were added. The mixture

was stirred for 60 min, then TFA-Leu-Leucinol (93.0 mg, 270 µmol, 1.0 eq) and DIPEA (69.8 mg, 540 µmol, 2.0 eq) were added. After stirring for 16 h at 23 °C the reaction mixture was transferred to a separatory funnel that was charged with 10% citric acid and extracted with EtOAc. The combined organic phases were washed with saturated $NaHCO_3$ solution and brine. The combined organic phases were dried over Na_2SO_4, filtered and the solvent was evaporated *in vacuo*. Compound **168** (145 mg, 249 µmol, 92%) was obtained as a pale yellow solid.

Attribution of NMR signals was not possible due to overlap and missing 2D signals.

^{1}H NMR (800 MHz, CD_3OD, 27 °C) δ = 7.75 (s, 1H, H-C(3)), 7.19 (s, 1H, H-C(6)), 5.52 (d, *J* = 15.1 Hz, 1H, H-C(7)), 5.43 – 5.40 (d, *J* = 15.1 Hz, 1H, H-C(7)), 4.46 (dd, *J* = 9.9, 4.9 Hz, 1H), 4.38 (dd, *J* = 9.6, 5.5 Hz, 1H), 4.16 (dd, *J* = 8.8, 6.4 Hz, 1H), 3.99 – 3.93 (m, 4H, H-C(16) and H-C(22)), 3.91 (s, 3H, H-C(23)), 3.48 – 3.41 (m, 2H, H-C(17)), 1.75 – 1.54 (m, 5H, H-C(20)), 1.44 – 1.32 (m, 2H, H-C(19)), 0.98 – 0.85 (m, 18H, H-C(21)).

^{13}C NMR (201 MHz, CD_3OD, 27 °C) δ = 175.14, 174.18, 173.06, 158.09, 155.35 (C-1), 149.61 (C-2), 140.82 (C-4 or C-5)), 129.53 (C-4 or C-5), 111.08 (C-6), 109.33 (C-3), 65.52, 64.64 (C-7), 56.99, 56.82, 55.02, 53.80, 53.31, 50.83, 50.67, 41.96, 41.73, 41.44, 41.17, 41.05, 25.96, 25.92, 25.85, 25.77, 23.84, 23.75, 23.41, 22.27, 22.21, 22.02, 21.99, 21.91.

HR-MS (ESI^+), [M] calc. for [$C_{28}H_{47}N_4O_9$]: 583.3343, found: 583.3350.

Compound 169

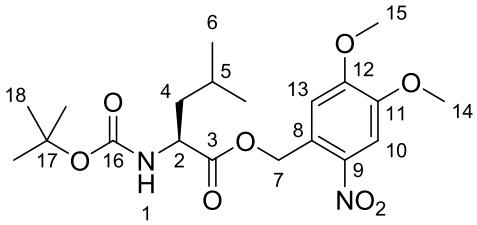

[426.466]

$C_{20}H_{30}N_2O_8$

Boc-Leu-OH (1.00 g, 4.32 mmol, 1.0 eq), 4,5-dimethoxy-2-nitrobenzyl alcohol (992 mg, 4.32 mmol, 1.0 eq), DCC (981 mg, 4.76 mmol, 1.1 eq) and DMAP (52.8 mg, 4.76 mmol, 0.1 eq) in CH_2Cl_2 (30 mL) were stirred for 20 h at 23 °C in the dark. The reaction mixture was filtered and partitioned between EtOAc and 10% citric acid and the aqueous phase was extracted with EtOAc. The combined organic phases were washed with saturated $NaHCO_3$ solution and brine, dried over Na_2SO_4, filtered and the solvent was evaporated *in vacuo*. After flash column

chromatography (SiO_2, *i*-Hex:EtOAc = 8:2) compound **169** (1.28 g, 3.00 mmol, 69%) was obtained as a yellow solid that crystallized under high vacuum.

^{1}H NMR (599 MHz, $CDCl_3$, 27 °C) δ = 7.73 (s, 1H, H-C(10)), 7.08 (s, 1H, H-C(13)), 5.66 (d, *J* = 15.3 Hz, 1H, H-C(7)), 5.52 (d, *J* = 15.0 Hz, 1H, H-C(7)), 4.87 (d, *J* = 8.5 Hz, 1H, H-N(1)), 4.40 (td, *J* = 9.1, 5.5 Hz, 1H, H-C(2)), 4.03 (s, 3H, H-C(15)), 3.96 (s, 3H, H-C(14)), 1.78 – 1.71 (m, 1H, H-C(5)), 1.66 (ddd, *J* = 13.7, 8.2, 5.5 Hz, 1H, H-C(4)), 1.61 – 1.51 (m, 1H, H-C(4)), 1.42 (d, *J* = 1.6 Hz, 9H, H-C(18)), 0.97 (m, 6H, H-C(6)).

^{13}C NMR (151 MHz, $CDCl_3$, 27 °C) δ = 173.38 (C-3), 155.70 (C-16), 154.01 (C-12), 148.27 (C-11), 139.66 (C-8), 127.47 (C-9), 109.99 (C-13), 108.28 (C-10), 80.20 (C-17), 63.96 (C-7), 56.79 (C-14), 56.56 (C-15), 52.49 (C-2), 41.59 (C-4), 28.45 (C-18), 25.04 (C-5), 23.00 (C-6), 22.00 (C-6).

IR: $\tilde{\nu}$ = 3450 (w), 2963 (w), 1747 (m), 1706 (s), 1522 (m), 1502 (s), 1325 (m), 1277 (m), 1226 (s), 1156 (vs), 1067 (m), 1051 (m), 987 (m), 887 (m), 853 (m), 796 (m), 757 (m).

HR-MS (ESI$^+$), $[M+NH_4]^+$ calc. for $[C_{20}H_{34}N_3O_8]$: 444.2340, found: 444.2349.
EA calc.: C: 56.33; H, 7.09; N, 6.57; found: C: 56.12; H: 7.09; N: 6.53.

Compound 170

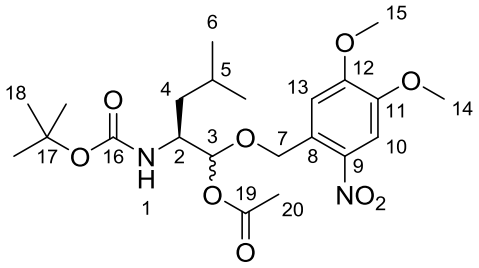

[470.519]

$C_{22}H_{34}N_2O_9$

In a flame dried Schlenk flask compound **169** (1.00 g, 2.35 mmol, 1.0 eq) was dissolved in CH_2Cl_2 (5.0 mL) under nitrogen. The solution was cooled to –78 °C and DIBAL-H (1 M in hexanes, 4.70 mL, 4.70 mmol, 2.0 eq) was added dropwise. After stirring for 45 min pyridine (7.20 mL, 7.07 mg, 8.94 mmol, 3.8 eq), DMAP (561 mg in 5 mL CH_2Cl_2, 4.59 mmol, 1.92 eq) and acetic anhydride (1.30 mL, 13.8 mmol, 6.0 eq) were added. The reaction mixture was stirred for another 20 h at –78 °C, warmed to 0 °C and after another 35 min the reaction was stopped

by addition of saturated ammonium chloride solution and saturated Rochelle salt solution. The mixture was stirred for 50 min at 23 °C and then extracted with CH_2Cl_2. The combined organic phases were washed with ice cold 1 M potassium bisulfate solution, saturated sodium bicarbonate solution and brine. The organic phase was dried over Na_2SO_4, filtered and the solvent was evaporated *in vacuo*. After flash column chromatography (SiO_2, *i*-Hex:EtOac = 3:7) compound **170** (mixture of diastereomers (1:1), 199 mg, 423 µmol, 18%) was obtained as a brown oil that crystallized within days.

Mixture of diastereomers

^{1}H NMR (800 MHz, CD_2Cl_2, 27 °C) δ = 7.68 (s, 2H, H-C(10)), 7.28 (s, 1H, H-C(13)), 7.20 (s, 1H, H-C(13)), 5.88 (d, *J* = 3.5 Hz, 1H, H-C(3)), 5.85 (d, *J* = 2.7 Hz, 1H, H-C(3)), 5.10 – 5.00 (m, 4H, H-C(7)), 4.62 – 4.57 (m, 2H, H-N(1)), 4.03 – 3.95 (m, 8H, H-C(2) and H-C(15)), 3.91 (m, 6H, H-C(14)), 2.07 (s, 3H, H-C(20)), 2.04 (s, 3H, H-C(20)), 1.71 – 1.67 (m, 2H, H-C(5)), 1.45 – 1.38 (m, 19H, H-C(4) and H-C(18)), 1.36 – 1.31 (m, 1H, H-C(4)), 0.96 – 0.91 (m, 12H, H-C(6)).

^{13}C NMR (151 MHz, $CDCl_3$, 27 °C) δ = 171.13 (C-19), 171.04 (C-19), 156.15 (C-16), 156.02 (C-16), 154.48 (C-12), 154.30 (C-12), 148.64 (C-11), 148.53 (C-11), 140.00 (C-9), 139.77 (C-9), 129.91 (C-8), 129.54 (C-8), 110.74 (C-13), 110.61 (C-13), 108.63 (C-10), 108.52 (C-10), 98.65 (C-3), 98.29 (C-3), 79.70 (C-17), 79.67 (C-17), 69.16 (C-7), 69.03 (C-7), 56.97 (C-15), 56.86 (C-15), 56.83 (C-14), 51.96 (C-2), 51.46 (C-2), 39.56 (C-4), 39.48 (C-4), 28.62 (C-18), 28.58 (C-18), 25.21 (C-5), 25.10 (C-5), 23.78 (C-6), 23.61 (C-6), 22.18 (C-6), 22.03 (C-6), 21.43 (C-20), 21.36 (C-20).

HR-MS (ESI$^+$), $[M+NH_4]^+$ calc. for $[C_{22}H_{38}N_3O_9]$: 488.2602, found: 488.2611.

Compound 171

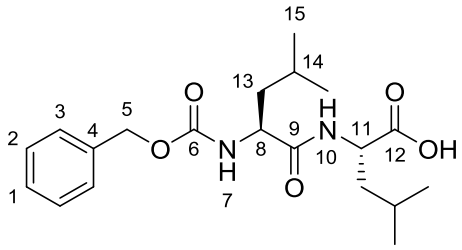

[378.469]

$C_{20}H_{30}N_2O_5$

A solution of *Z*-Leu-OH (2.80 g, 10.8 mmol, 1.0 eq) and Leu-OMe · HCl (1.96 g, 10.8 mmol, 1.0 eq) in CH_2Cl_2 (40 mL) was treated with PyBOP (5.60 g, 10.8 mmol, 1.0 eq) and DIPEA (3.65 mL, 21.5 mmol, 2.0 eq) and stirred for 4 h at 23 °C. The reaction mixture was extracted with aqueous 1 M HCl, saturated $NaHCO_3$ solution and brine. The organic phase was dried over Na_2SO_4, filtered and the solvent was evaporated *in vacuo*. After flash column chromatography (SiO_2, CH_2Cl_2:MeOH = 97:3) and (SiO_2, *i*-Hex:EtOAc = 7:3) *Z*-Leu-Leu-OMe (3.14 g, 8.00 mmol, 74%) was obtained as a colorless oil that was used directly in next synthetic step.

To a solution of *Z*-Leu-Leu-OMe (3.12 g, 7.95 mmol, 1.0 eq) in 1,4-dioxane (30 mL) and methanol (10 mL) was added sodium hydroxide (420 mg, 10.5 mmol, 1.32 eq) as aqueous 4 M solution. After stirring for 4 h at 23 °C the reaction mixture was acidified to pH 2 using aqueous 1 M HCl and concentrated *in vacuo*. The residue was taken up in EtOAc. The organic phase was extracted with water and brine, dried over Na_2SO_4, filtered and the solvent was evaporated *in vacuo*. After recrystallization from *i*-Hex/EtOAc compound **171** (2.32 g, 6.12 mmol, 77%, 57% over two steps) was obtained as a colorless solid.

^{1}H NMR (599 MHz, $CDCl_3$, 27 °C) δ = 7.36 – 7.28 (m, 5H, H-C(1), H-C(2) and H-C(3)), 6.86 (d, *J* = 8.2 Hz, 1H, H-N(10)), 5.73 (d, *J* = 8.7 Hz, 1H, H-N(7)), 5.09 (s, 2H, H-C(5)), 4.59 (td, *J* = 8.6, 4.6 Hz, 1H, H-C(11)), 4.32 – 4.26 (m, 1H, H-C(8)), 1.73 – 1.47 (m, 6H, H-C(13) and H-C(14)), 0.94 – 0.85 (m, 12H, H-C(15)).

^{13}C NMR (151 MHz, $CDCl_3$, 27 °C) δ = 176.00 (C-12), 172.88 (C-9), 156.63 (C-6), 136.21 (C-4), 128.66 (C-2), 128.33 (C-1), 128.07 (C-3), 67.29 (C-5), 53.54 (C-8), 50.96 (C-11), 41.27 (C-13), 24.94 (C-14), 24.70 (C-14), 22.92 (C-15), 22.23 (C-15), 21.96 (C-15).

IR: $\tilde{\nu}$ = 3298 (w), 2957 (m), 2871 (w), 1700 (vs), 1637 (vs), 1536 (s), 1232 (s), 1211 (s), 1151 (m), 1042 (s), 1028 (m), 736 (m), 695 (s).

HR-MS (ESI$^+$), $[M+H]^+$ calc. for $[C_{20}H_{31}N_2O_5]$: 379.2227, found: 379.2229.

Compound 173

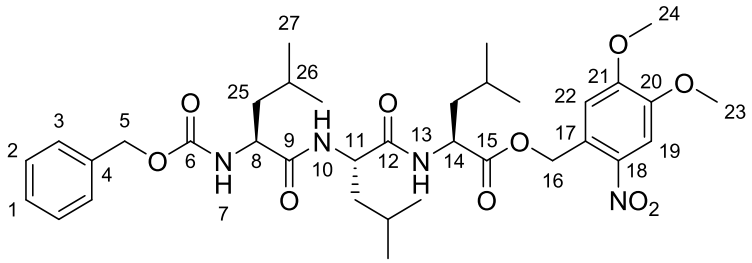

[686.803]

$C_{35}H_{50}N_4O_{10}$

To a stirring solution of Boc-Leu-NVOC (compound **169**, 500 mg, 1.17 mmol, 1.0 eq) in CH_2Cl_2 (4.0 mL) at 0 °C was added trifluoroacetic acid (1.0 mL). The solution was stirred for 2 h at 23 °C and the solvent was evaporated *in vacuo*. The amount of residual trifluoroacetic acid was calculated from the difference to 100% yield and neutralized in the following step with additional DIPEA (1:1).

TFA-Leu-NVOC (1.17 mmol, 1.0 eq), compound **171** (433 mg, 1.17 µmol, 1.0 eq), HOBt · H_2O (197 mg, 1.29 mmol, 1.1 eq) and DCC (266 mg, 1.29 mmol, 1.1 eq) in THF (5.0 mL) were cooled to 0 °C. DIPEA (408 mL, 303 mg, 2.34 mmol, 2.0 eq) was added and the reaction mixture was stirred at 23 °C for 16 h. The mixture was partitioned between EtOAc and 10% citric acid and the aqueous phase was extracted with EtOAc. The combined organic phases were washed with saturated $NaHCO_3$ solution and brine, dried over Na_2SO_4, filtered and the solvent was evaporated *in vacuo*. After flash column chromatography (SiO_2, CH_2Cl_2:MeOH = 97:3) compound **173** (620 mg, 903 µmol, 77%) was obtained as a colorless solid.

Mixture of diastereomers

^{1}H NMR (599 MHz, $CDCl_3$, 27 °C) δ = 7.71 (s, 1H, H-C(19)), 7.37 – 7.27 (m, 5H, H-C(1) to H-C(3)), 7.03 (s, 1H, H-C(22)), 6.87 (d, *J* = 7.8 Hz, 1H, H-N(13)), 6.63 (d, *J* = 7.9 Hz, 1H, H-N(10)), 5.60 – 5.51 (m, 2H, H-C(16)), 5.38 (d, *J* = 8.1 Hz, 1H, H-N(7)), 5.12 – 5.05 (m, 2H, H-C(5)), 4.66 – 4.59 (m, 1H, H-C(14)), 4.50 – 4.43 (m, 1H, H-C(11)), 4.22 – 4.16 (m, 1H, H-C(8)), 4.01 (s, 3H, H-C(24)), 3.94 (s, 3H, H-C(23)), 1.72 – 1.54 (m, 7H, H-C(25) and H-C(26)), 1.52 – 1.44 (m, 2H, H-C(25)), 0.94 – 0.81 (m, 18H, H-C(27)).

^{13}C NMR (151 MHz, $CDCl_3$, 27 °C) δ = 172.43 (C-9), 172.35 (C-15), 171.89 (C-12), 156.43 (C-6), 153.91 (C-21), 148.33 (C-20), 139.74 (C-18), 136.15 (C-4), 128.67 (C-2), 128.37 (C-1), 128.09 (C-3), 127.08 (C-17), 110.27 (C-22), 108.28 (C-19), 67.26 (C-5), 64.10 (C-16), 56.78 (C-24), 56.52 (C-23), 53.66 (C-8), 51.72 (C-11), 51.10 (C-14), 41.33 (C-25), 41.02 (C-25), 40.57 (C-25), 24.95 (C-26), 24.80 (C-26), 22.98 (C-27), 22.83 (C-27), 22.22 (C-27), 22.12 (C-27), 21.84 (C-27).

IR: $\tilde{\nu}$ = 3324 (m), 2927 (s), 2850 (m), 1704 (w), 1645 (m), 1625 (vs), 1572 (s), 1523 (vs), 1436 (m), 1311 (m), 1273 (s), 1242 (s), 1221 (s), 1185 (m), 1156 (m), 1087 (m), 1067 (s), 1045 (m), 983 (w), 891 (m), 870 (w), 796 (w), 733 (w).

HR-MS (ESI$^+$), $[M+NH_4]^+$ calc. for $[C_{35}H_{54}N_5O_{10}]$: 704.3865, found: 704.3876.

Compound 174

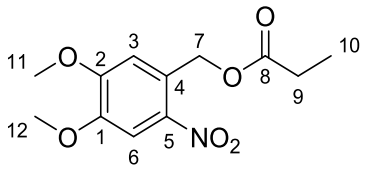

[269.253]

$C_{12}H_{15}NO_6$

To a stirring solution of 6-nitroveratryl alcohol (426 mg, 2.00 mmol, 1.0 eq) and DMAP (24.4 mg, 0.20 mmol, 0.1 eq) in CH_2Cl_2 (20.0 mL) was added TEA (405 mg, 4.00 mmol, 2.0 eq) and propionyl chloride (204 mg, 2.20 mmol, 1.1 eq). The solution was stirred for 3 d at 23 °C before it was transferred to a separatory funnel charged with aqueous 2 M HCl solution. The aqueous phase was extracted with CH_2Cl_2 and the combined organic phases were washed with saturated $NaHCO_3$ solution and brine, dried over Na_2SO_4, filtered and the solvent was evaporated *in vacuo*. After flash column chromatography (SiO_2, *i*-Hex:EtOAc = 3:2) compound **174** (398 mg, 1.48 mmol, 74%) was obtained as a pale yellow solid.

^{1}H NMR (599 MHz, $CDCl_3$, 27 °C) δ = 7.72 (s, 1H, H-C(6)), 7.00 (s, 1H, H-C(3)), 5.51 (s, 2H, H-C(7)), 3.98 (s, 3H, H-C(11)), 3.96 (s, 3H, H-C(12)), 2.48 – 2.42 (m, 2H, H-C(9)), 1.22 – 1.19 (m, 3H, H-C(10)).

^{13}C NMR (151 MHz, $CDCl_3$, 27 °C) δ = 173.86 (C-8), 153.58 (C-2), 148.37 (C-1), 140.18 (C-5), 127.33 (C-4), 110.56 (C-3), 108.41 (C-6), 63.24 (C-7), 56.57 (C-11), 56.51 (C-12), 27.75 (C-9), 9.32 (C-10).

HR-MS (ESI^+), $[M+NH_4]^+$ calc. for $[C_{12}H_{19}N_2O_6]$: 287.1243, found: 287.1239.

Compound 175

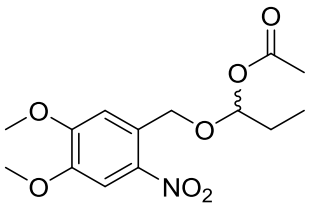

[313.306]

$C_{14}H_{19}NO_7$

In a flame dried Schlenk flask compound **174** (389 mg, 1.44 mmol, 1.0 eq) was dissolved in CH_2Cl_2 (9.0 mL) under nitrogen. The solution was cooled to –78 °C and DIBAL-H (1 M in hexanes, 2.89 mL, 2.89 mmol, 2.0 eq) was added dropwise. After stirring for 45 min pyridine (342 mg, 4.33 mmol, 3.0 eq), DMAP (353 mg in 4 mL CH_2Cl_2, 2.89 mmol, 2.0 eq) and acetic anhydride (885 mg, 8.67 mmol, 6.0 eq) were added. The reaction mixture was stirred for another 20 h at –78 °C, warmed to 0 °C and after another 35 min the reaction was stopped by addition of saturated ammonium chloride solution and saturated Rochelle salt solution. The mixture was stirred for 50 min at 23 °C and then extracted with CH_2Cl_2. The combined organic phases were washed with ice cold 1 M potassium bisulfate solution, saturated sodium bicarbonate solution and brine. The organic phase was dried over Na_2SO_4, filtered and the solvent was evaporated *in vacuo*. After flash column chromatography (SiO_2, *i*-Hex:EtOac = 7:3) compound **175** (mixture of diastereomers (1:1), 400 mg, 1.28 mmol, 88%) was obtained as a yellow solid.

^{1}H NMR (400 MHz, $CDCl_3$, 21 °C) δ = (s, 1H), 7.26 (s, 2H), 5.92 (t, *J* = 5.4 Hz, 1H), 5.06 (q, *J* = 15.2 Hz, 2H), 3.99 (s, 3H), 3.95 (s, 3H), 2.08 (d, *J* = 0.9 Hz, 3H), 1.91 – 1.79 (m, 2H), 1.00 (t, *J* = 7.4 Hz, 3H).

HR-MS (ESI^+), $[M+NH_4]^+$ calc. for $[C_{14}H_{23}N_2O_7]$: 331.1505, found: 331.1500.

9.3 Crystal structural data

Table 14 Crystal structural data for **A-81** and **C-81**.

	A-81 (CCDC 1838943)	**C-81 (CCDC 1838944)**
net formula	$C_{34}H_{33}N_3O_6S$	$C_{38}H_{41.97}N_3O_{7.48}S$
M_r/g mol^{-1}	611.69	692.51
crystal size/mm	0.090 × 0.050 × 0.010	0.100 × 0.020 × 0.020
T/K	293.(2)	103.(2)
radiation	MoKα	MoKα
diffractometer	'Bruker D8 Venture TXS'	'Bruker D8 Venture TXS'
crystal system	orthorhombic	monoclinic
space group	'P b c a'	'C 1 2/c 1'
a/Å	19.4202(17)	24.6040(12)
b/Å	9.7114(7)	10.2215(4)
c/Å	32.390(3)	27.4181(14)
α/°	90	90
β/°	90	103.143(2)
γ/°	90	90
V/Å^3	6108.7(9)	6714.8(5)
Z	8	8
calc. density/g cm^{-3}	1.330	1.370
μ/mm^{-1}	0.157	0.155
absorption correction	Multi-Scan	Multi-Scan
transmission factor range	0.9321–0.9705	0.92–1.00
refls. measured	66888	27226
R_{int}	0.0841	0.0909
mean σ(I)/I	0.0315	0.1048
θ range	3.222–25.026	3.138–25.345
observed refls.	3803	4422
x, y (weighting scheme)	0.0411, 2.8816	0.0647, 20.0750
hydrogen refinement	constr	constr
refls in refinement	5390	6121
parameters	434	444
restraints	23	10
$R(F_{obs})$	0.0450	0.0689
$R_w(F^2)$	0.1103	0.1861
S	1.031	1.035
shift/error$_{max}$	0.001	0.001
max electron density/e Å^{-3}	0.192	0.959
min electron density/e Å^{-3}	−0.214	−0.665

Table 15 Crystal structural data for disuflide **88**.

	88 (CCDC not assigned)
net formula	$C_{14}H_{12}Br_2O_2S_2$
M_r/g mol^{-1}	436.18
crystal size/mm	0.090 × 0.060 × 0.040
T/K	296.(2)
radiation	MoKα
diffractometer	'Bruker D8Quest'
crystal system	monoclinic
space group	'P 1 2/c 1'
a/Å	8.8327(2)
b/Å	9.0721(3)
c/Å	10.1000(3)
α/°	90
β/°	102.8310(10)
γ/°	90
V/Å^3	789.12(4)
Z	2
calc. density/g cm^{-3}	1.836
μ/mm^{-1}	5.398
absorption correction	Multi-Scan
transmission factor range	0.64–0.81
refls. measured	1743
R_{int}	0.0361
mean σ(*I*)/*I*	0.0182
θ range	2.365–27.103
observed refls.	1442
x, *y* (weighting scheme)	0.0298, 0.5835
hydrogen refinement	constr
refls in refinement	1743
parameters	93
restraints	0
$R(F_{obs})$	0.0342
$R_w(F^2)$	0.0795
S	1.048
shift/error$_{max}$	0.001
max electron density/e Å^{-3}	0.431
min electron density/e Å^{-3}	−0.478

Table 16 Crystal structural data for *E*-**99**.

	***E*-99 (CCDC not assigned)**
net formula	$C_{36}H_{37}N_3O_6S$
M_r/g mol^{-1}	639.74
crystal size/mm	0.100 × 0.090 × 0.080
T/K	298.(2)
radiation	MoKα
diffractometer	'Bruker D8 Venture TXS'
crystal system	triclinic
space group	'P -1'
a/Å	11.2739(5)
b/Å	12.1235(4)
c/Å	12.5935(5)
α/°	99.4830(10)
β/°	104.9920(10)
γ/°	96.9140(10)
V/Å^3	1615.78(11)
Z	2
calc. density/g cm^{-3}	1.315
μ/mm^{-1}	0.151
absorption correction	Multi-Scan
transmission factor range	0.91–0.99
refls. measured	17285
R_{int}	0.0223
mean σ(*I*)/*I*	0.0301
θ range	3.408–27.101
observed refls.	5558
x, *y* (weighting scheme)	0.0459, 0.4841
hydrogen refinement	constr
refls in refinement	7080
parameters	419
restraints	0
$R(F_{obs})$	0.0415
$R_w(F^2)$	0.1119
S	1.046
shift/error$_{max}$	0.001
max electron density/e Å^{-3}	0.241
min electron density/e Å^{-3}	−0.247

Table 17 Crystal structural data for **A_R-95** and **C_R-95**.

	A_R-95 (CCDC 1943797)	**C_R-95 (CCDC 1943796)**
net formula	$C_{195.76}H_{221.89}N_{15}O_{33}S_5$	$C_{36}H_{37}N_3O_6S$
M_r/g mol^{-1}	3473.24	639.74
crystal size/mm	0.090 × 0.070 × 0.040	0.100 × 0.060 × 0.050
T/K	107.(2)	296.(2)
radiation	MoKα	MoKα
diffractometer	'Bruker D8 Venture TXS'	'Bruker D8Quest'
crystal system	triclinic	triclinic
space group	'P -1'	'P -1'
a/Å	16.5519(9)	14.0134(5)
b/Å	17.2861(8)	14.8150(5)
c/Å	33.8162(18)	19.7182(8)
α/°	76.712(2)	107.2530(10)
β/°	76.864(2)	98.0000(10)
γ/°	74.084(2)	107.3370(10)
V/Å^3	8914.9(8)	3613.7(2)
Z	2	4
calc. density/g cm^{-3}	1.294	1.176
μ/mm^{-1}	0.144	0.135
absorption correction	Multi-Scan	Multi-Scan
transmission factor range	0.96–0.99	0.96–0.99
refls. measured	81264	63288
R_{int}	0.0657	0.0686
mean σ(I)/I	0.1008	0.0479
θ range	2.279–25.027	2.214–25.062
observed refls.	17012	8816
x, y (weighting scheme)	0.1968, 19.9762	0.1058, 1.7910
hydrogen refinement	constr	constr
refls in refinement	30428	12794
parameters	2444	919
restraints	280	64
$R(F_{obs})$	0.1087	0.0655
$R_w(F^2)$	0.3415	0.1998
S	1.025	1.029
shift/error$_{max}$	0.001	0.003
max electron density/e Å^{-3}	1.536	0.471
min electron density/e Å^{-3}	−0.538	−0.295

Table 18 Crystal structural data for *E*-**103**.

	***E*-103 (CCDC 1962416)**
net formula	$C_{29}H_{28}O_4S$
M_r/g mol^{-1}	472.57
crystal size/mm	0.090 × 0.070 × 0.050
T/K	105.(2)
radiation	MoKα
diffractometer	'Bruker D8 Venture TXS'
crystal system	triclinic
space group	'P -1'
a/Å	10.0447(3)
b/Å	11.1668(3)
c/Å	12.5448(4)
α/°	91.1770(10)
β/°	90.0490(10)
γ/°	97.0430(10)
V/Å^3	1396.19(7)
Z	2
calc. density/g cm^{-3}	1.124
μ/mm^{-1}	0.145
absorption correction	Multi-Scan
transmission factor range	0.94–0.99
refls. measured	26793
R_{int}	0.0296
mean σ(*I*)/*I*	0.0336
θ range	2.427–30.508
observed refls.	6672
x, *y* (weighting scheme)	0.0743, 0.5310
hydrogen refinement	constr
refls in refinement	8485
parameters	347
restraints	20
$R(F_{obs})$	0.0479
$R_w(F^2)$	0.1443
S	1.036
shift/error$_{max}$	0.001
max electron density/e Å^{-3}	0.431
min electron density/e Å^{-3}	−0.330

Table 19 Crystal structural data for *E*1-**110** and *E*2-**110**.

	***E*1-110 (CCDC not assigned)**	***E*2-110 (CCDC not assigned)**
net formula	$C_{36}H_{36}FN_3O_6S$	$C_{36}H_{36}FN_3O_6S$
M_r/g mol^{-1}	657.74	657.74
crystal size/mm	0.080 × 0.020 × 0.020	0.100 × 0.080 × 0.050
T/K	102.(2)	106.(2)
radiation	MoKα	MoKα
diffractometer	'Bruker D8 Venture TXS'	'Bruker D8 Venture TXS'
crystal system	monoclinic	monoclinic
space group	'P 1 21/n 1'	'P 1 21/n 1'
a/Å	14.0335(8)	13.6424(7)
b/Å	16.8939(12)	14.3381(7)
c/Å	14.5159(10)	16.1666(8)
α/°	90	90
β/°	113.292(2)	102.415(2)
γ/°	90	90
V/Å^3	3161.0(4)	3088.3(3)
Z	4	4
calc. density/g cm^{-3}	1.382	1.415
μ/mm^{-1}	0.161	0.165
absorption correction	Multi-Scan	Multi-Scan
transmission factor range	0.92–1.00	0.83–0.99
refls. measured	36062	7146
R_{int}	0.1120	0.0589
mean σ(*I*)/*I*	0.0763	0.0363
θ range	2.956–25.345	2.274–26.372
observed refls.	3447	6188
x, *y* (weighting scheme)	0.0782, 8.3158	0, 5.0801
hydrogen refinement	constr	constr
refls in refinement	5776	7146
parameters	404	429
restraints	94	5
$R(F_{obs})$	0.0844	0.0524
$R_w(F^2)$	0.2232	0.1208
S	1.019	1.133
shift/error$_{max}$	0.001	0.001
max electron density/e Å^{-3}	0.704	0.351
min electron density/e Å^{-3}	−0.648	−0.318

Table 20 Crystal structural data for *Z*2-**110**.

	***Z*2-110 (CCDC not assigned)**
net formula	$C_{36}H_{36}FN_3O_6S$
M_r/g mol^{-1}	657.74
crystal size/mm	0.090 × 0.030 × 0.020
T/K	106.(2)
radiation	MoKα
diffractometer	'Bruker D8 Venture TXS'
crystal system	monoclinic
space group	'C 1 2/c 1'
a/Å	24.6324(13)
b/Å	14.5874(6)
c/Å	21.5145(11)
α/°	90
β/°	107.913(2)
γ/°	90
V/Å^3	7355.9(6)
Z	8
calc. density/g cm^{-3}	1.188
μ/mm^{-1}	0.139
absorption correction	Multi-Scan
transmission factor range	0.85–1.00
refls. measured	40491
R_{int}	0.0711
mean σ(*I*)/*I*	0.0466
θ range	2.780–25.348
observed refls.	5038
x, *y* (weighting scheme)	0.0928, 20.3238
hydrogen refinement	constr
refls in refinement	6730
parameters	438
restraints	0
$R(F_{obs})$	0.0675
$R_w(F^2)$	0.1945
S	1.067
shift/error$_{max}$	0.001
max electron density/e Å^{-3}	0.760
min electron density/e Å^{-3}	−0.442

Table 21 Crystal structural data for *E*-**115**.

	***E*-115 (CCDC not assigned)**
net formula	$C_{36}H_{37}N_3O_7S$
M_r/g mol^{-1}	655.74
crystal size/mm	0.100 × 0.080 × 0.020
T/K	103.(2)
radiation	MoKα
diffractometer	'Bruker D8 Venture TXS'
crystal system	orthorhombic
space group	'P 21 21 21'
a/Å	11.4625(4)
b/Å	21.6925(7)
c/Å	26.3562(8)
α/°	90
β/°	90
γ/°	90
V/Å^3	6553.5(4)
Z	8
calc. density/g cm^{-3}	1.329
μ/mm^{-1}	0.153
absorption correction	Multi-Scan
transmission factor range	0.91–1.00
refls. measured	31641
R_{int}	0.0557
mean σ(*I*)/*I*	0.0803
θ range	3.214–25.379
observed refls.	9228
x, *y* (weighting scheme)	0.0365, 0.7946
hydrogen refinement	constr
refls in refinement	−0.03(4)
parameters	11947
restraints	855
$R(F_{obs})$	0
$R_w(F^2)$	0.0493
S	0.0953
shift/error$_{max}$	1.034
max electron density/e Å^{-3}	0.001
min electron density/e Å^{-3}	0.308

10 Bibliography

1. Friedländer, P. Ueber schwefelhaltige Analoga der Indigogruppe. *Berichte der Dtsch. Chem. Gesellschaft* **39**, 1060–1066 (1906).

2. Petermayer, C. & Dube, H. Indigoid Photoswitches: Visible Light Responsive Molecular Tools. *Acc. Chem. Res.* **51**, 1153–1163 (2018).

3. Zimmerman, H. E. & Ahramjian, L. Overlap Control of Carbanionoid Reactions. II.1 The Stereochemistry of the Perkin Reaction and Related Condensation Reactions. *J. Am. Chem. Soc.* **81**, 2086–2091 (1959).

4. Réamonn, L. S. S. & O'Sullivan, W. I. Configuration of 2-arylmethylene-2,3-dihydro-5-methylbenzo[b]thiophen-3-ones. *J. Chem. Soc., Perkin Trans. 1* 1009–1012 (1977).

5. Yamaguchi, T., Seki, T., Tamaki, T. & Ichimura, K. Photochromism of Hemithioindigo Derivatives. I. Preparation and Photochromic Properties in Organic Solvents. *Bulletin of the Chemical Society of Japan* **65**, 649–656 (1992).

6. Wiedbrauk, S. & Dube, H. Hemithioindigo - An emerging photoswitch. *Tetrahedron Lett.* **56**, 4266–4274 (2015).

7. Ichimura, K., Seki, T., Tamaki, T. & Yamaguchi, T. Fatigue-resistant Photochromic Hemithioindigoes. *Chem. Lett.* **19**, 1645–1646 (1990).

8. Maerz, B. *et al.* Making fast photoswitches faster - Using hammett analysis to understand the limit of donor-acceptor approaches for faster hemithioindigo photoswitches. *Chem. - A Eur. J.* **20**, 13984–13992 (2014).

9. Navrátil, R., Wiedbrauk, S., Jašík, J., Dube, H. & Roithová, J. Transforming hemithioindigo from a two-way to a one-way molecular photoswitch by isolation in the gas phase. *Phys. Chem. Chem. Phys.* **20**, 6868–6876 (2018).

10. Cordes, T., Schadendorf, T., Priewisch, B., Rück-Braun, K. & Zinth, W. The Hammett relationship and reactions in the excited electronic state: Hemithioindigo Z/E-photoisomerization. *J. Phys. Chem. A* **112**, 581–588 (2008).

11. Cordes, T., Schadendorf, T., Rück-Braun, K. & Zinth, W. Chemical control of

Hemithioindigo-photoisomerization - Substituent-effects on different molecular parts. *Chem. Phys. Lett.* **455**, 197–201 (2008).

12. Wiedbrauk, S. *et al.* Twisted Hemithioindigo Photoswitches: Solvent Polarity Determines the Type of Light-Induced Rotations. *J. Am. Chem. Soc.* **138**, 12219–12227 (2016).

13. Wiedbrauk, S. *et al.* Ingredients to TICT Formation in Donor Substituted Hemithioindigo. *J. Phys. Chem. Lett.* **8**, 1585–1592 (2017).

14. Wang, J. & Rueck-Braun, K. The Effect of Substituent-Dependent Photoinduced Intramolecular Charge Transfer on the Photochromism of Hemithioindigos. *ChemPhotoChem* **1**, 493–498 (2017).

15. Liu, R. S. H. & Asato, A. E. The primary process of vision and the structure of bathorhodopsin: A mechanism for photoisomerization of polyenes. *Proc. Natl. Acad. Sci. U. S. A.* **82**, 259–263 (1985).

16. Gerwien, A., Schildhauer, M., Thumser, S., Mayer, P. & Dube, H. Direct evidence for hula twist and single-bond rotation photoproducts. *Nat. Commun.* **9**, 1–9 (2018).

17. Balomenou, I. & Pistolis, G. Torsional photoisomerization proceeding adiabatically through a volume-conserving pathway in uninhibited fluid media. *Chem. - A Eur. J.* **15**, 4228–4232 (2009).

18. Jung, Y. O. *et al.* Volume-conserving trans-cis isomerization pathways in photoactive yellow protein visualized by picosecond X-ray crystallography. *Nat. Chem.* **5**, 212–220 (2013).

19. Kelly, T. R., De Silva, H. & Silva, R. A. Unidirectional rotary motion in a molecular system. *Nature* **401**, 150–152 (1999).

20. Koumura, N., Zijistra, R. W. J., Van Delden, R. A., Harada, N. & Feringa, B. L. Light-driven monodirectional molecular rotor. *Nature* **401**, 152–155 (1999).

21. Koumura, N., Geertsema, E. M., Meetsma, A. & Feringa, B. L. Light-driven molecular rotor: Unidirectional rotation controlled by a single stereogenic center. *J. Am. Chem. Soc.* **122**, 12005–12006 (2000).

22. Koumura, N., Geertsema, E. M., Van Gelder, M. B., Meetsma, A. & Feringa, B. L. Second generation light-driven molecular motors. Unidirectional rotation controlled by a single stereogenic center with near-perfect photoequilibria and acceleration of the speed of rotation by structural modification. *J. Am. Chem. Soc.* **124**, 5037–5051 (2002).

23. Pollard, M. M., Meetsma, A. & Feringa, B. L. A redesign of light-driven rotary molecular motors. *Org. Biomol. Chem.* **6**, 507–512 (2008).

24. Pollard, M. M., Klok, M., Pijper, D. & Feringa, B. L. Rate acceleration of light-driven rotary molecular motors. *Adv. Funct. Mater.* **17**, 718–729 (2007).

25. Kistemaker, J. C. M., Štacko, P., Visser, J. & Feringa, B. L. Unidirectional rotary motion in achiral molecular motors. *Nat. Chem.* **7**, 890–896 (2015).

26. Wezenberg, S. J. & Feringa, B. L. Supramolecularly directed rotary motion in a photoresponsive receptor. *Nat. Commun.* **9**, 1–7 (2018).

27. Villarón, D. & Wezenberg, S. J. Stiff-Stilbene Photoswitches: From Fundamental Studies to Emergent Applications. *Angew. Chemie - Int. Ed.* 2–13 (2020).

28. Lehn, J. M. Conjecture: Imines as unidirectional photodriven molecular motors-motional and constitutional dynamic devices. *Chem. - A Eur. J.* **12**, 5910–5915 (2006).

29. Greb, L. & Lehn, J. M. Light-driven molecular motors: Imines as four-step or two-step unidirectional rotors. *J. Am. Chem. Soc.* **136**, 13114–13117 (2014).

30. Guentner, M. *et al.* Sunlight-powered kHz rotation of a hemithioindigo-based molecular motor. *Nat. Commun.* **6**, (2015).

31. Huber, L. A. *et al.* Direct Observation of Hemithioindigo-Motor Unidirectionality. *Angew. Chemie - Int. Ed.* **56**, 14536–14539 (2017).

32. Schildhauer, M. *et al.* A Prospective Ultrafast Hemithioindigo Molecular Motor. *ChemPhotoChem* **3**, 365–371 (2019).

33. Štacko, P. *et al.* Locked Synchronous Rotor Motion in a Molecular Motor. *Science* **356**, 964–968 (2017).

34. Pedersen, C. J. Cyclic Polyethers and Their Complexes with Metal Salts. *J. Am. Chem.*

Soc. **89**, 7017–7036 (1967).

35. Pedersen, C. J. Crystalline Salt Complexes of Macrocyclic Polyethers. *J. Am. Chem. Soc.* **92**, 386–391 (1970).

36. Pedersen, C. J. & Frensdorff, H. K. Macrocyclic Polyethers and Their Complexes. *Angew. Chemie Int. Ed. English* **11**, 16–25 (1972).

37. Frensdorff, H. K. Stability Constants of Cyclic Polyether Complexes with Univalent Cations. *J. Am. Chem. Soc.* **93**, 600–606 (1971).

38. Steed, J. W. First- and second-sphere coordination chemistry of alkali metal crown ether complexes. *Coord. Chem. Rev.* **215**, 171–221 (2001).

39. Domasevitch, K. V., Ponomareva, V. V. & Rusanov, E. B. Synthesis and crystal structure of a caesium α-cyanobenzothiazole-α-carbaldehyde oximate complex with a crown ether (L): New evidence for the stability of $[Cs_2L_3]^{2+}$ club sandwiches. *J. Chem. Soc. - Dalt. Trans.* **2**, 1177–1180 (1997).

40. Hope, H., Olmstead, M. M., Power, P. P. & Xu, X. X-ray Crystal Structures of the Diphenylphosphide and -arsenide Anions: Use of a Crown Ether To Effect Complete Metal Cation and Organometalloid Anion Separation. *J. Am. Chem. Soc.* **106**, 819–821 (1984).

41. Watson, K. A. *et al.* Synthesis, NMR spectroscopy, and crystal structure of the 1:2 host: guest complex of 18-crown-6 with lithium phenoxide. *Can. J. Chem.* **68**, 1201–1207 (1990).

42. Antsyshkina, A.S.; Madikov, G.G.; Poraj-Koshits, M.A.; Konoplev, V.N.; Silina, T.A.; Sizareva, A. S. Crystal and molecular structure of $2LiBH_1 \cdot 18K6$. *Koord. Khim.* **20**, 274–278 (1994).

43. Dietrich, B., Lehn, J. M. & Sauvage, J. P. Diaza-polyoxa-macrocycles et macrobicycles. *Tetrahedron Lett.* **10**, 2885–2888 (1969).

44. Lehn, J. M. Cryptates: The Chemistry of Macropolycyclic Inclusion Complexes. *Acc. Chem. Res.* **11**, 49–57 (1978).

45. Dietrich, B., Lehn, J. -M & Sauvage, J. -P. Kryptate: makrocyclische Metallkomplexe.

Chemie unserer Zeit **7**, 120–128 (1973).

46. Dietrich, B., Lehn, J. M. & Sauvage, J. P. Cryptates: Control over bivalent/monovalent cation selectivity. *J. Chem. Soc. Chem. Commun.* 15–16 (1973).

47. Cram, D. J. The Design of Molecular Hosts, Guests, and Their Complexes. *Science* **240**, 760–767 (1988).

48. Gu, X.-P., Ikeda, I., Okahara, M. & Kim, J. Synthesis of 3,5-Bis(2,5,8-trioxaeicosyl)-18-crown-6 and Its Formation of Bilayer Membranes. *Chem. Lett.* **15**, 1715–1718 (1986).

49. Gokel, G. W. *et al.* Lariat ethers: From cation complexation to supramolecular assemblies. *Pure Appl. Chem.* **60**, 461–465 (1988).

50. Frisch, H. L. & Wasserman, E. Chemical Topology. *J. Am. Chem. Soc.* **83**, 3789–3795 (1961).

51. Gil-Ramírez, G., Leigh, D. A. & Stephens, A. J. Catenane: fünfzig Jahre molekulare Verschlingungen. *Angew. Chemie* **127**, 6208–6249 (2015).

52. Wasserman, E. The Preparation of Interlocking Rings: A Catenane. *J. Am. Chem. Soc.* **82**, 4433–4434 (1960).

53. Harrison, I. T. & Harrison, S. The Synthesis of a Stable Complex of a Macrocycle and a Threaded Chain. *J. Am. Chem. Soc.* **89**, 5723–5724 (1967).

54. Schill, G. & Lüttringhaus, A. Gezielte Synthese von Catena-Verbindungen [1]. *Angew. Chemie* **76**, 567–568 (1964).

55. Dietrich-Buchecker, C. O., Sauvage, J. P. & Kintzinger, J. P. Une nouvelle famille de molecules : les metallo-catenanes. *Tetrahedron Lett.* **24**, 5095–5098 (1983).

56. Cesario, M., Dietrich-Buchecker, C. O., Guilhem, J., PScard, C. & Sauvage, J.-P. Molecular structure of a catenand and its copper(I) catenate: complete rearrangement of the interlocked macrocyclic ligands by complexation. *J. Chem. Soc. Chem. Commun.* 244–247 (1985).

57. Mohr, B., Sauvage, J.-P., Grubbs, R. H. & Weck, M. High-Yield Synthesis of [2]Catenanes by Intramolecular Ring-Closing Metathesis. *Angew. Chemie Int. Ed.*

English **36**, 1308–1310 (1997).

58. Allwood, B. L., Shahriari-Zavareh, H., Stoddart, J. F. & Williams, D. J. Complexation of Paraquat and Diquat by a bismetaphenylene-32-crown-10 derivative. *J. Chem. Soc. Chem. Commun.* 1058–1061 (1987).

59. Allwood, B. L. & Williamsa, D. J. Complexation of Paraquat and Diquat. **20**, 72–74 (1987).

60. Ashtona, P. R. *et al.* Complexation of diquat and paraquat by macrocyclic polyethers incorporating two dibydroxynaphthalene residues. *Tetrahedron Lett.* **28**, 6367–6370 (1987).

61. Ashton, P. R. *et al.* A [2] Catenane Made to Order. *Angew. Chemie Int. Ed. English* **28**, 1396–1399 (1989).

62. Barin, G., Coskun, A., Fouda, M. M. G. & Stoddart, J. F. Mechanically Interlocked Molecules Assembled by π-π Recognition. *Chempluschem* **77**, 159–185 (2012).

63. Erbas-Cakmak, S., Leigh, D. A., McTernan, C. T. & Nussbaumer, A. L. Artificial Molecular Machines. *Chem. Rev.* **115**, 10081–10206 (2015).

64. Baroncini, M., Silvi, S. & Credi, A. Photo- And Redox-Driven Artificial Molecular Motors. *Chem. Rev.* **120**, 200–268 (2020).

65. Qiu, Y., Feng, Y., Guo, Q. H., Astumian, R. D. & Stoddart, J. F. Pumps through the Ages. *Chem* **6**, 1952–1977 (2020).

66. Huang, Z. *et al.* Method to derive restoring forces of strained molecules from kinetic measurements. *J. Am. Chem. Soc.* **131**, 1407–1409 (2009).

67. Hammerich, M. *et al.* Heterodiazocines: Synthesis and Photochromic Properties, Trans to Cis Switching within the Bio-optical Window. *J. Am. Chem. Soc.* **138**, 13111–13114 (2016).

68. Qian, H., Pramanik, S. & Aprahamian, I. Photochromic Hydrazone Switches with Extremely Long Thermal Half-Lives. *J. Am. Chem. Soc.* **139**, 9140–9143 (2017).

69. Li, Q., Qian, H., Shao, B., Hughes, R. P. & Aprahamian, I. Building Strain with Large

Macrocycles and Using It to Tune the Thermal Half-Lives of Hydrazone Photochromes. *J. Am. Chem. Soc.* **140**, 11829–11835 (2018).

70. Wiberg, K. B. The Concept of Strain in Organic Chemistry. *Angew. Chemie Int. Ed. English* **25**, 312–322 (1986).

71. Reuter, R. & Wegner, H. A. Oligoazobenzenophanes - Synthesis, photochemistry and properties. *Chem. Commun.* **47**, 12267–12276 (2011).

72. Bassotti, E. *et al.* Effect of strain on the photoisomerization and stability of a congested azobenzenophane: A combined experimental and computational study. *J. Phys. Chem. A* **110**, 12385–12394 (2006).

73. Schweighauser, L., Häussinger, D., Neuburger, M. & Wegner, H. A. Symmetry as a new element to control molecular switches. *Org. Biomol. Chem.* **12**, 3371–3379 (2014).

74. Dorel, R., Miró, C., Wei, Y., Wezenberg, S. J. & Feringa, B. L. Cation-Modulated Rotary Speed in a Light-Driven Crown Ether Functionalized Molecular Motor. *Org. Lett.* **20**, 3715–3718 (2018).

75. Wezenberg, S. J., Chen, K. Y. & Feringa, B. L. Visible-Light-Driven Photoisomerization and Increased Rotation Speed of a Molecular Motor Acting as a Ligand in a Ruthenium(II) Complex. *Angew. Chemie - Int. Ed.* **54**, 11457–11461 (2015).

76. Faulkner, A., Van Leeuwen, T., Feringa, B. L. & Wezenberg, S. J. Allosteric Regulation of the Rotational Speed in a Light-Driven Molecular Motor. *J. Am. Chem. Soc.* **138**, 13597–13603 (2016).

77. Berova, N., Bari, L. Di & Pescitelli, G. Application of electronic circular dichroism in configurational and conformational analysis of organic compounds. *Chem. Soc. Rev.* **36**, 914–931 (2007).

78. Li, H., Wang, C., Liao, X., Xie, M. & Sun, R. Hybrid triazolium and ammonium ions-contained hyperbranched polymer with enhanced ionic conductivity. *Polymer* **112**, 297–305 (2017).

79. Walker, J. A. *et al.* Substrate Design Enables Heterobifunctional, Dual 'click' Antibody Modification via Microbial Transglutaminase. *Bioconjug. Chem.* **30**, 2452–2457 (2019).

80. Punna, S., Meunier, S. & Finn, M. G. A hierarchy of aryloxide deprotection by boron tribromide. *Org. Lett.* **6**, 2777–2779 (2004).

81. McKillop, A. & Kemp, D. Further functional group oxidations using sodium perborate. *Tetrahedron* **45**, 3299–3306 (1989).

82. Karunakaran, C. & Kamalam, R. Mechanism and reactivity in perborate oxidation of anilines in acetic acid. *J. Chem. Soc. Perkin Trans. 2* 2011–2018 (2002).

83. Uhl, E., Thumser, S., Mayer, P. & Dube, H. Transmission of Unidirectional Molecular Motor Rotation to a Remote Biaryl Axis. *Angew. Chemie - Int. Ed.* **57**, 11064–11068 (2018).

84. Grein, F. Twist angles and rotational energy barriers of biphenyl and substituted biphenyls. *J. Phys. Chem. A* **106**, 3823–3827 (2002).

85. Chappell, M. D., Conner, S. E., Tripp, A. E., Zhu, G. Glucagon Receptor Antagonists, Preparation and Therapeutic Uses. WO 2006/086488 A2, 17 August 2006.

86. Uhl, E., Mayer, P. & Dube, H. Active and Unidirectional Acceleration of Biaryl Rotation by a Molecular Motor. *Angew. Chemie - Int. Ed.* **59**, 5730–5737 (2020).

87. Megerle, U., Lechner, R., König, B. & Riedle, E. Laboratory apparatus for the accurate, facile and rapid determination of visible light photoreaction quantum yields. *Photochem. Photobiol. Sci.* **9**, 1400–1406 (2010).

88. Cox, P. A. *et al.* Base-Catalyzed Aryl-$B(OH)_2$ Protodeboronation Revisited: From Concerted Proton Transfer to Liberation of a Transient Aryl Anion. *J. Am. Chem. Soc.* **139**, 13156–13165 (2017).

89. Otomo, A., Aoki, I., Yamada, T., Electro-Optic Polymer. US 2019/0225728 A1. 25 July 2019.

90. Aston, P. R. *et al.* Self-assembling [2]- and [3]Rotaxanes from Secondary Dialkylammonium Salts and Crown Ethers. *Chem. - A Eur. J.* **2**, 729–736 (1996).

91. Claessens, C. G. & Stoddart, J. F. π – π INTERACTIONS IN SELF-ASSEMBLY. **10**, 254–272 (1997).

92. Rebek, J. Molecular Recognition with Model Systems. *Angew. Chemie Int. Ed. English* **29**, 245–255 (1990).

93. Williams, K. *et al.* Molecular Recognition with Convergent Functional Groups. 7. Energetics of Adenine Binding with Model Receptors. *J. Am. Chem. Soc.* **111**, 1090–1094 (1989).

94. Faraoni, R. *et al.* New Rebek imide-type receptors for adenine featuring acetylene-linked π-stacking platforms. *Org. Biomol. Chem.* **2**, 1962–1964 (2004).

95. Sygula, A., Fronczek, F. R., Sygula, R., Rabideau, P. W. & Olmstead, M. M. A double concave hydrocarbon buckycatcher. *J. Am. Chem. Soc.* **129**, 3842–3843 (2007).

96. Mignon, P., Loverix, S., Steyaert, J. & Geerlings, P. Influence of the π-π interaction on the hydrogen bonding capacity of stacked DNA/RNA bases. *Nucleic Acids Res.* **33**, 1779–1789 (2005).

97. Lerman, L. S. Structural considerations in the interaction of DNA and acridines. *J. Mol. Biol.* **3**, 18–30 (1961).

98. Sinnokrot, M. O., Valeev, E. F. & Sherrill, C. D. Estimates of the ab initio limit for π-π interactions: The benzene dimer. *J. Am. Chem. Soc.* **124**, 10887–10893 (2002).

99. Hunter, C. A. Meldola Lecture. The Role of aromatic interactions in molecular recognition. *Chem. Soc. Rev.* **23**, 101–109 (1994).

100. Hunter, C. A. & Sanders, J. K. M. The Nature of π-π Interactions. *J. Am. Chem. Soc.* **112**, 5525–5534 (1990).

101. Hunter, C. A., Lawson, K. R., Perkins, J. & Urch, C. J. Aromatic interactions. *J. Chem. Soc. Perkin Trans. 2* 651–669 (2001).

102. Grimme, S. Do special noncovalent π-π stacking interactions really exist? *Angew. Chemie - Int. Ed.* **47**, 3430–3434 (2008).

103. Bloom, J. W. G. & Wheeler, S. E. Taking the aromaticity out of aromatic interactions. *Angew. Chemie - Int. Ed.* **50**, 7847–7849 (2011).

104. Wheeler, S. E. Understanding substituent effects in noncovalent interactions involving

aromatic rings. *Acc. Chem. Res.* **46**, 1029–1038 (2013).

105. Ringer, A. L., Sinnokrot, M. O., Lively, R. P. & Sherrill, C. D. The effect of multiple substituents on sandwich and T-shaped π-π interactions. *Chem. - A Eur. J.* **12**, 3821–3828 (2006).

106. Gung, B. W., Xue, X. & Zou, Y. Enthalpy (ΔH) and entropy (ΔS) for π-stacking interactions in near-sandwich configurations: Relative importance of electrostatic, dispersive, and charge-transfer effects. *J. Org. Chem.* **72**, 2469–2475 (2007).

107. Sinnokrot, M. O. & Sherrill, C. D. Unexpected substituent effects in face-to-face π-stacking interactions. *J. Phys. Chem. A* **107**, 8377–8379 (2003).

108. Lee, E. C. *et al.* Understanding of assembly phenomena by aromatic-aromatic interactions: Benzene Dimer and the substituted systems. *J. Phys. Chem. A* **111**, 3446–3457 (2007).

109. Tsuzuki, S., Honda, K., Uchimaru, T. & Mikami, M. Ab initio calculations of structures and interaction energies of toluene dimers including CCSD(T) level electron correlation correction. *J. Chem. Phys.* **122**, (2005).

110. Wheeler, S. E., McNeil, A. J., Müller, P., Swager, T. M. & Houk, K. N. Probing Substituent Effects in Aryl-Aryl Interactions Using Stereoselective Diels-Alder Cycloadditions. *J. Am. Chem. Soc.* **132**, 3304–3311 (2010).

111. Wheeler, S. E. & Houk, K. N. Substituent effects in the benzene dimer are due to direct interactions of the substituents with the unsubstituted benzene. *J. Am. Chem. Soc.* **130**, 10854–10855 (2008).

112. Wheeler, S. E. Local nature of substituent effects in stacking interactions. *J. Am. Chem. Soc.* **133**, 10262–10274 (2011).

113. Riwar, L. J., Trapp, N., Kuhn, B. & Diederich, F. Substituent Effects in Parallel-Displaced π–π Stacking Interactions: Distance Matters. *Angew. Chemie - Int. Ed.* **56**, 11252–11257 (2017).

114. Cram, D. J. & Cram, J. M. Host-Guest Chemistry. *Science* **183**, 803–809 (1974).

115. Chen, C. W. & Whitlock, H. W. Molecular Tweezers: A Simple Model of Bifunctional

Intercalation. *J. Am. Chem. Soc.* **100**, 4921–4922 (1978).

116. Klärner, F. G. *et al.* Molecular tweezer and clip in aqueous solution: Unexpected self-assembly, powerful host-guest complex formation, quantum chemical ^{1}H NMR shift calculation. *J. Am. Chem. Soc.* **128**, 4831–4841 (2006).

117. Klärner, F. G., Panitzky, J., Bläser, D. & Boese, R. Synthesis and supramolecular structures of molecular clips. *Tetrahedron* **57**, 3673–3687 (2001).

118. Zimmerman, S. C., Zeng, Z., Wu, W. & Reichert, D. E. Synthesis and Structure of Molecular Tweezers Containing Active Site Functionality. *J. Am. Chem. Soc.* **113**, 183–196 (1991).

119. Zimmerman, S. C. & Wu, W. A Rigid Molecular Tweezer with an Active Site Carboxylic Acid: An Exceptionally Efficient Receptor for Adenine in an Organic Solvent. *J. Am. Chem. Soc.* **111**, 8054–8055 (1989).

120. Ragazzon, G., Baroncini, M., Silvi, S., Venturi, M. & Credi, A. Light-powered autonomous and directional molecular motion of a dissipative self-assembling system. *Nat. Nanotechnol.* **10**, 70–75 (2015).

121. Pijper, D., Jongejan, M. G. M., Meetsma, A. & Feringa, B. L. Light-controlled supramolecular helicity of a liquid crystalline phase using a helical polymer functionalized with a single chiroptical molecular switch. *J. Am. Chem. Soc.* **130**, 4541–4552 (2008).

122. Dube, H. & Rebek, J. Selective guest exchange in encapsulation complexes using light of different wavelenghts. *Angew. Chemie - Int. Ed.* **51**, 3207–3210 (2012).

123. Clever, G. H., Tashiro, S. & Shionoya, M. Light-triggered crystallization of a molecular host-guest complex. *J. Am. Chem. Soc.* **132**, 9973–9975 (2010).

124. Merino, E. & Ribagorda, M. Control over molecular motion using the cis-trans photoisomerization of the azo group. *Beilstein J. Org. Chem.* **8**, 1071–1090 (2012).

125. Hua, Y. & Flood, A. H. Flipping the switch on chloride concentrations with a light-active foldamer. *J. Am. Chem. Soc.* **132**, 12838–12840 (2010).

126. Khan, A. & Hecht, S. Towards photocontrol over the helix-coil transition in foldamers:

Synthesis and photoresponsive behavior of azobenzene-core amphiphilic oligo(meta-phenylene ethynylene)s. *Chem. - A Eur. J.* **12**, 4764–4774 (2006).

127. Khan, A., Kaiser, C. & Hecht, S. Prototype of a photoswitchable foldamer. *Angew. Chemie - Int. Ed.* **45**, 1878–1881 (2006).

128. Shinkai, S., Nakaji, T., Ogawa, T., Shigematsu, K. & Manabe, O. Photoresponsive Crown Ethers. 2. Photocontrol of Ion Extraction and Ion Transport by a Bis(crown ether) with a Butterfly-like Motion. *J. Am. Chem. Soc.* **103**, 111–115 (1981).

129. Choi, Y. R. *et al.* Azobenzene-based chloride transporters with light-controllable activities. *Chem. Commun.* **50**, 15305–15308 (2014).

130. Kawai, S. H. Photochromic bis(monoaza-crown ether)s. Alkali-metal cation complexing properties of novel diarylethenes. *Tetrahedron Lett.* **39**, 4445–4448 (1998).

131. Takeshita, M. & Irie, M. Photoresponsive Tweezers for Alkali Metal Ions. Photochromic Diarylethenes Having Two Crown Ether Moieties. *J. Org. Chem.* **63**, 6643–6649 (1998).

132. Güntner, M. Molekulare Motoren und Rezeptoren auf Basis von Hemithioindigo. (2016).

133. Guentner, M., Uhl, E., Mayer, P. & Dube, H. Photocontrol of Polar Aromatic Interactions by a Bis-Hemithioindigo Based Helical Receptor. *Chem. - A Eur. J.* **22**, 16433–16436 (2016).

134. Perrotta, R. R., Winter, A. H. & Falvey, D. E. Photochemical heterolysis of 3,5-Bis(dimethylamino)benzyl alcohols and esters: Generation of a benzyl cation with a low-energy triplet state. *Org. Lett.* **13**, 212–215 (2011).

135. Comins, D. L. & Brown, J. D. Ortho Metalation Directed by α-Amino Alkoxides. *J. Org. Chem.* **49**, 1078–1083 (1984).

136. Stavber, S., Jereb, M. & Zupan, M. Selectfluor^{TM} F-TEDA-BF_4 mediated and solvent directed iodination of aryl alkyl ketones using elemental iodine. *Chem. Commun.* 488–489 (2002).

137. Brynn Hibbert, D. & Thordarson, P. The death of the Job plot, transparency, open science and online tools, uncertainty estimation methods and other developments in supramolecular chemistry data analysis. *Chem. Commun.* **52**, 12792–12805 (2016).

138. Wiedbrauk, S., Bartelmann, T., Thumser, S., Mayer, P. & Dube, H. Simultaneous complementary photoswitching of hemithioindigo tweezers for dynamic guest relocalization. *Nat. Commun.* **9**, 1–9 (2018).

139. Hough, R., Pratt, G. & Rechsteiner, M. Purification of two high molecular weight proteases from rabbit reticulocyte lysate. *J. Biol. Chem.* **262**, 8303–8313 (1987).

140. Wilk, S. & Orlowski, M. Evidence that Pituitary Cation-Sensitive Neutral Endopeptidase Is a Multicatalytic Protease Complex. *J. Neurochem.* **40**, 842–849 (1983).

141. Arrigo, A. P., Tanaka, K., Goldberg, A. L. & Welch, W. J. Identity of the 19S 'prosome' particle with the large multifunctional protease complex of mammalian cells (the proteasome). *Nature* **331**, 192–194 (1988).

142. Peters, J. M., Franke, W. W. & Kleinschmidt, J. A. Distinct 19 S and 20 S subcomplexes of the 26 S proteasome and their distribution in the nucleus and the cytoplasm. *J. Biol. Chem.* **269**, 7709–7718 (1994).

143. Kopp, F., Steiner, R., Dahlmann, B., Kuehn, L. & Reinauer, H. Size and shape of the multicatalytic proteinase from rat skeletal muscle. *Biochim. Biophys. Acta (BBA)/Protein Struct. Mol.* **872**, 253–260 (1986).

144. Löwe, J. *et al.* Crystal structure of the 20S proteasome from the archaeon T. acidophilum at 3.4 Å resolution. *Science* **268**, 533–539 (1995).

145. Kisselev, A. F. *et al.* The caspase-like sites of proteasomes, their substrate specificity, new inhibitors and substrates, and allosteric interactions with the trypsin-like sites. *J. Biol. Chem.* **278**, 35869–35877 (2003).

146. Arendt, C. S. & Hochstrasser, M. Identification of the yeast 20S proteasome catalytic centers and subunit interactions required for active-site formation. *Proc. Natl. Acad. Sci. U. S. A.* **94**, 7156–7161 (1997).

147. Kisselev, A. F., Akopian, T. N., Castillo, V. & Goldberg, A. L. Proteasome active sites allosterically regulate each other, suggesting a cyclical bite-chew mechanism for protein breakdown. *Mol. Cell* **4**, 395–402 (1999).

148. Groll, M. *et al.* Structure of 20S proteasome from yeast at 2.4 Å resolution. *Nature* **386**,

463–471 (1997).

149. Seemüller, E. *et al.* Proteasome from Thermoplasma acidophilum: A threonine protease. *Science* **268**, 579–582 (1995).

150. Kisselev, A. F., Songyang, Z. & Goldberg, A. L. Why does threonine, and not serine, function as the active site nucleophile in proteasomes? *J. Biol. Chem.* **275**, 14831–14837 (2000).

151. Liu, C. W. *et al.* ATP Binding and ATP Hydrolysis Play Distinct Roles in the Function of 26S Proteasome. *Mol. Cell* **24**, 39–50 (2006).

152. Glickman, M. H. *et al.* A subcomplex of the proteasome regulatory particle required for ubiquitin-conjugate degradation and related to the COP9-signalosome and eIF3. *Cell* **94**, 615–623 (1998).

153. Tomko, R. J. & Hochstrasser, M. Molecular Architecture and Assembly of the Eukaryotic Proteasome. *Annu. Rev. Biochem.* **82**, 415–445 (2013).

154. Bedford, L., Paine, S., Sheppard, P. W., Mayer, R. J. & Roelofs, J. Assembly, structure, and function of the 26S proteasome. *Trends Cell Biol.* **20**, 391–401 (2010).

155. Pathare, G. R. *et al.* The proteasomal subunit Rpn6 is a molecular clamp holding the core and regulatory subcomplexes together. *Proc. Natl. Acad. Sci. U.S.A.* **109**, 149–154 (2012).

156. Prakash, S., Tian, L., Ratliff, K. S., Lehotzky, R. E. & Matouschek, A. An unstructured initiation site is required for efficient proteasome-mediated degradation. *Nat. Struct. Mol. Biol.* **11**, 830–837 (2004).

157. Yu, H., Kago, G., Yellman, C. M. & Matouschek, A. Ubiquitin-like domains can target to the proteasome but proteolysis requires a disordered region. *EMBO J.* **35**, 1522–1536 (2016).

158. Lee, C., Schwartz, M. P., Prakash, S., Iwakura, M. & Matouschek, A. ATP-dependent proteases degrade their substrates by processively unraveling them from the degradation signal. *Mol. Cell* **7**, 627–637 (2001).

159. Olszewski, M. M., Williams, C., Dong, K. C. & Martin, A. The Cdc48 unfoldase

prepares well-folded protein substrates for degradation by the 26S proteasome. *Commun. Biol.* **2**, (2019).

160. Finley, D., Ulrich, H. D., Sommer, T. & Kaiser, P. The ubiquitin-proteasome system of Saccharomyces cerevisiae. *Genetics* **192**, 319–360 (2012).

161. Collins, G. A. & Goldberg, A. L. The Logic of the 26S Proteasome. *Cell* **169**, 792–806 (2017).

162. Braten, O. *et al.* Numerous proteins with unique characteristics are degraded by the 26S proteasome following monoubiquitination. *Proc. Natl. Acad. Sci. U.S.A.* **113**, E4639–E4647 (2016).

163. Dimova, N. V. *et al.* APC/C-mediated multiple monoubiquitylation provides an alternative degradation signal for cyclin B1. *Nat. Cell Biol.* **14**, 168–176 (2012).

164. Samant, R. S., Livingston, C. M., Sontag, E. M. & Frydman, J. Distinct proteostasis circuits cooperate in nuclear and cytoplasmic protein quality control. *Nature* **563**, 407–411 (2018).

165. Yau, R. G. *et al.* Assembly and Function of Heterotypic Ubiquitin Chains in Cell-Cycle and Protein Quality Control. *Cell* **171**, 918-933.e20 (2017).

166. Thrower, J. S. Recognition of the polyubiquitin proteolytic signal. *EMBO J.* **19**, 94–102 (2000).

167. Finley, D. Recognition and Processing of Ubiquitin-Protein Conjugates by the Proteasome. *Annu. Rev. Biochem.* **78**, 477–513 (2009).

168. Worden, E. J., Dong, K. C. & Martin, A. An AAA Motor-Driven Mechanical Switch in Rpn11 Controls Deubiquitination at the 26S Proteasome. *Mol. Cell* **67**, 799-811.e8 (2017).

169. Kisselev, A. F., Akopian, T. N., Woo, K. M. & Goldberg, A. L. The sizes of peptides generated from protein by mammalian 26 and 20 S proteasomes. Implications for understanding the degradative mechanism and antigen presentation. *J. Biol. Chem.* **274**, 3363–3371 (1999).

170. Lecker, S. H., Goldberg, A. L. & Mitch, W. E. Protein degradation by the ubiquitin-

proteasome pathway in normal and disease states. *J. Am. Soc. Nephrol.* **17**, 1807–1819 (2006).

171. Grana, X. & Reddy, E. P. Cell cycle control in mammalian cells: Role of cyclins, cyclin dependent kinases (CDKs), growth suppressor genes and cyclin-dependent kinase inhibitors (CKIs). *Oncogene* **11**, 211–219 (1995).

172. Morgan, D. O. Cyclin-dependent kinases: engines, clocks, and microprocessors. *Annu. Rev. Cell Dev. Biol.* **13**, 261–291 (1997).

173. Perry, J. A. & Kornbluth, S. Cdc25 and Wee1: Analogous opposites? *Cell Div.* **2**, 1–12 (2007).

174. Zheng, N. *et al.* Structure of the Cul1–Rbx1–Skp1–F box Skp2 SCF ubiquitin ligase complex. *Nature* **416**, 703–709 (2002).

175. Cardozo, T. & Pagano, M. The SCF ubiquitin ligase: Insights into a molecular machine. *Nat. Rev. Mol. Cell Biol.* **5**, 739–751 (2004).

176. Peters, J. M. The anaphase promoting complex/cyclosome: A machine designed to destroy. *Nat. Rev. Mol. Cell Biol.* **7**, 644–656 (2006).

177. Bassermann, F., Eichner, R. & Pagano, M. The ubiquitin proteasome system – Implications for cell cycle control and the targeted treatment of cancer. *Biochim. Biophys. Acta - Mol. Cell Res.* **1843**, 150–162 (2014).

178. Nasmyth, K. Disseminating the Genome: Joining, Resolving, and Separating Sister Chromatids During Mitosis and Meiosis. *Annu. Rev. Genet.* **35**, 673–745 (2001).

179. Shinohara, K. *et al.* Apoptosis induction resulting from proteasome inhibition. *Biochem. J.* **317**, 385–388 (1996).

180. Drexler, H. C. A. Activation of the cell death program by inhibition of proteasome function. *Proc. Natl. Acad. Sci. U.S.A.* **94**, 855–860 (1997).

181. Crawford, L. J., Walker, B. & Irvine, A. E. Proteasome inhibitors in cancer therapy. *J. Cell Commun. Signal.* **5**, 101–110 (2011).

182. Traenckner, E. B., Wilk, S. & Baeuerle, P. A. A proteasome inhibitor prevents activation

of NF-kappa B and stabilizes a newly phosphorylated form of I kappa B-alpha that is still bound to NF-kappa B. *EMBO J.* **13**, 5433–5441 (1994).

183. Nooka, A. K., Kastritis, E., Dimopoulos, M. A. & Lonial, S. Treatment options for relapsed and refractory multiple myeloma. *Blood* **125**, 3085–3099 (2015).

184. Guo, N. & Peng, Z. MG132, a proteasome inhibitor, induces apoptosis in tumor cells. *Asia. Pac. J. Clin. Oncol.* **9**, 6–11 (2013).

185. Josefsberg, L. B.-Y., Galiani, D., Dantes, A., Amsterdam, A. & Dekel, N. The Proteasome Is Involved in the First Metaphase-to-Anaphase Transition of Meiosis in Rat Oocytes. *Biol. Reprod.* **62**, 1270–1277 (2000).

186. Holloway, S. L., Glotzer, M., King, R. W. & Murray, A. W. Anaphase is initiated by proteolysis rather than by the inactivation of maturation-promoting factor. *Cell* **73**, 1393–1402 (1993).

187. Surana, U. *et al.* Destruction of the CDC28/CLB mitotic kinase is not required for the metaphase to anaphase transition in budding yeast. *EMBO J.* **12**, 1969–1978 (1993).

188. Clute, P. & Pines, J. Temporal and spatial control of cyclin B1 destruction in metaphase. *Nat. Cell Biol.* **1**, 82–87 (1999).

189. Stevens, D., Gassmann, R., Oegema, K. & Desai, A. Uncoordinated loss of chromatid cohesion is a common outcome of extended metaphase arrest. *PLoS One* **6**, (2011).

190. Stein, M. L. *et al.* Systematic comparison of peptidic proteasome inhibitors highlights the α-ketoamide electrophile as an auspicious reversible lead motif. *Angew. Chemie - Int. Ed.* **53**, 1679–1683 (2014).

191. Huber, E. M. *et al.* A unified mechanism for proteolysis and autocatalytic activation in the 20S proteasome. *Nat. Commun.* **7**, 1–10 (2016).

192. Potapova, T. A. *et al.* The reversibility of mitotic exit in vertebrate cells. *Nature* **440**, 954–958 (2006).

193. Zhang, S. *et al.* Covalent complexes of proteasome model with peptide aldehyde inhibitors MG132 and MG101: Docking and molecular dynamics study. *J. Mol. Model.* **15**, 1481–1490 (2009).

194. Meng, L. *et al.* Epoxomicin, a potent and selective proteasome inhibitor, exhibits in vivo antiinflammatory activity. *Proc. Natl. Acad. Sci. U.S.A.* **96**, 10403–10408 (1999).

195. Hansen, M. J., Velema, W. A., Lerch, M. M., Szymanski, W. & Feringa, B. L. Wavelength-selective cleavage of photoprotecting groups: Strategies and applications in dynamic systems. *Chem. Soc. Rev.* **44**, 3358–3377 (2015).

196. Vorobev, A. Y. & Moskalensky, A. E. Long-wavelength photoremovable protecting groups: On the way to in vivo application. *Comput. Struct. Biotechnol. J.* **18**, 27–34 (2020).

197. Klán, P. *et al.* Photoremovable protecting groups in chemistry and biology: Reaction mechanisms and efficacy. *Chem. Rev.* **113**, 119–191 (2013).

198. Il'ichev, Y. V. & Wirz, J. Rearrangements of 2-nitrobenzyl compounds. 1. Potential energy surface of 2-nitrotoluene and its isomers explored with ab initio and density functional theory methods. *J. Phys. Chem. A* **104**, 7856–7870 (2000).

199. Wang, P. Photolabile protecting groups: Structure and reactivity. *Asian J. Org. Chem.* **2**, 452–464 (2013).

200. Il'ichev, Y. V., Schwörer, M. A. & Wirz, J. Photochemical Reaction Mechanisms of 2-Nitrobenzyl Compounds: Methyl Ethers and Caged ATP. *J. Am. Chem. Soc.* **126**, 4581–4595 (2004).

201. Papageorgiou, G. & Corrie, J. E. T. Synthesis and properties of carbamoyl derivatives of photolabile benzoins. *Tetrahedron* **53**, 3917–3932 (1997).

202. Reichmanis, E., Gooden, R., Wilkins, C. W. & Schonhorn, H. STUDY OF THE PHOTOCHEMICAL RESPONSE OF o-NITROBENZYL CHOLATE DERIVATIVES IN P(MMA-MAA) MATRICES. *J. Polym. Sci. A1*. **21**, 1075–1083 (1983).

203. Reichmanis, E., Gooden, R., Wilkins, C. W. & Schonhorn, H. A study of the photochemical response of *o*-nitrobenzyl cholate derivatives in P(MMA-MAA) matrices. *J. Polym. Sci. A1*. **21**, 1075–1083 (1983).

204. Specht, A. & Goeldner, M. 1-(O-Nitrophenyl)-2,2,2-Trifluoroethyl Ether Derivatives As Stable and Efficient Photoremovable Alcohol-Protecting Groups. *Angew. Chemie - Int.*

Ed. **43**, 2008–2012 (2004).

205. Cameron, J. F. & Fréchet, J. M. J. Photogeneration of Organic Bases from O-Nitrobenzyl-Derived Carbamates. *J. Am. Chem. Soc.* **113**, 4303–4313 (1991).

206. Baldwin, J. E., McConnaughie, A. W., Moloney, M. G., Pratt, A. J. & Bo Shin, S. New photolabile phosphate protecting group. *Tetrahedron* **46**, 6879–6884 (1990).

207. Aujard, I. *et al.* O-nitrobenzyl photolabile protecting groups with red-shifted absorption: Syntheses and uncaging cross-sections for one- And two-photon excitation. *Chem. - A Eur. J.* **12**, 6865–6879 (2006).

208. Patchornik, A., Amit, B. & Woodward, R. B. Photosensitive Protecting Groups. *J. Am. Chem. Soc.* **92**, 6333–6335 (1970).

209. Lu, M., Fedoryak, O. D., Moister, B. R. & Dore, T. M. Bhc-diol as a photolabile protecting group for aldehydes and ketones. *Org. Lett.* **5**, 2119–2122 (2003).

210. Hébert, J. & Gravel, D. o-Nitrophenylethylene Glycol: a Photosensitive Protecting Group for Aldehydes and Ketones . *Can. J. Chem.* **52**, 187–189 (1974).

211. Robles, J. L. & Bochet, C. G. Photochemical release of aldehydes from α-acetoxy nitroveratryl ethers. *Org. Lett.* **7**, 3545–3547 (2005).

212. Hansen, M. J. *et al.* Proteasome inhibitors with photocontrolled activity. *ChemBioChem* **16**, 2053–2057 (2015).

213. Blanco, B., Palasis, K. A., Adwal, A., Callen, D. F. & Abell, A. D. Azobenzene-containing photoswitchable proteasome inhibitors with selective activity and cellular toxicity. *Bioorganic Med. Chem.* **25**, 5050–5054 (2017).

214. Shin, D. S. *et al.* Automated maskless photolithography system for peptide microarray synthesis on a chip. *J. Comb. Chem.* **12**, 463–471 (2010).

215. Ma, Y. *et al.* Synthesis and SAR study of novel peptide aldehydes as inhibitors of 20S proteasome. *Molecules* **16**, 7551–7564 (2011).

216. Stanton-Humphreys, M. N. *et al.* Wavelength-orthogonal photolysis of neurotransmitters in vitro. *Chem. Commun.* **48**, 657–659 (2012).

217. Verdoes, M. *et al.* Mixing of peptides and electrophilic traps gives rise to potent, broad-spectrum proteasome inhibitors. *Org. Biomol. Chem.* **5**, 1416–1426 (2007).

218. Kopecky, D. J. & Rychnovsky, S. D. Improved procedure for the reductive acetylation of acyclic esters and a new synthesis of ethers. *J. Org. Chem.* **65**, 191–198 (2000).

219. Krafft, G. A., Cummings, R. T. & Sutton, W. R. Photoactivable Fluorophores. 3. Synthesis and Photoactivation of Fluorogenic Difunctionalized Fluoresceins. *J. Am. Chem. Soc.* **110**, 301–303 (1988).

220. Uhl, E., Wolff, F., Mangal, S., Dube, H. & Zanin, E. Light Controlled Cell-Cycle Arrest and Apoptosis. *Angew. Chemie Int. Ed.* **60**, 1187–1196 (2021).